EPFL

Thèse n°7992

Photoactivatable Silicon Rhodamines for Super-Resolution Microscopy

Présentée le 25 septembre 2020

à la Faculté des sciences de base
Laboratoire d'ingénierie des protéines
Programme doctoral en chimie et génie chimique

pour l'obtention du grade de Docteur ès Sciences

par

Michelle Susanne FREI

Acceptée sur proposition du jury

Prof. B. Fierz, président du jury
Prof. K. Johnsson, directeur de thèse
Dr S. Pitsch , rapporteur
Prof. S. Matile, rapporteur
Prof. P. Rivera Fuentes, rapporteur

École polytechnique fédérale de Lausanne

2020

Acknowledgements

First of all, I would like to thank Professor Kai Johnsson for giving me the opportunity to pursue this PhD and be part of his research group. I immensely enjoyed working on such intriguing projects. He always encouraged me to study things I was interested in and allowed me to take the time to learn new techniques and methods. His guidance allowed me to evolve as an independent scientist and enabled me to design and plan my projects by myself. I really enjoyed the time in the Johnsson lab.

I would like to thank the members of my PhD defence jury committee Professor Pablo Rivera-Fuentes, Professor Stefan Matile, and Dr. Stefan Pitsch as well as the jury president Professor Beat Fierz for taking the time to review this thesis work and all their suggestions and inputs.

During my PhD, I had the pleasure to interact with a number of different research labs in three main places: EPFL, MPI for Medical Research (MPI-MR), and the European Molecular Biology Laboratory (EMBL). The three different places taught me different things and it was especially interesting to be part of the group moving from EPFL to MPI-MR and setting up the lab again from scratch.

Starting at the beginning of my PhD, I would like to thank the LIP family: Aleksandar Salim, Helen Farrants, Silvia Scarabelli, Qiuliyang Yu, Nicolas Goeldel, Yann Pierson, Julien Hiblot, Lin Xue, Shinnosuke Uno, Johannes Broichhagen, Gordon Brown, Ruud Hovius, Luc Reymond, Alberto Schena, and Rudolf Griss for welcoming me to the family. I really enjoyed my time in Lausanne and I will always remember the many brilliant moments we shared, which were usually connected to an apéro. A special thanks goes to Luc Reymond without whom the PA-SiR project would not exist and who introduced me to the most important techniques and instruments in our lab. I admire his creativity and I would have liked to work a little longer on his side to learn even more from him. Thank you for supporting the project also after the move to MPI-MR.

During my time at EPFL, I also found important collaborators outside of the LIP family. Dr. Joël Teuscher (Moser group, EPFL) had the clever idea to use a photography flash to enable some of my early photoactivation experiments and I am thankful for his input. Dr. Christian Sieben (Manley group, EPFL) introduced me to the world of SMLM and explained me so many microscopy mysteries. Without him the start into microscopy would have been a lot more difficult.

With the move to Heidelberg things changed and also people changed. We started a new family that grew even bigger than the LIP ever was. I would like to thank all the members of the CB-family, present and past, for always creating a fun atmosphere in the lab. I am glad we continued the coffee corner tradition from Lausanne and I always enjoy hanging out there discussing world politics over a coffee, beer or a glass of wine. Unfortunately, the family is too numerous to mention everyone by name. Nonetheless, I would like to mention a few key people.

Helen Farrants: for answering all my questions also the nagging ones; for all the walks, hikes, bike rides, and swimming adventures; for all the pep talks, punching bag sessions, and emergency runs or walk; for all the advice, and proof-reading of almost all my written work (I really owe you a lot of Swiss cheese and chocolate); my PhD would have been a lot less fun without her.

Julien Hiblot: for being my source of biochemistry knowledge and working with me on all the exciting HaloTag structures. I highly value his efforts for the whole group and he taught me many things starting from how to plan and execute biochemistry experiments efficiently to the every-day organisation of a lab. I also appreciate all the

discussions we had on how to change the academic system and I hope we will both succeed in making academic science a more open and more collaborative space.

Bettina Mathes and Andrea Bergner: for taking care of instruments and providing me and others with electrocompetent cells, proteins, fluorophores, and really good company. They are the two best technicians I could imaging and without them nothing would run as it does in the CB lab.

A special thanks also goes to the members of office 216 (Aleksandar Salim, Nicole Mertes, Nicolas Lardon and Mai Tran). It was a pleasure to share an office with all of you and I hope we will have a blast in the new wing.

Aleksandar Salim: for being Aleks, for talking through my crazy ideas and for sharing his, for laughing out loud in the middle of the day and distracting me when I was stuck.

Nicole Mertes: for sharing all the silly and stupid moments that happen in a lab and sharing my passion to organise things even though we never organised anything together.

Nicolas Lardon: for all our discussions on fluorophores, microscopy, super-resolution, and most importantly Swiss-German Music. Good luck on continuing the Swiss legacy in fluorophore development in the Johnsson lab.

Judith Notbohm: who was briefly part of office 216 as my research intern, for performing fabulous work on the wavelength extension of PA-SiR. I immensely enjoyed teaching her and working together with her.

Big thanks goes to Nicole Mertes, Helen Farrants, Nicolas Lardon, Magnus Huppertz, Vincent Grenier, Julien Hiblot, Corentin Gondrand, and Birgit Koch for proof-reading this thesis. Thank you for pointing out all my silly spelling mistakes and for all the constructive input.

Outside of our own group, I would like to thank Mirek Tarnawski (BMM, MPI-MR) for all the work regarding the crystal structures, without him this would not have been possible. I would like to thank Jochen Reinstein (BMM, MPI-MR) for help with UV-Vis spectroscopy and his introduction to the MPI-MR. I would like to thank Elisa D'Este (ON, MPI-MR) from the Optical Microscopy Facility for helping me with STED imaging.

Last but not least, I also spent considerable amount of time at EMBL mostly at the Advanced Light Microscopy Facility (ALMF) in the Cherry room. I would like to thank Marko Lampe (ALMF, EMBL) for all the help with the GSDIM. I really enjoyed his endless curiosity and I would wish that I could synthesis all the probes he ever dreamed of. Besides the time at ALMF, I also spent time in the group of Jonas Ries (EMBL) and got to perform exciting experiments with Philipp Hoess (EMBL). I would also like to thank Philipp Hoess for all the discussions on SMLM, the things he taught me about Adobe Illustrator and all the good moments we shared over French cheese and wine.

Outside of the laboratory, I would like to thank the PhD-representatives, Egle Maximowitsch (BMM, MPI-MR), Martin Schröter (CBP, MPI-MR), Marcus Held (ON, MPI-MR), Aleksandar Salim (CB, MPI-MR), and our Postdoc representative Sarah Duponchel (BMM, MPI-MR) for shaping the social and scientific life at MPI-MR together with me. A huge thank you also goes to Lindsey Bultema from the PhDnet who embarked together with me on the adventure of the Mental Health Awareness Week 2019. I would like to thank Ruth Signorell (ETHZ) for being my mentor during the last part of my PhD, I hope I will stay in contact with her beyond this.

I would like to thank the ETH crew: Andri Mani, Barbara Günthardt, Urs Lustenberger, Valentina Gasser und Andreas Gantenbein for exchanging all the wisdom over beers whenever I was in Zurich.

Finally, I would like to thank my parents Franziska and Willi Frei, and my two sisters Stefanie and Simone Frei for all their support throughout all my PhD and even way before that. A special thanks also goes to Deeke Ehmen who always believed in me and without whom I would not finish this PhD.

Lausanne, 17th may 2020

Abstract

Fluorescence microscopy is the method of choice to monitor dynamic processes in living cells due to its non-invasive nature. A variety of different fluorophores and labeling systems are currently used to selectively visualise structures or biomolecules of interest. However, recent progress in the field of fluorescence microscopy towards super-resolution microscopy (SRM) has increased the requirements for fluorophores, as well as labeling strategies. In order to make these techniques available for routine live-cell imaging, brighter, cell-permeable fluorophores and adequate labeling strategies are necessary. This thesis explores methods to improve both fields through developing a new photoactivatable fluorophore, as well as optimising the self-labeling protein tag HaloTag with regard to brightness.

Photoactivatable fluorophores are important tools for single-molecule localisation based SRM as well as tracking experiments. In here, the development of a photoactivatable fluorophore based on silicon rhodamine (SiR) is described. This photoactivatble SiR (PA-SiR) activates via an unprecedented light induced protonation and forms a bright photoproduct. In contrast to other photoactivatable fluorophores, no caging groups are required, nor are there any undesired side-products released. PA-SiRs are environmentally sensitive and therefore allowed to create a HaloTag probe that was not only photoactivatable but also fluorogenic. This leads to high signal-to-background ratios in live-cell microscopy and makes the probe a powerful tool for SRM. Its use in both fixed-cell and live-cell single-molecule localisation microscopy (SMLM) was demonstrated and it became possible to follow the fast dynamics of mitochondria in live cells. Most excitingly, the unlabeled lumen of the mitochondria could be distinguished from their labeled outer membrane, showcasing the power of this probe in combination with SRM.

With most fluorophores HaloTag shows higher fluorogenicity when compared to the self-labeling protein tag SNAP-tag. To characterize the underlying reasons and to identify brighter HaloTag variants, a screening based approach was established to identify amino acid residues that affect fluorogenicity. HaloTag variants harbouring mutations on the surface in close proximity to the rhodamine binding site were found that showed both increased and decreased fluorescence intensities compared to parental HaloTag. Multiple rounds of directed evolution subsequently led to the isolation of a variant that showed increases in fluorescence intensity as high as 300% when combined with several fluorogenic rhodamines *in vitro*. Expression in mammalian cells and analysis by live-cell confocal microscopy revealed similar trends. Mechanistic studies revealed that all the variants that decreased the fluorescence intensity of rhodamine fluorophores did so due to quenching via the introduced tryptophans. In contrast, a clear explanation of how the isolated brighter variants increased fluorescence could not be identified. Regardless, these results highlight that the properties of fluorogenic fluorophores cannot only be tuned by synthetic strategies but also by modifications of the protein surface. It is expected that the identified variants will be beneficial to SRM as well as conventional live-cell microscopy as they both profit from brighter fluorescent probes.

Keywords

Self-labeling protein tags, HaloTag, Fluorogenicity, Photoactivatable fluorophores, Fluorogenic fluorophores, Silicon rhodamine, Live-cell microscopy, Super-resolution microscopy (SRM), Single-molecule localisation microscopy (SMLM)

Résumé

La microscopie de fluorescence est la méthode de choix pour suivre les processus cellulaires dynamiques au sein des cellules vivantes en raison de sa nature non invasive. Une variété de fluorophores et de systèmes de marquage sont actuellement utilisés pour mettre en évidence de manière sélective des structures ou des biomolécules d'intérêt. Cependant, le récent développement de la microscopie à super-résolution (SRM) a augmenté les exigences imposées aux fluorophores et aux stratégies de marquage. Afin de rendre accessible ces techniques pour en routine, le développement de fluorophores plus brillants, perméables aux membranes cellulaires ainsi que de stratégies de marquage adéquates est nécessaire. Cette thèse explore des méthodes en vue d'améliorer ces deux aspects en développant notamment un nouveau fluorophore photoactivable, ainsi qu'en optimisant la luminosité de fluorescence de la protéine d'auto-étiquetage HaloTag.

Les fluorophores photoactivables sont des outils importants pour la SRM basée sur la localisation de molécules uniques ainsi que pour les expériences de traçage. Ici, le développement d'un fluorophore photoactivable à base de silicium rhodamine (SiR) est décrit. Cette SiR photoactivable (PA-SiR) s'active via un mécanisme inédit de protonation induite par la lumière qui génère un photoproduit brillant. Contrairement à d'autres fluorophores photoactivables, aucun groupe cage n'est requis, et aucun produit secondaire indésirable n'est libéré. Les PA-SiRs sont sensibles à l'environnement et ont permis de créer une sonde HaloTag qui était non seulement photoactivable mais également fluorogène. Ces propriétés apportent un rapport signal/signal bruit de fond élevé en microscopie de cellules vivantes faisant de cette sonde un outil puissant pour la SRM. Son utilisation en microscopie de localisation de molécules uniques (SMLM) sur cellules fixées et vivantes a été démontrée. Il est devenu possible de suivre la dynamique rapide des mitochondries en cellules vivantes. De manière notable, le lumen non marqué des mitochondries a pu être distingué de leur membrane externe marquée, mettant en évidence la puissance de cette sonde en combinaison avec la SRM.

En comparaison à la protéine d'auto-étiquetage SNAP-tag, HaloTag présente une fluorogenicity supérieur avec la plupart des fluorophores. Pour en caractériser les raisons sous-jacentes et afin d'identifier des variantes plus brillantes, des variantes de HaloTag ont été criblés pour identifier les acides aminés affectant la fluorogénicité. Des variantes avec des mutations de surface à proximité du site de liaison à la rhodamine présentaient une intensité de fluorescence à la fois augmentée et diminuée par rapport à la protéine parentale. Après plusieurs cycles d'évolution dirigée, une variante présentant jusqu'à 300% d'augmentation de l'intensité de fluorescence *in vitro* fut identifié (combiné avec différents substrats rhodamines fluorogènes). L'étude en cellules de mammifères par microscopie confocale dans des cellules vivantes a confirmé ces tendances. Des investigations mécaniques ont révélé que tous les variantes dont l'intensité de fluorescence diminuait présentaient des mutations de type tryptophane ayant la capacité d'atténuer la fluorescence par ''quenching''. A l'opposé, une explications claire de la façon dont les variantes plus brillantes ont augmenté la fluorescence n'a pas pu être identifiée. Ces résultats mettent néanmoins en évidence que les propriétés des fluorophores fluorogènes peuvent non seulement être ajustées par ingénierie des fluorophores eux-mêmes mais également par ingénierie des protéines cibles. Les variantes identifiées devraient trouver leurs applications en SRM ainsi qu'en microscopie conventionnelle, car toutes deux profitent de l'utilisation de sondes fluorescentes plus brillantes.

Mots-clés

Protéine d'auto-étiquetage, HaloTag, Fluorogénicité, Fluorophores photoactivables, Fluorophores fluorogènes, Silicium rhodamine, Microscopie des cellules vivantes, Microscopie à super-résolution (SRM), Microscopie de localisation de molécules uniques (SMLM)

Zusammenfassung

Die Fluoreszenzmikroskopie ist aufgrund seiner nicht-invasiven Natur die Methode der Wahl, um dynamische Prozesse in lebenden Zellen zu beobachten. Derzeit werden verschiedene Fluorophore und Markierungssysteme verwendet, um Strukturen oder Biomoleküle von Interesse selektiv zu visualisieren. Die jüngsten Fortschritte auf dem Gebiet der Fluoreszenzmikroskopie in Richtung eines höheren Auflösungsvermögens (SRM) haben jedoch die Anforderungen an Fluorophore sowie an verfügbare Markierungssysteme erhöht. Um diese Techniken für die routinemäßige Bildgebung lebender Zellen zu adaptieren, sind hellere, zellpermeable Fluorophore und geeignetere Markierungsstrategien erforderlich. In der vorliegenden Dissertation werden Methoden zur Verbesserung beider Bereiche durch die Entwicklung eines neuen photoaktivierbaren Fluorophors, sowie die Optimierung des selbstmarkierenden Protein-Tags HaloTag im Hinblick auf Hellichkeit untersucht.

Photoaktivierbare Fluorophore sind wichtige Werkzeuge für die auf Einzelmolekül-Lokalisierung basierende hochauflösende Mikroskopie (SRM) sowie für Tracking-Experimente. Hier wird die Entwicklung eines photoaktivierbaren Fluorophors auf Basis von Siliziumrhodamin (SiR) beschrieben. Dieses photoaktivierbare SiR (PA-SiR) wird über eine vorher unbekannte lichtinduzierte Protonierung aktiviert und bildet ein helles Photoprodukt. Im Gegensatz zu anderen photoaktivierbaren Fluorophoren sind weder Käfiggruppen erforderlich, noch werden unerwünschte Nebenprodukte freigesetzt. PA-SiRs werden von ihrer Umgebung beeinflusst; daher wurde es möglich eine HaloTag-Sonde zu kreieren, die nicht nur photoaktivierbar, sondern auch fluorogen ist. Dies führt zu hohen Signal-Hintergrund-Verhältnissen in der Lebendzellmikroskopie und macht die Sonde zu einem leistungsstarken Werkzeug für die SRM. Seine Anwendung in der Einzelmolekül-Lokalisationsmikroskopie (SMLM) von fixierten und lebenden Zellen konnte gezeigt werden. Zudem war es mit diesem Fluorophor möglich, schnelle Dynamiken von Mitochondrien in lebenden Zellen zu verfolgen. Ausserdem konnte das nicht markierte Lumen der Mitochondrien von der markierten Aussenmembran unterschieden werden, was die Leistungsfähigkeit dieser Sonde in Kombination mit SRM demonstriert.

Im Vergleich zu dem selbstmarkierenden Protein-Tag SNAP-Tag, zeigt HaloTag mit vielen Fluorophoren eine erhöhte Fluorogenizität. Um die zugrundeliegenden Ursachen zu charakterisieren und hellere HaloTag Varianten zu generieren, wurde ein Screening-basierter Ansatz etabliert, der erlaubt Aminosäurereste zu identifizieren, die die Fluorogenizität beeinflussen. Es wurden HaloTag Varianten gefunden, die Mutationen auf der Oberfläche des HaloTags in unmittelbarer Nähe der Rhodamin-Bindungsstelle aufweisen und sowohl erhöhte als auch verringerte Fluoreszenzintensität im Vergleich zum parentalen HaloTag zeigten. Mehrere Runden gerichteter Evolution führten daraufhin zur Isolierung einer Variante, die in Kombination mit mehreren fluorogenen Rhodaminen *in vitro* einen Anstieg der Fluoreszenzintensität um bis zu 300% zeigte. Die Expression in Säugetierzellen und die Analyse durch konfokale Mikroskopie lebender Zellen zeigten ähnliche Trends. Mechanistische Analysen zeigten, dass alle Varianten, die die Fluoreszenzintensität von Rhodaminen verringerten, dies aufgrund der eingeführten Tryptophane durch ''Quenchen'' taten. Im Gegensatz dazu konnte keine klare Erklärung gefunden werden, wie die helleren Varianten die Fluoreszenz erhöhen. Unabhängig davon zeigen diese Ergebnisse, dass die Eigenschaften fluorogener Fluorophore nicht nur durch Synthesestrategien, sondern auch durch Modifikationen an der Proteinoberfläche justiert werden können. Es wird erwartet, dass die identifizierten Varianten sowohl für die SRM als auch für die konventionelle Mikroskopie lebender Zellen von grossem Vorteil sind, da beide von helleren fluoreszierenden Sonden profitieren.

Schlüsselwörter

Selbstmarkierende Protein-Tags, HaloTag, Fluorogenität, Photoaktivierbare Fluorophore, Fluorogene Fluorophore, Silizium-Rhodamin, Lebendzellmikroskopie, Hochauflösende Mikroskopie (SRM), Einzelmolekül-Lokalisationsmikroskopie (SMLM)

Abbreviations

°C	degree Celsius
β-2-AR	β-adrenergic receptor 2
ϕ	quantum yield
ε	extinction coefficient
µ	micro
λ	wavelength
A	absorbance
abs	absorbance
ACN	acetonitrile
BG	O^6-benzylguanine
BODIPY	boron dipyrromethenes
BSA	bovine serum albumin
c	centi
CA	chloroalkane
CP	benzylchloropyrimidine
CPY	carbopyronine
D_{50}	dielectric constant at which half the molecules are in their closed form
DAPI	4',6-diamidino-2-phenylindole
DMSO	dimethyl sulfoxide
DNA	desoxyribonucleic acid
dSTORM	direct stochastic optical reconstruction microscopy
EC_{50}	effective concentration at half maximal value
EGFP	enhanced green fluorescent protein
EGS	ethyleneglycol-bis-succinimidyl-succinate
em	emission
EPR	electron paramagnetic resonance
ER	endoplasmic reticulum
EWG	electron withdrawing group
ex	excitation
FP(s)	fluorescent protein(s)
g	gram(s)
GFP	green fluorescent protein
GSH	glutathione
h	hour(s)
HOMO	highest occupied molecular orbital
I	intensity
^{i}Pr	*iso*-propyl

k	rate constant
kW	killowatts(s)
LC-MS	liquid chromatography coupled to mass spectrometry
LUMO	lowest unoccupied molecular orbital
M	molarity
m	milli/meter(s)
max	maximum
MHz	megahertz(s)
min	minute(s)
N	number of repeats
NBS	*N*-bromosuccinimid
n	nano
NMR	nuclear magnetic resonance
NPC	nuclear pore complex
Nuc	nucleophile
PA	photoactivatble
PA-FP	photoactivatable fluorescent protein
PA-SiR	photoactivatable silicon rhodamine
PAINT	point accumulation for imaging in nanoscale tomography
PBS	phosphate buffered saline
PC	photochromic
PEG	polyethylene glycol
POI	protein of interest
ppm	parts per million
PS	photoswitching
PSF	point spread function
rt	room temperature
S	singlet state
s	second(s)
SiR	silicon rhodamine
SMLM	single-molecule localisation microscopy
SRM	super-resolution microscopy
STED	stimulated emission depletion fluorescence microscopy
T	triplet state
TICT	twisted intramolecular charge transfer
TIRF	total internal reflection microscopy
TMR	tetra-methyl rhodamine
TSTU	*N*,*N*,*N*',*N*'-tetramethyl-*O*-(*N*-succinimidyl)uroniumtetrafluorborat
$t_{1/2}$	half-life
t_R	retention time
UV	ultraviolet
UV-Vis	ultraviolet-visible
VR	vibrational relaxation

Contents

Acknowledgements ..... **i**

Abstract **3**

Keywords **3**

Résumé **5**

Mots-clés **6**

Zusammenfassung **7**

Schlüsselwörter **8**

Abbreviations **9**

List of Figures **15**

List of Tables **17**

Chapter 1 Introduction **1**

1.1 Fluorescence and photophysics 1

1.2 Fluorescence microscopy 2

1.2.1 SMLM 3

1.2.2 STED 5

1.2.3 Live-cell microscopy 6

1.3 Labeling strategies for live cells 7

1.3.1 Self-labeling protein tags 7

1.3.2 Targeting ligands 8

1.4 Small-molecule fluorophores 8

1.4.1 Rhodamines 9

1.4.2 Silicon rhodamines (SiR) 9

1.5 Tuning of small-molecule fluorophore properties 10

1.5.1 Fluorogenicity and cell permeability 10

1.5.2 Spectral properties 11

1.5.3 Photon budget: brightness and photostability 12

1.5.4 Switching mechanisms 13

1.6 Previous work 15
1.6.1 Photoactivatable silicon rhodamine 15
1.6.2 Related compounds and reactions of PA-SiR 15
1.7 Scope of this thesis 16
1.7.1 PA-SiR 16
1.7.2 Exploring the fluorogenicity of HaloTag 17
Chapter 2 PA-SiR 19
2.1 Synthesis of PA-SiRs 19
2.2 Extension to other wavelengths 21
2.3 Characterisation of PA-SiR 23
2.3.1 Computational analysis 26
2.4 Equilibrium investigation by UV-Vis 27
2.4.1 Light dependence of the PA-SiR equilibrium system 27
2.4.2 pH dependence of the PA-SiR equilibrium system 29
2.4.3 Influence of solvent polarity on the PA-SiR equilibrium system 29
2.4.4 Influence of cysteamine on the PA-SiR equilibrium system 29
2.4.5 PA-SiR analogues 30
2.5 Probe synthesis and characterisation 31
2.5.1 UV-Vis characterisation 32
2.5.2 Influence of cysteamine on the equilibrium system of HaloTag probes 35
2.6 Widefield and confocal live-cell microscopy 35
2.6.1 Transfection free probes 39
2.7 *In vitro* single-molecule experiments 40
2.8 SMLM and single-particle tracking of PA-SiR probes 43
2.8.1 Fixed-cell SMLM of PA-SiR probes 43
2.8.2 Fixed-cell SMLM of transfection-free PA-SiR probes 44
2.8.3 Live-cell single particle tracking using PA-SiR-CA 45
2.8.4 Live-cell SMLM of PA-SiR-CA 46
2.9 STED 47
2.10 Conclusion and Outlook 48
Chapter 3 HaloTag's interaction with fluorogenic fluorophores 51
3.1 Screening of focused libraries of HaloTag in combination with SiR-CA 51
3.2 Characterisation of HaloTag variants 53
3.2.1 Labeling kinetic studies of HaloTag variants 53
3.2.2 Fluorophore screen 54

3.2.3 Quantum yields 55
3.2.4 Structural analysis 57
3.3 Mammalian cell assay 58
3.3.1 Live-cell confocal microscopy 59
3.4 Conclusion and Outlook 59
Chapter 4 Conclusion 61
Chapter 5 Materials and methods 63
5.1 Materials and general information for chemical synthesis 63
5.2 Materials and general information for *in vitro* and *in cellulo* experiments for Chapter 2 93
5.3 Materials and general information for *in vitro* and *in cellulo* experiments for Chapter 3 99
References 105
Curriculum Vitae 119
Chapter 6 Appendix 121
6.1 Supplementary figures 121
6.2 Supplementary tables 134
6.3 Supplementary equations 150
6.4 Supplementary NMR spectra 151

List of Figures

Figure 1: Jabłoński diagram and other diagrams relevant to photophysics. 2
Figure 2: Concepts of SRM. 5
Figure 3: Mechanism of the reaction of self-labeling protein tags with their substrates. 7
Figure 4: Structures of several targeting ligands specifically binding to F-actin (jasplakinolide **6**), microtubules (docetaxel **7**), DNA (bisbenzimide **8**), lysosomes (pepstatin A **9**), and the ER (gilbenclamide **10**). 8
Figure 5: Structures of several rhodamine analogues. 9
Figure 6: Fluorogenicity and cell permeability. 10
Figure 7: Spectral properties of rhodamine analogues substituted at X. 12
Figure 8: Structures of four rhodamine fluorophores with increased brightness and or photostability. 13
Figure 9: Different mechanisms to switch fluorophores between an emissive and a non-emissive state. 14
Figure 10: Equilibrium system and structure of PA-SiR. 15
Figure 11: Relevant structures and reactions for the PA-SiR equilibrium. 16
Figure 12: Synthesis of PA-SiR and its derivatives. 20
Figure 13: All successfully isolated PA-SiR derivatives. 21
Figure 14: Synthetic strategies to access PA-SiRs with different colours. 22
Figure 15: Characterisation of PA-SiR **41**. 24
Figure 16: ^{1}H NMR analysis of the PA-SiR equilibrium. 25
Figure 17: Possible photoactivation mechanism and calculations of HOMO and LUMO. 26
Figure 18: Simplified equilibrium system of PA-SiR as used for the UV-Vis analysis. 27
Figure 19: Influence of light and pH on the equilibrium system of PA-SiR **41**. 28
Figure 20: Influence of different environmental factors such as solvents and nucleophiles on the equilibrium system. 30
Figure 21: Photoactivation measurements of different PA-SiR analogues. 31
Figure 22: Synthetic route and structures of PA-SiR probes. 32
Figure 23: UV-Vis characterisation of different probes. 34
Figure 24: Reaction with cysteamine of PA-SiR analogues after photoactivation. 35
Figure 25: Live-cell microscopy images of PA-SiR probes in combination with self-labeling protein tags. 37
Figure 26: Quantification of live-cell microscopy. 38
Figure 27: Confocal microscopy images of HeLa and U-2 OS cells stained with several different transfection free probes. 39
Figure 28: Single-molecule assay. 42

Figure 29: Fixed-cell SMLM visualizing microtubules. 44
Figure 30: Super-resolved SMLM images. 45
Figure 31: Single-particle tracking experiments and their quantification. 46
Figure 32: Live-cell SMLM of mitochondria. 47
Figure 33: Live-cell confocal and STED images of vimentin-Halo. 48
Figure 34: Crystal structure of HaloTag bound to TMR-CA. 52
Figure 35: Screening of HaloTag variants with different fluorophores. 55
Figure 36: Crystal structures of HaloTag and Q165H-P174R reacted with TMR-CA. 57
Figure 37: Ratios of SiR and EGFP intensity in mammalian cells for ten HaloTag variants. .59

List of Tables

Table 1: All synthesised and tested PA-SiR probes. 33

Table 2: Kinetic characterisation of the brightest and dimmest HaloTag variants. 54

Table 3: Quantum yields of the brightest and dimmest HaloTag variants. 56

Table 4: Structural parameters measured in the preliminary X-ray crystal structures and from the calculated structures for TMR in water. 58

Chapter 1 Introduction

Light microscopy is an indispensable tool in biology and medicine, and has contributed enormously to our understanding of cell biology. Due to the non-invasive nature of light, optical microscopy techniques are compatible with live-cell experiments, making them the method of choice to monitor dynamic processes inside of cells. However, images only obtained through the interaction of light with a specimen are rarely sufficient to study cellular structures and processes in detail, due to poor contrast. This is why specific staining procedures and dye molecules have become of utmost importance. Starting from the use in histology over immunohistochemistry to the most advanced fluorophores and labeling strategies, both dye molecules and staining/labeling strategies have been developed in concordance with advances in optical microscopy.[1,2] Especially fluorescence microscopy has become increasingly popular over the years, aided by the discovery and the cloning of green fluorescent protein (GFP). Fluorescent proteins (FPs) enabled labelling of cellular proteins with high selectivity and to perform live-cell experiments with unprecedented ease.[3,4]

However, recent progress in the field of fluorescence microscopy has increased the requirements for fluorophores. Brighter, more photostable and far-red fluorophores are desired. This has shifted the focus from FPs back to small-molecule fluorophores, which were used during the early days of fluorescence microscopy.[5] In addition, it has spurred both the development of more specialised small-molecule fluorophores as well as clever labeling strategies compatible with living cells. Only the combination of the two allows us to use the newest microscopy techniques in a biological context to their full potential. The presented work contributes to both fields. First, a new type of photoactivatable fluorophore was developed and successfully applied in live-cell super-resolution microscopy (SRM). Secondly, a currently available labeling system was optimised with regard to fluorescence intensity, opening up new avenues to tune the properties of fluorogenic fluorophores. In the following, the fundamental principles of the most advanced fluorescence microscopy techniques, as well as labeling strategies and fluorophore scaffolds relevant to this work are outlined.

1.1 Fluorescence and photophysics

Fluorescence, an interaction between light and matter, is the process of spontaneous light emission upon excitation with light (F). It is described in the Jabłoński diagram (Figure 1A).[6–8] First, a molecule absorbs light (A) from the visible or ultraviolet (UV) part of the spectrum and is excited from the ground state (S_0) to a singlet excited state (S_1, S_2, etc.; Figure 1A, C). The wavelength absorbed (λ) is dictated by the molecule's electronic structure and its energy levels. The strength of the transition is described by the extinction coefficient (ε_λ). Both the absorbance maximum (λ_{max}) and the extinction coefficient at λ_{max} ($\varepsilon_{\lambda max}$) are used to characterise fluorophores and can be read out from an absorbance spectrum (Figure 1B). Upon excitation, the molecule rapidly decays to the lowest vibrational level of S_1 through loss of energy via vibrational relaxation (VR) and/or internal conversion (IC). This is followed by the emission of a photon (fluorescence, F) and the return of the molecule to the ground state. The emission wavelength is red-shifted compared to the absorbed wavelength due to the energy loss during VR. This shift is called Stokes shift after G. G. Stokes.[9] The efficiency of fluorescence is characterised by its quantum yield (ϕ) defined as the number of emitted photons divided by the number of absorbed photons. The ideal quantum yield is one. The product of ϕ and $\varepsilon_{\lambda max}$ is referred to as the brightness of a fluorophore and together with the photostability these parameters define the photon budget, corresponding to the overall number of emitted photons. However, the number of emitted photons is often reduced through a variety of competing photophysical processes.[10]

There are several photophysical processes that lead to diminished quantum yields. For example, molecules in the first excited singlet state can dissipate their energy via non-radiative transitions such as vibrational relaxations with the surrounding solvent, during which energy is released as heat. Alternatively, they can undergo inter system crossing (ISC) to a long-lived triplet state (T_1), which can undergo vibrational relaxation or phosphorescence (P) by the emission of a photon. All these secondary processes make a fluorophore less suitable for fluorescence microscopy. In addition, the generation of triplet states together with the population of higher excited singlet states (S_2, S_3, etc.) can lead to photobleaching of fluorophores reducing their photostability (Section 1.5.3). Molecules in these states are highly reactive and readily react with surrounding molecules or degrade through cleavage of covalent bonds. Nevertheless, several of these processes were exploited to elicit blinking in otherwise non-blinking fluorophores (Section 1.5.4).[11]

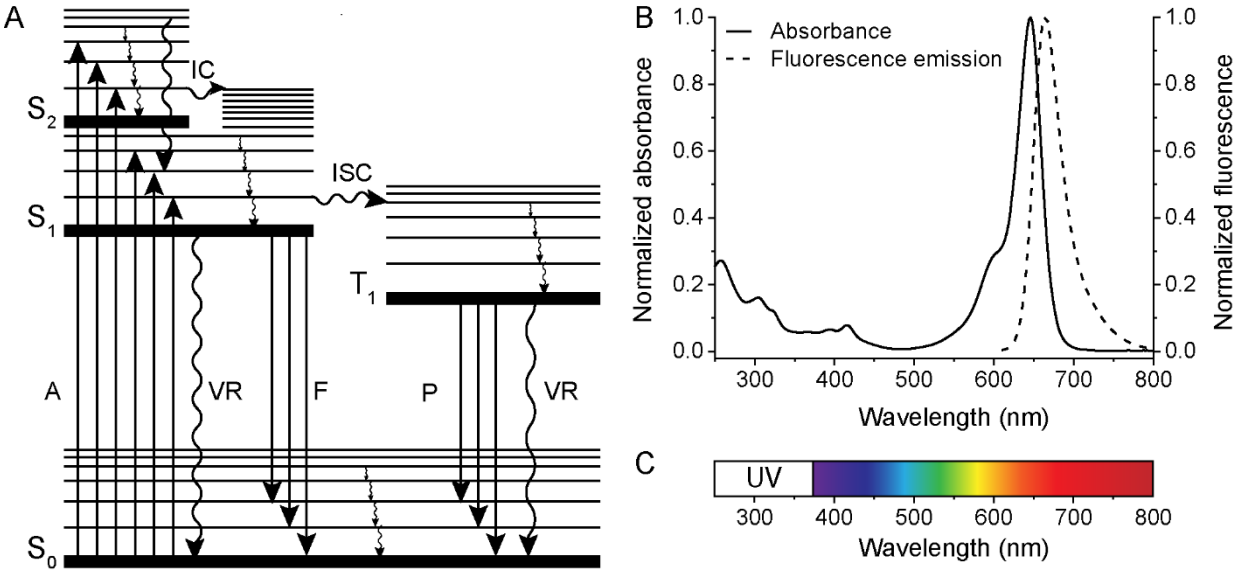

Figure 1: Jabłoński diagram and other diagrams relevant to photophysics. (A) Jabłoński diagram showing the most important radiative and non-radiative transitions between the electronic ground state (S_0) the singlet excited states ($S_1$and S_2) as well as the triplet excited state (T_1). Straight arrows correspond to radiative transitions whereas curly arrows to non-radiative transitions, which do not involve the absorbance or emission of a photon. A = absorbance, VR = vibrational relaxation, F = fluorescence, P = phosphorescence, IC = internal conversion, ISC = intersystem crossing. (B) Representative absorbance and fluorescence spectra. (C) Spectrum of light including the UV and visible range.

1.2 Fluorescence microscopy

Fluorescence microscopy makes use of intrinsic or extrinsic fluorophores probing their location through their fluorescence emission upon excitation. Due to the Stokes shift, emission and excitation light can be separated using optical elements such as filters and dichroic mirrors. The emitted light is then detected selectively, while the excitation light is filtered out. Type of illumination and detection vary from technique to technique. In widefield microscopy, the entire specimen is irradiated and the resulting fluorescence collected and read out by a camera from the same side as the excitation light (epi-illumination). Scanning confocal fluorescence microscopy, on the other hand, focuses the irradiation onto a single point and scans this point over the specimen. Fluorescence is read out with a single detector and out of focus light can be cut-off using a pinhole, allowing for optical sectioning and improvements in resolution. This is especially true for the z-direction, in comparison to widefield microscopy.[12] However, resolution in light microscopy is inherently limited to about 200 nm, due to the diffraction limit of light, as discovered by Ernst Abbe in 1873.[13] This is unfortunate as many biological structures have dimensions between 10 – 100 nm (e.g. nuclear pores, clathrin coated pits, protein complexes etc.) and are therefore not resolved by conventional fluorescence microscopy. Hence, breaking the diffraction limit had been a holy grail for many years. It was not until the first SRM techniques emerged in the 1990s and 2000s that the diffraction limit was broken.[14] The two first established methods both rely on the switching of fluorophores between an emissive (‘on’) and a non-emissive (‘off’) state to obtain a super-resolved image.[15] However, the strategies through which they achieve these distinguishable states differ. In the

following two sections, the concepts of the two methods single-molecule localisation microscopy (SMLM) and stimulated emission depletion (STED) microscopy as well as recent advances in these fields are summarised.

1.2.1 SMLM

The basis for SMLM was laid in 1989 with the first optical detection of a single molecule by W. E. Moerner and L. Kador.[16] Six years later, in 1995, E. Betzig proposed how to achieve molecular resolution through the separation of molecules in higher dimensional space.[17] However, only when the first photoactivatable fluorescent protein PA-GFP was developed,[18] it became possible to separate fluorescence emission in time. In 2006, four independent groups reported for the first time SRM based on the detection of single-molecules.[19–22] In the coming years many techniques using the same fundamental concept were reported, each bearing a different acronym (e.g. photoactivated light microscopy (PALM),[19] stochastic optical reconstruction microscopy (STORM),[21] point accumulation for imaging in nanoscale tomography (PAINT),[22] or ground-state depletion with individual molecule return (GSDIM))[23] to name just a few. Within this work, all of them will be abbreviated by SMLM.

In SMLM super-resolution images are acquired through repeated imaging of temporally separated single molecules. More specifically, at a certain time point only a sparse sub-set of molecules is in the fluorescent form and allows for precise localisation through fitting with a suitable model function (e.g. Gaussian function). Fitting of the measured photon distribution makes it possible to determine the most likely position of the single emitter well below the diffraction limit. Over time, different sub-sets of fluorophores are fluorescent and it becomes possible to combine the localisations gathered in each frame into a final super-resolved image (Figure 2A). The spatial resolution obtained is related to the localisation precision of a single molecule, which scales with the inverse square root of the number of detected photons.[24] Additionally, the fraction of time a fluorophore spends in the “on” state versus the “off” state defined as the duty cycle (“on”/”off”) plays a crucial role for the attainable spatial resolution and acquisition time.[25] The attainable spatial resolution is moreover connected to the labeling density via the Nyquist-Shannon sampling theorem, which states that at least two fluorophores need to be localised within the smallest distance of resolution.[15,26] Altogether, these criteria restrict the pool of suitable fluorophores and labeling strategies. An ideal fluorophore should be able to switch between an ‘off’ and an ‘on’ state with high on–off contrast ratio, show a high photon budget, corresponding to the overall number of emitted photons, and have a low duty cycle.[27] Switching a fluorophore between an ‘off’ and an ‘on’ state is most often achieved through photocontrollable fluorophores, albeit other principles are also harnessed (Section 1.5.4). In general, three different categories of fluorophores are used in SMLM: FPs, small-molecule fluorophores or quantum dots. Due to the limited applicability of quantum dots in live cells, they will not be further discussed here. Excellent reviews can be found elsewhere.[27]

A variety of different photocontrollable FPs with different spectral properties are available. In general, these photocontrollable FPs belong to one of three classes: photoactivatable (PA), photoconvertible (PC, wavelength-shifting) and photoswichable (PS) FPs. PA-FPs and PC-FPs are activated or converted through irradiation with violet-blue light, localised and then irreversibly photobleached by the excitation laser. The density of activated FPs is controlled by tuning the intensity of the activation laser such that the activated FPs are well separated in space, which allows for precise localisation. PS-FPs can be reversibly switched between two spectral states using two different wavelengths and the density of emitters can be controlled through adjustments of the two laser intensities.[28,29] Photocontrollable FPs often show low duty cycles, which is necessary for good temporal separation.[27] Due to their genetic encodability, which is specific and highly efficient, FPs have been extensively used in SMLM especially in live-cell experiments.[24,29] Three main points should be kept in mind when choosing a FP for SMLM. First, a major concern of their use has been their tendency to dimerise or form higher state oligomers, which could lead to localisation artifacts. Many monomeric versions were therefore developed by the introduction of mutations at the dimer interface. Second, the maturation time of the chromophore needs to be taken into account. FPs with long maturation times can lead to reduced effective labeling densities due to incompletely matured and hence non-fluorescent proteins. [28–30] Third, FPs are generally dimmer and have a lower photon budget than small-molecule fluorophores,

which limits the achievable localisation precision and therefore resolution.[27] Consequently much attention has been drawn to small-molecule fluorophores over the last years.

Photoactivatable or photoswitchable small-molecule fluorophores are known throughout many different classes of fluorophores and can be used analogously to PA-FPs or PS-FPs.[31] Photoactivation often relies on photocleavable protecting groups (caging groups) that render the fluorophores non-fluorescent but can be removed irreversibly through light irradiation. Photoswitchable, often also referred to as photochromic, small-molecule fluorophores exist in an equilibrium between two distinct spectral states, which can be modulated by light of different wavelength.[27] More recently, spontaneously blinking fluorophores were reported, which switch between two equilibrium forms without the need for light irradiation.[32–36] In addition, many conventional (non PA or PS) small-molecule fluorophores were made available through the concept of direct stochastic optical reconstruction microscopy (dSTORM), where blinking behaviour was induced by intense illumination of the sample creating long lived dark states.[23,37–40] It was also found that this photophysical blinking can be influenced by using additives such as thiols, copper,[41,42] or oxygen scavenging systems.[11] Over time sophisticated imaging cocktails were developed to favour suitable blinking kinetics for different classes of fluorophores.[27] Clearly not all additives or the intense irradiation are compatible with live-cell imaging and this is why the class of spontaneously blinking fluorophores is a very promising step into a new direction. The four principles presented (PA, PS, spontaneously blinking, and photophysical blinking) will be further discussed and exemplified on the class of rhodamine fluorophores (Section 1.5.4).

Over the past 15 years several major advances were made in the field of SMLM technology. First, multichannel measurements were made possible through different approaches. Two or even three spectrally well-resolved fluorophores can be imaged in separate channels. The associated challenges lie in finding suitable fluorophore pairs that show optimal single-molecule behaviour in the same buffer condition. In addition, chromatic aberrations for the different channels have to be corrected for.[43] In order to circumvent chromatic aberrations, fluorophores with similar excitation spectra but distinguishable emission spectra can be imaged by the same excitation laser. Their identity is then revealed though spectral imaging.[44–50] Exactly the same fluorophore can also be imaged either in combination with multiple activating fluorophores in different spectral ranges,[51] or sequentially over time bound to different targets. The latter was made more readily available through exchange-PAINT, where oligonucleotides are used to selectively but reversibly label different targets with the same fluorophore.[52]

The second major advance in the field of SMLM was its expansion to 3D measurements. The most commonly used implementation encodes z information in the point spread function (PSF). This can be realised using a cylindrical lens that creates elliptic images (astigmatism). The z position can be read out from the ellipticity of the single-molecule.[53] Similarly, a helical PSF was used to modulate the emitted light such that the image of a single molecule shows two lobes and the angle between them encodes the z information.[54] Alternatively, biplane detection of defocused molecules[55] or interferometry can be used.[56,57]

In addition to multi-channel and 3D imaging, a major advancement has been the development of several different software packages to detect and localise single molecules. A quantitative comparison between the different 2D methods was performed in 2013.[58] A newer 3D SMLM challenge was concluded in 2016, but both the 2D and 3D challenge remain open and the newest information can be found on the webpage of the SMLM challenge.[59]

Finally, SMLM was combined with a variety of different microscopy techniques such as single-particle tracking,[60] light sheet microscopy,[61] or in correlative approaches with other microscopy techniques most prominently electron microscopy.[62] However, further description is beyond this thesis and the reader is referred to the indicated reviews.

Despite extensive development of SMLM and the associated techniques and tools, it still exhibits limitations. The resolution improvement is dictated by the photon budget of the fluorophores and the background signal. Hence, only ideal samples allow to obtain resolutions in the single digit nanometer range. In addition, SMLM inherently trades spatial resolution for temporal resolution, and therefore makes dynamic measurements challenging. The often required high light intensities further impose challenges to live-cell microscopy experiments (Section 1.2.3).

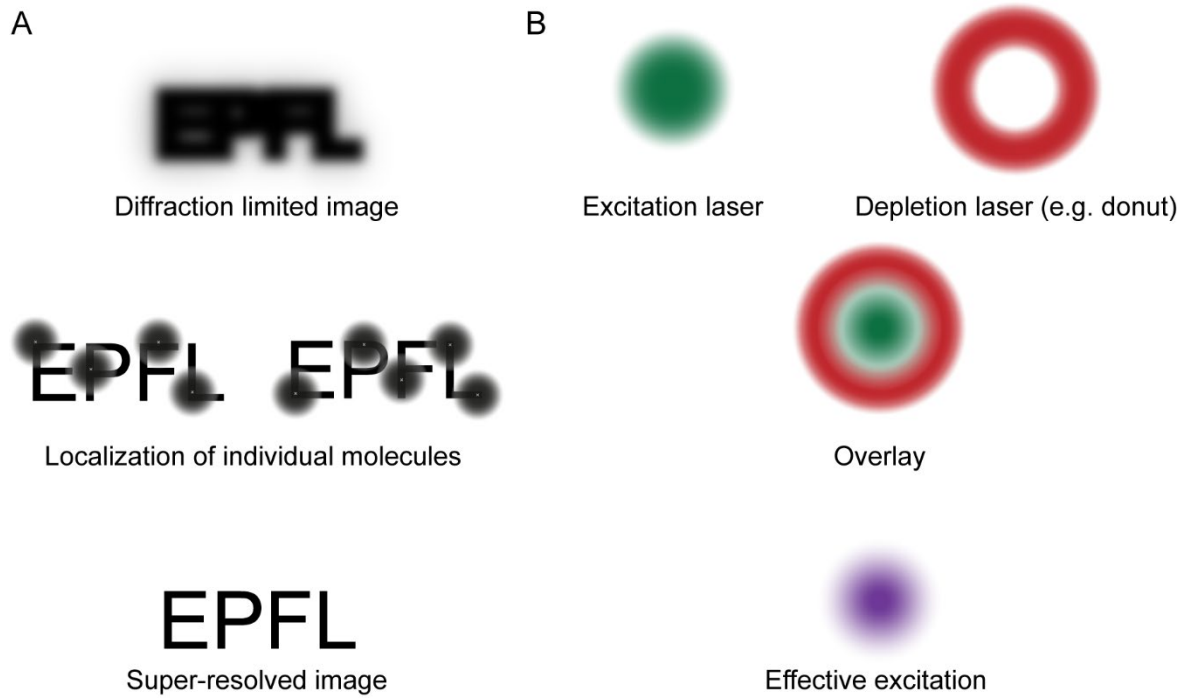

Figure 2: Concepts of SRM. (A) In SMLM, individual molecules, from an otherwise diffraction limited image, are separated in time and localised with high precision. A super-resolved image is then reconstructed from multiple frames each with a different set of emitting fluorophores. (B) STED microscopy uses a second depletion laser to decrease the effective excitation spot in size and hence increases the resolution.

1.2.2 STED

STED fluorescence microscopy was proposed in 1994 by Hell and Wichmann[14] and experimentally demonstrated five years later by Klar and Hell.[63] STED is based on scanning confocal microscopy and uses an additional 'depletion' laser to switch fluorophores between two distinguishable photophysical states. More specifically, fluorophores in the outer region of the excitation volume undergo stimulated emission, induced by the donut shaped spot of the depletion laser ($S_1 \rightarrow S_0$). This reduces the size of the effective excitation volume below the diffraction limit (Figure 2B).[64–66] The wavelength of the depletion laser needs to be well matched to the stimulated emission transition, which is usually red-shifted compared to the excitation and emission. The excitation and depletion lasers are then simultaneously scanned over the specimen and a super-resolved image is obtained. Due to the high intensity of especially the depletion laser, fluorophores for STED imaging must show high brightness (extinction coefficient and quantum yield) as well as high photostability. In addition, fluorophores that are not excited by the depletion laser (re-excitation) or do not undergo excitation into higher excited states (S_n or T_n) are preferable. Re-excitation decreases the efficiency of depletion and therefore limits the attainable resolution. Population of higher excited states contribute to photobleaching and therefore diminishes the signal obtained from the sample. In general, small-molecule fluorophores are better suited for STED than the less bright and less photostable FPs.[66,67]

STED microscopy enables multicolour and 3D measurements. Multicolour implementations of STED most often rely on a single depletion laser even though the use of two depletion lasers is also possible.[68,69] However, this requires the alignment of the two depletion lasers with nanometer precision. One depletion laser on the other hand guarantees intrinsic alignment.[70] Fluorophores are either distinguished through their excitation as with long-stokes shift fluorophores,[71] through their emission in spectrally distinct fluorophores or both excitation and emission.[72–74] Similarly to strategies used for SMLM, other photophysical parameters such as fluorescence lifetime[70] or photochromism[75] can be used to distinguish spectrally similar fluorophores. In addition, the concept of sequential imaging using labeled oligonucleotides can be used for STED.[76] 3D implementations of STED generally use face masks to create a depletion beam that has a local zero not only in two but in three dimensions.[66,77]

STED was combined with fluorescence correlation spectroscopy used to study dynamics of fluorescent species and efficiently decreases the detection volume allowing to investigate these dynamics at higher resolutions. [66,67,78] Analogously to SMLM, STED has been combined with several other microscopy methods including electron microscopy for correlative approaches.[62]

Nevertheless, also STED exhibits several limitations. The resolution in STED is theoretically only limited by the intensity of the depletion laser. However, practically resolution is limited by the photostability of the fluorophore and hence once more by its photon budget. STED also experiences similar challenges as SMLM when combined with live-cell measurements and phototoxicity is a concern (Section 1.2.3).

1.2.3 Live-cell microscopy

Live-cell imaging aims at elucidating structural features and observing dynamic processes within living cells and has become more and more important as scientists move away from fixed-cell experiments. Fixation and immunolabeling run the risk to introduce artefacts and to destroy ultra structures.[79] Due to these limitations of fixed samples, there is an increasing need to combine SRM with live-cell measurements.[80,81] However, SRM imposes several challenges on live-cell imaging.

First, the increased illumination intensities used to control the density of the activated fluorophores in SMLM or to deplete fluorophores in STED can have phototoxic effects on live cells.[80,81] Studies showed that especially shorter wavelengths can have detrimental effects on live cells.[82] Especially the intensities of the 405 nm laser used to control photoactivation in SMLM should be limited, making it difficult to control the emitter densities appropriately. Similarly, far-red wavelengths are preferred in STED imaging.[83] In the case of SMLM the commonly used additives need to be carefully chosen such that they do not harm the cells or interfere with the processes of interest.[31]

Second, live-cell microscopy relies on a sufficiently fast acquisition rate in order to resolve dynamic processes. However, the gain in spatial resolution in SRM is usually connected to a loss in temporal resolution as super-resolution images are made up of several hundreds to thousands of frames (for SMLM) and of several thousand scanning points (for STED). In order to obtain highly precise localisations in SMLM, enough photons need to be collected from every single fluorophore. However, photon emission rates are inherently limited, and therefore the speed at which a single frame with sufficient signal for localisation can be acquired. In addition, the fluorophores need to be well separated in time, increasing the number of frames that need to be acquired to reconstruct one image and further putting time constraints on dynamic measurements. Similarly, in STED scanning speeds need to be adjusted such that sufficient signal can be obtained from the sample but once more, this is inherently limited by the photon emission rate of a fluorophore.

All three points, spatial resolution, temporal resolution and phototoxicity are connected. Increasing one of them usually leads to decreases in another area. Efforts are currently focused on overcoming these challenges. In SMLM for instance, efforts have been raised to improve high density analysis methods and optimisation in microscopic systems have already lead to an improved time resolution.[80,84] However, the main focus still remains on improving the signal-to-noise ratio by either decreasing the noise level of the detector or by increasing the photon budget of the fluorophores.[81] Photon budget including fluorophore brightness and photostability are also points of active research to improve fluorophores for STED imaging.[85] In addition, a third SRM technique called MINFLUX was introduced in 2017.[86] MINFLUX probes the position of single-molecules through the absence of fluorescence and therefore requires substantially less photons, making it ideal for live-cell microscopy.[87] MINFLUX requires switchable fluorophores, whose switching behaviour can be tightly regulated and which show very low background levels.[86–88] Further discussion of this very exciting new technology is beyond the scope of this thesis.

1.3 Labeling strategies for live cells

Live-cell imaging requires different labeling strategies than fixed-cell applications as many conventionally used small-molecule fluorophores, as well as antibodies, are not cell permeable. FPs on the other hand do not exhibit this problem as they can be genetically encoded and expressed in live cells. This is why they have been the method of choice for live-cell imaging for many years and also found applications in SRM.[24] For labeling with small-molecule fluorophores, which are often preferred in SRM, several different strategies were established over the last two decades. However, not all of them show the necessary specificity and selectivity to label intracellular structures. In this section, two such strategies will be discussed, self-labeling protein tags and targeting ligands, excellent reviews on further labeling strategies can be found elsewhere.[89–95]

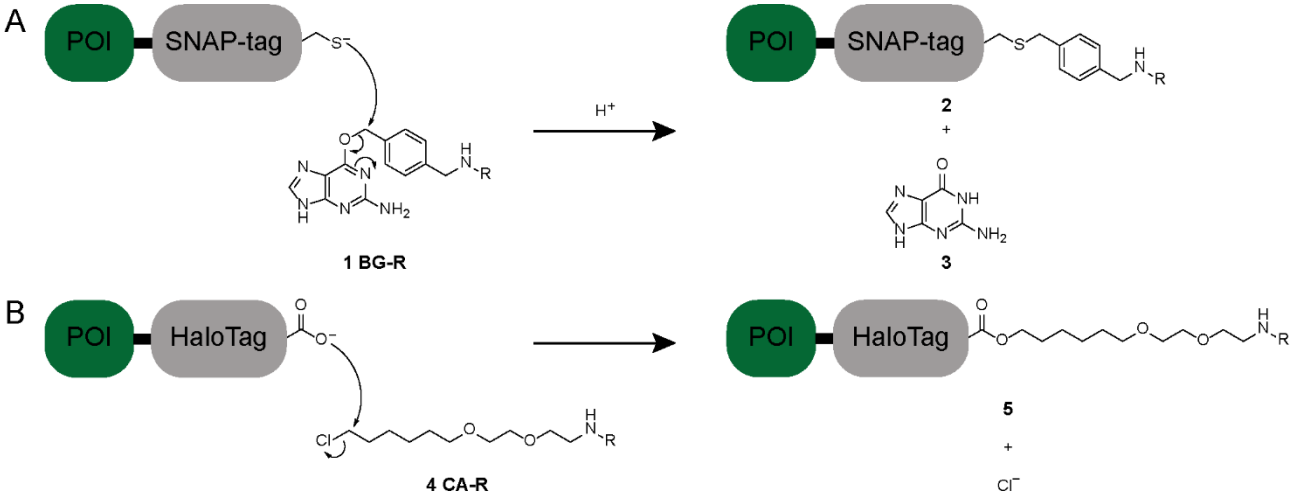

Figure 3: Mechanism of the reaction of self-labeling protein tags with their substrates. (A) SNAP-tag reacting with BG attached to a desired label (R, compound **1**). The desired label remains covalently bound to SNAP-tag **2** and compound **3** is released. (B) HaloTag reacting with CA-R (**4**) releasing a Cl^- and R being covalently bound to HaloTag **5**.

1.3.1 Self-labeling protein tags

One of the most prominent strategies for labeling of protein targets in live cells are self-labeling protein tags, which can be genetically encoded and fused to proteins of interest (POI). The two most commonly used self-labeling protein tags are SNAP-tag and HaloTag, which are derived from the human DNA repair enzyme O^6-alkylguanine-DNA alkyltransferase and the *Rhodococcus* dehalogenase DhaA, respectively. Their active site residues (SNAP-tag: cystein, HaloTag: aspartic acid) specifically react with distinct ligands forming a covalent bond. In the case of SNAP-tag this is a substituted O^6-benzylguanine (BG-R **1**),[96] and for HaloTag it is a synthetic chloroalkane ligand (CA-R **4**).[97,98] The two self-labeling protein tags and ligands are orthogonal to each other and can therefore be used at the same time, labeling two different targets (Figure 3). In contrast to previously available labeling tags such as FLAsH, SNAP-tag and HaloTag show the high reaction rates and specificities that are necessary for live-cell labeling.[91–94] A disadvantage of self-labeling protein tags is their size (3–4 nm diameter), which they add to the POI. SNAP-tag (20 kDa) and HaloTag (33 kDa) have a similar size as GFP (27 kDa) and often previously tested POI-GFP fusions are used, simply replacing the GFP with SNAP-tag or HaloTag. Nevertheless, it is possible that the fusion proteins are not functional or do not localise properly and control experiments have to be performed. A possible solution is to vary the position of attachment of the self-labeling protein tag (N-, C- terminus or insertion into a loop). Especially in the context of SRM, one has to take into account that the size of these tags add to the linkage error and that the obtained microscopy image indicates the position of the fluorophore and not the POI per se.[31,99] In addition, commonly used over-expression from plasmids with exogenous promoters can lead to mislocalisation. This can be circumvented by the creation of knock-in cell lines through gene-editing methods, which has recently been used for SRM.[100,101] Nonetheless, this does not ensure proper function or localisation, both of which require verification.

1.3.2 Targeting ligands

Despite self-labeling protein tags, several cellular organelles and biomolecules can be labeled using targeting ligands. These ligands have high affinity and specificity for their target or accumulate in a specific organelle or in a membrane. They can be coupled to a desired label such as a small-molecule fluorophore. Affinity labeling was used to label biopolymers such as filamentous actin (jasplakinolide **6**, Figure 4),[102] microtubules (docetaxel **7** and its derivatives),[103,104] and DNA (e.g. bisbenzimides **8**).[90] In addition, a variety of affinity based ligands were developed from inhibitors targeting enzymes such as cathepsin D located in lysosomes (pepstatin A **9**),[105] or sulfonylurea receptors of ATP-sensitive K^+ channels in the endoplasmic reticulum (ER, gilbenclamide **10**)[90] along with many others (Figure 4).[90,93,106] Ligands that accumulate in specific organelles were developed for mitochondria using positively charged groups that accumulated in negatively charged mitochondria (ammonium or phosphonium groups, intrinsically positively charged fluorophores).[107] Probes accumulating in lysosomes on the other hand use a change in pH to trap weakly basic groups in the acidic vesicles (amines).[90] Ceramide derivatives integrate into the membranes of the ER or the Golgi apparatus, depending on the temperature used during labeling.[108,109] The advantage of this system is that they do not require genetic manipulation of the target, which can be complex in primary cells or whole animals. Additionally, not only proteins but also DNA and membranes can be labeled. However, it is possible that probes derived from inhibitors still show residual activity perturbing the biological target/ system and also here careful control experiments need to be performed to rule out artifacts.[110] This could eventually be circumvented by designing ligands that are derived from binders that show no pharmacological effects.

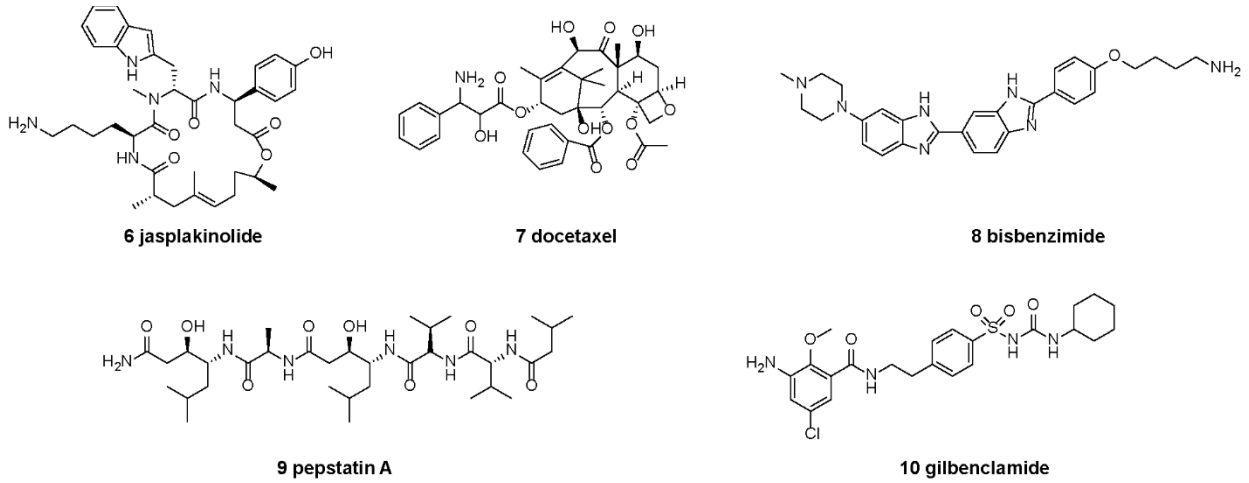

Figure 4: Structures of several targeting ligands specifically binding to F-actin (jasplakinolide **6**), microtubules (docetaxel **7**), DNA (bisbenzimide **8**), lysosomes (pepstatin A **9**), and the ER (gilbenclamide **10**).

1.4 Small-molecule fluorophores

As previously outlined, small-molecule fluorophores have several beneficial properties over FPs, most notably a higher photon budget. However, in order to be applied to live-cell SRM they need to be cell membrane permeable.[15,24,31] That is why current research is focused on finding even brighter and cell-permeable small-molecule fluorophores that could help to overcome current challenges in live-cell SRM. The ideal properties of a small-molecule fluorophore for live-cell SMR include: high brightness (high extinction coefficient (ε) and high quantum yield (ϕ)), good cell permeability, ideally excitation and emission in the far-red, and low background signal from unspecific staining. SMLM additionally requires blinking, switchable, convertible, or photoactivatable fluorophores with high contrast ratios between the 'on' and the 'off' state and favourable activation or switching kinetics.[25] STED on the other hand demands high photostability, good stimulated emission rates, and low re-excitation through the depletion laser.[66]

Many different classes of small-molecule fluorophores exist such as coumarins, boron dipyrromethenes (BODIPY), fluoresceins, rhodamines, oxazines, and cyanines but not all analogues fulfil the above mentioned criteria.[111] Many

variants have been optimised for their use in fixed-cell applications without taking permeability into account, which is why most commercially available small-molecule fluorophores are not suitable for live-cell imaging. Other classes are of limited use due to their lower brightness and excitation and emission maxima in the blue/green. One of the remaining most promising classes for live-cell SRM or microscopy in general is the class of rhodamines.[85,112,113]

1.4.1 Rhodamines

Rhodamine fluorophores and their derivatives are based on a xanthene core and bear an extra aromatic ring. Their first representative tetramethyl rhodamine (TMR **13**) was synthesised from 3-(*N*,*N*)-aminophenol **11** and phtalic anhydride **12** at the end of the 19th century (Figure 5A).[114] Due to its strong pink colour TMR was of high interest at the time and soon it was found that depending on the environment (solvent) TMR exists in either a coloured, fluorescent quinoid form **13** or in a non-coloured, non-fluorescent spirolactone form **14**.[115] Even earlier, similar equilibria had been found for fluorescein **15** (Figure 5B, C).[116] It is due to this equilibrium that many rhodamine derivatives show good cell-permeability.[117] These zwitterionic molecules can adapt to their environment and are on one hand soluble in aqueous solution but can also penetrate the lipophilic plasma membrane in their spirolactone form (Figure 6).

Rhodamines have been extensively derivatised since their discovery. New analogues with shifted spectral properties, enhanced photophysical characteristics, and even chemosensors using the open-close equilibrium have been developed.[112,118–120] Doing so, almost all positions on the xanthene core and the appended aromatic ring were modified (R^1-R^6). A very common modification is the introduction of a second carboxylic acid functionality at position 6' (compound **16**, less common at position 5' or 4')[121], which acts as a suitable handle for derivatisation with targeting ligands. The derivatised fluorophores can then be targeted to an intracellular target and used for live-cell applications (Figure 5D, E).

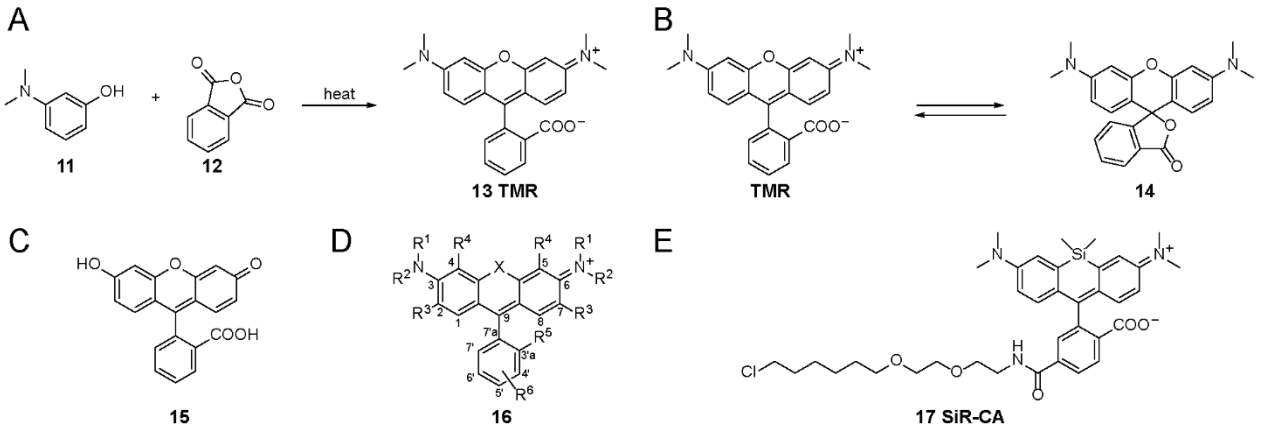

Figure 5: Structures of several rhodamine analogues. (A) Synthesis of TMR **13**. (B) Equilibrium between the quinoid **13** and the spirolactone form **14** of TMR. (C) Fluorescein **15**, which is another xanthene analogue. (D) Generalised rhodamine structure **16**. (E) Siliconrhodamine (SiR)-CA **17**.

1.4.2 Silicon rhodamines (SiR)

SiRs make up a class of far-red fluorophores with broad applications in bioimaging. They are rhodamine analogues, where the oxygen atom is substituted by a silicon (compound **16** X = Si, Figure 5D, E). SiR derivatives have several properties that are highly desirable for live-cell imaging, such as membrane permeability, high ε, high Φ, photostability, and excitation and emission in the far-red (ε = 100,000 $M^{-1}\,cm^{-1}$, Φ_{aq} = 0.39, $\lambda_{ex,\,max}$ = 645 nm; $\lambda_{em,\,max}$ = 661 nm).[117] In addition, they show fluorogenicity due to their open-close equilibrium (Section 1.5.1). SiR derived probes e.g. SiR-CA **17** have found broad applications in microscopy and were even used for live-cell SRM in both STED[74,104,117,122–124] and SMLM.[32,33]

1.5 Tuning of small-molecule fluorophore properties

In the following sections, several strategies to tune the most important properties of small-molecule fluorophores, in particular rhodamines and SiRs with regard to live-cell SRM, will be discussed.

1.5.1 Fluorogenicity and cell permeability

Fluorogenicity, the ability to increase fluorescence upon interaction with a target, has proven to be a crucial property of small-molecule fluorophores over recent years.[125,126] Fluorogenic fluorophores generally show lower background fluorescence than their non-fluorogenic analogues and often do not even require washing steps. This is especially beneficial in contexts where low background is crucial such as SRM or where removing excess probe is difficult e.g. in tissues or whole animals.

Generally, fluorogenic fluorophores fall into two categories. The first uses a quencher moiety that reduces the fluorophore's fluorescence through either Förster resonance energy transfer, photoinduced electron transfer or through bond energy transfer.[127,128] Upon reaction or binding, the quenching is released and an increase in fluorescence can be seen. The second class uses environmentally sensitive fluorophores that shift their equilibrium from a non-fluorescent to a fluorescent form upon interaction with a target (Figure 6). Certain of these probes are also believed to form non-fluorescent aggregates in water which further increases the fluorescence turn-on.[104,117]

Rhodamine fluorophores exhibit exactly such an environmentally sensitive equilibrium and are therefore prime candidates for the development of fluorogenic probes (Figure 5B). However, the original TMR is not suitable as it exists predominantly in its fluorescent form in water and cannot exhibit a further turn-on upon target binding. This is only possible if the fluorophore is partly or fully closed in aqueous solution. Hence, the position of the open-close equilibrium as well as the target environment determine whether a fluorophore is suited for the further development of fluorogenic probes. This type of fluorogenicity also contributes to cell permeability as it allows fluorophores to adopt the non-fluorescent, non-charged, spirolactone form **18**. This apolar form **18** diffuses passively through the cell membrane, which is the main uptake route together with active transport and endocytosis (Figure 6).[129] Shifting the equilibrium towards the closed form **18** therefore increases cell permeability. This approach of fluorogenicity has attracted a lot of attention over recent years due to its dual advantages for both signal-to-background and cell permeability.[130] It is of high interest for live-cell SRM.[130]

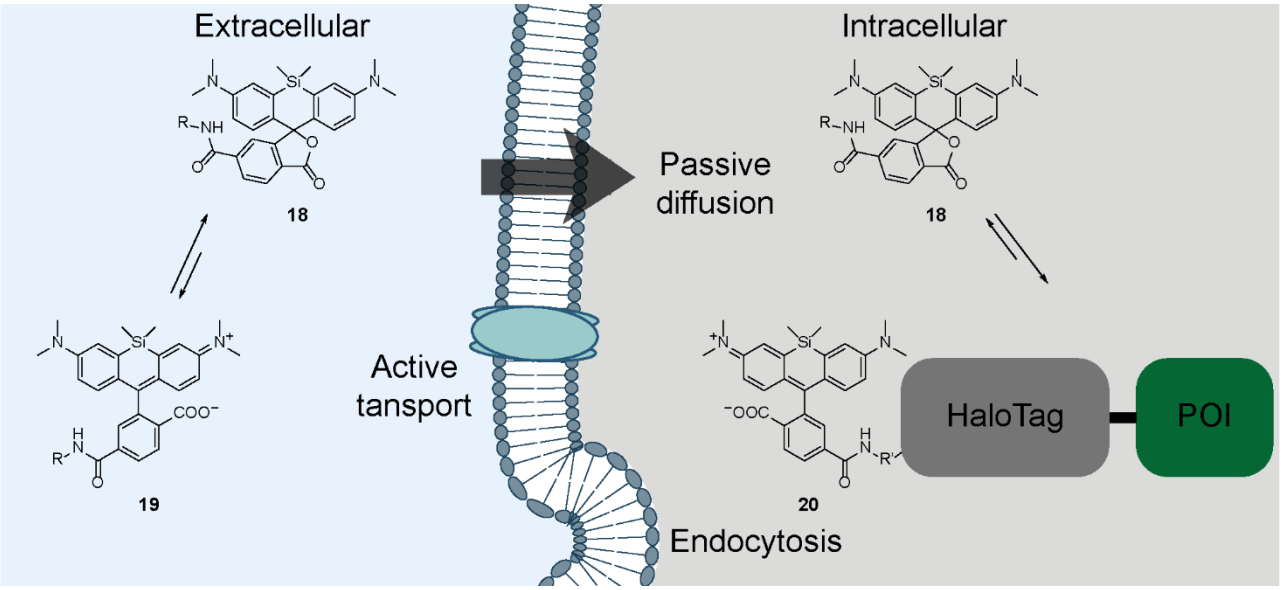

Figure 6: Fluorogenicity and cell permeability. The equilibrium between the closed form **18** and the open form **19** is shifted toward the closed form **18** in aqueous solution, which allows for better penetration of the cell membrane. Binding or reaction with the target then shifts the equilibrium toward the open form **20**, making live-cell microscopy with minimal background possible.

Studies focusing on the development of fluorogenic fluorophores based on rhodamines and its derivatives concentrated their attention primarily on the open-close equilibrium. The equilibrium has been studied both theoretically[131,132] and experimentally, revealing that the equilibrium depends on solvent polarity, pH, and the hydrogen bonding character of the solvent as well as on electronic and steric factors of the fluorophore itself.[115,133–135] This is why pH titrations and water-dioxane titrations have become the gold standards to assess the position of the open-close equilibrium.[32,117,136] Especially, the D_{50} value obtained from water-dioxane titrations, corresponding to the dielectric constant at which half the molecules are in their closed form, is commonly used. In addition, probes are usually tested against their specific target *in vitro* such that the fluorescence turn-on of the probe can be defined.[117,122,123] One has found that both the electrophilicity (LUMO) of the xanthene core and the nucleophilicity (HOMO) of the intramolecular nucleophile are crucial determinants for the open-close equilibrium. Making the core more electron poor or the nucleophile more electron rich both shift the equilibrium toward the closed state. By now chemical modifications have been introduced to virtually all available positions and fluorogenic rhodamines are now available over the whole spectral range.[36,117,124,137–143] Electron withdrawing groups (EWG) such as fluorines and cyanine groups were introduced on the xanthene core (R^3) and the aniline substituents to shift the equilibrium more towards the closed state.[36,137–140,143] In contrast introduction of EWGs on the appended aromatic ring leads to a more open equilibrium.[141,143] Modifications can also be directly introduced to the intramolecular nucleophile modifying R^5.[142] This position also opens up interesting new avenues to create photoactivatable or spontaneously blinking fluorophores (Sections 1.5.4).

Most of the presented studies only investigated intrinsic factors of the fluorophores and did not take the environment of the target into account. However, recent theoretical calculations showed that the contribution of hydrogen-bonding is stronger than polarity only.[132] This indicates that more specific interactions with the target environment could make crucial contributions to the extent of the fluorogenic response. It is therefore not surprising that different self-labeling tags and protein targets do not elicit the same fluorogenic response in the same fluorophore and different fluorophores might be optimal for different targets.[117,122,123,142,144] This clearly requires more investigation.

1.5.2 Spectral properties

Shifting the absorbance and emission spectrum of fluorophores to the far-red facilitates live-cell SRM as phototoxicity at longer wavelengths (lower energy) is diminished. In addition, fluorophores in the near-infrared window (650 – 950 nm) are crucial for tissue and *in vivo* applications as the penetration depth of light is highest due to decreased absorbance and scattering at these wavelengths.[145] Furthermore, autofluorescence of cells is reduced, which also benefits live-cell SRM. Consequently, considerable efforts have been made to shift the absorbance and emission spectra of rhodamine fluorophores. The most substantial being the substitution of the oxygen atom with atoms with different electronic properties changing the gap between the highest-occupied molecular orbital (HOMO) and the lowest unoccupied molecular orbital (LUMO) of the fluorophore and therefore its spectral properties. Oxygen was substituted with atoms of group 16 (S, Se, Te),[146,147] group 15 (N),[148] and group 14 (C, Si, Ge, Sn)[149–152] bearing none, one or two methyl groups (Figure 7, compound **21**). More recently, substituted phosphorous[153–155] and sulfons[156] were used to access the spectrum past 670 nm. However, not all of these fluorophores show suitable extinction coefficients, quantum yields or open-close equilibria for live-cell imaging. Especially the latter is directly interconnected with the spectral properties, as changing the spectral properties requires to change the HOMO-LUMO gap and with this the electrophilicity of the xanthene core which then influences the open-close equilibrium. Red-shifted fluorophores generally tend to have a more closed equilibrium and are more fluorogenic, as they are more electrophilic (lower LUMO). The two most popular variants of this series remain carbopyronines (CPYs) and SiRs.

Smaller spectral shifts can be realised through modifications on the xanthene core or the aniline substituents using EWGs such as fluorines.[124,138,140]

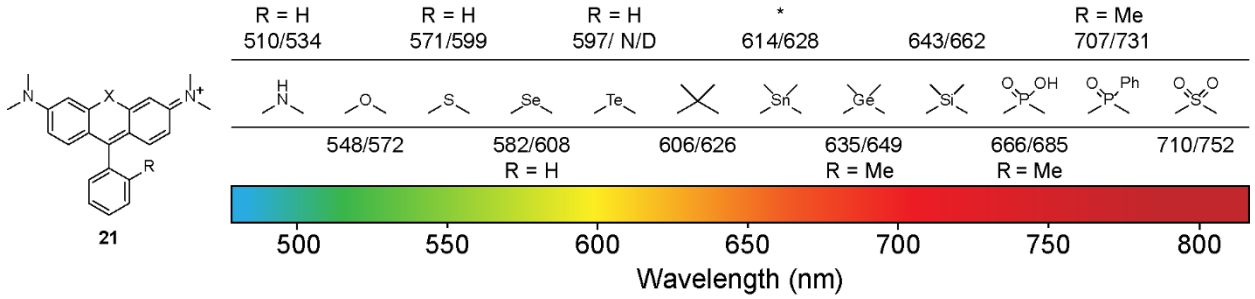

Figure 7: Spectral properties of rhodamine analogues substituted at X. Excitation and emission maxima are given in nm. R = COOH unless otherwise stated. N/D not determined * Values reported correspond to the pyronine lacking the appended aromatic ring. Values were obtained from the following references N,[148] O, C, Si,[136] S, Se,[146] Te,[147] Sn, Ge,[152] P,[154,155] and sulfone.[156]

1.5.3 Photon budget: brightness and photostability

Brightness and photostability define the photon budget of fluorophores and with this the attainable spatial and temporal resolution in SRM. In addition, they define the overall duration of an experiment.

Strategies to increase the brightness of rhodamines have often focused on decreasing the likelihood for alternative non-radiative pathways. Suppressing such vibrational transitions often went hand in hand with rigidification of the xanthene scaffold. As a consequence, many of these brighter analogues showed decreased cell permeability.[112] In two very elegant strategies introduced more recently, the *N,N*-dimethylamino moiety was replaced by 7-azanorbornane (compound **22**) or a four-membered azetidine ring (compound **23**, Figure 8), leaving cell permeability and spectral properties unaffected.[136,157] Introduction of these cyclic amines prohibits the excited state fluorophore to undergo twisted intramolecular charge transfer (TICT), which relaxes through a non-emissive pathway reducing the quantum yield.

Instability of rhodamine fluorophores and its derivatives to photobleaching most commonly stems from processes originating from the triplet state, which is highly reactive due to its high energy and long lifetime.[158,159] Firstly, the triplet state can react with molecular oxygen generating highly reactive singlet oxygen ($^1O_2$) or other reactive oxygen species. These in turn can react again with the fluorophore and cause its degradation. Alternatively, they react with their cellular environment leading to photodamage. Secondly, triplet states can also react with oxidizing or reducing species forming non-fluorescent adducts. Despite many photophysical studies and the relevance of these mechanisms to triplet state blinking (Section 1.5.4)[11,160] most photobleaching pathways remain poorly understood. One of the best studied pathways in rhodamines is photodealkylation, where the reaction with oxygen leads to the formation of a nitrogen centered radical cation, which is deprotonated, then recombines with triplet oxygen and finally dealkylates.[161–163] This pathway was successfully suppressed using *tert*-alkyl substituted rhodamines (compound **24**, Figure 8) lacking the α-proton required for deprotonation of the radical cation.[163] An alternative pathway of forming such a radical cation is TICT and hence the previously introduced strategies substituting the *N,N*-dimethylamino moiety with small cyclic amines benefits photostability as well.[136,157]

Considerable efforts were also spent in reducing reactions with oxygen, either through the introduction of EWGs (fluorines, compound **25**, Figure 8), which reduce the reactivity of the fluorophore,[164] or through addition or coupling with triplet state quenchers.[165,166] However, the former also influences fluorogenicity and often decreases quantum yield and the latter generally reduces cell permeability due to the attachment of large non-polar triplet state quenchers such as 1,3,5,7-cyclooctatetraene.[85] Therefore both approaches have limited applicability for live-cell microscopy.

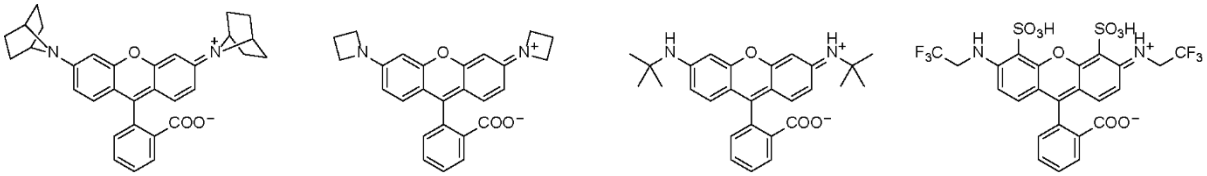

Figure 8: Structures of four rhodamine fluorophores with increased brightness and or photostability.

1.5.4 Switching mechanisms

Rhodamines and SiRs can be rendered switchable in terms of their emissive state and used for SMLM. To do so several different strategies were harnessed including: excited state blinking, photochromism, ground state equilibria and photoactivation. Early on, it was discovered that rhodamine fluorophores show dark states upon strong laser irradiation. This behaviour could be enhanced and the dark states prolonged, when using redox additives. In addition, recovery to the ground state can be aided by UV irradiation. It was later found that rhodamine fluorophores undergo photo reduction of their triplet state forming a radical anion. This dark state then returns to the ground state via oxidation with molecular oxygen, closing the switching cycle (Figure 9A).[40,167,168] Especially thiol additives such as cysteamine and glutathion (GSH) fit the redox properties of rhodamines and efficiently contribute to the formation of dark states. A variety of rhodamine fluorophores were systematically tested for their switching properties in fixed cells and Atto 488, Alexa Fluor 488, and Alexa Fluor 568 **26** were among the best rhodamine fluorophores for SMLM (Figure 9B).[25] The redox pair GSH/GSSG is also present in living cells and this strategy can therefore be used for live-cell SMLM.[31,117,169,170] However, it has limited applicability as GSH concentrations vary in different subcellular locations and it is difficult to control the density of fluorescent molecules.

The open-close equilibrium of rhodamines is also an ideal starting point for photochromic and spontaneously blinking fluorophores. For instance, lactam derivatives (compound **27**, Figure 9C) were found to show photochromism as early as 1977.[171] The lactam is predominantly in its non-fluorescent, closed form **27** but undergoes opening upon irradiation with UV light (375 nm, compound **28**) and then thermally reverts to the closed state. Both the spectral properties of the fluorophore and the wavelength required for switching were modified through structural changes to the fluorophore.[44,172–174] This has been used for SMLM in fixed cells,[175,176] and recently for live-cell measurements.[174,177] However, most of the described applications were in fixed cells as they require strong UV irradiation increasing phototoxicity. Spontaneously blinking fluorophores on the other hand do not require light irradiation but interchange spontaneously between a fluorescent, open and a non-fluorescent, closed form at room temperature.[32] The first reported spontaneously blinking fluorophore HM-SiR **32** (Figure 9E) was readily applied in live-cell SMLM.[32,33] Optimal candidates, were identified based on pH titrations measuring the compounds pK_{cycl}, the value at which half the molecules are in their open form **33** and which should ideally lie below 6. This guarantees that at physiological pH only few percent of the molecules will be in their fluorescent form. Using similar strategies the concept was also extended to different spectral regions.[34,36] However, the kinetics of the forward and backward reaction and hence the equilibrium position determine the imaging speed and the density of fluorescent molecules. This in turn limits the quality and resolution of the images depending on the structures imaged. This is why a combined approach using photoactivation and spontaneously blinking fluorophores (compound **29**, Figure 9D) is more adaptable to different environments and structurally different targets. The photoactivation converting compound **29** to compound **30** acts as an additional lever through which the density of the emitting fluorophores (compound **31**) can be adjusted.[35]

The primary strategy to render rhodamines photoactivatable is to attach one variant of the most commonly used caging group *ortho*-nitrobenzyl.[178–182] Through the newly formed amide bond rhodamine **34** is locked into its spirolactone form and is therefore non-fluorescent (Figure 9F).[183,184] Only upon irradiation with UV-light the underlying fluorophore compound **35** is released. This strategy was not only applied to rhodamines, but also to CPY and SiR and was used both in fixed,[137,185] and live-cell SMLM.[186] One major disadvantage of *ortho*-nitrobenzyl protected compounds is the stoichiometric formation of very electrophilic nitroso-aldehydes or ketones, which are

coloured, highly reactive, and therefore toxic and of concern in live-cell imaging.[187] In addition, these groups are bulky and add to the overall lipophilicity of the probes making them less soluble and less cell permeable and ultimately not suitable for live-cell microscopy.

An alternative strategy to render rhodamines photoactivatable was discovered in 2010 making use of a diazoketone group. Due to the smaller nature of the caging group the cell permeability of the resulting probes is not reduced (compound **36**).[188] The approach was expanded to fluorophores in different spectral ranges[189,190] and with enhanced quantum yield.[191] It was successfully applied to live-cell SMLM using both the rhodamine and the SiR analogue.[191] The major downside of this approach is the formation of a dark side-product **40** along the two fluorescent compounds **38** and **39** during photoactivation (Figure 9G). This lowers photoactivation efficiencies to variable degrees depending on the structure and environment of the fluorophore, making the application of the diazoketone approach more complicated. Moreover, photoactivation proceeds through a carbene intermediate **37**, which is reactive toward intracellular nucleophiles.[192]

Altogether, many advances have been made in the field of rhodamine fluorophores and many parameters can be tuned for desired microscopy experiments. However, further advances have to be made to keep up with the development of microscopy techniques. One such area is the development of new photoactivation strategies compatible with live-cell SMLM. Such fluorophores are not only useful for SMLM but allow also to study protein dynamics within cells using tracking experiments.[193]

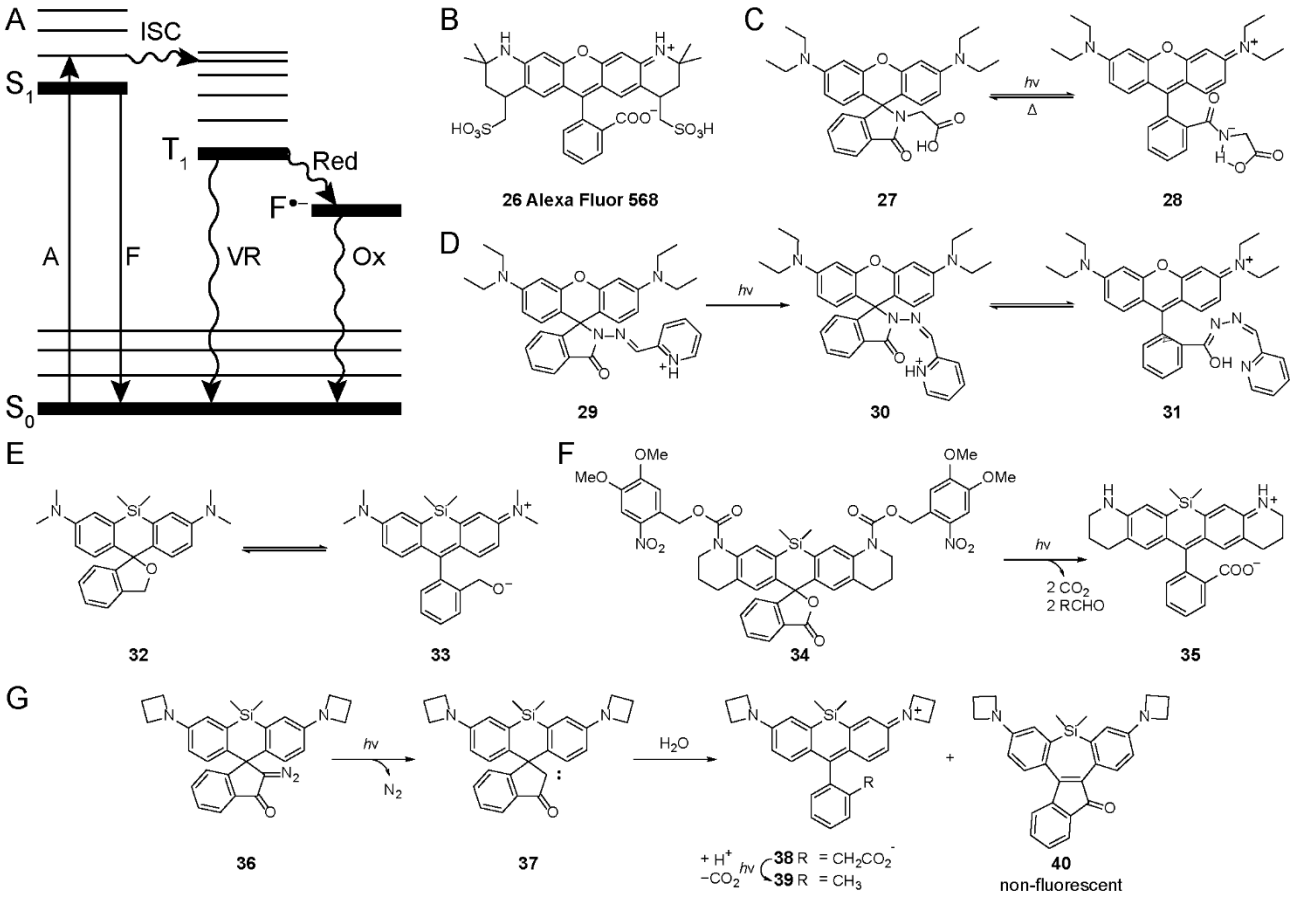

Figure 9: Different mechanisms to switch fluorophores between an emissive and a non-emissive state. (A) Simplified Jabłoński diagram including radical anions $F^{\bullet}$, which are formed via reduction from the T_1 state. (B) Structure of Alexa Fluor 568 **26** that exhibits excited state blinking in the presence of reducing agents such as GSH. (C) Photochromic equilibrium of spiroamide **27** used in live-cell SMLM. (D) Photoactivatable and spontaneously blinking (fluxional) rhodamine **29**. (E) Equilibrium of the first spontaneously blinking fluorophore HM-SiR **32**. (F) *ortho*-Nitrobenzyl caged SiR **34** and its photoproduct(s). (G) Photoactivation of diazoketone caged SiR **36** and subsequent reactions.

1.6 Previous work

1.6.1 Photoactivatable silicon rhodamine

During his work on SiRs, Dr. Luc Reymond in the Johnsson group, serendipitously synthesised a photoactivatable silicon rhodamine (PA-SiR **41**)[1] from 3,3'-(dimethylsilanediyl)bis(4-bromo-*N*,*N*-dimethylaniline) and glutaric anhydride via a later published synthesis route.[141] Instead of the expected compound **42**, the synthesis yielded the non-coloured, non-fluorescent PA-SiR **41**, which in preliminary tests was shown to undergo photoactivation by irradiation with UV light (290–365 nm), forming the desired product **42** (Figure 10). However, the colour and fluorescence of the solution were not sustained over longer times, indicating reversibility or a secondary process such as nucleophilic attack at position 9 analogous to spirolactone formation of SiRs.[117] Nucleophilic attack could not only proceed intramolecularly forming spirolactone **44** but also via intermolecular nucleophiles such as water forming hydrol **43** or a generic nucleophile Nuc^- giving compound **45**. It was not clear under which conditions PA-SiR activates (k_1) and through which mechanism. In addition, it was unknown if nucleophilic attack of **42** was relevant and if yes, through which nucleophiles it would proceed and to which extent the different processes (k_{-1}, k_2, k_3, k_4) contribute to the disappearance of the colour and whether one process could be favoured over the others (Figure 10).

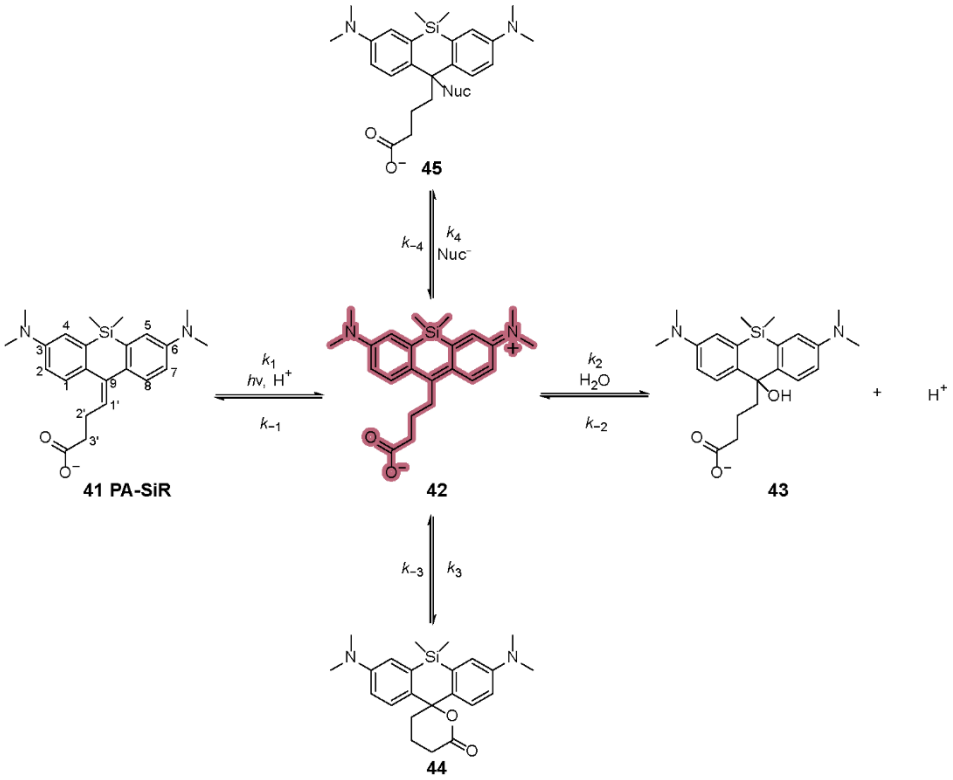

Figure 10: Equilibrium system and structure of PA-SiR.

1.6.2 Related compounds and reactions of PA-SiR

Few hints towards a better understanding of this equilibrium system were found in the literature. Similar structures bearing an exocyclic double bond to the xanthene scaffold were previously reported for fluorescein **49** and CPY derivatives (compound **50**, Figure 11A and B). None of which was reported to be photoactivatable but to be in

[1] Technically PA-SiR **41** does not belong to the class of rhodamines as it is lacking the extra aromatic ring. However, throughout this thesis they will be referred to as PA-SiRs similarly to succinylfluorescein (*vide infra*).

equilibrium with their quinoid forms at room temperature.[194,195] The structurally most related compound that has been reported to undergo a light induced transformation of similar sort is 1,1-bis[4-(dimethyl-amino)phenyl]-1-alkene (**51**), which was reported to exhibit photochromism in acidic solution converting to compound **52** (Figure 11C). However, the phenomenon was not further explored.[196]

More information was available on possible reactions with nucleophiles. SiRs are indeed susceptible to nucleophilic attack by intramolecular nucleophiles such as glutathione.[197] It is also known that sterically unhindered xanthenes, such as alkyl substituted fluorescein, exhibit poor stability toward water.[194,198] For instance, succinylfluorescein **49** was reported to interchange at room temperature between four different forms including the lactone **46**, the quinoid **47**, the hydrolic form **48** and the ethylenic form **49** (omitting all remaining charged forms). The interchange between the last two is believed to proceed via a 1,2-elimination and is also observed in alcoholic solvents. In general, this equilibrium depends on the solvent as well as on other ions present (Figure 11A).[194] The energy difference between the quinoid and the ethylenic form was calculated for a fluorescein analogue showing that the quinoid form is favoured.[199,200] These four forms correspond exactly to the proposed forms for PA-SiR **41** (Figure 10). However, the energy levels of the PA-SiR system must be different allowing for photoactivation. In addition, it was not possible to isolate all reported ethylenic fluorescein and CPY derivatives and they are often only described as equilibrium species in solution.[194,195] Two synthetic routes both starting from protected xanthenone **53** were reported to give access to non-functionalised ethylenic fluoresceins (compounds **54**) and this might be envisaged as an alternative synthesis route for PA-SiRs (Figure 11D).[199,201,202]

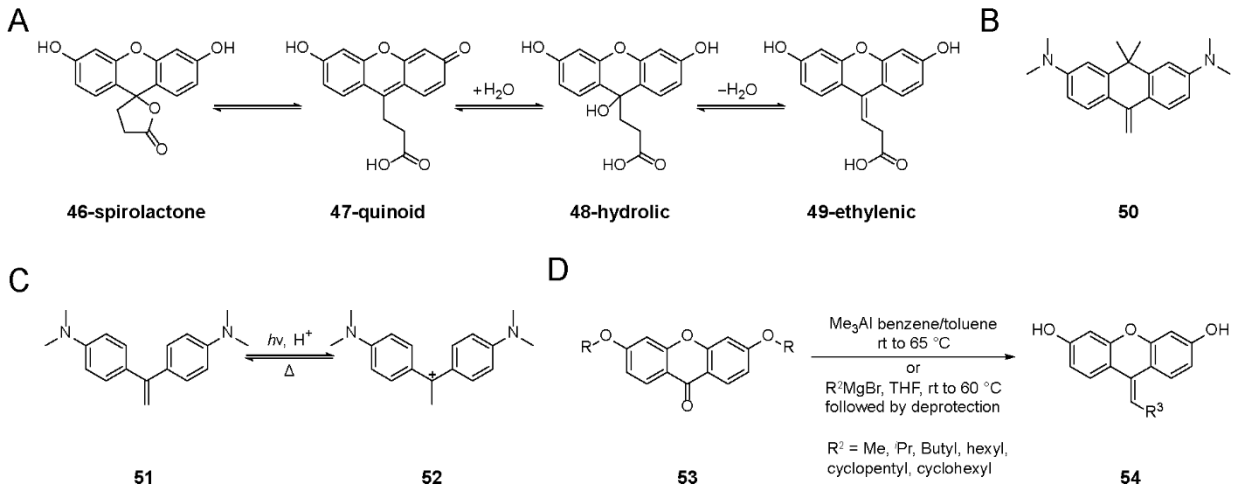

Figure 11: Relevant structures and reactions for the PA-SiR equilibrium. (A) Simplified equilibrium system described for succinylfluorescein showing spirolactone **46**, quinoid form **47**, hydrolic form **48**, and the ethylenic form **49**. (B) Analogous CPY derivative compound **50**. (C) Structure and mechanism of the reported photochromism of the structurally relevant compound 1,1-bis[4-(dimethylamino)phenyl]-1-alkene (**51**). (D) Synthetic pathway towards ethylenic fluoresceins starting from xanthenone **53**.

1.7 Scope of this thesis

1.7.1 PA-SiR

The main goal of this project was to develop photoactivatable, small-molecule fluorophore probes based on PA-SiR **41** with suitable photophysical properties for live-cell SMLM. To this end, the equilibrium system of PA-SiR **41** was characterised using spectroscopic methods. Additionally, synthesis and analysis of different PA-SiR analogues were used to establish a structure-activity-relationship to further understand the equilibrium system. This served as a basis for the rational design of PA-SiR analogues with improved photophysical and chemical properties. The best candidates were selected for the development of probes for self-labeling protein tags and targets such as DNA, microtubules, and F-actin. Moreover, characterisation by widefield and confocal fluorescence microscopy in live cells allowed further restriction of the pool of candidates. In parallel, *in vitro* single-molecule measurements were used to

investigate the probe's photoactivation and blinking characteristics on a single molecule level. The best fluorophore was used in fixed-cell SMLM using HaloTag fused to different proteins and jasplakinolide **6** visualizing F-actin. Ultimately, live-cell SMLM was demonstrated for the HaloTag probe investigating the dynamics of mitochondria. The developed probes were additionally tested for STED microscopy. Lastly, it was attempted to broaden the scope of the photoactivation reaction to rhodamines. Parts of this project have been previously published[203] (Springer Nature under CC BY 4.0) and a patent application was filed.[204] Data thereof was adapted for this thesis.

1.7.2 Exploring the fluorogenicity of HaloTag

The same fluorophore can show different photophysical and chemical properties when bound to different self-labeling protein tags. This phenomena is most pronounced for red-shifted and fluorogenic fluorophores.[142,144] In the context of live-cell microscopy especially brightness and fluorogenicity are of importance as they allow longer experiments and higher signal-to-background ratios. For instance, PA-SiR **41** in combination with HaloTag showed increased photoactivation and higher fluorogenicity when compared to SNAP-tag (Section 2.5). Motivated by this observation, it was set out to understand the increased fluorogenicity of HaloTag in combination with fluorogenic rhodamine fluorophores. To this end, mutations on the HaloTag surface were probed via site-saturation mutagenesis and coupled to a bacterial lysates screening approach. The most promising candidates featured modulations in fluorescence intensity as compared to parental HaloTag and were further characterised. In addition, two rounds of site-saturation mutagenesis combining beneficial mutations were carried out targeting HaloTag variants with enhanced fluorogenicity properties. The best candidates were characterised by X-ray crystallography and their properties were tested in combination with several rhodamine fluorophores using spectroscopic methods. They were further examined *in cellulo* by confocal microscopy demonstrating that the identified HaloTag variants also enhance the fluorescence intensity in cells.

Chapter 2 PA-SiR

2.1 Synthesis of PA-SiRs

PA-SiR and its derivatives were synthesised via a synthetic route that was published during the preparation of this thesis (Materials and Methods).[141] Starting from *N*-dimethyl-bromoaniline (**55**) compound **57** was accessed via lithiation at −78 °C and reaction with dichlorodimethylsilane (**56**) in a yield of 67%. Bromination of compound **57** by means of *N*-bromosuccinimid (NBS) delivered compound **58** in good yield (80%). Finally, closure of the xanthene core and formation of PA-SiR **41** via lithium halogen exchange and reaction with glutaric anhydride (**59**) proceeded in substantially lower yield (5%). In addition, a major side-product **60** was isolated (19%), which most likely formed upon abstraction of an α-proton of glutaric anhydride (Figure 12A). Depending on the acidity of the substrate, this undesired reaction pathway could be disfavoured. For instance, higher yields were obtained for derivatives **62** and **69**, obtained from reaction of **58** with ethylacetate (**61**) and methyl butyrate, respectively. All attempts to isolate the corresponding quinoid **42**, hydrol **43** or spirolactone **44** forms of PA-SiR **41** failed. However, analogues bearing shorter alkyl linkers obtained from reaction with different succinic anhydrides could be isolated as the spirolactone, only converting to the photoactivatable derivative when treated with highly acidic solutions. This is in agreement with the greater hydrolytic inertness of γ-butyrolactone compared to δ-valerolactone under acidic conditions[205] and hence 5-membered spirolactones obtained by reaction with succinic anhydride are more kinetically stable than the 6-membered spirolactones (formed by reaction with glutaric anhydride). It is assumed that spirolactone **44** is formed during the synthesis of PA-SiR **41** but is hydrolysed under the acidic conditions on silica gel and hence conversion to the ethylenic form occurs during workup.

In order to facilitate the access of PA-SiR analogues two directions were pursued. First, an attempt to increase the yields of the conventional PA-SiR synthesis described above was taken. The less acidic δ-valerolactone was used instead of glutaric anhydride. However, this approach did not lead to the isolation of the desired product (Supplementary Table 1). Alternatively, related protocols for the synthesis of xanthene fluorophores through bis-arymalgnesium species have recently been published, and it will be of interest to see if these strategies give higher yields than the bis-aryllithium approach described here.[141,206,207207] Second, two alternative synthetic routes were attempted but neither Grubbs metathesis of **62** nor Wittig reaction with an analogue ketone **65** led to product formation (Figure 12B, C). It is possible that reagents **62** and **65** were both too sterically hindered to react with the Grubbs II catalyst or compound **66**. Alkylation of xanthenone **65** as previously mentioned using alkyl-magnesium/lithium or Me_3Al reagents would be another possibility.[199,201,202] However, these strategies would only give access to unsubstituted PA-SiRs, which are already available through the conventional synthesis in low but acceptable yields and therefore this route was not further investigated (Figure 11D).

Several different PA-SiR analogues were synthesised but it was found that not all modifications were tolerated regarding the formation or isolation of PA-SiR derivatives. Analogues were successfully isolated when scaffolds substituted on the Si (R^2 = ^{i}Pr, compound **72**) and N (compound **74**) were used. However, only EWGs (R^4 = F, compound **73**) were tolerated as substituents on the aromatic core. Methyl substituents (R^3 or R^4 = Me) increasing the electron density of the aromatic core did not lead to formation of the desired products. The di-anion intermediate of the methyl substituted substrates is probably too reactive, leading to the formation of side-products. Even the use of ethyl acetate instead of glutaric anhydride did not lead to product formation (Supplementary Table 1).

Alternative anhydrides or esters were successfully used to access derivatives lacking the carboxylic acid handle (compounds **62** and **69**) or bearing shorter alkyl linkers (PA-SiR-C3 **70**). Methyl substituents on the extra alkyl chain

were only tolerated on position 3'[204] and 2' (compound **71**) but whereas position 3' allowed for geminal methyl groups position 2' only tolerated one methyl group. However, the 2',2'-dimethyl analogue could be isolated as the spirolactone (Supplementary Table 1), and it is hypothesised that unfavourable steric interactions of the methyl groups with the protons at positions 1 and 8 of the xanthene core prevented the formation of the ethylenic form. Interestingly spirolactones could also be isolated for analogues forming a five-membered ring but not for those forming six-membered rings (Supplementary Table 1).[204] Conversion of the five-membered spirolactones to the corresponding photoactivatable ethylenic analogues and isolation was only possible in distinct cases (e.g. compound **70**, and **74** albeit to a lesser extent). One derivative with a C3 linker substituted at position 2' (Me) even interchanged between the different forms at room temperature analogous to fluorescein (Supplementary Table 1). Taken together these observations indicate that the relative energies of the different forms depend on both steric and electronic factors. This then determines which form is isolated via the chosen workup protocol.

All successfully isolated PA-SiRs are depicted below (Figure 13). In addition, all attempted PA-SiRs (successful and unsuccessful) are listed in the Appendix (Supplementary Table 1).

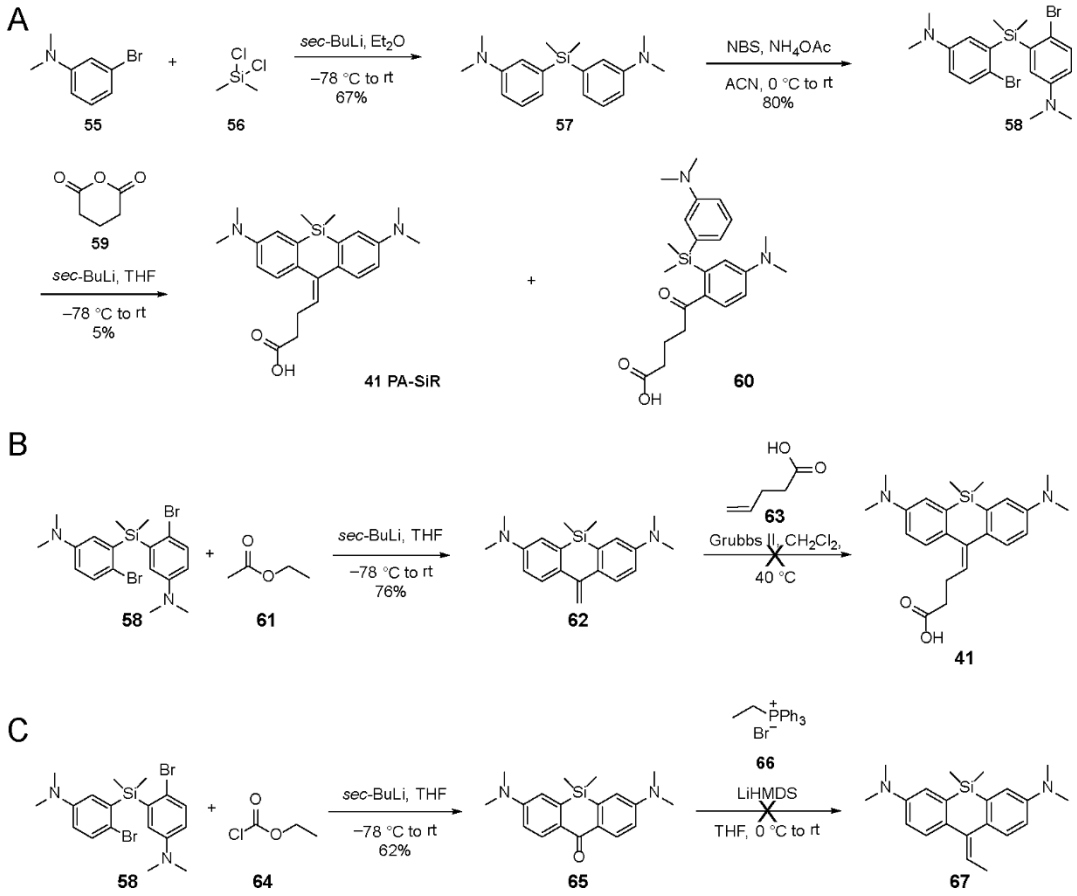

Figure 12: Synthesis of PA-SiR and its derivatives. (A) Reaction scheme for the synthesis of PA-SiR **41** in three steps, also showing the major side-product **60**. (B) Alternative synthesis via Grubbs metathesis. (C) Alternative synthesis via Wittig reaction of compound **65** and compound **66**. Compound **67** could not be isolated.

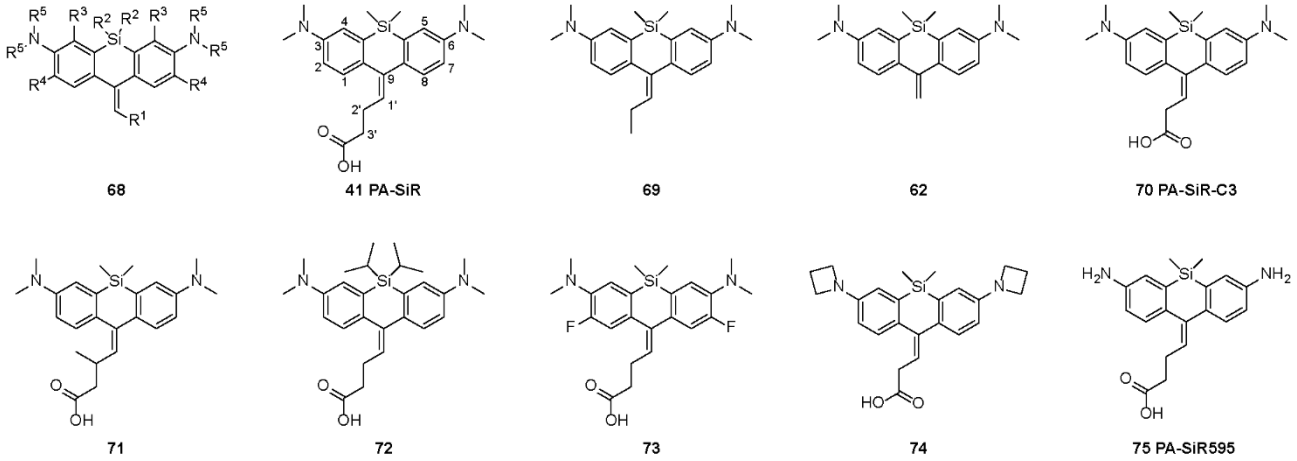

Figure 13: All successfully isolated PA-SiR derivatives. Analogue **75** was synthesised via a tetra-allyl analogue followed by ally-deprotection using palladium catalysis (Figure 14B).

2.2 Extension to other wavelengths

Strategies to shift the absorbance and emission spectrum of fluorophores are inherently linked to a change in HOMO and LUMO energies of the molecules in question. These energies and their relative position are also crucial for the isolation and photoactivatablilty of PA-SiRs, as found during the synthesis and characterisation of PA-SiR analogues, which showed that not all modifications of the xanthene core were tolerated. It is therefore difficult to predict if the ethylenic form can be isolated or if the different forms exist in equilibrium at room temperature as for succinylfluorescein[194] and the simplest carbopyronine (Section 1.6.2).[195] It was therefore decided to first shift the spectral properties while keeping the Si atom. Two strategies were employed. First, introduction of an indoline ring, resulting in a bathochromic shift of the excitation and emission maxima by 50 nm,[208] was explored. Isolation of a PA-SiR analogue **77** was possible but the product degraded rapidly and characterisation was impossible (Figure 14A). Second, removal of the methyl substituents on the aniline is known to shift the absorbance maximum to about 595 nm.[209,210] PA-SiR595 **75** was successfully isolated via a two-step synthesis starting from tetra-allyl substituted compound **79** via the conventional reaction with glutaric anhydride, followed by allyl deprotection with tetrakis(triphenylphospine)-palladium (Figure 14B).

A suitable alternative to silicon rhodamines are rhodamine analogues, which fit the 532 nm or even the 488 nm laser of a SMLM microscope. The first attempt to synthesise a photoactivatable TMR derivative via copper-catalysed arylation of aminophenol **81**,[211] alkylation and bromination of the intermediate products **82** and **84** respectively and finally followed by closure of the xanthene core was unsuccessful. Only the fluorescent, quinoid compound **88** was detected, but not the ethylenic form (Figure 14C). Next, TMR derivatives bearing EWGs were targeted, as previously synthesised electron poor PA-SiRs (compound **73**) were isolated in higher yields and similar strategies were used to create more fluorogenic rhodamines and CPYs, as well as spontaneously blinking rhodamines.[34,36,138,164] Following the same synthetic strategy as for unsubstituted TMR **88**, 2,7-difluoro substituted TMR was isolated as the quinoid form 550R **89** (13% yield), which was confirmed by LC-MS in acidic aqueous solution and the compound's characteristic absorbance at 550 nm (Figure 14C, Supplementary Figure 1). However, ^{1}H NMR measurements in aprotic solvents (DMSO-d_6 and CD_3CN) only revealed the signals of the ethylenic compound **90** (Section 5.1). This demonstrated that depending on the solvent used, 550R **89** adopted a different form, similarly to succinylfluorescein.[194] Additionally, a second electron poor rhodamine 490R **97**, whose anilines carry CH_2CF_3 substituents, was synthesised. However, initial attempts to synthesise 490R via the presented synthetic route were unsuccessful due to the alkylation of compound **82** with trifluoro-2-iodoethane that did not yield the desired product. However, the CH_2CF_3 substituted precursor **95** could be accessed via Buchwald-Hartwig coupling of bis(2,2,2-trifluoroethyl)amine (**94**) with compound **93**, which in turn was synthesised by Lam-Chan-Evans coupling.[212–214] Bromination by means of NBS and closure of the xanthene core led to the isolation of an inseparable mixture of quinoid 490R **97** and ethylenic **98** (Figure 14D). The ratio

between the quinoid and ethylenic form as estimated from LC-MS was 1.5:1 in acidic aqueous solution at 254 nm (Supplementary Figure 1). ^{1}H NMR measurements in CD_3CN showed a slightly shifted ratio of 3:1, indicating that also for this compound solvatochromic effects were important (Supplementary Figure 2).

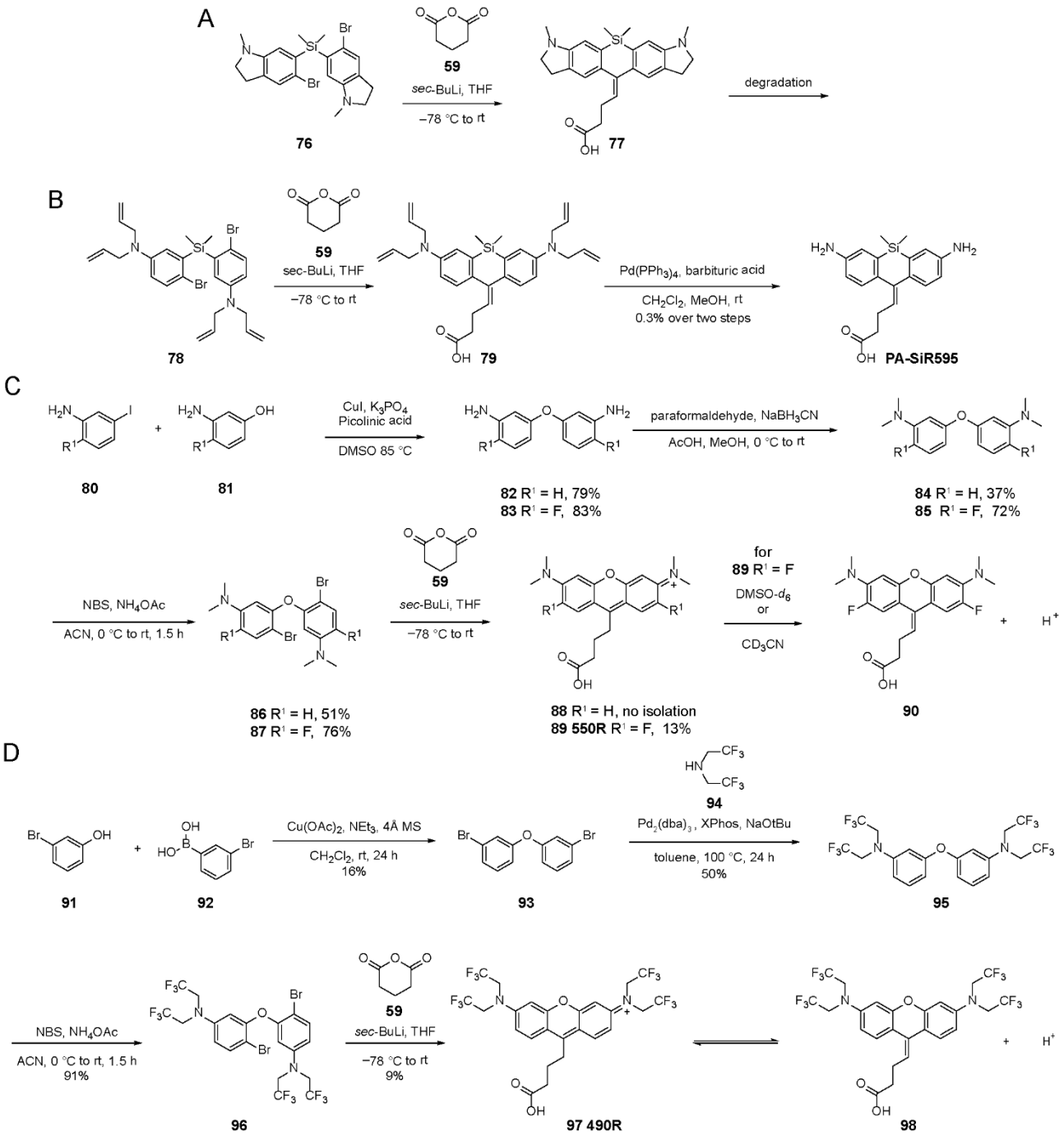

Figure 14: Synthetic strategies to access PA-SiRs with different colours. (A) Indoline substituted PA-SiR analogue **77** could be isolated but degraded rapidly. (B) Synthesis of PA-SiR595 via tetra-allyl-PA-SiR **79**. Precursor **78** was obtained from Dr. A. Salim. (C) Four-step synthesis to access two rhodamine derivatives, both led to isolation of the fluorescent quinoid product **88** and 550R **89**. However, compound 550R converted to ethylenic **90** in aprotic NMR solvents. Synthesis and characterization of compounds **83**, **85**, **87**, **89**, and **90** was performed by J. Notbohm. (D) Four-step synthesis via Lam-Chan-Evans coupling of arylboronic acid **92** with bromo-phenol **91** followed by Buchwald-Hartwig coupling of bis(2,2,2-trifluoroethyl)amine (**94**) with dibromide **93**. Finally, dibromination and closure of the xanthene core using glutaric anhydride (**59**) resulted in the isolation of an inseparable mixture of compounds 490R **97** and **98**. Synthesis and characterization was performed by J. Notbohm.

2.3 Characterisation of PA-SiR

PA-SiR **41** and its equilibria were extensively characterised and its properties experimentally investigated under various conditions. UV-Vis spectra of PA-SiR **41** in aqueous buffer confirmed that the two aromatic ring systems were not conjugated, as only a single absorbance maximum of $\lambda_{abs,\ max}$ = 290 nm was found (Figure 15A). NMR measurements of PA-SiR **41** and X-ray crystal structure analysis of PA-SiR analogue **62** corroborated the structure and position of the double bonds (Figure 15B, C and Material and Methods). Unfavourable steric interactions are reduced through the bent conformation of compound **62**. This further indicates that PA-SiRs are cross-conjugated π-systems, bearing two separate π-systems, one formed by the aniline and the extracyclic double bond and the other by the second aniline.

Upon UV irradiation in aqueous solution PA-SiR **41** underwent protonation as found by LC-MS studies in deuterated water (Figure 15D, E). Photoactivation is quantitative (φ_{act} = 13.3±2.3% at 340 nm (mean±sem, N = 3 samples)), which became clear when the conversion of PA-SiR **41** was examined by ^{1}H NMR (Figure 16). The photoproduct showed strong absorbance at $\lambda_{abs,\ max}$ = 646 nm and emitted around 660–670 nm, confirming the reestablishment of the fluorescent xanthene core (Figure 15A, B). The extinction coefficient and quantum yield of the photoproduct **42** were determined to be ε_{646} = 90,000±18,000 M^{-1} cm^{-1} and φ = 19.0±2.4% in aqueous buffer (mean±95% confidence interval, N = 3 and 4 samples respectively).

Photoproduct **42** was susceptible to nucleophilic attack, which led to rapid establishment of a secondary equilibrium with a half-life of about 1.5 min, as measured by UV-Vis spectroscopy (Figure 15F, G). In order to characterise the nature of the product(s) of the nucleophilic attack, NMR experiments in H_2O/D_2O were performed. While the detection of photoproduct **42** was not possible, these measurements clearly showed that only one product formed upon the subsequent nucleophilic attack. However, the assignment to the hydrolic **43** or spirolactone form **44** from the ^{1}H NMR experiments was challenging. As the protons of the hydroxyl or the carboxylic acid group exchanged with deuterium under the chosen conditions, few characteristic signals were present. However, ^{13}C NMR revealed a peak at 183.7 ppm characteristic of carboxylates whereas the carbonyl carbon in δ-valerolactone would show a chemical shift of 171.2 ppm.[215] The structure of the product of the nucleophilic attack was therefore unambiguously assigned to the hydrolic form **43** under the chosen conditions. Nevertheless, it might be possible that spirolactionisation becomes relevant in different pH regimes or for different analogues.

In addition, ^{1}H NMR experiment revealed that the equilibrium system was reversible on the time scale of days (Figure 16B). However, it is not clear from these experiments if this reversibility proceeds through k_{-2} and k_{-1} (approximately k_{-1}) or through an additional process k_5 linking **43** and **41** directly. Such a potential process is a 1,2-elimination of the hydroxy group directly re-establishing the exocyclic double bond. Similar processes are also known for succinylfluorescein **49**[194] and 1,1-bis[4-(dimethyl-amino)phenyl]-1-alkene (**51**).[196] The kinetic constant of this process was determined to be k_5 or k_{-1} = 9.9±1.8 · 10^{-6} s^{-1} (fit parameter±standard error of the fit; Supplementary Figure 3, Supplementary Table 3). In addition, ^{1}H NMR experiments at higher pH showed that the reversibility is pH dependent and is effectively suppressed at higher pH. This would support a back reaction via k_{-2} and k_{-1} as k_{-2} is especially disfavoured at higher pH (Section 2.4) but it does not exclude other unknown processes. Unfortunately, the pH range between 5 and 7 was not accessible for ^{1}H NMR measurements in H_2O/ D_2O as the compound was not soluble at the necessary concentrations (mM).

It should be noted that none of the experimental methods used to characterise the equilibrium so far (LC-MS, UV-VIS or NMR) allowed the identification of all four species at the same time under all relevant conditions. This complicated the unambiguous characterisation of the underlying equilibria. Nevertheless, UV-Vis measurements could give insights with respect to the formation of the coloured, fluorescent species, which was relevant for microscopy experiments. PA-SiR **41** as well as several of its analogues were therefore further characterised using UV-Vis spectroscopy (Section 2.4).

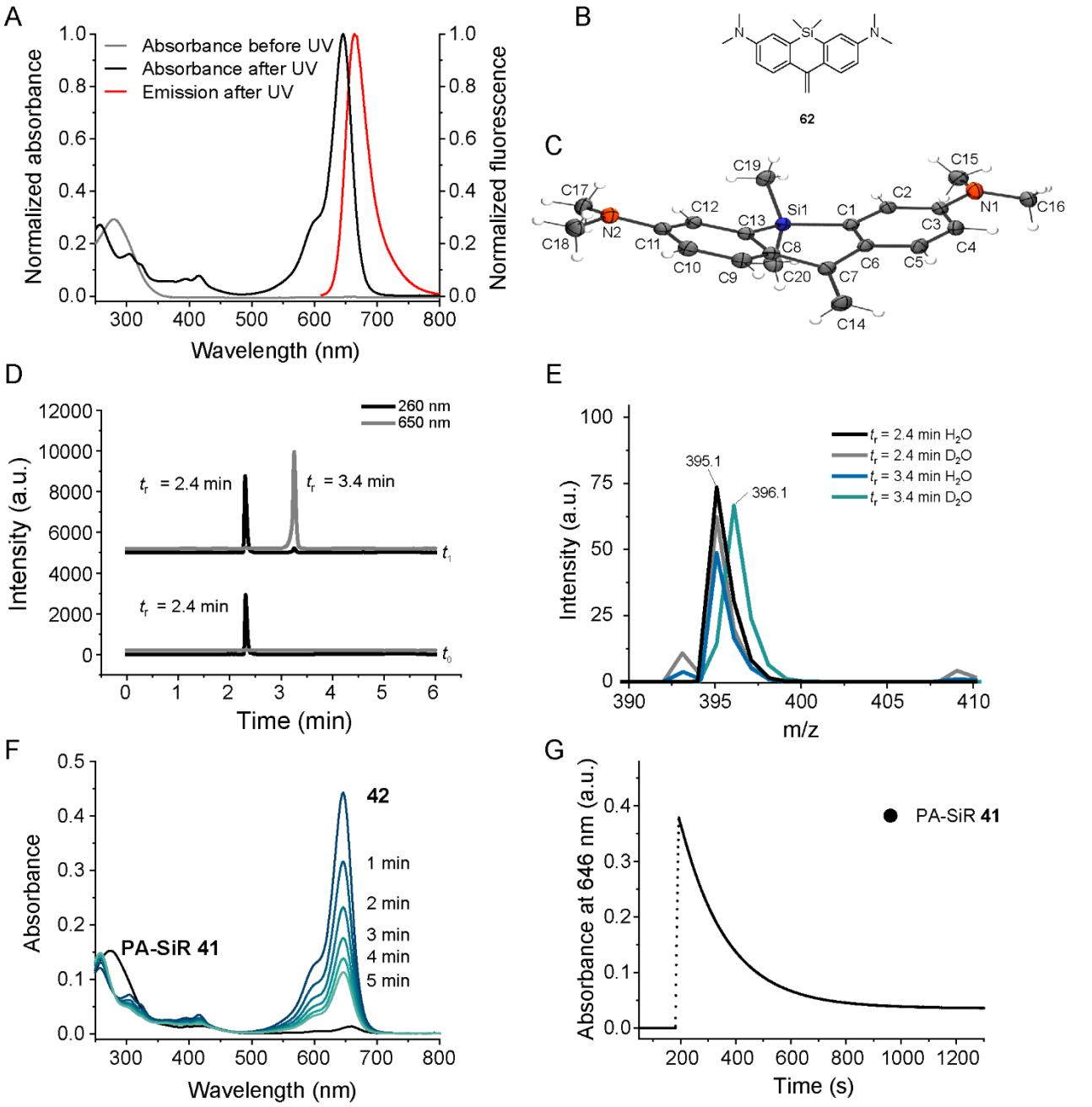

Figure 15: Characterisation of PA-SiR **41**. (A) UV-Vis and fluorescence spectra before and after UV-irradiation. (B) Structure of PA-SiR **62**. (C) X-ray crystal structure of PA-SiR **62** given is its Oak Ridge Thermal Ellipsoid Plot (ORTEP), arbitrary numbering. Atomic displacement parameters are drawn at 50% probability level. Selected bond lengths (Å) and torsion angles (°): C4-C5 1.380(2), C5-C6 1.3999(19), C6-C7 1.4896(19), C7-C8 1.4929(19), C7-C14 1.344(2), C1-C6-C7-C14 145.94(15), C5-C6-C7-C14 –31.9(2), C7-C8-C13-Si1 –2.91(17), C14-C7-C8-C9 33.4(2). The C7-C14 bond was the shortest bond confirming its double bond character. It is followed by the aromatic bonds exemplified by C4-C5 or C5-C6. Bonds C6-C7 and C7-C8 were considerably longer. Further information can be found in Supplementary Table 15. The X-ray crystal structure was determined by H. Haungs and H. Wadepohl. (D) LC-MS time traces before (t_0) and after (t_1) UV irradiation at two different wavelengths, showing the formation of a blue coloured product. (E) Mass analysis of the two peaks indicated in D when experiments were performed either in H_2O or D_2O. (F) UV-Vis spectra of PA-SiR **41** before, during and after photoactivation. (G) Time dependent absorbance measurements at 646 nm of PA-SiR **41** (10 µM) after brief excitation with UV light after 3 min.

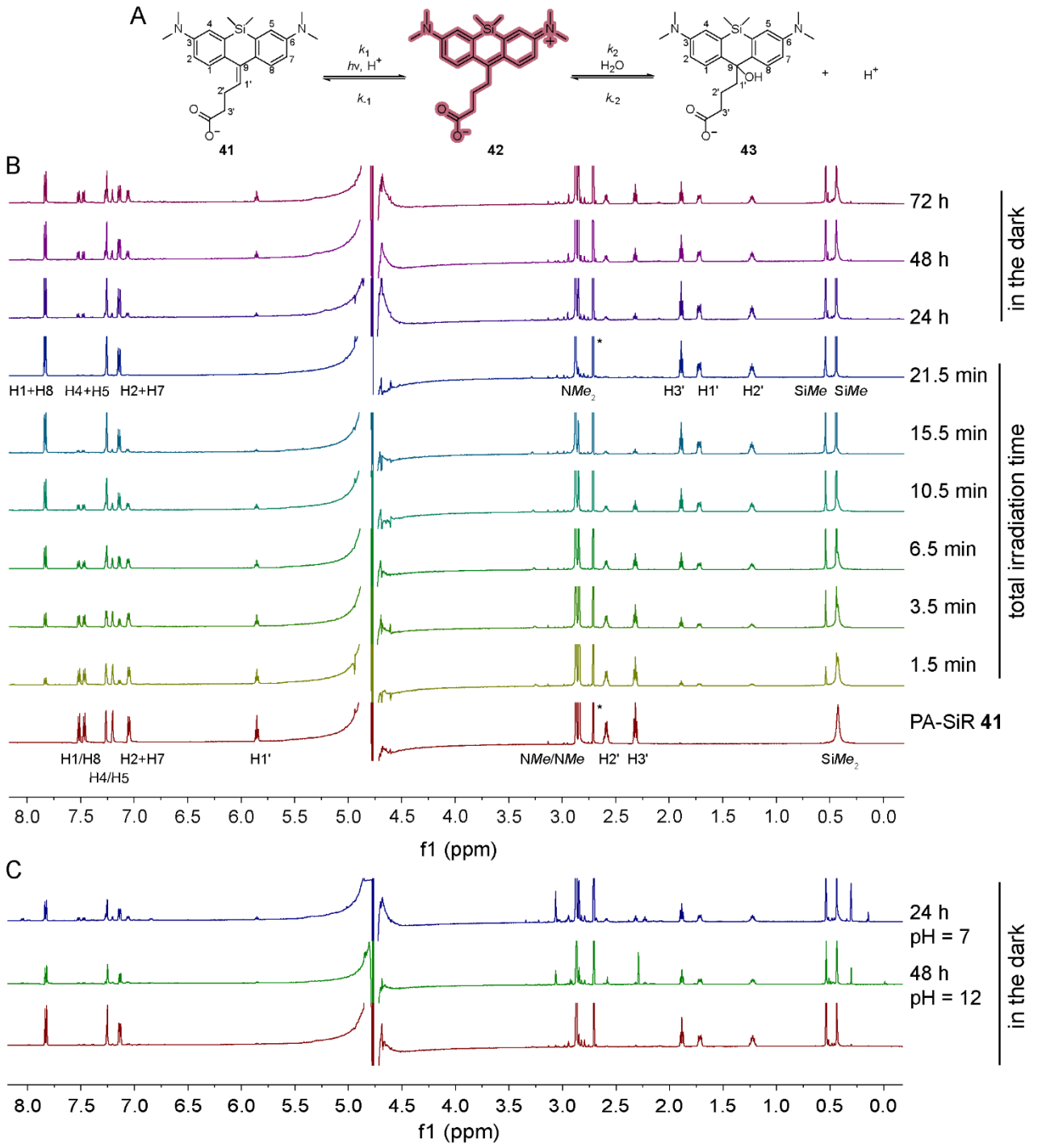

Figure 16: ^{1}H NMR analysis of the PA-SiR equilibrium. (A) Equilibrium system of PA-SiR. (B) ^{1}H NMR spectra of PA-SiR at distinct time points during photoactivation. Peak assignment of the spectra of PA-SiR **41** and of compound **43** after 21.5 min of irradiation: ^{1}H NMR (PA-SiR **41**, 600 MHz, H_2O + D_2O): δ 7.52 (d, J = 8.5 Hz, 1H; CH_{ar}), 7.46 (d, J = 8.5 Hz, 1H; CH_{ar}), 7.26 (d, J = 2.8 Hz, 1H; CH_{ar}), 7.20 (d, J = 2.8 Hz, 1H; CH_{ar}), 7.05 (dd, J = 8.5, 2.8 Hz, 2H; CH_{ar}), 5.85 (t, J = 7.4 Hz, 1H; C*H*), 2.87 (s, 6H; N*Me*), 2.84 (s, 6H; N*Me*), 2.71 (s, 2H; DMSO reference = *), 2.59 (q, J = 7.5 Hz, 2H; CH_2), 2.32 (t, J = 7.5 Hz, 2H; CH_2), 0.43 (s, 6H; SiMe_2); and ^{1}H NMR (21.5 min **43**, 600 MHz, H_2O + D_2O): δ 7.83 (d, J = 8.8 Hz, 2H; CH_{ar}), 7.26 (d, J = 2.8 Hz, 2H; CH_{ar}), 7.14 (dd, J = 8.9, 2.8 Hz, 2H; CH_{ar}), 2.87 (s, 12H; NMe_2), 2.71 (s, 3H; DMSO reference = *), 1.89 (t, J = 7.4 Hz, 2H; CH_2), 1.76 – 1.68 (m, 2H; CH_2), 1.31 – 1.17 (m, 2H; CH_2), 0.54 (s, 3H; Si*Me*), 0.44 (s, 3H; Si*Me*). Despite water suppression a residual H_2O signal was seen around 4.7 ppm. **42** was not detected under the chosen conditions (pH= 7–8). Over a time scale of days the photoactivation reaction was reversible as the peaks of PA-SiR **41** reappeared. (C) pH dependency of the reversibility of the photoactivation. At higher pH the photoactivation was not reversible anymore. Even after a fully converted sample was kept at pH = 12 for 48 h, no peaks of PA-SiR **41** were visible. However, changing the pH back to pH = 7 for further 24 h allowed for conversion back to PA-SiR **41**.

2.3.1 Computational analysis

In addition to the experimental characterisation of the equilibrium system, calculations of HOMO and LUMO were performed. As previously seen in its X-ray crystal structure, PA-SiR **62** was bent and showed two separate, cross-conjugated π-systems. Therefore, PA-SiR **62** was compared to the cross-conjugated model compound 1,1-bis[4-(dimethyl-amino)phenyl]-1-alkene (**51**). HOMO and LUMO were calculated for both compounds and it was found that both LUMOs showed major contributions from the exocyclic double bond whereas the HOMOs were located to the anilines (Figure 17B, C). A HOMO-LUMO transition as induced by light (photoactivation) would therefore lead to an intramolecular charge transfer from the aniline to the exocyclic double bond. Indeed such intramolecular charge transfers are known for 1,1-diphenylethenes in polar solvents and therefore also likely for PA-SiRs. Specifically, 1,1-diphenylethenes show TICT states, forming diradicals for which several resonance structures can be drawn. In contrast to the TICT states described for rhodamines, where the aniline twists, it is likely that the major contributions for PA-SiR **41** stem from resonance structures where the bond connecting C9 and C1' is rotated, releasing unfavourable steric interactions (Figure 17A). In addition, the alkyl radical is stabilised through H-bonding by the solvent. TICT is then followed by protonation of the excited state. A similar photoinduced protonation was reported for *N*-methyl-*N*-phenylamino-6-naphtalen derivatives (Supplementary Figure 4).[216,217] Further experimental and theoretical experiments are required to elucidate the mechanism fully.

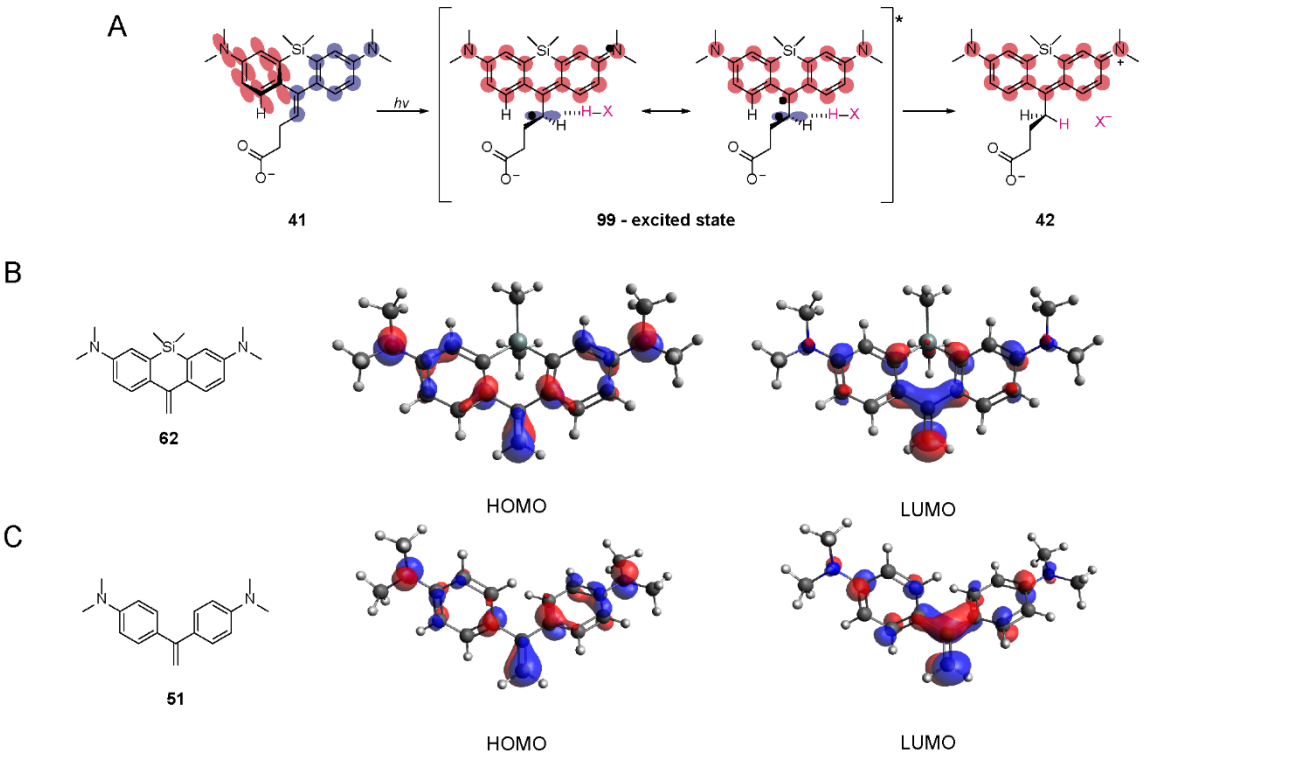

Figure 17: Possible photoactivation mechanism and calculations of HOMO and LUMO. (A) Possible photoactivation mechanism for PA-SiR **41**. Unfavourable steric interactions are minimised in the bent structure of PA-SiRs. They show two separate, cross-conjugated π-systems (indicated in red and purple), which become conjugated after irradiation with UV-light. In the diradical excited state **99** the bond connecting C9 and C1' is rotated, releasing steric constraints. Additionally, the alkyl radical on C1' is stabilised by solvent H-bonding. Electron transfer from the π-system to the alkyl radical and protonation gives the photoproduct **42**. (B) Calculated HOMO and LUMO (B3LYP/6-31G(d), only contributions bigger than 0.05 are shown) of model PA-SiR **62**, along with its structure. (C) Structure of model compound 1,1-bis[4-(dimethyl-amino)phenyl]-1-alkene (**51**) and its calculated HOMO and LUMO.

2.4 Equilibrium investigation by UV-Vis

The equilibrium system of PA-SiR **41** was best investigated by means of UV-Vis measurements. Specifically, the absorbance at 646 nm, corresponding to the formation of the photoproduct **42**, was followed. To this end, PA-SiR solutions were directly irradiated at 340 nm during the running UV-Vis experiment such that the increase in absorbance at 646 nm could be measured with the necessary temporal resolution. The obtained time dependent measurements were then analysed according to a generalised PA-SiR equilibrium system (Figure 18), because in several experiments nucleophilic attack by species other than H_2O might be relevant. The formed colourless species could not be distinguished by UV-Vis measurements at 646 nm and therefore universal kinetic constants (k_2 and k_{-2}) were used. Additionally, the second equilibrium was treated as pseudo-first order assuming that the nucleophile (H_2O among others) was present in excess. Accordingly, several different parameters were investigated A_{max}, A_{eq}, $A_{norm,\,eq}$, ΔA, k_1 and $k_{app} = k_2 + k_{-2}$ for different experiments. From these parameters the equilibrium and kinetic constants can be deduced (Figure 19A).

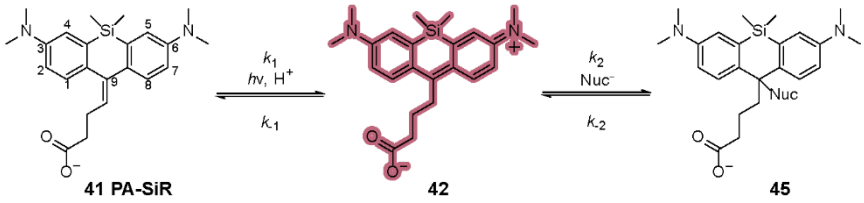

Figure 18: Simplified equilibrium system of PA-SiR as used for the UV-Vis analysis. Kinetic constants are indicated.

2.4.1 Light dependence of the PA-SiR equilibrium system

First of all, the influence of UV light was investigated in depth. Saturation experiments were performed irradiating PA-SiR **41** solutions until the maximum (A_{max}, Figure 19B, first section) and finally the equilibrium absorbance (A_{eq}) was reached (second section). Assuming that both the back reaction via k_{-1} and the second equilibrium (k_2 and k_{-2}) are negligible during photoactivation, the kinetic constant k_1 was found to be 19.4±0.4 s (mean±sd, N = 3 samples) when fitting the first section with a mono-exponential increase. It can be seen that irradiation for 12 s, which was chosen as ideal irradiation duration for all subsequent experiments, lay well within the linear range of the photoactivation. Furthermore, the contribution of the second equilibrium can be neglected during photoactivation, decoupling the photoactivation and the second equilibrium from each other (Figure 19C).

Interestingly the equilibrium established during irradiation (second and fourth section) was different from the one in absence of UV-irradiation (third section). More specifically the back-reaction ($k_{-2,UV} > k_{-2}$) was increased during irradiation whereas nucleophilic attack ($k_{2,\,UV} < k_2$) was decreased, indicating that the second equilibrium depends on UV-irradiation similarly to photochromic spiroamide derivatives (Section 1.5.4) or as reported for 1,1-bis[4-(dimethyl-amino)phenyl]-1-alkene (**51**).[196] The parameters fitted in the absence of UV-irradiation (k_2 and A_{eq}, third section) were additionally used to calculate the theoretical extinction coefficient of the photoproduct (Section 2.3).

The photochromic nature of the second equilibrium was additionally demonstrated in a fatigue experiment (Figure 19D). The total increase in absorbance (ΔA_{tot} = 1.089) calculated from the individual increases after each activation (ΔA_i) is higher than the theoretical absorbance of **42** at the concentration used (0.900) and demonstrates once more that the equilibrium between **42** and **43** is light dependent. This photochromism could be used as an additional handle to tune the density of fluorescent species in SMLM.

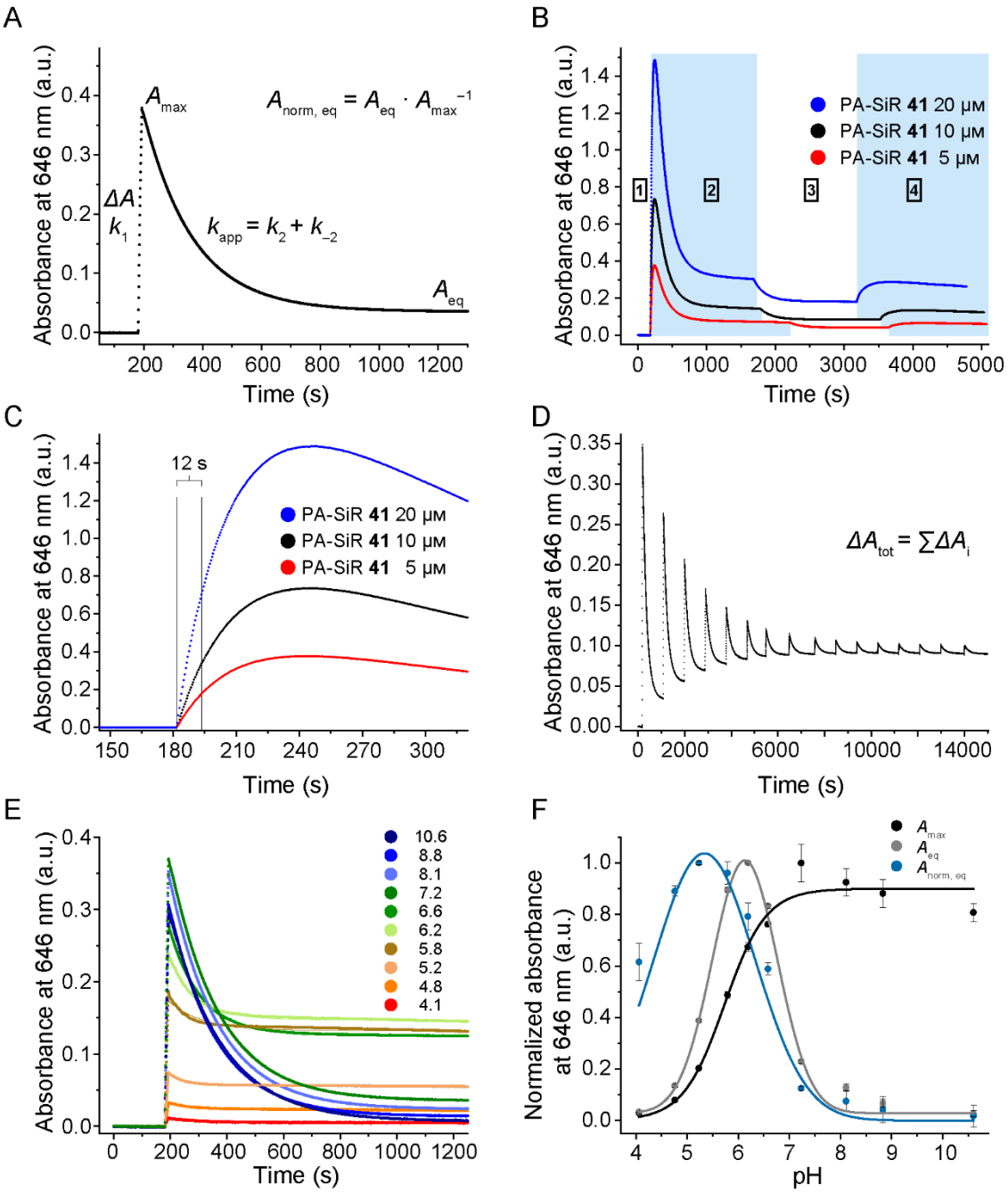

Figure 19: Influence of light and pH on the equilibrium system of PA-SiR **41**. (A) Exemple photoactivation experiment where a solution of PA-SiR **41** in PBS was irradiated (12 s, 340 nm) after 3 min in the dark. The change in absorbance at 646 nm was followed over time. The parameters extracted for the different experiments include: A_{max}, A_{eq}, $A_{norm, eq}$, ΔA, k_1 and $k_{app} = k_2 + k_{-2}$ as defined in the figure. (B) Saturation experiment of PA-SiR **41** solutions in PBS (5, 10 and 20 µM). During the first and second section (light blue colour), the samples were continuously irradiated with UV light. Irradiation was then discontinued for the third section and restarted for the fourth (light blue colour). (C) Zoom in, into the graph from B, showing the time range from 150–300 s. The range of the commonly used 12 s irradiation duration is indicated. (D) UV-Vis trace of repeated activation of PA-SiR **41** in PBS (10 µM). The increase in absorbance after each activation ΔA_i was calculated and summed up (ΔA_{tot}). After seven iterations the sum exceeds the theoretical absorbance of **42** and hence all PA-SiR **41** is converted to **42**. However, the absorbance still increases upon UV-irradiation demonstrating the photochromism of the second equilibrium. (E) Absorbance measurements over time for PA-SiR solutions in PBS (10 µM) at different pH (4.1–10.6). All traces were fitted with a mono-exponential decay function. However, curves measured at pH values between 6.6 and 4.8 show a bi-exponential decay and it is likely that under these conditions, the reaction k_{-1} becomes relevant. Nevertheless, the approximation considering the second equilibrium only (k_2 and k_{-2}) was made and the fitted parameters can be compared with each other. (F) Normalised absorbance values directly after activation (A_{max}), in equilibrium (A_{eq}), or in equilibrium normalised to A_{max} ($A_{norm, eq}$). Data is extracted from panel E and values displayed are means from three individual measurements, error bars correspond to 95% confidence intervals.

2.4.2 pH dependence of the PA-SiR equilibrium system

PA-SiR **41** was photoactivated in solutions at different pH values ranging from 4.1 to 10.6 and both the photoactivation as well as the secondary equilibrium were found to be pH dependent (Figure 19E, F). Photoactivation was most efficient above pH = 6 (A_{max}). Below this pH value, the aniline groups are protonated and prevent the photoactivation, as a doubly charged species (2^+) would be formed. The decay rates (k_{app}) were highest at high pH and lowest in the intermediary range between pH = 5–6 and hence the maximal absorbance in equilibrium normalised to A_{max} ($A_{norm,\ eq}$) was also between pH = 5–6. The maximal concentration of **42** in equilibrium was reached at pH = 6.1 (A_{eq}), where about 61% of the activated PA-SiR **41** was present as **42** ($A_{norm,\ eq}$). At physiological pH, however, only 10% of the activated PA-SiR **41** was fluorescent. This is of disadvantage for diffraction limited microscopy as only 10% of the initial fluorescence intensity would be detected after a few minutes. However, for SMLM this is less relevant as the detection period of single molecules is in the range of milliseconds. The reaction of **42** with nucleophiles should therefore not prevent SMLM but could even be beneficial as this dynamic equilibrium might show suitable kinetics (k_2 and k_{-2}) for spontaneous blinking. Even though the pK_{nuc} = 6.9 (pH at half maximal absorbance) of PA-SiR **41** was one unit higher than for HM-SiR **32** (pK_{cycl} = 5.8)[32] resulting in a higher density of fluorescent molecules, the proportion of molecules in the 'on' state could still be adjusted through the photoactivation, activating more or fewer molecules at a given time.

2.4.3 Influence of solvent polarity on the PA-SiR equilibrium system

The activation of PA-SiR **41** was also measured in four different solvent systems (30% organic solvent in PBS) with decreasing polarity (PBS > ACN > DMSO >1,4-dioxane).[218] Solvent polarity was found to have an effect on both photoactivation and the secondary equilibrium (Figure 20A). Generally, more polar solvents allowed for faster activation, assuming that the extinction coefficients of PA-SiR **41** were comparable in the different solvents. This might be due to better excited state stabilisation by polar solvents. ACN and PBS showed about 10% absorbance signal at equilibrium ($A_{norm,\ eq}$) compared to complete decay in DMSO and 1,4-dioxane. The decay kinetics on the other hand were fastest in DMSO and slowest in ACN or 1,4-dioxane and no clear trends could be made out. More data points and a full water-dioxane titration would be required to get further insight. However, the solvent dependence of both the activation and the secondary equilibrium complicates analysis and therefore it was decided to perform further experiments directly with the specific probes on their protein targets.

2.4.4 Influence of cysteamine on the PA-SiR equilibrium system

The influence of stronger nucleophiles than H_2O itself was also tested. Cysteamine was selected as a strong thiol based nucleophile, and because it is commonly used as a blinking additive in fixed-cell SMLM. Addition of only 1 mM cysteamine to a PA-SiR **41** solution in PBS led to no discernible activation (Figure 20B). At intermediary concentrations photoactivation was still visible followed by a slow decrease in absorbance. The rate of the nucleophilic attack at this concentration was likely to be as fast as the photoactivation and the equilibrium between **42** and **45** was therefore rapidly established and almost complete at the time when UV-irradiation was stopped. In addition, stepwise activation and addition of cysteamine was performed, revealing an effective concentration at which half maximal fluorescence intensity was reached (EC_{50}) of 0.192±0.019 mM (mean±95% confidence interval, N = 24 samples, Figure 24A).

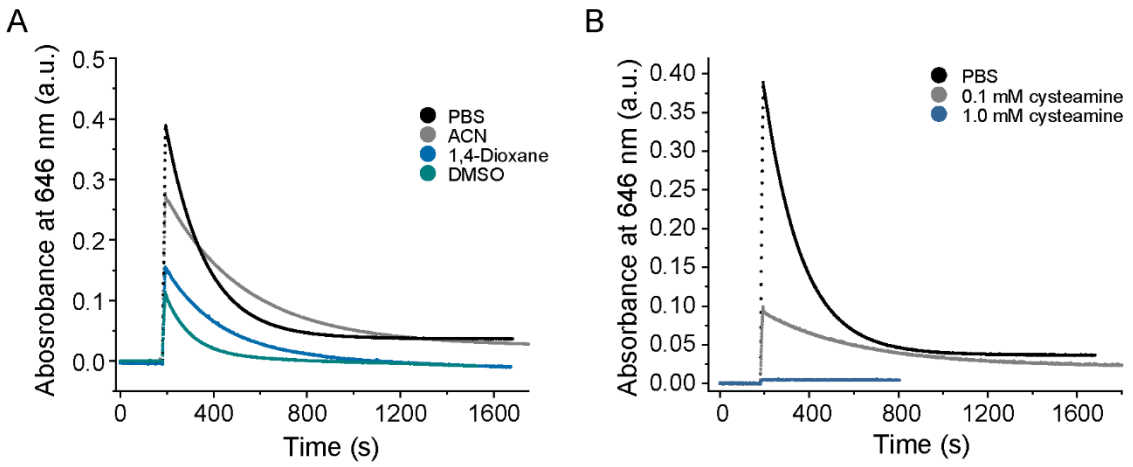

Figure 20: Influence of different environmental factors such as solvents and nucleophiles on the equilibrium system. (A) Absorbance measurements at 646 nm over time of PA-SiR **41** (10 µM) in different solvents (PBS, PBS/ACN 7:3, PBS/1,4-dioxane 7:3, PBS/DMSO 7:3). The activation and decay rates depend on the solvent mixture chosen. (B) Absorbance measurements at 646 nm over time of PA-SiR **41** solutions in PBS (10 µM) at different cysteamine concentrations. Already at 1 mM no activation was seen anymore. Under these conditions, the nucleophilic attack by cysteamine (k_2) became as fast as the photoactivation (k_1).

2.4.5 PA-SiR analogues

The photoactivation and equilibrium system of six out of the nine previously synthesised PA-SiR analogues were investigated (Figure 21). The introduced structural modifications clearly influenced the equilibrium system. First of all, analogues lacking the carboxylic acid (compounds **62** and **69**) showed disappearance of the absorbance at 646 nm after photoactivation. This confirmed that the reaction with H_2O dominated over the spirolactone formation, making the hydrol the major product of the nucleophilic attack of PA-SiRs at physiological pH. Nevertheless, for compounds PA-SiR-C3, **72** and **73** and in general for compounds bearing a carboxylic acid under different conditions (e.g. pH) it was not possible to exclude a contribution of spirolactonisation to the disappearance of the absorbance. NMR experiments would need to be performed under the relevant conditions in order to identify the involved species. However, this is not always possible due to the limited solubility of these compound in H_2O at the high concentrations required for NMR experiments.

Structural variations also lead to both faster and slower reaction rates (k_{app}) and changes in equilibria position (A_{eq} and $A_{norm,\,eq}$) compared to PA-SiR **41**. The introduction of the bulky ^{i}Pr substituents on the Si (compound **72**) decreased the reaction rate of the nucleophilic attack drastically and increased the percentage of the fluorescent form in equilibrium after photoactivation to 47%. This might be explained by steric and electronic reasons. The sterically demanding ^{i}Pr substituents of compound **72** could prevent nucleophilic attack to a certain degree. In comparison to PA-SiR **41** the antibonding Si-^{i}Pr σ* orbital is higher in energy and therefore also the LUMO of compound **72**, making it less electrophilic after activation.[152] Indeed, the calculated LUMO of the photoproduct of a simplified ^{i}Pr substituted PA-SiR (Supplementary Figure 4B) was higher in energy than the LUMO of the photoproduct of PA-SiR **62** (Supplementary Table 9). The decreased reactivity towards nucleophiles makes compound **72** an interesting candidate to develop photoactivatable probes for single-molecule tracking where long 'on'-times are required. On the other hand, fluorination of the xanthene core resulted in compound **73** which only showed an increase in absorbance after prolonged UV irradiation and always fully lost its absorbance in equilibrium. EWGs are assumed to increase the electrophilicity of the fluorescent form and therefore also its reactivity towards nucleophiles (k_{app}).

The different compounds also exhibited different A_{max} directly after photoactivation for 12 s. However, as all of them exhibited different extinction coefficients at 646 nm, direct comparison was not possible. The extinction coefficients were only determined for PA-SiR **41** and PA-SiR-C3 via saturation experiments (Supplementary Figure 6A). Normalisation of the signal of PA-SiR-C3 by its extinction coefficient to PA-SiR **41** showed that there were only small

differences in activation efficiency that were within the error of the extinction coefficient measurement (Supplementary Figure 6B).

Compounds **71**, **74**, and **75** were not available in sufficient amounts and only preliminary experiments were performed to confirm photoactivation (Supplementary Figure 6C, D) and additional experiments should be performed. Further characterisation should also be executed with rhodamine derivatives **90** and **98**. However, due to their equilibration of the quinoid and ethylenic form at room temperature UV-Vis measurements need to be combined with ^{1}H NMR experiments. Their behaviour in different solvent systems, especially in H_2O/D_2O, is of utmost interest and results from such experiments will enhance the understanding of their equilibrium systems. Measurements under UV irradiation should be used to inquire if the ethylenic forms show photoactivatble properties. Alternatively, the interconversion of the ethylenic and quinoid form could lead to ground state blinking, which should be tested in an *in vitro* single-molecule assay (Section 2.7).

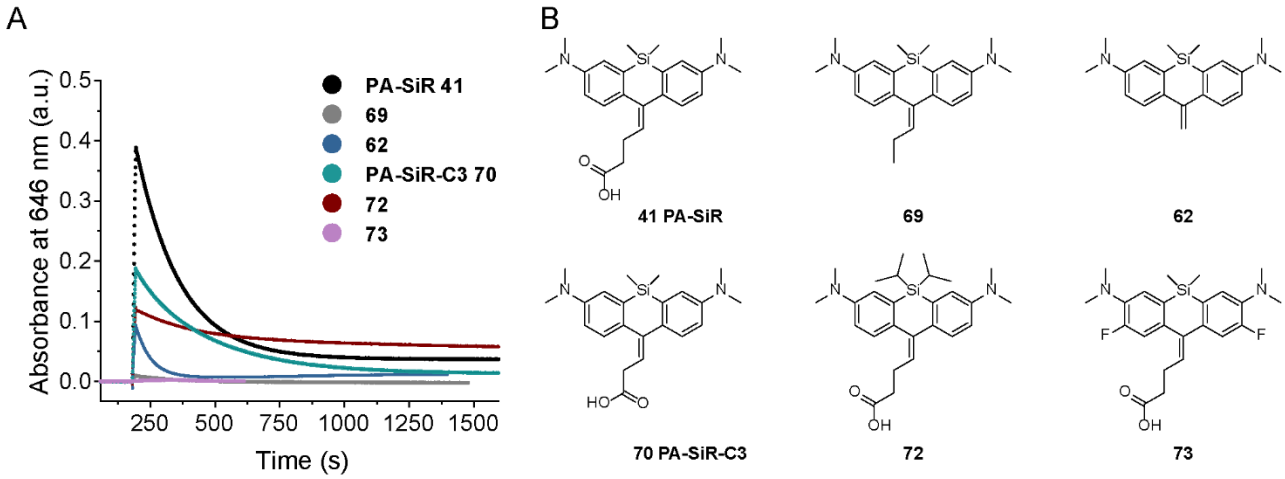

Figure 21: Photoactivation measurements of different PA-SiR analogues. (A) Time dependent absorbance measurements were performed at 646 nm in PBS solution (10 µM). (B) Structures of compounds **41**, **69**, **62**, **70**, **72**, and **73**.

2.5 Probe synthesis and characterisation

In order to test the use of PA-SiRs in combination with different labeling systems for live-cell applications, several probes were synthesised via amide coupling with the ligands for SNAP-tag and HaloTag as well as various targeting ligands (Figure 22 and Table 1). They were tested both *in vitro* and *in cellulo* and more detailed information about their synthesis is given in the Materials and Methods.

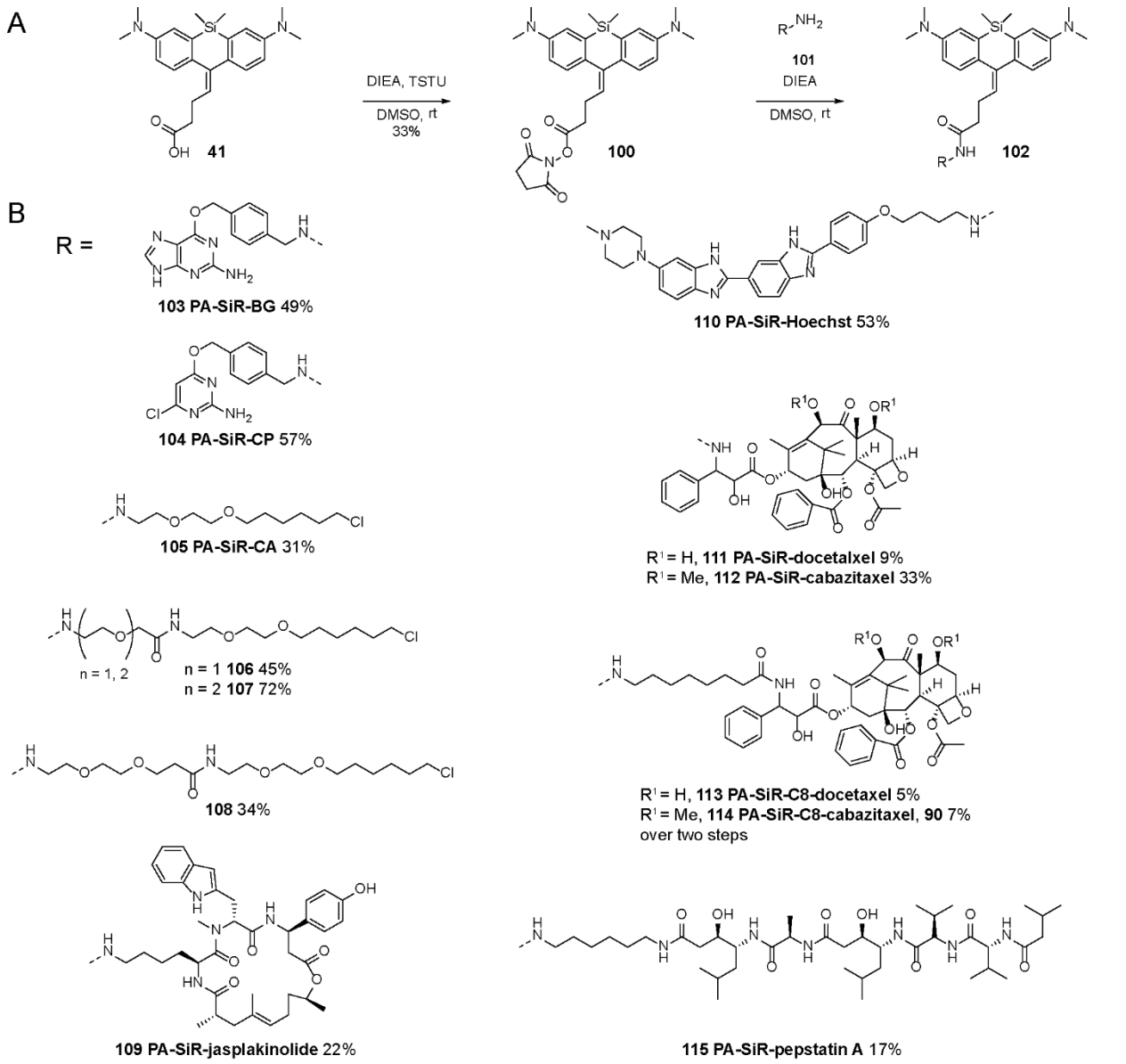

Figure 22: Synthetic route and structures of PA-SiR probes. (A) Synthesis of PA-SiR probes via amide coupling. In general, *N*,*N*,*N*',*N*'-tetramethyl-*O*-(*N*-succinimidyl)uroniumtetrafluorborat (TSTU) was used to activate the carboxylic acid of PA-SiR **41**, which was followed by addition of the ligands bearing an amino group (R-NH_2 **101**), unless otherwise stated. (B) Structures of all PA-SiR probes derived from PA-SiR **41**. Another three CA probes were synthesised starting from PA-SiRs with different substitutions (Table 1).

2.5.1 UV-Vis characterisation

To test the environmental sensitivity of several probes upon reaction or binding with their protein tag UV-Vis experiments were performed. Surprisingly, it was found that PA-SiR-CA conjugated to HaloTag was photoactivated efficiently and the photoproduct was stable over time ($A_{norm,eq}$ = 0.98). In contrast, if PA-SiR-CA was not attached to HaloTag it showed only modest activation and reacted quickly with nucleophiles (Figure 23A). The difference in the probes behaviour depending on conjugation with HaloTag is reminiscent of the fluorogenicity of SiR[117] and most likely increases the signal-to-background ratio in live-cell imaging as the unconjugated probe is non-fluorescent. Saturation experiments revealed an extinction coefficient of ε_{646} = 180,000±30,000 M^{-1} cm^{-1} and a fluorescence quantum yield of φ = 29.2±1.2% for the photoproduct in aqueous buffer (Figure 23C, mean±95% confidence interval, *N* = 3 samples). Additionally, the photoactivation showed a first order rate constant of k_1 = 28.24±1.99 s (mean±sd, *N* = 3 samples) and a quantum yield of activation of φ_{act} = 0.86±0.07% at 340 nm (mean±sem, *N* = 3 samples), which is comparable to PA-JF_{549}.[191]

Table 1: All synthesised and tested PA-SiR probes. Their properties *in vitro* are briefly summarised. N/D not determined N/A not applicable. $A_{norm,\,eq} = A_{max} \cdot A_{eq}^{-1}$ on the protein target and its **sd**, $A_{eq\text{-}target}\,A_{eq\text{-}BSA}^{-1}$ and its **sd**.

Probe	PA-SiR	Linker	Ligand	$A_{norm,\,eq}$ ± sd	$A_{eq\text{-}target} \cdot A_{eq\text{-}BSA}^{-1}$ ± sd
PA-SiR-BG 103	PA-SiR	-	BG-NH_2	0.73±0.26	11±7
PA-SiR-CP 104	PA-SiR	-	CP-NH_2	N/D	N/D
PA-SiR-CA 105	PA-SiR	-	CA-NH_2	0.98±0.03	102±30
106	PA-SiR	PEG-1-CH_2	CA-NH_2	0.65±0.12	12.1±2.0
107	PA-SiR	PEG-2-CH_2	CA-NH_2	0.68±0.14	3.8±0.8
108	PA-SiR	PEG-2-CH_2CH_2	CA-NH_2	N/D	N/D
PA-SiR-jasplakinolide 109	PA-SiR	-	Jasplakinolide	0.06±0.05	N/A
PA-SiR-Hoechst 110	PA-SiR	C4	Hoechst	N/D	N/D
PA-SiR-docetaxel 111	PA-SiR	-	Docetaxel	N/D	N/D
PA-SiR-cabazitaxel 112	PA-SiR	-	Cabazitaxel	N/D	N/D
PA-SiR-C8-docetaxel 113	PA-SiR	C8	Docetaxel	N/D	N/D
PA-SiR-C8-cabazitaxel 114	PA-SiR	C8	Cabazitaxel	N/D	N/D
PA-SiR-pepstatin A 115	PA-SiR	C6	Pepstatin A	N/D	N/D
PA-SiR-C3-CA 116	PA-SiR-C3	-	CA-NH_2	0.60±0.02	N/A
117	**72**	-	CA-NH_2	N/D	N/D
118	**73**	-	CA-NH_2	N/D	N/D

In order, to better understand the remarkable characteristics of PA-SiR-CA, derivatives with different linker lengths (compounds **106**, **107**, and PA-SiR-C3-CA) were tested (Figure 23B). Longer linkers did not affect the stability gained upon activation when conjugated to HaloTag (compounds **106** and **107**). However, the fluorogenicity (BSA vs. HaloTag) was substantially decreased as both the conjugated and unconjugated probes activated similarly. This was on one hand due to a decreased activation of the conjugated probe but also due to an increase of activation of the unconjugated probe, which might be mediated through the PEG linker changing the local environment of the unconjugated probe in solution. Shortening the alkyl chain (PA-SiR-C3-CA) partially retained the difference in activation of the conjugated compared to the unconjugated probe. The probe was stable over time but very fast initial decay kinetics were observed, diminishing $A_{norm,eq}$ = 0.60 as compared to PA-SiR-CA (0.98). In addition, PA-SiR-C3-CA exhibited a smaller extinction coefficient of ε_{646} = 15,000±3,000 M^{-1} cm^{-1}, making it less suitable for microscopy than PA-SiR-CA (Figure 23A, D). Taken together, this highlights that the proximity and positioning of the fluorophore on the protein-tag, and therefore the specific microenvironment is crucial for its photophysical properties. HaloTag was evolved using TMR-CA as a ligand[97] and it is therefore likely that it forms specific interactions with the open, fluorescent form of rhodamines and hence the activated probe. Unfortunately, none of the attempts to co-crystallise PA-SiR-CA on HaloTag either in the photoactivatable or the activated form yielded suitable protein crystals for X-ray analysis. A crystal structure of HaloTag-TMR-CA was available and will be further discussed (Chapter 3).

PA-SiR-BG also showed increased stability after photoactivation, albeit to a lesser degree than PA-SiR-CA (Figure 23E). In both conditions, conjugated as well as unconjugated, the activated PA-SiR-BG was initially attacked by nucleophiles. The equilibrium of conjugated PA-SiR-BG was shifted more toward the photoproduct than the unconjugated probe showing a higher $A_{norm,eq}$ (0.73 vs. 0.18). This also renders PA-SiR-BG fluorogenic, though to a lesser degree than PA-SiR-CA. PA-SiR-jasplakinolide only activated in the presence of F-actin but still decayed over time (Figure 23F). However, due to the non-covalent nature of the jasplakinolide-F-actin bond it was unclear if the decrease in absorbance was due to unbinding of the probe and decay in free solution or nucleophilic attack to the bound probe. In general, probes which show normalised absorbance values in equilibrium below $A_{norm,eq}$ = 0.9, translating to a slight shift of the equilibrium away from the fluorescent form, might exhibit spontaneous blinking albeit with rather high 'on'-times.

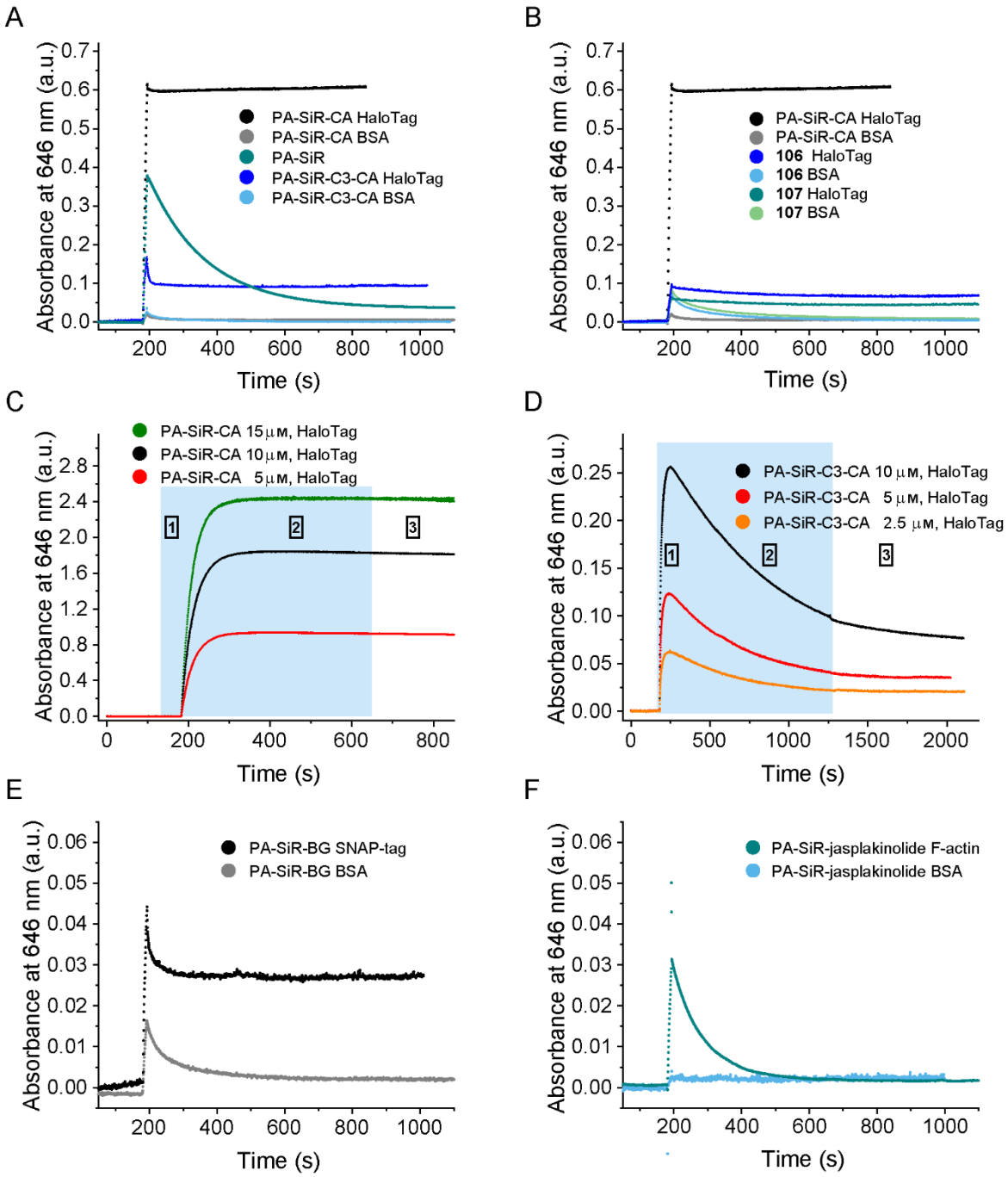

Figure 23: UV-Vis characterisation of different probes. (A-B) Time dependent absorbance measurements for different PA-SiR-CA analogous (10 µM) with addition of BSA or HaloTag (20 µM). (C-D) Saturation experiments of PA-SiR-CA and PA-SiR-C3-CA on HaloTag. During the first and second section the samples were continuously irradiated with UV-light (light blue colour). The light source was then switched off during the third section. (E) Time dependent absorbance measurements at 646 nm for PA-SiR-BG (10 µM) in the presence of BSA or SNAP-tag (20 µM). (F) Absorbance measurements over time for PA-SiR-jasplakinolide (10 µM) in the presence of BSA or F-actin.

2.5.2 Influence of cysteamine on the equilibrium system of HaloTag probes

The behaviour of PA-SiR-CA and PA-SiR-C3-CA conjugated to HaloTag towards addition of cysteamine, commonly used in fixed-cell SMLM, was assessed as for PA-SiR **41** (Section 2.4.4). Indeed, the conjugated probes showed greater stability toward cysteamine (Figure 24A). The EC_{50} for PA-SiR-CA was 16-fold and for PA-SiR-C3-CA 3-fold higher than for PA-SiR **41**. Additionally, the reversibility of the reaction with cysteamine was demonstrated using a thiol scavenger (maleimide) that irreversibly reacts with cysteamine and rescued the absorbance (Figure 24B). In respect to SMLM experiments, care has to be taken when using PA-SiR-CA in combination with fluorophores requiring thiol addition. Choosing the appropriate concentration is crucial and depends on the effect that should be achieved.

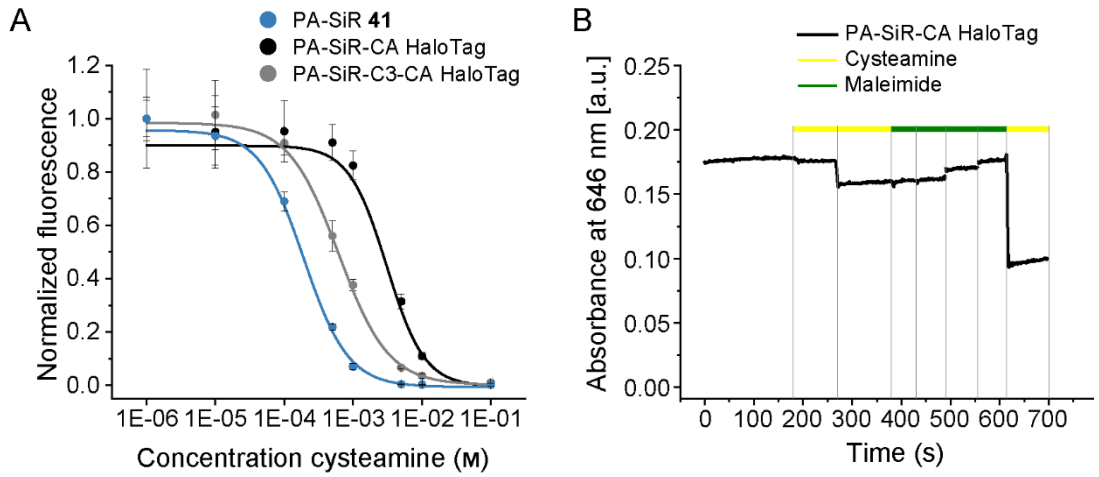

Figure 24: Reaction with cysteamine of PA-SiR analogues after photoactivation. (A) Equilibrium fluorescence intensity of fully activated PA-SiR **41**, PA-SiR-CA, and PA-SiR-C3-CA (1 µM) reacted with HaloTag (2 µM). The absorbance decreased upon addition of cysteamine (0.001–100 mM) and the EC_{50} for the three compounds were determined to be 0.192±0.019 mM for PA-SiR **41**, 3.1±0.5 mM for PA-SiR-CA conjugated to HaloTag, and 0.62±0.06 mM for PA-SiR-C3-CA conjugated to HaloTag (mean±95% confidence interval, all *N* = 24 samples, error bars correspond to 95% confidence intervals). (B) Absorbance measurements upon addition of cysteamine and maleimide to a fully activated solution of PA-SiR-CA reacted with HaloTag. The nucleophilic attack by cysteamine is reversible and the absorbance is reinstalled after quenching the cysteamine with maleimide. Final cysteamine concentrations in solution: 10 µM (180 s), 110 µM (270 s), and 1.11 mM (610 s). Final maleimide concentrations in solution: 100 µM (380 s), 200 µM (430 s), 700 µM (500 s), and 1.2 mM (560 s).

2.6 Widefield and confocal live-cell microscopy

PA-SiR-CA was tested for its behaviour in live-cell microscopy. U-2 OS cells expressing histone H2B-Halo were incubated with the probe (0.5 µM, 2 h) and imaged before and after UV activation on either a widefield or a scanning-confocal microscope (Figure 25A-D). PA-SiR-CA showed good cell membrane permeability under the chosen conditions as well as a clear and stable fluorescence signal with good selectivity for the nucleus after brief activation (Figure 26A, C). The signal-to-background ratio upon activation, representing the fluorogenicity of the fluorophore *in cellulo*, was found to be 32±5 (mean±95% confidence interval, *N* = 119 cells) under no wash conditions and was later compared to other probes (*vide infra*).

Motivated by this excellent results, different CA probes (compounds **106**, **107**, **108**, **117**, and **118**) were tested under similar conditions on the scanning-confocal setup (0.5 µM, 3 h, 1 wash). Probes bearing PEG linkers (**106**, **107**, and **108**; Figure 25G, H, and I) showed good localisation to the nucleus but the signal obtained was only marginally over the background signal and therefore much lower than for PA-SiR-CA (Figure 25E, F), as expected from the *in vitro* experiments. ^{i}Pr substituted CA probe **117** did not specifically localise to the nucleus but rather to mitochondria, making it inutile for live-cell imaging (Figure 25J). The fluorine substituted probe **118**, on the other hand, localised to the nucleus and a weak signal could be observed when using the appropriate imaging conditions (Figure 25K). In a later experiment PA-SiR-C3-CA was also measured on the same setup, albeit with different imaging parameters and a

modified labeling protocol (0.25 µM, 1 h, no wash) and therefore the images cannot be directly compared (Figure 25L). PA-SiR-C3-CA showed good signal from the nucleus but relatively high background signal from the surrounding, which resulted in a lower signal-to-background ratio 6.8±0.9 (*N* = 86 cells) than PA-SiR-CA (Figure 26C).

Additionally, PA-SiR-BG and PA-SiR-CP were tested in U-2 OS cells expressing histone H2B-SNAP and imaged as previously described by confocal microscopy (Figure 25M, N). However, both showed much lower staining specificity than PA-SiR-CA, with a signal-to-background ratio for PA-SiR-BG of 4.1±0.4 (*N* = 82 cells, Figure 26D). Additionally, the signal of PA-SiR-BG was found to decay over time as measured by widefield microscopy (Figure 26A).

PA-SiR-CA clearly showed the most suitable properties for live-cell imaging and was therefore used to image several other target proteins such as Cep41-Halo, LifeAct-Halo, and TOMM20-Halo visualizing microtubules, F-actin, and mitochondria respectively (Figure 25O, P, Supplementary Figure 7G, H).

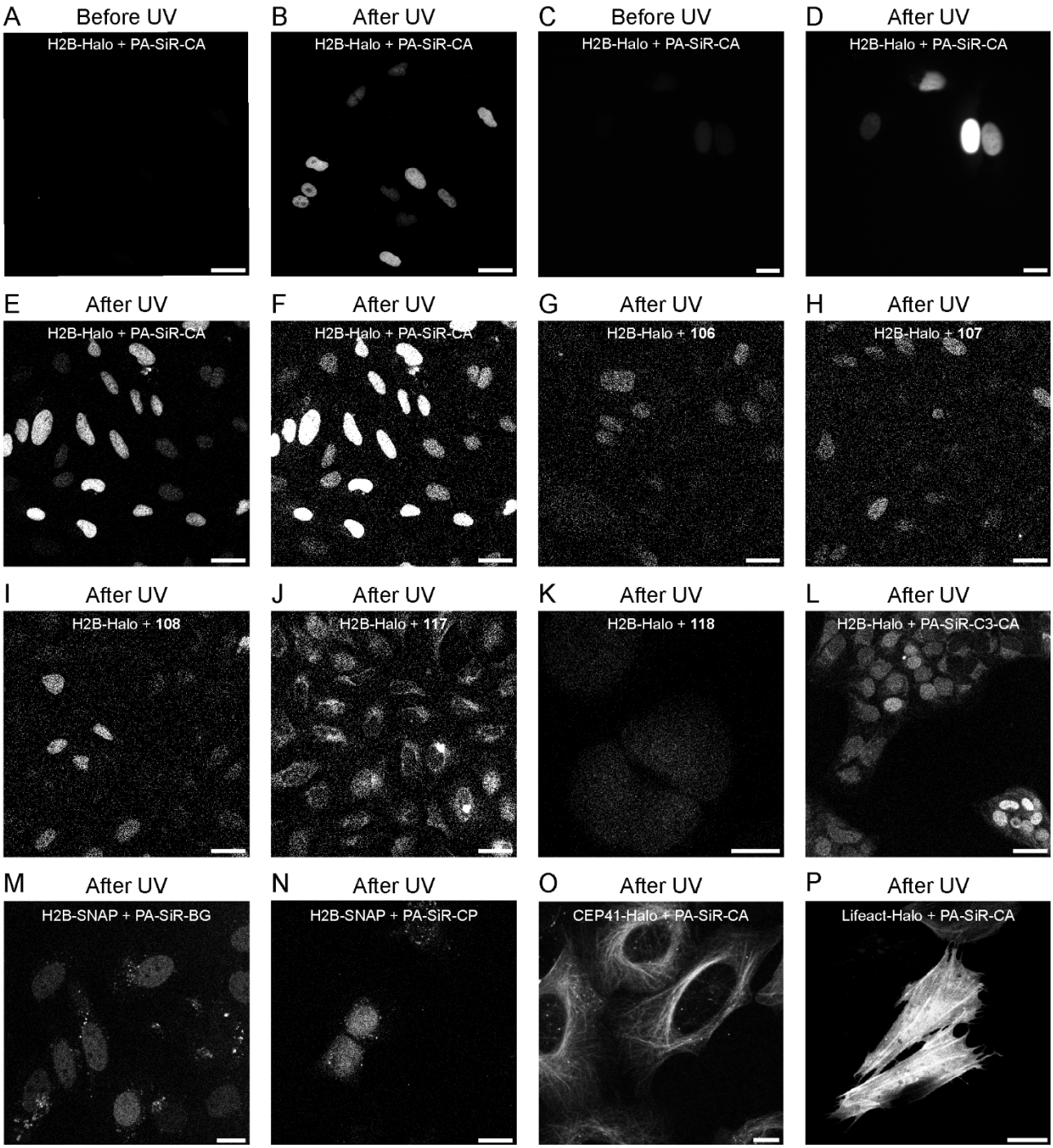

Figure 25: Live-cell microscopy images of PA-SiR probes in combination with self-labeling protein tags. (A-B) U-2 OS cells expressing H2B-Halo (nucleus) stained with PA-SiR-CA (0.5 µM, 2 h) imaged by confocal microscopy before (A) and after activation (B) using a 355 nm laser for photoactivation. Maximum projections of z-stacks are displayed. Scale bars, 40 µm. (C-D) Widefield microscopy image of U-2 OS cells expressing H2B-Halo (nucleus) stained with PA-SiR-CA (0.5 µM, 2 h) before (C) and after (D) activation with the DAPI channel (430/35 nm). Scale bars, 40 µm. (E-K) Confocal microscopy images of U-2 OS cells expressing H2B-Halo (nucleus) stained with various CA probes (0.5 µM, 3 h) after activation: (E) PA-SiR-CA, contrast settings optimised for the strong signal. (F) PA-SiR-CA, contrast adjusted for weaker signals and the same in all subsequent images. (G) Compound **106**. (H) Compound **107**. (I) Compound **108**. (J) Compound **117**. (K) Compound **118**, with adjusted imaging and contrast parameters. Scale bars, 40 µm except (K) 10 µm. (L) Confocal microscopy images of U-2 OS cells expressing H2B-Halo (nucleus) stained with PA-SiR-C3-CA (0.25 µM, 1 h) after activation with a 355 nm laser. Scale bar, 40 µm. (M-N) Confocal microscopy images of U-2 OS cells expressing H2B-SNAP (nucleus) stained with PA-SiR-SNAP (0.25 µM, 1 h, M) or PA-SiR-CP (0.5 µM, 3 h, N) after activation with a 355 nm laser. Scale bars, 20 µm. (O-P) Confocal microscopy images of U-2 OS cells expressing Cep41-Halo (microtubules, O) or LifeAct-Halo (F-actin, P) stained with PA-SiR-CA (0.5 µM, 1.5 h). Scale bars, 10 µm and 20 µm, respectively.

In addition, the properties of PA-SiR-CA were further characterised and compared to the only other available photoactivatable fluorophore for live-cell microscopy in the far-red: PA-JF$_{646}$-CA.[191] The stability of the fluorescence signal after activation of the two were comparable, whereas PA-JF$_{646}$-CA showed faster activation kinetics, which might be due to a higher quantum yield of photoactivation. However, PA-SiR-CA showed a 14-fold turn-on upon complete photoactivation compared to a 3.5-fold turn-on for PA-JF$_{646}$-CA. The signal-to-background ratios were measured for both SNAP-tag and HaloTag based probes and compared to the non-activatable analogues SiR-BG and SiR-CA. PA-SiR-CA showed a signal-to-background ratio 2.4 times higher than PA-JF$_{646}$-CA and was comparable to HM-SiR. As previously mentioned both PA-SiR-C3-CA and PA-SiR-BG showed lower values between 4 and 7 and are therefore less suitable for live-cell imaging.

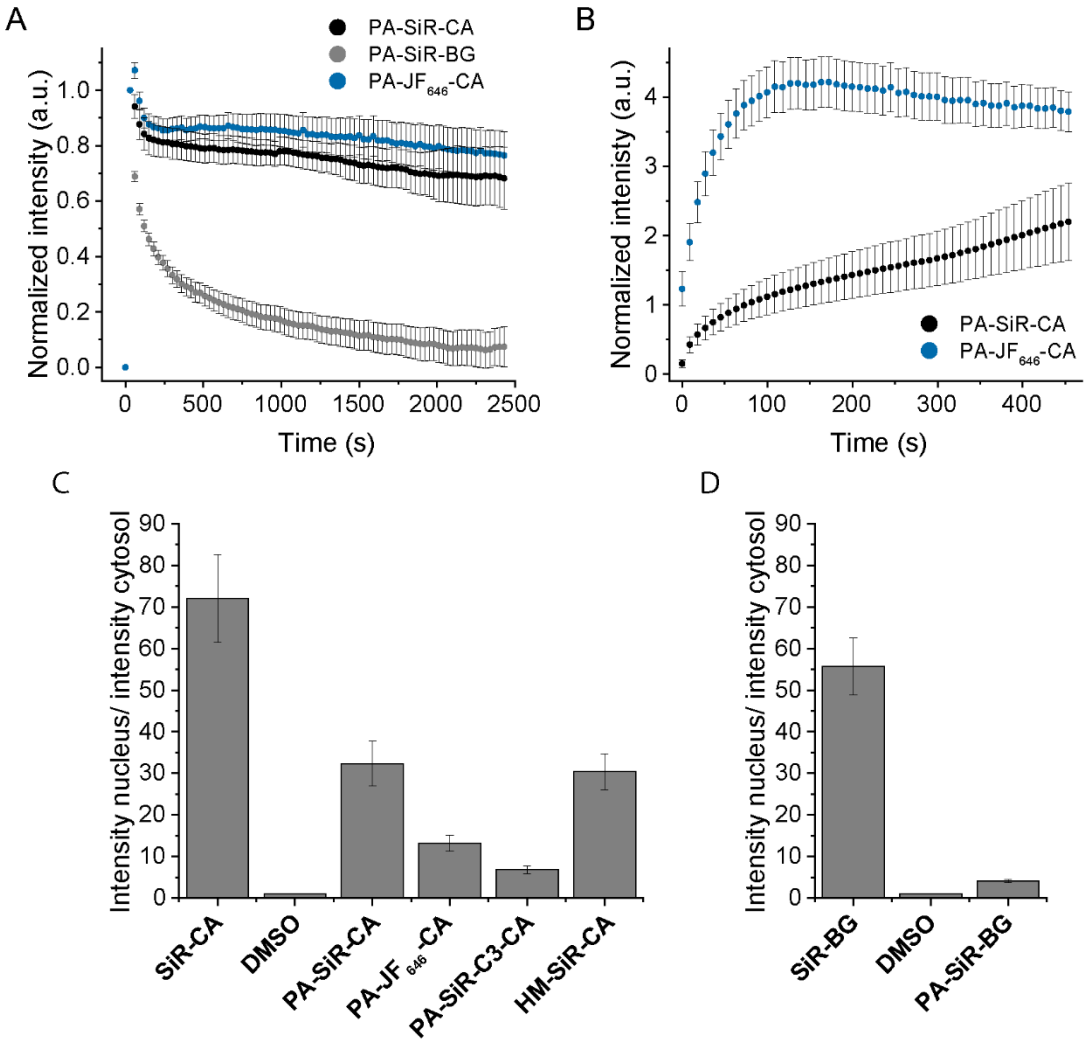

Figure 26: Quantification of live-cell microscopy. (A) Time dependent widefield microscopy measurements of the fluorescence signal of PA-SiR-CA and PA-JF$_{646}$-CA localised to H2B-Halo in U-2 OS cells after a single photoactivation pulse (mean±95% confidence interval, *N* = 30 cells for PA-SiR-CA and 70 cells for PA-JF$_{646}$-CA). (B) Time dependent widefield microscopy measurements during repeated photoactivation of PA-SiR-CA and PA-JF$_{646}$-CA in U-2 OS cells expressing H2B-Halo (0.5 µM, 2 h, mean±95% confidence interval, *N* = 26 cells for PA-SiR-CA, *N* = 54 cells for PA-JF646-CA). (C-D) Signal-to-background measurements for CA probes (C) and BG probes (D) performed in U-2 OS cells expressing H2B-Halo-T2A-EGFP or H2B-SNAP-T2A-EGFP stained with the respective probes (250 nm, 1 h) and imaged by confocal microscopy (mean±95% confidence interval): SiR-CA (72±11, *N* = 135 cells), DMSO (1.04±0.07, *N* = 126 cells), PA-SiR-CA (32±5, *N* = 119 cells), PA-JF646-CA (13.2±1.9, *N* = 121 cells), PA-SiR-C3-CA (6.8±0.9, *N* = 86 cells), HM-SiR-CA (30±4, *N* = 123 cells), SiR-BG (56±7, *N* = 117 cells), DMSO (1.03±0.10, *N* = 129 cells), PA-SiR-BG (4.1±0.4, *N* = 82 cells), all after activation.

2.6.1 Transfection free probes

Different probes based on targeting ligands were tested for their cell-permeability in HeLa or U-2 OS cells. The PA-SiR-jasplakinolide probe worked especially well and allowed the visualisation of the F-actin network upon activation (Figure 27A, B). PA-SiR-Hoechst specifically stained DNA in the nucleus but photoactivation required longer UV-irradiation (Figure 27C, D). This might be due to a decreased photoactivation quantum yield as absorbance of UV-light by the PA-SiR moiety inducing photoactivation competes with absorbance followed by fluorescence of the Hoechst part. PA-SiR-pepstatin A targeting cathepsin D located in lysosomes showed many vesicular structures corresponding to lysosomes upon photoactivation (Figure 27E, F). Several tubulin staining probes were synthesised based on docetaxel and cabazitaxel with or without a C8 linker in between the targeting ligand and PA-SiR. The C8-docetaxel probe showed (Figure 27G, H) more specific staining than the docetaxel probe without a linker, which predominantly showed unspecific staining. However, for the cabazitaxel based probes no linker resulted in better staining of microtubules than C8-cabazitaxel (Supplementary Figure 7). Comparing C8-docetaxel to the cabazitaxel probe was difficult and further co-localisation experiments are required to select the best candidate.

The fluorescence signal of the PA-SiR-jasplakinolide and the microtubule probes decayed over time and obtaining these images was only possible using line-scanning instead of frame-wise activation/read-out as used for PA-SiR-CA. The signals of PA-SiR-Hoechst and PA-SiR-pepstatin A were more stable over time. Further *in vitro* experiments would be required to quantify the extent of these effects. In the case of PA-SiR-pepstatin A the pH of lysosomes (around 5) influences the signal favourably, as the highest signal $A_{norm,eq}$ and the lowest kinetic constants k_{2app} were observed in this range for the parent PA-SiR **41**.

Two other probes targeting the Golgi and ER via a ceramide and the plasma membrane via a C16 alky chain were synthesised but did either not activate or localise to the desired target.

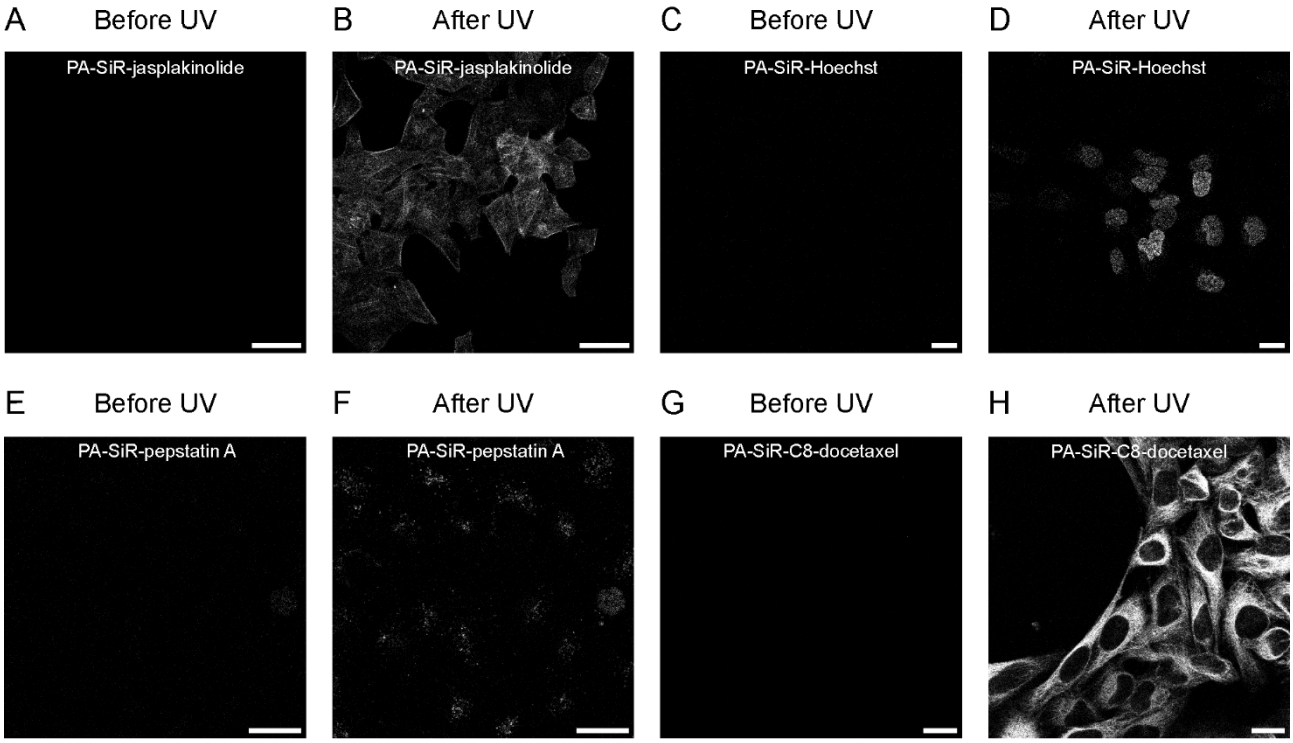

Figure 27: Confocal microscopy images of HeLa and U-2 OS cells stained with several different transfection free probes. (A-B) HeLa cells stained with PA-SiR-jasplakinolide (1 µM, 1.5 h) before (A) and after (B) photoactivation revealing F-actin. Scale bars, 40 µm. (C-D) HeLa cells stained with PA-SiR-Hoechst (1 µM, 1 h). Images were taken before (C) and after (D) UV irradiation using the 355 nm laser of the confocal microscope. Scale bars, 20 µm. (E-F) Confocal images of U-2 OS cells stained with PA-SiR-pepstatin A (1 µM, 1 h). Images shown before (E) and after (F) UV irradiation at 355 nm. Scale bars, 20 µm. (G-H) U-2 OS cells stained with PA-SiR-C8-docetaxel (1 µM, 2 h) before (G) and after (H) photoactivation. Scale bars, 20 µm.

2.7 *In vitro* single-molecule experiments

In order to characterise the three most promising probes for self-labeling protein tags (PA-SiR-CA, PA-SiR-C3-CA, and PA-SiR-BG) an *in vitro* single-molecule assay was established. A small flow channel was assembled using clean, PEG-coated coverslips that were sparsely functionalised with PEG-biotin. A solution containing streptavidin was flowed through the channel followed by a solution of doubly labeled SNAP:EGFP:Halo protein. One self-labeling protein tag was labeled with a biotin handle and the other with the fluorophore of interest. The immobilised but well separated fluorophores were then imaged by total-internal reflection fluorescence (TIRF) microscopy at 642 nm using 405 nm for photoactivation. The fluorophores could therefore be investigated directly bound to the relevant self-labeling protein tag and upon addition of different buffer systems, if necessary (Figure 28A).

The numbers of photons per particle per frame were analysed first, as they determine the localisation precision. These numbers depend on the laser power and were therefore measured in two relevant regimes. At lower power densities (1.2 kW cm^{-2}) relevant for live-cell measurements PA-SiR-CA (668, 518; mean, median; *N* = 170171 localisations) showed photon numbers about 30% higher than both PA-SiR-C3-CA (497, 348; *N* = 43787 localisations) and PA-JF_{646}-CA (474, 414; *N* = 339443 localisations) and about two-fold higher than PA-SiR-BG (380, 244; *N* = 9674 localisations). The fluorescent protein mEOS3.2, which is commonly used in live-cell single-particle tracking experiments and for live-cell SMLM, showed considerably lower numbers (187, 132; *N* = 123045 localisations) as expected from literature (Figure 28B). At a higher power density (4.2 kW cm^{-2}) used for fixed-cell SMLM, PA-SiR-CA (1265, 951; *N* = 131068 localisations), PA-SiR-C3-CA (1070, 754; *N* = 22404 localisations), and PA-JF_{646}-CA (1287, 1075; *N* = 78575 localisations) all showed similar photon numbers, which were considerably higher than for PA-SiR-BG (674, 562; *N* = 8895 localisations). However, the gold standard fluorophore for dSTORM Alexa647-CA (2327, 2056; *N* = 276806 localisations) in Glox buffer, containing cysteamine and an oxygen scavenging system, and the more recently developed HM-SiR-CA (2734, 1625; *N* = 10788 localisations) both showed increased photon numbers. Nevertheless, the photon numbers for PA-SiR-CA were promising in both regimes and made it therefore the best candidate for further experiments of the PA-SiR fluorophores.

Parameters characterizing the blinking behaviour of the three probes were also investigated. However, it proved to be difficult to compare the blinking behaviour of Alexa647-CA and HM-SiR-CA with PA-SiR fluorophores. Many of these parameters are not distributed according to a normal distribution (e.g. photon numbers), which made comparison between different fluorophores difficult. Several parameters are of high importance for purely blinking fluorophores but less important for photoactivatable fluorophores. The duty-cycle can, for instance, be tuned by varying the illumination time of photoactivation and is therefore not a suitable measure for photoactivatable fluorophores. In addition, the adjustment of the different imaging parameters (power densities, frame rate) to obtain optimal time-recordings allowing extraction of all relevant parameters for each and every fluorophore was challenging. Finally, the numbers of blinks over time at the same power density for every fluorophore were displayed (4.2 kW cm^{-2} at 642 nm and 7.2 W cm^{-2} at 405 nm; except for HM-SiR-CA were no 405 nm laser was used). Roughly one minute into the recordings an equilibrium state was established. Alexa647-CA and HM-SiR-CA clearly showed blinking. The average number of blinks was highest for Alexa647-CA followed by HM-SiR-CA, whereas the non-blinking PA-JF_{646}-CA only showed few reappearances after 60 s and most of the fluorophores were activated and irreversibly bleached in the first 1.5 min (Figure 28D). While the blinking mechanism of Alexa647-CA is attributed to a thiol adduct[27] and HM-SiR-CA cycles between its two equilibrium forms,[32] the few reappearances of PA-JF_{646}-CA might stem from photophysical transitions and the formation of radical anions known for rhodamines.[31] However, this contribution should be small as the buffers used did not contain reducing agents commonly employed in blinking buffers.[27] The PA-SiR derivatives showed two distinct behaviours. PA-SiR-CA blinked more than PA-JF_{646} but less than HM-SiR-CA. PA-SiR-C3-CA and PA-SiR-BG showed many blinks over time and it is possible that they blink spontaneously as predicted by the UV-Vis experiments. However, care has to be taken as both fluorophores showed rather low photon numbers per particle per frame. This increases the possibility that the fluorophore was not localised over subsequent frames, artificially increasing the number of blinks reported (Figure 28E).

To test the suitability of PA-SiR-CA for single-particle tracking experiments, where blinking is undesired, the on-time of the fluorophore was investigated at a lower power density (1.2 kW cm^{-2}) and compared with probes previously used for tracking experiments. PA-SiR-CA showed on-times similar to PA-JF_{646}-CA, meaning that blinking did not substantially influence the on-time (Figure 31D). Nevertheless, it was not clear from these measurements if the blinking components in all three fluorophores stemmed from photophysical processes or changes in the open-close equilibrium. In order to clarify this further measurements under different conditions such as different power densities, with the addition of blinking buffers (triplet state quenchers, oxygen scavenging system) or at different pH would need to be performed. However, as the considered applications were live-cell SMLM or single-particle tracking, the fluorophores were directly tested *in cellulo*.

Altogether, PA-SiR-CA showed the required photon numbers and its blinking characteristics were promising for both SMLM in live and fixed cells and possibly for single-particle tracking at lower power densities. PA-SiR-C3 and PA-SiR-BG showed highly interesting blinking characteristics but lower photon numbers. In addition, they performed poorly in live-cell confocal experiments and should therefore only be considered for fixed-cell SMLM.

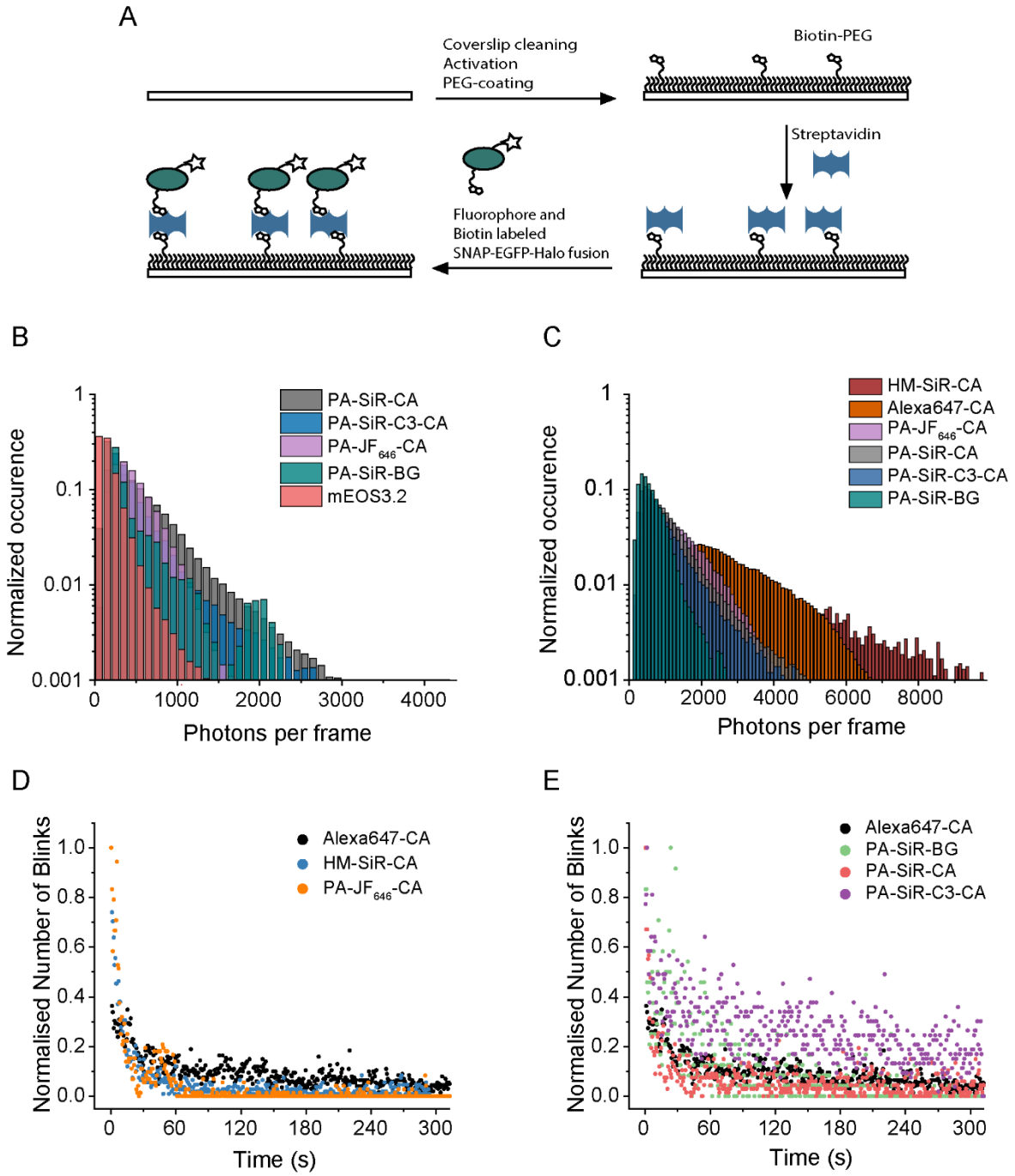

Figure 28: Single-molecule assay. (A) Schematic drawing of the coverslip functionalisation for fluorescence measurements by TIRF microscopy. Coverslips are first cleaned followed by surface activation and coating with amino-silane, which is reacted with PEG and PEG-Biotin. Streptavidin is bound to the sparse biotin moieties followed by binding to SNAP:EGFP:Halo labeled with biotin and a fluorophore. (B) Distribution of the photons per particle per frame for different fluorophores under 1.2 kW cm^{-2} 642 nm irradiation, which corresponds to the live-cell tracking regime. PA-SiR-CA (668, 518; mean, median; *N* = 170171 localisations), PA-SiR-C3-CA (497, 348; *N* = 43787 localisations), PA-JF_{646}-CA (474, 414; *N* = 339443 localisations), PA-SiR-BG (380, 244; *N* = 9674 localisations), and mEOS3.2 (187, 132; *N* = 123045 localisations; mEOS3.2:Halo, 0.9 kW cm^{-2} at 532 nm). (C) Photons per particle per frame in the high intensity regime used for dSTORM in fixed-cells (4.2 kW cm^{-2}). HM-SiR-CA (2734, 1625; mean, median; *N* = 10788 localisations), Alexa647-CA (Glox buffer, 2327, 2056; *N* = 276806 localisations), PA-JF_{646}-CA (1287, 1075; *N* = 78575 localisations), PA-SiR-CA (1265, 951; *N* = 131068 localisations), PA-SiR-C3-CA (1070, 754; *N* = 22404 localisations), and PA-SiR-BG (674, 562; *N* = 8895 localisations). (D-E) Normalised number of blinks over time for the three model compounds Alexa647-CA, spontaneously blinking HM-SiR-CA and the non-blinking PA-JF_{646}-CA (D) and the three PA-SiR derivatives (E), Alexa647-CA is depicted a second time for orientation.

2.8 SMLM and single-particle tracking of PA-SiR probes

2.8.1 Fixed-cell SMLM of PA-SiR probes

First, all three PA-SiR analogues were tested in a stable cell line expressing the microtubule binding protein Cep41 as a HaloTag or SNAP-tag fusion. Super-resolved images of microtubules with good quality were obtained for samples stained with both PA-SiR-CA and PA-SiR-C3-CA (Figure 29A-C and Supplementary Figure 8A, B) but not for the BG analogue, which was not bright enough, as expected. Accordingly, the microtubule diameters were determined to be $FWHM_{PA\text{-}SiR\text{-}CA}$ = 38.7±7.7 nm and $FWHM_{PA\text{-}SiR\text{-}C3\text{-}CA}$ = 39.2±5.3 nm (Figure 29D) for the two samples (mean±95% confidence interval, N = 20 tubules each). This is in good correspondence with the diameter of a microtubule (25 nm) coated by Cep41-Halo (74 kDa, ca. 5 nm). In order to demonstrate the power of the self-labeling protein tag strategy compared to antibody staining, which introduces even higher linkage errors, direct tagging of α- and β-tubulin, the main constituents of microtubules, was attempted. Whereas N-terminal fusion of HaloTag to α-tubulin did not result in optimal localisation, β-tubulin gave better images as confirmed by confocal microscopy. However, SMLM using PA-SiR-CA resulted in discontinuous structures and mislocalisations in between different tubules, which made quantification of the microtubule diameter unreliable (Figure 29E, F). The observed mislocalisation artefacts might be due to overexpression, as unusually high amounts of Halo-β-tubulin diffuse in the cytosol without polymerisation. The discontinues microtubules most likely stem from incomplete incorporation of Halo-β-tubulin into polymerised microtubules as endogenous β-tubulin is preferred over the fusion protein. Gene knockdown experiments or the generation of homozygous knock-in cell lines could circumvent this problem. Super-resolved images of similar quality were obtained when PA-SiR-CA was imaged in the presence of cysteamine (1 mM), demonstrating its compatibility with thiol containing blinking buffers and eventual dual colour experiments (Supplementary Figure 8C, D).

Both PA-SiR-CA and PA-SiR-C3-CA were further imaged when localised to the nuclear pore complex (NPC) via Nup96-Halo (Figure 30A-C and Supplementary Figure 8E-G).[101] This endogenously tagged cell line allowed quantification of the effective labeling efficiency of the fluorophores as exactly 32 copies of Nup96-Halo are present on one NPC. The effective labeling efficiency is a measure for the number of fluorophores localised when compared to the overall amount of protein theoretically present. It takes more parameters into account than just the labeling efficiency. Its value is reduced if HaloTag is not expressed, truncated or not located to the NPC, if the labeling reaction did not proceed, the fluorophore does not fluoresce anymore (e.g. modification during fixation), the signal was too weak for localisation, or the fluorophore is not activated in the time course of the experiment. A high effective labeling efficiency is essential to obtain images of good quality as it limits the attainable effective labeling density. They also have to be taken into account if quantitative information should be extracted from SMLM images. The effective labeling efficiencies of PA-SiR-CA and PA-SiR-C3-CA were found to be 16.8±1.5% and 21±3%, which are comparable to the reported value for $PA\text{-}JF_{549}$-CA 21±4%[101] (mean±sd, *N* = 5, 4 and 17 cells respectively; in each individual cell 150-300 NPCs were quantified).[101] Due to the many parameters influencing the effective labeling efficiency, it is difficult to take measures to improve this value for PA-SiRs and it might be more promising to engineer the labeling systems at the same time.

The two probes were also tested for labeling in yeast but neither live-cell labeling nor fixed-cell labeling resulted in usable images. The probes did not permeate the cell wall of yeast as tested during live-cell labeling and only showed unspecific staining when applied after fixation and permeabilisation. PA-SiR **41** and some of its derivatives PA-SiR-CA and PA-SiR-BG were additionally tested by collaborators for SMLM at cryogenic temperatures for correlative imaging with electron microscopy. It was hypothesised that PA-SiR could be activated due to its unusual photoactivation mechanism. Few fluorophores are currently known that can be activated under cryogenic conditions and alternatives are therefore urgently searched for.[219] PA-SiR is a good candidate as photoinduced protonation was reported to work in PC-FP's under cryogenic conditions.[220] Unfortunately, none of the trials succeeded in activating the fluorophore at these temperatures. Nevertheless, PA-SiR-CA and PA-SiR-C3-CA are suitable probes for fixed-cell SMLM and they even allow to circumvent permeabilisation steps during fixation and hence to reduce artifacts as live-cell labeling can be employed.

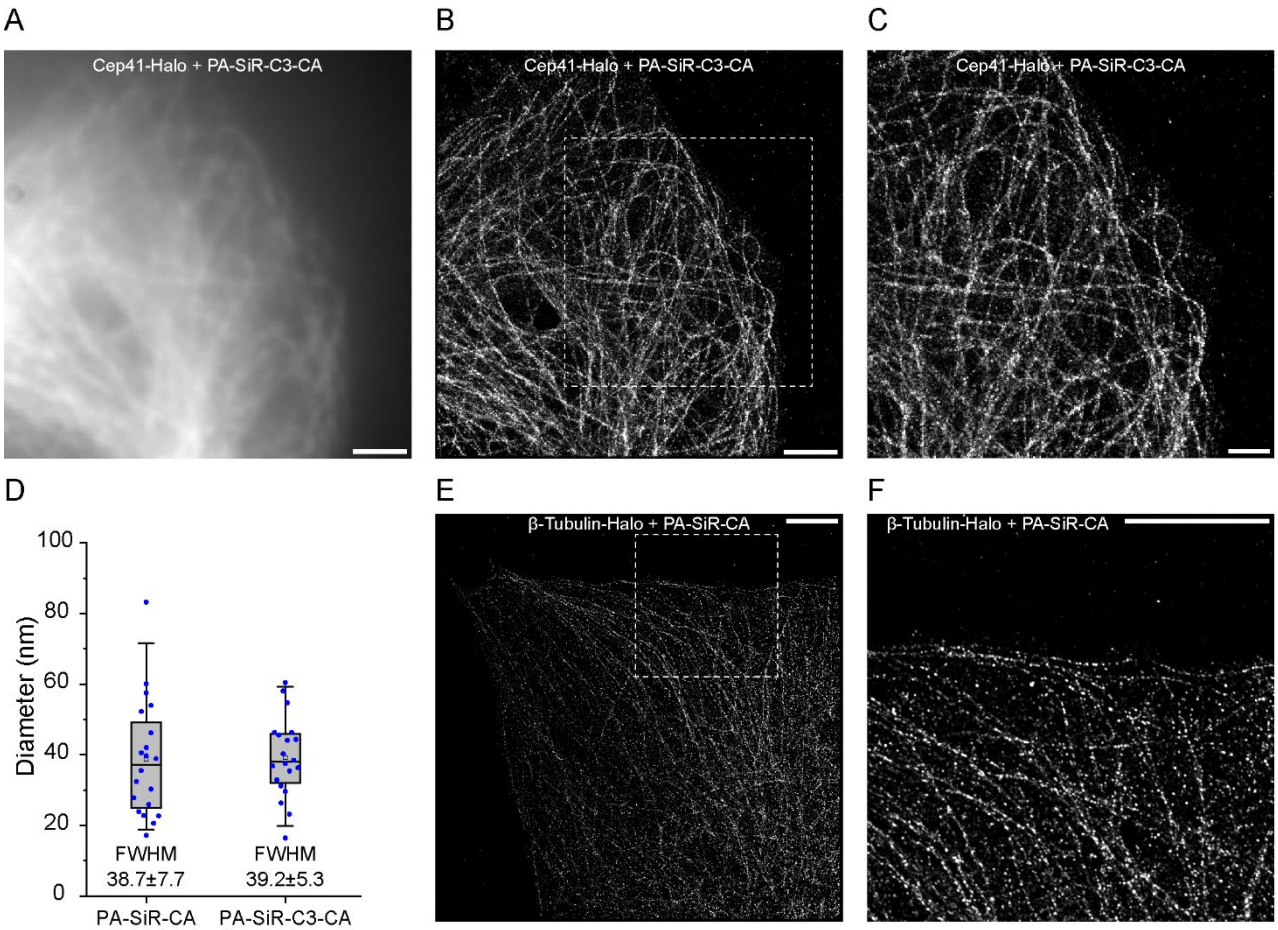

Figure 29: Fixed-cell SMLM visualizing microtubules. (A-C) Fixed U-2 OS cells expressing Cep41-Halo stained with PA-SiR-C3-CA (1 µM, 2 h). Diffraction limited image (A), super-resolved image (B), zoom-in indicated in panel B (C). Despite its suboptimal performance in live cells, PA-SiR-C3-CA allowed acquiring fixed-cell SMLM images of good quality, which were comparable to images of PA-SiR-CA localised to the same target (Supplementary Figure 8A). Scale bars, 2 µm and 1 µm (C). (D) Boxplots of the microtubule diameter measured by the FWHM obtained via fitting intensity profiles of microtubule cross-sections (Supplementary Figure 8A, B, box= 25%–75% percentile, whiskers 5%–95% percentile, black line = median, box= mean, individual data points in blue). Microtubule diameter quantification was performed by P. Hoess. (E-F) Super-resolved images of microtubules in fixed U-2 OS cells labeled by staining β-tubulin-Halo with PA-SiR-CA (1 µM, 2 h). Full image (E), zoom-in indicated in panel E (F). Scale bars, 5 µm.

2.8.2 Fixed-cell SMLM of transfection-free PA-SiR probes

Probes targeting F-actin, microtubules and DNA were tested in fixed-cell SMLM. Super-resolved images of PA-SiR-jasplakinolide revealed stress fibers and connecting thinner fibers of the F-actin network in fixed COS-7 cells. In order to visualise the thin fibers long acquisition times of several hours were required, so as to ideally separate all molecules in time. Additionally, minimal spatial drift was crucial. SMLM of the two best tubulin probes (PA-SiR-C8-docetaxel and PA-SiR-cabazitaxel) proved to be more challenging. Methanol and PFA fixation were previously shown to destroy the binding site of the taxol derivative and therefore fixation with ethyleneglycol-bis-succinimidyl-succinate (EGS) was used.[122] However, staining followed by fixation did not yield super-resolved images of sufficient quality. Only when poststaining was employed could the microtubule network be visualised albeit with poor image quality. In particular, close to interconnecting microtubules, the resolution was not optimal as many diffuse localisations created patches. In addition, circular structures reminiscent of vesicles were visible. Both the patches and the circular structures are likely to be artefacts from fixation as nothing similar was observed in live-cell confocal microscopy of the tubulin probes. Further optimisation of the fixation strategy would be required and would eventually allow the measurement of the tubulin diameter with almost no linkage error. PA-SiR-Hoechst did not lead to the desired super-resolved images of DNA in the nucleus as the density of activated fluorophores was too high for localisation. Optimisation of the fluorophore concentration might enable SMLM of nuclear DNA.

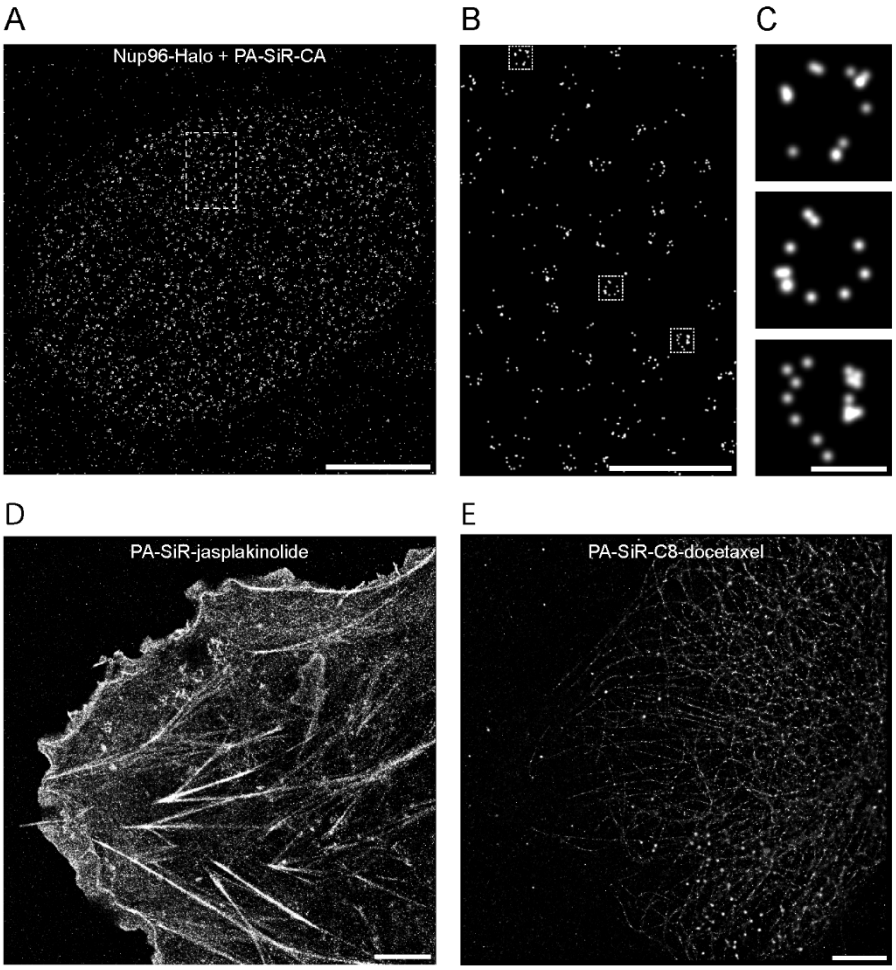

Figure 30: Super-resolved SMLM images. (A-C) Genome edited U-2 OS cells expressing Nup96-Halo under the endogenous promotor stained with PA-SiR-CA (1 µM, 2 h) revealing NPCs. Overview image (A), zoom-in of the indicated area in A (B), and single nuclear pores from the indicated areas in B (C). Scale bars, 5 µm, 1 µm, 100 nm. Experiments were performed together with P. Hoess. (D) SMLM image of actin-skeleton stained with PA-SiR-jasplakinolide (0.5 µM, 2 h) in fixed COS-7 cells. Scale bar, 5 µm. (E) Super-resolved image of microtubules stained with PA-SiR-C8-docetaxel (0.5 µM, 4 h) in EGS fixed U-2 OS cells. Scale bar, 5 µm.

2.8.3 Live-cell single particle tracking using PA-SiR-CA

To test the suitability of PA-SiR-CA for single-particle tracking, the G-protein coupled receptor β-2-adrenergic-receptor (β-2-AR) was expressed as a HaloTag fusion in U-2 OS cells and the receptor was tracked on the plasma membrane using TIRF. PA-SiR-CA showed sufficient signal-to-background ratios to track the receptors reliably at power densities as low as 0.3 kW cm^{-2} and it was possible to track the receptor for several hundreds of milliseconds. The tracklengths commonly found for fusions with PA-FPs or PC-FPs are considerably shorter.[191] Direct comparison with PA-JF$_{646}$-CA under identical labeling and imaging conditions showed similar tracklengths and both receptors moved with comparable mean speeds (Figure 31B, C). This was expected as the two fluorophores also showed similar on-times in the *in vitro* single-molecule assay (Figure 31D). Small differences might stem from the higher propensity of PA-SiR-CA to blink or a slightly reduced photostability. Nevertheless, PA-SiR-CA is an excellent fluorophore to perform live-cell single-particle tracking and might prove especially useful in intracellular applications where even higher signal-to-background ratios are required. Its higher fluorogenicity might help the fluorophore to outperform PA-JF$_{646}$-CA in this context and provide an alternative in a field of research where brighter and more photostable, activatable fluorophores are sought after.

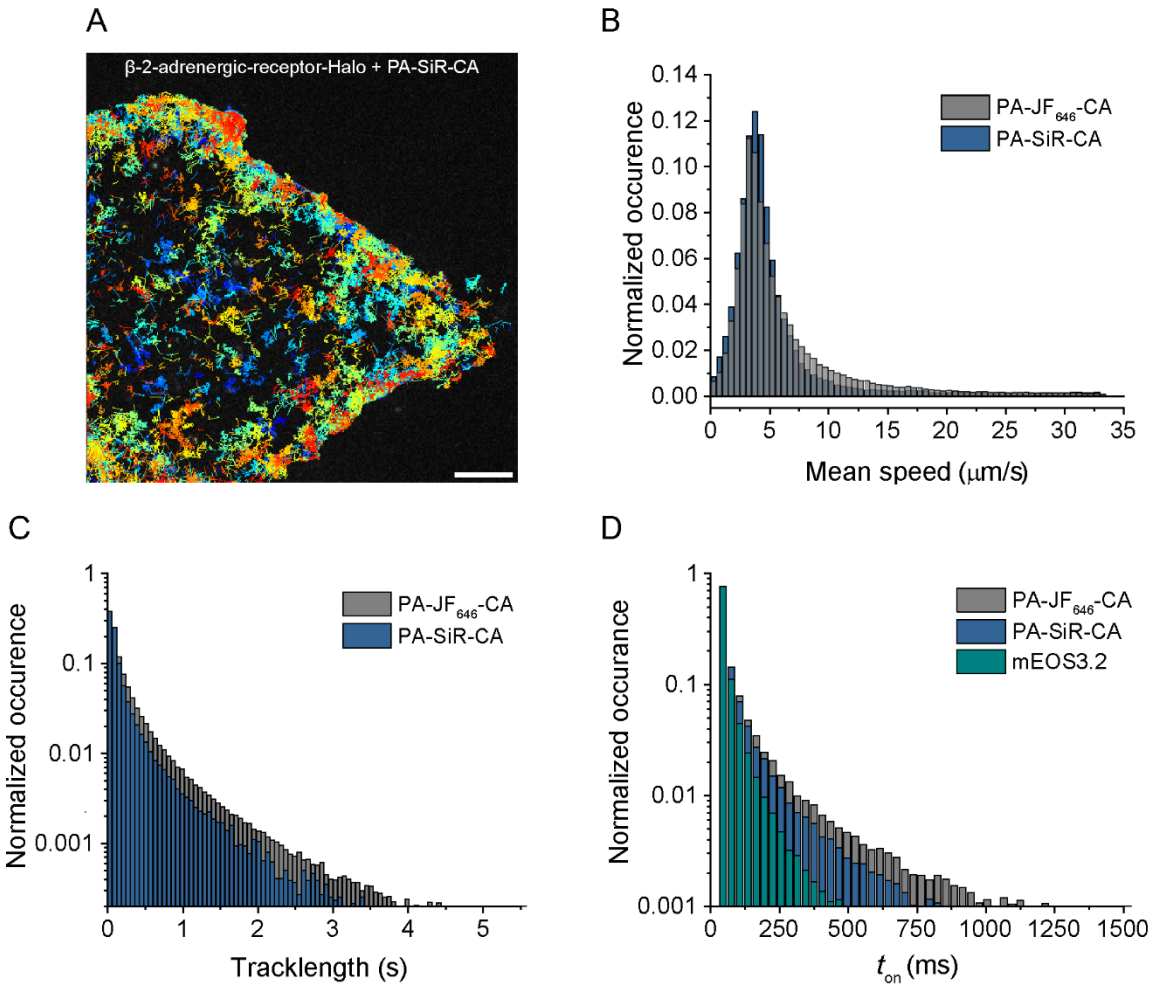

Figure 31: Single-particle tracking experiments and their quantification. (A) Cumulative tracks of the β-2-AR-Halo expressed in U-2 OS cells and stained with PA-SiR-CA (0.5 μM, 1 h) measured in TIRF mode during 2 min. Differently coloured lines represent the movement of individual receptors. Tracks are only displayed if their overall displacement was larger than 0.28 μm. Scale bar, 5 μm. (B) Histogram of the average speeds of the receptors. The means were determined to be PA-SiR-CA (5.55±0.05 μm s^{-1}, median = 4.1 μm s^{-1}, *N* = 51,408 tracks) and PA-JF_{646}-CA (6.36±0.02 μm s^{-1}, median = 4.4 μm s^{-1}, *N* = 233,871 tracks) (mean±95% confidence interval, median). (C) Comparison of the tracklengths found for PA-SiR-CA (208 ms, *N* = 51,408 tracks) and PA-JF_{646}-CA (338 ms, *N* = 233,871 tracks) under identical labeling and imaging conditions (0.3 kW cm^{-2} at 642 nm, mean; no standard deviation given as not normally distributed). (D) Histogram of on-times determined in the single-molecule assay for PA-SiR-CA and PA-JF_{646}-CA at 642 nm (1.2 kW cm^{-2}), and mEOS3.2 at 532 nm (0.9 kW cm^{-2}).

2.8.4 Live-cell SMLM of PA-SiR-CA

After showcasing both the use of PA-SiR-CA in fixed-cell SMLM and live-cell single-particle tracking, its potential for live-cell SMLM was investigated. To this end, live U-2 OS cells expressing the mitochondrial marker Tomm20-Halo located in the outer mitochondrial membrane were labeled with PA-SiR-CA (0.5 μM, 1 h) and imaged by SMLM continuously for up to 4 min. High emitter densities were targeted in order to capture fast structural changes and the partially overlapping signals were fitted using the localisation algorithm HAWK.[84] A movie was then reconstructed from overlapping 10 s snapshots revealing the fast dynamics of mitochondria (Figure 32, Movie available in [203]). The combination of PA-SiR-CA and SMLM allowed for the first time to distinguish the outer membrane of the mitochondria from the matrix in live cells (red arrowheads). In addition, the sporadic formation of thin tubules between adjacent mitochondria (blue arrowheads) or the fission of entire segments (yellow arrowheads) could be observed (Figure 32, Supplementary Figure 9), as previously demonstrated with MitoTracker Red.[221] Taken together these measurements demonstrate that PA-SiR-CA allowed to access both suitable temporal and spatial resolutions to follow the fast dynamics of mitochondria in great detail. Hence, PA-SiR-CA enables live-cell SMLM of intracellular

targets, which might be used to study the dynamics of further protein targets at super-resolution in the future. It should be borne in mind that strong light irradiation can cause photobleaching and have phototoxic effects on live cells. For instance, in these experiments, prolonged live-cell SMLM measurements past 4 min were not possible as the image quality generally deteriorated. However, different biological questions require different spatial and temporal resolutions such that the imaging speed (frame rate) and the power densities (or pulse frequencies) of the excitation and the activation laser can be adjusted. For instance, in order to extend the duration of a biological experiment without extending the overall acquisition time the recording might be discontinued and restarted several times.

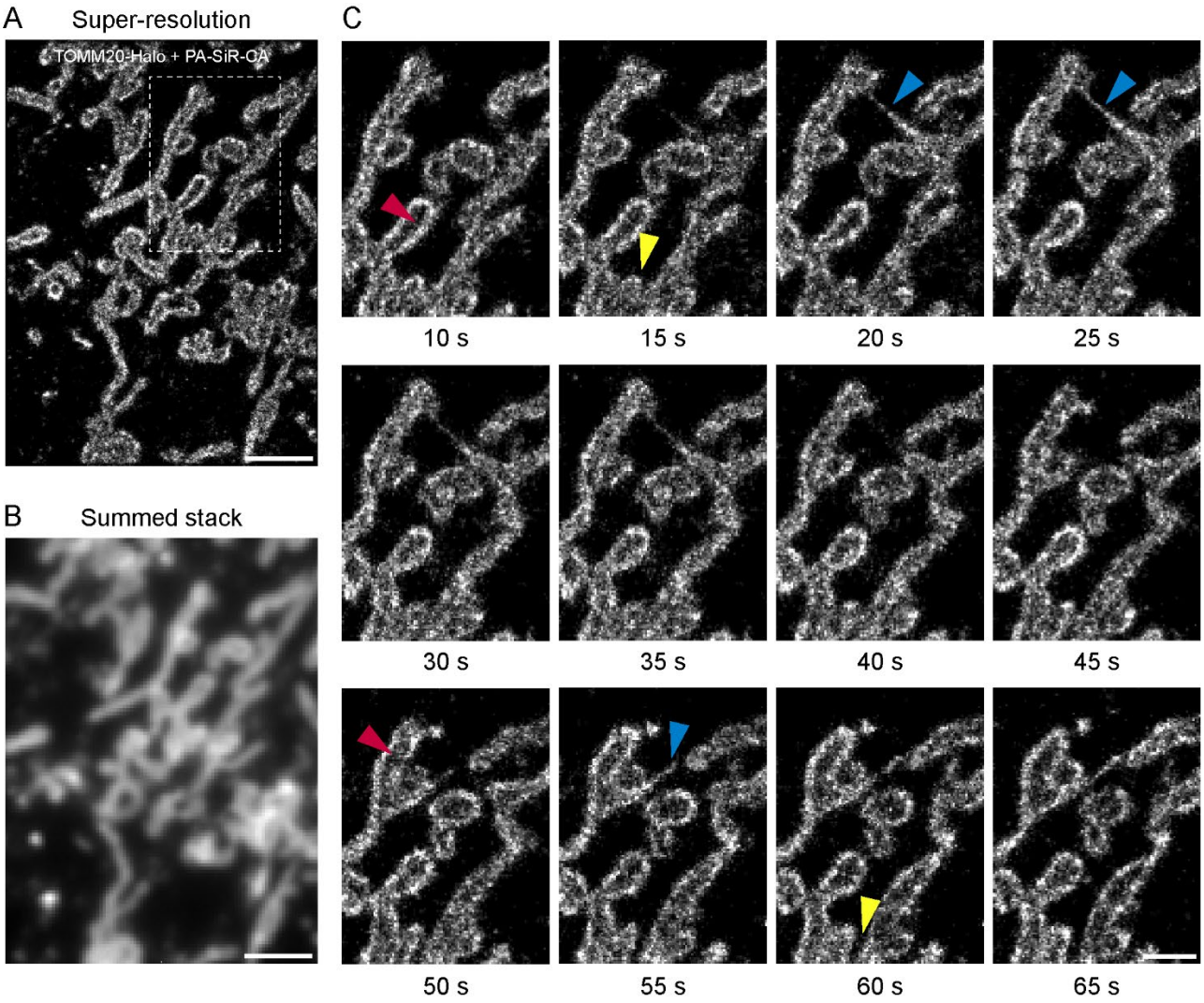

Figure 32: Live-cell SMLM of mitochondria. (A) Super-resolved overview image of Tomm20-Halo (outer mitochondrial membrane) labeled with PA-SiR-CA (0.5 µM, 1 h) acquired in the first 10 s. Scale bar, 2 µm. (B) Summed stack of the frames within the first 10 s reflecting the diffraction limited image. Scale bar, 2 µm. (C) Zoom-in of the indicated region in (A) at different time points. Mitochondria that are observed to be hollow are marked with a red, formation of thin tubules with a blue and disconnecting areas with a yellow arrowhead. Scale bar, 1 µm.

2.9 STED

In addition to SMLM imaging, PA-SiR-CA and PA-SiR-Hoechst were tested for STED imaging. To this end, U-2 OS cells expressing vimentin-Halo,[222] a component of the cytoskeleton, were stained with PA-SiR-CA (0.5 µM, 1 h) and imaged on a STED microscope. After photoactivation with the 355 nm laser, both a confocal and a STED image were acquired showing clear resolution enhancement of the filamentous vimentin structure (Figure 33B, C). PA-SiR-Hoechst was imaged in fixed U-2 OS cells and photoactivation was attempted with the 355 nm and the 405 nm laser

lines, as well as by two-photon activation with the 755 nm depletion laser. Many trials to optimise the dwell time and the power densities of the two or three lasers (activation, excitation and depletion) with respect to photobleaching, photoactivation and signal intensity were made. However, so far satisfactory imaging parameters to observe super-resolved DNA in the nucleus were not found. The 405 nm laser for instance could not convert sufficient amounts of PA-SiR-Hoechst, whereas both the 355 nm and the 755 nm depletion laser caused photobleaching of the fluorophore and led to no discernible signal.

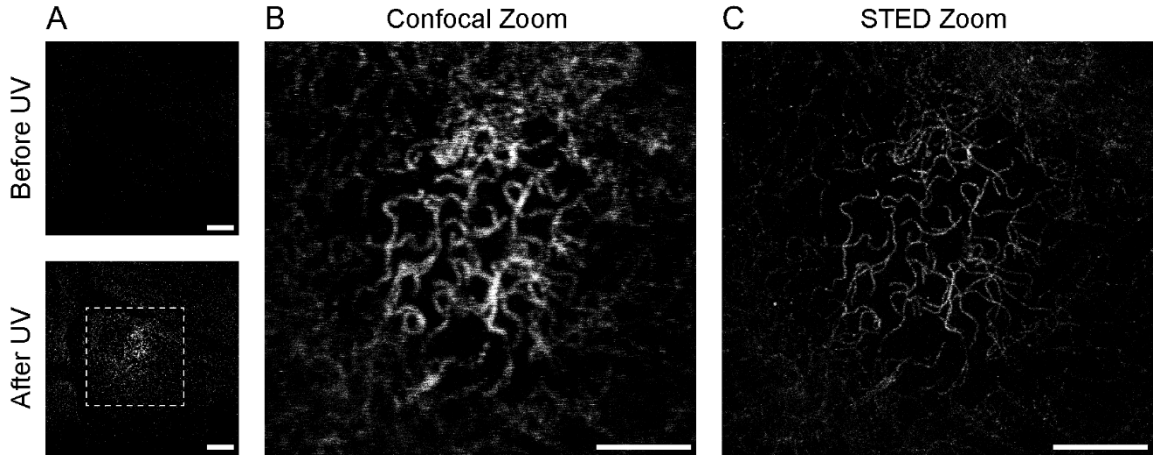

Figure 33: Live-cell confocal and STED images of vimentin-Halo. (A) Confocal overview images of U-2 OS cells expressing vimentin-Halo labeled with PA-SiR-CA (0.5 µM, 1 h) before (top) and after (bottom) UV irradiation. Scale bar, 10 µm. (B-C) Zoom-in of the region indicated in (A) after photoactivation. Confocal image (B) and STED image (C). Scale bar, 5 µm. Experiment was performed together with Dr. E. D'Este.

2.10 Conclusion and Outlook

This thesis describes the discovery and characterisation of PA-SiRs and adds to the rich chemistry of SiR and xanthene based fluorophores in general. Replacing the appended aromatic ring with an alkyl chain opened up the possibility of isolating the ethylenic form. Furthermore, it was demonstrated that tuning electronic structure and steric effects not only influenced the equilibrium involving the nucleophilic attack at C9 but could also be harnessed to favour the ethylenic form and even render it photoactivatable. PA-SiRs and the new type of photoactivation via a light-induced protonation were then used for live-cell microscopy. They were suitable for this purpose as no side-products were formed during photoconversion and no caging groups were required that would otherwise affect the solubility and permeability of the fluorophores. In addition, it was found that in combination with the environmental sensitivity of the secondary equilibrium, the created probes were not only photoactivatble but also fluorogenic. The fluorogenic properties were then examined for a variety of different probes, including a series of HaloTag probes bearing different linker lengths. The trends found *in vitro* also translated to the signal-to-background ratios measured by live-cell confocal microscopy. Specifically, PA-SiR-CA and PA-SiR-jasplakinolide performed best in both *in vitro* and *in cellulo* experiments. PA-SiR-CA's use was further demonstrated using both widefield and confocal microscopy investigating diverse targets in live cells. The application of the synthesised probes was further showcased in single-particle tracking experiments by TIRF microscopy, as well as diffraction unlimited microscopy of fixed and live cells using primarily SMLM but also STED microscopy. The presented photoactivatable, fluorogenic probes demonstrate how two non-fluorescent forms, initially considered a nuisance, can be exploited in microscopy experiments. Nevertheless, further experiments, as described below, should be performed.

The scope of this photoactivation and the possibility of isolating the ethylenic form of other xanthene analogues then the Si substituted PA-SiRs was only briefly touched upon in this thesis. More work should be dedicated toward the theoretical and experimental characterisation of the ethylenic form as well as the photoactivation in order to design and synthesise more (photoactivatable) fluorophores with tailored photophysical and chemical properties. The presented compounds **90** and **98** present starting points for two such equilibrium systems. In addition, calculations of

the ground state energies of ethylenic, quinoid, and hydrolic forms could help to choose scaffolds with increased propensities to from the ethylenic form and would hence optimise synthesis success. Improving the yield of the final step of the synthetic route via the use of bis-arylmagnesium species as proposed in Section 2.1,[141,206,207] would not only increase the amounts of compound available for extended spectroscopic measurements but might also help to find compounds which are only formed in trace amounts.

The photoactivation could be further studied using spectroscopic methods including ultrafast time-resolved absorbance and fluorescence spectroscopy or electron paramagnetic resonance (EPR). The former would be the method of choice to investigate the life-times of the transition states and the latter could be used to test the hypothesis of triplet diradical formation. It has to be noted that the created diradicals might be too short lived to be detected by EPR. Nevertheless, the results from these spectroscopic methods could be combined with theoretical calculations of transition states and help to get a better picture of the mechanism of photoactivation. In addition, the currently used spectroscopic methods could be refined. For instance, ^{1}H NMR measurements with in situ irradiation could be performed using a NMR setup where a light guide can be directly introduced into the NMR tube[223–225] and could even be combined with simultaneous UV-Vis measurements.[226] This might allow to capture the formation of the fluorescent form. However, finding a light source and light guide fitting the dimensions of an NMR tube and exhibiting the required power density to convert sufficient amounts of PA-SiR to observe compound **42** will be essential.

Moreover, the equilibrium system should be investigated further in the context of target binding. The obtained stability of the absorbance signal of photoactivated PA-SiR-CA conjugated to HaloTag were so far not equalled by any other synthesised probe. Structural information on PA-SiR-CA would be informative. Unfortunately, trials to obtain crystals of PA-SiR-CA conjugated to HaloTag were so far unsuccessful. Alternatively, solution protein NMR could be used to investigate the interactions of HaloTag with PA-SiR-CA and it might even be possible to perform a photoactivation experiment following the changes in surface interactions. In addition, probes which have not yet been fully characterised (e.g. PA-SiR-Hoechst) should be characterised in depth by UV-Vis to further understand their properties and behaviour. Additionally, new probes could be synthesised using alternative ligands. For instance, it would be of high interest to investigate the probes behaviour when localised to membranes instead of proteins and whether this apolar environment allows for photoactivation and/or fluorogenicity.

In terms of future microscopy applications, one can imagine a variety of different directions. First, different targets could be investigated using PA-SiR-CA in combination with POI-HaloTag fusion proteins in live cells. PA-SiR-CA could be advantageous in single-particle tracking experiments of intracellular targets, such as transcription factors, as longer tracklengths can be measured than with commonly used FPs. SRM of alternative targets could also be performed using live-cell SMLM or STED. Second, different cell lines and even tissues could be investigated using the PA-SiR technology. Third, as correlative SRM with electron microscopy becomes more and more important and despite the unsuccessful trials to use PA-SiR at cryogenic temperatures, it would be of high interest to test its behaviour in resin embedded samples.

This thesis and the associated publication[203] has set the stage for further research and applications of PA-SiR and its derivatives. It is hoped that the presented results will spark interest in underexploited alkyl substituted xanthenes and their equilibrium systems. Future work could not only lead to the eventual isolation of photoactivatable derivatives in other spectral ranges but might also lead to the development of spontaneously blinking fluorophores, both of which would be of enormous benefit for advanced microscopy purposes. Regardless of future developments, it is expected that the presented probes, especially PA-SiR-CA, will become useful tools in bioimaging.

Chapter 3 HaloTag's interaction with fluorogenic fluorophores

In order to investigate the influence of HaloTag's surface environment on fluorogenic rhodamines, site-saturation mutagenesis libraries were designed based on the crystal structure of HaloTag bound to TMR-CA (Figure 34A).[227] These libraries were designed to modulate the HaloTag-fluorophore interface and therefore the fluorescence intensity of fluorogenic fluorophores. Characterisation of the identified variants should allow to better understand and engineer the ability of HaloTag to influence the open-close equilibrium of fluorogenic rhodamine fluorophores and/or their brightness in general. Originally the self-labeling protein tag HaloTag was engineered from the *Rhodococcus* dehalogenase DhaA via directed evolution using site-saturation mutagenesis and error-prone PCR. The screens were focused on increasing three key parameters namely labeling kinetics with TMR-CA, protein stability, and expression yields.[98] Fluorophore brightness, on the other hand, was not taken into account. The resulting HaloTag carried 21 mutations compared to wild type DhaA and the C-terminus was extended by four amino acids.[98]

3.1 Screening of focused libraries of HaloTag in combination with SiR-CA

First, the previously solved crystal structure of HaloTag bound to TMR-CA was scrutinised for specific interactions between the protein and the fluorophore core (Figure 34A).[227] TMR-CA, as a non-fluorogenic fluorophore, should be bound to HaloTag in its open, fluorescent form. Fluorogenic analogues are expected to adopt a similar conformation on the surface of HaloTag and therefore HaloTag bound to TMR-CA served as a model to identify amino acid residues to randomise. The crystal structure revealed that the xanthene moiety lay on one of the α-helices (167-171). The carboxylic acid of the appended aromatic ring was solvent exposed and in solution probably stabilised via hydrogen-bonding with solvent molecules. This suggested that interactions of the α-helix with the xanthene core and (specific) interactions with the anilines mostly contribute to the stabilisation of the open form of fluorophores on the protein surface. It is possible that the delocalised positive charge is efficiently stabilised in this conformation. Based on these assumptions, ten amino acid residues were selected for site-saturation mutagenesis and screened for fluorescence intensity modulations of SiR-CA. All ten amino acids were in close proximity to the fluorophore and were mostly located in the α-helix (167-171) or in adjacent loops (Figure 34B). They comprise the amino acids F144, T148, L161, Q165, V167, E170, G171, T172, P174, and M175. While V167, T172, and M175 were known to be relevant for reaction kinetics the remaining seven amino acids were not modified going from wild type DhaA to HaloTag.[98]

The chosen amino acids were individually[228] randomised, resulting in ten libraries, which were screened in *Escherichia coli* lysate insuring full library coverage (77 colonies each). EGFP, C-terminally fused to HaloTag, was used to estimate the protein concentration and served to distinguish variants with decreased fluorescence intensity from low expressing variants. Cell lysates were screened for changes in fluorescence intensity (increases and decreases) after addition of a limiting amount of SiR-CA. The best hits in both directions (increasing and decreasing) were sequenced and the proteins purified on a 100 ng scale. Validation of the results with purified proteins lead to the identification of seven variants with significantly higher fluorescence intensity upon reaction with SiR-CA. The increases and decreases were later confirmed in protein constructs without the EGFP tag and in the following only the values from these measurements are reported. Selected variants showed an overall fluorescence increase of 10% as compared to parental HaloTag ($I_{rel} = I_{mut} \cdot I_{Halo}^{-1} = 1.10$, Section 3.2.2, Supplementary Table 20). On the other hand, many variants showed decreased fluorescence intensities as low as −76% ($I_{rel} = 0.24$, Supplementary Table 17 and Supplementary Table 21). Throughout this thesis, variants showing a fluorescence intensity increase will be referred to as brighter

variants, while for the ones decreasing the fluorescence intensity the term dimmer variant will be used. While the variant itself is not fluorescent the fluorophore-HaloTag couple is.

While seven brighter variants were found, their mutations were localized in only four of the ten randomized positions (Q165, E170, P174, and M175), making these sites hotspots for further rounds of mutagenesis. Hence, to further engineer HaloTag, the brightest first round variants were subjected to a second round of site-saturation mutagenesis. Previously mutated sites were fixed while sampling the remaining three sites separately (e.g. Q165H-E170X, Q165H-P174X, and Q165H-M175X; Supplementary Table 18). Only brighter variants were considered for validation in an assay with purified protein, which confirmed seven proteins (Supplementary Table 20). The three best ones (Q165H-P174R, Q165H-P174L, and E170K-M175L) with fluorescence intensity ratios between 1.12 and 1.17 were chosen for a third screening round, fixing the two selected mutations and sampling the other two sites (e.g. Q165H-P174R-M175X and Q165H-P174R-E170X; Supplementary Table 19). However, no substantial increases over the underlying parental proteins were found and no further screenings were conducted (Supplementary Table 20). In order to find variants that show further improvements, the library design and screening strategies would need to be adjusted. For instance, an unbiased library design based on error-prone PCR combined with high-throughput screening approaches could be employed, allowing to identify beneficial mutations distal to the HaloTag-fluorophore interface.

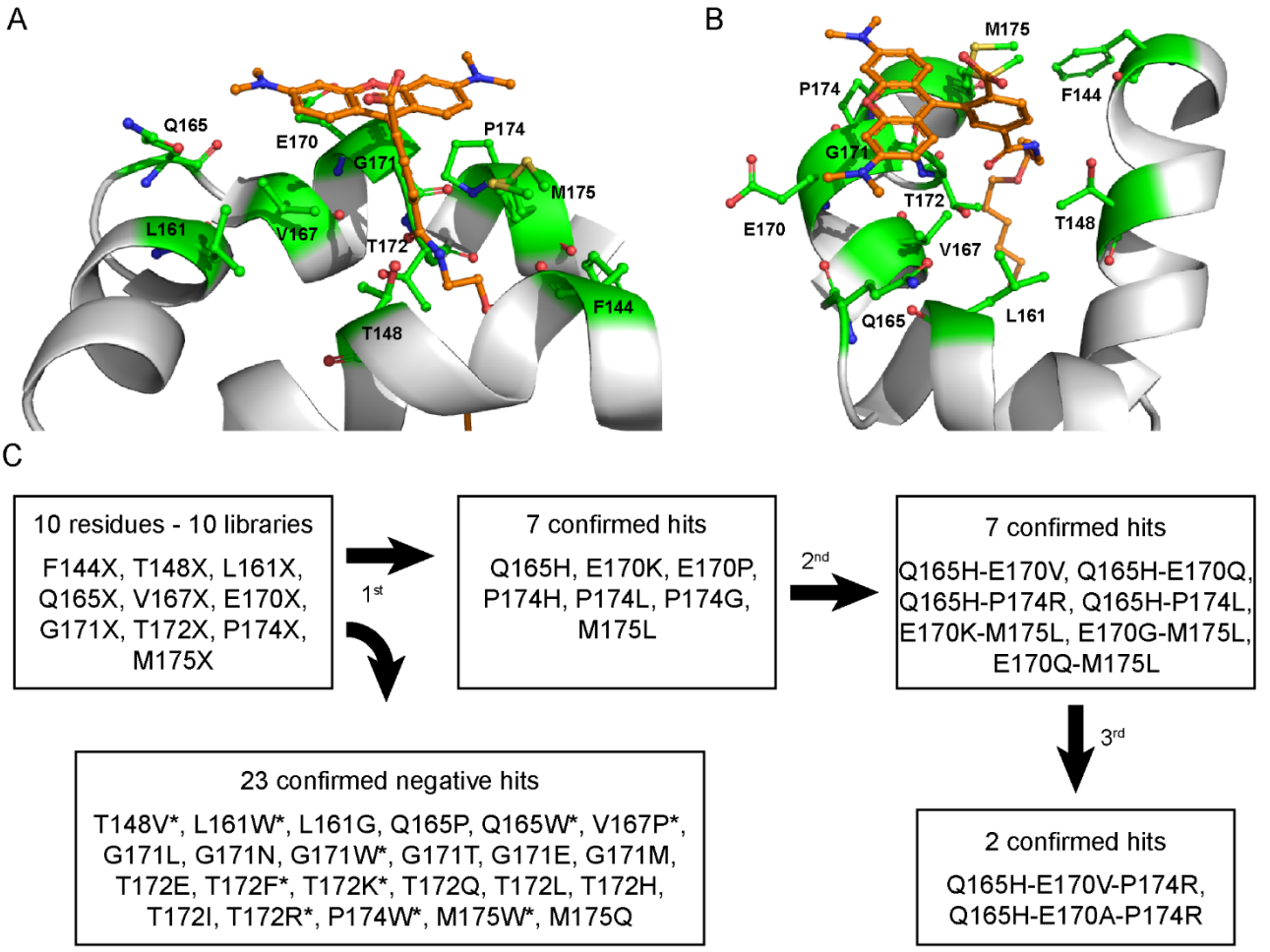

Figure 34: Crystal structure of HaloTag bound to TMR-CA. (A-B) HaloTag (142-177) in grey, TMR-CA in orange stick representation (oxygen – red, nitrogen – blue, carbon – orange). The ten residues chosen for site-saturation mutagenesis are highlighted in green (oxygen – red, nitrogen – blue, carbon – green, sulfur – yellow).[227] (C) Work flow of directed evolution of HaloTag screening for variants of HaloTag that give decreased (1st round) or increased fluorescence intensity (1st – 3rd round). * Variants among the 23 negative hits selected for further analysis.

The analysis of the sequences of the brighter and dimmer variants allowed the classification of the ten amino acid sites into three groups. Four positions resulted in fluorescence decreases (L161X, V167X, G171X, and T172X). Since V167X, G171X, and T172X were located directly underneath the xanthene core of the fluorophore, their mutation might prevent proper fluorophore binding, disfavouring spirolactone opening. Mutations at the two positions (F144X and T148X) on the opposite helix (137-153) did not seem to influence the fluorophore's fluorescence properties, probably being located too far from the fluorophore. The remaining positions (Q165X, E170X, P174X, and M175X) yielded the most interesting results with respect to fluorescence intensity enhancement. P174X located in α-helix (173-177), breaking the continuity of the α-helix starting at 167 towards 177, was mutated in several cases, potentially allowing the protein adopting a more favourable conformation with an intact α-helix. In addition, brighter variants often presented positively charged amino acids (K, H, and R). These amino acids were found in positions Q165H, E170K, and P174H/P174R, all close to the xanthene core. This was unexpected as the fluorophore itself is zwitterionic and the positive charge is delocalised over the xanthene core. In addition, one non-polar residue was found (L) at positions P174L and M175L. On the other hand, aromatic amino acids (W and F) were found in dimmer variants. Structural analysis of the best variants might help to investigate the interactions with the different amino acids in more detail (Section 3.2.4).

3.2 Characterisation of HaloTag variants

The 16 brighter variants, as well as ten selected dimmer variants, were subjected to further characterisation (Supplementary Table 17). Identified variants were sub-cloned into a vector without the EGFP reporter tag, and prepared for crystallography studies (His-TEV-HaloTag, Section 5.3 and Section 3.2.4). The changes in fluorescence intensity ($I_{rel\text{-}SiR}$) in combination with SiR-CA were confirmed and the number of proteins was further restricted (7 brighter and 9 dimmer variants, Table 2, Supplementary Table 20 and Supplementary Table 21).

3.2.1 Labeling kinetic studies of HaloTag variants

Reaction kinetics were measured for the 16 variants and compared with parental HaloTag. This was most important for the dimmer variants, as incomplete labeling would also result in a decreased fluorescence intensity as compared to parental HaloTag. This could not be distinguished from a variant that influences the brightness of the bound fluorophore in the endpoint screening assay and therefore variants with slow reaction kinetics needed to be filtered out. The reaction kinetics of all 16 variants were investigated using fluorescence polarisation measurements with the non-fluorogenic fluorophore TMR-CA. The obtained time-dependent polarisation measurements were fitted with a mono-exponential function, giving access to apparent first order rate constants k_{1app} under the chosen reaction conditions. Side-by-side comparison with parental HaloTag allowed filtering out variants with more than 4-fold decreased reaction kinetics (Table 2). This encompassed V167P, T172F, T172K, and T172R, which is in agreement with data from the development of HaloTag, during which V167 and T172 were introduced for increased labeling kinetics with TMR-CA.[98] Interestingly the mutation of M175, which was also known to influence labeling kinetics,[98] did not lead to a decreased k_{1app} neither for M175L nor for M175W. The variants bearing a tryptophan showed moderate decreases in labeling kinetics, while the variant Q165W (k_{1app} = 0.47±0.04 s^{-1}) even reacted faster with TMR-CA than HaloTag (k_{1app} = 0.373±0.012 s^{-1}, mean±sd N = 3 samples).

The different variants also reached different maximum polarisation values (y_0) after completion of the reaction (plateau). As the influence of the mutations on the size of the variants tested was negligible, this change in polarisation should originate from a change in the fluorophore's flexibility on the protein surface. Most of the brighter variants showed lower polarisation values which corresponds to higher flexibility of TMR-CA than on HaloTag (y_0 = 300.3±0.7 mP). Only P174H (y_0 = 331.46±0.14 mP, mean±sd N = 3 samples) showed a substantially increased value, indicating a higher rigidity of TMR-CA bound to the protein surface. All the dimmer variants (except L161W), on the other hand, showed plateaus above 300 mP. Their fluorophores are therefore likely to be more rigidly bound, which would indicate that tryptophan undergoes favourable interactions with the fluorophore. Rigidification disfavours non-radiative decay and potentially increases the quantum yield. On the other hand, rigidification can also lock the

fluorophore in an unfavourable position, decreasing absorbance and/ or emission. In light of these contradicting interpretations, fluorescence polarisation values do not allow conclusions to be made about the observed changes in brightness.

Table 2: Kinetic characterisation of the brightest and dimmest HaloTag variants. Three parameters are given including the ratio of intensities found for SiR-CA ($I_{rel\text{-}SiR} = I_{mut} \cdot I_{Halo}^{-1}$); the apparent first order rate constant k_{1app} and the maximal fluorescence polarisation value reached y_0. Results are given as means±90% confidence interval ($I_{rel\text{-}SiR}$: N = 4 samples) except for k and A, which are means±sd of N measurements. * The measured reaction kinetics were so slow that a mono-exponential curve fit was not possible in the time window recorded.

	Variant	$I_{rel\text{-}SiR}$	k_{1app} [s^{-1}]	y_0 [mP]	N (kinetics)
Brighter variants	**M175L**	1.094±0.030	0.35±0.07	307.5±3	2
	E170K	1.150±0.010	0.18±0.03	287.74±0.19	3
	Q165H	1.149±0.014	0.40±0.14	273±4	2
	P174H	1.151±0.016	0.308±0.017	331.46±0.14	3
	P174L	1.161±0.023	0.2279±0.0004	288.9±0.6	3
	Q165H-P174R	1.200±0.025	0.45±0.20	271±3	3
	Q165H-P174L	1.128±0.022	0.37±0.05	271.8±0.8	3
	HaloTag	1.000±0.012	0.373±0.012	300.3±0.7	3
Dimmer variants	**M175W**	0.570±0.011	0.22±0.11	340±3	2
	V167P	0.327±0.020	*	*	2
	L161W	0.454±0.005	0.13±0.03	300±70	2
	Q165W	0.476±0.005	0.47±0.04	358.5±0.5	3
	T172F	0.256±0.004	*	*	3
	T172K	0.340±0.006	*	*	3
	T172R	0.150±0.004	*	*	3
	G171W	0.234±0.004	0.15±0.08	334±5	3
	P174W	0.267±0.004	0.040±0.013	360±40	3

3.2.2 Fluorophore screen

The 26 most interesting variants were tested in combination with seven additional fluorophores in addition to SiR-CA. The fluorophores were chosen from different spectral ranges and showed varying fluorogenicity properties as expressed by their D_{50} values referring to the dielectric constant at which half maximal absorbance is reached in dioxane-water mixtures (Figure 35A). Based on this, the most interesting variants were evaluated to be Q165H-P174L and Q165H-P174R followed by Q165H, P174H, and P174L (Figure 35B, Supplementary Table 20). Their fluorescence intensity ratios in combination with SiR-CA ($I_{rel\text{-}SiR} = I_{SiR,\ variant} \cdot I_{SiR,\ HaloTag}^{-1}$) were found to be $I_{rel\text{-}SiR}$ = 1.109±0.017 (Q165H), 1.16±0.03(P174H), 1.147±0.018 (P174L), 1.20±0.03 (Q165H-P174R), and 1.17±0.03 (Q165H-P174L; Supplementary Table 20). Even more interestingly for Q165H-P174R the ratios were even higher when measured in combination with different fluorophores $I_{rel\text{-}JF614}$ = 4.07±0.16, $I_{rel\text{-}JF635}$ = 1.51±0.12, $I_{rel\text{-}CPY}$ = 1.32±0.04, and $I_{rel\text{-}MaP618}$ = 1.51±0.05. Increases of up to 300% enhance the potential of these fluorophores for live-cell applications enormously. On the other hand, the dimmest variants were G171W and P174W for all the fluorophores measured (Supplementary Figure 11). Their intensity ratios were $I_{rel\text{-}SiR}$ = 0.235±0.010 (G171W) and 0.268±0.005 (P174W, mean±90% confidence interval, N = 4 samples; Supplementary Figure 11 and Supplementary Table 21).

The intensity ratios (I_{rel}) varied depending on the fluorophore used (Figure 35B). For instance, TMR-CA showed small changes when compared to MaP618-CA or JF_{614}-CA. In general, highly fluorogenic fluorophores (high D_{50}) showed greater increases than fluorophores that are barely fluorogenic (low D_{50}). It was found that the increase in fluorescence intensity correlated with the D_{50} of the fluorophores (Figure 35C). Unfortunately, the D_{50} for JF_{614}-CA and JF_{635}-CA could not be determined as the fluorophores were not fully open in water. The correlation indicated that the fluorescence intensity increase might result, at least partly, from a shift in the open-close equilibrium toward the open

form. This then leads to an increase in apparent extinction coefficient. Fluorophores that were inherently more closed (e.g. JF_{614}-CA, JF_{635}-CA or MaP618-CA) experienced a greater opening on the brighter variants than on HaloTag compared to almost fully open fluorophores (e.g. SiR-CA). Non-fluorogenic fluorophores such as TMR-CA are believed to be fully open on protein surfaces and should therefore not present a fluorescence intensity increase through a shift in equilibrium position. Nevertheless, also TMR-CA showed increased intensity ratios in combination with Q165H-P174R ($I_{rel\text{-}TMR}$ =1.10±0.04). Therefore, it is likely that other factors than the open-close equilibrium influence the fluorescence intensity of rhodamine fluorophores on protein surfaces.

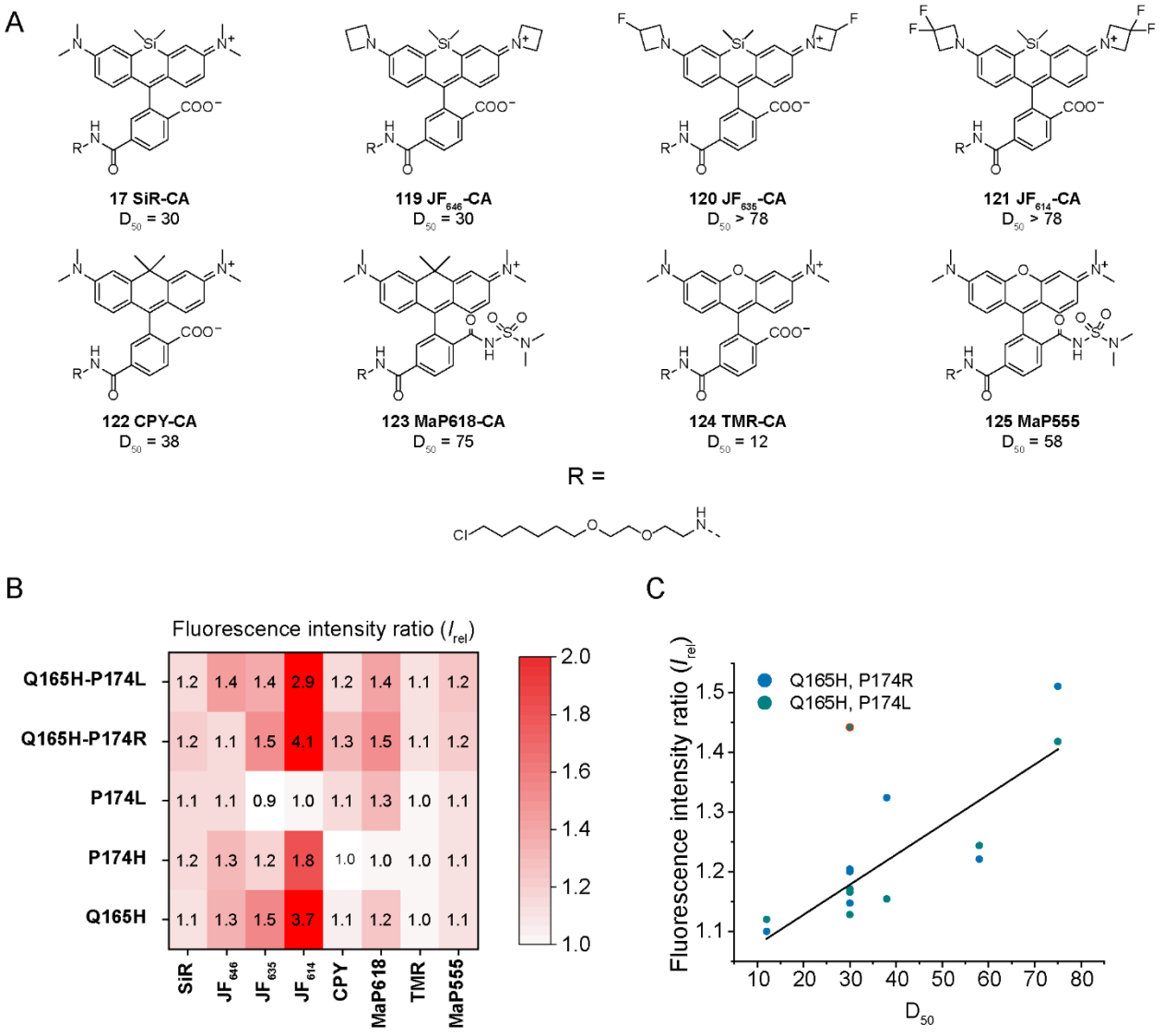

Figure 35: Screening of HaloTag variants with different fluorophores. (A) Structures of all fluorophores used SiR-CA **17**, JF_{646}-CA **119**, JF_{635}-CA **120**, JF_{614}-CA **121**, CPY-CA **122**, MaP618-CA **123**, TMR-CA **124**, and MaP555-CA **125**, together with their D_{50} values.[117,140,142,229] JF_{635}-CA and JF_{614}-CA do not fully open in water and hence determination of the D_{50} value was not possible. Fluorophores were synthesised by B. Mathes. (B) Ratios of fluorescence intensity (I_{rel}) for different fluorophore protein combinations (mean of N = 4 samples). (C) D_{50} dependent fluorescence intensity ratios (I_{rel}) of the two best variants showcasing a correlation between the open-close equilibrium and the ratios obtained. Only fluorophores with a D_{50} value below 78 were taken into account. The outlier marked in red was excluded from the fit.

3.2.3 Quantum yields

The brightness of fluorophores is determined by the quantum yield and the extinction coefficient, which in the case of rhodamines is influenced by the open-close equilibrium. The quantum yield was measured for SiR-CA as well as TMR-CA bound to several variants (Table 3). The ratios of the quantum yield $\phi_{rel} = \phi_{variant} \cdot \phi_{Halo}^{-1}$ were

compared with the ratios of fluorescence intensity I_{rel} and it was found that only few variants showed statistically relevant differences in quantum yield. For SiR-CA the changes in quantum yield were smaller than the changes in fluorescence intensity. Specifically, for variants P174L, Q165H-P174R, and Q165H-P174L changes in quantum yield up to 7% ($\phi_{rel\text{-}SiR}$) were found but the changes in fluorescence intensity were 2-fold higher and between 13% and 20% ($I_{rel\text{-}SiR}$). Hence, for SiR-CA the increases in quantum yield only partially explained the overall fluorescence intensity increase. However, for TMR-CA the ratios of fluorescence intensity $I_{rel\text{-}TMR}$ corresponded well with the ratios in quantum yield $\phi_{rel\text{-}TMR}$ (e.g. Q165H-P174R $I_{rel\text{-}TMR}$ = 1.10±0.04 and $\phi_{rel\text{-}TMR}$ = 1.100±0.021). The change in quantum yield was therefore the major contribution to the observed increase in brightness. This is also in accordance with the fact that the fluorophore is thought to be fully open on the protein surface.

Greatly diminished quantum yields were found for the dimmer variants that contain a tryptophan. Specifically, the two variants G171W and P174W both showed quantum yields of about 12-13% for SiR-CA and 4-15% for TMR-CA. The corresponding ratios ϕ_{rel} were in good agreement with their fluorescence intensity ratios I_{rel}. The tryptophan residue in these variants is therefore likely to be in close proximity to the fluorophore, quenching its fluorescence through photoinduced electron transfere.[230] In order to account for the efficient quenching, it is possible that the fluorophore undergoes π-stacking with the tryptophan. In addition, this would also explain the increased polarisation values (higher rigidity) found in the kinetic assays for TMR-CA on these variants.

Table 3: Quantum yields of the brightest and dimmest HaloTag variants. Six parameters are given including the ratio of intensities for SiR-CA ($I_{rel\text{-}SiR} = I_{SiR\text{-}mut} \cdot I_{SiR\text{-}Halo}^{-1}$) and TMR-CA ($I_{rel\text{-}TMR} = I_{TMR\text{-}mut} \cdot I_{TMR\text{-}Halo}^{-1}$); the quantum yields in combination with SiR-CA (ϕ_{SiR}) and TMR-CA (ϕ_{TMR}) along with their ratio in quantum yield $\phi_{rel\text{-}SiR} = \phi_{SiR,\,mut} \cdot \phi_{SiR,\,Halo}^{-1}$ and $\phi_{rel\text{-}TMR} = \phi_{TMR,\,mut} \cdot \phi_{TMR,\,Halo}^{-1}$. Results are given as means±90% confidence interval (I_{rel}: N = 4 samples; ϕ: N = 3 samples; ϕ_{rel}: N = 3 samples). N/D not determined.

Name	$I_{rel\text{-}SiR}$	ϕ_{SiR} [%]	$\phi_{rel\text{-}SiR}$	$I_{rel\text{-}TMR}$	ϕ_{TMR} [%]	$\phi_{rel\text{-}TMR}$
M175L	1.094±0.030	52.0±1.5	1.01±0.04	0.87±0.07	N/D	N/D
E170K	1.150±0.010	52.9±1.1	1.02±0.03	0.96±0.05	N/D	N/D
Q165H	1.149±0.014	51.3±1.1	0.99±0.03	1.00±0.05	N/D	N/D
P174H	1.151±0.016	51.6±1.0	1.00±0.03	1.00±0.04	N/D	N/D
P174L	1.161±0.023	54.7±1.3	1.06±0.03	1.00±0.04	56.9±0.3	1.016±0.007
Q165H-P174R	1.200±0.025	55.3±1.5	1.07±0.04	1.10±0.04	61.2±1.2	1.100±0.021
Q165H-P174L	1.128±0.022	55.1±1.1	1.07±0.03	1.12±0.04	62.8±0.7	1.122±0.013
HaloTag	1.000±0.012	51.7±0.9	1.00±0.03	1.00±0.04	56.00±0.24	1.000±0.006
G171W	0.234±0.004	13.6±0.8	0.26±0.02	0.070±0.003	3.8±0.3	0.067±0.006
P174W	0.267±0.004	12.0±0.8	0.23±0.02	0.28±0.03	14.93±0.21	0.267±0.004

3.2.4 Structural analysis

In order to better understand the modulation of the fluorescence intensity by HaloTag, the X-ray structures of different variants bound to TMR-CA were obtained. Crystals were obtained for eight out of eleven trials and preliminary structures were solved for seven of them, which were all brighter variants. The final refinements are still pending and therefore the structures are only briefly discussed here (Supplementary Figure 13). The observed changes are exemplified on the brightest candidate Q165H-P174R, whose crystal structure was solved with a resolution of 1.40 Å (Figure 36A, B). The most striking change in the crystal structure of almost all variants was a shift of the fluorophore toward the α-helix (156-165). This was measured as the mean shift of the nitrogen atoms ($d_{N\text{-}N}$, Figure 36C) when compared to parental HaloTag. This shift was highest for Q165H-P174R ($d_{N\text{-}N}$ = 2.00±0.14 Å), Q165H-P174L ($d_{N\text{-}N}$ = 1.65±0.07 Å), and P174L ($d_{N\text{-}N}$ = 1.45±0.07 Å, mean±sd *N* = 2 distances; Table 4). This shift repositions the xanthene, whose centre was over G170 in parental HaloTag but now lies closer to the beginning of the α-helix (167-171), over F168. The fluorophore therefore extended to the adjacent loop (165-167) coming into close contact with H165X. Interaction with this residue could potentially prevent vibrational decays and increase the quantum yield through rigidification of the fluorophore. However, rigidification was only found to be important for P174H (Section 3.2.1), the only variant with no discernible shift toward α-helix (156-165). Up to now, it is unclear if or how the shifted position of the fluorophore leads to an increase in extinction coefficient or a change in quantum yield compared to parental HaloTag.

None of the mutations leading to brighter variants of HaloTag allowed for the formation of hydrogen bonds or salt bridges with the fluorophore, despite the positively charged nature of the residues. However, it might be possible that these positively charged amino acids influence the local hydrogen bond network of water and the associated local pH. Through this, they might indirectly stabilise the carboxylate group and therefore the open form of the fluorophore. Modeling of the electrostatic potential on the protein surface might help to better understand this effect.

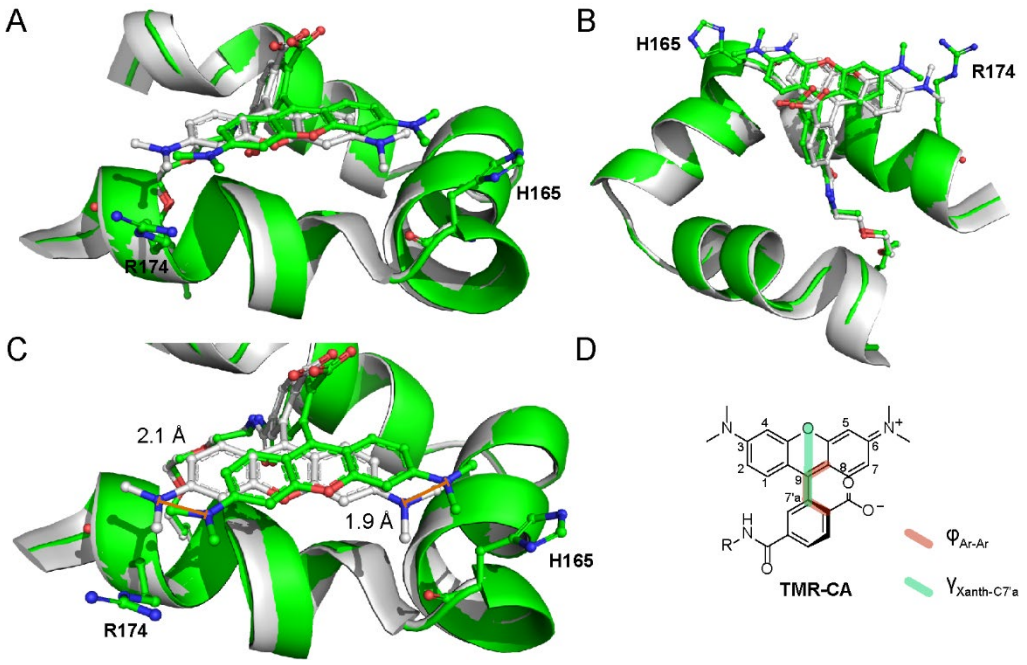

Figure 36: Crystal structures of HaloTag and Q165H-P174R reacted with TMR-CA. (A) View from α-helix (167-171) towards the fluorophore. (B) View from the opposite side over α-helix (146-152). (C) Zoom in showing only the fluorophores and the two α-helixes (167-171) and (156-165). The shift toward α-helix (156-165) is indicated. HaloTag (142-177) in grey and Q165H-P174R (142-177) in green. TMR-CA and the mutated amino acids are given in stick representation (oxygen – red, nitrogen – blue, carbon – grey/green). (D) Structure of TMR-CA (R = CA) indicating the dihedral angle $\varphi_{Ar\text{-}Ar}$ and the angle γ measured between the xanthene plane (O-C9) and C7'a. Crystallisation trials, optimisation and X-ray diffraction were performed by Dr. M. Tarnawski and Professor I. Schlichting.

Differences were also found in the angle γ by which C7'a-C9 is tilted out of the xanthene plane (Figure 36D, Table 4). This angle is a measure for the deviation from an ideal sp^2 hybridisation of C9 adopted in the open, fluorescent form (closed form sp^3). TMR-CA on HaloTag showed an angle of γ = 8.7° whereas the brightest variants showed angles γ closer to 0°. This is in accordance with the calculated structures of the open and closed form of TMR in water where the open form showed an angle around 5.6° (Supplementary Figure 12). This might indicate a greater sp^2 character of C9 and therefore a higher contribution of the p orbital to the molecular orbitals relevant to the chromophore. This could positively influence the extinction coefficient. In addition, the dihedral angle $\varphi_{Ar\text{-}Ar}$ between the appended aromatic ring and the xanthene core was investigated. Surprisingly, all variants including HaloTag showed angles around $\varphi_{Ar\text{-}Ar}$ = 115.0°, corresponding rather to the angle calculated for the closed form $\varphi_{Ar\text{-}Ar}$ = 115.1° than the open form $\varphi_{Ar\text{-}Ar}$ = 94.3° of TMR in water (Supplementary Figure 12). These findings could indicate that rotation around the C9-C7'a bond is restricted by the protein as it positions the alkane and the amid bond in its binding pocket. This angle might therefore not be indicative for the equilibrium position. Similarly, rotations of the carboxylate out of the plane of the appended aromatic ring, is believed to be dictated by the crystal water and the crystal packing and therefore not relevant for processes in solution. Altogether, further analysis of the fully refined crystal structures might aid in understanding the origins of fluorogenicity of HaloTag fluorophore couples and enable rational design of even more enhanced HaloTag variants in terms of fluorescence intensities of fluorogenic rhodamines.

Table 4: Structural parameters measured in the preliminary X-ray crystal structures and from the calculated structures for TMR in water. The following parameters are given: the mean distance between the aniline nitrogen atom of TMR-CA on HaloTag and the aniline nitrogen atom of TMR-CA on the respective variant ($d_{N\text{-}N}$), its standard deviation ($sd_{dN\text{-}N}$), the dihedral angle between the xanthene and the appended aromatic ring ($\varphi_{Ar\text{-}Ar}$), and the tilt angle of the C9-C7'a bond out of the xanthene plane (γ). In addition, the previously listed ratio of intensities $I_{rel\text{-}SiR} = I_{mut} \cdot I_{Halo}^{-1}$ is given. Results are given as means±90% confidence interval for $I_{rel\text{-}SiR}$ (N = 4 samples); as a mean and its sd (N = 2 distances) for $d_{N\text{-}N}$, and as single measurements from the crystal structures or the calculated structures for $\varphi_{Ar\text{-}Ar}$ and γ. Values in brackets are taken from the indicated publication.* Upward shift.

Name	$I_{rel\text{-}SiR}$	$d_{N\text{-}N}$ [Å]	$sd_{dN\text{-}N}$ [Å]	$\varphi_{Ar\text{-}Ar}$ [°]	γ [°]
M175L	1.094±0.030	0.60	-	113.6	6.1
E170K	1.150±0.010	1.30	-	119.3	5.7
Q165H	1.149±0.014	1.20	0.14	116.8	7.5
P174H	1.151±0.016	0.40*	0.14	116.6	7.0
P174L	1.161±0.023	1.45	0.07	117.8	2.8
Q165H-P174R	1.200±0.025	2.00	0.14	119.0	3.6
Q165H-P174L	1.128±0.022	1.65	0.07	114.2	3.4
HaloTag	1.000±0.012	-	-	119.0	8.7
TMR open	-	-	-	94.3 (95.4)[131]	5.6 (7)[131]
TMR closed	-	-	-	115.1 (115.4)[131]	37.8

3.3 Mammalian cell assay

In order to test if the *in vitro* engineered variants perform similarly in mammalian cells, and especially in live-cell microscopy applications, the brighter HaloTag variants (Q165H, E170K, M174L, P175H, P175L, Q165H-P175L, and Q165H-P175R) and three dimmer variants (G161W, Q165W, and P175W) were sub-cloned for cytosolic expression in mammalian cells. In addition, co-translational expression of EGFP via the self-cleaving peptide T2A allowed for expression level normalisation.[231]

3.3.1 Live-cell confocal microscopy

Proteins were expressed in U-2 OS cells and imaged by confocal microscopy. The resulting z-stacks were summed up and analysed with regards to their SiR and EGFP fluorescence intensities. Whereas the single variants (M17L, E170K, Q165H) did not result in significantly higher ratios than parental HaloTag, the double variants (Q165H-P175L and Q165H-P175R) and the two single variants (P175H and P175L) showed clear SiR fluorescence intensity increases (Figure 37A). The ratios $I_{rel\text{-}SiR} = I_{mut} \cdot I_{Halo}^{-1}$ for these four variants were $I_{rel\text{-}SiR}$ = 1.16±0.06 (P175H), 1.18±0.05 (P175L), 1.17±0.05 (Q165H-P175R), and 1.12±0.05 (Q165H-P175L, Supplementary Table 23). The three dimmer variants showed significant changes and gave ratios of $I_{rel\text{-}SiR}$ = 0.49±0.03 (Q165W), 0.162±0.009 (G161W), and 0.25±0.01 (P175W). These were in good comparison with the values obtained *in vitro* and demonstrate that the *in vitro* engineering work translated with similar performance to *in cellulo* experiments. These brighter variants can thus be used to obtain up to 20% higher fluorescence intensity from SiR-CA in live-cell microscopy. It remains to be seen if the *in vitro* results are also transferrable for other fluorogenic fluorophores, such as JF_{614}-CA, JF_{635}-CA and MaP618-CA which are predicted to lead to even higher fluorescence intensity increases in combination with the variants Q165H-P175L and Q165H-P175R. This would benefit live-cell microscopy enormously as increases in brightness of cell-permeable, fluorogenic fluorophores are rather limited trough structural modifications of the fluorophore. In comparison, the introduction of azetidines lead to a 2.78-fold increase in brightness for TMR but only 1.42-fold for SiR and 1.05-fold for CPY.[136] Other commonly used strategies that often work via rigidification of fluorophores usually entail decreases in solubility and cell permeability, making them unsuitable for live-cell experiments. As brighter fluorophores allow using lower irradiation powers to obtain the same signal-to-noise ratios while reducing photobleaching, the brighter HaloTag-fluorophore combinations could be used for long-term live-cell microscopy experiments. In addition, other imaging strategies that require high signal-to-background ratios such as SRM and tracking experiments could benefit as well.

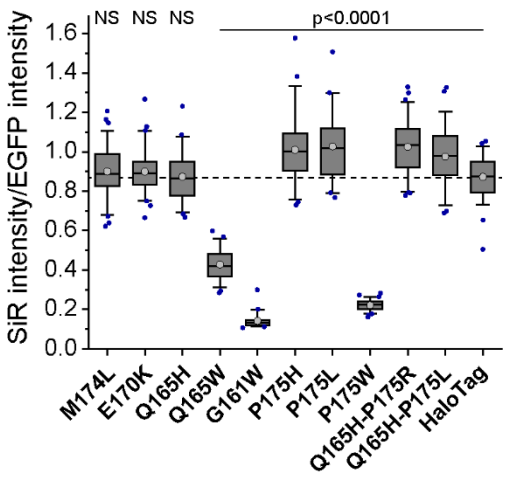

Figure 37: Ratios of SiR and EGFP intensity in mammalian cells for ten HaloTag variants. Boxplots of the ratio distributions measured by confocal microscopy. Measurements are from three biological replicates (*N* = 67, 63, 54, 55, 58, 55, 55, 60, 61, 57, and 49 cells; from left to right; Supplementary Table 23). Box = 25%–75% percentile, whiskers = 5%–95% percentile, black line = median, circle = mean, individual data points in blue, dashed line = mean of HaloTag for comparison. p-Values are given based on pairwise, one-sided t-tests. NS: not significant.

3.4 Conclusion and Outlook

In this chapter, it was demonstrated that the self-labeling protein tag HaloTag can be optimised for higher fluorescence intensities in combination with fluorogenic rhodamines. The screening based approach using iterative site-saturation mutagenesis in combination with a fluorescence read-out in bacterial cell lysate enabled the rapid identification of HaloTag variants with both increased and decreased fluorescence intensities when labeled with (fluorogenic) rhodamines. The analysis of the isolated variants generated valuable information for future HaloTag

engineering endeavours. Seven of the ten investigated amino acid sites have previously not been inspected, neither during the optimisation of HaloTag[97,98] nor the development of the halo-based oligonucleotide binder (HOB), where negatively charged surface residues were substituted for lysine in order to increase reaction rates with DNA.[232] Out of the remaining three amino acid sites, all of which were reported to be of importance for labeling kinetics,[98] only one tolerated further mutation without compromising labeling kinetics. Three rounds of directed evolution led to the isolation of a variant (Q165H-P174R) that significantly increased the fluorescence intensity of the tested fluorophores, reaching up to 300% *in vitro* (JF_{614}). In general, fluorophores with a higher D_{50} showed higher increases as compared to fluorophores with low D_{50}. Several dimmer variants (Q165W, G171W, and P174W) showed fluorescence intensity decreases down to 20% compared to parental HaloTag. They exhibited quantum yield decreases in the same range, indicating that the introduced tryptophan most probably quenched fluorescence. For most of the brighter variants a combination of an increased quantum yield and (apparent) extinction coefficient seemed responsible. Full X-ray structure refinement, closer analysis and modeling of surface properties such as the electrostatic potential could assist to get a better understanding of these phenomena. Nevertheless, it was shown that the selected variants exhibited similar fluorescence intensity changes when tested in mammalian cells. Especially the brighter variants might turn-out valuable for microscopy experiments as brighter fluorophores are in constant need. Above all, SRM could profit from the use of these variants and therefore their brightness should be characterised on a single-molecule level to evaluate their suitability for SMLM or tracking experiments. In addition, the brighter variants should be tested for altered properties such as increased bleaching stability in STED microscopy or changes in fluorescence lifetime. The dimmer variants, on the other hand, should be investigated for their blinking behaviour as the quenching might be dynamic.

Overall, the presented work is another example of how the photophysical and chemical properties of small-molecule fluorophores can be tuned using protein engineering instead of molecular engineering of fluorophores. Protein engineering is commonly used to improve the properties of FP's,[3] and was more recently also applied to optimize proteins that bind fluorogenic small-molecule fluorophores such as single-chain antibodies, photoactive yellow protein (PYP-tag) and fluorescence-activating and absorption-shifting tag (FAST).[130] However, it had thus far not been used to improve the brightens of fluorophores bound to the more classic self-labeling protein tags HaloTag or SNAP-Tag. In their context most attention was focused on optimising the small-molecule fluorophores used.[112] Moreover, as fluorophore binding to surfaces can not only induce changes in brightness but also affect other properties such as excitation and emission wavelength or pH sensitivity, it is envisioned that, as long as a screening assay can be set up, all these properties can be tuned through surface modifications. In this regard, proteins, and especially self-labeling protein tags, represent an ideal target as the fluorophores are usually tightly bound and their surface can be easily modified using directed evolution approaches. Nevertheless, other biopolymers such as DNA, RNA or lipids can be used in a similar manner. For instance, light-up RNA aptamers binding to fluorophores have become very attractive tools for RNA imaging and is an active field of research.[233–235] Lately, a SiR binding aptameter (SiRA) was presented and it would be of high interest to obtain and analyse a co-crystal structure of SiRA and SiR, in order to obtain insight as to which interactions are crucial for this system.[236] In addition, HaloTag could be optimised for different classes of fluorophores such as BODIPYs or cyanine fluorophores. The fluorophores of choice to perform such screenings are those that are environmentally sensitive and therefore have a high propensity to be influenced by the protein surface. Ideally, all these efforts would help to generate more powerful self-labeling protein tag-fluorophore combinations with tailored properties for their respective applications in microscopy. In addition, instead of developing specific self-labeling protein tag-fluorophore couples such screenings could also be used in combination with a panel of different substrates, improving self-labeling protein tags for broad applications creating an even more universal tag. Not only brighter fluorophores are crucial for advanced microscopy methods such as SRM but also other properties such as blinking or photostability are of utmost importance. This work represents an example how the performance of synthetic fluorophores bound to a self-labeling protein tag can be improved through protein engineering of the tag, which eventually should result in better tools for optical microscopy.

Chapter 4 Conclusion

The presented work of this thesis demonstrates the development of a small-molecule fluorophore and the optimization of a self-labeling protein tag. It shows how synthetic chemistry and protein engineering can generate protein-fluorophore couples that advance fluorescence microscopy. It is expected that both PA-SiR with its photoactivation via light-induced protonation and the brighter HaloTag will become useful additions to the toolbox for live-cell fluorescence microscopy.

Chapter 5 Materials and methods

5.1 Materials and general information for chemical synthesis

Parts of this chapter have been previously published. For completeness reasons several compounds were listed again and were therefore adapted from ref [203] published by Springer under Nature CC BY 4.0 or ref [204]. This is indicated by the number of the reference after the compound name. For several probes only small amounts of product (<1 mg, MW > 600 g mol^{-1}) were isolated, thus measuring full NMR characterisations especially ^{13}C spectra was not possible. ^{13}C spectra where hence only acquired for probes that were used for spectroscopic experiments.

All chemical reagents and anhydrous solvents for synthesis were purchased from commercial suppliers (Acros, Apollo, Armar, Bachchem, Biomatrik, Fluka, Fluorochem, LC Laboratories, Merck, Reseachem, Roth, Sigma-Aldrich, TCI, and TOCRIS) and used without further purification. BG-NH_2 **135**, CP-NH_2 **136**, CA-NHBoc **137**, Hoechst-linker **145**, and HM-SiR-CA were synthesised according to literature procedures.[32,96,97,123] Jasplakinolide-NHBoc **144** was obtained from a custom synthesis by Spirochrome AG. PA-JF_{646}-NHS and Alexa647-NHS were purchased from TOCRIS and ThermoFisher and the amid bond coupling witch CA-NH_2 was carried out as described by the vendor and confirmed by LC-MS and HRMS. JF_{646}-CA, JF_{635}-CA, JF_{614}-CA, TMR-CA, CPY-CA, MaP555-CA, MaP618-CA, were synthesised by B. Matthes (MPI-MR), and precursor **78** was synthesised by Dr. A. Salim (MPI-MR). Compounds **83**, **85**, **87**, **89**, **90**, **93**, **95**, **96**, **97**, **98** and **115** were synthesised by my student J. Notbohm (MPI-MR). Composition of mixed solvents is given by volume ratio (v/v). Reactions in the absence of air and moisture were performed in oven-dried glassware under Ar or N_2 atmosphere. Flash column chromatography was performed using a CombiFlash Rf system (Teledyne ISCO) using SiO_2 RediSep® Rf columns at 25 °C or a Biotage (Isolera™) flash system using SiliaSep™ columns. The used solvent compositions are reported individually in parentheses. Analytical thin layer chromatography was performed on glass plates coated with silica gel 60 F254 (Merck). Visualisation was achieved using UV light (254 nm). Evaporation *in vacuo* was performed at 25–60 °C and 900–10 mbar. ^{1}H, ^{13}C, and ^{19}F NMR spectra were recorded on AV 400, Ascend™ 400, and AV 600 Bruker spectrometers at 400 MHz or 600 MHz (^{1}H), 101 MHz or 151 MHz (^{13}C), 377 MHz or 566 MHz (^{19}F) respectively. All spectra were recorded at 298 K. Chemical shifts δ are reported in ppm downfield from tetramethylsilane using the residual deuterated solvent signals as an internal reference ($CDCl_3$: δ_H = 7.26 ppm, δ_C = 77.16 ppm; CD_3OD: δ_H = 3.31 ppm, δ_C = 49.00 ppm; DMSO-*d*$_6$: δ_H = 2.50 ppm, δ_C = 39.52 ppm; CD_3CN: δ_H = 1.94 ppm, δ_C = 118.26 ppm). For ^{1}H, ^{13}C, and ^{19}F NMR, coupling constants *J* are given in Hz and the resonance multiplicity is described as s (singlet), d (doublet), t (triplet), q (quartet), quint (quintet), sext (sextet), sept (septet), m (multiplet), and br. (broad). High-resolution mass spectrometry (HRMS) was performed by the MS-service of the EPF Lausanne (SSMI) on a Waters Xevo® G2-S Q-Tof spectrometer with electron spray ionisation (ESI) or by the MS-facility of the Max Planck Institute for Medical Research on a Bruker maXis II™ ETD. Liquid chromatography coupled to mass spectrometry (LC-MS) was performed on a Shimadzu MS2020 connected to a Nexera UHPLC system equipped with a Waters ACQUITY UPLC BEH C18 (1.7 µm, 2.1 x 50 mm) column or a Supelco Titan C18 80 Å (1.9 µm, 2.1 x 50 mm). Buffer A: 0.05% HCOOH in H_2O Buffer B: 0.05% HCOOH in ACN. Analytical gradient was from 10% to 90% B within 6 min with 0.5 mL min^{-1} flow unless otherwise stated. Preparative reverse phase high-performance liquid chromatography (RP-HPLC) was carried out on a Dionex system equipped with an UltiMate 3000 diode array detector for product visualisation on a Waters Symmetry C18 column (5 µm, 3.9 x 150 mm), Waters SunFire™ Prep C18 OBD™ (5 µm, 10 x 150 mm) column, Supleco Ascentis® C18 column (5 µm, 10 x 250 mm) or on a Supleco Ascentis® C18 column (5 µm, 21.2 x 250 mm). Buffer A: 0.1% TFA in H_2O Buffer B: ACN. Typical gradient was from 10% to 90% B within 32 min with 2, 4 or 8 mL min^{-1} flow.[203]

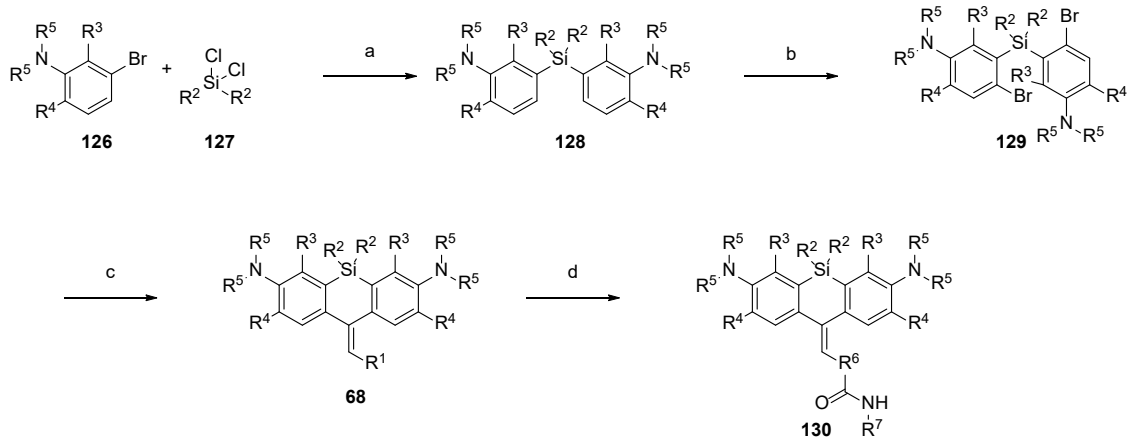

Scheme 1. Synthetic route to PA-SiR derivatives[141,207]. (a) *sec*-BuLi, Et_2O, −78 °C to room temperature 1 h; (b) NBS, NH_4OAc, ACN, 0 °C to room temperature, 2 h; (c) *sec*-BuLi, THF, anhydride or ester, −78 °C to room temperature 1 h; (d) TSTU, DIPEA, R^7-NH_2, DMSO, room temperature 30 min.

General procedure A for the silane introduction

3-Bromo-*N,N*-dimethylaniline (**55**) (3.20 g, 16.00 mmol, 2.0 eq.) was dissolved in dry Et_2O (45 mL) and cooled down to −78 °C. *sec*-BuLi (14.0 mL, 18.40 mmol, 2.3 eq., 1.3 M in cyclohexane) was added dropwise over 15 min and the mixture was stirred for 30 min at −78 °C. Dichlorodimethylsilane (**56**) (1.0 mL, 8.00 mmol, 1.0 eq.) was added dropwise over 10 min at −78 °C. The mixture was stirred for 10 min at −78 °C and then warmed up to room temperature and stirred for 1 h. The mixture was quenched with aqueous saturated $NaHCO_3$ solution. The aqueous layer was extracted with Et_2O (3 x 150 mL) and the combined organic layers were dried over $MgSO_4$, filtered, and evaporated to afford the crude product.[203]

General procedure B for the bromination

A solution of **57** (1.85 g, 6.18 mmol, 1.0 eq.) and ammonium acetate (95 mg, 1.24 mmol, 0.2 eq.) in ACN (30 mL) was cooled down to 0 °C. NBS (2.3 g, 12.98 mmol, 2.1 eq.) was added portion wise over 10 min. The mixture was stirred at 0 °C for 30 min and then warmed up to room temperature and stirred for 2 h. A mixture of aqueous saturated $NaHCO_3$ solution and water 1:1 was added. The aqueous layer was extracted with CH_2Cl_2 (3 x 100 mL) and the combined organic layers were dried over $MgSO_4$, filtered, and evaporated to afford the crude product.[203]

General procedure C for the ring closure

A solution of **58** (365 mg, 0.8 mmol, 1.0 eq.) in dry THF (8 mL) was cooled down to −78 °C. *sec*-BuLi (1.4 mL, 1.76 mmol, 2.2 eq., 1.3 M in cyclohexane) was added dropwise over 5 min and the mixture was stirred for 30 min at −78 °C. A solution of glutaric anhydride (**59**) (100 mg, 0.88 mmol, 1.1 eq.) in dry THF (1.0 mL) was added to the mixture. The mixture was stirred at −78 °C for 15 min and then warmed up to room temperature and stirred for 30 min. Acetic acid (2 mL) was added to the mixture. The blue mixture was adsorbed on SiO_2 (2 g).[203]

3,3'-(Dimethylsilanediyl)bis(*N*,*N*-dimethylaniline) (57)[203]

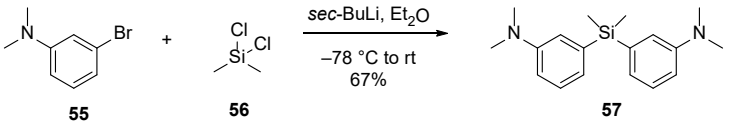

55 56 57

Following general procedure **A**, flash column chromatography (SiO_2, hexane/EtOAc 100:0 → 70:30) gave **57** (1.598 g, 67%) as a colourless oil.

^{1}H NMR (400 MHz, $CDCl_3$): δ 7.31 – 7.22 (m, 2H), 6.98 – 6.92 (m, 4H), 6.78 (ddd, J = 8.3, 2.8, 1.0 Hz, 2H), 2.94 (s, 12H), 0.56 (s, 6H); ^{13}C NMR (101 MHz, $CDCl_3$): δ 150.0, 139.1, 128.6, 122.9, 118.5, 113.7, 40.8, −2.0; HRMS (*m/z*): $[M + H]^+$ calcd. for $C_{18}H_{27}N_2Si^+$, 299.1938; found, 299.1940.

3,3'-(Dimethylsilanediyl)bis(4-bromo-*N*,*N*-dimethylaniline) (58)[203]

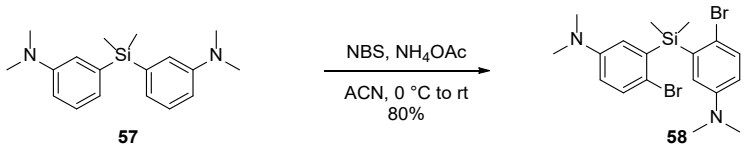

57 58

Following general procedure **B**, flash column chromatography (SiO_2, hexane/CH_2Cl_2 100:0 → 0:100) gave **58** (2.270 g, 80%) as a beige solid.

^{1}H NMR (400 MHz, $CDCl_3$): δ 7.35 (d, J = 8.7 Hz, 2H), 6.84 (d, J = 3.2 Hz, 2H), 6.60 (dd, J = 8.7, 3.2 Hz, 2H), 2.88 (s, 12H), 0.75 (s, 6H); ^{13}C NMR (101 MHz, $CDCl_3$): δ 149.0, 138.9, 133.1, 121.9, 116.9, 115.4, 40.7, −0.8; HRMS (m/z): $[M + H]^+$ calcd. for $C_{18}H_{25}Br_2N_2Si^+$, 455.0148; found, 455.0145.

10-(3-Carboxypropylidene)-7-(dimethylamino)-*N*,*N*,5,5-tetramethyl-5,10-dihydrodibenzo[*b*,*e*]-silin-3-aminium trifluoroacetate; PA-SiR (41)[203]

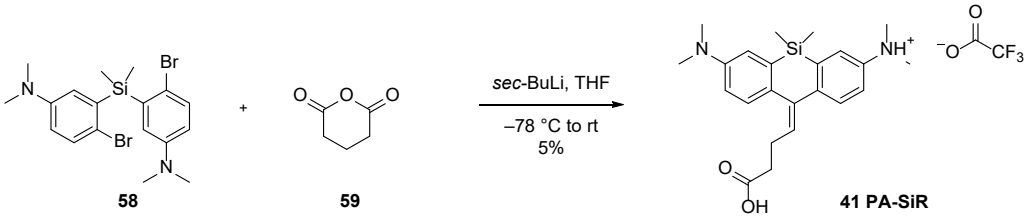

58 59 41 PA-SiR

Following general procedure **C**, flash column chromatography (SiO_2, CH_2Cl_2/MeOH 100:0 → 90:10) and RP-HPLC (4 mL min^{-1}, 10% to 90% B in 32 min) gave PA-SiR **41** (23 mg, 5%) as a light green solid.

^{1}H NMR (400 MHz, CD_3OD): δ 7.70 (t, J = 2.9 Hz, 2H), 7.66 (d, J = 8.5 Hz, 1H), 7.61 (d, J = 8.4 Hz, 1H), 7.55 (dd, J = 8.5, 2.6 Hz, 1H), 7.50 (dd, J = 8.5, 2.7 Hz, 1H), 6.03 (t, J = 7.3 Hz, 1H), 3.27 (s, 6H), 3.26 (s, 6H), 2.68 (q, J = 7.4 Hz, 2H), 2.45 (t, J = 7.2 Hz, 2H), 0.52 (br. s, 6H); ^{13}C NMR (101 MHz, CD_3OD): δ 176.3, 162.3 (q, J = 36.0 Hz), 150.1, 144.5, 143.4, 143.2, 141.0, 140.3, 138.5, 134.1, 131.3, 128.6, 123.8, 123.7, 121.7, 120.0, 117.8 (q, J = 291.0 Hz), 46.4, 45.7, 34.8, 26.6, −3.8; ^{19}F NMR (376 MHz, CD_3OD): δ −77.11; HRMS (*m/z*): $[M - H]^-$ calcd. for $C_{23}H_{29}N_2O_2Si^-$, 393.2004; found, 393.1992.

Note: All attempts (HPLC: triethylammonium acetate/ACN pH = 8; triethylammonium bicarbonate/ACN pH = 8 buffer system) to isolate the fluorescent SiR **42** were not successful. Also work up with aqueous saturated NH_4Cl instead of acetic acid did not lead to the isolation of the spirolactone **44** as the compound converted during column chromatography.

4-(3,7-Bis(dimethylamino)-10-hydroxy-5,5-dimethyl-5,10-dihydrodibenzo[*b*,*e*]silin-10-yl)butanoate (43)[203]

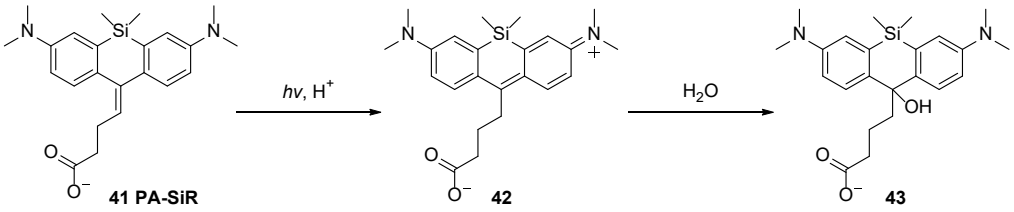

Photoactivation experiment as described in Section 5.2 giving compound **43**.

^{1}H NMR (600 MHz, H_2O + D_2O): δ 7.83 (d, J = 8.8 Hz, 2H; C*H*$_{ar}$), 7.26 (d, J = 2.8 Hz, 2H; C*H*$_{ar}$), 7.14 (dd, J = 8.9, 2.8 Hz, 2H; C*H*$_{ar}$), 2.87 (s, 12H; N*Me*$_2$), 2.71 (s, 3H; DMSO reference), 1.89 (t, J = 7.4 Hz, 2H; C*H*$_2$), 1.66 – 1.80 (m, 2H; C*H*$_2$), 1.12 – 1.29 (m, 2H; C*H*$_2$), 0.54 (s, 3H; Si*Me*), 0.44 (s, 3H; Si*Me*); ^{13}C NMR (151 MHz, H_2O + D_2O): δ 183.7, 163.7, 163.5, 150.2, 144.5, 135.2, 127.2, 120.3, 117.9, 116.0, 77.7, 49.7, 41.9, 39.4, 37.9, 21.9, −2.0.

3-((2-(4-Carboxybutanoyl)-5-(dimethylamino)phenyl)dimethylsilyl)-*N*,*N*-dimethylbenzen-aminium trifluoroacetate (60)[203]

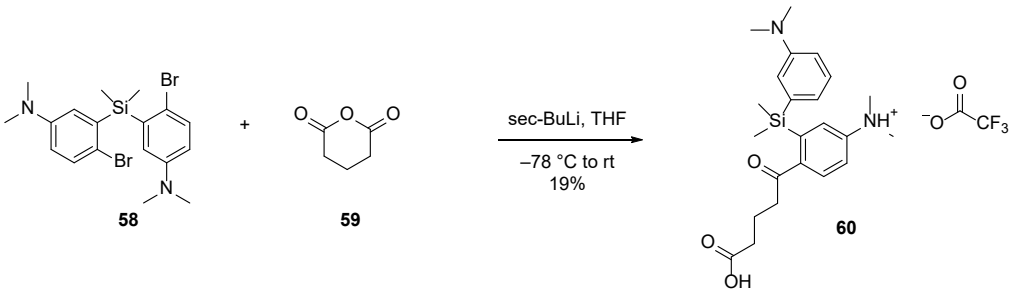

Compound **60** is the major side product isolated during preparation of PA-SiR **41**. Following general procedure **C**, flash column chromatography (SiO_2, hexane/EtOAc 100:0 → 0:100 then CH_2Cl_2/MeOH 100:0 → 90:10) and RP-HPLC (8 mL min^{-1}, 10% to 90% B in 32 min) also gives **60** (65 mg, 19%) as a light blue solid.

^{1}H NMR (400 MHz, CD_3OD): δ 7.97 (d, J = 8.9 Hz, 1H), 7.67 (dd, J = 2.6, 0.8 Hz, 1H), 7.58 – 7.51 (m, 2H), 7.48 (dd, J = 8.2, 7.0 Hz, 1H), 7.02 (d, J = 2.8 Hz, 1H), 6.79 (dd, J = 8.9, 2.7 Hz, 1H), 3.27 (s, 6H), 3.05 (s, 6H), 2.86 (t, J = 7.2 Hz, 2H), 2.12 (t, J = 7.4 Hz, 2H), 1.76 (p, J = 7.3 Hz, 2H), 0.57 (s, 6H); ^{13}C NMR (101 MHz, CD_3OD): δ 200.2, 176.9, 161.92 (d, J = 36.1 Hz), 153.9, 147.4, 143.4, 141.6, 136.2, 133.7, 130.6, 130.3, 126.0, 121.6, 120.4, 117.63 (q, J = 290.4 Hz), 112.3, 47.2, 40.1, 37.3, 33.9, 21.5, −0.3; ^{19}F NMR (376 MHz, CD_3OD): δ −77.15; HRMS (*m/z*): $[M + 2H]^{2+}$ calcd. for $C_{23}H_{34}N_2O_3Si^{2+}$, 207.1164; found, 207.1163.

***N*^{3},*N*^{3},*N*^{7},*N*^{7},5,5-Hexamethyl-10-methylene-5,10-dihydrodibenzo[*b*,*e*]siline-3,7-diamine (62)**[203]

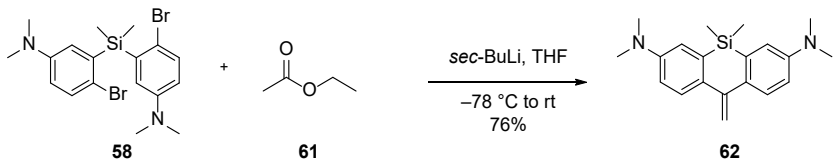

Following general procedure **C**, washing the crude solid with MeOH instead of absorption to SiO_2 gave **62** (195 mg, 76%) as a white solid.

^{1}H NMR (400 MHz, $CDCl_3$): δ 7.59 (d, J = 8.7 Hz, 2H), 6.93 (d, J = 2.8 Hz, 2H), 6.79 (dd, J = 8.7, 2.8 Hz, 2H), 5.41 (s, 2H), 2.99 (s, 12H), 0.44 (s, 6H); ^{13}C NMR (101 MHz, $CDCl_3$): δ 149.2, 147.7, 135.2, 134.8, 126.9, 115.9, 114.2, 111.3, 40.9, −2.1; HRMS (*m/z*): $[M + H]^+$ calcd. for $C_{20}H_{27}N_2Si^+$, 323.1938; found, 323.1936.

3,7-Bis(dimethylamino)-5,5-dimethyldibenzo[*b,e*]silin-10(5*H*)-one (65)

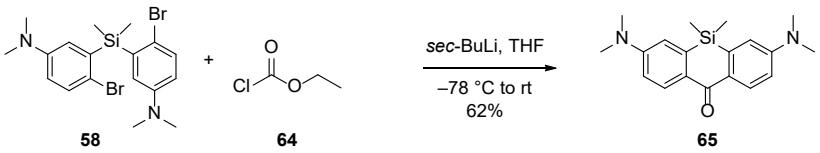

Following general procedure **C**, flash column chromatography (SiO2, hexane/EtOAc 100:0 → 50:50) gave **65** (130 mg, 62%) as a yellow solid.

^{1}H NMR (400 MHz, $CDCl_3$): δ 8.40 (d, J = 9.0 Hz, 2H), 6.84 (dd, J = 9.0, 2.8 Hz, 2H), 6.79 (d, J = 2.8 Hz, 2H), 3.10 (s, 12H), 0.47 (s, 6H); ^{13}C NMR (101 MHz, $CDCl_3$): δ 185.4, 151.6, 140.6, 131.8, 129.8, 114.4, 113.3, 40.2, −0.8; HRMS (m/z): $[M + H]^+$ calcd. for $C_{19}H_{25}N_2OSi^+$, 325.1731; found, 325.1726.

7-(Dimethylamino)-*N*,*N*,5,5-tetramethyl-10-propylidene-5,10-dihydrodibenzo[*b*,*e*]silin-3-aminium trifluoroacetate (69)[203]

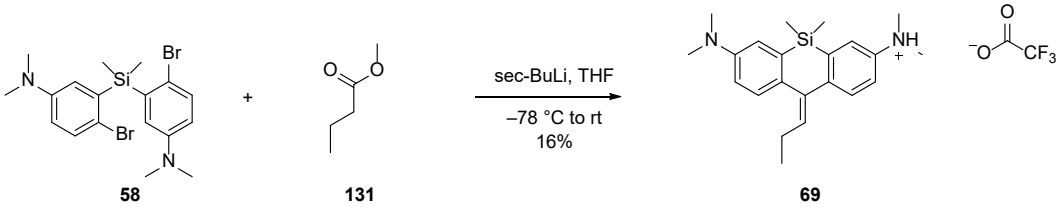

Following general procedure **C**, flash column chromatography (SiO_2, hexane/EtOAc 90:10 → 70:30) and RP-HPLC (8 mL min^{-1}, 20% to 100% B in 32 min) gave **69** (61 mg, 16%) as a light blue solid.

^{1}H NMR (400 MHz, CD_3OD): δ 7.68 – 7.60 (m, 2H), 7.60 (d, J = 2.7 Hz, 1H), 7.54 – 7.47 (m, 2H), 7.40 (dd, J = 8.5, 2.7 Hz, 1H), 6.01 (t, J = 7.5 Hz, 1H), 3.25 (s, 6H), 3.22 (s, 6H), 2.39 (p, J = 7.5 Hz, 2H), 1.07 (t, J = 7.5 Hz, 1H), 0.50 (br. s, 6H); ^{13}C NMR (101 MHz, CD_3OD): δ 162.2 (q, J = 36.0 Hz), 150.0, 145.0, 143.6, 142.4, 139.8, 139.7, 138.3, 137.2, 131.2, 128.4, 123.3, 122.8, 121.3, 119.2, 117.7 (q, J = 283.5 Hz), 46.1, 45.2, 24.4, 14.6, −3.8; ^{19}F NMR (376 MHz, CD_3OD): δ −77.15; HRMS (*m/z*): $[M + 2H]^{2+}$ calcd. for $C_{22}H_{32}N_2Si^{2+}$, 176.1162; found, 176.1160.

3,7-Bis(dimethylamino)-5,5-dimethyl-3',4'-dihydro-5*H*,5'*H*-spiro[dibenzo[*b*,*e*]siline-10,2'-furan]-5'-one (133)[203]

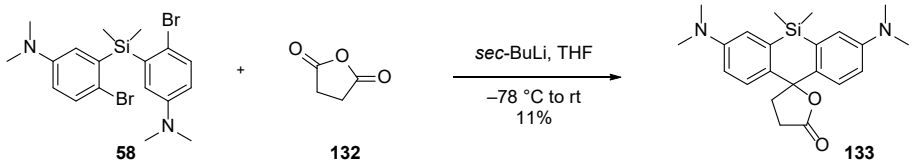

A solution of **58** (296 mg, 0.65 mmol, 1.0 eq.) in dry THF (9 mL) was cooled down to −78 °C. *sec*-BuLi (1.2 mL, 1.7 mmol, 2.6 eq., 1.3 M in cyclohexane) was added dropwise over 5 min and the mixture was stirred for 30 min at −78 °C. A solution of succinic anhydride (**132**) (72 mg, 0.72 mmol, 1.1 eq.) in dry THF (2.0 mL) was added to the mixture. The mixture was stirred at −78 °C for 15 min and then warmed up to room temperature and stirred for 30 min. Aqueous saturated NH_4Cl was added and the aqueous layer was extracted with EtOAc (2 x 25 mL). The combined organic layers were dried over $MgSO_4$, filtered, and evaporated to afford the crude product. Flash column chromatography (SiO_2, hexane/EtOAc 100:0 → 0:100) gave **133** (28 mg, 11%) as a white solid.

^{1}H NMR (400 MHz, CD_3CN): δ 7.34 (d, J = 8.8 Hz, 2H), 7.06 (d, J = 2.8 Hz, 2H), 6.79 (dd, J = 8.8, 2.9 Hz, 2H), 2.95 (s, 12H), 2.52 (td, J = 7.9, 0.7 Hz, 2H), 2.30 (td, J = 8.4, 0.7 Hz, 2H), 0.58 (s, 3H), 0.42 (s, 3H); ^{13}C NMR (101 MHz, CD_3CN): δ 178.6, 150.2, 138.8, 134.8, 124.2, 118.6, 114.3, 88.7, 42.9, 40.7, 29.2, 0.5, −2.4; HRMS (m/z): $[M + H]^+$ calcd. for $C_{22}H_{29}N_2O_2Si^+$, 381.1993; found, 381.1993.

10-(2-Carboxyethylidene)-7-(dimethylamino)-*N*,*N*,5,5-tetramethyl-5,10-dihydrodibenzo[b,e]-silin-3-aminium trifluoroacetate; PA-SiR-C3 (70)[203]

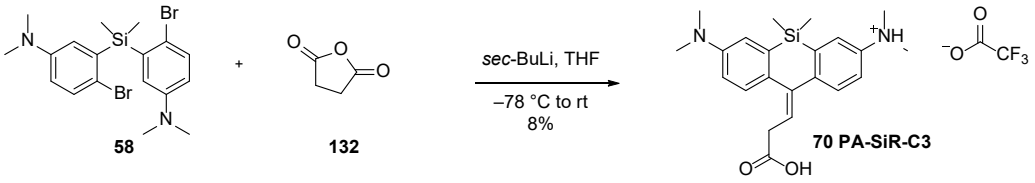

A solution of **58** (296 mg, 0.65 mmol, 1.0 eq.) in dry THF (9 mL) was cooled down to −78 °C. *sec*-BuLi (1.2 mL, 1.7 mmol, 2.6 eq., 1.3 M in cyclohexane) was added dropwise over 5 min and the mixture was stirred for 30 min at −78 °C. A solution of succinic anhydride (**132**) (72 mg, 0.72 mmol, 1.1 eq.) in dry THF (2.0 mL) was added to the mixture. The mixture was stirred at −78 °C for 15 min and then warmed up to room temperature and stirred for 30 min. Aqueous saturated NH_4Cl was added and the aqueous layer was extracted with EtOAc (2 x 25 mL). The combined organic layers were dried over $MgSO_4$, filtered, and evaporated to afford the crude product. Flash column chromatography (SiO_2, hexane/EtOAc 100:0 → 0:100) gave **133** (28 mg, 11%) as a white solid. The compound was dissolved in water with 0.1% TFA. The blue solution was frozen and lyophilised overnight. RP-HPLC (8 mL min^{-1}, 20% to 90% B in 32 min) gave PA-SiR-C3 (27 mg, 8%) as a light blue solid.

^{1}H NMR (400 MHz, CD_3CN): δ 7.60 – 7.57 (m, 2H), 7.48 (d, J = 2.7 Hz, 1H), 7.43 (d, J = 8.5 Hz, 1H), 7.40 (dd, J = 8.5, 2.6 Hz, 1H), 7.23 (dd, J = 8.5, 2.7 Hz, 1H), 6.06 (t, J = 7.6 Hz, 1H), 3.33 (d, J = 7.7 Hz, 2H), 3.11 (s, 6H), 3.08 (s, 6H), 0.45 (s, 6H); ^{13}C NMR (101 MHz, CD_3CN): δ 173.1, 147.4, 146.2, 144.4, 142.3, 139.0, 138.6, 137.5, 130.4, 127.8, 125.1, 123.1, 121.9, 120.9, 118.5, 45.3, 43.9, 35.6, −3.7; ^{19}F NMR (376 MHz, CD_3CN): δ −76.26; HRMS (m/z): $[M + 2H]^{2+}$ calcd. for $C_{22}H_{30}N_2O_2Si_2^+$, 191.1033; found, 191.1032.

Note: For reaction with succinic anhydride both PA-SiR-C3 and compound **131** could be isolated. Analogues work up and isolation procedure for PA-SiR **41** did not lead to the isolation of the spirolactone **44** but only PA-SiR **41**.

(E)-10-(3-Carboxy-2-methylpropylidene)-7-(dimethylamino)-*N*,*N*,5,5-tetramethyl-5,10-dihydrodibenzo[*b*,*e*]silin-3-aminium trifluoroacetate (71)

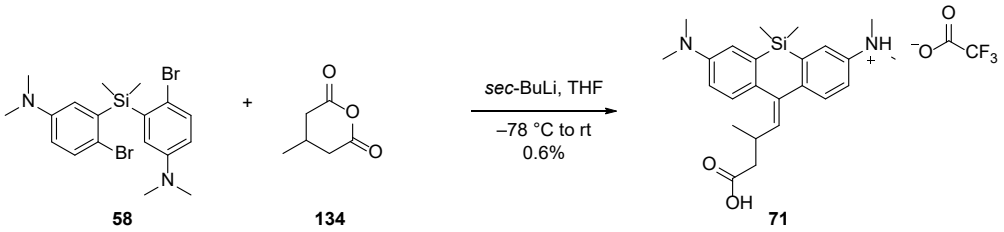

Following general procedure **C**, flash column chromatography (SiO_2, CH_2Cl_2/MeOH 100:0 → 90:10) and RP-HPLC (3 mL min^{-1}, 10% to 65% B in 32 min) gave **71** (0.9 mg, 0.6%) as a light blue solid.

^{1}H NMR (400 MHz, DMSO-d_6): δ 7.38 – 7.21 (m, 2H), 7.03 (br. s, 2H), 6.95 – 6.77 (m, 2H), 5.51 (d, J = 10.3 Hz, 1H), 2.95 (s, 6H), 2.94 (s, 6H), 2.52 (d, J = 6.8 Hz, 2H), 2.26 (br. s, 1H), 1.04 (t, J = 7.0 Hz, 3H), 0.37 (s, 6H); HRMS (m/z): $[M - H]^-$ calcd. for $C_{24}H_{31}N_2O_2Si^-$ 407.2160; found, 407.2155.

(E)-7-(Dimethylamino)-10-(4-((2,5-dioxopyrrolidin-1-yl)oxy)-4-oxobutylidene)-*N*,*N*,5,5-tetramethyl-5,10-dihydrodibenzo[*b*,*e*]silin-3-aminium trifluoroacetate (100)

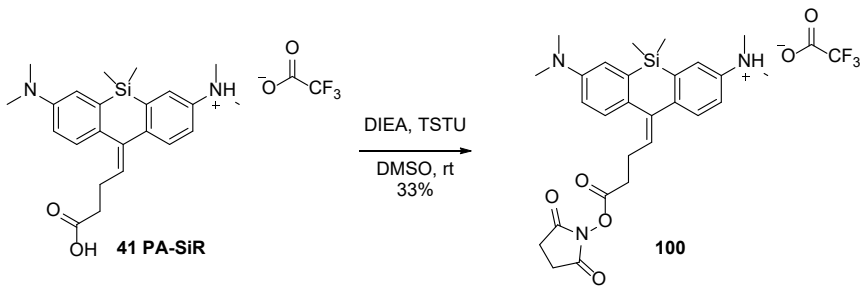

A solution of PA-SiR **41** (5.1 mg, 13.0 µmol, 1.0 eq.) in DMSO (300 µL) was treated with DIEA (6.0 µL, 39 µmol, 3.0 eq.) and TSTU (4.7 mg, 15.6 µmol, 1.2 eq.). The mixture was shaken for 30 min at room temperature and then acidified with TFA (2 µL). RP-HPLC (3 mL min^{-1}, 0% to 90% B in 32 min) gave **100** (2.1 mg, 33%) as a light green solid.

^{1}H NMR (400 MHz, CD_3OD): δ 7.69 (d, *J* = 8.5 Hz, 1H), 7.64 (d, *J* = 2.6 Hz, 1H), 7.60 (d, *J* = 2.7 Hz, 1H), 7.57 (d, *J* = 8.5 Hz, 1H), 7.51 (dd, *J* = 8.4, 2.6 Hz, 1H), 7.41 (dd, *J* = 8.5, 2.7 Hz, 1H), 6.05 (t, *J* = 7.0 Hz, 1H), 3.25 (s, 6H), 3.22 (s, 6H), 2.87 – 2.77 (m, 8H), 0.50 (s, 6H); ^{13}C NMR (101 MHz, CD_3OD): δ 171.9, 169.7, 149.4, 145.4, 143.8, 142.0, 141.0, 139.9, 138.5, 131.8, 131.1, 128.6, 123.2, 122.7, 121.2, 119.2, 46.1, 44.9, 31.6, 26.5, 26.1, −3.9; ^{19}F NMR (376 MHz, CD_3OD): δ −77.1; HRMS (m/z): $[M + H]^+$ calcd. for $C_{27}H_{34}N_3O_4Si^+$ 492.2312; found, 492.2311.

10-(4-((4-(((2-Amino-9*H*-purin-6-yl)oxy)methyl)benzyl)amino)-4-oxobutylidene)-7-(dimethyl-amino)-*N*,*N*,5,5-tetramethyl-5,10-dihydrodibenzo[*b*,*e*]silin-3-aminium trifluoroacetate; PA-SiR-BG (103)[203]

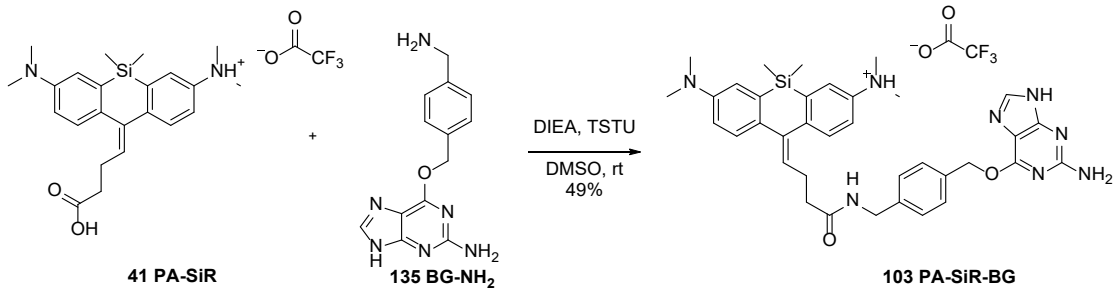

A solution of PA-SiR **41** (4.0 mg, 8.0 µmol, 1.0 eq.) in DMSO (300 µL) was treated with DIEA (5.0 µL, 30.1 µmol, 3.8 eq.) and TSTU (3.6 mg, 12.0 µmol, 1.5 eq.). The mixture was shaken for 20 min and BG-NH_2 (3.4 mg, 12.8 µmol, 1.6 eq.) was added. The mixture was shaken for 10 min at room temperature and then acidified with TFA (15 µL). RP-HPLC (8 mL min^{-1}, 10% to 90% B in 32 min) gave PA-SiR-BG (3.0 mg, 49%) as a light green solid.

^{1}H NMR (400 MHz, CD_3OD): δ 8.32 (s, 1H), 7.58 – 7.47 (m, 4H), 7.42 – 7.36 (m, 3H), 7.30 – 7.25 (m, 3H), 5.95 (t, J = 7.2 Hz, 1H), 5.60 (s, 2H), 4.35 (s, 2H), 3.21 (s, 6H), 3.17 (s, 6H), 2.73 (q, J = 7.2 Hz, 2H), 2.41 (t, J = 7.2 Hz, 2H), 0.46 (s, 6H); ^{13}C NMR (101 MHz, CD_3OD): δ 174.9, 162.2 (d, J = 36.2 Hz), 161.1, 158.6, 153.8, 148.3, 146.1, 144.6, 143.2, 141.5, 140.8, 140.4, 139.6, 138.1, 135.4, 132.4, 131.1, 130.1, 128.7, 128.3, 122.4, 121.8, 120.5, 118.2, 117.8 (d, J = 290.6 Hz), 108.7, 70.6, 45.4, 44.3, 43.7, 37.0, 27.6, −2.6; ^{19}F NMR (376 MHz, CD_3OD): δ −77.14; HRMS (*m/z*): $[M + H]^+$ calcd. for $C_{37}H_{43}N_8O_2Si^+$, 647.3278; found, 647.3274.

(Z)-10-(4-((4-(((2-Amino-6-chloropyrimidin-4-yl)oxy)methyl)benzyl)amino)-4-oxobutylidene)-7-(dimethylamino)-*N*,*N*,5,5-tetramethyl-5,10-dihydrodibenzo[*b*,*e*]silin-3-aminium trifluoroacetate; PA-SiR-CP (104)

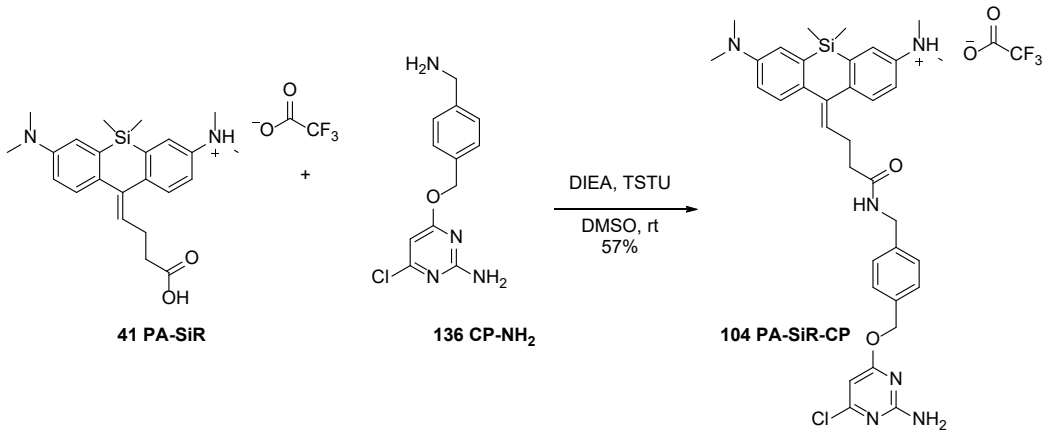

A solution of PA-SiR **41** (1.3 mg, 3.3 µmol, 1.0 eq.) in DMSO (150 µL) was treated with DIEA (1.6 µL, 9.9 µmol, 3.0 eq.) and TSTU (1.2 mg, 4.0 µmol, 1.2 eq.). The mixture was shaken for 20 min at room temperature. CP-NH_2 (1.22 mg, 4.6 µmol, 1.4 eq.) was added. The mixture was shaken for 20 min and then acidified with TFA (3 µL). RP-HPLC (3 mL min^{-1}, 10% to 90% B in 32 min) gave PA-SiR-CP (1.2 mg, 57%) as a light blue solid.

^{1}H NMR (400 MHz, DMSO-d_6): δ 8.34 (t, J = 5.9 Hz, 1H), 7.42 – 7.29 (m, 2H), 7.29 – 7.25 (m, 2H), 7.18 (d, J = 8.0 Hz, 2H), 7.12 – 7.05 (m, 3H), 6.99 – 6.82 (m, 3H), 6.11 (s, 1H), 5.69 (t, J = 7.1 Hz, 1H), 5.24 (s, 2H), 4.22 (d, J = 5.9 Hz, 2H), 3.02 – 2.91 (m, 14H), 2.62 – 2.54 (m, 2H), 0.35 (s, 6H); HRMS (m/z): $[M + H]^+$ calcd. for $C_{35}H_{42}ClN_6O_2Si^+$ 641.2822; found, 641.2820.

10-(4-((2-(2-((6-Chlorohexyl)oxy)ethoxy)ethyl)amino)-4-oxobutylidene)-7-(dimethylamino)-*N*,*N*,5,5-tetramethyl-5,10-dihydrodibenzo[*b*,*e*]silin-3-aminium trifluoroacetate; PA-SiR-CA (105)[203]

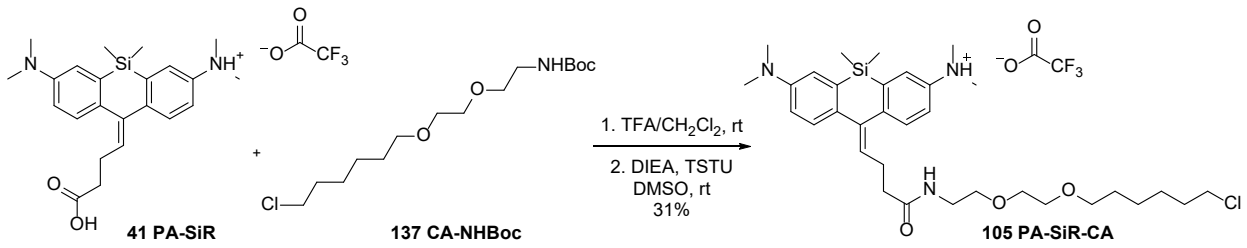

A solution of PA-SiR **41** (4.0 mg, 8.0 µmol, 1.0 eq.) in DMSO (300 µL) was treated with DIEA (5.0 µL, 30.1 µmol, 3.8 eq.) and TSTU (3.6 mg, 12.0 µmol, 1.5 eq.). The mixture was shaken for 20 min at room temperature. In a separate vial a solution of CA-NHBoc (4.0 mg, 12.3 µmol, 1.5 eq.) in TFA/CH_2Cl_2 (2:8, 80 µL) was shaken for 5 min. The solution was evaporated and dried on the high vacuum for 1 h. The residue was taken up in DMSO (50 µL) and added to the other mixture. The mixture was shaken for 10 min and then acidified with TFA (3 µL). RP-HPLC (4 mL min^{-1}, 10% to 90% B in 32 min) gave PA-SiR-CA (1.8 mg, 31%) as a light blue solid.

^{1}H NMR (400 MHz, CD_3OD): δ 7.61 (d, J = 8.5 Hz, 1H), 7.56 – 7.48 (m, 3H), 7.41 (dd, J = 8.5, 2.7 Hz, 1H), 7.30 (dd, J = 8.5, 2.7 Hz, 1H), 5.95 (t, J = 7.2 Hz, 1H), 3.52 – 3.48 (m, 8H), 3.45 (t, J = 6.5 Hz, 2H), 3.33 (d, J = 5.7 Hz, 2H), 3.22 (s, 6H), 3.19 (s, 6H), 2.69 (q, J = 7.3 Hz, 2H), 2.36 (t, J = 7.3 Hz, 2H), 1.73 (p, J = 6.9 Hz, 2H), 1.56 (p, J = 6.8 Hz, 2H), 1.30 – 1.47 (m, 4H), 0.49 (s, 6H); ^{13}C NMR (101 MHz, CD_3OD): δ 175.0, 163.2 (d, J = 34.2 Hz), 148.7, 145.9, 144.4, 141.3, 139.6, 138.8, 138.2, 132.7, 131.1, 128.4, 122.5, 121.9, 120.6, 118.4, 117.7 (d, J = 291.1 Hz), 72.2, 71.2, 71.2, 70.6, 45.7, 45.6, 44.5, 40.4, 36.9, 33.7, 30.5, 27.7, 27.6, 26.5, −7.1; ^{19}F NMR (376 MHz, CD_3OD): δ −77.21; HRMS (*m/z*): $[M + H]^+$ calcd. for $C_{33}H_{51}ClN_3O_3Si^+$, 600.3383; found, 600.3386.

(9*H*-Fluoren-9-yl)methyl(18-chloro-5-oxo-3,9,12-trioxa-6-azaoctadecyl)carbamate (139)

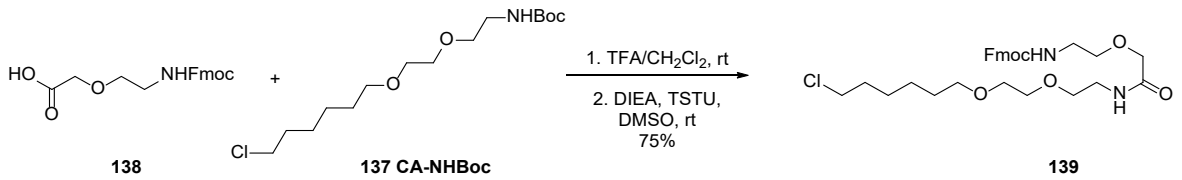

138 **137 CA-NHBoc** **139**

A solution of **138** (22 mg, 66.0 µmol, 1.1 eq.) in DMSO (625 µL) was treated with DIEA (50 µL, 300.0 µmol, 5.0 eq.) and TSTU (21 mg, 72.0 µmol, 1.2 eq.). The mixture was shaken for 10 min at room temperature. In a separate vial a solution of CA-NHBoc (19 mg, 60.0 µmol, 1.0 eq.) in TFA/CH_2Cl_2 (2:8, 750 µL) was shaken for 5 min. The solution was evaporated and dried on the high vacuum for 1 h. The residue was taken up in DMSO (50 µL) and added to the other mixture. The mixture was shaken for 10 min and then acidified with TFA (25 µL). RP-HPLC (8 mL min^{-1}, 10% to 90% B in 32 min) gave **139** (24 mg, 75%) as a colourless oil.

^{1}H NMR (400 MHz, CD_3CN): δ 7.83 (dt, J = 7.6, 0.9 Hz, 2H), 7.65 (d, J = 7.5 Hz, 2H), 7.41 (tt, J = 7.5, 1.0 Hz, 2H), 7.33 (td, J = 7.5, 1.2 Hz, 2H), 7.00 (s, 1H), 5.96 (s, 1H), 4.37 (d, J = 6.8 Hz, 2H), 4.23 (t, J = 6.8 Hz, 1H), 3.88 (s, 2H), 3.39 – 3.62 (m, 10H), 3.26 – 3.36 (m, 6H), 1.65 – 1.78 (m, 2H), 1.48 (p, J = 6.8 Hz, 2H), 1.34 – 1.43 (m, 2H), 1.25 – 1.34 (m, 2H); ^{13}C NMR (101 MHz, CD_3CN): δ 170.5, 157.5, 145.2, 142.1, 128.6, 128.1, 126.0, 120.9, 71.5, 71.2, 70.9, 70.8, 70.6, 70.0, 66.9, 48.1, 46.2, 41.4, 39.2, 33.3, 30.2, 27.3, 26.1; HRMS (*m/z*): $[M + H]^+$ calcd. for $C_{29}H_{40}ClN_2O_6^+$, 547.2569; found, 547.2568.

10-(23-Chloro-4,10-dioxo-8,14,17-trioxa-5,11-diazatricosylidene)-7-(dimethylamino)-*N*,*N*,5,5-tetramethyl-5,10-dihydrodibenzo[*b*,*e*]silin-3-aminium trifluoroacetate (106)

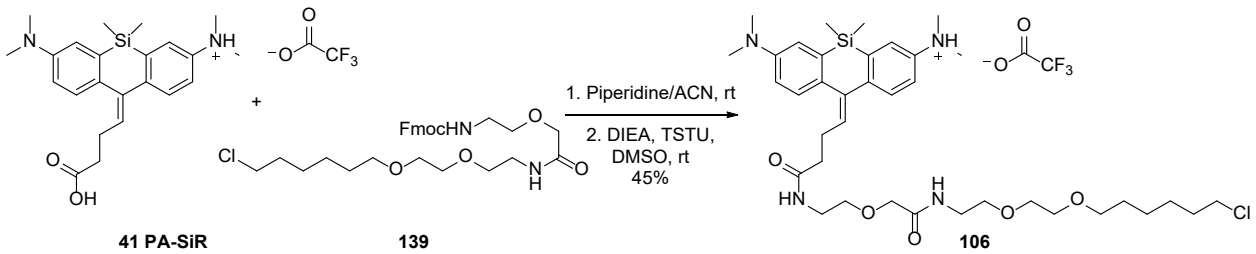

41 PA-SiR **139** **106**

A solution of PA-SiR **41** (1.0 mg, 2.0 µmol, 1.0 eq.) in DMSO (150 µL) was treated with DIEA (1.3 µL, 7.8 µmol, 3.9 eq.) and TSTU (0.9 mg, 3.0 µmol, 1.5 eq.). The mixture was shaken for 20 min at room temperature. In a separate vial a solution of **139** (1.9 mg, 3.5 µmol, 1.8 eq.) in piperidine/ACN (1:9, 100 µL) was shaken for 15 min. The solution was evaporated and dried on the high vacuum for 1 h. The residue was taken up in DMSO (50 µL) and added to the other mixture. The mixture was shaken for 10 min and then acidified with TFA (3 µL). RP-HPLC (8 mL min^{-1}, 20% to 90% B in 34 min) gave **106** (0.7 mg, 45%) as a blue oil.

^{1}H NMR (400 MHz, CD_3CN): δ 7.45 (d, J = 8.5 Hz, 1H), 7.38 (d, J = 8.5 Hz, 1H), 7.34 (d, J = 2.6 Hz, 1H), 7.26 (d, J = 2.7 Hz, 1H), 7.14 (dd, J = 8.5, 2.6 Hz, 1H), 7.01 (dd, J = 8.6, 2.8 Hz, 1H), 6.95 (s, 1H), 6.64 (t, J = 5.9 Hz, 1H), 5.80 (t, J = 7.2 Hz, 1H), 3.80 (s, 2H), 3.44 – 3.58 (m, 10H), 3.38 (t, J = 6.6 Hz, 2H), 3.30 – 3.33 (m, 4H), 3.04 (s, 6H), 3.02 (s, 6H), 2.62 (q, J = 7.3 Hz, 2H), 2.05 – 2.14 (m, 2H), 1.71 (q, J = 7.0 Hz, 2H), 1.50 (p, J = 6.8 Hz, 2H), 1.40 (dd, J = 10.8, 5.0 Hz, 2H), 1.31 (dt, J = 8.9, 3.8 Hz, 2H), 0.42 (s, 6H); ^{19}F NMR (376 MHz, CD_3CN): δ −75.25 ppm; HRMS (*m/z*): $[M + 2H]^{2+}$ calcd. for $C_{37}H_{57}ClN_4O_5Si^{2+}$, 351.1966; found, 351.1962.

(9*H*-Fluoren-9-yl)methyl(21-chloro-8-oxo-3,6,12,15-tetraoxa-9-azahenicosyl)carbamate (141)

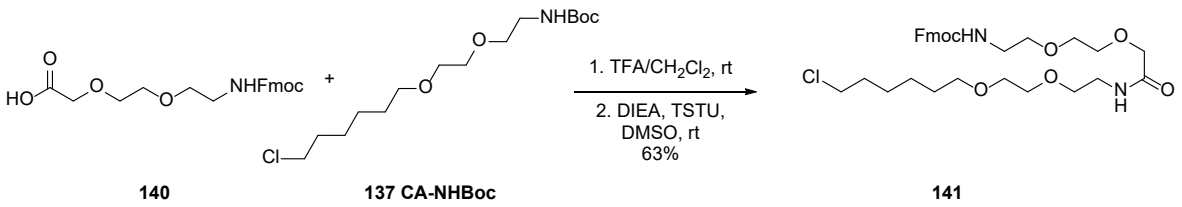

140 **137 CA-NHBoc** **141**

A solution of **140** (21.2 mg, 55.0 µmol, 1.1 eq.) in DMSO (625 µL) was treated with DIEA (41 µL, 250.0 µmol, 5.0 eq.) and TSTU (18.1 mg, 60.0 µmol, 1.2 eq.). The mixture was shaken for 20 min at room temperature. In a separate vial a solution of CA-NHBoc (16.2 mg, 50.0 µmol, 1.0 eq.) in TFA/CH_2Cl_2 (2:8, 750 µL) was shaken for 5 min. The solution was evaporated and dried on the high vacuum for 1 h. The residue was taken up in DMSO (100 µL) and added to the other mixture. The mixture was shaken for 10 min and then acidified with TFA (20 µL). RP-HPLC (4 mL min^{-1}, 10% to 90% B in 32 min) gave **141** (19 mg, 63%) as a colourless oil.

^{1}H NMR (400 MHz, CD_3CN): δ 7.83 (d, J = 7.5 Hz, 2H), 7.65 (d, J = 7.4 Hz, 2H), 7.41 (t, J = 7.4 Hz, 2H), 7.33 (t, J = 7.5 Hz, 2H), 7.16 (s, 1H), 5.90 (d, J = 7.2 Hz, 1H), 4.37 (d, J = 6.6 Hz, 2H), 4.22 (t, J = 6.7 Hz, 1H), 3.89 (s, 2H), 3.64 – 3.52 (m, 6H), 3.52 – 3.46 (m, 4H), 3.47 – 3.39 (m, 4H), 3.40 – 3.27 (m, 4H), 3.26 (q, J = 5.5 Hz, 2H), 1.97 – 1.61 (m, 2H), 1.55 – 1.40 (m, 2H), 1.42 – 1.34 (m, 2H), 1.34 – 1.23 (m, 2H); ^{13}C NMR (101 MHz, CD_3CN): δ 170.8, 157.3, 145.2, 142.1, 128.6, 128.0, 126.0, 120.9, 71.7, 71.5, 71.0, 70.9, 70.6, 70.6, 70.6, 70.3, 66.7, 48.1, 46.2, 41.5, 39.2, 33.3, 30.2, 27.3, 26.1; HRMS (*m/z*): $[M + H]^+$ calcd. for $C_{31}H_{44}ClN_2O_7^+$, 591.2832; found, 591.2831.

10-(26-Chloro-4,13-dioxo-8,11,17,20-tetraoxa-5,14-diazahexacosylidene)-7-(dimethylamino)-*N*,*N*,5,5-tetramethyl-5,10-dihydrodibenzo[*b*,*e*]silin-3-aminium trifluoroacetate (107)

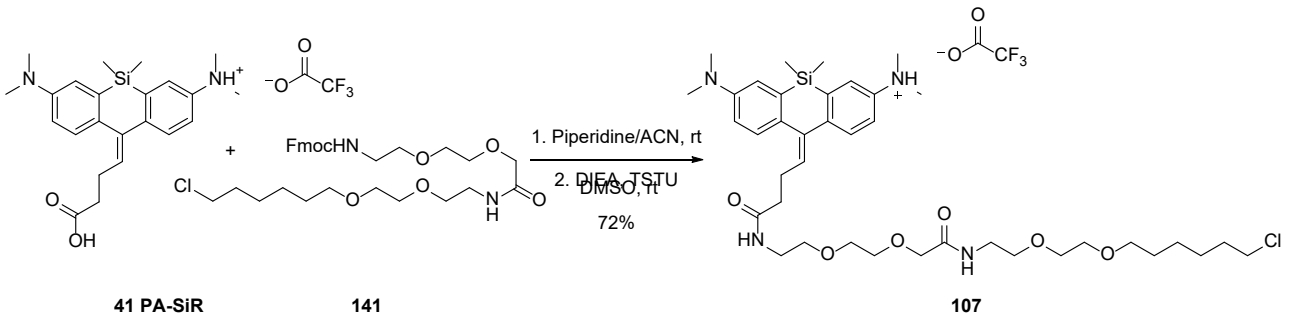

41 PA-SiR **141** **107**

A solution of PA-SiR **41** (1.0 mg, 2.0 µmol, 1.0 eq.) in DMSO (150 µL) was treated with DIEA (1.3 µL, 7.8 µmol, 3.9 eq.) and TSTU (0.9 mg, 3.0 µmol, 1.5 eq.). The mixture was shaken for 20 min at room temperature. In a separate vial a solution of **141** (2.1 mg, 3.5 µmol, 1.8 eq.) in piperidine/ACN (1:9, 100 µL) was shaken for 15 min. The solution was evaporated and dried on the high vacuum for 1 h. The residue was taken up in DMSO (50 µL) and added to the other mixture. The mixture was shaken for 10 min and then acidified with TFA (3 µL). RP-HPLC (8 mL min^{-1}, 20% to 90% B in 34 min) gave **107** (1.2 mg, 72%) as a blue oil.

^{1}H NMR (400 MHz, CD_3CN): δ 7.36 (d, J = 8.5 Hz, 1H), 7.30 (d, J = 8.5 Hz, 1H), 7.11 (s, 1H), 7.08 (dd, J = 5.2, 2.8 Hz, 2H), 6.89 (dd, J = 8.6, 2.8 Hz, 1H), 6.84 (dd, J = 8.5, 2.8 Hz, 1H), 6.58 (s, 1H), 5.70 (t, J = 7.2 Hz, 1H), 3.87 (s, 2H), 3.50 – 3.58 (m, 8H), 3.44 – 3.48 (m, 6H), 3.32 – 3.39 (m, 4H), 3.27 – 3.30 (m, 2H), 2.97 (s, 6H), 2.96 (s, 6H), 2.60 (q, J = 7.3 Hz, 2H), 2.11 (dt, J = 4.9, 2.5 Hz, 2H), 1.68 – 1.76 (m, 2H), 1.51 (tt, J = 7.8, 6.4 Hz, 2H), 1.24 – 1.45 (m, 4H), 0.39 (s, 6H); ^{19}F NMR (376 MHz, CD_3CN): δ −75.29 ppm; HRMS (*m/z*): $[M + H]^+$ calcd. for $C_{39}H_{62}ClN_4O_6Si^+$, 745.4122; found, 745.4124.

(9*H*-Fluoren-9-yl)methyl (22-chloro-9-oxo-3,6,13,16-tetraoxa-10-azadocosyl)carbamate (143)

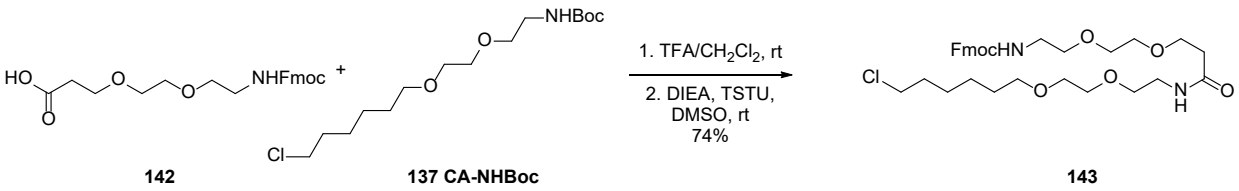

142 **137 CA-NHBoc** **143**

A solution of compound **142** (26 mg, 66 µmol, 1.1 eq.) in DMSO (625 µL) was treated with DIEA (50 µL, 300.0 µmol, 5.0 eq.) and TSTU (21 mg, 72 µmol, 1.2 eq.). The mixture was shaken for 10 min at room temperature. In a separate vial a solution of CA-NHBoc (19 mg, 60 µmol, 1.0 eq.) in TFA/CH_2Cl_2 (2:8, 750 µL) was shaken for 5 min. The solution was evaporated and dried on the high vacuum for 1 h. The residue was taken up in DMSO (50 µL) and added to the other mixture. The mixture was shaken for 10 min and then acidified with TFA (25 µL). RP-HPLC (8 mL min^{-1}, 30% to 100% B in 32 min) gave **143** (24 mg, 74%) as a colourless oil.

^{1}H NMR (400 MHz, CD_3CN): δ 7.83 (d, J = 7.5 Hz, 2H), 7.66 (d, J = 7.5 Hz, 2H), 7.42 (t, J = 7.5 Hz, 2H), 7.34 (t, J = 7.4 Hz, 2H), 6.67 (s, 1H), 5.92 (t, J = 5.7 Hz, 1H), 4.35 (d, J = 6.8 Hz, 2H), 4.23 (t, J = 6.8 Hz, 1H), 3.65 (t, J = 6.0 Hz, 2H), 3.56 (t, J = 6.7 Hz, 2H), 3.55 – 3.44 (m, 10H), 3.42 (t, J = 5.6 Hz, 2H), 3.37 (t, J = 6.6 Hz, 2H), 3.33 – 3.18 (m, 4H), 2.33 (t, J = 6.0 Hz, 2H), 1.73 (p, J = 6.9 Hz, 2H), 1.51 (p, J = 6.8 Hz, 2H), 1.45 – 1.25 (m, 4H); ^{13}C NMR (101 MHz, CD_3CN): δ 171.9, 157.3, 145.2, 142.1, 128.6, 128.1, 126.1, 120.9, 71.6, 70.9, 70.8, 70.8, 70.7, 70.4, 70.3, 67.8, 66.8, 48.1, 46.2, 41.5, 39.8, 37.4, 33.3, 30.3, 27.3, 26.1; HRMS (m/z) $[M + H]^+$ calcd. for $C_{32}H_{45}ClN_2O_7^+$, 605.2988; found, 605.2988.

(E)-10-(27-Chloro-4,14-dioxo-8,11,18,21-tetraoxa-5,15-diazaheptacosylidene)-7-(dimethylamino)-*N*,*N*,5,5-tetramethyl-5,10-dihydrodibenzo[*b*,*e*]silin-3-aminium trifluoroacetate (108)

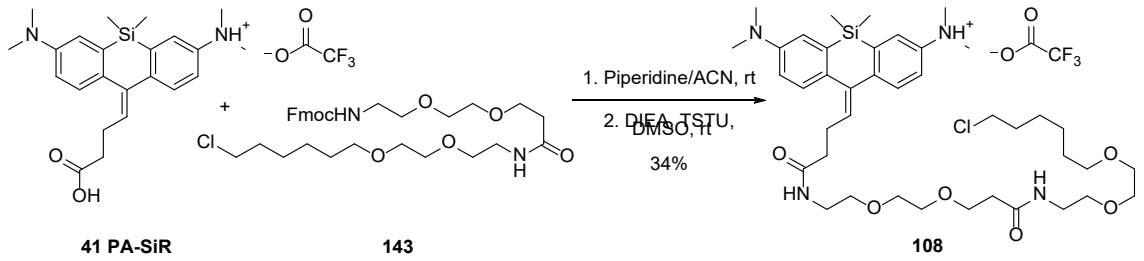

41 PA-SiR **143** **108**

A solution of PA-SiR **41** (1.0 mg, 2.5 µmol, 1.0 eq.) in DMSO (150 µL) was treated with DIEA (1.3 µL, 7.5 µmol, 3.0 eq.) and TSTU (0.9 mg, 3.0 µmol, 1.2 eq.). The mixture was shaken for 20 min at room temperature. In a separate vial a solution of **143** (2.1 mg, 3.5 µmol, 1.4 eq.) in piperidine/ACN (1:9, 100 µL) was shaken for 15 min. The solution was evaporated and dried on the high vacuum for 1 h. The residue was taken up in DMSO (50 µL) and added to the other mixture. The mixture was shaken for 10 min and then acidified with TFA (3 µL). RP-HPLC (8 mL min^{-1}, 20% to 90% B in 34 min) gave **108** (0.7 mg, 34%) as a blue oil.

^{1}H NMR (400 MHz, CD_3CN): δ 7.40 (d, J = 8.5 Hz, 1H), 7.34 (d, J = 8.5 Hz, 1H), 7.20 (d, J = 2.6 Hz, 1H), 7.16 (d, J = 2.8 Hz, 1H), 7.02 (dd, J = 8.5, 2.6 Hz, 1H), 6.91 (dd, J = 8.4, 2.8 Hz, 1H), 6.68 (s, 2H), 5.75 (t, J = 7.2 Hz, 1H), 3.63 (t, J = 5.9 Hz, 2H), 3.56 (t, J = 6.7 Hz, 2H), 3.53 – 3.44 (m, 10H), 3.43 – 3.39 (m, 4H), 3.27 (q, J = 5.8 Hz, 4H), 3.00 (s, 12H), 2.60 (q, J = 7.3 Hz, 2H), 2.32 (t, J = 6.0 Hz, 2H), 2.12 – 2.10 (m, 2H), 1.69 – 1.76 (m, 2H), 1.52 (p, J = 6.9 Hz, 2H), 1.37 (dq, J = 27.3, 8.2 Hz, 4H), 0.40 (s, 6H); ^{19}F NMR (376 MHz, CD_3CN): δ −75.27; HRMS (*m/z*): $[M + 2H]^{2+}$ calcd. for $C_{40}H_{65}ClN_4O_6Si^{2+}$, 380.2175; found, 380.2177.

10-(4-((4-((4*R*,7*R*,10*S*,13*S*,19*S*,*E*)-7-((1*H*-Indol-2-yl)methyl)-4-(4-hydroxyphenyl)-8,13,15,19-tetramethyl-2,6,9,12-tetraoxo-1-oxa-5,8,11-triazacyclononadec-15-en-10-yl)butyl)amino)-4-oxobutylidene)-7-(dimethylamino)-*N*,*N*,5,5-tetramethyl-5,10-dihydrodibenzo[*b*,*e*]silin-3-aminium trifluoroacetate; PA-SiR-jasplakinolide (109)[203]

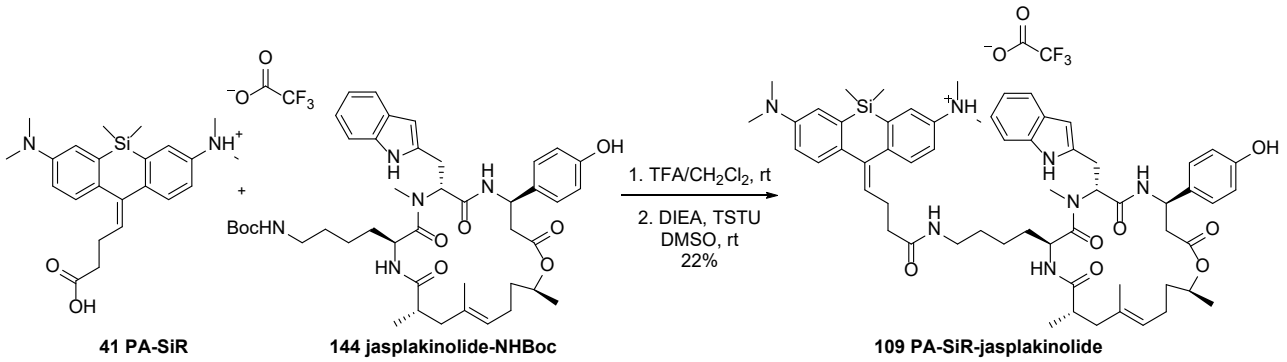

A solution of PA-SiR **41** (4.0 mg, 8.0 µmol, 1.0 eq.) in DMSO (300 µL) was treated with DIEA (5.0 µL, 30.1 µmol, 3.8 eq.) and TSTU (3.6 mg, 12.0 µmol, 1.5 eq.). The mixture was shaken for 20 min at room temperature. In a separate vial a solution of jasplakinolide-NHBoc (9.5 mg, 12.3 µmol, 1.5 eq.) in TFA/CH_2Cl_2 (2:8, 80 µL) was shaken for 2 min. The solution was evaporated and dried on the high vacuum for 1 h. The residue was taken up in DMSO (50 µL) and added to the other mixture. The mixture was shaken for 30 min and then acidified with TFA (3 µL). RP-HPLC (4 mL min^{-1}, 10% to 90% B in 32 min) gave PA-SiR-jasplakinolide (2.6 mg, 22%) as a light blue solid.

^{1}H NMR (400 MHz, CD_3OD): δ 8.42 (d, J = 8.6 Hz, 1H), 7.64 (d, J = 8.5 Hz, 1H), 7.61 – 7.53 (m, 4H), 7.47 (dd, J = 8.4, 2.7 Hz, 1H), 7.37 – 7.32 (m, 1H), 7.30 – 7.24 (m, 1H), 7.10 – 6.95 (m, 5H), 6.81 – 6.72 (m, 2H), 5.96 (t, J = 7.3 Hz, 1H), 5.60 (dd, J = 10.1, 6.4 Hz, 1H), 5.27 (dt, J = 9.8, 5.0 Hz, 1H), 5.04 (t, J = 7.0 Hz, 1H), 4.85 – 4.78 (m, 1H), 4.67 (t, J = 5.7 Hz, 1H), 3.23 (s, 6H), 3.18 (s, 6H), 3.15 – 2.99 (m, 4H), 2.93 (s, 3H), 2.79 – 2.66 (m, 4H), 2.61 (ddd, J = 10.2, 6.8, 3.0 Hz, 1H), 2.35 (t, J = 7.2 Hz, 2H), 2.33 – 2.26 (m, 1H), 1.95 – 1.84 (m, 3H), 1.64 – 1.57 (m, 1H), 1.55 (s, 3H), 1.41 (td, J = 13.3, 7.7 Hz, 1H), 1.23 (s, 2H), 1.18 (d, J = 6.3 Hz, 3H), 1.07 (d, J = 6.8 Hz, 3H), 0.95 (d, J = 5.5 Hz, 2H), 0.86 (d, J = 8.1 Hz, 2H), 0.53 (d, J = 3.6 Hz, 6H); ^{13}C NMR (101 MHz, CD_3OD): δ 178.0, 174.9, 174.4, 172.3, 171.7, 157.8, 149.0, 145.8, 144.2, 141.3, 139.6, 138.3, 138.0, 135.4, 134.7, 133.6, 132.9, 131.1, 128.5, 128.4, 128.2, 125.8, 124.4, 122.9, 122.4, 120.9, 119.8, 119.5, 119.0, 118.6, 116.3, 112.3, 110.7, 71.9, 57.4, 50.7, 50.1, 45.7, 44.6, 44.5, 41.9, 40.3, 40.1, 37.0, 36.6, 32.6, 31.3, 30.0, 27.5, 25.9, 24.6, 23.2, 20.3, 20.0, 16.6, −0.2; ^{19}F NMR (376 MHz, CD_3OD): δ −77.26; HRMS (*m/z*): $[M + H]^+$ calcd for $C_{61}H_{80}N_7O_7Si^+$, 1050.5883; found, 1050.5902.

(Z)-7-(Dimethylamino)-*N*,*N*,5,5-tetramethyl-10-(4-((4-(4-(6-(4-methylpiperazin-1-yl)-1*H*,3'*H*-[2,5'-bibenzo[*d*]-imidazol]-2'-yl)phenoxy)butyl)amino)-4-oxobutylidene)-5,10-dihydrodibenzo[*b*,*e*]silin-3-aminium; PA-SiR-Hoechst (110)

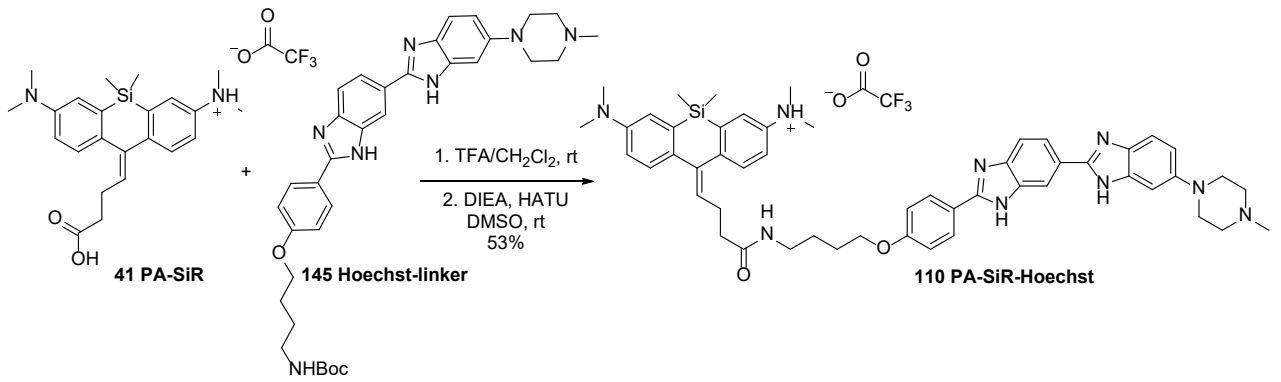

A solution of PA-SiR **41** (1.1 mg, 3.0 µmol, 1.0 eq.) in DMSO (150 µL) was treated with DIEA (1.5 µL, 9.0 µmol, 3.0 eq.) and HATU (1.4 mg, 3.6 µmol, 1.2 eq.). The mixture was shaken for 20 min at room temperature. In a separate vial a

solution of Hoechst-linker (2.1 mg, 3.6 µmol, 1.2 eq.) in TFA/CH_2Cl_2 (2:8, 80 µL) was shaken for 5 min. The solution was evaporated and dried on the high vacuum for 1 h. The residue was taken up in DMSO (50 µL) and added to the other mixture. The mixture was shaken for 15 min and then acidified with TFA (3 µL) and diluted with water (200 µL). RP-HPLC (3 mL min^{-1}, 0% to 90% B in 32 min) gave PA-SiR-Hoechst (1.4 mg, 53%) as a light green solid.

^{1}H NMR (400 MHz, CD_3OD): δ 8.40 (d, J = 1.7 Hz, 1H), 8.11 (d, J = 8.6 Hz, 2H), 8.04 (dd, J = 8.6, 1.7 Hz, 1H), 7.90 (d, J = 8.6 Hz, 1H), 7.73 (d, J = 9.0 Hz, 1H), 7.58 (d, J = 8.5 Hz, 1H), 7.52 – 7.45 (m, 2H), 7.44 – 7.38 (m, 2H), 7.35 – 7.29 (m, 2H), 7.23 (dd, J = 8.5, 2.7 Hz, 1H), 7.14 (d, J = 8.7 Hz, 2H), 5.93 (t, J = 7.2 Hz, 1H), 4.07 (t, J = 6.2 Hz, 2H), 4.03 – 3.90 (m, 4H), 3.77 – 3.61 (m, 4H), 3.25 (t, J = 6.9 Hz, 2H), 3.17 (s, 6H), 3.15 (s, 6H), 3.02 (s, 3H), 2.71 (q, J = 7.3 Hz, 2H), 2.36 (t, J = 7.3 Hz, 2H), 1.89 – 1.75 (m, 2H), 1.75 – 1.59 (m, 2H), 0.49 (d, J = 7.8 Hz, 6H); HRMS (m/z): $[M + H]^+$ calcd. for $C_{52}H_{62}N_9O_2Si^+$ $[M + H]^+$ 872.4790; found, 872.4797.

(Z)-10-(4-((3-(((2αR,4S,4αS,6R,9S,11S,12S,12αR,12βS)-12β-Acetoxy-12-(benzoyloxy)-4,6,11-trihydroxy-4α,8,13,13-tetramethyl-5-oxo-2α,3,4,4α,5,6,9,10,11,12,12α,12β-dodecahydro-1*H*-7,11-methanocyclodeca[3,4]benzo[1,2-β]oxet-9-yl)oxy)-2-hydroxy-3-oxo-1-phenylpropyl)amino)-4-oxobutylidene)-7-(dimethylamino)-*N*,*N*,5,5-tetramethyl-5,10-dihydrodibenzo[*b*,*e*]silin-3-aminium trifluoroacetate; PA-SiR-docetaxel (111)

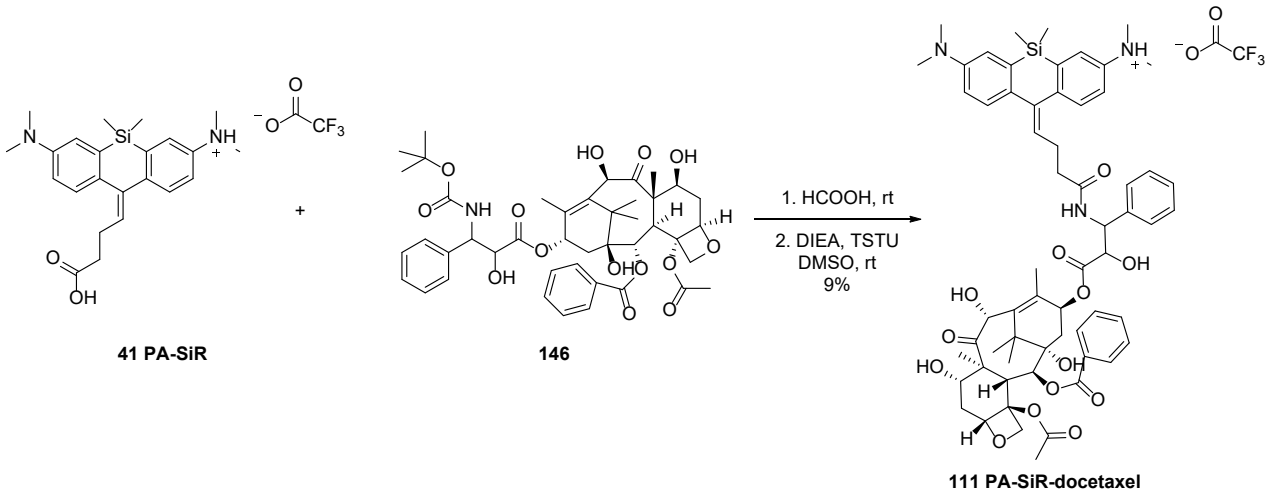

41 PA-SiR **146** **111 PA-SiR-docetaxel**

A solution of PA-SiR **41** (1.8 mg, 4.6 µmol, 1.0 eq.) in DMSO (130 µL) was treated with DIEA (2.3 µL, 13.8 µmol, 3.0 eq.) and TSTU (1.7 mg, 5.5 µmol, 1.2 eq.). The mixture was shaken for 20 min at room temperature. In a separate vial a solution of docetaxel **146** (20 mg, 25.2 µmol, 5.5 eq.) in formic acid (370 µL) was shaken for 45 min. The solution was evaporated, coevaporated with toluene (3 x 500 µL), and dried on the high vacuum for 1 h. The residue was taken up in DMSO (200 µL) and a quarter of this solution (50 µL, 6.3 µmol, 1.4 eq.) was added to the other mixture. The mixture was shaken for 1 h and then acidified with TFA (3 µL). RP-HPLC (3 mL min^{-1}, 10% to 90% B in 32 min) gave PA-SiR-docetaxel (0.5 mg, 9%) as a light blue solid.

^{1}H NMR (400 MHz, CD_3OD) δ 8.14 – 8.08 (m, 2H), 7.66 – 7.49 (m, 5H), 7.45 – 7.36 (m, 4H), 7.33 – 7.25 (m, 4H), 7.11 (d, J = 8.4 Hz, 1H), 6.11 (t, J = 9.2 Hz, 1H), 5.91 (t, J = 7.3 Hz, 1H), 5.64 (d, J = 7.1 Hz, 1H), 5.50 (d, J = 3.8 Hz, 1H), 5.25 (s, 1H), 5.03 – 4.96 (m, 1H), 4.62 (d, J = 3.9 Hz, 1H), 4.25 – 4.15 (m, 3H), 3.87 (d, J = 7.1 Hz, 1H), 3.20 (s, 6H), 3.09 (s, 6H), 2.72 – 2.67 (m, 2H), 2.66 (s, 3H), 2.47 (t, J = 7.1 Hz, 2H), 2.33 (s, 3H), 1.90 (d, J = 1.4 Hz, 2H), 1.69 (s, 3H), 1.29 (s, 2H), 1.10 (s, 3H), 1.07 (s, 3H), 0.43 – 0.40 (m, 6H); HRMS (m/z): $[M + H]^+$ calcd. for $C_{61}H_{74}N_3O_{13}Si^+$ 1084.4985; found, 1084.5005.

(Z)-10-(4-((3-(((2αR,4S,4αS,6R,9S,11S,12S,12αR,12βS)-12β-Acetoxy-12-(benzoyloxy)-11-hydroxy-4,6-dimethoxy-4α,8,13,13-tetramethyl-5-oxo-2α,3,4,4α,5,6,9,10,11,12,12α,12β-dodecahydro-1*H*-7,11-methanocyclodeca-[3,4]benzo[1,2-β]oxet-9-yl)oxy)-2-hydroxy-3-oxo-1-phenylpropyl)amino)-4-oxobutylidene)-7-(dimethylamino)-N,N,5,5-tetramethyl-5,10-dihydrodibenzo[*b*,*e*]silin-3-aminium trifluoroacetate; PA-SiR-cabazitaxel (112)

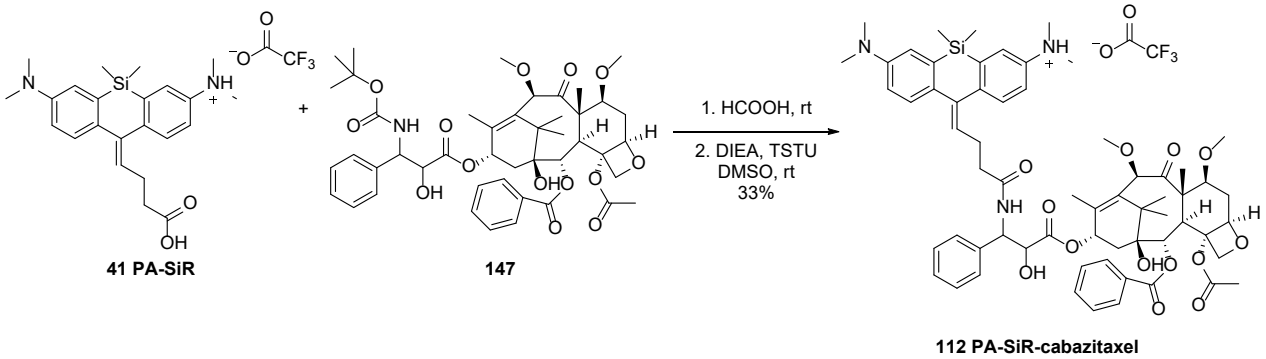

41 PA-SiR **147** **112 PA-SiR-cabazitaxel**

A solution of PA-SiR **41** (1.3 mg, 3.3 µmol, 1.0 eq.) in DMSO (150 µL) was treated with DIEA (1.6 µL, 9.9 µmol, 3.0 eq.) and TSTU (1.2 mg, 4.0 µmol, 1.2 eq.). The mixture was shaken for 20 min at room temperature. In a separate vial a solution of cabazitaxel **147** (2.9 mg, 4.0 µmol, 1.2 eq.) in formic acid (370 µL) was shaken for 45 min. The solution was evaporated, coevaporated with toluene (3 x 500 µL), and dried on the high vacuum for 1 h. The residue was taken up in DMSO (200 µL) and added to the other mixture. The mixture was shaken for 1 h and then acidified with TFA (3 µL). RP-HPLC (3 mL min^{-1}, 10% to 100% B in 32 min) gave PA-SiR-cabazitaxel (1.2 mg, 33%) as a light blue solid.

^{1}H NMR (400 MHz, DMSO-d_6): δ 8.44 (d, J = 9.0 Hz, 1H), 7.98 (d, J = 7.7 Hz, 2H), 7.67 (d, J = 7.4 Hz, 1H), 7.58 (t, J = 7.6 Hz, 2H), 7.35 – 7.13 (m, 7H), 6.97 – 6.87 (m, 2H), 6.72 (s, 2H), 5.94 (t, J = 9.8 Hz, 1H), 5.65 (t, J = 7.0 Hz, 1H), 5.39 (d, J = 7.0 Hz, 1H), 5.34 – 5.25 (m, 1H), 4.96 (d, J = 9.7 Hz, 1H), 4.68 (d, J = 14.1 Hz, 2H), 4.44 (s, 1H), 4.02 (s, 3H), 3.20 (s, 1H) 3.17 (s, 6H), 2.91 (s, 6H), 2.91 (s, 6H), 2.56 – 2.52 (m, 4H), 2.21 (s, 2H), 2.07 (s, 2H), 1.82 (s, 2H), 1.52 (s, 4H), 1.24 (s, 3H), 1.03 (d, J = 10.2 Hz, 4H), 0.97 (s, 3H), 0.33 (d, J = 15.7 Hz, 6H); HRMS (m/z): $[M + H]^+$ calcd. for $C_{63}H_{78}N_3O_{13}Si^+$ 1112.5298; found, 1112.5283.

(Z)-10-(4-((8-((3-(((2αR,4S,4αS,6R,9S,11S,12S,12αR,12βS)-12β-acetoxy-12-(benzoyloxy)-4,6,11-trihydroxy-4α,8,13,13-tetramethyl-5-oxo-2α,3,4,4α,5,6,9,10,11,12,12α,12β-dodecahydro-1*H*-7,11-methanocyclodeca-[3,4]benzo[1,2-β]oxet-9-yl)oxy)-2-hydroxy-3-oxo-1-phenylpropyl)amino)-8-oxooctyl)amino)-4-oxobutylidene)-7-(dimethylamino)-*N*,*N*,5,5-tetramethyl-5,10-dihydrodibenzo[*b*,*e*]silin-3-aminium trifluoroacetate; PA-SiR-C8-docetaxel (113)

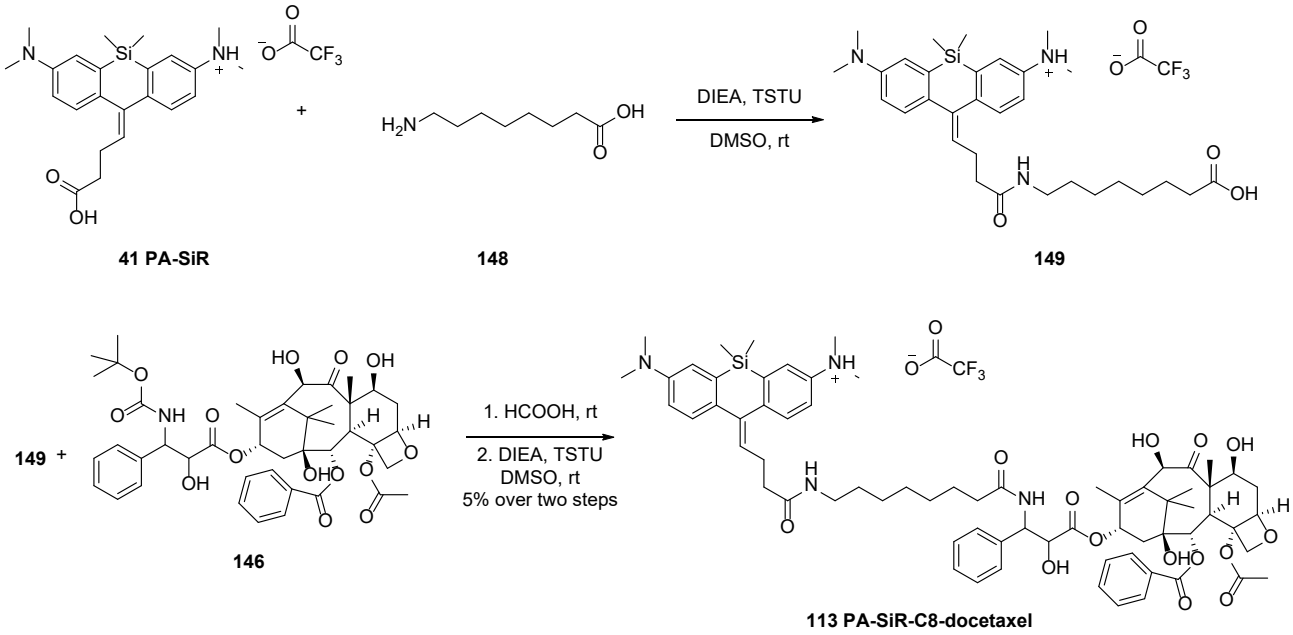

41 PA-SiR 148 149

149 + 146

113 PA-SiR-C8-docetaxel

A solution of PA-SiR **41** (1.6 mg, 4.0 µmol, 1.0 eq.) in DMSO (120 µL) was treated with DIEA (4.6 µL, 28.0 µmol, 7.0 eq.) and TSTU (1.4 mg, 4.8 µmol, 1.2 eq.). The mixture was shaken for 20 min at room temperature. Amino-octanoic acid (**148**) (1.5 mg, 9.2 µmol, 2.3 eq.) was added to the mixture. The mixture was shaken for 10 min and then acidified with TFA (3 µL). RP-HPLC (3 mL min^{-1}, 10% to 90% B in 32 min) gave **149**. A solution of **149** (1.0 mg, 2.0 µmol, 0.5 eq.) in DMSO (120 µL) was treated with DIEA (1.0 µL, 6.0 µmol, 1.5 eq.) and TSTU (0.7 mg, 2.4 µmol, 0.6 eq.). The mixture was shaken for 20 min at room temperature. In a separate vial a solution of docetaxel **146** (20 mg, 25.2 µmol, 6.3 eq.) in formic acid (370 µL) was shaken for 45 min. The solution was evaporated, coevaporated with toluene (3 x 500 µL), and dried on the high vacuum for 1 h. The residue was taken up in DMSO (200 µL) and a tenth of this solution (20 µL, 2.5 µmol, 1.3 eq.) was added to the other mixture. The combined mixture was shaken for 1 h and then acidified with TFA (3 µL). RP-HPLC (3 mL min^{-1}, 10% to 90% B in 32 min) gave PA-SiR-C8-docetaxel (0.2 mg, 5%) as a light blue solid.

^{1}H NMR (400 MHz, DMSO-d_6): δ 8.35 (d, J = 9.1 Hz, 1H), 8.02 – 7.95 (m, 2H), 7.75 (t, J = 5.6 Hz, 1H), 7.68 (t, J = 7.3 Hz, 1H), 7.59 (t, J = 7.6 Hz, 2H), 7.40 – 7.15 (m, 7H), 6.98 (br. s, 2H), 6.79 (br. s, 2H), 5.90 (t, J = 9.2 Hz, 1H), 5.70 – 5.53 (m, 1H), 5.41 (d, J = 7.1 Hz, 1H), 5.26 (dd, J = 9.0, 5.9 Hz, 1H), 5.09 (s, 1H), 4.90 (d, J = 9.5 Hz, 1H), 4.58 (s, 1H), 4.40 (d, J = 6.0 Hz, 1H), 4.03 (p, J = 8.2, 7.7 Hz, 3H), 3.68 (d, J = 7.2 Hz, 1H), 3.17 (s, 1H), 3.01 – 2.93 (m, 2H), 2.94 (s, 6H), 2.91 (s, 6H), 2.54 – 2.50 (m, 2H), 2.30 – 2.21 (m, 4H), 2.14 (t, J = 7.4 Hz, 2H), 2.02 – 1.91 (m, 2H), 1.86 – 1.77 (m, 2H), 1.74 (s, 2H), 1.71 – 1.60 (m,2H), 1.52 (s, 2H), 1.47 – 1.42 (m, 2H), 1.32 – 1.22 (m, 6H), 1.22 – 1.12 (m, 6H), 1.09 – 1.00 (m, 4H), 0.98 (s, 3H), 0.36 (s, 6H); HRMS (m/z): $[M + H]^+$ calcd. for $C_{69}H_{89}N_4O_{14}Si^+$ 1225.6139; found, 1225.6103.

(Z)-10-(4-((8-((3-(((2αS,4R,4αR,6S,9R,11R,12R,12αS,12βR)-12β-Acetoxy-12-(benzoyloxy)-11-hydroxy-4,6-dimethoxy-4α,8,13,13-tetramethyl-5-oxo-2α,3,4,4α,5,6,9,10,11,12,12α,12β-dodecahydro-1*H*-7,11-methanocyclodeca[3,4]-benzo[1,2-β]oxet-9-yl)oxy)-2-hydroxy-3-oxo-1-phenylpropyl)amino)-8-oxooctyl)amino)-4-oxobutylidene)-7-(dimethylamino)-*N*,*N*,5,5-tetramethyl-5,10-dihydrodibenzo[*b*,*e*]silin-3-aminium trifluoroacetate; PA-SiR-C8-cabazitaxel (114)

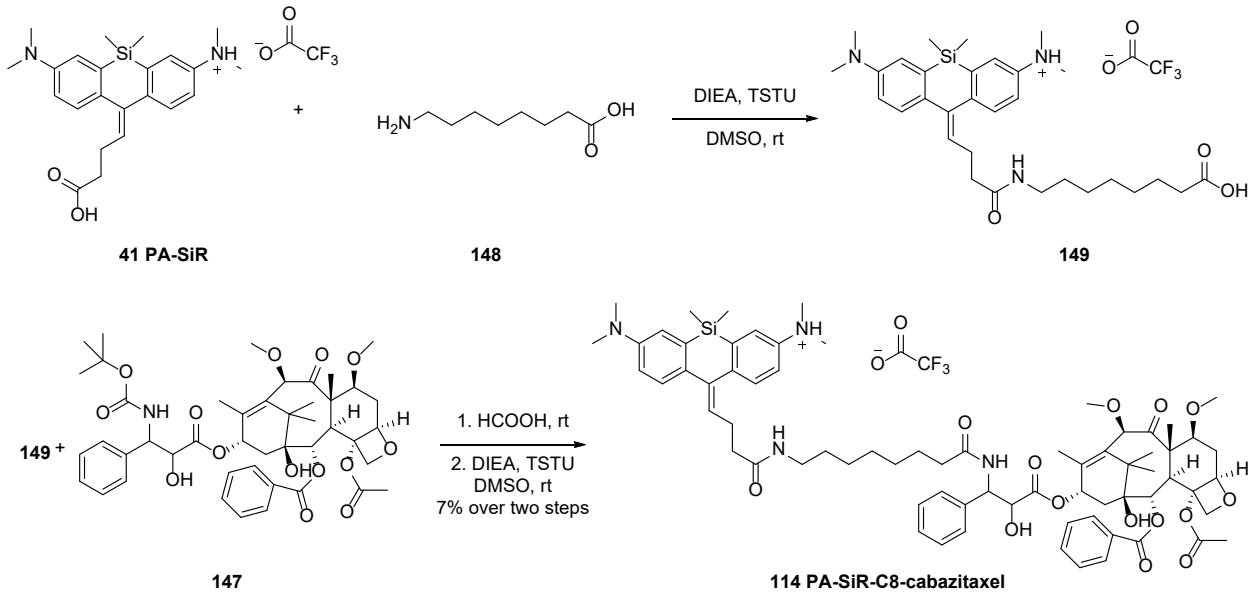

41 PA-SiR 148 149

147 114 PA-SiR-C8-cabazitaxel

A solution of PA-SiR **41** (1.3 mg, 3.3 µmol, 1.0 eq.) in DMSO (150 µL) was treated with DIEA (1.6 µL, 9.9 µmol, 3.0 eq.) and TSTU (1.2 mg, 4.0 µmol, 1.2 eq.). The mixture was shaken for 20 min at room temperature. Amino-octanoic acid (**148**) (0.74 mg, 4.6 µmol, 1.4 eq.) was added to the mixture. The mixture was shaken and sonicated for 10 min and then acidified with TFA (3 µL). RP-HPLC gave **149** (3 mL min^{-1}, 10% to 90% B in 32 min). The residue was dissolved in dry DMSO (150 µL). DIEA (1.6 µL, 9.9 µmol, 3.0 eq.) and TSTU (1.2 mg, 4.0 µmol, 1.2 eq.) were added. The mixture was shaken for 20 min at room temperature. In a separate vial a solution of cabazitaxel **147** (2.9 mg, 4.0 µmol, 1.2 eq.) in formic acid (370 µL) was shaken for 45 min. The solution was evaporated, coevaporated with toluene (3 x 500 µL), and dried on the high vacuum for 1 h. The residue was taken up in DMSO (200 µL) and added to the other mixture. The mixture was shaken for 1 h and then acidified with TFA (3 µL). RP-HPLC (3 mL min^{-1}, 10% to 100% B in 32 min) gave PA-SiR-C8-cabazitaxel (0.3 mg, 7%) as a light blue solid over two steps.

^{1}H NMR (400 MHz, DMSO-d_6): δ 8.36 (d, J = 9.1 Hz, 1H), 7.98 (d, J = 7.3 Hz, 2H), 7.76 (t, J = 6.2 Hz, 1H), 7.69 (t, J = 7.3 Hz, 1H), 7.60 (t, J = 7.7 Hz, 2H), 7.41 – 7.17 (m, 7H), 6.98 – 6.84 (m, 2H), 6.72 (br. s, 2H), 5.95 (d, J = 7.3 Hz, 1H), 5.59 (t, J = 7.2 Hz, 1H), 5.39 (d, J = 6.9 Hz, 1H), 5.28 (dd, J = 7.9, 6.6 Hz, 1H), 4.96 (d, J = 9.3 Hz, 1H), 4.71 (s, 1H), 4.65 (s, 1H), 4.46 – 4.37 (m, 1H), 4.03 (s, 3H), 3.21 (s, 1H), 3.17 (s, 6H), 2.92 (s, 6H), 2.88 (s, 6H), 2.57 – 2.55 (m, 4H), 2.25 (s, 2H), 2.14 (t, J = 6.5 Hz, 2H), 2.08 (s, 3H), 1.83 (s, 2H), 1.52 (s, 3H), 1.39 (s, 2H), 1.34 – 1.22 (d, J = 15.9 Hz, 7H), 1.22 – 1.44 (m, 6H), 1.07 – 1.03 (m, 4H), 0.98 (s, 3H), 0.35 (s, 6H); HRMS (m/z): $[M + H]^+$ calcd. for $C_{71}H_{93}N_4O_{14}Si^+$ 1253.6452; found,1253.6447.

(Z)-10-((6R,9S,12R,13R,17R,20R,21R)-13,21-Dihydroxy-12,20-diisobutyl-6,9-diisopropyl-2,17-dimethyl-4,7,10,15,18,23,32-heptaoxo-5,8,11,16,19,24,31-heptaazapentatriacontan-35-ylidene)-7-(dimethylamino)-*N*,*N*,5,5-tetramethyl-5,10-dihydrodibenzo[*b*,*e*]silin-3-aminium trifluoroacetate; PA-SiR-pepstatin A (115)

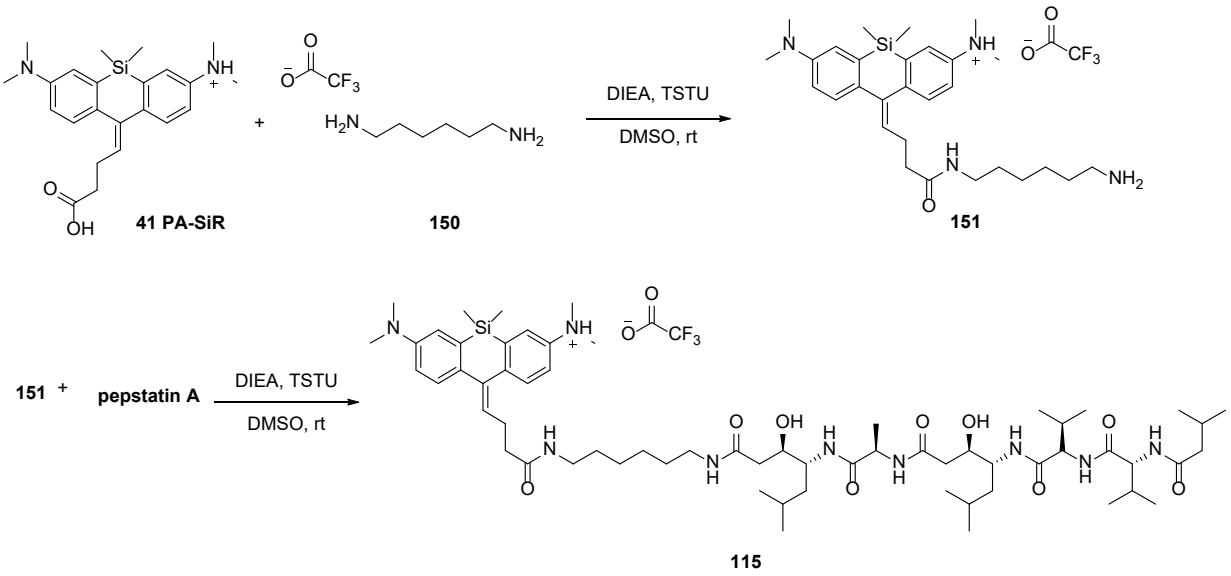

A solution of PA-SiR **41** (1.0 mg, 2.5 µmol, 1.0 eq.) in DMSO (150 µL) was treated with DIEA (1.4 µL, 7.5 µmol, 3.0 eq.) and TSTU (0.85 mg, 2.8 µmol, 1.1 eq.). The mixture was shaken for 20 min at room temperature. A solution of diaminohexane (**150**) (2.94 mg, 25.3 µmol, 10.0 eq.) in DMSO (100 µL) was added. The mixture was shaken for 1 h at room temperature and then acidified with TFA (3 µL). RP-HPLC gave **151** (3 mL min^{-1}, 20% to 100% B in 32 min). A solution of pepstatin A (**9**) (1.7 mg, 2.5 µmol, 1.0 eq.) in DMSO (100 µL) was treated with DIEA (12 µL, 76.0 µmol, 30.0 eq.) and TSTU (1.5 mg, 5.0 µmol, 2.0 eq.). The mixture was shaken for 20 min at room temperature. **151** (1.25 mg, 2.5 µmol, 1 eq.) were dissolved in DMSO (200 µL) and added to the other mixture. The mixture was shaken for 1 h and then acidified with TFA (12 µL). RP-HPLC (3 mL min^{-1}, 10% to 90% B in 32 min) gave PA-SiR-pepstatin A as a green solid.

HRMS (m/z): $[M + 2H]^{2+}$ calcd. for $C_{63}H_{107}N_9O_9Si^+$ 580.8975; found, 580.8972.

10-(3-((2-(2-((6-Chlorohexyl)oxy)ethoxy)ethyl)amino)-3-oxopropylidene)-7-(dimethylamino)-*N*,*N*,5,5-tetramethyl-5,10-dihydrodibenzo[*b*,*e*]silin-3-aminium trifluoroacetate; PA-SiR-C3-CA (116)[203]

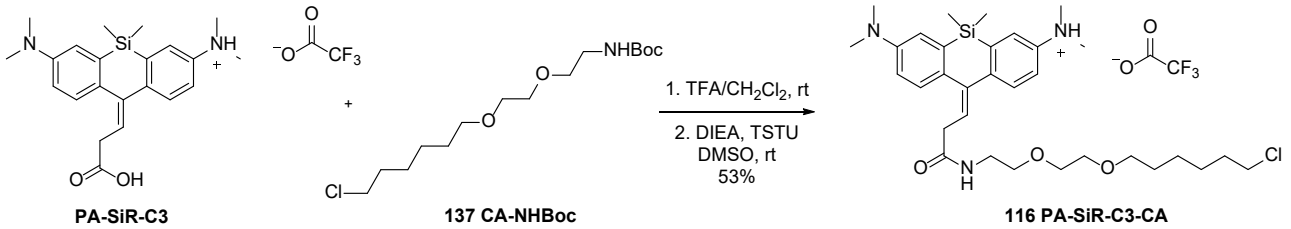

A solution of PA-SiR-C3 (4.0 mg, 8.1 µmol, 1.0 eq.) in DMSO (250 µL) was treated with DIEA (5.2 µL, 31.5 µmol, 4.0 eq.) and TSTU (3.8 mg, 12.6 µmol, 1.6 eq.). The mixture was shaken for 20 min at room temperature. In a separate vial a solution of CA-NHBoc (4.8 mg, 14.7 µmol, 1.8 eq.) in TFA/CH_2Cl_2 (2:8, 200 µL) was shaken for 5 min. The solution was evaporated and dried on the high vacuum for 1 h. The residue was taken up in DMSO (150 µL) and added to the other mixture. The mixture was shaken for 10 min and then acidified with TFA (15 µL). RP-HPLC (4 mL min^{-1}, 20% to 100% B in 32 min) gave PA-SiR-C3-CA (3.0 mg, 53%) as a light blue solid.

^{1}H NMR (400 MHz, CD_3OD): δ 7.70 (d, *J* = 8.5 Hz, 1H), 7.59 (d, *J* = 2.6 Hz, 1H), 7.55 (d, *J* = 8.5 Hz, 1H), 7.50 – 7.41 (m, 2H), 7.24 (dd, *J* = 8.5, 2.7 Hz, 1H), 6.13 (t, *J* = 7.6 Hz, 1H), 3.64 – 3.48 (m, 6H), 3.52 (t, J = 6.6 Hz, 2H), 3.46 (t, J = 6.5 Hz,

2H), 3.39 (t, J = 5.4 Hz, 2H), 3.30 (d, J = 3.3 Hz, 2H), 3.24 (s, 6H), 3.16 (s, 6H), 1.72 (dq, J = 7.9, 6.7 Hz, 2H), 1.55 (tt, J = 7.5, 6.4 Hz, 2H), 1.49 – 1.22 (m, 4H), 0.49 (s, 6H); ^{13}C NMR (101 MHz, CD_3OD): δ 173.7, 161.9 (q, J = 36.5 Hz), 149.0, 147.0, 144.2, 143.2, 139.3, 138.7, 138.5, 131.0, 128.5, 126.3, 122.8, 121.2, 120.8, 117.7, 117.7 (q, J = 290.2 Hz), 72.2, 71.2, 71.2, 70.5, 45.8, 45.7, 43.8, 40.5, 38.1, 33.7, 30.5, 27.7, 26.4, −3.5; ^{19}F NMR (376 MHz, CD_3OD): δ −77.2; HRMS (m/z): $[M + H]^+$ calcd. for $C_{32}H_{49}ClN_3O_3Si^+$, 586.3226; found, 586.3226.

3,3'-(Diisopropylsilanediyl)bis(*N*,*N*-dimethylaniline) (153)[203]

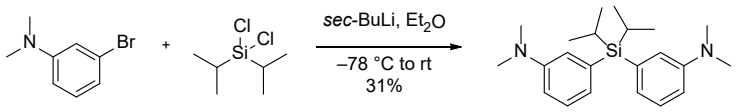

55 152 153

Following general procedure **A**, flash column chromatography (SiO_2, hexane/EtOAc 100:0 → 80:20) gave **153** (0.440 g, 31%) as a colourless oil.

^{1}H NMR (400 MHz, $CDCl_3$): δ 7.29 – 7.21 (m, 2H), 7.00 – 6.90 (m, 4H), 6.81 (ddd, J = 8.3, 2.7, 1.0 Hz, 2H), 2.92 (s, 12H), 1.56 (hept, J = 7.3 Hz, 2H), 0.97 (d, J = 7.4 Hz, 12H); ^{13}C NMR (101 MHz, $CDCl_3$): δ 149.7, 133.9, 128.1, 125.2, 120.9, 113.7, 41.0, 17.8, 10.0; HRMS (*m/z*): $[M + H]^+$ calcd. for $C_{22}H_{35}N_2Si^+$, 355.2564; found, 355.2567.

3,3'-(Diisopropylsilanediyl)bis(4-bromo-*N*,*N*-dimethylaniline) (154)[203]

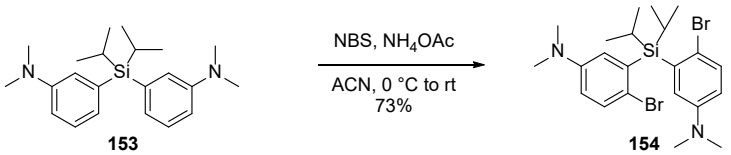

153 154

Following general procedure **B**, flash column chromatography (SiO_2, hexane/CH_2Cl_2 100:0 → 0:100) gave **154** (1.087 g, 73%) as a white solid.

^{1}H NMR (400 MHz, $CDCl_3$): δ 7.33 (d, J = 8.7 Hz, 2H), 6.97 (d, J = 3.2 Hz, 2H), 6.60 (dd, J = 8.8, 3.3 Hz, 2H), 2.92 (s, 12H), 2.00 (p, J = 7.4 Hz, 2H), 1.17 (d, J = 7.5 Hz, 12H); ^{13}C NMR (101 MHz, $CDCl_3$): δ 148.6, 136.8, 133.4, 122.8, 117.6, 115.1, 40.8, 19.1, 12.7; HRMS (*m/z*): $[M + H]^+$ calcd. for $C_{22}H_{33}Br_2N_2Si^+$, 511.0774; found, 511.0779.

10-(3-Carboxypropylidene)-7-(dimethylamino)-5,5-diisopropyl-*N*,*N*-dimethyl-5,10-dihydrodibenzo[*b*,*e*]silin-3-aminium trifluoroacetate (72)[203]

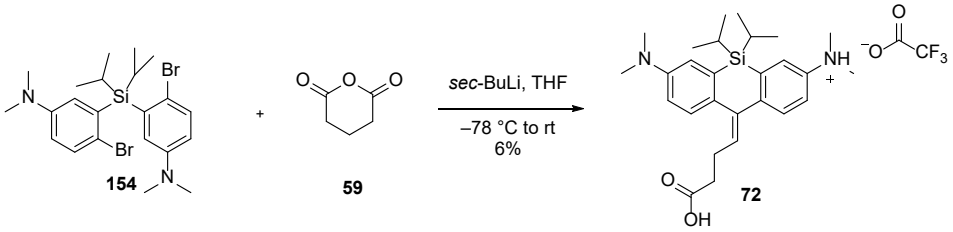

154 59 72

Following general procedure **C**, flash column chromatography (SiO_2, hexane/EtOAc 100:0 → 50:50) and RP-HPLC (2 mL min^{-1}, 10% to 90% B in 32 min) gave **72** (6.7 mg, 6%) as a light blue solid.

^{1}H NMR (400 MHz, CD_3OD): δ 7.69 (d, J = 8.5 Hz, 1H), 7.61 – 7.48 (m, 4H), 7.37 (dd, J = 8.6, 2.7 Hz, 1H), 5.90 (t, J = 7.2 Hz, 1H), 3.24 (s, 6H), 3.20 (s, 6H), 2.65 (q, J = 7.6 Hz, 2H), 2.41 (t, J = 7.4 Hz, 2H), 1.57 (br. s, 2H), 1.09 (br. s, 12H); ^{13}C NMR (101 MHz, CD_3OD): δ 176.5, 161.9 (q, J = 36.2 Hz), 150.5, 145.7, 143.9, 142.2, 141.7, 136.0, 134.7, 133.7, 131.6, 128.7, 123.9, 123.0, 121.0, 116.3 (q, J = 292.8 Hz), 45.8, 44.5, 34.8, 26.9, 18.4, 12.9; ^{19}F NMR (376 MHz, CD_3OD): δ −77.16; HRMS (*m/z*): $[M - H]^-$ calcd. for $C_{27}H_{37}N_2O_2Si^-$, 449.2630; found, 449.2622.

(Z)-10-(4-((2-(2-((6-Chlorohexyl)oxy)ethoxy)ethyl)amino)-4-oxobutylidene)-7-(dimethylamino)-5,5-diisopropyl-*N*,*N*-dimethyl-5,10-dihydrodibenzo[*b*,*e*]silin-3-aminium trifluoroacetate (117)

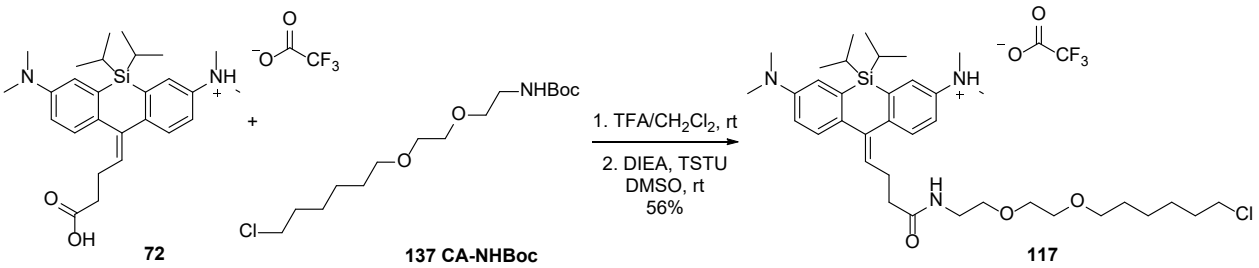

72 137 CA-NHBoc 117

A solution of **72** (1.3 mg, 3.0 µmol, 1.0 eq.) in DMSO (150 µL) was treated with DIEA (1.5 µL, 9.0 µmol, 3.0 eq.) and TSTU (1.1 mg, 3.6 µmol, 1.2 eq.). The mixture was shaken for 20 min at room temperature. In a separate vial a solution of CA-NHBoc (1.3 mg, 4.0 µmol, 1.3 eq.) in TFA/CH_2Cl_2 (2:8, 80 mL) was shaken for 3 min. The solution was evaporated and dried on the high vacuum for 1 h. The residue was taken up in DMSO (50 mL) and added to the other mixture. The mixture was shaken for 10 min and then acidified with TFA (3 µL). RP-HPLC (3 mL min^{-1}, 10% to 90% B in 32 min) gave **117** (1.0 mg, 55%) as a light blue oil.

^{1}H NMR (400 MHz, CD_3CN): δ 7.51 (d, J = 8.6 Hz, 1H), 7.41 (d, J = 8.5 Hz, 1H), 7.33 (d, J = 2.7 Hz, 1H), 7.26 (d, J = 2.7 Hz, 1H), 7.14 – 7.22 (m, 1H), 7.04 (dd, J = 8.5, 2.7 Hz, 1H), 6.43 (s, 1H), 5.72 (t, J = 7.2 Hz, 1H), 3.56 – 3.61 (m, 2H), 3.48 – 3.53 (m, 4H), 3.45– 3.42 (m, 2H), 3.40 – 3.36 (m, 2H), 3.23 – 3.31 (m, 2H), 3.04 (s, 6H), 3.03 (s, 6H), 2.51 – 2.63 (m, 2H), 2.19 (t, J = 7.4 Hz, 2H), 1.69 – 1.76 (m, 2H), 1.48 – 1.57 (m, 4H), 1.29 – 1.44 (m, 4H), 1.03 (d, J = 7.4 Hz, 12H); HRMS (*m/z*): $[M + H]^+$ calcd. for $C_{37}H_{59}ClN_3O_3Si^+$, 656.4009; found, 656.4009.

5-Bromo-2-fluoro-*N*,*N*-dimethylaniline (156)[203]

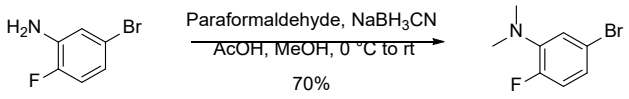

155 156

A solution of 5-bromo-2-fluoroaniline (**155**) (5.0 g, 26.3 mmol, 1.0 eq.) in MeOH (30 mL) was treated with acetic acid (40 mL) and paraformaldehyde (3.9 g, 131.6 mmol, 5.0 eq.). The mixture was cooled down to 0 °C and stirred for 15 min. $NaBH_3CN$ (5.0 g, 78.9 mmol, 3.0 eq.) was added portion wise to the mixture over 10 min. The mixture was warmed up to room temperature and was stirred for 16 h. The mixture was evaporated and then neutralised with aqueous NaOH solution (4 mL, 5 M). The aqueous layer was extracted with CH_2Cl_2 (3 x 100 mL). The combined organic layers were dried over $MgSO_4$, filtered, and evaporated to afford the crude product. Flash column chromatography (SiO_2, hexane/EtOAc 100:0 → 85:15) gave **156** (3.990 g, 70%) as a yellow oil.

^{1}H NMR (400 MHz, $CDCl_3$): δ 6.99 – 6.82 (m, 3H), 2.85 (d, J = 1.0 Hz, 6H); ^{13}C NMR (101 MHz, $CDCl_3$): δ 154.1 (d, J = 245.3 Hz), 142.1 (d, J = 9.7 Hz), 123.3 (d, J = 7.9 Hz), 121.2 (d, J = 3.9 Hz), 117.6 (d, J = 22.8 Hz), 116.9 (d, J = 3.3 Hz), 42.7 (d, J = 4.5 Hz); ^{19}F NMR (376 MHz, $CDCl_3$): δ −124.69 – −124.58 (m); HRMS (*m/z*): $[M + H]^+$ calcd. for $C_8H_{10}BrFN^+$, 217.9975; found, 217.9978.

5,5'-(Dimethylsilanediyl)bis(2-fluoro-*N*,*N*-dimethylaniline) (157)[203]

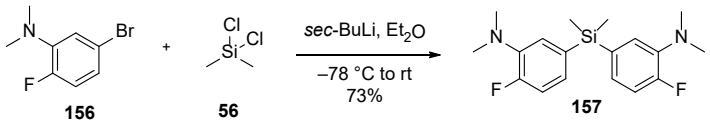

156 56 157

Following general procedure **A**, flash column chromatography (SiO_2, hexane/EtOAc 100:0 → 85:15) gave **157** (2.110 g, 73%) as a yellow oil.

^{1}H NMR (400 MHz, $CDCl_3$): δ 7.06 – 6.98 (m, 6H), 2.83 (d, J = 0.9 Hz, 12H), 0.52 (s, 6H); ^{13}C NMR (101 MHz, $CDCl_3$): δ 156.3 (d, J = 248.0 Hz), 140.3 (d, J = 8.0 Hz), 134.0 (d, J = 4.3 Hz), 127.6 (d, J = 7.5 Hz), 124.0 (d, J = 3.4 Hz), 115.9 (d, J = 19.8 Hz), 43.0 (d, J = 3.9 Hz), −1.9; ^{19}F NMR (376 MHz, $CDCl_3$): δ −121.34 – −121.21 (m); HRMS (*m/z*): $[M + H]^+$ calcd. for $C_{18}H_{25}F_2N_2Si^+$, 335.1750; found, 335.1754.

5,5'-(Dimethylsilanediyl)bis(4-bromo-2-fluoro-*N*,*N*-dimethylaniline) (158)[203]

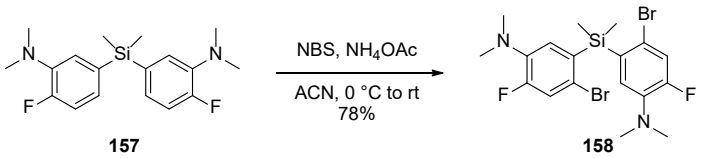

Following general procedure **B**, flash column chromatography (SiO_2, hexane/CH_2Cl_2 100:0 → 0:100) gave **158** (2.329 g, 78%) as a beige solid.

^{1}H NMR (400 MHz, $CDCl_3$): δ 7.20 (d, J = 12.5 Hz, 2H), 6.94 (d, J = 10.2 Hz, 2H), 2.80 (d, J = 1.0 Hz, 12H), 0.74 (s, 6H); ^{13}C NMR (101 MHz, $CDCl_3$): δ 155.6 (d, J = 252.7 Hz), 139.4 (d, J = 7.5 Hz), 134.1 (d, J = 4.0 Hz), 126.7 (d, J = 4.0 Hz), 120.9 (d, J = 23.2 Hz), 119.9 (d, J = 8.6 Hz), 42.7 (d, J = 4.0 Hz), −0.8; ^{19}F NMR (376 MHz, $CDCl_3$): δ −118.89 (t, J = 11.3 Hz); HRMS (*m/z*): $[M + H]^+$ calcd. for $C_{18}H_{23}Br_2F_2N_2Si^+$, 490.9960; found, 490.9954.

10-(3-Carboxypropylidene)-7-(dimethylamino)-2,8-difluoro-*N*,*N*,5,5-tetramethyl-5,10-dihydrodibenzo[*b*,*e*]silin-3-aminium trifluoroacetate (73)[203]

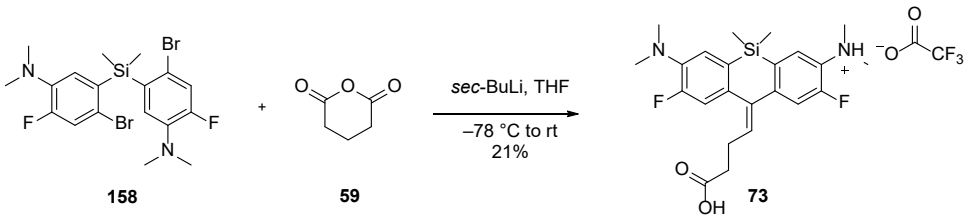

Following general procedure **C**, flash column chromatography (SiO_2, hexane/EtOAc 80:20 → 0:100) and RP-HPLC (3 mL min^{-1}, 10% to 90% B in 32 min) gave **73** (24 mg, 21%) as a white solid.

^{1}H NMR (400 MHz, CD_3OD): δ 7.58 (d, J = 9.0 Hz, 1H), 7.54 (d, J = 9.3 Hz, 1H), 7.40 (d, J = 13.3 Hz, 1H), 7.35 (d, J = 13.6 Hz, 1H), 6.00 (t, J = 7.3 Hz, 1H), 3.15 (s, 6H), 3.10 (s, 6H), 2.69 (q, J = 7.2 Hz, 2H), 2.47 (t, J = 7.1 Hz, 2H), 0.48 (s, 6H); ^{13}C NMR (101 MHz, CD_3OD): δ 176.4, 163.2 (d, J = 34.8 Hz), 161.1 (q, J = 38.1 Hz), 157.8 (d, J = 85.7 Hz), 155.3 (d, J = 84.7 Hz), 150.0 (d, J = 7.1 Hz), 142.5 (d, J = 5.5 Hz), 139.9, 135.7 (d, J = 8.2 Hz), 134.9 (d, J = 3.5 Hz), 134.5, 133.7 (d, J = 11.7 Hz), 133.3 (d, J = 3.9 Hz), 124.9, 118.0 (d, J = 20.3 Hz), 117.2 (q, J = 288.5 Hz), 115.3 (d, J = 20.0 Hz), 45.3 (d, J = 2.5 Hz), 44.7 (d, J = 2.9 Hz), 34.7, 26.5, −3.4; ^{19}F NMR (376 MHz, CD_3OD): δ −77.45, −123.44 (dd, J = 13.3, 9.3 Hz); HRMS (*m/z*): $[M - H]^-$ calcd. for $C_{23}H_{27}F_2N_2O_2Si^-$, 429.1815; found, 429.1816.

10-(4-((2-(2-((6-Chlorohexyl)oxy)ethoxy)ethyl)amino)-4-oxobutylidene)-7-(dimethylamino)-2,8-difluoro-*N*,*N*,5,5-tetramethyl-5,10-dihydrodibenzo[*b*,*e*]silin-3-aminium trifluoroacetate (118)

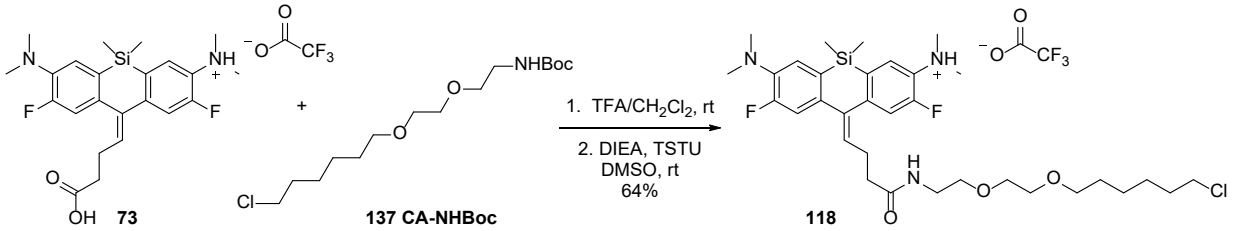

A solution of **73** (1.3 mg, 2.4 µmol, 1.0 eq.) in DMSO (120 µL) was treated with DIEA (1.5 µL, 9.0 µmol, 3.8 eq.) and TSTU (1.1 mg, 3.6 µmol, 1.5 eq.). The mixture was shaken for 20 min at room temperature. In a separate vial a solution of CA-NHBoc (1.4 mg, 4.0 µmol, 1.8 eq.) in TFA/CH_2Cl_2 (2:8, 80 µL) was shaken for 3 min. The solution was evaporated and dried on the high vacuum for 1 h. The residue was taken up in DMSO (50 µL) and added to the other mixture. The mixture was shaken for 10 min and then acidified with TFA (3 µL). RP-HPLC (8 mL min^{-1}, 20% to 100% B in 32 min) gave **118** (1.2 mg, 64%) as a light blue oil.

^{1}H NMR (400 MHz, CD_3OD): δ 7.38 (d, J = 2.8 Hz, 1H), 7.36 (d, J = 2.6 Hz, 1H), 7.31 (d, J = 13.9 Hz, 1H), 7.25 (d, J = 14.0 Hz, 1H), 5.91 (t, J = 7.3 Hz, 1H), 3.48 – 3.54 (m, 8H), 3.44 (t, J = 6.5 Hz, 2H), 3.34 (d, J = 5.5 Hz, 2H), 3.02 (s, 6H), 3.00 (s, 6H), 2.70 (q, J = 7.4 Hz, 2H), 2.37 (t, J = 6.9 Hz, 2H), 1.67 – 1.78 (m, 2H), 1.56 (dt, J = 13.9, 6.8 Hz, 2H), 1.30 – 1.49 (m, 4H), 0.44 (s, 6H); ^{19}F NMR (376 MHz, CD_3OD): δ −76.95 (s), −122.91 – −122.79 (m), −123.34 – −123.21 (m); HRMS (*m/z*): $[M + H]^+$ calcd. for $C_{33}H_{49}F_2N_3O_3Si^+$, 636.3194; found, 636.3197.

1-(3-Bromophenyl)azetidine (161)

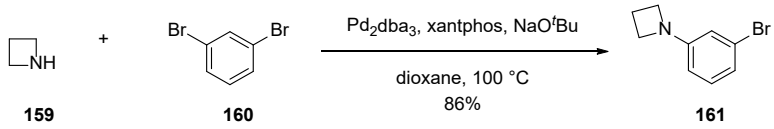

A solution of 1,3-dibromobenzene (**160**) (2.3 g, 10.0 mmol, 1.5 eq.), Pd_2dba_3 (305 mg, 0.3 mmol, 0.05 eq.), xantphos (387 mg, 0.7 mmol, 0.1 eq.) and NaO^{t}Bu (1.9 g, 20.0 mmol, 3.0 eq.) in 1,4-dioxane (50 mL) was degassed with argon for 5 min. Azetidine **159** (452 µL, 6.7 mmol, 1.0 eq.) was added and the mixture was again degassed with argon for 10 min. The mixture was stirred at 100 °C for 2 h. The mixture was cooled down to room temperature and diluted with EtOAc and aqueous saturated $NaHCO_3$ solution. The organic layer was washed with aqueous saturated $NaHCO_3$ (2 x 50 mL), brine, dried over $MgSO_4$, filtered, and evaporated to afford the crude product. Flash column chromatography (SiO_2, hexane/EtOAc 100:0 → 80:20) gave **161** (1.224 g, 86%) as a yellow oil.

^{1}H NMR (400 MHz, $CDCl_3$): δ 7.04 (t, J = 8.0 Hz, 1H), 6.82 (ddd, J = 7.9, 1.9, 0.9 Hz, 1H), 6.56 (t, J = 2.1 Hz, 1H), 6.34 (ddd, J = 8.1, 2.2, 0.9 Hz, 1H), 3.87 (t, J = 7.3 Hz, 4H), 2.37 (p, J = 7.3 Hz, 2H); ^{13}C NMR (101 MHz, $CDCl_3$): δ 153.3, 130.3, 123.1, 120.0, 114.2, 109.9, 52.4, 17.0; HRMS (m/z): $[M + H]^+$ calcd. for $C_9H_{11}BrN^+$ 212.0069; found, 221.0065.

Bis(3-(azetidin-1-yl)phenyl)dimethylsilane (162)

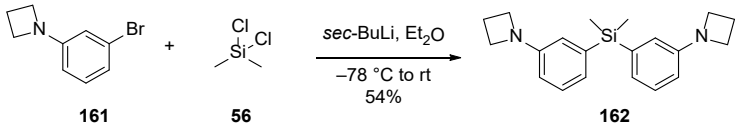

Following general procedure **A**, flash column chromatography (SiO_2, hexane/EtOAc 100:0 → 60:40) gave **162** (0.473 g, 54%) as a colourless oil.

^{1}H NMR (400 MHz, $CDCl_3$): δ 7.20 (t, J = 7.6 Hz, 2H), 6.90 (dt, J = 7.2, 1.1 Hz, 2H), 6.61 (d, J = 2.1 Hz, 2H), 6.47 (ddd, J = 8.1, 2.4, 0.8 Hz, 2H), 3.86 (t, J = 7.2 Hz, 8H), 2.34 (p, J = 7.2 Hz, 4H), 0.54 – 0.47 (m, 6H); ^{13}C NMR (101 MHz, $CDCl_3$): δ 151.6, 138.9, 128.3, 123.4, 116.9, 112.3, 52.6, 17.2, −2.1; HRMS (m/z): $[M + H]^+$ calcd. for $C_{20}H_{27}N_2Si^+$ 323.1938; found, 323.1944.

Bis(5-(azetidin-1-yl)-2-bromophenyl)dimethylsilane (163)

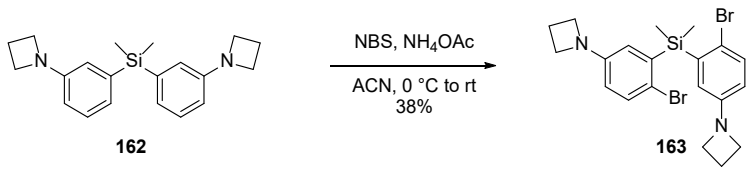

Following general procedure **B**, flash column chromatography (SiO_2, hexane/EtOAc 100:0 → 80:20) gave **163** (0.085 g, 38%) as a beige solid.

^{1}H NMR (400 MHz, $CDCl_3$): δ 7.31 (d, J = 8.5 Hz, 2H), 6.51 (d, J = 3.0 Hz, 2H), 6.31 (dd, J = 8.5, 2.9 Hz, 2H), 3.81 (t, J = 7.2 Hz, 8H), 2.33 (p, J = 7.2 Hz, 4H), 0.71 (s, 6H); ^{13}C NMR (101 MHz, $CDCl_3$): δ 150.6, 138.9, 132.9, 120.4, 117.5, 114.1, 52.6, 17.0, −0.9; HRMS (m/z): $[M + H]^+$ calcd. for $C_{20}H_{25}Br_2N_2Si^+$ 479.0148; found, 479.0146.

3,7-Di(azetidin-1-yl)-5,5-dimethyl-3',4'-dihydro-5*H*,5'*H*-spiro[dibenzo[*b*,*e*]siline-10,2'-furan]-5'-one (164)

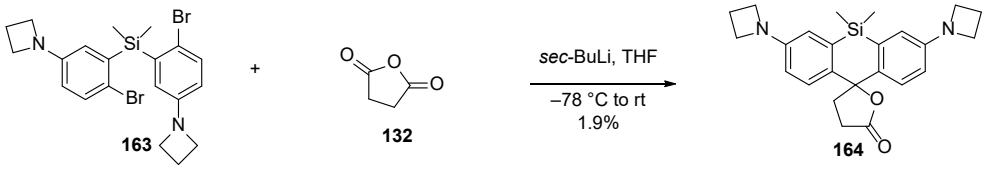

A solution of **163** (91 mg, 0.19 mmol, 1.0 eq.) in dry THF (3 mL) was cooled down to −78 °C. *sec*-BuLi (0.4 mL, 0.56 mmol, 3.0 eq., 1.3 M in cyclohexane) was added dropwise over 5 min and the mixture was stirred for 30 min at −78 °C. A solution of succinic anhydride (**132**) (21 mg, 0.21 mmol, 1.1 eq.) in dry THF (1.0 mL) was added to the mixture. The mixture was stirred at –78 °C for 15 min and then warmed up to room temperature and stirred for 30 min. Aqueous sat. NH_4Cl was added and extracted with EtOAc (2 x 25 mL). The combined organic layers were dried over $MgSO_4$, filtered, and evaporated to afford the crude product. Flash column chromatography (SiO_2, hexane/EtOAc 90:10 → 70:30) gave **164** (1.4 mg, 1.9%) as a colourless solid.

^{1}H NMR (400 MHz, CD_3CN): δ 7.32 (d, J = 8.6 Hz, 2H), 6.74 (d, J = 2.6 Hz, 2H), 6.47 (dd, J = 8.6, 2.6 Hz, 2H), 3.86 (t, J = 7.2 Hz, 8H), 2.50 (td, J = 8.0, 0.7 Hz, 2H), 2.41 – 2.24 (m, 6H), 0.53 (s, 3H), 0.40 (s, 3H); ^{13}C NMR (101 MHz, CD_3CN): δ 178.5, 151.8, 139.5, 134.7, 124.0, 117.4, 113.0, 88.8, 53.2, 42.9, 29.2, 17.6, 0.4, −2.5.

(E)-1-(7-(Azetidin-1-yl)-10-(2-carboxyethylidene)-5,5-dimethyl-5,10-dihydrodibenzo[*b*,*e*]silin-3-yl)azetidin-1-ium trifluoroacetate (74)

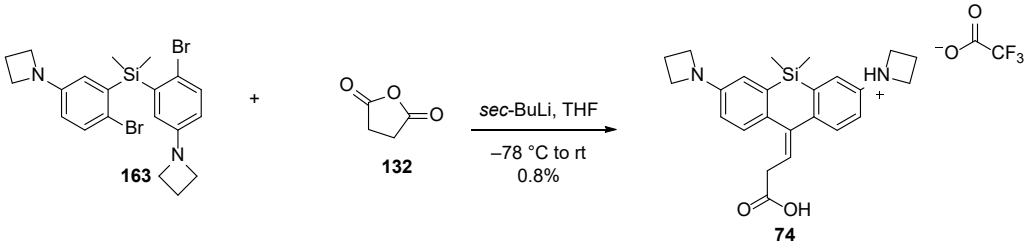

A solution of **163** (91 mg, 0.19 mmol, 1.0 eq.) in dry THF (3 mL) was cooled down to –78 °C. *sec*-BuLi (0.4 mL, 0.56 mmol, 3.0 eq., 1.3 M in cyclohexane) was added dropwise over 5 min and the mixture was stirred for 30 min at −78 °C. A solution of succinic anhydride (**132**) (21 mg, 0.21 mmol, 1.1 eq.) in dry THF (1.0 mL) was added to the mixture. The mixture was stirred at −78 °C for 15 min and then warmed up to room temperature and stirred for 30 min. Aqueous sat. NH_4Cl was added and extracted with EtOAc (2 x 25 mL). The combined organic layers were dried over $MgSO_4$, filtered, and evaporated to afford the crude product. Flash column chromatography (SiO_2, hexane/EtOAc 90:10 → 70:30) and RP-HPLC (3 mL min^{-1}, 10% to 90% B in 32 min) gave **74** (0.6 mg, 0.8%) as a light blue solid.

^{1}H NMR (400 MHz, CD_3CN): δ 7.32 (d, J = 8.4 Hz, 1H), 7.22 (d, J = 8.3 Hz, 1H), 6.73 (d, J = 2.5 Hz, 1H), 6.68 (d, J = 2.6 Hz, 1H), 6.49 (ddd, J = 11.0, 8.3, 2.6 Hz, 2H), 5.80 (t, J = 7.6 Hz, 1H), 3.89 (td, J = 7.2, 3.3 Hz, 8H), 3.32 – 3.24 (m, 2H), 1.77 (p, J = 2.5 Hz, 4H), 0.35 (s, 6H); HRMS (m/z): $[M + H]^+$ calcd. for $C_{24}H_{29}N_2O_2Si^+$ 405.1993; found, 405.1994.

6-Bromo-1-methylindoline (166)

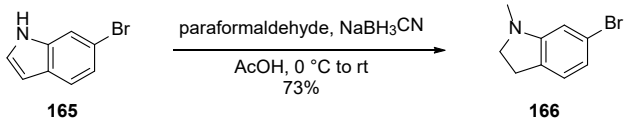

165 **166**

A solution of 6-bromoindol (**165**) (3.7 g, 19.0 mmol, 1.0 eq.) in AcOH (45 mL) was treated with paraformaldehyde (2.8 g, 95.0 mmol, 5.0 eq.) and stirred at room temperature for 10 min. The mixture was cooled down to 0 °C. $NaBH_3CN$ (2.8 g, 45.6 mmol, 2.4 eq.) was added portion wise to the mixture over 10 min. The mixture was warmed up to room temperature and was stirred for 2 h. The mixture was cooled down to 4 °C and neutralised with aqueous NaOH solution (160 mL, 5 M). The aqueous layer was extracted with EtOAc (3 x 300 mL). The combined organic layers were dried over $MgSO_4$, filtered, and evaporated to afford the crude product. Flash column chromatography (SiO_2, hexane/EtOAc 100:0 → 70:30) gave **166** (2.930 g, 73%) as a yellow oil.

^{1}H NMR (400 MHz, $CDCl_3$): δ 6.90 (dt, J = 7.6, 1.2 Hz, 1H), 6.76 (dd, J = 7.7, 1.7 Hz, 1H), 6.56 (d, J = 1.7 Hz, 1H), 3.34 (t, J = 8.2 Hz, 2H), 2.89 (td, J = 8.2, 1.1 Hz, 2H), 2.74 (s, 3H); ^{13}C NMR (101 MHz, $CDCl_3$): δ 154.8, 129.4, 125.4, 121.2, 120.2, 110.2, 56.2, 35.8, 28.3; HRMS (m/z): $[M + H]^+$ calcd. for $C_9H_{11}BrN^+$ 212.0069; found, 212.0067.

Dimethylbis(1-methylindolin-6-yl)silane (167)

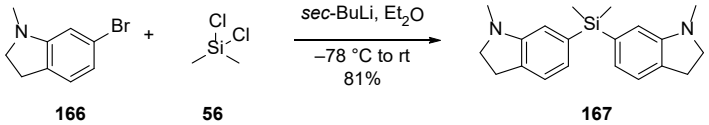

166 **56** **167**

Following general procedure **A**, flash column chromatography (SiO_2, hexane/EtOAc 100:0 → 70:30) gave **167** (1.710 g, 81%) as a yellow oil.

^{1}H NMR (400 MHz, $CDCl_3$): δ 7.11 (dq, J = 7.1, 0.9 Hz, 2H), 6.89 (dd, J = 7.1, 0.9 Hz, 2H), 6.68 (s, 2H), 3.30 (t, J = 8.1 Hz, 4H), 2.96 (t, J = 8.4 Hz, 4H), 2.77 (s, 6H), 0.53 (s, 6H); ^{13}C NMR (101 MHz, $CDCl_3$): δ 152.8, 137.4, 131.8, 124.5, 124.0, 112.5, 56.1, 36.5, 28.9, −1.7; HRMS (m/z): $[M + H]^+$ calcd. for $C_{20}H_{27}N_2Si^+$ 323.1938; found, 323.1935.

Bis(5-bromo-1-methylindolin-6-yl)dimethylsilane (76)

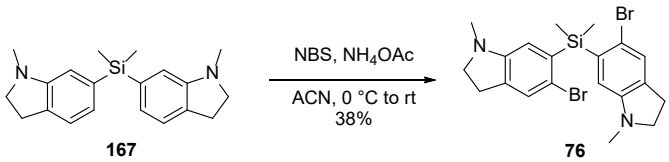

Following general procedure **B**, flash column chromatography (SiO_2, hexane/CH_2Cl_2 100:0 → 0:100) gave **76** (0.977 g, 38%) as a beige solid.

^{1}H NMR (400 MHz, $CDCl_3$): δ 7.21 (s, 2H), 6.57 (s, 2H), 3.30 (t, J = 8.2 Hz, 4H), 2.93 (t, J = 8.0 Hz, 4H), 2.71 (s, 6H), 0.73 (s, 6H); ^{13}C NMR (101 MHz, $CDCl_3$): δ 152.0, 137.0, 134.2, 128.8, 118.0, 115.2, 56.2, 36.3, 28.5, −0.6; HRMS (m/z): $[M + H]^+$ calcd. for $C_{20}H_{25}Br_2N_2Si^+$ 481.0128; found, 481.0127.

(Z)-7-Amino-10-(3-carboxypropylidene)-5,5-dimethyl-5,10-dihydrodibenzo[*b*,*e*]silin-3-aminium trifluoroacetate; PA-SiR595 (75)

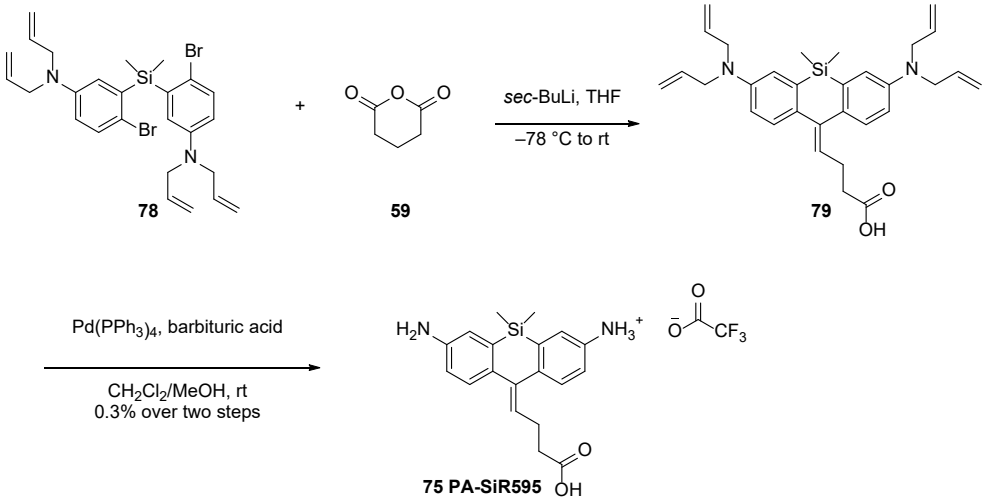

Following general procedure **C**, flash column chromatography (SiO_2, hexane/EtOAc 100:0 → 0:100) and RP-HPLC (3 mL min^{-1}, 20% to 100% B in 32 min) gave a **79** (6 mg) as an impure green oil, which was used in the next step.

A solution of impure **79** (6 mg, 12.0 µmol, 1.0 eq.) in CH_2Cl_2/MeOH (9:1, 2 mL) was degassed with argon for 5 min. Barbituric acid (13 mg, 8.4 µmol, 7.0 eq.) was added and the solution was again degassed with argon. $Pd(PPh_3)_4$ (3 mg, 0.2 µmol, 0.2 eq.) was added and the mixture was stirred at room temperature for 30 min. The solution was evaporated. The residue was taken up in DMSO (200 µL), filtered through a syringe filter and then acidified with TFA (3 µL). RP-HPLC (8 mL min^{-1}, 20% to 100% B in 34 min) gave PA-SiR595 (0.1 mg, 0.3%) as a light blue-green solid.

^{1}H NMR (400 MHz, CD_3OD): δ 7.55 (d, J = 8.2 Hz, 1H), 7.47 (d, J = 8.2 Hz, 1H), 7.41 (d, J = 2.5 Hz, 1H), 7.39 (d, J = 2.4 Hz, 1H), 7.23 (dd, J = 8.3, 2.5 Hz, 1H), 7.18 (dd, J = 8.2, 2.4 Hz, 1H), 5.94 (t, J = 7.3 Hz, 1H), 2.68 (q, J = 7.2 Hz, 2H), 2.43 (t, J = 7.3 Hz, 2H), 0.45 (s, 6H); HRMS (m/z): $[M + H]^+$ calcd. for $C_{19}H_{23}N_2O_2Si^+$ 339.1529; found, 339.1523.

3,3'-Oxydianiline (82)

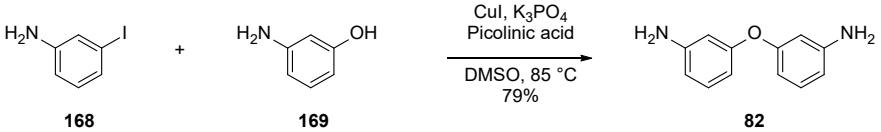

A solution of 3-iodo-aniline (**168**) (2.2 g, 10.0 mmol, 1.0 eq.), 3-aminophenol (**169**) (1.3 g, 12.0 mmol, 1.2 eq.), K_3PO_4 (4.25 g, 20.0 mmol, 2.0 eq.), picolinic acid (246 mg, 2.0 mmol, 0.2 eq.), and CuI (190 mg, 1.0 mmol, 0.1 eq.) in DMSO (50 mL) was degassed with argon for 5 min. The mixture was heated to 85 °C for 16 h. The mixture was cooled down, diluted with water and EtOAc. The aqueous layer was extracted with EtOAc (3 x 200 mL). The combined organic layers were dried over $MgSO_4$, filtered, and evaporated to afford the crude product. Flash column chromatography (SiO_2, hexane/EtOAc 90:10 → 40:60) gave **82** (1.570 g, 79%) as a yellow solid.

^{1}H NMR (400 MHz, $CDCl_3$): δ 7.08 (t, J = 8.0 Hz, 2H), 6.41 (dtd, J = 8.0, 2.3, 0.9 Hz, 4H), 6.33 (t, J = 2.2 Hz, 2H), 3.66 (s, 4H); ^{13}C NMR (101 MHz, $CDCl_3$): δ 158.4, 148.0, 130.4, 110.1, 109.3, 105.8; HRMS (m/z): $[M + H]^+$ calcd. for $C_{12}H_{13}N_2O^+$ 201.1022; found, 201.1023.

3,3'-Oxybis(*N*,*N*-dimethylaniline) (84)

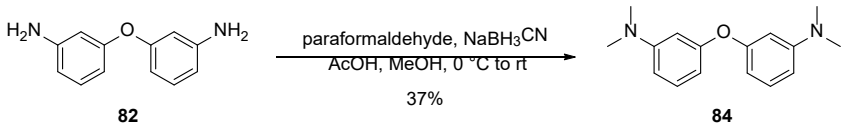

82 **84**

A solution of compound **82** (1.2 g, 6.0 mmol, 1.0 eq.) in MeOH (10 mL) was treated with AcOH (15 mL) and paraformaldehyde (1.9 g, 60.0 mmol, 10.0 eq.) and stirred at room temperature for 10 min. The mixture was cooled down to 0 °C. $NaBH_3CN$ (2.2 g, 36.0 mmol, 6.0 eq.) was added portion wise to the mixture over 10 min. The mixture was warmed up to room temperature and stirred for 16 h. The mixture was cooled down to 4 °C and neutralised with aqueous NaOH solution (50 mL, 5 M). The aqueous layer was extracted with EtOAc (3 x 100 mL). The combined organic layers were dried over $MgSO_4$, filtered, and evaporated to afford the crude product. Flash column chromatography (SiO_2, hexane/EtOAc 100:0 → 50:50) gave **84** (575 mg, 37%) as a pinkish oil.

^{1}H NMR (400 MHz, $CDCl_3$): δ 7.16 (t, J = 8.1 Hz, 2H), 6.53 – 6.44 (m, 4H), 6.43 – 6.34 (m, 2H), 2.93 (s, 12H); ^{13}C NMR (101 MHz, $CDCl_3$): δ 158.4, 152.1, 129.9, 107.6, 106.9, 103.5, 40.7; HRMS (m/z): $[M + H]^+$ calcd. for $C_{16}H_{21}N_2O^+$ 257.1648; found, 257.1650.

3,3'-Oxybis(4-bromo-*N*,*N*-dimethylaniline) (86)

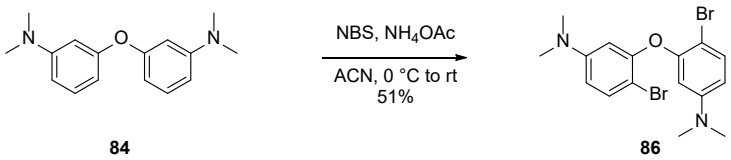

84 **86**

Following general procedure **B**, flash column chromatography (SiO_2, hexane/CH_2Cl_2 100:0 → 0:100) gave **86** (0.431 g, 51%) as a beige solid.

^{1}H NMR (400 MHz, $CDCl_3$): δ 7.39 (d, J = 8.9 Hz, 2H), 6.37 (dd, J = 8.9, 2.9 Hz, 2H), 6.23 (d, J = 2.9 Hz, 2H), 2.86 (s, 12H); ^{13}C NMR (101 MHz, $CDCl_3$): δ 153.8, 151.1, 133.4, 109.3, 103.9, 99.9, 40.6; HRMS (m/z): $[M + H]^+$ calcd. for $C_{16}H_{19}Br_2N_2O^+$ 414.9839; found, 414.9836.

5,5'-Oxybis(2-fluoroaniline) (83)

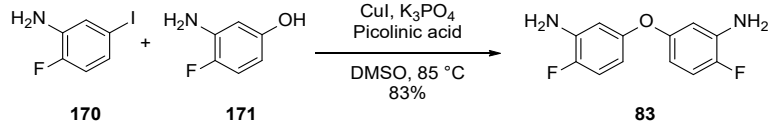

170 171 83

A Schlenk flask fitted with a magnetic stir bar was baked out under vacuum and flooded with nitrogen. 2-Fluoro-5-iodoaniline (**170**) (1.19 g, 5.0 mmol, 1.0 eq.), 3-amino-4-fluorophenol (**171**) (0.76 g, 6.0 mmol, 1.2 eq.), copper (I) iodide (0.05 g, 0.3 mmol, 0.05 eq.), picolinic acid (0.06 g, 0.5 mmol, 0.1 eq.), and K_2CO_3 (2.12 g, 10.0 mol, 2.0 eq.) were added under nitrogen backflow. The flask was evacuated and backfilled with nitrogen three times. Dry DMSO (10 mL) was added and the solution degassed with argon for 5 min. The mixture was heated to 85 °C for 24 h, then cooled down to room temperature. The mixture was quenched with brine/EtOAc 1:10 and filtered over Celite. The layers were separated and the aqueous layer extracted with EtOAc (3 x 400 mL). The combined organic layers were washed with brine, dried over $MgSO_4$, filtered over Celite, and concentrated to give the crude product. Purification via column chromatography, (SiO_2 hexane/EtOAc 100:0 → 50:50) gave **83** (0.976 g, 83%) as a yellow oil.

^{1}H NMR (400 MHz, $CDCl_3$): δ 6.90 (dd, J = 10.6, 8.8 Hz, 2H), 6.40 (dd, J = 7.6, 2.9 Hz, 2H), 6.28 (ddd, J = 8.8, 3.7, 2.9 Hz, 2H), 3.73 (s, 4H); ^{13}C NMR (101 MHz, $CDCl_3$): δ 153.9 (d, J = 2.3 Hz), 147.9 (d, J = 234.3 Hz), 135.5 (d, J = 14.6 Hz), 115.8 (d, J = 20.4 Hz), 108.3 (d, J = 6.8 Hz), 107.3 (d, J = 3.5 Hz); ^{19}F NMR (376 MHz, $CDCl_3$) δ −142.12 (ddd, J = 11.0, 7.5, 3.7 Hz); HRMS (m/z): $[M + H]^+$ calcd. for $C_{12}H_{11}F_2N_2O^+$ 237.0834; found, 237.0831.

5,5'-Oxybis(2-fluoro-*N*,*N*-dimethylaniline) (85)

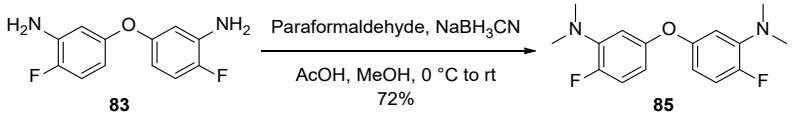

83 85

A solution of **83** (0.45 g, 1.9 mmol, 1.0 eq.) in MeOH (3 mL) was treated with acetic acid (4.5 mL) and paraformaldehyde (0.57 g, 19.1 mmol, 10.0 eq.) and stirred at 0 °C for 15 min. $NaBH_3CN$ (0.72 g, 11.4 mmol, 6.0 eq.) was added portionwise over 5 min, the mixture was then warmed up to room temperature and stirred for 24 h. The mixture was quenched with NaOH (5 M), diluted with EtOAc and the layers were separated. The aqueous layer was extracted with EtOAc (3 x 100 mL), and the combined organic layers were dried over $MgSO_4$, filtered, and evaporated to afford the crude product. Flash column chromatography (SiO_2, hexane/EtOAc 100:0 → 95:05) gave **85**(0.400 g, 72%) as a colourless oil.

^{1}H NMR (400 MHz, $CDCl_3$): δ 6.92 (dd, J = 12.6, 8.7 Hz, 2H), 6.56 (dd, J = 7.6, 2.9 Hz, 2H), 6.39 (dt, J = 8.7, 3.2 Hz, 2H), 2.83 (d, J = 1.0 Hz, 12H); ^{13}C NMR (101 MHz, $CDCl_3$): δ 153.7 (d, J = 2.4 Hz), 151.08 (d, J = 240.4 Hz), 141.8 (d, J = 10.4 Hz), 116.5 (d, J = 23.1 Hz), 109.8 (d, J = 7.9 Hz), 109.1 (d, J = 3.7 Hz), 42.8 (d, J = 4.5 Hz); ^{19}F-NMR (376 MHz, CDCl3): δ −129.0 – −129.7 (m); HRMS (m/z): $[M + H]^+$ calcd. for $C_{16}H_{19}F_2N_2O^+$ 293.1460; found, 293.1461.

5,5'-Oxybis(4-bromo-2-fluoro-*N*,*N*-dimethylaniline) (87)

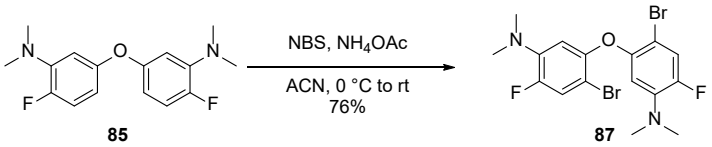

85 87

Following general procedure **B**, flash column chromatography (SiO_2, hexane/EtOAc 100:0 → 90:10) gave **87** (0.471 g, 76%) as a yellow oil.

^{1}H NMR (400 MHz, $CDCl_3$): δ 7.25 (d, J = 12.1 Hz, 2H), 6.34 (d, J = 8.1 Hz, 2H), 2.78 (d, J = 1.0 Hz, 12H); ^{13}C NMR (101 MHz, $CDCl_3$): 151.90, 149.65 (d, J = 37.8 Hz), 141.07, 120.72 (d, J = 25.9 Hz), 108.71 (d, J = 4.2 Hz), 102.39, 42.56

(d, J = 4.6 Hz); ^{19}F NMR (376 MHz, $CDCl_3$) δ −126.25 (dd, J = 12.1, 8.2 Hz); HRMS (m/z): $[M + H]^+$ calcd. for $C_{16}H_{17}Br_2F_2N_2O^+$ 448.9670; found, 448.9664.

_N_-(9-(3-Carboxypropyl)-6-(dimethylamino)-2,7-difluoro-3_H_-xanthen-3-ylidene)-_N_-methylmethanaminium trifluoroacetate (89) or (E)-9-(3-carboxypropylidene)-6-(dimethylamino)-2,7-difluoro-_N_,_N_-dimethyl-9_H_-xanthen-3-aminium trifluoroacetate (90)

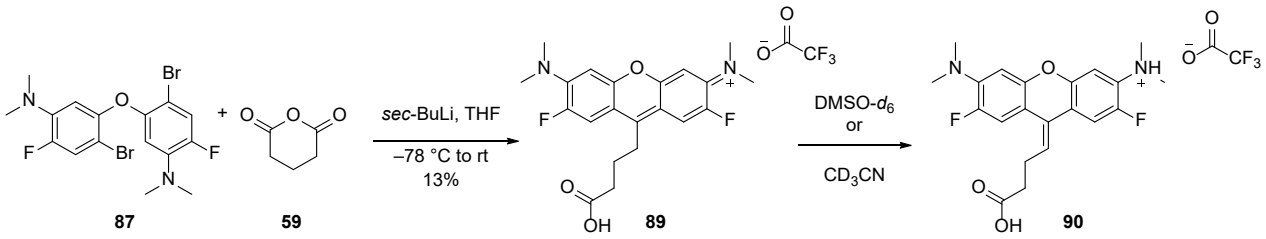

87 59 89 90

Following general procedure **C**, flash column chromatography (SiO_2, hexane/EtOAc 70:30 → 0:100, CH_2Cl_2/MeOH 100:0 → 0:10) and RP-HPLC (3 mL min^{-1}, 10% to 90% B in 32 min) gave **89** (11 mg, 13%) as a red solid. NMR of **90** is reported.

^{1}H NMR (400 MHz, DMSO-d_6): δ 7.34 (d, J = 2.8 Hz, 1H), 7.30 (d, J = 2.4 Hz, 1H), 6.64 (d, J = 8.3 Hz, 1H), 6.60 (d, J = 8.0 Hz, 1H), 5.68 (t, J = 6.8 Hz, 1H), 2.85 (d, J = 1.1 Hz, 6H), 2.80 (d, J = 1.0 Hz, 6H) (CH_2 groups hidden by solvent signal and water signal); ^{1}H NMR (400 MHz, CD_3CN): δ 7.31 (d, J = 14.9 Hz, 1H), 7.22 (d, J = 14.5 Hz, 1H), 6.62 (d, J = 8.2 Hz, 1H), 6.58 (d, J = 8.1 Hz, 1H), 5.63 (t, J = 7.0 Hz, 1H), 2.88 (d, J = 1.1 Hz, 6H), 2.84 (d, J = 1.0 Hz, 6H), 2.75 (q, J = 7.2 Hz, 2H), 2.52 (t, J = 7.3 Hz, 2H); HRMS (m/z): $[M + H]^+$ calcd. for $C_{21}H_{23}F_2N_2O_3^+$ 389.1671; found, 389.1670.

3,3'-Oxybis(bromobenzene) (93)

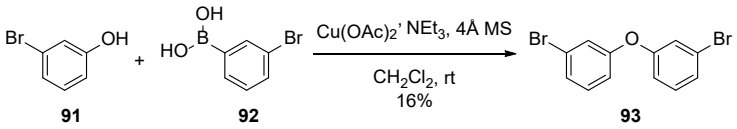

91 92 93

A 250 mL flask was charged with 4 Å MS (5.4 g), 3-bromophenol (**91**) (1.07 g, 6.2 mmol, 1.0 eq.), 3-bromophenylboronic acid (**92**) (2.49 g, 12.3 mmol, 2.0 eq.), Cu(II)$(OAc)_2$ (1.13 g, 6.2 mmol, 1.0 eq.), and triethylamine (4.32 mL, 31.0 mmol, 5.0 eq.), dissolved in dry CH_2Cl_2 (55 mL) and stirred for 24 h at room temperature, then filtered over Celite with CH_2Cl_2, concentrated to dryness and dissolved in Et_2O/H_2O. The layers were separated and the aqueous layer extracted with Et_2O (3 x 400 mL). The combined organic layers were dried over $MgSO_4$, filtered, and evaporated to afford the crude product. Purification via flash column chromatography (SiO_2, hexane) gave **93** (0.323 g, 16%) as a clear oil.

^{1}H NMR (400 MHz, $CDCl_3$): δ 7.31 – 7.21 (m, 4H), 7.19 (t, J = 2.1 Hz, 2H), 6.97 (ddd, J = 8.1, 2.4, 1.1 Hz, 2H); ^{13}C NMR (101 MHz, $CDCl_3$): δ 157.6, 131.1, 127.1, 123.1, 122.4, 117.8; HRMS (m/z): $[M]^+$ calcd. for $C_{12}H_8Br_2O^+$ 325.8936; found, 325.8933 (APCI).

3,3'-Oxybis(_N_,_N_-bis(2,2,2-trifluoroethyl)aniline) (95)

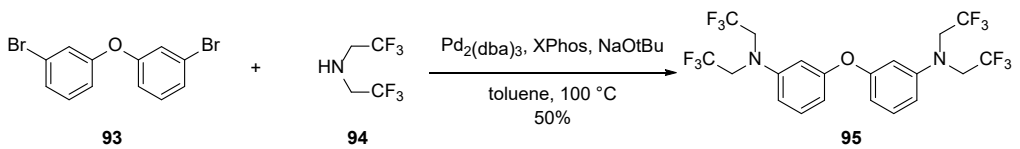

93 94 95

A Schlenk tube fitted with a magnetic stirbar was baked out under vacuum and flooded with nitrogen. **93** (0.2 g, 0.6 mmol, 1.0 eq.) was dissolved in dry toluene (7 mL). XPhos (0.087 g, 0.18 mmol, 0.3 eq.), tris(dibenzylidene-

acetone)dipalladium(0) (0.055 g, 0.06 mmol, 0.1 eq.), and sodium *tert*-butoxide (0.164 g, 1.7 mmol, 2.8 eq.) were added under nitrogen backflow and the mixture was degassed with argon for 10 min. Bis(2,2,2-trifluoroethyl)amine (**94**) (0.33 mL, 1.8 mmol, 3.0 eq.) was added and stirred at 100 °C for 20 h. The mixture was cooled down to room temperature, diluted with EtOAc and washed with H_2O (3 x 100 mL) and brine. The organic layer was dried over $MgSO_4$, filtered, and evaporated to afford the crude product. Flash column chromatography (SiO_2, hexane/EtOAc 100:0 → 90:10) gave **95** (0.161 g, 50%) as an orange oil.

^{1}H NMR (400 MHz, $CDCl_3$): δ 7.23 (t, J = 8.2 Hz, 2H), 6.65 (dd, J = 8.4, 2.7 Hz, 2H), 6.58 (t, J = 2.4 Hz, 2H), 6.53 (ddd, J = 8.2, 2.2, 0.7 Hz, 2H), 4.01 (q, J = 8.6 Hz, 8H); ^{13}C NMR (101 MHz, $CDCl_3$): δ 158.14, 148.16, 130.57, 125.22 (d, J = 283.5 Hz), 110.59, 109.46, 105.55, 51.98 (d, J = 33.1 Hz); ^{19}F NMR (376 MHz, $CDCl_3$): δ = −69.39 (t, J = 8.5 Hz); HRMS (m/z): $[M + H]^+$ calcd. for $C_{20}H_{17}F_{12}N_2O^+$ 529.1144; found, 529.1140.

3,3'-Oxybis(4-bromo-*N*,*N*-bis(2,2,2-trifluoroethyl)aniline) (96)

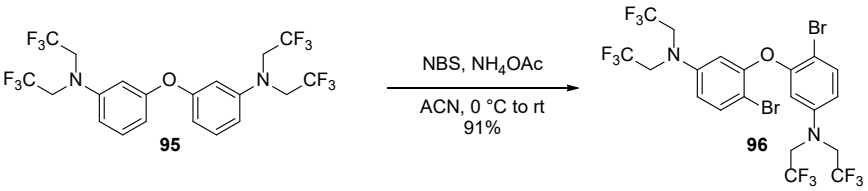

Following general procedure **B**, flash column chromatography (SiO_2, hexane/EtOAc 100:0 → 90:10) gave **96** (0.291 g, 91%) as a yellow oil.

^{1}H-NMR (400 MHz, $CDCl_3$): δ 7.50 (d, J = 8.9 Hz, 2H), 6.60 (dd, J = 8.9, 3.0 Hz, 2H), 6.37 (d, J = 3.0 Hz, 2H), 3.92 (q, J = 8.4 Hz, 8H); ^{13}C-NMR (101 MHz, $CDCl_3$): δ 153.7, 147.3, 134.3, 124.96 (d, *J* = 281.9 Hz), 111.6, 106.3, 104.4, 52.10 (d, *J* = 33.8 Hz); ^{19}F-NMR (377 MHz, $CDCl_3$): δ −69.57 (t, *J* = 8.3 Hz); HRMS (m/z): $[M + H]^+$ calcd. for $C_{20}H_{15}Br_2F_{12}N_2O^+$ 686.9335; found, 686.9332.

Inseparable mixture of (*E*)-6-(Bis(2,2,2-trifluoroethyl)amino)-9-(3-carboxypropylidene)-*N*,*N*-bis(2,2,2-trifluoroethyl)-9*H*-xanthen-3-aminium trifluoroacetate (97) and *N*-(6-(bis(2,2,2-trifluoroethyl)amino)-9-(3-carboxypropyl)-3*H*-xanthen-3-ylidene)-2,2,2-trifluoro-*N*-(2,2,2-trifluoroethyl)ethan-1-aminium trifluoroacetate (98)

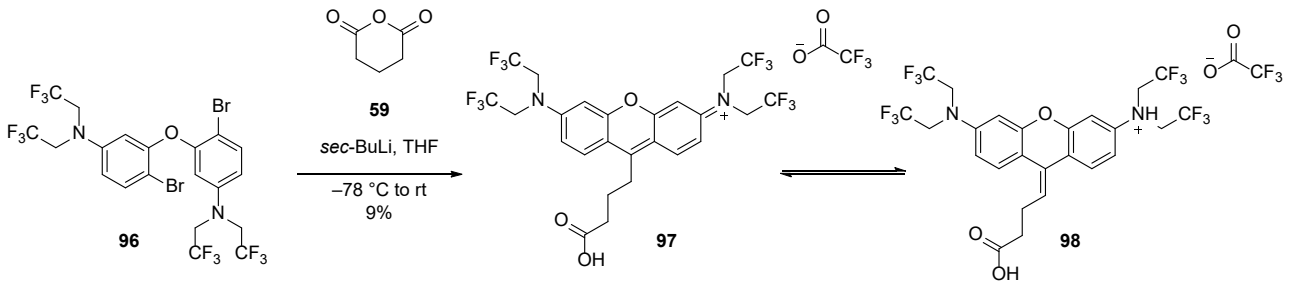

Following general procedure **C**, flash column chromatography (SiO_2, hexane/EtOAc 70:30 → 0:100, CH_2Cl_2/MeOH 100:0 → 0:10) and RP-HPLC (3 mL min^{-1}, 20% to 100% B in 32 min) gave two products, which were in equilibrium, **97** and **98** (16 mg, 9%) as an orange solid. Equilibrium between the fluorescent and activatable forms **97** and **98** is dependent on solvent. LC-MS analysis at 254 nm under acidic aqueous conditions revealed a ratio of 1.5:1 (**97**:**98**).

^{1}H NMR measurements revealed two sets of peaks as confirmed by COSY measurements. They correspond to **97** (75%) and **98** (25%):

^{1}H NMR (400 MHz, CD_3CN, signals of **97** are marked with [a], those from compound **98** with [b]; ratio a b^{-1} = 3:1): δ 8.45[a] (d, J = 9.6 Hz, 2H), 7.56[a] (dd, J = 9.5, 2.7 Hz, 2H), 7.48[b] (d, J = 8.9 Hz, 1H), 7.37[a] (d, J = 2.7 Hz, 2H), 6.87 – 6.76[b] (m, 4H), 6.70[b] (d, J = 2.8 Hz, 1H), 5.71[b] (t, J = 6.9 Hz, 1H), 4.56[a] (q, J = 8.4 Hz, 8H), 4.29 – 4.13[b] (m, 8H), 3.67 – 3.54[a] (m, 2H),

2.75[b] (q, J = 7.2 Hz, 2H), 2.59[a] (t, J = 6.7 Hz, 2H), 2.51[b] (d, J = 7.2 Hz, 2H), 2.04 – 1.95[a] (m, 2H); ^{19}F NMR (376 MHz, CD_3CN): δ −69.85 (t, J = 8.3 Hz), −76.62; HRMS (m/z): $[M + H]^+$ calcd. for $C_{25}H_{21}F_{12}N_2O_3^+$ 625.1355; found, 625.1351.

7-(Dimethylamino)-*N*,*N*,4',4',5,5-hexamethyl-5'-oxo-4',5'-dihydro-3'*H*,5*H*-spiro[dibenzo[*b*,*e*]siline-10,2'-furan]-3-aminium trifluoroacetate (173)

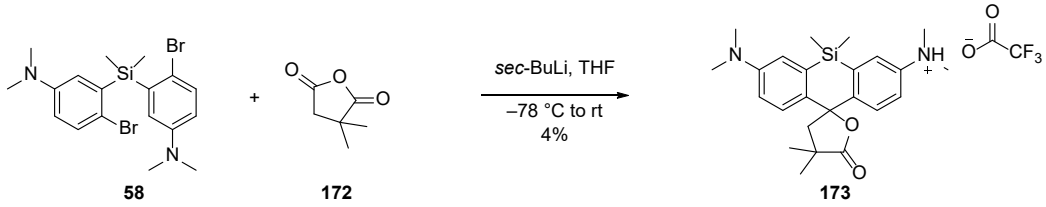

58 **172** **173**

Following general procedure **C**, flash column chromatography (SiO_2, hexane/EtOAc 70:30 → 0:100) and RP-HPLC (3 mL min^{-1}, 10% to 100% B in 32 min) gave **173** (8.4 mg, 4%) as a white solid.

^{1}H NMR (400 MHz, DMSO-*d*$_6$): δ 7.26 (d, J = 8.8 Hz, 2H), 7.00 (d, J = 2.8 Hz, 2H), 6.77 (dd, J = 8.8, 2.8 Hz, 2H), 2.90 (s, 12H), 2.25 (s, 2H), 1.09 (s, 6H), 0.56 (s, 3H), 0.41 (s, 3H); ^{13}C NMR (101 MHz, DMSO-*d*$_6$): δ 182.3, 147.7, 141.7, 133.6, 122.4, 117.0, 114.1, 83.8, 56.3, 40.9, 40.4, 26.9, 0.4, −2.8; ^{19}F NMR (376 MHz, DMSO-*d*$_6$): δ −73.47; HRMS (m/z): $[M + H]^+$ calcd. for $C_{24}H_{33}N_2O_2Si^+$ 409.2306; found, 409.2304.

3-Bromo-*N*,*N*,2-trimethylaniline (175)

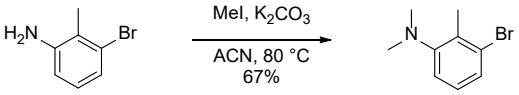

174 **175**

A suspension of 3-bromo-2-methylaniline (**174**) (3.0 g, 16.5 mmol, 1.0 eq.), K_2CO_3 (5.02 g, 36.3 mmol, 2.2 eq.) and MeI (2.25 mL, 36.3 mmol, 2.2 eq.) in dry ACN (80 mL) was heated to 80 °C for 16 h. The mixture was cooled down to room temperature, diluted with water to dissolve the residual salt and evaporated. The obtained solution was diluted with aqueous saturated $NaHCO_3$ solution. The aqueous layer was extracted with CH_2Cl_2 (3 x 100 mL) and the combined organic layers were dried over $MgSO_4$, filtered, and evaporated to afford the crude product. Flash column chromatography (SiO_2, hexane/EtOAc 100:0 → 85:15) gave **175** (2.380 g, 67%) as a colourless oil.

^{1}H NMR (400 MHz, $CDCl_3$): δ 7.53 (dd, J = 7.2, 2.0 Hz, 1H), 7.33 – 7.22 (m, 2H), 2.95 (s, 6H), 2.69 (s, 3H); ^{13}C NMR (101 MHz, $CDCl_3$): δ 154.5, 132.3, 127.2, 126.8, 126.7, 117.6, 44.5, 18.8; HRMS (m/z): $[M + H]^+$ calcd. for $C_9H_{13}BrN^+$ $[M + H]^+$ 214.0226; found, 214.0228.

3,3'-(Dimethylsilanediyl)bis(*N*,*N*,2-trimethylaniline) (176)

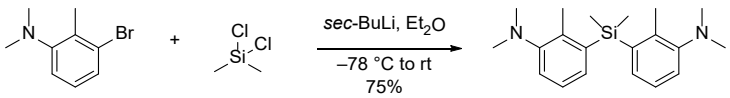

175 **56** **176**

Following general procedure **A**, flash column chromatography (SiO_2, hexane/EtOAc 100:0 → 70:30) gave **176** (1.280 g, 75%) as a colourless oil.

^{1}H NMR (400 MHz, $CDCl_3$): δ 7.23 (d, J = 7.3 Hz, 2H), 7.17 (t, J = 7.5 Hz, 2H), 7.11 (d, J = 7.4 Hz, 2H), 2.64 (s, 12H), 2.20 (s, 6H), 0.61 (s, 6H); ^{13}C NMR (101 MHz, $CDCl_3$): δ 152.7, 139.5, 138.3, 129.6, 125.9, 119.9, 44.7, 18.4, −0.1; HRMS (m/z): $[M + H]^+$ calcd. for $C_{20}H_{31}N_2Si^+$ 327.2251; found, 327.2248.

3,3'-(Dimethylsilanediyl)bis(4-bromo-*N,N*,2-trimethylaniline) (177)

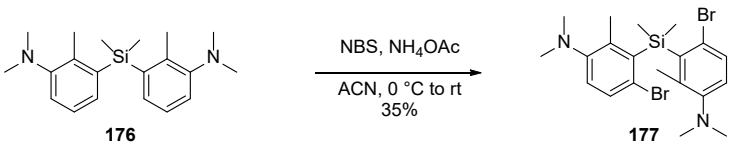

Following general procedure **B**, flash column chromatography (SiO_2, hexane/CH_2Cl_2 100:0 → 0:100) gave **177** (0.640 g, 35%) as a beige solid.

^{1}H NMR (400 MHz, $CDCl_3$): δ 7.28 (d, J = 8.6 Hz, 2H), 6.88 (d, J = 8.5 Hz, 2H), 2.60 (s, 12H), 2.34 (s, 6H), 0.87 (s, 6H); ^{13}C NMR (101 MHz, $CDCl_3$): δ 152.0, 142.4, 140.1, 131.6, 123.4, 120.9, 44.5, 19.1, 6.8; HRMS (m/z): $[M + H]^+$ calcd. for $C_{20}H_{29}Br_2N_2Si^+$ 483.0461; found, 483.0454.

5-Bromo-*N,N*,2-trimethylaniline (179)

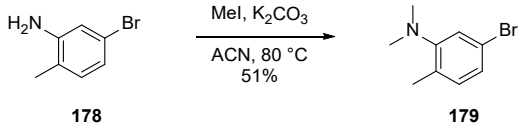

A suspension of 5-bromo-2-methylaniline (**178**) (4.10 g, 22.0 mmol, 1.0 eq.), K_2CO_3 (6.70 g, 48.4 mmol, 2.2 eq.) and MeI (3.0 mL, 48.4 mmol, 2.2 eq.) in dry ACN (140 mL) was heated to 80 °C for 16 h. The mixture was cooled down to room temperature, diluted with water to dissolve the residual salt and evaporated. The obtained solution was diluted with aqueous saturated $NaHCO_3$ solution. The aqueous layer was extracted with CH_2Cl_2 (3 x 100 mL) and the combined organic layers were dried over $MgSO_4$, filtered, and evaporated to afford the crude product. Flash column chromatography (SiO_2, hexane/EtOAc 100:0 → 70:30) gave **179** (2.380 g, 51%) as a colourless oil.

^{1}H NMR (400 MHz, $CDCl_3$): δ 7.15 (d, J = 1.6 Hz, 1H), 7.08 (dd, J = 8.1, 1.7 Hz, 1H), 7.03 (d, J = 8.1 Hz, 1H), 2.71 (s, 6H), 2.29 (s, 3H); ^{13}C NMR (101 MHz, $CDCl_3$): δ 154.2, 132.5, 130.9, 125.3, 121.8, 119.7, 44.0, 18.2; HRMS (m/z): $[M + H]^+$ calcd. for $C_9H_{13}BrN^+$ 214.0226; found, 214.0232.

5,5'-(Dimethylsilanediyl)bis(*N,N*,2-trimethylaniline) (180)

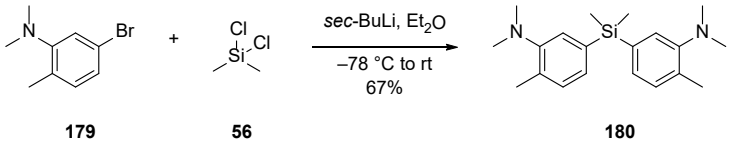

Following general procedure **A**, flash column chromatography (SiO_2, hexane/EtOAc 100:0 → 80:20) gave **180** (1.200 g, 67%) as a colourless oil.

^{1}H NMR (400 MHz, $CDCl_3$): δ 7.22 (s, 2H), 7.18 (d, J = 7.3 Hz, 2H), 7.14 (d, J = 7.3 Hz, 2H), 2.71 (s, 12H), 2.35 (s, 6H), 0.54 (s, 6H); ^{13}C NMR (101 MHz, $CDCl_3$): δ 152.2, 136.3, 133.3, 130.9, 128.7, 123.9, 44.4, 18.6, −1.8; HRMS (m/z): $[M + H]^+$ calcd. for $C_{20}H_{31}N_2Si^+$ 327.2251; found, 327.2252.

5,5'-(Dimethylsilanediyl)bis(4-bromo-*N,N*,2-trimethylaniline) (181)

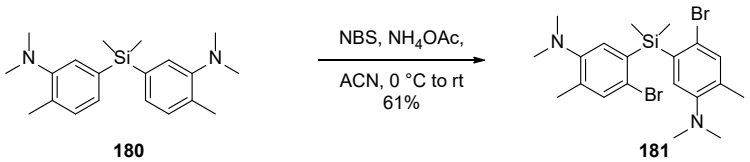

180 **181**

Following general procedure **B**, flash column chromatography (SiO_2, hexane/CH_2Cl_2 100:0 → 0:100) gave **181** (1.098 g, 61%) as a beige solid.

^{1}H NMR (400 MHz, $CDCl_3$): δ 7.32 (s, 2H), 7.09 (s, 2H), 2.63 (s, 12H), 2.28 (s, 6H), 0.75 (s, 6H); ^{13}C NMR (101 MHz, $CDCl_3$): δ 151.3, 136.1, 135.8, 135.2, 127.6, 123.4, 44.2, 18.2, −0.79; HRMS (m/z): $[M + H]^+$ calcd. for $C_{20}H_{29}Br_2N_2Si^+$ 483.0461; found, 483.0458.

5.2 Materials and general information for *in vitro* and *in cellulo* experiments for Chapter 2

General considerations: PA-SiRs were prepared as stock solutions in dry DMSO and diluted in the respective buffer such that the final concentration of DMSO did not exceed 5% v/v. A fiber coupled LED (Omicron, 340 nm, 3 mm liquid light guide) was used to perform UV irradiation unless otherwise stated. PBS (6.7 mM, Lonza) was used in all experiments.

UV-Vis measurements: Spectra and time traces were measured in 1.5 mL stirrable quartz cuvettes (Hellma Analytics) on a JASCO V770 spectrophotometer with a Peltier element (PAC743R) under continuous stirring and at 21 °C. PA-SiRs were diluted in PBS (10 µM unless otherwise stated). A blank was measured before starting the measurement. UV irradiation was performed directly inside the spectrophotometer during the ongoing experiment for 12 s unless otherwise stated. PBS solutions of different pH were adjusted by addition of HCl or NaOH solution using a pH meter. ACN, DMSO, and 1,4-dioxane PBS mixtures (3:7) were freshly prepared before each measurement. Cysteamine and maleimide concentrations were adjusted by addition of concentrated cysteamine or maleimide solutions (1 M each).

PA-SiR-CA (C4, C3, PEG1, and PEG2), PA-SiR-BG, and PA-SiR-jasplakinolide probes (10 µM) were directly added to the target protein (20 µM SNAP-tag, 20 µM HaloTag or 0.4 mg mL^{-1} G-actin), or to a bovine serum albumin (BSA) (Sigma) solution in PBS. The mixture was incubated for 1 h (HaloTag) or 2 h (SNAP-tag) at room temperature. In the case of the actin probe, buffer containing 5 mM Tris-HCl (pH 8.0), 0.2 mM $CaCl_2$, and 0.2 mM ATP was used. This buffer was supplemented with 50 mM KCl, 2 mM $MgCl_2$, 5 mM guanidine carbonate, and 1 mM ATP to obtain F-actin. Both buffers are components of the actin polymerisation fluorescence assay kit (Cytoskeleton). The samples were incubated for 2–3 h at 37 °C. All measurements were performed in triplicates expect the saturation experiment with 405 nm and the fatigue experiment as duplicates and the measurements for PA-SiR **71**, **74**, and **75** only once. For PA-SiR **74** activation was performed using a monochromator (Polychrome V, FEI, at 330 nm for 12 s). Saturation experiments at 405 nm were performed using a Solis405C High-Power LED (Thorlabs). Fitted parameters such as decay constants etc. are reported as the average of three fits. Representative measurements are displayed. Where given X^2 (the reduced chi-squared) corresponds to the residual sum of square and R^2 is the squared correlation coefficient. They are defined according to Supplementary Equation 10 and Supplementary Equation 11.

Fluorescence and quantum yield: Fluorescence spectra were measured on a JASCO FP-8600 fluorimeter in 1.4 mL fluorescence cuvettes (Hellma Analytics). Emission spectra were collected from 610–1000 nm exciting at 580 nm; excitation spectra were recorded at 664 nm exciting from 400–655 nm unless otherwise stated. Fluorescence intensity upon addition of cysteamine was measured on a plate reader (TECAN Spark® 20M) equipped with a monochromator exciting at 640/10 nm and collecting the emission at 670/10 nm. Quantum yields were determined using a Hamamatsu Quantaurus QY.

Extinction coefficient and quantum yield of activation: Extinction coefficients at 646 nm after activation were calculated from the equilibrium constants (K_2) obtained in the 12 s activation experiments (Figure 21A, and Figure 23A, B; Supplementary Table 8, and Supplementary Table 10) assuming that during the activation the decay (k_2 and k_{-2}) is negligible, and the absorbance reached in equilibrium in the saturation experiment (Figure 19B, Figure 23C, D, and Supplementary Figure 6A; Supplementary Table 5). Quantum yields of activation were determined using standard ferroxialate actinometry[237] along with the activation rates determined in the saturation experiments (Supplementary Table 6). This calculation does not take into account the decay kinetics but was good enough to give an estimate of the quantum yields of activation. Saturation experiments under 405 nm irradiation were performed using a Solis405C High-Power LED (Thorlabs) coupled to a 3 mm liquid light guide.

Computational chemistry: Optimisation of the PA-SiR **62** structure as well as HOMO/LUMO calculations were performed at the B3LYP/6-31G(d) or at the B3LP/6-31G(d,p) (compound **184** and **185**) level of theory by using the software package Gaussian 16.[238]

X-ray crystal structure determination: Colourless needle shaped crystals were grown from slow evaporation of a CH_2Cl_2/MeOH solution at 4 °C. X-ray crystal structure determination was then performed by H. Haungs and H. Wadepohl (Uni Heidelberg).

Crystal data and details of the structure determinations are compiled in Supplementary Table 15. A full shell of intensity data was collected at low temperature with an Agilent Technologies Supernova-E CCD diffractometer (Mo-K_α radiation, microfocus X-ray tube, multilayer mirror optics). Detector frames (typically ω-, occasionally ϕ-scans, scan width 0.5°) were integrated by profile fitting.[239,240] Data were corrected for air and detector absorption, Lorentz and polarisation effects[239] and scaled essentially by application of appropriate spherical harmonic functions.[239,241,242] Absorption by the crystal was treated numerically (Gaussian grid).[241,243] An illumination correction was performed as part of the numerical absorption correction.[241] The structures were solved by ab initio dual space methods involving difference Fourier syntheses (VLD procedure)[244,245] and refined by full-matrix least squares methods based on F^2 against all unique reflections.[246–249] All non-hydrogen atoms were given anisotropic displacement parameters. The positions of most hydrogen atoms (except those of the methyl groups, which were treated as variable metric rigid groups with local C_3 symmetry) were taken from difference Fourier syntheses and refined.

CCDC 1942173 contains the supplementary crystallographic data for this paper. These data can be obtained free of charge from the Cambridge Crystallographic Data Centre's and FIZ Karlsruhe's joint Access Service via https://www.ccdc.cam.ac.uk/structures/?.

Visualisation was performed using ORTEP III[250] and POV-Ray 3.7.0.[251]

LC-MS analysis: LC-MS was performed on a Shimadzu MS2020 connected to a Nexera UHPLC system equipped with a Supelco Titan C18 80 Å (1.9 µm, 2.1 x 50 mm) column. Buffer A: 0.05% HCOOH in H_2O Buffer B: 0.05% HCOOH in ACN. PA-SiR **41** was dissolved in MQ water (~20 µM). UV irradiation was performed for 1 min in a quartz cuvette (Hellma Analytics) and aliquots were taken to measure LC-MS at defined time points using an analytical gradient from 10% to 90% B within 6 min with 0.5 mL min^{-1} flow.

^{1}H and ^{13}C NMR analysis: PA-SiR **41** (1 mg, 2.0 µmol) was dissolved in H_2O/D_2O (1 mL, 90:10) and NaOH (1 µL, 5 M) was added to achieve better solubility as PA-SiR **41** was isolated as its TFA salt (pH = 7–8, pH paper). ^{1}H NMR spectra were measured on a Bruker AV 600 spectrometer at 600 MHz and 298 K. Chemical shifts δ are reported in ppm downfield from tetramethylsilane using the DMSO signal (δ_H = 2.50 ppm) instead of the residual deuterated solvent signal as an internal reference. Spectra were measured with NS = 128 using a water suppression pre-saturation sequence. UV irradiation was performed outside of the spectrometer for the indicated times with a transilluminator (Biometra TI 1, 312 nm). After each UV irradiation step the NMR sample was transferred to the NMR spectrometer. The pH was adjusted by addition of HCl (1 M) or NaOH (1 M). ^{13}C NMR was measured after full conversion with NS = 3000.

Plasmids: A pcDNA5/FRT/TO vector (ThermoFisher Scientific) was used for transient expression in mammalian cells and generation of stable cell lines. A pET51b(+) vector (Novagen) was used for protein production in *Escherichia coli*. Proteins were tagged Strep and His_{x10} N- and C-terminal, respectively. SNAP-tag and HaloTag7 were fused to the N or C terminus of the genes of interest (GOI) and a T2A-EGFP sequence was introduced. Cloning was performed by Gibson assembly.[252] GOI: H2B (NEB, pSNAPf-H2B), CEP41 (Genecopoeia (GC-V1653 and GC-V1653-CF))[117], mEOS3.2 (Addgene #54525)[253], LifeAct (Addgene #36201)[254], TOMM20 (Addgene #55146, gift from Michael Davidson), β-2-adrenergic-receptor-Halo (Addgene #66994, gift from Catherine Berlot), and β-tubulin (Addgene #AG64691)[32] were used as entry plasmids.

Protein production and purification: Proteins were expressed in *Escherichia coli* strain BL21(DE3)-pLysS. Luria-Bertani broth (LB) cultures were grown at 37 °C to optical density at 600 nm (OD_{600nm}) of 0.8, induced by the addition of 0.5 mM isopropyl-β-D-thiogalactopyranoside and grown at 17 °C overnight in the presence of 1 mM $MgCl_2$. The cells were harvested by centrifugation (4,500 g, 10 min, 4 °C) and lysed by sonication. The cell lysate was cleared by centrifugation (20,000 g, 20 min, 4 °C). All proteins were purified using affinity-tag Ni-NTA (Qiagen) leading to higher than 95% pure proteins (verified by SDS-PAGE coomassie staining). mEOS3.2-Halo was purified analogously but using an additional Strep-Tactin (IBA) column purification step to reach higher purity and following the suppliers' instructions. Proteins were finally concentrated using an Ultra-0.5 mL centrifugal filter device (Amicon) with a molecular weight cut-off according to the protein size and then stored in a glycerol 45% solution at −20 °C. Proteins were used from glycerol stocks and were further diluted. The amino acid sequences can be found below. mEOS3.2-Halo and SNAP-tag:EGFP:HaloTag were produced and purified by H. Farrants (MPI-MR).

Protein sequences

>Strep-HaloTag-His

MASWSHPQFEKGADDDDKVPHGSEIGTGFPFDPHYVEVLGERMHYVDVGPRDGTPVLFLHGNPTSSYVWRNIIPHVAPTHRCIAPDLI
GMGKSDKPDLGYFFDDHVRFMDAFIEALGLEEVVLVIHDWGSALGFHWAKRNPERVKGIAFMEFIRPIPTWDEWPEFARETFQAFRTT
DVGRKLIIDQNVFIEGTLPMGVVRPLTEVEMDHYREPFLNPVDREPLWRFPNELPIAGEPANIVALVEEYMDWLHQSPVPKLLFWGTPG
VLIPPAEAARLAKSLPNCKAVDIGPGLNLLQEDNPDLIGSEIARWLSTLEISGAPGFSSISAHHHHHHHHHH

Green: Strep-tag, Red: HaloTag, Purple: His-tag

>Strep-SNAP-tag-His

MASWSHPQFEKGADDDDKVPHMDKDCEMKRTTLDSPLGKLELSGCEQGLHEIIFLGKGTSAADAVEVPAPAAVLGGPEPLMQATAW
LNAYFHQPEAIEEFPVPALHHPVFQQESFTRQVLWKLLKVVKFGEVISYSHLAALAGNPAATAAVKTALSGNPVPILIPCHRVVQGDLDV
GGYEGGLAVKEWLLAHEGHRLGKPGLGAPGFSSISAHHHHHHHHHH

Green: Strep-tag, Red: SNAP-tag, Purple: His-tag

>Strep-mEOS3.2:HaloTag-His

MASWSHPQFEKGADDDDKVPHMSAIKPDMKIKLRMEGNVNGHHFVIDGDGTGKPFEGKQSMDLEVKEGGPLPFAFDILTTAFHYGN
RVFAKYPDNIQDYFKQSFPKGYSWERSLTFEDGGICNARNDITMEGDTFYNKVRFYGTNFPANGPVMQKKTLKWEPSTEKMYVRDGV
LTGDIEMALLLEGNAHYRCDFRTTYKAKEKGVKLPGAHFVDHCIEILSHDKDYNKVKLYEHAVAHSGLPDNARRGRLEVLFQGPKAFLEG
SEIGTGFPFDPHYVEVLGERMHYVDVGPRDGTPVLFLHGNPTSSYVWRNIIPHVAPTHRCIAPDLIGMGKSDKPDLGYFFDDHVRFMD
AFIEALGLEEVVLVIHDWGSALGFHWAKRNPERVKGIAFMEFIRPIPTWDEWPEFARETFQAFRTTDVGRKLIIDQNVFIEGTLPMGVVR
PLTEVEMDHYREPFLNPVDREPLWRFPNELPIAGEPANIVALVEEYMDWLHQSPVPKLLFWGTPGVLIPPAEAARLAKSLPNCKAVDIG
PGLNLLQEDNPDLIGSEIARWLSTLEISGAPGFSSISAHHHHHHHHHH

Green: Strep-tag, Red: HaloTag, Blue: mEOS3.2, Purple: His-tag

>Strep-SNAP-tag:EGFP:HaloTag-His

MASWSHPQFEKGADDDDKVPHMDKDCEMKRTTLDSPLGKLELSGCEQGLHEIIFLGKGTSAADAVEVPAPAAVLGGPEPLMQATAW
LNAYFHQPEAIEEFPVPALHHPVFQQESFTRQVLWKLLKVVKFGEVISYSHLAALAGNPAATAAVKTALSGNPVPILIPCHRVVQGDLDV
GGYEGGLAVKEWLLAHEGHRLGKPGLGGRLEVLFQGPKAFLEMVSKGEELFTGVVPILVELDGDVNGHKFSVSGEGEGDATYGKLTLKF
ICTTGKLPVPWPTLVTTLTYGVQCFSRYPDHMKQHDFFKSAMPEGYVQERTIFFKDDGNYKTRAEVKFEGDTLVNRIELKGIDFKEDGNI
LGHKLEYNYNSHNVYIMADKQKNGIKVNFKIRHNIEDGSVQLADHYQQNTPIGDGPVLLPDNHYLSTQSALSKDPNEKRDHMVLLEFVT
AAGITLGMDELYKIGTGFPFDPHYVEVLGERMHYVDVGPRDGTPVLFLHGNPTSSYVWRNIIPHVAPTHRCIAPDLIGMGKSDKPDLGY
FFDDHVRFMDAFIEALGLEEVVLVIHDWGSALGFHWAKRNPERVKGIAFMEFIRPIPTWDEWPEFARETFQAFRTTDVGRKLIIDQNVFI
EGTLPMGVVRPLTEVEMDHYREPFLNPVDREPLWRFPNELPIAGEPANIVALVEEYMDWLHQSPVPKLLFWGTPGVLIPPAEAARLAKS
LPNCKAVDIGPGLNLLQEDNPDLIGSEIARWLSTLEISGAPGFSSISAHHHHHHHHHH

Green: Strep-tag, Red: SNAP-tag, Brown: EGFP, Blue: HaloTag, Purple: His-tag

Polyacrylamide gel electrophoresis (PAGE): HaloTag protein (4 µM) was labeled using PA-SiR-CA (0, 1, 2, 3, 4 or 6 µM) in activity buffer (50 mM HEPES, 50 mM NaCl, pH 7.3) for 2 h at room temperature. After labeling, the proteins were separated by PAGE (4-20% 10 well Mini-Protean TGX, BioRad) as recommended by the manufacturer and revealed by in gel fluorescence using a ChemiDoc MD Imaging System (BioRad). PA-SiR-CA labeled proteins were imaged using red epi illumination (695/55 nm). PA-SiR-CA was activated using the UV-transilluminator of the ChemiDoc MD Imaging System.

Cell culture and transfection: HeLa, U-2 OS (both ATCC), COS-7 (Gift from Dr. R. Sprengel, MPI-MR) or U-2 OS Nup96-Halo (generously provided by the Ellenberg lab, EMBL) cells were cultured in high-glucose phenol red free DMEM (Life Technologies) medium supplemented with GlutaMAX (Life Technologies), sodium pyruvate (Life Technologies) and 10% FBS (Life Technologies) in a humidified 5% CO_2 incubator at 37 °C. Cells were split every 3–4 days or at confluency. These cell lines were regularly tested for mycoplasma contamination. Cells were seeded on glass bottom 35 mm dishes (Mattek or Greiner bio-one), 10 well glass bottom dishes (Greiner bio-one) or 24 mm high precision round coverslips #1.5 (Carl Roth GmbH) one day before imaging. Transient transfection of cells was performed using Lipofectamine™ 2000 reagent (Life Technologies) according to the manufacturer's recommendations: DNA (2.5 µg) was mixed with OptiMEM I (100 µL, Life Technologies) and Lipofectamine™ 2000 (6 µL) was mixed with OptiMEM I (100 µL). The solutions were incubated for 5 min at room temperature, then mixed, and incubated for additional 20 min at room temperature. The prepared DNA-Lipofectamine complex was added to a glass bottom 35 mm dish with cells at 50–70% confluency. After 12 h incubation in a humidified 5% CO_2 incubator at 37 °C the medium was changed to fresh medium. The cells were incubated for 24–48 h before imaging.

Stable cell line establishment: The Flp-In™ T-REx™ System (ThermoFisher Scientific) was used to generate stable cell lines exhibiting tetracycline-inducible expression of the gene of interest (GOI). Briefly, pcDNA5-FRT-TO-GOI and pOG44 were co-transfected into the host cell line U-2 OS FlpIn TREx.[255] Homologous recombination between the FRT sites in pcDNA5-FRT-TO-GOI and on the host cell chromosome, catalysed by the Flp recombinase expressed from pOG44, produced the U-2 OS Flp-In T-REx cells expressing stable and inducible the GOI. Selection was performed using 100 µg mL^{-1} hygromycin B (ThermoFisher Scientific) and 15 µg mL^{-1} blasticidine (ThermoFisher Scientific). Stable cell lines were seeded on glass bottom dishes as described in the previous section, and induced using 100 µg mL^{-1} doxycycline (Sigma Aldrich) for 24–48 h previous to imaging. The Cep41-Halo and H2B-SNAP-T2A-EGFP cell lines were established together with Dr. B. Koch (MPI-MR).

Staining: Cells were stained with 0.2–1 µM PA-SiRs (1–3 h, 37 °C) in phenol-red free DMEM medium supplemented with GlutaMAX, sodium pyruvate, and 10% FBS (all Life Technologies, imaging medium), washed with the same medium or PBS (once for 3 min, 37 °C) and imaged in the same medium.

Sample preparation for SMLM: U-2 OS CEP41-Halo cells were seeded on 24 mm glass coverslips and stained with PA-SiR as described above. Methanol fixation was performed as follows: growth medium was removed, cells were

incubated for 7 min in −20 °C cold methanol and washed twice with PBS. Fixed-cell samples were mounted in PBS on cavity slides (VWR™) sealed with twinsil® 22 (Picodent) and imaged therein.

COS-7 cells were seeded on 24 mm glass coverslips and stained with PA-SiR-jasplakinolide as described above. The cells were fixed as previously described.[256] Briefly, they were fixed and extracted for 1 min using a solution of 0.3% [w/v] glutaraldehyde and 0.25% [v/v] Triton X-100 in CB buffer (CB: 10 mM MES, pH 6.1, 150 mM NaCl, 5 mM EGTA, 5 mM glucose, and 5 mM $MgCl_2$), and then post-fixed for 10 min in 2% [w/v] glutaraldehyde in CB. They were treated with freshly prepared 0.1% sodium borohydride for 7 min. Short additional post-staining was performed with 0.5 µM PA-SiR-jasplakinolide (1 h, 25 °C). Fixed-cell samples were mounted in PBS on cavity slides (VWR™) sealed with twinsil® 22 (Picodent) and imaged therein.

U-2 OS cells were seeded on 24 mm glass coverslips and stained with PA-SiR-C8-docetaxel or PA-SiR-cabazitaxel as described above. The cells were fixed as previously described.[122] Briefly, the medium was replaced with BRB80 buffer (80 mM K-PIPES, pH 6.8, 1 mM $MgCl_2$, 1 mM EGTA) containing 0.2% IGEPAL-630 for 1 min, and cells were then incubated in BRB80 buffer containing 2 mM EGS for 10 min. They were washed twice with PBS 10 min each. Post-staining was performed in PBS (0.5 µM, 1 h) followed by one wash in PBS. Fixed-cell samples were mounted in PBS on cavity slides (VWR™) sealed with twinsil® 22 (Picodent) and imaged therein.

U-2 OS cells were seeded on 24 mm glass coverslips and transiently transfected (TOMM20-Halo or β-2-adrenergic-receptor-Halo). The next day the cells were stained with PA-SiR-CA as described above and the coverslips were mounted into attofluor cell chambers (Life technologies) and the imaging medium was supplemented with HEPES (20 mM). Cells were directly imaged after mounting.

Genome-edited U-2 OS cells with Halo-tagged NUP96[101] were seeded on 24 mm round coverslips (No. 1.5H; 117640; Marienfeld). Cells were cultured under adherent conditions at 37 °C, 5% CO_2, and 100% humidity in DMEM (high-glucose, without phenol red) supplemented with 10% [v/v] FBS, 2 mM l-glutamine, nonessential amino acids, and ZellShield. Before sample preparation, the respective fluorophore was added to the medium to a final concentration of 1 µM and incubated for 2 h. All following incubations were carried out at room temperature and all incubations longer than 1 min were performed on an orbital shaker in the dark to prevent preactivation of the dye. Cells were prefixed in 2.4% [w/v] formaldehyde (FA) in PBS for 30 s, permeabilised in 0.4% [v/v] Triton X-100 in PBS for 3 min and fixed in 2.4% [w/v] FA in PBS for 30 min. Subsequently, the FA was quenched by incubating the coverslip for 5 min in 100 mM NH_4Cl in PBS. After washing 3 times for 5 min in PBS, the coverslips were mounted and imaged in PBS.

Sample preparation for STED: Genome-edited U-2 OS cells expressing Vimentin-Halo,[222] were seeded on glass by C. Gürth (MPI-MR) and stained with PA-SiR-CA as described above. Cells were imaged in imaging medium at room temperature.

Single-molecule assay: Sample preparation was adapted from two literature procedures.[257,258] Briefly, 18 x 18 mm high precision coverslips (Carl Roth) were sonicated for 10 min in MQ water, 10 min in acetone, 10 min in MeOH, 10 min in KOH (1 M, prepared from 99.98% purity Carl Roth) and rinsed with MQ water after each step. The coverslips were cleaned with piranha solution (1:3, H_2O_2/H_2SO_4) twice for 30 min. After extensive rinsing with MQ water they were dried under a N_2 stream. A solution of 2% [v/v] *N*-[3-(trimethoxysilyl)propyl]ethylendiamine (Sigma-Aldrich) in dry acetone was prepared and the clean coverslips where immersed in the dark for 1 h. The coverslips were rinsed with acetone, MQ water and then dried with N_2. A solution of 1 mg biotin-PEG-SVA (MW 5000, Laysan Bio) and 54 mg mPEG-SVA (MW 5000, Laysan Bio) was prepared in 230 µL sodium bicarbonate buffer (10 mM freshly prepared) and applied to three coverslip pairs. After 3 h in the dark the coverslips were washed with MQ water, blow dried with N_2 and stored under N_2 at −20 °C. Flow chambers were assembled at need from one glass slide (Carl Roth) and one coated coverslip separated by double sided tape and fixed with epoxy glue.

100 µL of a 0.2 mg mL^{-1} solution of streptavidin (Life Technologies) in PBS was applied to the flow chamber and incubated for 10 min. The channel was washed with 400 µL PBS. A solution of SNAP-tag:EGFP:HaloTag (5 µM),

fluorophore (2.5 µM), biotin-ligand (5 µM; SNAP-Biotin™ (NEB), HaloTag Biotin (Promega)), in PBS was prepared and incubated for 1 h. 100 µL of a 1:1000–1:500 dilution thereof was applied to the flow chamber and incubated for 10 min. The channel was washed with 400 µL PBS and filled with PBS. They were imaged in TIRF mode using a Leica SR GSD (Supplementary Table 14).

Widefield microscopy: Imaging was performed using a Leica DMi8 microscope (Leica Microsystems) equipped with a Leica DFC9000 GT sCMOS camera; a CoolLED Pe4000 LED light source (635 nm, 635/18; 470 nm, 474/27; 365 nm, 378/52); a HC PL APO 40.0x1.10 water objective and standard GFP (515/40) and Cy5 (720/100) filter sets. Activation of the fluorophores was achieved by irradiation with the 365 nm LED and the DAPI filter set (430/35) at 100% LED output for the indicated durations. The microscope was equipped with a CO_2 and temperature controllable incubator (PeCon, 37 °C).

For stability measurement images were taken in the Cy5 (500 ms, ex: 10%), transmission (100 ms), and the GFP channel (100 ms, ex: 5%) every 30 s. Activation was performed for 1 s once.

For activation experiment images were taken in the Cy5 (500 ms, ex: 10%), transmission (100 ms), and the GFP channel (100 ms, ex: 5%) consecutively every 9 s. Activation was performed for 50 ms after each acquisition cycle.

Confocal microscopy: Confocal imaging was performed on a Leica DMi8 microscope (Leica Microsystems) equipped with a Leica TCS SP8 X scanhead; a SuperK white light laser, a 355 nm CW laser (Coherent), a HC PL APO 63x1.47 oil objective or a HC PL APO 40.0x1.10 water objective; emission was collected as indicated in Supplementary Table 14. Photoactivation was performed for one frame by using a 355 nm laser. The microscope was equipped with a CO_2 and temperature controllable incubator (Life Imaging Services, 37 °C).

For signal-to-background measurement cells were focused in the transmission channel and z-stacks were recorded with 0.4 µm step size before and after activation. The summed stacks were analysed as following: the mean of a rectangular ROI within the nucleus was divided by the mean of a rectangular ROI adjacent to the nucleus. Staining with Hoechst was used to distinguish the nucleus from the cytosol in the case of the DMSO control.

SMLM: SMLM was performed on a Leica SR GSD (Leica Microsystems) microscope equipped with an Andor iXon3 897 EMCCD camera (Andor) using a central 180 pixel x 180 pixel or 400 pixel x 400 pixel subregion of the camera chip. The system was equipped with the following lasers for excitation and photoactivation: a 642 nm (500 mW; MPBC, Inc.), a 532 nm (1000 mW; MPBC, Inc.), a 488 nm (500 mW; MPBC, Inc.), and a 405 nm (30 mW; Coherent, Inc) diode laser for photoactivation. The standard Leica filter sets for SR GSD systems were used - in brief: Leica set 488 for 405 nm and 488 nm excitation: DBP 405/10 488/10 excitation filter, LP 505 dichroic mirror and 555/100 suppression / emission filter; Leica set 532 for 405 nm and 532 nm excitation: DBP 405/10 532/10 excitation filter, LP 550 dichroic mirror and 600/100 suppression / emission filter; Leica set 642 for 405 nm and 642 nm excitation: DBP 405/10 642/10 excitation filter, LP 650 dichroic mirror and 710/100 suppression / emission filter. Fluorescence was collected through a high-numerical-aperture (NA) oil-immersion objective (Leica HC PL APO 160x1.43). Lateral drift was minimised by the suppressed motion (SuMo) stage of the Leica SR GSD and by keeping the temperature of the environment stable via an incubation box (T = 21±0.1 °C, instrument parameter) covering the entire microscope. The microscope was operated by the Leica LAS X software (version 1.9.0.13747). The specific parameters can be found in Supplementary Table 14.

NUP96-Halo samples were imaged together with P. Hoess (EMBL) on a custom-built epi-fluorescence microscope with homogenous high power illumination.[259] The output of a commercial LightHub laser box (Omicron-Laserage Laserprodukte) with 405 nm, 488 nm, 561 nm, and 640 nm laser lines and an additional 640 nm booster laser (Toptica) were focused on a speckle reducer (LSR-3005-17S-VIS; Optotune) and coupled into a multi-mode fiber (M105L02S-A; Thorlabs). The output of this fiber is magnified by an achromatic lens, cleaned up by a quadband filter (390/482/563/640 HC Quad; AHF) and focused into the sample. Fluorescence was collected through a high-NA oil-immersion objective (160x/1.43-NA; Leica), filtered by a 700/100 bandpass filter (AHF) and focused onto an

Evolve512D EMCCD camera (Photometrics). The focus was stabilised by a total internally reflected IR laser that was focused onto a quadrant photodiode, which was coupled into a closed-loop with the piezo objective positioner. Typically, 15,000 to 30,000 frames with 50 ms exposure time and laser power densities of about 13 kW cm^{-2} were acquired. Data was acquired until no more activated fluorophores were observed. The pulse-length of the 405 nm laser was adjusted during the acquisition to maintain a similar number of localisations per frame. The different components of the microscope are managed by a field-programmable gate array (Mojo; Embedded Micro) which is controlled using a custom-written plugin for µManager.[260]

STED imaging: was performed together with Dr. E. D'Este (MPI-MR) on an Abberior easy3D STED/RESOLFT QUAD scanning microscope (Abberior Instruments GmbH, Göttingen, Germany) built on a motorised inverted microscope IX83 (Olympus, Tokyo, Japan). The microscope is equipped with pulsed STED lasers at 595 nm and 775 nm, and with 355 nm, 405 nm, 485 nm, 561 nm, and 640 nm excitation lasers. Spectral detection is performed with avalanche photodiodes (APD) in the following spectral window. 650–750 nm. Images were acquired with a 100x1.40 UPlanSApo oil immersion objective lens (Olympus). Pixel sizes were 200 nm and 30 nm (zoom in). The specific parameters can be found in Supplementary Table 14.

Software and image processing: Statistical analysis as well as curve fitting was performed using OriginLab.[261] All images except the NUP96-Halo images were processed with ImageJ/Fiji.[262,263] Super-resolution images and TIRF data from the single-molecule assay were processed with the ImageJ plugin ThunderSTORM.[264] Tracking data were analyzed using the TrackMate plugin.[265] Single-molecule assay data were further processed by a costume written MatLab[266] script provided by Dr. Christian Sieben (EPFL) based on the Crocker, Weeks, and Grier Algorithm.[267] For the quantification of microtubule width, a perpendicular line profile from a 250 nm long section of the microtubule was constructed by P. Hoess (EMBL) and then fitted with a Gaussian distribution (bin width 2 nm). The FWHM was plotted in a boxplot (*N* = 20 line segments per fluorophore). Live-cell SMLM data was additionally processes using the HAWK plugin using 3 levels and time grouping, followed by multi-emitter fit in ThunderSTORM allowing for 5 emitters per fitting region.[84] Costume written MatLab code was used to produce the rolling frame video. The movie presented was convoluted with a Gaussian function (sigma = 12 nm).

The reconstruction analysis of super-resolved images of NUP96-Halo was performed by P. Hoess (EMBL) using the custom-written software SMAP (Superresolution Microscopy Analysis Platform, https://github.com/jries/SMAP). First, localisations were detected using a difference of Gaussians algorithm and a dynamic threshold to exclude random signal fluctuations. Then the localisations were fit by a pixelated Gaussian function. Dim localisations (localisation precision > 30 nm) and out-of-focus localisations (fitted size of the Gaussian > 160 nm) were filtered out. Localisations that were found within 75 nm of each other in consecutive frames with maximum 1 frame dark time were grouped into one localisation. Images were reconstructed by plotting all localised emitters at the fitted positions as Gaussians with a width proportional to their localisation precision. Effective labeling efficiencies were calculated as reported.[101]

5.3 Materials and general information for *in vitro* and *in cellulo* experiments for Chapter 3

General considerations: Fluorophores were prepared as stock solutions in dry DMSO and diluted in the respective buffer such that the final concentration of DMSO did not exceed 1% v/v. Activity buffer (50 mM HEPES, 150 mM NaCl, pH 7.2) was used in all experiments unless otherwise stated. Clean 96-well plates (black, flat bottom, non-binding, (Corning) were used unless otherwise stated. Fluorescence intensity was measured on a plate reader (TECAN Spark® 20M) equipped with filter cubes exciting at 620/20 and collecting the emission at 680/30 for SiR, JF_{646}, JF_{635}, and JF_{614}; 535/25 and 595/35 for TMR and MaP555; 535/25 and 625/35 for CPY and MaP618; 485/20 and 535/25 for EGFP. The system was additionally equipped with an injector system for kinetic experiments. Measurements were performed in triplicates unless otherwise stated. The one letter amino acid code was used throughout this document.

Plasmids: A pET51b(+) vector (Novagen) was used for protein production in *Escherichia coli*. Proteins were tagged with His_{x10} N-terminally, followed by a TEV cleavage site (GAAAACCTGTATTTTCAGGGC). In addition, for *in vitro* screening EGFP was fused to the C terminus of HaloTag. A pcDNA5/FRT/TO vector (ThermoFisher Scientific) was used for transient expression in mammalian cells. No purification tags were fused to HaloTag but a T2A-EGFP sequence was fused C-terminally. Cloning was performed by Gibson assembly.[252] EGFP and T2A-EGFP (Addgene #135443)[203] were used as template plasmids.

Protein sequences

>His-TEV-Halo-EGFP

MHHHHHHHHHHENLYFQGIGTGFPFDPHYVEVLGERMHYVDVGPRDGTPVLFLHGNPTSSYVWRNIIPHVAPTHRCIAPDLIGMGKS
DKPDLGYFFDDHVRFMDAFIEALGLEEVVLVIHDWGSALGFHWAKRNPERVKGIAFMEFIRPIPTWDEWPEFARETFQAFRTTDVGRK
LIIDQNVFIEGTLPMGVVRPLTEVEMDHYREPFLNPVDREPLWRFPNELPIAGEPANIVALVEEYMDWLHQSPVPKLLFWGTPGVLIPPA
EAARLAKSLPNCKAVDIGPGLNLLQEDNPDLIGSEIARWLSTLEIVSKGEELFTGVVPILVELDGDVNGHKFSVSGEGEGDATYGKLTLKFIC
TTGKLPVPWPTLVTTLTYGVQCFSRYPDHMKQHDFFKSAMPEGYVQERTIFFKDDGNYKTRAEVKFEGDTLVNRIELKGIDFKEDGNILG
HKLEYNYNSHNVYIMADKQKNGIKVNFKIRHNIEDGSVQLADHYQQNTPIGDGPVLLPDNHYLSTQSALSKDPNEKRDHMVLLEFVTA
AGITLGMDELYK

Red: His-tag, Purple: TEV-cleavage site, Blue: HaloTag, Black: Sites of mutations, Green: EGFP.

>His-TEV-Halo

MHHHHHHHHHHENLYFQGIGTGFPFDPHYVEVLGERMHYVDVGPRDGTPVLFLHGNPTSSYVWRNIIPHVAPTHRCIAPDLIGMGKS
DKPDLGYFFDDHVRFMDAFIEALGLEEVVLVIHDWGSALGFHWAKRNPERVKGIAFMEFIRPIPTWDEWPEFARETFQAFRTTDVGRK
LIIDQNVFIEGTLPMGVVRPLTEVEMDHYREPFLNPVDREPLWRFPNELPIAGEPANIVALVEEYMDWLHQSPVPKLLFWGTPGVLIPPA
EAARLAKSLPNCKAVDIGPGLNLLQEDNPDLIGSEIARWLSTLEI

Red: His-tag, Purple: TEV-cleavage site, Blue: HaloTag, Black: Sites of mutations

>Halo cut

GIGTGFPFDPHYVEVLGERMHYVDVGPRDGTPVLFLHGNPTSSYVWRNIIPHVAPTHRCIAPDLIGMGKSDKPDLGYFFDDHVRFMDA
FIEALGLEEVVLVIHDWGSALGFHWAKRNPERVKGIAFMEFIRPIPTWDEWPEFARETFQAFRTTDVGRKLIIDQNVFIEGTLPMGVVRP
LTEVEMDHYREPFLNPVDREPLWRFPNELPIAGEPANIVALVEEYMDWLHQSPVPKLLFWGTPGVLIPPAEAARLAKSLPNCKAVDIGP
GLNLLQEDNPDLIGSEIARWLSTLEI

Purple: remainder TEV-cleavage site, Blue: HaloTag, Black: Sites of mutations

>Halo-T2A-EGFP (mammalian cells)

MEIGTGFPFDPHYVEVLGERMHYVDVGPRDGTPVLFLHGNPTSSYVWRNIIPHVAPTHRCIAPDLIGMGKSDKPDLGYFFDDHVRFMD
AFIEALGLEEVVLVIHDWGSALGFHWAKRNPERVKGIAFMEFIRPIPTWDEWPEFARETFQAFRTTDVGRKLIIDQNVFIEGTLPMGVVR
PLTEVEMDHYREPFLNPVDREPLWRFPNELPIAGEPANIVALVEEYMDWLHQSPVPKLLFWGTPGVLIPPAEAARLAKSLPNCKAVDIG
PGLNLLQEDNPDLIGSEIARWLSTLEISGGSGEGRGSLLTCGDVEENPGPVSKGEELFTGVVPILVELDGDVNGHKFSVSGEGEGDATYGK
LTLKFICTTGKLPVPWPTLVTTLTYGVQCFSRYPDHMKQHDFFKSAMPEGYVQERTIFFKDDGNYKTRAEVKFEGDTLVNRIELKGIDFKE
DGNILGHKLEYNYNSHNVYIMADKQKNGIKVNFKIRHNIEDGSVQLADHYQQNTPIGDGPVLLPDNHYLSTQSALSKDPNEKRDHMVL
LEFVTAAGITLGMDELYK

Blue: HaloTag, Black: Sites of mutations, Orange: Linker, Purple: T2A, Green: EGFP.

Protein production and purification: Proteins were expressed in the *Escherichia coli* strain BL21(DE3)-pLysS. Luria-Bertani broth (LB) cultures were grown at 37 °C to an optical density at 600 nm (OD_{600nm}) of 0.8, induced by the

addition of 0.5 mM isopropyl-β-D-thiogalactopyranoside and grown at 17 °C overnight in the presence of 1 mM $MgCl_2$. The cells were harvested by centrifugation (4,500 g, 10 min, 4 °C) and lysed by sonication (5 min, 70%). The cell lysate was cleared by centrifugation (20,000 g, 20 min, 4 °C). Proteins were purified using affinity-tag Ni-NTA (Qiagen) leading to higher than 95% pure proteins (verified by SDS-PAGE coommassi staining). Proteins were finally concentrated using an Ultra-0.5 mL centrifugal filter device (Amicon) with a molecular weight cut-off according to the protein size and then stored in a glycerol 45% solution at −20 °C. Proteins were used from glycerol stocks and were further diluted. The amino acid sequences are listed above.

For X-ray crystallography, proteins were produced as described above but were purified using a HisTRAP FF affinity column (GE-Healthcare) on an ÄKTAPure M FPLC (GE-Healthcare). The proteins were concentrated using an Ultra-4 mL centrifugal filter device (Amicon) and were diluted to a final concentration of ~0.3 mg mL^{-1} (ca. 40 mL) in TEV-cleavage buffer (25 mM Na_2HPO_4, 200 mM NaCl). β-mercaptoethanol (10 µL) and TEV protease (~1 mg, TEV protease: produced and purified by A. Bergner (MPI-MR)) were added and incubated at 30 °C overnight. The solution was filtered (0.22 µm) and cleaved protein was harvested by reverse purification on a HisTRAP FF affinity column (GE-Healthcare), collecting the flow through. Proteins were concentrated using an Ultra-4 mL centrifugal filter device (Amicon) and further purified by size exclusion chromatography on a HiLoad 26/600 Superdex 75 pg column (GE-Healthcare) exchanging the buffer to activity buffer. Proteins were concentrated again and prepared to a final concentration of 5 µM in activity buffer. 3 mg of protein was incubated in presence of TMR-CA (10 µM) and incubated at room temperature overnight. Labeled proteins were concentrated and an illustra MicroSPin G-50 desalting column (GE-Healthcare) was employed to remove excess of unreacted fluorophore. The final protein concentration was adjusted to 12 mg mL^{-1} using the absorbance at 280 nm, correcting the extinction coefficient of the protein by $\varepsilon_{280,\,TMR\text{-}CA} = 0.16$.

Crystallisation and X-ray crystal structure determination: Crystallisation trials, optimisation and X-ray diffraction were performed by Dr. M. Tarnawski and Professor I. Schlichting (MPI-MR). Partially refined structure models were provided by Dr. M. Tarnawski. Current structural analysis were performed using PyMOL.[268]

Polyacrylamide gel electrophoresis (PAGE): HaloTag proteins (10 µM) were labeled using SiR-CA (100 µM) in activity buffer for 1 h at room temperature. After labeling, the proteins were separated by PAGE (4-20% 10 well Mini-Protean TGX, BioRad) as recommended by the manufacturer and revealed by in gel fluorescence using a ChemiDoc MD Imaging System (BioRad). SiR-CA labeled proteins were imaged using red epi illumination (695/55 nm). Coommassie staining (BioRad) was performed overnight, followed by destaining in H_2O for 24 h and imaging with brightfield illumination.

Library construction: The plasmid libraries aiming to saturate specific sites were prepared using degenerated primers according to Kille et al. (2014).[228] The degenerated primers (Eurofins, exemplary sequences see below) were mixed in a ratio of NDT:VHG:TGG = 12:9:1. Plasmid libraries were prepared using standard PCR (KOD Hot Start DNA polymerase, Merck) and Gibson assembly.[252] After electroporation in the *Escherichia coli* strain *E. cloni* 10G (Lucigen), the library size was evaluated by cascade dilution and incubation overnight at 37 °C on selective LB-agar plates in order to verify the proper coverage of the complete library (number of colonies ≥ 1000). Concomitantly, the library was amplify in selective LB liquid culture overnight (3 mL) at 37 °C in a prior to plasmid purification (Qiagen kit). Purified plasmid libraries were sequenced to verify incorporation of degenerated codons. *Escherichia coli* strain BL21(DE3)-pLysS was transformed with the plasmid library and spread out on LB agar plates containing 100 µg mL^{-1} ampicillin. After overnight incubation at 37 °C, single colonies were inoculated into 2 mL 96-deep-well plates containing 400 µL LB medium (50 µg mL^{-1} ampicillin). Five wells were reserved for parental HaloTag, five wells for Clip-tag as a negative control and eight wells for sterility controls. The bacterial culture was incubated overnight at 37 °C and 500 rpm. Then, 50 µL of the stationary phase cultures were transferred to 2 mL 96-deep-well plates containing 950 µL LB medium (50 µg mL^{-1} ampicillin) and were incubated at 37 °C for 4 h at 500 rpm. The rest of the culture was spun down and stored at 4 °C. Protein expression was induced by the addition of 0.5 mM isopropyl-β-D-thiogalactopyranoside and grown at 17 °C overnight at 500 rpm. The cells were harvested by centrifugation (5,000 g,

15 min, 4 °C). The bacterial pellet was frozen and thawed for two cycles before being lysed using 300 µL lysis buffer (50 mM K_2HPO_4, pH = 8) containing 1 mg mL^{-1} lysozyme, 2 mM $MgCl_2$, and 2.5 units mL^{-1} benzonase (Turbo Nuclease, Jena Bioscience) at 37 °C for 1 h. The cell lysate was cleared by centrifugation (5,000 g, 20 min, 4 °C). The cleared supernatant was transferred into clean 96-well plates for the screening assay.

Exemplary primer sequences

forward_G171X_NDT	AACGTTTTTATCGAGNDTACGCTGCCGATGGGT
forward_G171X_VHG	AACGTTTTTATCGAGVHGACGCTGCCGATGGGT
forward _G171X_TGG	AACGTTTTTATCGAGTGGACGCTGCCGATGGGT
reverse _G171X_NDT	ACCCATCGGCAGCGTAHNCTCGATAAAAACGTT
reverse _G171X_VHG	ACCCATCGGCAGCGTCDBCTCGATAAAAACGTT
reverse_G171X_TGG	ACCCATCGGCAGCGTCCACTCGATAAAAACGTT

Screening assay: In a clean 96-well plate, the supernatant (20 µL) was diluted into activity buffer (80 µL) containing 0.5 mg mL^{-1} BSA (Sigma). Basal SiR and GFP fluorescence intensity was measured. SiR-CA (5 µL) was spiked to a final concentration of 5 nM, the plate was incubated at room temperature for 1 h after which SiR fluorescence intensity was measured. SiR-CA (5 µL) was added again to a final concentration of 10 nM followed by incubation at room temperature for 1 h. SiR fluorescence intensity was again measured after incubation. The mean and sd of the fluorescence intensities (GFP and SiR) of the parental protein was calculated from the five test wells. Wells with GFP intensities lower than $0.1 \cdot mean_{par}$ were discarded due to low expression. Wells with SiR fluorescence intensities larger or smaller than $mean_{par} \pm 3 \cdot sd_{par}$ (second and third round: $mean_{par} \pm 2 \cdot sd_{par}$) were selected. If more than 20 candidates were identified 10–15 were chosen at random (only relevant for lower SiR fluorescence intensities than HaloTag). Plasmids of selected wells were obtained from stored bacterial cultures and sequenced. Selected variants were purified from 50 mL LB bacterial cultures (as described above) and characterised as follows:

The proteins were diluted to a concentration of 1 µM in activity buffer containing 0.5 mg mL^{-1} BSA (Sigma). 90 µL were distributed into a 96-well plate and 10 µL SiR-CA (1 µM) were added. After incubation at room temperature for 2 h, the SiR and GFP fluorescence intensities were measured in triplicates. Mean and 90% confidence intervals were calculated for every variant and compared to the parental protein. Variants with significant changes in SiR fluorescence intensity compared to the parental protein (one-sided t test, $\alpha = 5\%$) were picked for further investigation.

Validation and fluorophore screening: For further validation, the most promising variants were subcloned into a pET51b(+) vector lacking the C-terminal EGFP. Variant proteins were purified from bacteria cultures (500 mL) as described above and characterised as follows:

Fluorophores (SiR-CA, TMR-CA, etc.) were distributed into a black 96-well plate (100 µL, 100 nM) and incubated at 4 °C overnight. The plate was warmed to room temperature. Proteins were diluted to a concentration of 1 µM in activity buffer containing 0.5 mg mL^{-1} BSA (Sigma), 100 µL were added to the black fluorophore containing 96-well plate. After incubation at room temperature for 4 h, the respective fluorescence intensities were measured with a plate reader. The measurements were performed in quadruplicates. Mean and 90% confidence intervals were calculated for every variant and compared to the parental protein. Variants were compared to parental HaloTag (one sided t-test, $\alpha = 5\%$).

Kinetics: Labeling kinetics of HaloTag variants were measured by fluorescence polarisation with TMR-CA at room temperature on a plate reader using the above stated filters for TMR and the injector system. G-factor and gain were calculated from three control measurements (buffer only, fluorophore in buffer, fully labeled protein in buffer). A solution of TMR-CA (100 µL, 20 nM) in activity buffer supplemented with 0.5 mg mL^{-1} BSA was injected into 100 µL protein solution (80 nM) in the same buffer. The data was fitted with a mono-exponential function (Supplementary Equation 5.) using R.[269] Data was measured in triplicates.

Quantum yield: Quantum yields were determined using a Hamamatsu Quantaurus QY. SiR-CA (0.5 µM) was directly added to the target protein (2.5 µM) in activity buffer. The mixture was incubated for 1 h at room temperature and then measured in triplicates.

Computational chemistry: Optimisation of the quinoid form **13** and the spirolactone **14** structures were performed at the B3LYP/6-31G(d,p) level of theory by using the software package Gaussian 16.[238] Solvent effects were modeled using the polarizable continuum model SMD.

Cell culture and transfection: U-2 OS (ATCC) cells were cultured in high-glucose phenol red free DMEM (Life Technologies) medium supplemented with GlutaMAX (Life Technologies), sodium pyruvate (Life Technologies) and 10% FBS (Life Technologies) in a humidified 5% CO_2 incubator at 37 °C. Cells were split every 3–4 days or at confluency. The cell line was regularly tested for mycoplasma contamination. Cells were seeded on 10 well glass bottom dishes (Greiner bio-one) one day before imaging. Transient transfection of cells was performed using Lipofectamine™ 2000 reagent (Life Technologies) according to the manufacturer's recommendations: DNA (0.25 µg) was mixed with OptiMEM I (10 µL, Life Technologies) and Lipofectamine™ 2000 (0.5 µL) was mixed with OptiMEM I (10 µL). The solutions were incubated for 5 min at room temperature, then mixed and incubated for additional 20 min at room temperature. The prepared DNA-Lipofectamine complex was added to one well in a 10 well glass bottom dish with cells at 50–70% confluency. After 12 h incubation in a humidified 5% CO_2 incubator at 37 °C the medium was changed to fresh medium. The cells were incubated for 24–48 h before imaging.

Staining: Cells were stained with the respective fluorophore (1 µM, 1–2 h, 37 °C) in phenol-red free DMEM medium supplemented with GlutaMAX, sodium pyruvate, and 10% FBS (all Life Technologies), washed with the same medium or PBS (once for 3 min, 37 °C) and imaged in the same medium.

Confocal microscopy: Confocal imaging was performed on a Leica DMi8 microscope (Leica Microsystems) equipped with a Leica TCS SP8 X scanhead; a SuperK white light laser, a HC PL APO CS2 20x0.75 dry objective; emission was collected from 510–530 nm for EGFP (exciting at 489 nm), and from 680–700 nm for SiR-CA (exciting at 631 nm). The microscope was equipped with a CO_2 and temperature controllable incubator (Life Imaging Services, 37 °C). Cells were focused in the GFP channel and z-stacks were recorded with 1 µm step size over 22 µm. The summed stacks were analysed as following: the mean of a rectangular ROI within the cell was normalised by the GFP intensity using a custom written Fiji macro.[262,263]

Software and image processing: Statistical analysis as well as curve fitting was performed using OriginLab[261] or R[269] including packages readxl,[270] fBasics,[271] tidyverse,[272] gghighlight,[273] ggplot2,[274] ggrepel,[275] ggpubr,[276] broom.[277] All images were processed with ImageJ/Fiji[262,263] and macros written therein.

References

1. Alberts, B. *et al. Molecular biology of the cell*. (Taylor & Francis; Garland Science, 2015).

2. Hell, S. W. Nanoscopy with Focused Light (Nobel Lecture). *Angew. Chem. Int. Ed.* **54**, 8054–8066 (2015).

3. Rodriguez, E. A. *et al.* The Growing and Glowing Toolbox of Fluorescent and Photoactive Proteins. *Trends Biochem. Sci.* **42**, 111–129 (2017).

4. Celie, P. H. N., Parret, A. H. A. & Perrakis, A. Recombinant cloning strategies for protein expression. *Curr. Opin. Struct. Biol.* **38**, 145–154 (2016).

5. Lavis, L. D. Chemistry Is Dead. Long Live Chemistry! *Biochemistry* **56**, 5165–5170 (2017).

6. Jabłoński, A. Efficiency of Anti-Stokes Fluorescence in Dyes. *Nature* **131**, 839–840 (1933).

7. Jabłoński, A. Über den Mechanismus der Photolumineszenz von Farbstoffphosphoren. *Zeitschrift für Phys.* **94**, 38–46 (1935).

8. Kasha, M. The Triplet State: An Example of G. N. Lewis' Research Style. *J. Chem. Educ.* **61**, 204–215 (1984).

9. Stokes, G. G. On the Change of Refrangibility of Light. *Phil. Trans. R. Soc. London* **142**, 463–562 (1852).

10. Lakowicz, J. R. *Principles of Fluorescence Spectroscopy*. (Plenum Press, 1984).

11. Ha, T. & Tinnefeld, P. Photophysics of Fluorescent Probes for Single-Molecule Biophysics and Super-Resolution Imaging. *Annu. Rev. Phys. Chem.* **63**, 595–617 (2012).

12. Lacey, A. J. *Light Microscopy in Biology A Practical Approach*. (Oxford University Press, 1999).

13. Abbe, E. Beiträge zur Theorie des Mikroskops und der mikroskopischen Wahrnehmung. *Archive fuer mikroskopische Anatomie* **9**, 413–468 (1873).

14. Hell, S. W. & Wichmann, J. Breaking the diffraction resolution limit by stimulated-emission: stimulated-emission-depletion fluorescence microscopy. *Opt. Lett.* **19**, 780–782 (1994).

15. Patterson, G., Davidson, M., Manley, S. & Lippincott-Schwartz, J. Superresolution Imaging using Single-Molecule Localization. *Annu. Rev. Phys. Chem.* **61**, 345–367 (2010).

16. Moerner, W. E. & Kador, L. Optical Detection and Spectroscopy of Single Molecules in a Solid. *Phys. Rev. Lett.* **62**, 2535–2538 (1989).

17. Betzig, E. Proposed method for molecular optical imaging. *Opt. Lett.* **20**, 237–239 (1995).

18. Patterson, G. H. & Lippincott-Schwartz, J. A Photoactivatable GFP for Selective Photolabeling of Proteins and Cells. *Science* **297**, 1873–1877 (2002).

19. Betzig, E. *et al.* Imaging Intracellular Fluorescent Proteins at Nanometer Resolution. *Science* **313**, 1642–1645 (2006).

20. Hess, S. T., Girirajan, T. P. K. & Mason, M. D. Ultra-High Resolution Imaging by Fluorescence Photoactivation Localization Microscopy. *Biophys. J.* **91**, 4258–4272 (2006).

21. Rust, M. J., Bates, M. & Zhuang, X. Sub-diffraction-limit imaging by stochastic optical reconstruction microscopy (STORM). *Nat. Methods* **3**, 793–795 (2006).

22. Sharonov, A. & Hochstrasser, R. M. Wide-field subdiffraction imaging by accumulated binding of diffusing probes. *Proc. Natl. Acad. Sci.* **103**, 18911–18916 (2006).

23. Fölling, J. *et al.* Fluorescence nanoscopy by ground-state depletion and single-molecule return. *Nat. Methods*

5, 943–945 (2008).

24. Fernández-Suárez, M. & Ting, A. Y. Fluorescent probes for super-resolution imaging in living cells. *Nat. Rev. Mol. Cell Biol.* **9**, 929–943 (2008).

25. Dempsey, G. T., Vaughan, J. C., Chen, K. H., Bates, M. & Zhuang, X. Evaluation of fluorophores for optimal performance in localization-based super-resolution imaging. *Nat. Methods* **8**, 1027–1036 (2011).

26. Shannon, C. E. Communication in the Presence of Noise. *Proc. IEEE* **86**, 447–457 (1998).

27. Li, H. & Vaughan, J. C. Switchable Fluorophores for Single-Molecule Localization Microscopy. *Chem. Rev.* **118**, 9412–9454 (2018).

28. Shcherbakova, D. M., Sengupta, P., Lippincott-Schwartz, J. & Verkhusha, V. V. Photocontrollable Fluorescent Proteins for Superresolution Imaging. *Annu. Rev. Biophys.* **43**, 303–329 (2014).

29. Nienhaus, K. & Nienhaus, G. U. Fluorescent proteins for live-cell imaging with super-resolution. *Chem. Soc. Rev.* **43**, 1088–1106 (2014).

30. Wang, S., Moffitt, J. R., Dempsey, G. T., Xie, X. S. & Zhuang, X. Characterization and development of photoactivatable fluorescent proteins for single-molecule-based superresolution imaging. *Proc. Natl. Acad. Sci.* **111**, 8452–8457 (2014).

31. van de Linde, S., Heilemann, M. & Sauer, M. Live-Cell Super-Resolution Imaging with Synthetic Fluorophores. *Annu. Rev. Phys. Chem.* **63**, 519–540 (2012).

32. Uno, S. *et al.* A spontaneously blinking fluorophore based on intramolecular spirocyclization for live-cell super-resolution imaging. *Nat. Chem.* **6**, 681–689 (2014).

33. Takakura, H. *et al.* Long time-lapse nanoscopy with spontaneously blinking membrane probes. *Nat. Biotechnol.* **35**, 773–780 (2017).

34. Uno, S., Kamiya, M., Morozumi, A. & Urano, Y. A green-light emitting, spontaneously blinking fluorophore based on intramolecular spirocyclization for live-cell super-resolution imaging. *Chem. Commun.* **54**, 102–105 (2018).

35. Halabi, E. A., Pinotsi, D. & Rivera-Fuentes, P. Photoregulated fluxional fluorophores for live-cell super-resolution microscopy with no apparent photobleaching. *Nat. Commun.* **10**, 1232 (2019).

36. Zheng, Q. *et al.* Rational Design of Fluorogenic and Spontaneously Blinking Labels for Super-Resolution Imaging. *ACS Cent. Sci.* **5**, 1602–1613 (2019).

37. Bock, H. *et al.* Two-color far-field fluorescence nanoscopy based on photoswitchable emitters. *Appl. Phys. B Lasers Opt.* **88**, 161–165 (2007).

38. Heilemann, M. *et al.* Subdiffraction-Resolution Fluorescence Imaging with Conventional Fluorescent Probes. *Angew. Chem. Int. Ed.* **47**, 6172–6176 (2008).

39. Baddeley, D., Jayasinghe, I. D., Cremer, C., Cannell, M. B. & Soeller, C. Light-Induced Dark States of Organic Fluochromes Enable 30 nm Resolution Imaging in Standard Media. *Biophys. J.* **96**, L22–L24 (2009).

40. Heilemann, M., van de Linde, S., Mukherjee, A. & Sauer, M. Super-Resolution Imaging with Small Organic Fluorophores. *Angew. Chem. Int. Ed.* **48**, 6903–6908 (2009).

41. Vogelsang, J. *et al.* Make them Blink: Probes for Super-Resolution Microscopy. *ChemPhysChem* **11**, 2475–2490 (2010).

42. van de Linde, S. *et al.* Direct stochastic optical reconstruction microscopy with standard fluorescent probes. *Nat. Protoc.* **6**, 991–1009 (2011).

43. Sauer, M. & Heilemann, M. Single-Molecule Localization Microscopy in Eukaryotes. *Chem. Rev.* **117**, 7478–7509 (2017).

44. Bossi, M. *et al.* Multicolor Far-Field Fluorescence Nanoscopy through Isolated Detection of Distinct Molecular Species. *Nano Lett.* **8**, 2463–2468 (2008).

45. Baddeley, D. *et al.* 4D Super-Resolution Microscopy with Conventional Fluorophores and Single Wavelength Excitation in Optically Thick Cells and Tissues. *PLoS One* **6**, e20645 (2011).

46. Lampe, A., Haucke, V., Sigrist, S. J., Heilemann, M. & Schmoranzer, J. Multi-colour direct STORM with red emitting carbocyanines. *Biol. Cell* **104**, 229–237 (2012).

47. Zhang, Z., Kenny, S. J., Hauser, M., Li, W. & Xu, K. Ultrahigh-throughput single-molecule spectroscopy and spectrally resolved super-resolution microscopy. *Nat. Methods* **12**, 935–938 (2015).

48. Mlodzianoski, M. J., Curthoys, N. M., Gunewardene, M. S., Carter, S. & Hess, S. T. Super-Resolution Imaging of Molecular Emission Spectra and Single Molecule Spectral Fluctuations. *PLoS One* **11**, e0147506 (2016).

49. Dong, B. *et al.* Super-resolution spectroscopic microscopy via photon localization. *Nat. Commun.* **7**, 12290 (2016).

50. Zhang, Y. *et al.* Nanoscale subcellular architecture revealed by multicolor three-dimensional salvaged fluorescence imaging. *Nat. Methods* **17**, 225–231 (2020).

51. Bates, M., Huang, B., Dempsey, G. T. & Zhuang, X. Multicolor Super-Resolution Imaging with Photo-Switchable Fluorescent Probes. *Science* **317**, 1749–1753 (2007).

52. Jungmann, R. *et al.* Multiplexed 3D cellular super-resolution imaging with DNA-PAINT and Exchange-PAINT. *Nat. Methods* **11**, 313–318 (2014).

53. Huang, B., Wang, W., Bates, M. & Zhuang, X. Three-Dimensional Super-Resolution Imaging by Stochastic Optical Reconstruction Microscopy. *Science* **319**, 810–813 (2008).

54. Pavani, S. R. P. *et al.* Three-dimensional, single-molecule fluorescence imaging beyond the diffraction limit by using a double-helix point spread function. *Proc. Natl. Acad. Sci.* **106**, 2995–2999 (2009).

55. Juette, M. F. *et al.* Three-dimensional sub-100 nm resolution fluorescence microscopy of thick samples. *Nat. Methods* **5**, 527–529 (2008).

56. Shtengel, G. *et al.* Interferometric fluorescent super-resolution microscopy resolves 3D cellular ultrastructure. *Proc. Natl. Acad. Sci.* **106**, 3125–3130 (2009).

57. Aquino, D. *et al.* Two-color nanoscopy of three-dimensional volumes by 4Pi detection of stochastically switched fluorophores. *Nat. Methods* **8**, 353–359 (2011).

58. Sage, D. *et al.* Quantitative evaluation of software packages for single-molecule localization microscopy. *Nat. Methods* **12**, 717–724 (2015).

59. Single molecule localization microscopy Software benchmarking. Available at: http://bigwww.epfl.ch/smlm/index.html#&panel1-1.

60. Manley, S. *et al.* High-density mapping of single-molecule trajectories with photoactivated localization microscopy. *Nat. Methods* **5**, 155–157 (2008).

61. Gustavsson, A.-K., Petrov, P. N. & Moerner, A. W. E. Light sheet approaches for improved precision in 3D localization-based super- resolution imaging in mammalian cells. *Opt. Express* **26**, 13122–13147 (2018).

62. Hauser, M. *et al.* Correlative Super-Resolution Microscopy : New Dimensions and New Opportunities. *Chem. Rev.* **117**, 7428–7456 (2017).

63. Klar, T. A. & Hell, S. W. Subdiffraction resolution in far-field fluorescence microscopy. *Opt. Lett.* **24**, 954–956 (1999).

64. Hell, S. W. Far-Field Optical Nanoscopy. *Science* **2**, 1153–1158 (2007).

65. Müller, T., Schumann, C. & Kraegeloh, A. STED Microscopy and its Applications: New Insights into Cellular Processes on the Nanoscale. *ChemPhysChem* **13**, 1986–2000 (2012).

66. Blom, H. & Widengren, J. Stimulated Emission Depletion Microscopy. *Chem. Rev.* **117**, 7377–7427 (2017).

67. Vicidomini, G., Bianchini, P. & Diaspro, A. STED super-resolved microscopy. *Nat. Methods* **15**, 173–182 (2018).

68. Donnert, G. *et al.* Two-Color Far-Field Fluorescence Nanoscopy. *Biophys. J.* **92**, L67–L69 (2007).

69. Meyer, L. *et al.* Dual-Color STED Microscopy at 30-nm Focal-Plane Resolution. *Small* **4**, 1095–1100 (2008).

70. Bückers, J., Wildanger, D., Vicidomini, G., Kastrup, L. & Hell, S. W. Simultaneous multi-lifetime multi-color STED imaging for colocalization analyses. *Opt. Express* **19**, 3130–3143 (2011).

71. Pellett, P. A. *et al.* Two-color STED microscopy in living cells. *Biomed. Opt. Express* **2**, 2364–2371 (2011).

72. Tønnesen, J., Nadrigny, F., Willig, K. I., Wedlich-Söldner, R. & Nägerl, U. V. Two-color STED Microscopy of Living Synapses Using A Single Laser-Beam Pair. *Biophys. J.* **101**, 2545–2552 (2011).

73. Göttfert, F. *et al.* Coaligned Dual-Channel STED Nanoscopy and Molecular Diffusion Analysis at 20 nm Resolution. *Biophys. J.* **105**, L01–L03 (2013).

74. Bottanelli, F. *et al.* Two-colour live-cell nanoscale imaging of intracellular targets. *Nat. Commun.* **7**, 10778 (2016).

75. Willig, K. I., Stiel, A. C., Brakemann, T., Jakobs, S. & Hell, S. W. Dual-Label STED Nanoscopy of Living Cells Using Photochromism. *Nano Lett.* **11**, 3970–3973 (2011).

76. Beater, S., Holzmeister, P., Lalkens, B. & Tinnefeld, P. Simple and aberration-free 4color-STED - multiplexing by transient binding. *Opt. Express* **23**, 8630–8638 (2015).

77. Harke, B., Ullal, C. K., Keller, J. & Hell, S. W. Three-Dimensional Nanoscopy of Colloidal Crystals. *Nano Lett.* **8**, 1309–1313 (2008).

78. Sezgin, E. *et al. Measuring nanoscale diffusion dynamics in cellular membranes with super-resolution STED–FCS*. *Nature Protoc.* **14**, (2019).

79. Schnell, U., Dijk, F., Sjollema, K. A. & Giepmans, B. N. G. Immunolabeling artifacts and the need for live-cell imaging. *Nat. Methods* **9**, 152–158 (2012).

80. Cox, S. Super-resolution imaging in live cells. *Dev. Biol.* **401**, 175–181 (2015).

81. Cremer, C. & Birk, U. Perspectives in Super-Resolved Fluorescence Microscopy: What Comes Next? *Front. Phys.* **4**, 11 (2016).

82. Wäldchen, S., Lehmann, J., Klein, T., van de Linde, S. & Sauer, M. Light-induced cell damage in live-cell super-resolution microscopy. *Sci. Rep.* **5**, 15348 (2015).

83. Kilian, N. *et al.* Assessing photodamage in live-cell STED microscopy. *Nat. Methods* **15**, 755–756 (2018).

84. Marsh, R. J. *et al.* Artifact-free high-density localization microscopy analysis. *Nat. Methods* **15**, 689–692 (2018).

85. Zheng, Q. & Lavis, L. D. Development of photostable fluorophores for molecular imaging. *Curr. Opin. Chem. Biol.* **39**, 32–38 (2017).

86. Balzarotti, F. *et al.* Nanometer resolution imaging and tracking of fluorescent molecules with minimal photon

fluxes. *Science* **355**, 606–612 (2016).

87. Gwosch, K. C. *et al.* MINFLUX nanoscopy delivers 3D multicolor nanometer resolution in cells. *Nat. Methods* **17**, 217–224 (2020).

88. Eilers, Y., Ta, H., Gwosch, K. C., Balzarotti, F. & Hell, S. W. MINFLUX monitors rapid molecular jumps with superior spatiotemporal resolution. **115**, 6117–6122 (2018).

89. Marks, K. M. & Nolan, G. P. Chemical labeling strategies for cell biology. *Nat. Methods* **3**, 591–596 (2006).

90. Johnson, I. D. & Spence, M. T. Z. *The Molecular Probes Handbook : A Guide to Fluorescent Probes and Labeling Technologies*. (Molecular Probes, 2010).

91. Jing, C. & Cornish, V. W. Chemical Tags for Labeling Proteins Inside Living Cells. *Acc. Chem. Res.* **44**, 784–792 (2011).

92. Dean, K. M. & Palmer, A. E. Advances in fluorescence labeling strategies for dynamic cellular imaging. *Nat. Chem. Biol.* **10**, 512–523 (2014).

93. Xue, L., Karpenko, I. A., Hiblot, J. & Johnsson, K. Imaging and manipulating proteins in live cells through covalent labeling. *Nat. Chem. Biol.* **11**, 917–923 (2015).

94. Schneider, A. F. L. & Hackenberger, C. P. R. Fluorescent labelling in living cells. *Curr. Opin. Biotechnol.* **48**, 61–68 (2017).

95. Tamura, T. & Hamachi, I. Chemistry for Covalent Modification of Endogenous/Native Proteins: From Test Tubes to Complex Biological Systems. *J. Am. Chem. Soc.* **141**, 2782–2799 (2019).

96. Keppler, A. *et al.* A general method for the covalent labeling of fusion proteins with small molecules in vivo. *Nat. Biotechnol.* **21**, 86–89 (2003).

97. Los, G. V *et al.* HaloTag: A Novel Protein Labeling Technology for Cell Imaging and Protein Analysis. *ACS Chem. Biol.* **3**, 373–382 (2008).

98. Encell, L. P. *et al.* Development of a Dehalogenase-Based Protein Fusion Tag Capable of Rapid, Selective and Covalent Attachment to Customizable Ligands. *Curr. Chem. Genomics* **6**, 55–71 (2012).

99. Ries, J., Kaplan, C., Platonova, E., Eghlidi, H. & Ewers, H. A simple, versatile method for GFP-based super-resolution microscopy via nanobodies. *Nat. Methods* **9**, 582–584 (2012).

100. Ratz, M., Testa, I., Hell, S. W. & Jakobs, S. CRISPR/Cas9-mediated endogenous protein tagging for RESOLFT super-resolution microscopy of living human cells. *Sci. Rep.* **5**, 9592 (2015).

101. Thevathasan, J. V. *et al.* Nuclear pores as versatile reference standards for quantitative superresolution microscopy. *Nat. Methods* **16**, 1045–1053 (2019).

102. Tannert, R. *et al.* Synthesis and Structure-Activity Correlation of Natural-Product Inspired Cyclodepsipeptides Stabilizing F-Actin. *J. Am. Chem. Soc.* **132**, 3063–3077 (2010).

103. Dubois, J. *et al.* Fluorescent and Biotinylated Analogues of Docetaxel: Synthesis and Biological Evaluation. *Bioorganic Med. Chem.* **3**, 1357–1368 (1995).

104. Lukinavičius, G. *et al.* Fluorescent dyes and probes for super-resolution microscopy of microtubules and tracheoles in living cells and tissues. *Chem. Sci.* **9**, 3324–3334 (2018).

105. Chen, C.-S., Chen, W.-N. U., Zhou, M., Arttamangkul, S. & Haugland, R. P. Probing the cathepsin D using a BODIPY FL-pepstatin A: applications in fluorescence polarization and microscopy. *J. Biochem. Biophys. Methods* **42**, 137–151 (2000).

106. Kowada, T., Maeda, H. & Kikuchi, K. BODIPY-based probes for the fluorescence imaging of biomolecules in

living cells. *Chem. Soc. Rev.* **44**, 4953–4972 (2015).

107. Johnson, L. V., Walsh, M. L. & Chen, L. B. Localization of mitochondria in living cells with rhodamine 123. *Proc. Natl. Acad. Sci.* **77**, 990–994 (1980).

108. Erdmann, R. S. *et al.* Super-Resolution Imaging of the Golgi in Live Cells with a Bioorthogonal Ceramide Probe. *Angew. Chem. Int. Ed.* **53**, 10242–10246 (2014).

109. Thompson, A. D., Bewersdorf, J., Toomre, D. & Schepartz, A. HIDE Probes: A New Toolkit for Visualizing Organelle Dynamics, Longer and at Super-Resolution. *Biochemistry* **56**, 5194–5201 (2017).

110. Wang, L., Frei, M. S., Salim, A. & Johnsson, K. Small-Molecule Fluorescent Probes for Live-Cell Super-Resolution Microscopy. *J. Am. Chem. Soc.* **141**, 2770–2781 (2019).

111. Lavis, L. D. & Raines, R. T. Bright Building Blocks for Chemical Biology. *ACS Chem. Biol.* **9**, 855–866 (2014).

112. Lavis, L. D. Teaching Old Dyes New Tricks: Biological Probes Built from Fluoresceins and Rhodamines. *Annu. Rev. Biochem.* **86**, 825–843 (2017).

113. Jradi, F. M. & Lavis, L. D. Chemistry of Photosensitive Fluorophores for Single-Molecule Localization Microscopy. *ACS Chem. Biol.* **14**, 1077–1090 (2019).

114. Ceresole, M. Verfahren zur Darstellung von Farbstoffen aus der Gruppe des Meta-amidophenol-Phtaleïns. (1887).

115. Ramette, R. W. & Sandell, E. B. Rhodamine B Equilibria. *J. Am. Chem. Soc.* **78**, 4872–4878 (1956).

116. Orndorff, W. R. & Hemmer, A. J. Fluorescein And Some of Its Derivatives. *J. Am. Chem. Soc.* **49**, 1272–1280 (1927).

117. Lukinavičius, G. *et al.* A near-infrared fluorophore for live-cell super-resolution microscopy of cellular proteins. *Nat. Chem.* **5**, 132–139 (2013).

118. Beija, M., Afonso, C. A. M. & Martinho, J. M. G. Synthesis and applications of Rhodamine derivatives as fluorescent probes. *Chem. Soc. Rev.* **38**, 2410–2433 (2009).

119. Chen, X., Pradhan, T., Wang, F., Kim, J. S. & Yoon, J. Fluorescent Chemosensors Based on Spiroring-Opening of Xanthenes and Related Derivatives. *Chem. Rev.* **112**, 1910–1956 (2012).

120. Li, X., Gao, X., Shi, W. & Ma, H. Design Strategies for Water-Soluble Small Molecular Chromogenic and Fluorogenic Probes. *Chem. Rev.* **114**, 590–659 (2014).

121. Bucevičius, J., Kostiuk, G., Gerasimaitė, R., Gilat, T. & Lukinavičius, G. Enhancing biocompatibility of rhodamine fluorescent probes by a neighbouring group effect. *bioRxiv* 2020.03.11.986919 (2020).

122. Lukinavičius, G. *et al.* Fluorogenic probes for live-cell imaging of the cytoskeleton. *Nat. Methods* **11**, 731–733 (2014).

123. Lukinavičius, G. *et al.* SiR-Hoechst is a far-red DNA stain for live-cell nanoscopy. *Nat. Commun.* **6**, 8497 (2015).

124. Lukinavičius, G. *et al.* Fluorogenic Probes for Multicolor Imaging in Living Cells. *J. Am. Chem. Soc.* **138**, 9365–9368 (2016).

125. Lukinavičius, G. & Johnsson, K. Switchable fluorophores for protein labeling in living cells. *Curr. Opin. Chem. Biol.* **15**, 768–774 (2011).

126. Nadler, A. & Schultz, C. The Power of Fluorogenic Probes. *Angew. Chem. Int. Ed.* **52**, 2408–2410 (2013).

127. Kozma, E. & Kele, P. Fluorogenic probes for super-resolution microscopy. *Org. Biomol. Chem.* **17**, 215–233 (2019).

128. Kozma, E., Estrada Girona, G., Paci, G., Lemke, E. A. & Kele, P. Bioorthogonal double-fluorogenic siliconrhodamine probes for intracellular super-resolution microscopy. *Chem. Commun.* **53**, 6696–6699 (2017).

129. Yang, N. J. & Hinner, M. J. Getting Across the Cell Membrane: An Overview for Small Molecules, Peptides, and Proteins. in *Site-Specific Protein Labeling: Methods and Protocols; Methods in Molecular Biology* (eds. Gautier, A. & Hinner, M. J.) **1266**, 29–53 (Springer New York, 2015).

130. Péresse, T. & Gautier, A. Next-Generation Fluorogen-Based Reporters and Biosensors for Advanced Bioimaging. *Int. J. Mol. Sci.* **20**, 6142 (2019).

131. Cavallo, L., Moore, M. H., Corrie, J. E. T. & Fraternali, F. Quantum Mechanics Calculations on Rhodamine Dyes Require Inclusion of Solvent Water for Accurate Representation of the Structure. *J. Phys. Chem. A* **108**, 7744–7751 (2004).

132. Chi, W., Qi, Q., Lee, R., Xu, Z. & Liu, X. A Unified Push–Pull Model for Understanding the Ring-Opening Mechanism of Rhodamine Dyes. *J. Phys. Chem. C* **124**, 3793–3801 (2020).

133. Rosenthal, I., Peretz, P. & Muszkat, K. A. Thermochromic and Hyperchromic Effects in Rhodamine B Solutions. *J. Phys. Chem.* **83**, 350–353 (1979).

134. Hinckley, D. A., Seybold, P. G. & Borris, D. P. Solvatochromism and thermochromism of rhodamine solutions. *Spectrochim. Acta, Part A* **42**, 747–754 (1986).

135. Hinckley, D. A. & Seybold, P. G. Thermodynamics of the Rhodamine B Lactone-zwitterion Equilibrium: An Undergraduate Laboratory Experiment. *J. Chem. Educ.* **64**, 362–364 (1987).

136. Grimm, J. B. *et al.* A general method to improve fluorophores for live-cell and single-molecule microscopy. *Nat. Methods* **12**, 244–250 (2015).

137. Grimm, J. B. *et al.* Carbofluoresceins and Carborhodamines as Scaffolds for High-Contrast Fluorogenic Probes. *ACS Chem. Biol.* **8**, 1303–1310 (2013).

138. Butkevich, A. N. *et al.* Fluorescent Rhodamines and Fluorogenic Carbopyronines for Super-Resolution STED Microscopy in Living Cells. *Angew. Chem. Int. Ed.* **55**, 3290–3294 (2016).

139. Butkevich, A. N. *et al.* Hydroxylated Fluorescent Dyes for Live-Cell Labeling: Synthesis, Spectra and Super-Resolution STED** Microscopy. *Chem. - A Eur. J.* **23**, 1–7 (2017).

140. Grimm, J. B. *et al.* A general method to fine-tune fluorophores for live-cell and in vivo imaging. *Nat. Methods* **14**, 987–994 (2017).

141. Grimm, J. B., Brown, T. A., Tkachuk, A. N. & Lavis, L. D. General Synthetic Method for Si-Fluoresceins and Si-Rhodamines. *ACS Cent. Sci.* **3**, 975–985 (2017).

142. Wang, L. *et al.* A general strategy to develop cell permeable and fluorogenic probes for multicolour nanoscopy. *Nat. Chem.* **12**, 165–172 (2020).

143. Grimm, J. B. *et al.* Optimization and functionalization of red-shifted rhodamine dyes. *bioRxiv* 2019.12.20.881227 (2019).

144. Erdmann, R. S. *et al.* Labeling Strategies Matter for Super-Resolution Microscopy: A Comparison between HaloTags and SNAP-tags. *Cell Chem. Biol.* **26**, 584–592 (2019).

145. Smith, A. M., Mancini, M. C. & Nie, S. Second window for in vivo imaging. *Nat. Nanotechnol.* **4**, 710–711 (2009).

146. Detty, M. R. *et al.* Synthesis, properties, and photodynamic properties in vitro of heavy-chalcogen analogues of tetramethylrosamine. *Bioorganic Med. Chem.* **12**, 2537–2544 (2004).

147. Calitree, B. *et al.* Tellurium Analogues of Rosamine and Rhodamine Dyes: Synthesis, Structure, 125Te NMR,

and Heteroatom Contributions to Excitation Energies. *Organometallics* **26**, 6248–6257 (2007).

148. Van Duuren, B. L., Goldschmidt, B. M. & Seltzman, H. H. The Synthesis and Aggregation of 9-phenyl- and 9-s-Butyl-3,6- bisdimethylaminoacridine in Solution. The Dealkylation of 9-t-Butylacridans. *J. Chem. Soc. B Phys. Org.* 814–819 (1967).

149. Aaron, C. & Barker, C. C. Steric Effects in Di- and Tri-arylmethane Dyes. Part X. Electronic Absorption Spectra of Bridged Derivatives of Malachite Green and Crystal Violet. *J. Chem. Soc. B Phys. Org.* 319–324 (1971).

150. Arden-Jacob, J., Frantzeskos, J., Kemnitzer, N. U., Zilles, A. & Drexhage, K. H. New fluorescent markers for the red region. *Spectrochim. Acta, Part A* **57**, 2271–2283 (2001).

151. Fu, M., Xiao, Y., Qian, X., Zhao, D. & Xu, Y. A design concept of long-wavelength fluorescent analogs of rhodamine dyes: replacement of oxygen with silicon atom. *Chem. Commun.* 1780–1782 (2008).

152. Koide, Y., Urano, Y., Hanaoka, K., Terai, T. & Nagano, T. Evolution of Group 14 Rhodamines as Platforms for Near-Infrared Fluorescence Probes Utilizing Photoinduced Elctron Transfer. *ACS Chem. Biol.* **6**, 600–608 (2011).

153. Chai, X. *et al.* Near-Infrared Phosphorus-Substituted Rhodamine with Emission Wavelength above 700 nm for Bioimaging. *Chem. - A Eur. J.* **21**, 16754–16758 (2015).

154. Zhou, X., Lai, R., Beck, J. R., Li, H. & Stains, C. I. Nebraska Red: a phosphinate-based near-infrared fluorophore scaffold for chemical biology applications. *Chem. Commun.* **52**, 12290–12293 (2016).

155. Grzybowski, M. *et al.* A Highly Photostable Near-Infrared Labeling Agent Based on a Phospha-rhodamine for Long-Term and Deep Imaging. *Angew. Chem. Int. Ed.* **57**, 10137–10141 (2018).

156. Liu, J. *et al.* Sulfone-Rhodamines: A New Class of Near-Infrared Fluorescent Dyes for Bioimaging. *ACS Appl. Mater. Interfaces* **8**, 22953–22962 (2016).

157. Song, X., Johnson, A. & Foley, J. 7-Azabicyclo[2.2.1]heptane as a Unique and Effective Dialkylamino Auxochrome Moiety: Demonstration in a Fluorescent Rhodamine Dye. *J. Am. Chem. Soc.* **130**, 17652–17653 (2008).

158. Kuznetsova, N. A., Kaliya, O. L. & Lukyanets, E. A. Photochemistry of laser dyes for the visible spectrum. *Int. Conf. At. Mol. Pulsed Laser* **2619**, 161–165 (1995).

159. Zheng, Q. *et al.* Ultra-stable organic fluorophores for single-molecule research. *Chem. Soc. Rev.* **43**, 1044–1056 (2014).

160. Widengren, J., Chmyrov, A., Eggeling, C., Löfdahl, P.-Å. & Seidel, C. A. M. Strategies to Improve Photostabilities in Ultrasensitive Fluorescence Spectroscopy. *J. Phys. Chem. A* **111**, 429–440 (2007).

161. Evans, N. A. Photofading of Rhodamine Dyes II-Photode-alkylation of Rhodamine B. *J. Soc. Dye. Colour* **89**, 332 (1973).

162. Watanabe, T., Takizawa, T. & Honda, K. Photocatalysis through Excitation of Adsorbates. 1. Highly Efficient N-Deethylation of Rhodamine B Adsorbed to CdS. *J. Phys. Chem.* **81**, 1845–1851 (1977).

163. Butkevich, A. N., Bossi, M. L., Lukinavičius, G. & Hell, S. W. Triarylmethane Fluorophores Resistant to Oxidative Photobluing. *J. Am. Chem. Soc.* **141**, 981–989 (2019).

164. Mitronova, G. Y. *et al.* New Fluorinated Rhodamines for Optical Microscopy and Nanoscopy. *Chem. - A Eur. J.* **16**, 4477–4488 (2010).

165. Zheng, Q. *et al.* Intra-molecular triplet energy transfer is a general approach to improve organic fluorophore photostability. *Photochem. Photobiol. Sci.* **15**, 196–203 (2016).

166. Zheng, Q. *et al.* Electronic tuning of self-healing fluorophores for live-cell and single-molecule imaging. *Chem. Sci.* **8**, 755–762 (2017).

167. van de Linde, S. *et al.* Multicolor photoswitching microscopy for subdiffraction-resolution fluorescence imaging. *Photochem. Photobiol. Sci.* **8**, 465–469 (2009).

168. van de Linde, S. *et al.* Photoinduced formation of reversible dye radicals and their impact on super-resolution imaging. *Photochem. Photobiol. Sci.* **10**, 499–506 (2011).

169. Wombacher, R. *et al.* Live-cell super-resolution imaging with trimethoprim conjugates. *Nat. Methods* **7**, 717–719 (2010).

170. Jones, S. A., Shim, S.-H., He, J. & Zhuang, X. Fast, three-dimensional super-resolution imaging of live cells. *Nat. Methods* **8**, 499–505 (2011).

171. Knauer, K.-H. & Gleiter, R. Photochromism of Rhodamine Derivatives. *Angew. Chem. Int. Ed.* **16**, 113–113 (1977).

172. Fölling, J. *et al.* Fluorescence Nanoscopy with Optical Sectioning by Two-Photon Induced Molecular Switching using Continuous-Wave Lasers. *ChemPhysChem* **9**, 321–326 (2008).

173. Belov, V. N., Bossi, M. L., Fölling, J., Boyarskiy, V. P. & Hell, S. W. Rhodamine Spiroamides for Multicolor Single-Molecule Switching Fluorescent Nanoscopy. *Chem. - A Eur. J.* **15**, 10762–10776 (2009).

174. Lee, M. K., Rai, P., Williams, J., Twieg, R. J. & Moerner, W. E. Small-Molecule Labeling of Live Cell Surfaces for Three-Dimensional Super-Resolution Microscopy. *J. Am. Chem. Soc.* **136**, 14003–14006 (2014).

175. Fölling, J. *et al.* Photochromic Rhodamines Provide Nanoscopy with Optical Sectioning. *Angew. Chem. Int. Ed.* **46**, 6266–6270 (2007).

176. Belov, V. N. & Bossi, M. L. Photoswitching Emission with Rhodamine Spiroamides for Super-Resolution Fluorescence nanoscopies. *Isr. J. Chem.* **53**, 267–279 (2013).

177. Ye, Z. *et al.* Strategy to Lengthen the On-Time of Photochromic Rhodamine Spirolactam for Super-resolution Photoactivated Localization Microscopy. *J. Am. Chem. Soc.* **141**, 6527–6536 (2019).

178. Mitchison, T. J., Sawin, K. E., Theriot, J. A., Gee, K. & Mallavarapu, A. Caged Fluorescent Probes. *Methods Enzymol.* **291**, 63–78 (1998).

179. Pelliccioli, A. P. & Wirz, J. Photoremovable protecting groups: reaction mechanisms and applications. *Photochem. Photobiol. Sci.* **1**, 441–458 (2002).

180. Bley, F., Schaper, K. & Görner, H. Photoprocesses of Molecules with 2-Nitrobenzyl Protecting Groups and Caged Organic Acids. *Photochem. Photobiol.* **84**, 162–171 (2008).

181. Šolomek, T., Mercier, S., Bally, T. & Bochet, C. G. Photolysis of ortho-nitrobenzylic derivatives: the importance of the leaving group. *Photochem. Photobiol. Sci.* **11**, 548–555 (2012).

182. Klán, P. *et al.* Photoremovable Protecting Groups in Chemistry and Biology: Reaction Mechanisms and Efficacy. *Chem. Rev.* **113**, 119–191 (2013).

183. Gee, K. R., Weinberg, E. S. & Kozlowski, D. J. Caged Q-Rhodamine Dextran: A New Photoactivated Fluorescent Tracer. *Bioorganic Med. Chem. Lett.* **11**, 2181–2183 (2001).

184. Wysocki, L. M. *et al.* Facile and General Synthesis of Photoactivatable Xanthene Dyes. *Angew. Chem. Int. Ed.* **50**, 11206–11209 (2011).

185. Grimm, J. B. *et al.* Synthesis of a Far-Red Photoactivatable Silicon-Containing Rhodamine for Super-Resolution Microscopy. *Angew. Chem. Int. Ed.* **55**, 1723–1727 (2016).

186. Hauke, S., von Appen, A., Quidwai, T., Ries, J. & Wombacher, R. Specific protein labeling with caged fluorophores for dual-color imaging and super-resolution microscopy in living cells. *Chem. Sci.* **8**, 559–566 (2017).

187. Mayer, G. & Heckel, A. Biologically Active Molecules with a 'Light Switch'. *Angew. Chem. Int. Ed.* **45**, 4900–4921 (2006).

188. Belov, V. N., Wurm, C. A., Boyarskiy, V. P., Jakobs, S. & Hell, S. W. Rhodamines NN: A Novel Class of Caged Fluorescent Dyes. *Angew. Chem. Int. Ed.* **49**, 3520–3523 (2010).

189. Kolmakov, K. *et al.* Masked red-emitting carbopyronine dyes with photosensitive 2-diazo-1-indanone caging group. *Photochem. Photobiol. Sci.* **11**, 522–32 (2012).

190. Belov, V. N. *et al.* Masked Rhodamine Dyes of Five Principal Colors Revealed by Photolysis of a 2-Diazo-1-Indanone Caging Group: Synthesis, Photophysics, and Light Microscopy Applications. *Chem. - A Eur. J.* **20**, 13162–13173 (2014).

191. Grimm, J. B. *et al.* Bright photoactivatable fluorophores for single-molecule imaging. *Nat. Methods* **13**, 985–988 (2016).

192. Halabi, E. A., Thiel, Z., Trapp, N., Pinotsi, D. & Rivera-Fuentes, P. A Photoactivatable Probe for Super-Resolution Imaging of Enzymatic Activity in Live Cells. *J. Am. Chem. Soc.* **139**, 13200–13207 (2017).

193. Wysocki, L. M. & Lavis, L. D. Advances in the chemistry of small molecule fluorescent probes. *Curr. Opin. Chem. Biol.* **15**, 752–759 (2011).

194. Amat-Guerri, F., Martin, M. E., Martinez-Utrilla, R. (the late) & Pascual, C. Structures of Molecular and Ionic Forms of Succinylfluorescein in Solution and in the Solid State. *J. Chem. Res., Synop.* 184–185 (1988).

195. Aaron, C. & Barker, C. C. Steric Effects in Di- and Tri-arylmethanes. Part VIII.* Electronic Absorption Spectra of Planar Derivatives of Michler's Hydrol Blue. *J. Chem. Soc.* 2655–2662 (1963).

196. Matsui, M., Tsuge, M., Shibata, K. & Muramatsu, H. Photochromism of 1,1-Diaryl-1-alkanols. *Bull. Chem. Soc. Jpn.* **67**, 1753–1755 (1994).

197. Umezawa, K., Yoshida, M., Kamiya, M., Yamasoba, T. & Urano, Y. Rational design of reversible fluorescent probes for live-cell imaging and quantification of fast glutathione dynamics. *Nat. Chem.* **9**, 279–286 (2017).

198. Martínez-Peragón, Á. *et al.* Synthesis and Photophysics of a New Family of Fluorescent 9-Alkyl-Substituted Xanthenones. *Chem. - A Eur. J.* **20**, 447–455 (2014).

199. Šebej, P. *et al.* Fluorescein Analogues as Photoremovable Protecting Groups Absorbing at 520 nm. *J. Org. Chem.* **78**, 1833–1843 (2013).

200. Yamagami, A., Ishimura, H., Katori, A., Kuramochi, K. & Tsubaki, K. Syntheses and properties of the V-shaped dimeric xanthene dyes. *Org. Biomol. Chem.* **14**, 10963–10972 (2016).

201. Cui, J. *et al.* Design, Synthesis and Biological Evaluation of Rose Bengal Analogues as SecA Inhibitors. *ChemMedChem* **8**, 1384–1393 (2013).

202. Katori, A., Kuramochi, K. & Tsubaki, K. Oxidative cleavage of exo-alkylidene xanthenes. *Tetrahedron* **72**, 2997–3002 (2016).

203. Frei, M. S. *et al.* Photoactivation of silicon rhodamines via a light-induced protonation. *Nat. Commun.* **10**, 4580 (2019).

204. Johnsson, K., Reymond, L., Frei, M. S. & Pitsch, S. Novel Tunable Photoactivatable Silicon Rhodamine Fluorophores. (2019).

205. Pérez-Prior, M. T., Manso, J. A., Del Pilar García-Santos, M., Calle, E. & Casado, J. Reactivity of Lactones and GHB Formation. *J. Org. Chem.* **70**, 420–426 (2005).

206. Link, A., Fischer, C. & Sparr, C. Direct Transformation of Esters into Arenes with 1,5-Bifunctional Organomagnesium Reagents. *Angew. Chem. Int. Ed.* **54**, 12163–12166 (2015).

207. Fischer, C. & Sparr, C. Direct Transformation of Esters into Heterocyclic Fluorophores. *Angew. Chem. Int. Ed.* **57**, 2436–2440 (2018).

208. Koide, Y. *et al.* Development of NIR Fluorescent Dyes Based on Si-rhodamine for in Vivo Imaging. *J. Am. Chem. Soc.* **134**, 5029–5031 (2012).

209. Abdelfattah, A. S. *et al.* Bright and photostable chemigenetic indicators for extended in vivo voltage imaging. *Science* **364**, 699–704 (2019).

210. Salim, A. Fluorogenic probes for live-cell imaging. (EPFL PP - Lausanne, 2020).

211. Maiti, D. & Buchwald, S. L. Cu-Catalyzed Arylation of Phenols: Synthesis of Sterically Hindered and Heteroaryl Diaryl Ethers. *J. Org. Chem.* **75**, 1791–1794 (2010).

212. Lam, P. Y. S. *et al.* New Aryl/Heteroaryl C-N Bond Cross-coupling Reactions via Arylboronic Acid/Cupric Acetate Arylation. *Tetrahedron Lett.* **39**, 2941–2944 (1998).

213. Chan, D. M. T., Monaco, K. L., Wang, R.-P. & Winters, M. P. New N- and O-Arylations with Phenylboronic Acids and Cupric Acetate. *Tetrahedron Lett.* **39**, 2933–2936 (1998).

214. Evans, D. A., Katz, J. L. & West, T. R. Synthesis of Diaryl Ethers through the Copper-Promoted Arylation of Phenols with Arylboronic Acids. An Expedient Synthesis of Thyroxine. *Tetrahedron Lett.* **39**, 2937–2940 (1998).

215. Pretsch, E., Bühlmann, P. & Badertscher, M. *Spektroskopische Daten zur Strukturaufklärung organischer Verbindungen*. (Springer-Verlag Berlin, 2010).

216. Dodiuk, H. & Kosower, E. M. Multiple Fluorescences From The Excited State Of N-Methyl-2-N-Phenyl-Amino-6-Naphthalenesulphonate In Glycerol: Fast Proton Transfer. *Chem. Phys. Lett.* **34**, 253–257 (1975).

217. Kosower, E. M. & Dodiuk, H. Multiple Fluorescences. II. A New Scheme for 4-(N,N-Dimethylamino)benzonitrile Including Proton Transfer. *J. Am. Chem. Soc.* **98**, 924–929 (1976).

218. Reichardt, C. & Welton, T. Empirical Parameters of Solvent Polarity. in *Solvents and Solvent Effects in Organic Chemistry* (WILEY-VCH Verlag GmbH & Co. KGaA, Weinheim, 2010).

219. Wolff, G., Hagen, C., Grünewald, K. & Kaufmann, R. Towards correlative super-resolution fluorescence and electron cryo-microscopy. *Biol. Cell* **108**, 245–258 (2016).

220. Faro, A. R. *et al.* Low-temperature switching by photoinduced protonation in photochromic fluorescent proteins. *Photochem. Photobiol. Sci.* **9**, 254–262 (2010).

221. Shim, S.-H. *et al.* Super-resolution fluorescence imaging of organelles in live cells with photoswitchable membrane probes. *Proc. Natl. Acad. Sci.* **109**, 13978–13983 (2012).

222. Butkevich, A. N. *et al.* Two-Color 810 nm STED Nanoscopy of Living Cells with Endogenous SNAP-Tagged Fusion Proteins. *ACS Chem. Biol.* **13**, 475–480 (2018).

223. Kuprov, I. & Hore, P. J. Uniform illumination of optically dense NMR samples. *J. Magn. Reson.* **171**, 171–175 (2004).

224. Ball, G. E. In situ photochemistry with NMR detection of organometallic complexes. in *Spectroscopic Properties of Inorganic and Organometallic Compounds: Techniques, Materials and Applications* **41**, 262–287 (The Royal Society of Chemistry, 2010).

225. Feldmeier, C., Bartling, H., Riedle, E. & Gschwind, R. M. LED based NMR illumination device for mechanistic studies on photochemical reactions - Versatile and simple, yet surprisingly powerful. *J. Magn. Reson.* **232**, 39–44 (2013).

226. Seegerer, A., Nitschke, P. & Gschwind, R. M. Combined In Situ Illumination-NMR-UV/Vis Spectroscopy: A New Mechanistic Tool in Photochemistry. *Angew. Chem. Int. Ed.* **57**, 7493–7497 (2018).

227. Hiblot, J. & Tarnawski, M. *unpublished results*. (2020).

228. Kille, S. *et al.* Reducing Codon Redundancy and Screening Effort of Combinatorial Protein Libraries Created by Saturation Mutagenesis. *ACS Synth. Biol.* **2**, 83–92 (2013).

229. Deo, C. *et al.* Bright and tunable far-red chemigenetic indicators. *bioRxiv* 2020.01.08.898783 (2020).

230. Marmé, N., Knemeyer, J. P., Sauer, M. & Wolfrum, J. Inter- and Intramolecular Fluorescence Quenching of Organic Dyes by Tryptophan. *Bioconjug. Chem.* **14**, 1133–1139 (2003).

231. Liu, Z. *et al.* Systematic comparison of 2A peptides for cloning multi-genes in a polycistronic vector. *Sci. Rep.* **7**, 2193 (2017).

232. Koßmann, K. J. *et al.* A Rationally Designed Connector for Assembly of Protein-Functionalized DNA Nanostructures. *ChemBioChem* **17**, 1102–1106 (2016).

233. Eydeler, K., Magbanua, E., Werner, A., Ziegelmüller, P. & Hahn, U. Fluorophore Binding Aptamers as a Tool for RNA Visualization. *Biophys. J.* **96**, 3703–3707 (2009).

234. Ouellet, J. RNA Fluorescence with Light-Up Aptamers. *Front. Chem.* **4**, 29 (2016).

235. Bouhedda, F., Autour, A. & Ryckelynck, M. Light-Up RNA Aptamers and Their Cognate Fluorogens: From Their Development to Their Applications. *Int. J. Mol. Sci.* **19**, 44 (2018).

236. Wirth, R., Gao, P., Nienhaus, G. U., Sunbul, M. & Jäschke, A. SiRA: A Silicon Rhodamine-Binding Aptamer for Live-Cell Super-Resolution RNA Imaging. *J. Am. Chem. Soc.* **141**, 7562–7571 (2019).

237. Hatchard, C. G. & Parker, C. A. A new sensitive chemical actinometer. II. Potassium ferrioxalate as a standard chemical actinometer. *Proc. R. Soc. A* **235**, 518–536 (1956).

238. Frisch, M. J. *et al.* Gaussian 16 Rev. B.01. (2016).

239. CrysAlisPro. Agilent Technologies UK Ltd., Oxford, UK (2011-2014) and Rigaku Oxford Diffraction, Rigaku Polska Sp.z o.o., Wrocław, Poland (2015-2019).

240. Kabsch, K. *International Tables for Crystallography Vol. F, Ch. 11.3*. (Kluwer Academic Publishers, Dordrecht, The Netherlands, 2001).

241. SCALE3 ABSPACK, C. CrysAlisPro, Agilent Technologies UK Ltd., Oxford, UK (2011-2014) and Rigaku Oxford Diffraction, Rigaku Polska Sp.z o.o., Wrocław, Poland (2015-2019).

242. Blessing, R. H. An Empirical Correction for Absorption Anisotropy. *Acta Crystallogr. Sect. A* **51**, 33–38 (1995).

243. Busing, W. R. & Levy, H. A. High-Speed Computation of the Absorption Correction for Single-Crystal Diffraction Measurements. *Acta Crystallogr.* **10**, 180–182 (1957).

244. Burla, M. C. *et al.* SIR2019, CNR IC, Bari, Italy, (2019).

245. Burla, M. C., Giacovazzo, C. & Polidori, G. From a random to the correct structure: The VLD algorithm. *J. Appl. Crystallogr.* **43**, 825–836 (2010).

246. Sheldrick, G. M. SHELXL-20xx, University of Göttingen and Bruker AXS GmbH, Karlsruhe, Germany, (2012-2018).

247. Sheldrick, G. M. Crystal structure refinement with SHELXL. *Acta Crystallogr. Sect. C* **71**, 3–8 (2014).

248. Robinson, W. & Sheldrick, G. M. *Crystallographic Computing 4, Ch. 22,*. (IUCr and Oxford University Press, Oxford, UK, 1988).

249. Sheldrick, G. M. A short history of SHELX. *Acta Crystallogr. Sect. A* **64**, 112–122 (2008).

250. Farrugia, L. J. WinGX and ORTEP for Windows: an update. *J. Appl. Crystallogr.* **45**, 849–854 (2012).

251. Persistence of Vision Pty. Ltd., Persistence of Vision Raytracer (Version 3.6), (2004).

252. Gibson, D. G. *et al.* Enzymatic assembly of DNA molecules up to several hundred kilobases. *Nat. Methods* **6**, 343–345 (2009).

253. Zhang, M. *et al.* Rational design of true monomeric and bright photoactivatable fluorescent proteins. *Nat. Methods* **9**, 727–729 (2012).

254. Goedhart, J. *et al.* Structure-guided evolution of cyan fluorescent proteins towards a quantum yield of 93%. *Nat. Commun.* **3**, 751 (2012).

255. Malecki, M. J. *et al.* Leukemia-Associated Mutations within the NOTCH1 Heterodimerization Domain Fall into at Least Two Distinct Mechanistic Classes. *Mol. Cell. Biol.* **26**, 4642–4651 (2006).

256. Xu, K., Babcock, H. P. & Zhuang, X. Dual-objective STORM reveals three-dimensional filament organization in the actin cytoskeleton. *Nat. Methods* **9**, 185–188 (2012).

257. Jain, A., Liu, R., Xiang, Y. K. & Ha, T. Single-molecule pull-down for studying protein interactions. *Nat. Protoc.* **7**, 445–452 (2012).

258. Zhang, Z., Park, S. R., Pertsinidis, A. & Revyakin, A. Cloud-point PEG Glass Surfaces for Imaging of Immobilized Single Molecules by Total-internal-reflection Microscopy. *Bio-protocol* **6**, e1784 (2016).

259. Deschamps, J., Rowald, A. & Ries, J. Efficient homogeneous illumination and optical sectioning for quantitative single-molecule localization microscopy. *Opt. Express* **24**, 28080–28090 (2016).

260. Edelstein, A., Amodaj, N., Hoover, K., Vale, R. & Stuurman, N. Computer Control of Microscopes Using μManager. in *Current Protocols in Molecular Biology* (ed. John Wiley & Sons, I.) 14.20.1 (2010).

261. Origin(Pro), Version 2018b, OriginLab Corporation, Northampton, MA, USA.

262. Rueden, C. T. *et al.* ImageJ2: ImageJ for the next generation of scientific image data. *BMC Bioinformatics* **18**, 529 (2017).

263. Schindelin, J. *et al.* Fiji: An open-source platform for biological-image analysis. *Nat. Methods* **9**, 676–682 (2012).

264. Ovesný, M., Křížek, P., Borkovec, J., Švindrych, Z. & Hagen, G. M. ThunderSTORM: a comprehensive ImageJ plug-in for PALM and STORM data analysis and super-resolution imaging. *Bioinformatics* **30**, 2389–2390 (2014).

265. Tinevez, J.-Y. *et al.* TrackMate: An open and extensible platform for single-particle tracking. *Methods* **115**, 80–90 (2017).

266. MATLAB, Version 9.3.0.713579 (R2017b). (2010).

267. Crocker, J. C. & Grier, D. G. Methods of Digital Video Microscopy for Colloidal Studies. *J. Colloid Interface Sci.* **179**, 298–310 (1996).

268. Schrödinger, L. The PyMOL Molecular Graphics System, Version 2.1.1. (2015).

269. R Core Team. R: A Language and Environment for Statistical Computing. (2019).

270. Wickham, H. & Bryan, J. readxl: Read Excel Files. (2019).

271. Wuertz, D., Setz, T. & Chalabi, Y. fBasics: Rmetrics - Markets and Basic Statistics. (2017).

272. Wickham, H. *et al.* Welcome to the tidyverse. *J. Open Source Softw.* **4**, 1686 (2019).

273. Yutani, H. gghighlight: Highlight Lines and Points in 'ggplot2'. (2018).

274. Wickham, H. ggplot2: Elegant Graphics for Data Analysis. (2016).

275. Slowikowski, K. ggrepel: Automatically Position Non-Overlapping Text Labels with 'ggplot2'. (2019).

276. Kassambara, A. ggpubr: 'ggplot2' Based Publication Ready Plots. (2019).

277. Robinson, D. & Hayes, A. broom: Convert Statistical Analysis Objects into Tidy Tibbles. (2019).

278. Tsutsui, H., Karasawa, S., Shimizu, H., Nukina, N. & Miyawaki, A. Semi-rational engineering of a coral fluorescent protein into an efficient highlighter. *EMBO Rep.* **6**, 233–238 (2005).

Curriculum Vitae

MICHELLE FREI

Handschuhsheimer Landstrasse 12
69120 Heidelberg, Germany
michelle.frei@epfl.ch
ORCID iD: 0000-0002-4799-4554
Born 17th of August 1991

EDUCATION

Sept. 2016 – present	**PhD in Chemistry and Chemical Engineering** École Polytechnique Fédérale de Lausanne (EPFL), Switzerland and Max Planck Institute for Medical Research (MPI-MR), Heidelberg, Germany Supervisor: Professor Dr. Kai Johnsson
Sept. 2014 – Oct. 2015	**Master of Science ETH in Chemistry** Eidgenössische Technische Hochschule Zürich (ETH), Switzerland Master's thesis supervisor: Professor Dr. François Diederich
Sept. 2011 – Sept. 2014	**Bachelor of Science ETH in Chemistry** ETH Zürich, Switzerland
Aug. 2007 – June 2011	**Swiss Matura** Kantonsschule Wettingen, Switzerland

EMPLOYMENT HISTORY

Sept. 2017 – present	Visiting Scientist at the Advanced Light Microscopy Facility, EMBL Heidelberg, Germany
Oct. 2015 – June 2016	Chemistry Trainee, Actelion Pharmaceuticals Ltd., Allschwil, Switzerland (now Idorsia Pharmaceuticals Ltd.)
Oct. 2013 – Feb. 2014	Erasmus Exchange, University of Cambridge, United Kingdom Supervisor: Professor Dr. David R. Spring
July 2011 – Sept. 2011	Research Internship, Paul Scherrer Institute, Villigen, Switzerland

AWARDS

Sept. 2014 – Oct. 2015	Excellence Scholarship, ETH Zurich, Switzerland
Nov. 2012 – present	Member of the Swiss Study Foundation
July 2011	Bronze medal International Chemistry Olympiad, Ankara, Turkey
June 2011	2nd place Matura Examinations, Wettingen, Switzerland
Apr. 2011	1st place Swiss Chemistry Olympiad
July 2010	Invited member of the Swiss delegation: International Chemistry Olympiad, Tokyo, Japan
Apr. 2010	3rd place Swiss Chemistry Olympiad

PUBLICATIONS

Frei, M. S., Hoess, P., Lampe, M., Nijmeijer, B., Kueblbeck, M., Ellenberg, J., Wadepohl, H., Ries, J., Pitsch, S., Reymond, L., Johnsson, K. "Photoactivation of silicon rhodamines via a light-induced protonation" *Nat. Commun.* **2019**, *10*, 4580.

Wang, L., Frei, M. S., Salim, A., Johnsson, K. "Small-Molecule Fluorescent Probes for Live-Cell Super-Resolution Microscopy" *J. Am. Chem. Soc.* **2019**, *141*, 2770−2781.

Johnsson, K., Reymond, L., Frei, M. S., Pitsch, S., (Spirochrome AG), PCT Int. Appl. WO2019/122269 A1, **2019**, "Novel Tunable Photoactivatable Silicon Rhodamine Fluorophores".

Schwertz, G., Frei, M. S., Witschel, M. C., Rottmann, M., Leartsakulpanich, U., Chitnumsub, P., Jaruwat, A., Ittarat, W., Schäfer, A., Aponte, R. A., Trapp, N., Mark, K., Chaiyen, P., Diederich, F. "Conformational Aspects in the Design of Inhibitors for Serine Hydroxymethyltransferase (SHMT): Biphenyl, Aryl Sulfonamide, and Aryl Sulfone Motifs" *Chem. Eur. J.* **2017**, *23*, 14345−14357.

Frei, M. S., Bilyard, M. K., Alanine, T. A., Galloway, W. R. J. D., Stokes, J. E., Spring, D. R. "Studies towards the synthesis of indolizin-5(3*H*)-one derivatives and related 6,5-azabicyclic scaffolds by ring-closing metathesis" *Bioorg. Med. Chem.* **2015**, *23* (11), 2666−2679.

Chapter 6 Appendix

6.1 Supplementary figures

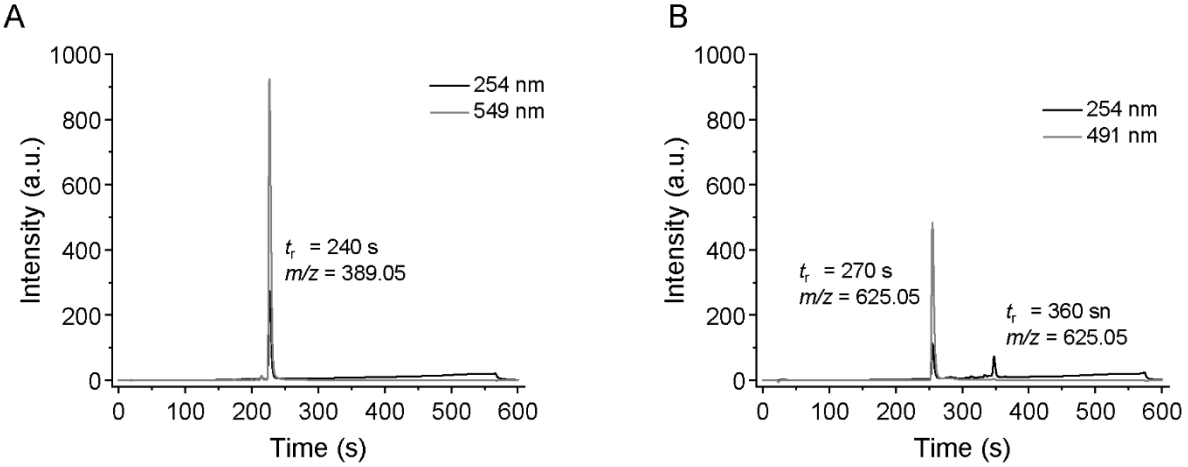

Supplementary Figure 1: LC-MS traces of 550R **89** and the mixture of quinoid 490R **97** and ethylenic **98**. (A) LC-MS traces of 550R **89** at 254 nm and 549 nm. The retention time with the corresponding mass is given. (B) LC-MS traces of the inseparable mixture of quinoid 490R **97** and ethylenic **98** at 254 nm and 491 nm. The peak at t_r = 240 s corresponds to 490R **97** an the one at t_r = 360 s to **98**. The ratio of the two peaks at 254 nm is 1.5:1 (**97**:**98**). Experiments were performed by J. Notbohm.

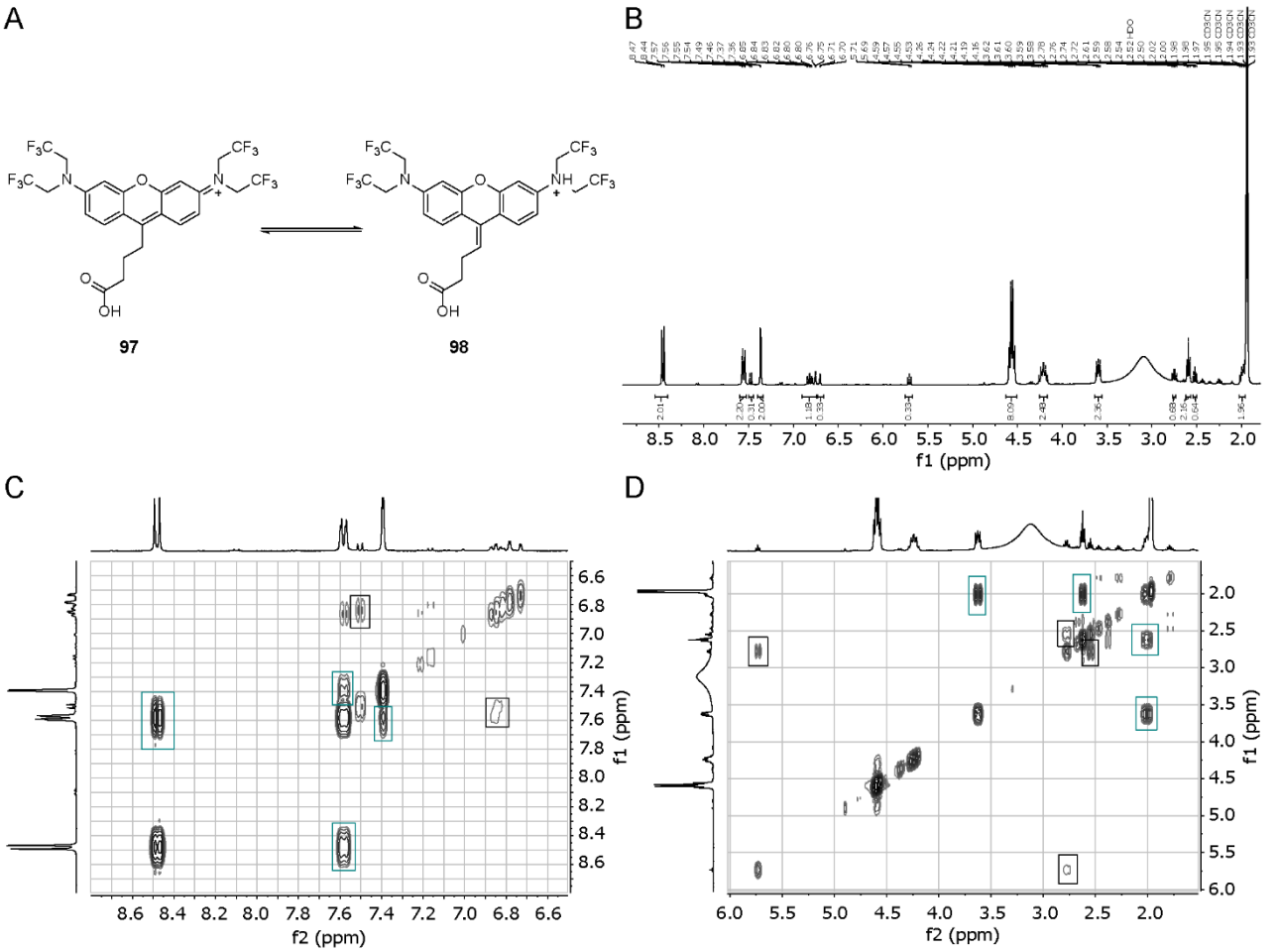

Supplementary Figure 2: ^{1}H NMR characterisation of the mixture of compounds **97** and **98**. (A) Chemical equilibrium of **97** and **98**. (B) ^{1}H NMR spectrum of the mixture. ^{1}H NMR (400 MHz, CD_3CN, signals of **97** are marked with [a], those from compound **98** with [b]; ratio **97** **98**$^{-1}$=3:1): δ 8.45[a] (d, J = 9.6 Hz, 2H), 7.56[a] (dd, J = 9.5, 2.7 Hz, 2H), 7.48[b] (d, J = 8.9 Hz, 1H), 7.37[a] (d, J = 2.7 Hz, 2H), 6.87 – 6.76[b] (m, 4H), 6.70[b] (d, J = 2.8 Hz, 1H), 5.71[b] (t, J = 6.9 Hz, 1H), 4.56[a] (q, J = 8.4 Hz, 8H), 4.29 – 4.13[b] (m, 8H), 3.67 – 3.54[a] (m, 2H), 2.75[b] (q, J = 7.2 Hz, 2H), 2.59[a] (t, J = 6.7 Hz, 2H), 2.51[b] (d, J = 7.2 Hz, 2H), 2.04 – 1.95[a] (m, 2H). The broad peak around 3.1 ppm could not be assigned (C-D) Excerpts from 2D homonuclear correlation spectroscopy (^{1}H COSY) spectrum. Aromatic region in (C) and aliphatic region in (D). Cross peaks corresponding to the two different compounds are highlighted (Compound **97** green, compound **98** black). Experiments were performed by J. Notbohm.

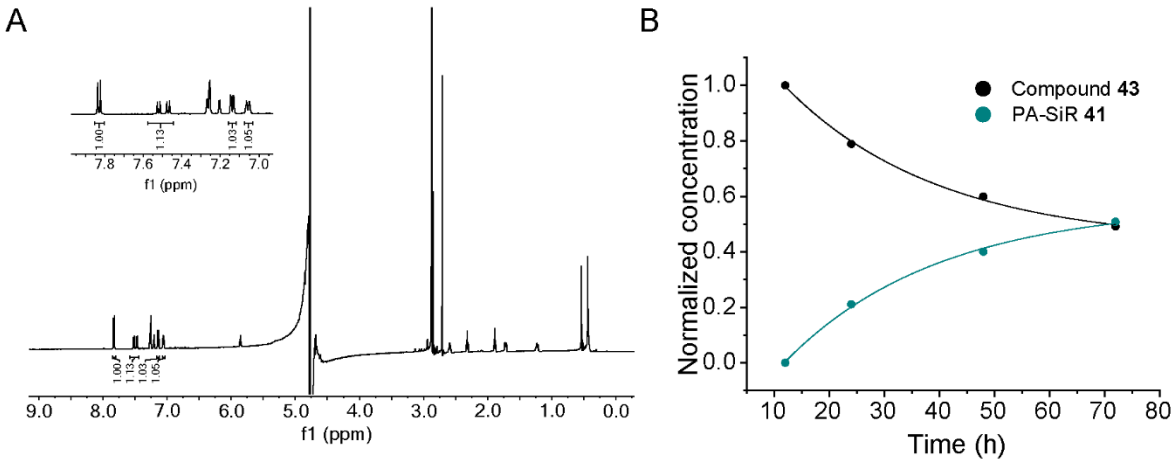

Supplementary Figure 3: Reaction kinetics of the back reaction to PA-SiR **41**. (A) ^{1}H NMR spectrum after full photoactivation of PA-SiR **41** and further 72 h in the dark. The peaks of PA-SiR **41** at 7.52, 7.46, 7.06, and 7.04 ppm as well as the peaks of compound **43** at 7.83 and 7.14 ppm were integrated and used to compare the relative amounts of both species. Similar measurements were performed after full conversion, 24 h and 48 h. After 72 h the experiment was stopped. (B) Normalised concentration of PA-SiR **41** and compound **43** over time. The kinetic constant k_5 or k_{-1} was determined to be 9.9±1.8 · 10^{-6} s^{-1} (fit parameter±standard error of the fit; Supplementary Table 3).

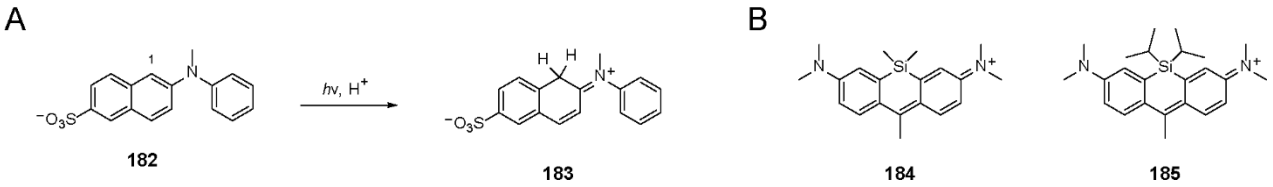

Supplementary Figure 4: Related photoinduced reaction and structure of activated PA-SiRs **184** and **185** for HOMO-LUMO calculations. (A) Photoinduced protonation of *N*-methyl-*N*-phenylamino-6-naphtalensulphonate (**182**) forming **183**. (B) Photoproducts of the photoactivation of PA-SiR **60** and a simplified, ^{i}Pr substituted PA-SiR whose HOMO and LUMO energies were calculated (Supplementary Table 9).

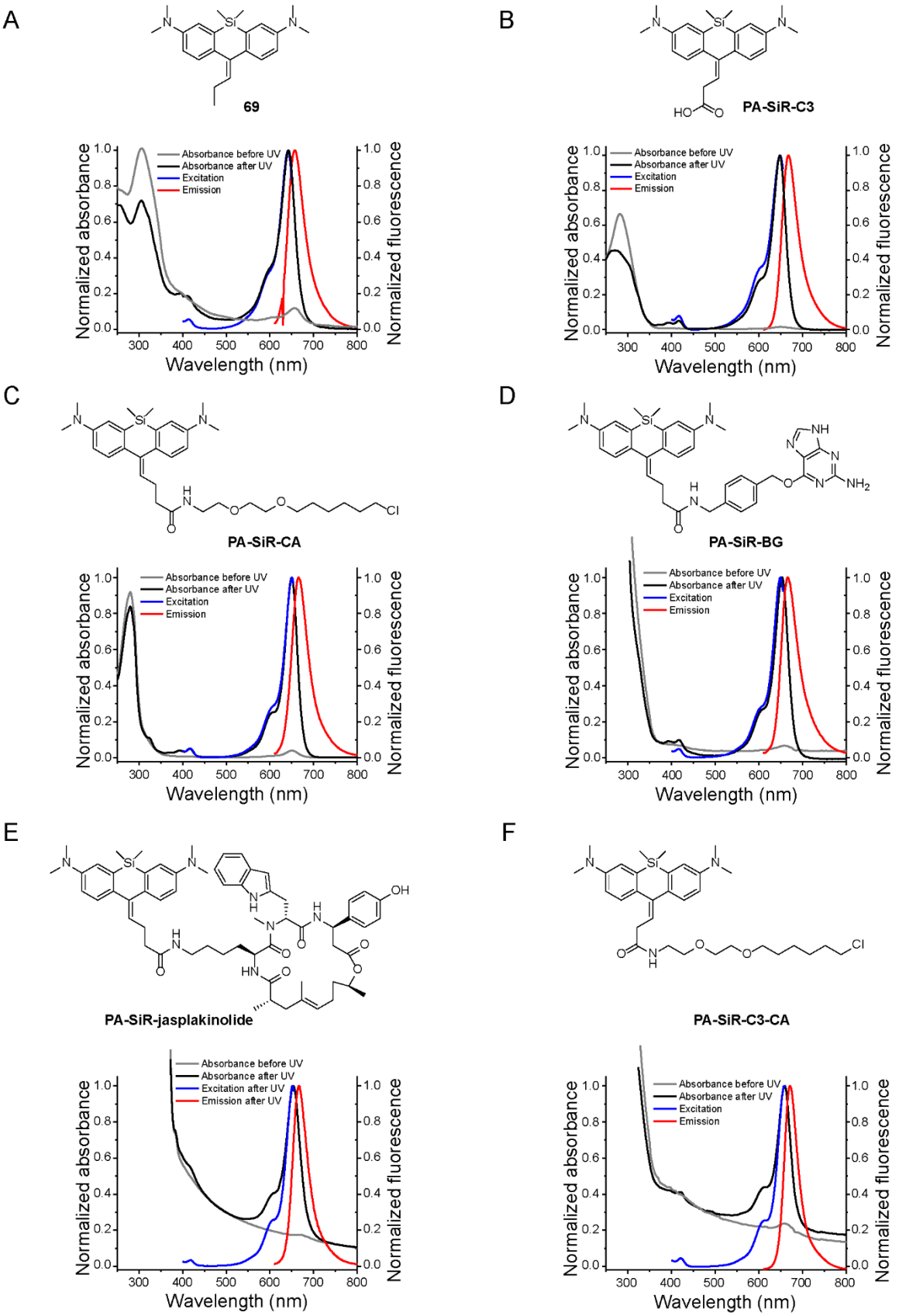

Supplementary Figure 5: Structures of six different PA-SiR derivatives and their absorbance spectra before and their excitation and emission spectra after UV-irradiation. (A) Compound **69**. (B) PA-SiR-C3. (C) PA-SiR-CA. (D) PA-SiR-BG. (E) PA-SiR-jasplakinolide. (F) PA-SiR-C3-CA.

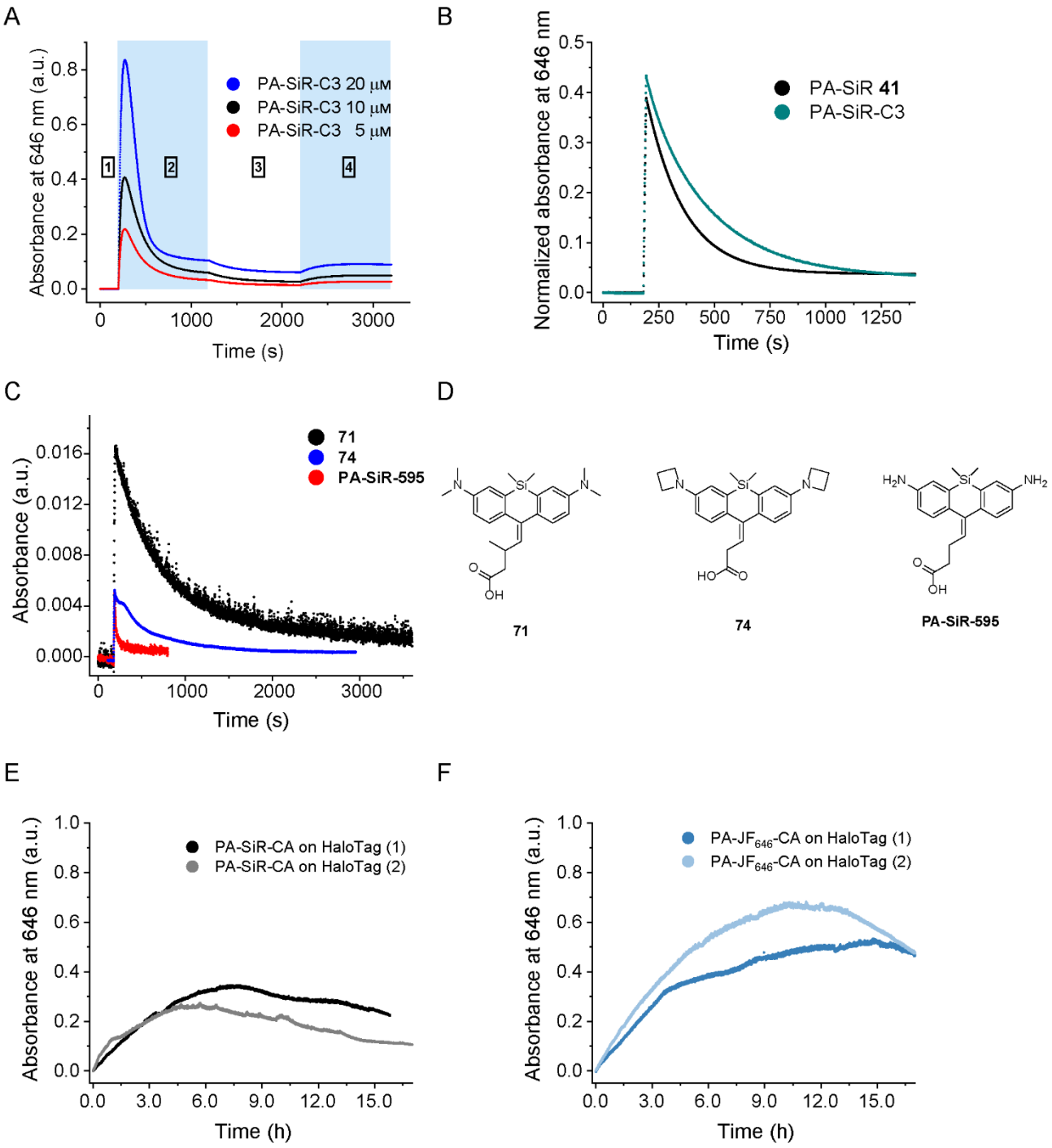

Supplementary Figure 6: Additional UV-Vis measurements. (A) Saturation experiment of PA-SiR-C3 at three different concentrations. The samples were irradiated during section 1, 2, and 4 (light blue color) but no irradiation was performed during section three. The fitted parameters from this experiment were used to calculate the extinction coefficient of the photoproduct at 646 nm. (B) Time dependent UV-Vis measurements of PA-SiR **41** and PA-SiR-C3 normalised to their extinction coefficients. The photoactivation efficiency of the two are very similar. (C) Preliminary time dependent absorbance measurements at 646 nm and 595 nm for compounds **71**, **74**, and PA-SiR595, respectively. For compound **74** photoactivation was performed using a monochromator (330 nm). (D) Structures of compounds **71**, **74**, and PA-SiR595. (E-F) Photoactivation of PA-SiR-CA and PA-JF_{646}-JF on HaloTag using 405 nm irradiation. Only when the solutions were exposed to 405 nm irradiation for multiple hours was full conversion reached.

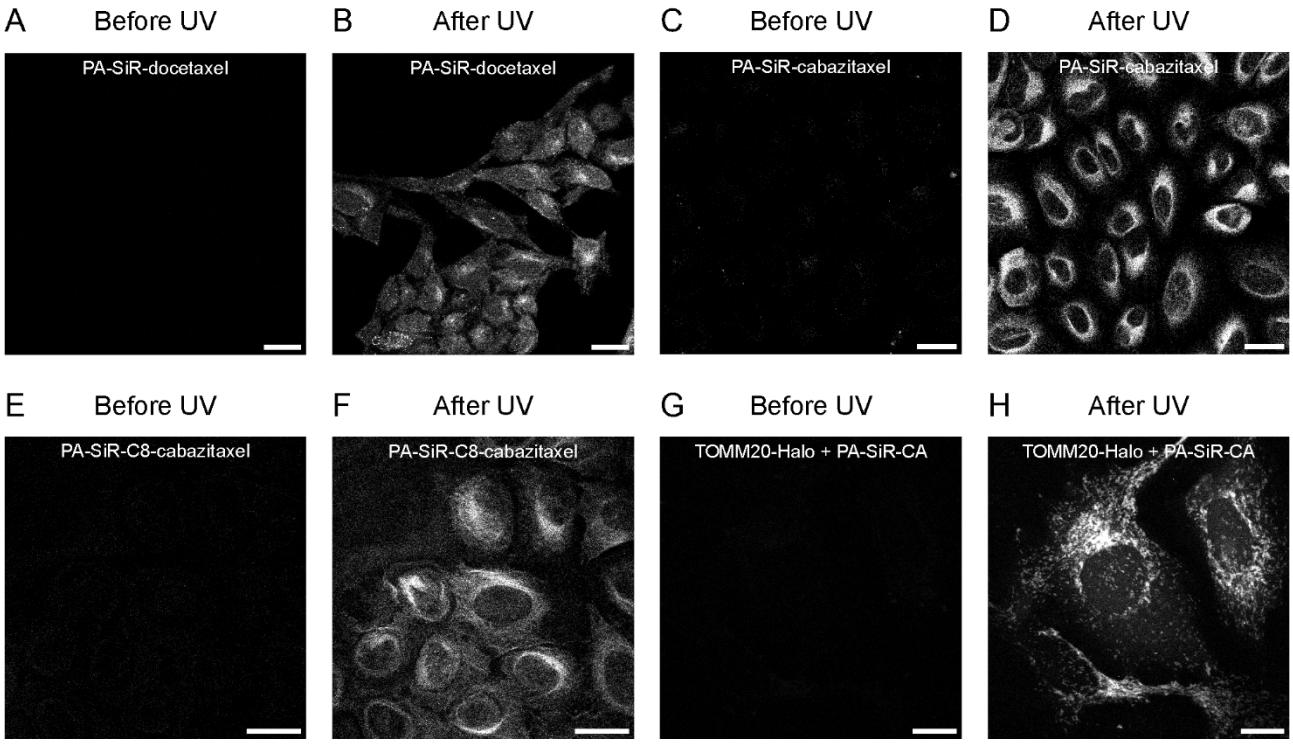

Supplementary Figure 7: Confocal microscopy images of transfection free probes and PA-SiR-CA. (A-B) U-2 OS cells stained with PA-SiR-docetaxel (1 µM, 2 h, microtubules) before (A) and after (B) photoactivation. Scale bars, 30 µm. (C-F) Confocal images of U-2 OS cells stained with PA-SiR-cabazitaxel (1 µM, 1 h, C-D, microtubules) or PA-SiR-C8-cabazitaxel (1 µM, 1 h, E-F, microtubules). Images shown before (C and E) and after (D and F) UV irradiation at 355 nm. Scale bars, 30 µm. (G-H) Confocal microscopy images of U-2 OS cells expressing Tomm20-Halo (outer mitochondrial membrane) stained with PA-SiR-CA (0.5 µM, 1.5 h) before (G) and after (H) photoactivation. Scale bar, 20 µm.

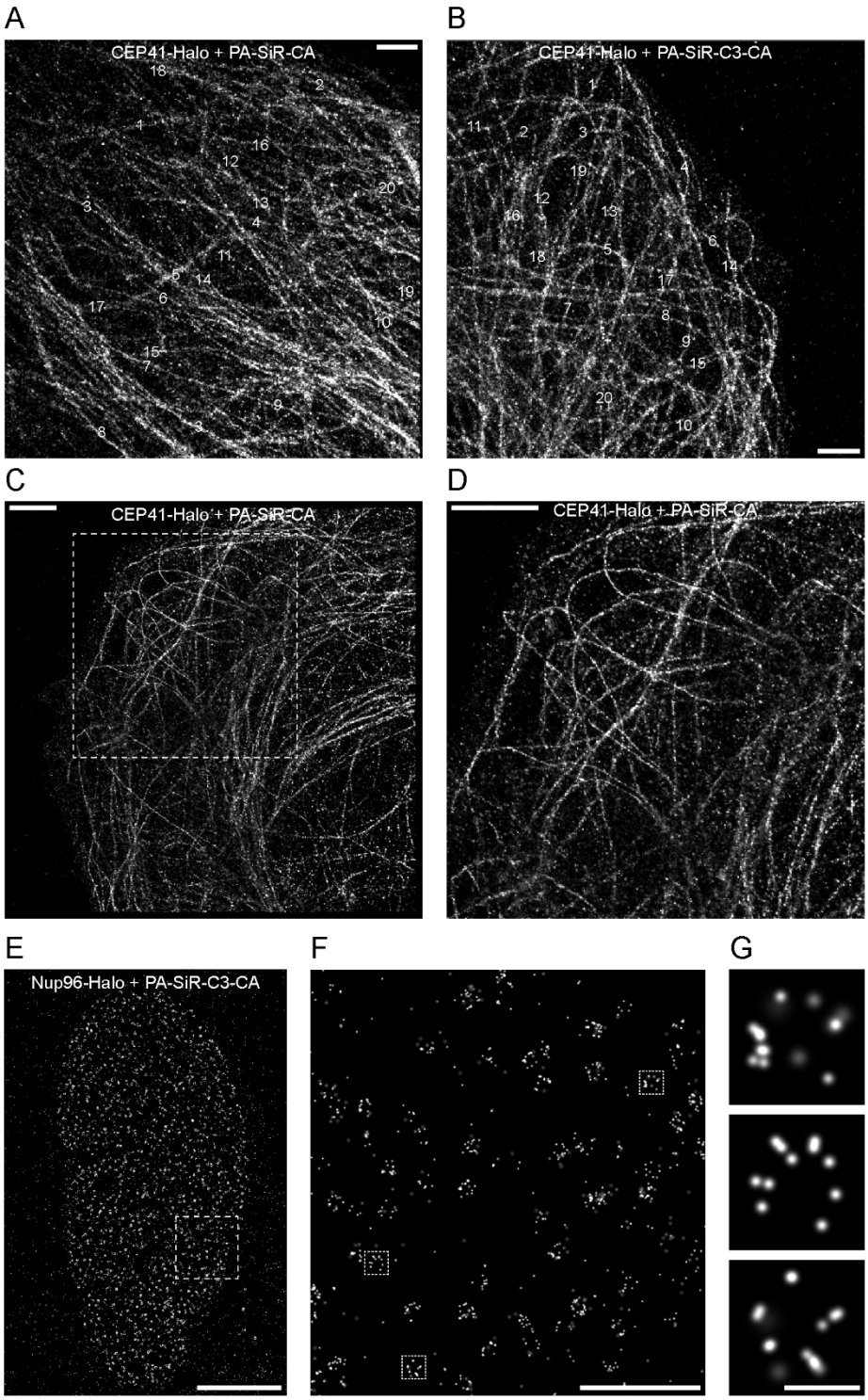

Supplementary Figure 8: Super-resolved images of HaloTag fusion proteins obtained by SMLM. (A-B) Fixed U-2 OS cells expressing Cep41-Halo (microtubules) stained with PA-SiR-CA (A) or PA-SiR-C3-CA (B, 1 µM, 2 h). The areas used for microtubule diameter quantification are indicated. Scale bars, 1 µm. (C-D) Fixed U-2 OS cells expressing Cep41-Halo (microtubules) stained with PA-SiR-CA (1 µM, 2 h) and treated with cysteamine (1 mM) right before image acquisition. Overview (C) and zoom-in of the indicated area in panel C (D). Scale bars, 2 µm. (E-G) Super-resolved images of U-2 OS cells expressing Nup96-Halo (nuclear pores) under their endogenous promotor stained with PA-SiR-C3-CA (1 µM, 2 h) Overview image (E), zoom-in from the region indicated in panel E (F), and three individual nuclear pores indicated in panel F following the same order top-bottom (G). Scale bars, 5 µm, 1 µm and 100 nm. Experiments were performed together with P. Hoess.

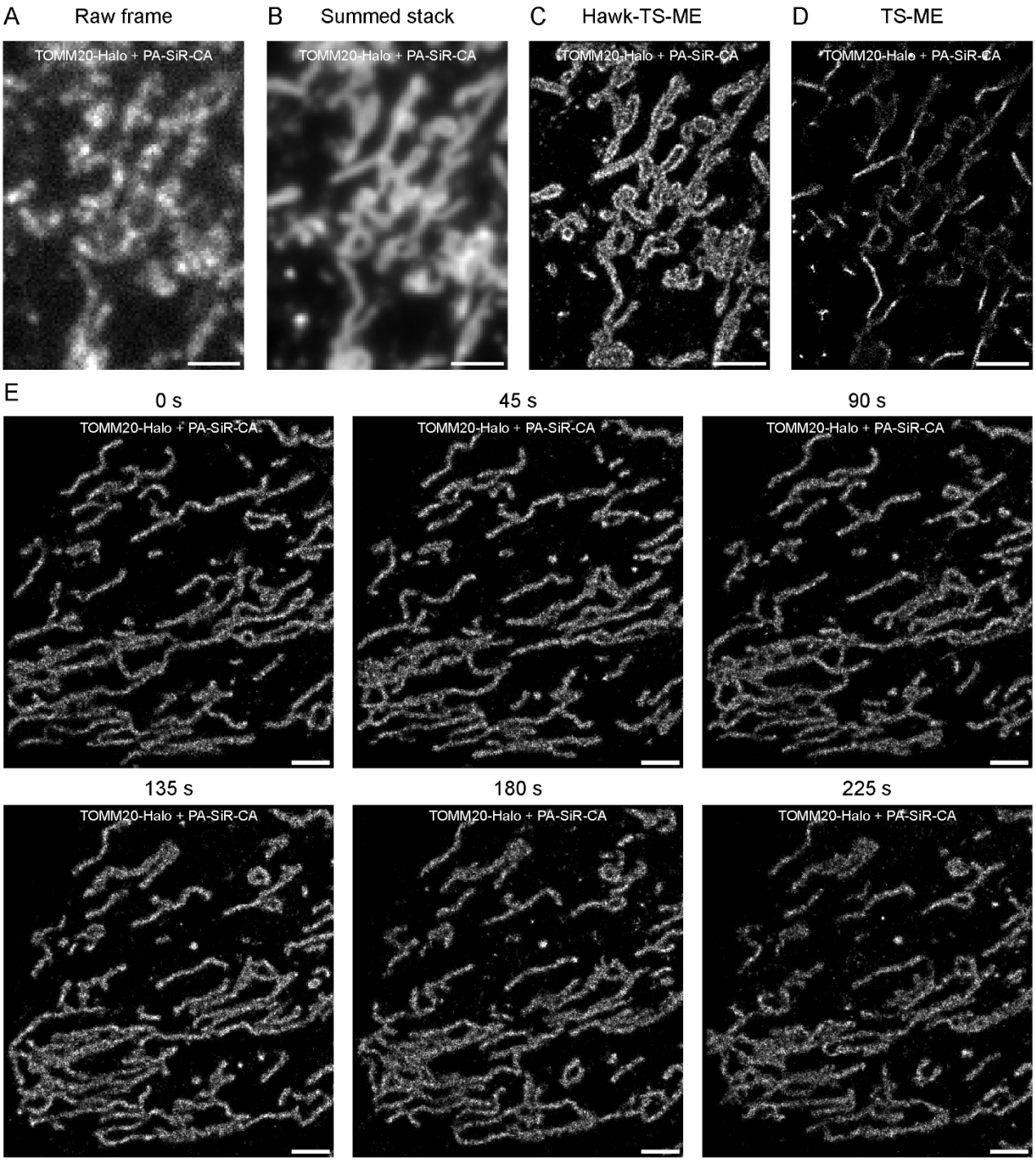

Supplementary Figure 9: Live-cell SMLM of TOMM20-Halo stained with PA-SiR-CA in live U-2 OS cells. (A) Single raw camera frame. (B) Summed stack over the first 10 s. (C) Super-resolved images reconstructed using Hawk[84] and multi-emitter fitting in ThunderSTORM. [264] (D) Super-resolved image reconstructed using only multi-emitter fitting in ThunderSTORM.[264] Scale bar, 2 µm. (E) Super-resolved images at different time points reconstructed using Hawk[84] and single-emitter fitting in ThunderSTORM.[264] Each image is reconstructed from 160 frames (8 s) over 4 min. Scale bar, 2 µm.

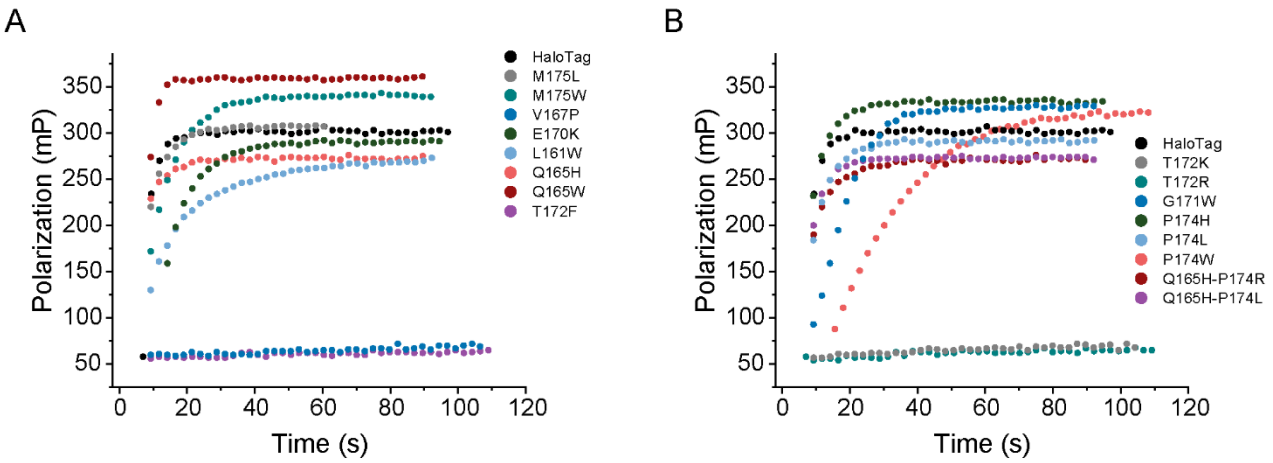

Supplementary Figure 10: Time-dependent polarisation measurements of HaloTag variants in combination with TMR-CA. (A-B) Measured data was split into panels (A) and (B), data points of HaloTag are depicted in both panels. Proteins (80 nM) were reacted with limiting amounts of TMR-CA (20 nM) to allow complete labeling of fluorophores. The data was fitted with a mono-exponential function (Supplementary Equation 5.) and the apparent first order rate constants k_{1app} and the values reached after reaction completion were compared with each other. Not all variants reached the plateau in 2 min. Representative of three replicates.

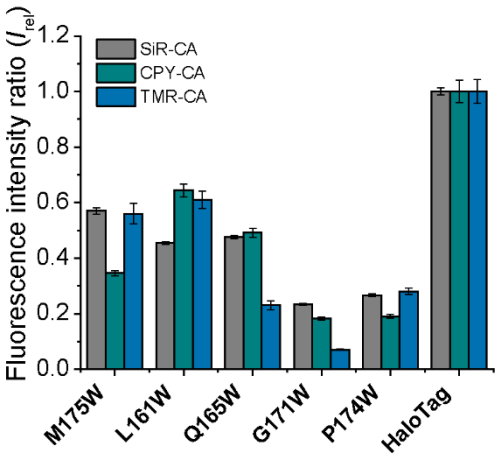

Supplementary Figure 11: Ratios of fluorescence intensity (I_{rel}) for five dimmer variants chosen to be investigated further. Values in combination with SiR-CA, CPY-CA, and TMR-CA are reported (mean±90% confidence interval, *N* = 4).

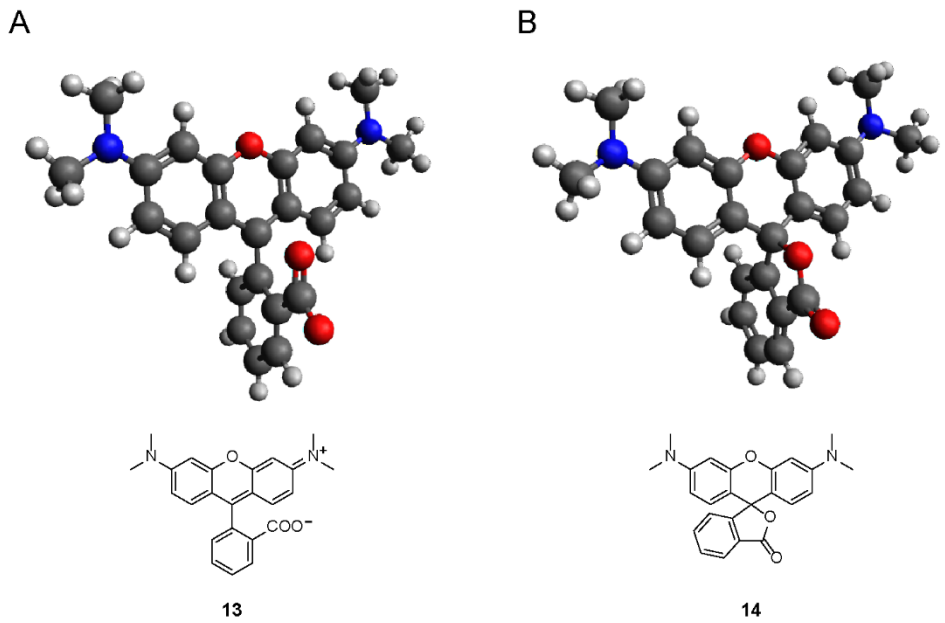

Supplementary Figure 12: Calculated structures of TMR in its quinoid **13** and spirolactone **14** form in water together with their chemical structures**.** (A) Quinoid **13**. (B) Spirolactone **14**.

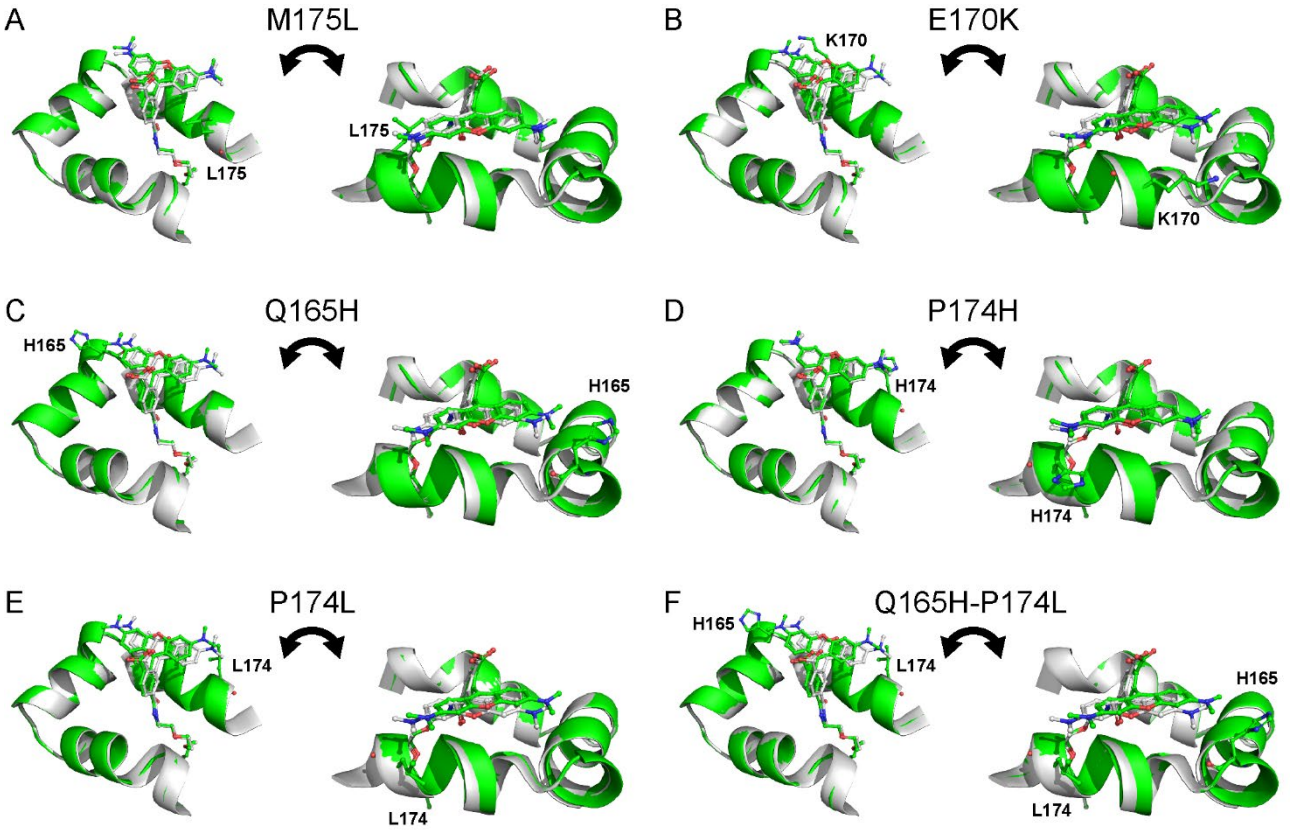

Supplementary Figure 13: Images of the crystal structures of six HaloTag variants. (A-F) HaloTag (142-177) in grey and the respective variant in green. TMR-CA (142-177) and the mutated amino acids are given in stick representation (oxygen – red, nitrogen – blue, carbon – grey/green). Two different views are given for each crystal structure. Crystallisation trials, optimisation and X-ray diffraction were performed by Dr. M Tarnawski and Professor I. Schlichting.

6.2 Supplementary tables

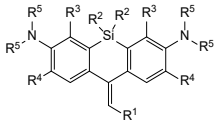

68

Supplementary Table 1: All attempted compounds. Yields of the different intermediates ant the final compounds isolated are given. * The product formed but interchanged between the ethylenic, quinoid, and spirolactone form at room temperature; ** The product formed but degraded in solution at room temperature; *** The product did not form.

Entry	R^1	R^2	R^3	R^4	R^5	128 (yield)	129 (yield)	68 (yield)
1	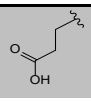	Me	H	H	Me	**57** (67%)	**58** (80%)	**41** (5%)
2	H	Me	H	H	Me	**57** (67%)	**58** (80%)	**62** (76%)
3		Me	H	H	Me	**57** (67%)	**58** (80%)	**69** (16%)
		Me	H	H	Me	**57** (67%)	**58** (80%)	**133** spiro (11%) **70** open (8%)
4		Me	H	H	Me	**57** (67%)	**58** (80%)	**173** Spiro (4%)
5		Me	H	H	Me	**57** (67%)	**58** (80%)	*
6		Me	H	H	Me	**57** (67%)	**58** (80%)	**71** (0.6%)
7		Me	H	H	Me	**57** (67%)	**58** (80%)	**
8		^{i}Pr	H	H	Me	**153** (31%)	**154** (73%)	**72** (6%)
9		Me	Me	H	Me	**176** (75%)	**177** (35%)	***
10	H	Me	Me	H	Me	**176** (75%)	**177** (35%)	***
11		Me	F	H	Me	**157** (73%)	**158** (78%)	**73** (21%)
12		Me	H	Me	Me	**180** (67%)	**181** (61%)	***
13	H	Me	H	Me	Me	**180** (67%)	**181** (61%)	***
14		Me	H	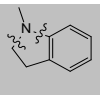		**167** (81%)	**76** (38%)	**
15		Me	H	H		**162** (54%)	**163** (38%)	**164** Spiro (1.9%) **74** open (0.8%)
16	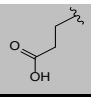	Me	H	H	H	Alternative synthesis	Alternative synthesis	**75** (0.3%)

Supplementary Table 2: Photophysical parameters of several PA-SiR analogues. $\lambda_{abs,max}$ absorption maximum, ε_{max} extinction coefficient, φ_{act} quantum yield of activation, $\lambda_{ex,\ max}$/ $\lambda_{em,\ max}$ excitation and emission maximum, φ quantum yield, τ and $\tau_{on\ POI}$ mean lifetime, N/D not determined, N/A not applicable, * $\lambda_{abs,\ max}$/ $\lambda_{em,\ max}$, ** from reference [117] , *** at 405 nm. Values are given as means±95% confidence interval. Except for φ_{act}±sem.[203]

	PA-SiR before photoactivation			Photoproduct				
#	$\lambda_{abs,max}$ [nm]	ε_{max} [$M^{-1}cm^{-1}$]	φ_{act} [%]	$\lambda_{ex,\ max}$/ $\lambda_{em,\ max}$ [nm]	$\varepsilon_{max,\ 646\ nm}$ [$M^{-1}cm^{-1}$]	φ [%]	$\tau_{PBS\ or\ BSA}$ [s]	$\tau_{on\ POI}$ [s]
PA-SiR	276	17,000±3,000 *N* = 10	13.3±2.3 *N* = 3	646/664	90,000±18,000 *N* = 3	19.0±2.4 *N* = 3	169±9 *N* = 3	N/A
SiR-COOH	N/A	N/A	N/A	645/661*,**	100,000**	39**	N/A	N/A
69	314	16,000±5,000 *N* = 9	N/D	642/656	N/D	13±10 *N* = 3	200±70 *N* = 3	N/A
62	N/D	N/D	N/D	N/D	N/D	11±8 *N* = 3	55±21 *N* = 3	N/A
PA-SiR-C3	281	16,000±3,000 *N* = 9	29±13 *N* = 3	648/668	39,000±7,000 *N* = 3	15.6±1.5 *N* = 3	271±15 *N* = 3	N/A
72	N/D	N/D	N/D	N/D	N/D	16.1±0.7 *N* = 3	460±60 *N* = 3	N/A
PA-SiR-CA	333	33,000±5,000 *N* = 9	0.86±0.07 *N* = 3 0.09±0.04 *N* = 2***	650/666	180,000±30,000 *N* = 3	29.2±1.2 *N* = 4	40±60 *N* = 3	6±3 *N* = 3
PA-SiR-C3-CA	329	20,000±3,000 *N* = 9	3.9±0.3 *N* = 3	658/672	15,000±3,000 *N* = 3	29±5 *N* = 3	100±18 *N* = 3	7±4 *N* = 3
PA-SiR-BG	294	19,000±6,000 *N* = 10	N/D	650/666	N/D	11.1±2.0 *N* = 3	84±19 *N* = 3	30±50 *N* = 3
PA-SiR-jasplakinolide	298	21,000±7,000 *N* = 9	N/D	651/666	N/D	3±6 *N* = 3	N/A	92±3 *N* = 3

Supplementary Table 3: Kinetic rate constant from the ^{1}H NMR measurements. It is not clear if this reaction proceeds through k_5 or k_{-2} and k_{-1}, in which case k_{-1} would be the rate determining step and the measured kinetic constant would correspond to k_{-1}. k kinetic constant and its standard error se_k (Supplementary Figure 3B).

Name	k [s^{-1}]	se_k [s^{-1}]
PA-SiR 41	9.95E−6	1.85E−6

Supplementary Table 4: Quantum yields of photoactivation of different photoactivatable fluorophores including the PA-FP mKikGR and kikGR. Values are given as mean±sem from three or two measurements (Supplementary Figure 6 C, D).[203]

Name	φ_{act} [%]	Condition	Citation
PA-SiR 41	13.3±2.3, *N* = 3	340 nm	This work
PA-SiR-C3	29±13, *N* = 3	340 nm	This work
PA-SiR-CA on HaloTag	0.86±0.07, *N* = 3	340 nm	This work
PA-SiR-CA on HaloTag	0.09±0.04, *N* = 2	405 nm	This work
PA-SiR-C3-CA on HaloTag	3.9±0.3, *N* = 3	340 nm	This work
PA-JF$_{549}$	2.2	365 nm	[191]
PA-JF$_{646}$	0.07±0.03, *N* = 2	405 nm	This work
PFF (Fluxional- Rhodamine)	0.4 and 0.5	405 nm pH = 5, 7.4	[35]
mKikGR	0.75	405 nm	[278]
kikGR	0.47	405 nm	[278]

Supplementary Table 5: Fit parameters from the saturation experiments fitting the third section of PA-SiR, PA-SiR-C3 (C3), and PA-SiR-C3-CA (C3Halo) with a mono-exponential curve according to Supplementary Equation 5. The respective values for PA-SiR-CA (Halo) were found through fitting the first section in a similar manner. The concentration at which the experiments were performed is given in µM. τ decay constant and its sd sd_τ; A amplitude and its sd sd_A; y_0 offset and its sd sd_{y0}, along with the derived parameters: $A_{eq} = y_0$; $A_{x=0} = A + A_{eq}$; $K_2 = (A_{x=0} - A_{eq}) \cdot A_{eq}^{-1}$; $k_{app} = \tau^{-1}$; $k_{-2} = k_{app} \cdot (K_2 + 1)^{-1}$; $k_2 = k_{app} - k_{-2}$; $K_{-1} = k_2 \cdot k_{-2}^{-1}$; K = equilibrium constant from Supplementary Table 8 and Supplementary Table 10 for the respective compound; $A_{sat} = K \cdot A_{eq} + A_{eq}$. These values were used to calculate the extinction coefficients at 646 nm. N/A not applicable (Figure 19B, Supplementary Figure 6A, and Figure 23C, D).[203]

	Fit Parameters						Calculated								
Name	τ [s]	sd_τ [s]	A [a.u.]	sd_A [a.u.]	y_0 [a.u.]	sd_{y0} [a.u.]	A_{eq} [a.u.]	$A_{x=0}$ [a.u.]	K_2	k_{app} [s^{-1}]	k_{-2} [s^{-1}]	k_2 [s^{-1}]	K_{-2}	K	A_{sat} [a.u.]
PA-SiR/5	171.26	0.16	0.028	1.5E−5	0.040	3.9E−6	0.040	0.069	0.69	5.84E−3	3.45E−3	2.39E−3	1.44	9.866	**0.440**
PA-SiR/10	173.14	0.16	0.057	3.3E−5	0.084	6.8E−6	0.084	0.141	0.68	5.78E−3	3.43E−3	2.35E−3	1.46	9.866	**0.911**
PA-SiR/20	172.73	0.12	0.125	4.9E−5	0.182	1.1E−5	0.182	0.307	0.69	5.79E−3	3.42E−3	2.36E−3	1.45	9.866	**1.974**
C3/5	268.05	0.36	0.018	9.0E−6	0.014	6.4E−6	0.014	0.032	1.34	3.73E−3	1.59E−3	2.14E−3	0.74	13.212	**0.192**
C3/10	274.48	0.26	0.031	1.1E−5	0.026	8.1E−6	0.026	0.057	1.23	3.64E−3	1.64E−3	2.01E−3	0.82	13.212	**0.363**
C3/20	269.74	0.27	0.041	1.5E−5	0.059	1.1E−5	0.059	0.101	0.70	3.71E−3	2.18E−3	1.52E−3	1.43	13.212	**0.843**
C3Halo/2.5	388.55	0.79	0.044	4.0E−5	0.020	1.9E−5	0.020	0.064	2.25	2.57E−3	7.93E−4	1.78E−3	0.45	0.657	**0.032**
C3Halo/5	441.00	0.69	0.091	5.6E−5	0.032	3.5E−5	0.032	0.123	2.82	2.27E−3	5.93E−4	1.67E−3	0.35	0.657	**0.053**
C3Halo/10	594.43	1.30	0.196	1.4E−4	0.065	1.3E−4	0.065	0.261	3.02	1.68E−3	4.19E−4	1.26E−3	0.33	0.657	**0.108**
Halo/5	N/A	N/A	N/A	N/A	0.929	1.7E-04	0.929	N/A	N/A	N/A	N/A	N/A	N/A	0.020	**0.947**
Halo/10	N/A	N/A	N/A	N/A	1.832	2.5E-04	1.832	N/A	N/A	N/A	N/A	N/A	N/A	0.020	**1.869**
Halo/15	N/A	N/A	N/A	N/A	2.432	2.5E-04	2.432	N/A	N/A	N/A	N/A	N/A	N/A	0.020	**2.480**

Supplementary Table 6: Fit parameters from the saturation experiments fitting the first section of PA-SiR, PA-SiR-CA, PA-SiR-C3-CA, and PA-SiR-C3-CA with a mono-exponential curve according to Supplementary Equation 5. τ decay constant and its sd sd_τ. (Figure 19B, Supplementary Figure 6A, and Figure 23C, D).[203]

Name	τ [s]	sd_τ [s]	*N*	Wavelength of irradiation
PA-SiR 41	19.40	0.36	3	340 nm
PA-SiR-CA	28.24	1.99	3	340 nm
PA-SiR-CA	12,000	6,000	2	405 nm
PA-SiR-C3	20.99	0.80	3	340 nm
PA-SiR-C3-CA	10.32	0.72	3	340 nm
PA-JF$_{646}$	15,000	1,000	2	405 nm

Supplementary Table 7: Fit parameters from the fatigue experiment fitting the repeated increase-decrease sequences with a mono-exponential curve according to Supplementary Equation 5. y_0 offset and its standard error se_{y0}; **A** amplitude and its standard error se_A; along with the derived parameters: $A_{eq} = y_0$; $A_{x=0} = A + A_{eq}$; $\Delta A = A_{x=0}[i] - y_0[i-1]$; $se_{\Delta A}$ propagated standard error; **ΣΔA** summed $\Delta A + A_{x=0}[1]$; $se_{\Sigma\Delta A}$ propagated standard error; theoretical $\Sigma\Delta A = K \cdot A_{eq} + A_{eq}$ (*K* from Supplementary Table 8); $se_{theor\ \Sigma\Delta A}$ propagated standard error (Figure 19D).

	Fit Parameters				Calculated Values				
Iteration	y_0 [a.u.]	se_{y0} [a.u.]	**A** [a.u.]	se_A [a.u.]	$A_{x=0}$ [a.u.]	**ΔA** [a.u.]	$se_{\Delta A}$ [a.u.]	**ΣΔA** [a.u.]	$se_{\Sigma\Delta A}$ [a.u.]
1	0.033	1.34E−5	0.313	3.19E−5	0.346	0.346	3.46E−5	0.346	3.46E−5
2	0.055	1.42 E−5	0.209	3.43E−5	0.264	0.231	3.95E−5	0.577	3.66E−3
3	0.069	1.11E−5	0.138	2.70E−5	0.207	0.152	3.25E−5	0.729	3.66E−3
4	0.078	8.74E−6	0.093	2.06E−5	0.171	0.102	2.49E−5	0.831	3.66E−3
5	0.083	1.01E−5	0.063	2.32E−5	0.146	0.069	2.67E−5	**0.900**	3.66E−3
6	0.086	1.02E−5	0.044	1.90E−5	0.130	0.047	2.38E−5	0.947	3.66E−3
7	0.089	7.66E−6	0.032	1.95E−5	0.120	0.034	2.34E−5	0.981	3.66E−3
8	0.090	6.39E−6	0.024	1.82E−5	0.114	0.025	2.08E−5	1.006	3.66E−3
9	0.090	7.70E−6	0.019	1.63E−5	0.110	0.020	1.91E−5	1.026	3.66E−3
10	0.091	7.66E−6	0.015	1.54E−5	0.106	0.015	1.88E−5	1.041	3.66E−3
11	0.091	7.83E−6	0.014	1.60E−5	0.105	0.014	1.94E−5	1.055	3.66E−3
12	0.091	8.45E−6	0.012	1.70E−5	0.103	0.012	2.05E−5	1.068	3.66E−3
13	0.091	8.08E−6	0.011	1.69E−5	0.102	0.011	2.05E−5	1.079	3.66E−3
14	0.090	8.14E−6	0.011	1.61E−5	0.101	0.011	1.98E−5	1.089	3.66E−3

Supplementary Table 8: Fit parameters from the UV-Vis experiments following the decay in absorbance of PA-SiR and its analogues under various conditions. The decay was fitted with a mono-exponential curve according to Supplementary Equation 5. τ decay constant and its sd sd_τ; A amplitude and its sd sd_A; y_0 offset and its sd sd_{y0}, along with the derived parameters: $A_{eq} = y_0$; $A_{x=0} = A + A_{eq}$; $K_2 = (A_{x=0} - A_{eq}) \cdot A_{eq}^{-1}$; $k_{app} = \tau^{-1}$; $k_{-2} = k_{app} \cdot (K_2 + 1)^{-1}$; $k_2 = k_{app} - k_{-2}$; $K_{-2} = k_2 \cdot k_{-2}^{-1}$. *Negative equilibrium values are within the experimental error of the instrument and were set to 0 for further calculations. ** Cysteamine (0.1 mM). N/D not determined. Values are given as means±sd from three measurements (Figure 19E, Figure 20A, B, and Figure 21A).[203]

	Fit Parameters						Calculated						
Name/pH	τ [s]	sd_τ [s]	A [a.u.]	sd_A [a.u.]	y_0 [a.u.]	sd_{y0} [a.u.]	A_{eq} [a.u.]	$A_{x=0}$ [a.u.]	K_2	k_{app} [s^{-1}]	k_{-2} [s^{-1}]	k_2 [s^{-1}]	K_{-2}
PA-SiR 41 PBS	169.50	3.49	0.347	0.008	0.035	0.002	0.035	0.382	9.87	5.90E−3	5.43E−4	5.36E−3	0.10
PA-SiR 41 PBS + UV	-	-	-	-	-	-	-	-	6.09	6.00E−3	8.46E−4	5.15E−3	0.16
10.6	180.19	8.60	0.283	0.014	0.004	0.005	0.004	0.287	74.93	5.55E−3	7.31E−5	5.48E−3	0.01
8.8	171.83	5.29	0.303	0.021	0.010	0.006	0.010	0.313	30.75	5.82E−3	1.83E−4	5.64E−3	0.03
8.1	171.83	4.12	0.310	0.021	0.019	0.006	0.019	0.329	16.63	5.82E−3	3.30E−4	5.49E−3	0.06
7.2	169.55	2.85	0.322	0.045	0.033	0.004	0.033	0.355	9.65	5.90E−3	5.54E−4	5.34E−3	0.10
6.6	114.99	0.65	0.150	0.003	0.121	0.003	0.121	0.271	1.23	8.70E−3	3.90E−3	4.80E−3	0.81
6.2	96.94	2.78	0.094	0.007	0.146	0.001	0.146	0.240	0.64	1.03E−2	6.27E−3	4.04E−3	1.55
5.8	93.18	22.73	0.043	0.004	0.130	0.004	0.130	0.173	0.33	1.07E−2	8.08E−3	2.65E−3	3.05
5.2	97.69	26.62	0.016	0.002	0.057	0.002	0.057	0.072	0.28	1.02E−2	8.02E−3	2.22E−3	3.62
4.8	115.09	65.13	0.009	0.001	0.020	0.002	0.020	0.028	0.45	8.69E−3	6.01E−3	2.68E−3	2.24
4.1	114.50	7.21	0.006	4.2E−4	0.005	2.3E−4	0.005	0.010	1.16	8.73E−3	4.05E−3	4.68E−3	0.87
PA-SiR 41 ACN	327.82	23.16	0.253	0.008	0.027	0.002	0.027	0.280	9.20	3.05E−3	2.99E−4	2.75E−3	0.11
PA-SiR 41 Dioxane	320.75	47.96	0.159	0.015	−0.020*	0.012	0.000	0.159	N/D	3.12E−3	N/D	N/D	N/D
PA-SiR 41 DMSO	157.26	12.47	0.119	0.016	−0.013*	0.015	0.000	0.119	N/D	6.36E−3	N/D	N/D	N/D
PA-SiR 41**	444.20	26.28	0.069	0.005	0.022	0.001	0.022	0.091	3.14	2.25E−3	5.43E−4	1.71E−3	0.32
69	202.87	28.89	0.009	0.001	−0.002*	0.001	0.000	0.009	N/D	4.93E−3	N/D	N/D	N/D
62	54.92	8.49	0.086	0.002	0.008	0.004	0.008	0.094	10.25	1.82E−2	1.62E−3	1.66E−2	0.10
PA-SiR-C3	271.19	6.02	0.172	0.003	0.013	0.001	0.013	0.185	13.21	3.69E−3	2.59E−4	3.43E−3	0.08
72	460.09	22.57	0.057	0.011	0.050	0.007	0.050	0.106	1.14	2.17E−3	1.02E−3	1.16E−3	0.88

Supplementary Table 9: HOMO and LUMO energies for the activated PA-SiRs **184** and **185**. Energies of the two molecular orbitals as well as the HOMO-LUMO gap is given. The LUMO of the activated PA-SiR **185** is higher in energy and therefore compound **185** is less electrophilic (Supplementary Figure 4B).

Name	HOMO [hartree]	LUMO [hartree]	Gap [hartree]
184	−0.29304	−0.21011	−0.08293
185	−0.29220	−0.20868	−0.08352

Supplementary Table 10: Fit parameters from the UV-Vis experiments of different PA-SiR probes following the decay in absorbance. The decay was fitted with a mono-exponential curve according to Supplementary Equation 5. τ decay constant and its sd sd_τ; A amplitude and its sd sd_A; y_0 offset and its sd sd_{y0}, along with the derived parameters: $A_{eq} = y_0$; $A_{x=0} = A + A_{eq}$; $K_2 = (A_{x=0} - A_{eq}) \cdot A_{eq}^{-1}$; $k_{app} = \tau^{-1}$; $k_{-2} = k_{app} \cdot (K_2 + 1)^{-1}$; $k_2 = k_{app} - k_{-2}$; $K_{-2} = k_2 \cdot k_{-2}^{-1}$. *negative equilibrium values are within the experimental error of the instrument and were set to 0 for further calculations. N/D not determined. Values are given as means±sd from three measurements (Figure 23A, B, E, F).[203]

	Fit Parameters						Calculated						
Name	τ [s]	sd_τ [s]	A [a.u.]	sd_A [a.u.]	y_0 [a.u.]	sd_{y0} [a.u.]	A_{eq} [a.u.]	$A_{x=0}$ [a.u.]	K_2	k_{app} [s^{-1}]	k_{-2} [s^{-1}]	k_2 [s^{-1}]	K_{-2}
PA-SiR-CA BSA	41.98	23.46	0.012	0.001	0.006	0.002	0.006	0.017	1.99	2.38E−2	7.97E−3	1.59E−2	0.50
PA-SiR-CA Halo	5.74	1.19	0.013	0.004	0.593	0.013	0.593	0.606	0.02	1.74E−1	1.70E−1	3.87E−3	43.99
PA-SiR-C3-CA BSA	105.02	7.34	0.018	4.4E−04	−0.000*	0.001	0.000	0.018	N/D	9.52E−3	N/D	N/D	N/D
PA-SiR-C3-CA Halo	6.51	1.55	0.062	0.002	0.095	0.002	0.095	0.157	0.66	1.54E−1	9.27E−2	6.09E−2	1.52
PA-SiR-PEG1-CA BSA	110.28	2.40	0.053	0.000	0.005	0.001	0.005	0.058	9.67	9.07E−3	8.50E−4	8.22E−3	0.10
PA-SiR-PEG1-CA Halo	239.92	53.17	0.035	0.012	0.066	0.008	0.066	0.101	0.53	4.17E−3	2.73E−3	1.44E−3	1.89
PA-SiR-PEG2-CA BSA	124.47	2.91	0.056	0.002	0.010	0.001	0.010	0.066	5.69	8.03E−3	1.20E−3	6.83E−3	0.18
PA-SiR-PEG2-CA Halo	240.14	18.60	0.018	0.002	0.038	0.006	0.038	0.055	0.47	4.16E−3	2.84E−3	1.32E−3	2.15
PA-SiR-BG BSA	84.10	7.49	0.011	0.001	0.002	0.001	0.002	0.014	4.68	1.19E−2	2.09E−3	9.80E−3	0.21
PA-SiR-BG SNAP	32.66	18.20	0.010	0.003	0.026	0.007	0.026	0.036	0.37	3.06E−2	2.23E−2	8.35E−3	2.67
PA-SiR-jasplakinolide	92.45	1.35	0.032	0.005	0.002	0.002	0.002	0.035	14.50	1.08E−2	6.98E−4	1.01E−2	0.07

Supplementary Table 11: Fit parameters from the pH experiments fitting peak shaped data with a Gaussian curve according to Supplementary Equation 6. y_0 offset and its standard error se_{y0}; **xc** center and its standard error se_{xc}; w width and its standard error se_w; A area and its standard error se_A; $X^2$the reduced chi-squared and R^2 the squared correlation coefficient are given (Figure 19F).[203]

Name	y_0 [a.u.]	se_{y0} [a.u.]	xc	se_{xc}	w	se_w	A	se_A	X^2	R^2
$A_{eq, norm}$	0.000	0.095	**5.339**	0.115	1.972	0.283	2.564	0.560	16.507	0.984
A_{eq}	0.028	0.003	**6.130**	0.017	1.274	0.028	1.568	0.034	15.462	0.999

Supplementary Table 12: Fitting parameters of the maximal absorbance directly after photoactivation fitted with a sigmoidal curve according to Supplementary Equation 7. a amplitude and its standard error se_a; **xc** center and its standard error se_{xc}; k coefficient and its standard error se_k; $X^2$the reduced chi-squared and R^2 the squared correlation coefficient are given (Figure 19F).[203]

Name	a [a.u.]	se_a [a.u.]	xc	se_{xc}	k	se_k	X^2	R^2
A_{max}	0.900	0.032	**5.731**	0.084	2.465	0.435	0.004	0.971

Supplementary Table 13: Fit parameters form the cysteamine experiment to evaluate the EC_{50} according to Supplementary Equation 8. **A1** and **A2** asymptotes and their standard errors sd_{A1} and sd_{A2}; **LOGx0** center and its standard error se_{LOGx0}; p hill slope and its standard error se_p; **EC50** derived parameter concentration at half response and its standard error se_{EC50}; $X^2$the reduced chi-squared and R^2 the squared correlation coefficient are given (Figure 24A).[203]

Name	A1	se_{A1}	A2	se_{A2}	Logx0	se_{Logx0}	p	se_p	EC50	se_{EC50}	X^2	R^2
PA-SiR 41	−0.0064	0.0083	0.9568	0.0103	−3.7167	0.0205	−1.3449	0.0647	**1.92E−4**	9.04E−6	0.001	0.997
PA-SiR-CA	−0.0043	0.0207	0.8989	0.0119	−2.5127	0.0326	−1.5812	0.1251	**3.07E−3**	2.30E−4	0.001	0.991
PA-SiR-C3-CA	0.0013	0.0108	0.9842	0.0097	−3.2101	0.0186	−1.2019	0.0699	**6.16E−4**	2.64E−5	0.001	0.997

Supplementary Table 14: Microscopy parameters.

Image	Label	Ligand	Microscope	Excitation [nm]	Exposure time / Pixel dwell time	Activation [nm]	Pinhole	Objective	Size	Fixed-live	Emission [nm]	Comment
25A, B	H2B-Halo	PA-SiR-CA	Confocal	631	0.6 µs	355	1	40x/1.10 water	1024x 1024	Live	777-800	Max projection
25C, D	H2B-Halo	PA-SiR-CA	Widefield	635 635/16	500 ms	365 365/10	-	40x/1.10 water	-	Live	720/100	
25E-J	H2B-Halo	Respective fluorophore	Confocal	631	0.25 µs	355	1	40x/1.10 water	2496x 2496	Live	751-779	
25K	H2B-Halo	PA-SiR-F-CA	Confocal	631	0.25 µs	355	1	40x/1.10 water	488x4 88	Live	751-779	
25L	H2B-Halo	PA-SiR-C3-CA	Confocal	631	0.6 µs	355	1	40x/1.10 water	1048x 1048	Live	777-800	
25M	H2B-SNAP	PA-SiR-BG	Confocal	631	0.6 µs	355	1	40x/1.10 water	1048x 1048	Live	777-800	
25N	H2B-SNAP	PA-SiR-CP	Confocal	631	0.7 µs	355	1	63x/1.20 water	1752x 1752	Live	751-779	
25O	CEP41-Halo	PA-SiR-CA	Confocal	631	0.25 µs	355	1	40x/1.10 water	2488x 2488	Live	751-779	
25P	LA-Halo	PA-SiR-CA	Confocal	631	0.475 µs	355	1	40x/1.10 water	1288x 1288	Live	751-779	
26A	H2B-Halo	Respective fluorophore	Widefield	635 635/16	500 ms	365 365/10	-	40x/1.10 water	-	Live	720/100	Stability
26B	H2B-Halo	Respective fluorophore	Widefield	635 635/16	500 ms	365 365/10	-	40x/1.10 water	-	Live	720/100	50 ms act
26C	H2B-Halo	Respective fluorophore	Confocal	631	0.6 µs	355	1	40x/1.10 water	1024x 1024	Live	777-800	Max projection
26D	H2B-SNAP	Respective fluorophore	Confocal	631	0.6 µs	355	1	40x/1.10 water	1048x 1048	Live	777-800	
27A,B	none	PA-SiR-jasplakinolide	Confocal	631	0.225 µs	355	1	63x/1.40 oil	2688x 2688	Live	751-779	
27C,D	none	PA-SiR-Hoechst	Confocal	631	0.225 µs	355	1	63x/1.40 oil	2640x 2640	Live	751-779	
27E,F	none	PA-SiR-pepstatin A	Confocal	631	0.875 µs	355	1	63x/1.20 water	1392x 1392	Live	751-779	
27G,H	none	PA-SiR-C8-docetaxel	Confocal	631	0.3 µs	355	1	63x/1.40 oil	2000x 2000	Live	751-779	
28B-E 31D	Halo:EGFP: SNAP	Respective dye	TIRF	642 642/10	30 ms	405 405/10	-	160x/1.43 oil	400x 400	-	LP 649 BP 710/100	10,000-20,000 frames
28B-C 31D	mEOS3.2: Halo	-	TIRF	532 532/10	30 ms	405 405/10	-	160x/1.43 oil	400x 400	-	LP 541 BP 600/100	10,000-20,000 frames
29A-C	CEP41-Halo	PA-SiR-C3-CA	GSD TIRF	642 642/10	100 ms	405 405/10	-	160x/1.43 oil	-	Fixed-MeOH	LP 649 BP 710/100	6,004 frames
29E, F	β-tubulin-Halo	PA-SiR-CA	GSD TIRF	642 642/10	150 ms	405 405/10	-	160x/1.43 oil	-	Fixed-MeOH	LP 649 BP 710/100	100,000 frames
30A-C	NUP96-Halo	PA-SiR-CA	Widefield (custom)	640 HC Quad	50 ms	405	-	160x/1.43 oil	-	Fixed-FA	700/100	
30D	-	PA-SiR-jasplakinolide	GSD TIRF	642 642/10	130 ms	405 405/10	-	160x/1.43 oil	-	Fixed-glutaraldehyde	LP 649 BP 710/100	30,000 frames
30E	-	PA-SiR-C8-docetaxel	GSD TIRF	642 642/10	100 ms	405 405/10	-	160x/1.43 oil	-	Fixed-EGS	LP 649 BP 710/100	2,337 frames
31A-C	β-2-adrenergic-receptor-Halo	PA-SiR-CA	GSD TIRF	642 642/10	30 ms	405 405/10	-	160x/1.43 oil	-	Live	LP 649 BP 710/100	10,046/ 4,000 frames

32	TOMM20-Halo	PA-SiR-CA	GSD TIRF	642 642/10	50 ms	405 405/10	-	160x/1.43 oil	-	Live	LP 649 BP 710/100	total 1,499 frames
33 A	Vimentin-Halo	PA-SiR-CA	Confocal	640	10 µs	355 nm	0.8	100x/1.40 oil	375x 375	Live	650-750	
33B	Vimentin-Halo	PA-SiR-CA	Confocal	640	10 µs	355 nm	0.8	100x/1.40 oil	760x7 27	Live	650-750	3 x line accumulation
33C	Vimentin-Halo	PA-SiR-CA	Confocal STED	640	10 µs	355 nm	0.8	100x/1.40 oil	760x7 27	Live	650-750	STED 775 nm 3 x line accumulation
37A	Halo/variant	SiR-CA	Confocal	631	0.2125 µs	-	1	20x0.75 dry	3992x 3992	Live	777-800	Max projection
S6A, B	none	PA-SiR-docetaxel	Confocal	631	0.375 µs	355	1	63x/1.40 oil	1584x 1584	Live	751-779	
S6C, D	none	PA-SiR-cabazitaxel	Confocal	631	0.35 µs	355	1	40x/1.10 water	3528x 3528	Live	751-779	
S6E, F	none	PA-SiR-C8-cabazitaxel	Confocal	631	0.5 µs	355	1	40x/1.10 water	1240x 1240	Live	751-779	
S6G, H	TOMM20-Halo	PA-SiR-CA	Confocal	631	1.2 µs	355	1	40x/1.10 water	410x 714	Live	751-779	
S7A	CEP41-Halo	PA-SiR-CA	GSD TIRF	642 642/10	100 ms	405 405/10	-	160x/1.43 oil	-	Fixed-MeOH	LP 649 BP 710/100	14,083 frames
S7C, D	CEP41-Halo	PA-SiR-CA	GSD TIRF	642 642/10	50 ms	405 405/10	-	160x/1.43 oil	-	Fixed-MeOH	LP 649 BP 710/100	25,935 frames cysteamine
S7E-G	NUP96-Halo	PA-SiR-C3-CA	Widefield (custom)	640 HC Quad	50 ms	405	-	160x/1.43 oil	-	Fixed-FA	700/100	
S8E	TOMM20-Halo	PA-SiR-CA	GSD TIRF	642 642/10	50 ms	405 405/10	-	160x/1.43 oil	-	Live	LP 649 BP 710/100	4,800 frames

Supplementary Table 15: Crystallography parameters for the structure determined of compound **62**.[203]

	Compound 62
formula	$C_{20}H_{26}N_2Si$
crystal system	orthorhombic
space group	$P\,2_12_12_1$
***a* /Å**	9.55658(9)
***b* /Å**	10.42713(10)
***c* /Å**	18.26555(18)
***V* /Å^3**	1820.12(3)
Z	4
M_r	322.52
F_{000}	696
d_c **/Mg m^{-3}**	1.177
μ /mm^{-1}	0.131
max., min. transmission factors	1.000, 0.483
X-radiation, *λ* /Å	Mo-K_α, 0.71073
data collect. temperat. /K	120(1)
***Θ* range /°**	2.2 to 34.7
index ranges *h,k,l*	−15 ... 15, −16 ... 16, −29 ... 29
reflections measured	157476
unique [R_{int}]	7733 [0.0556]
observed [$I \geq 2\sigma(I)$]	7006
data / restraints /parameters	7733 / 0 / 246
GooF on F^2	1.086
***R* indices [$F>4\sigma(F)$] $R(F)$, $wR(F^2)$**	0.0379, 0.0932
***R* indices (all data) $R(F)$, $wR(F^2)$**	0.0452, 0.0961
absolute structure parameter	−0.03(2)
largest residual peaks /e Å^{-3}	0.395, −0.152

Supplementary Table 16: First round of directed evolution on all ten positions, summarizing the number of mutations found that increase (+) and decrease (−) the fluorescence intensity of SiR-CA compared to parental HaloTag ($mean_{Halo}±3·sd_{Halo}$). In the case of more than 20 hits, a representative number of them were picked for sequencing and further analysis. The sequenced mutations are listed along with the ones that were later validated using purified variant-EGFP proteins. *might be an artefact; **sensitive positions; ***neutral positions.

Library		Hits found (picked)	Mutations (redundancy)	Validated
M175X	**+**	6 (6)	L(4), M, Q	L
	−	26 (8)	W(3), V, E(2), Q , M	W, Q
V167X**	**+**	6 (5)	V(5)	-
	−	37 (10)	G(2), E(4), D(2), P(2)	P
E170X	**+**	1 (1)	K	K, P*
	−	7 (7)	T, W(3), P(3)	-
T148X***	**+**	1 (1)	G	-
	−	2 (2)	V, I	V
L161X**	**+**	0	-	-
	−	39 (16)	W(7), K, P, T, G(4), A, C	W, G
Q165X	**+**	1 (1)	H	H
	−	5 (5)	P, Q, W(3),	W, P
T172X**	**+**	0	-	-
	−	48 (18)	E(5), F, K(4), Q(2), R(2), L(2), H, I	E, F, K, Q, R, L, H, I
F144X***	**+**	0	-	-
	−	11 (11)	S, L(2), F, H(3), N(2), G, I	-
G171X**	**+**	0	-	-
	−	39 (10)	L(3), H, N, W, T, E, P, M	L,N, W, T, E, M
P174X	**+**	4 (4)	H, L, G, Y	H, L, G
	−	23 (12)	Q(2), T(3), V, W(3), P(2), E	W

Supplementary Table 17: All validated variants from the first round of screening along with their fluorescence intensity ratios (I_{rel} = $I_{mut} \cdot I_{Halo}^{-1}$, sem, N = 3 samples) from the HaloTag-EGFP assay. * Variants selected for further characterisation.

Variant	I_{rel}	sem
M175L*	1.31	0.22
M175W*	0.51	0.09
M175Q	0.92	0.06
V167P*	0.39	0.03
E170K*	1.26	0.14
E170P*	1.21	0.14
T148V*	0.78	0.10
L161W*	0.49	0.09
L161G	0.81	0.10
Q165H*	1.24	0.16
Q165P	0.71	0.16
Q165W*	0.64	0.08
T172E	0.87	0.05
T172F*	0.56	0.05
T172K*	0.56	0.14
T172Q	0.63	0.13
T172L	0.86	0.05
T172H	0.61	0.05
T172I	0.79	0.05
T172R*	0.21	0.03
G171L	0.90	0.08
G171N	0.85	0.08
G171W*	0.49	0.06
G171T	0.68	0.06
G171E	0.80	0.08
G171M	0.67	0.06
P174H*	1.27	0.16
P174L*	1.43	0.33
P174W*	0.33	0.05
P174G*	1.15	0.14

Supplementary Table 18: Second round of directed evolution of the seven best variants (M175L, E170K, E170P, Q165H, P174H, P174G, and P174L), randomizing the remaining three positions individually. The number of mutations found to increase the fluorescence intensity of SiR-CA compared to parental HaloTag are summarised ($mean_{Halo}±2·sd_{Halo}$). The sequenced mutations are listed along with the ones that were later validated using purified variant-EGFP proteins. Additionally, variants that showed a SiR-CA fluorescence intensity ratio ($I_{rel\text{-}SiR} = I_{var\text{-}SiR} \cdot I_{Halo\text{-}SiR}^{-1}$, N = 3 samples) higher than 1.10 were selected for characterisation.

Library	Hits found (picked)	Mutation (redundancy)	Validated	$I_{rel\text{-}SiR}$ > 1.10
E170K, M175X	2 (2)	M(2)	-	-
E170X, M175L	12 (12)	E(5), G, A(2), Q, K, L, V	-	G, Q, K
E170P, M175X	6 (6)	M(4), S, K	-	-
Q165H, M175X	2 (2)	Y, M	-	-
Q165X, M175L	4 (4)	Q, V, L, A	-	-
Q165H, P174X	4 (4)	R(2), F, L	R, L	R, L
Q165X, P174H	2 (2)	V, Q	-	-
Q165X, P174L	1 (1)	V	-	-
Q165X, P174G	5 (5)	T, H, V, A, G	-	-
P174X, M175L	3 (3)	L, H, V	-	-
P174H, M175X	0	-	-	-
P174L, M175X	6 (6)	L(3), M(3)	-	-
Q165X, E170K	0	-	-	-
Q165H, E170X	2 (2)	V, Q	V	Q
E170K, P174X	0	-	-	-
E170X, P174H	7 (7)	E(4), K, Q, N	-	-
E170X, P174L	4 (4)	E(2), Q, A	-	-

Supplementary Table 19: Third round of directed evolutions on the three best variants, randomizing the remaining two positions individually. The number of mutations increasing the fluorescence intensity of SiR-CA compared to parental HaloTag ($mean_{Parent}±2·sd_{Parent}$, N = 5) are summarised. The sequenced mutations are listed along with the ones that were later validated using purified variant-EGFP proteins. Additionally, variants that showed a SiR-CA fluorescence intensity ratio ($I_{rel\text{-}SiR} = I_{var\text{-}SiR} \cdot I_{Halo\text{-}SiR}^{-1}$, N = 3 samples) higher than 1.10 were selected for further characterisation.

Library	Hits found (picked)	Mutation (redundancy)	Validated	$I_{rel\text{-}SiR}$ > 1.10
Q165H, P174R, M175X	1 (1)	V	-	-
Q165H, E170X, P174R	5 (5)	G(2), V, T, A	V, A	A
Q165H, P174L, M175X	3 (3)	L, V(2)	-	-
Q165H, E170X, P174L	10 (10)	E(5), H, V, G, A, Q	-	-
E170K, Q165X, M175L	1 (1)	R	-	-
E170K, P174X, M175L	10 (10)	L(3), Q(2), N, V, P(2), H	-	-

Supplementary Table 20: Fluorescence intensity ratios ($I_{rel} = I_{mut} \cdot I_{Halo}^{-1}$) of all brighter variants in combination with eight fluorophores. For SiR-CA three biological replicates with each $N = 4$ samples were measured and the mean of the three replicates is given with its sd. For all other measurements the mean of one replicate and its sem ($N = 4$ samples) is given. *One replicate only; mean and sem.

Variant	SiR	sd	JF_{646}	sem	JF_{635}	sem	JF_{614}	sem
M175L	1.10	0.04	1.12	0.01	N/D	N/D	N/D	N/D
E170K	1.13	0.07	1.02	0.01	N/D	N/D	N/D	N/D
E170P	1.02	0.04	1.36	0.02	N/D	N/D	N/D	N/D
Q165H	1.11	0.07	1.34	0.01	1.54	1.05	3.70	0.04
P174H	1.16	0.01	1.33	0.02	1.17	0.04	1.80	0.04
P174L	1.15	0.05	1.13	0.02	0.91	0.04	1.013	0.015
P174G	1.01	0.02	0.92	0.01	N/D	N/D	N/D	N/D
Q165H-P174R	1.20	0.00	1.15	0.01	1.51	0.05	4.07	0.07
Q165H-P174L	1.17	0.04	1.44	0.02	1.38	0.05	2.88	0.05
E170K-M175L	1.16	0.02	0.95	0.01	N/D	N/D	N/D	N/D
E170G-M175L	1.12	0.00	0.95	0.01	N/D	N/D	N/D	N/D
E170Q-M175L	1.07	0.10	0.88	0.02	N/D	N/D	N/D	N/D
E170V-Q165H	0.98*	0.04*	1.00	0.05	N/D	N/D	N/D	N/D
E170Q-Q165H	1.06*	0.04*	1.31	0.04	N/D	N/D	N/D	N/D
Q165H-E170V-P174R	1.03*	0.03*	1.16	0.04	N/D	N/D	N/D	N/D
Q165H-E170A-P174R	1.04*	0.05*	1.16	0.05	N/D	N/D	N/D	N/D

Variant	CPY	sem	MaP618	sem	TMR	sem	MaP555	sem
M175L	1.05	0.01	1.17	0.01	0.87	0.03	1.02	0.01
E170K	1.09	0.01	0.76	0.01	0.96	0.02	1.04	0.01
E170P	0.90	0.01	0.10	0.00	0.90	0.02	0.95	0.00
Q165H	1.06	0.02	1.24	0.01	1.00	0.02	1.10	0.01
P174H	0.97	0.01	1.03	0.01	1.00	0.02	1.13	0.01
P174L	1.14	0.02	1.32	0.02	1.00	0.02	1.12	0.01
P174G	0.82	0.02	0.62	0.01	0.89	0.01	0.95	0.01
Q165H-P174R	1.32	0.02	1.51	0.02	1.10	0.02	1.22	0.01
Q165H-P174L	1.15	0.02	1.42	0.02	1.12	0.02	1.24	0.01
E170K-M175L	1.04	0.02	0.87	0.01	0.97	0.01	0.98	0.01
E170G-M175L	0.99	0.02	0.87	0.01	0.88	0.02	0.88	0.01
E170Q-M175L	0.98	0.01	1.09	0.02	0.96	0.01	0.95	0.03
E170V-Q165H	0.79	0.01	0.92	0.06	0.92	0.01	1.03	0.03
E170Q-Q165H	0.97	0.01	1.20	0.08	1.00	0.01	1.08	0.03
Q165H-E170V-P174R	0.96	0.01	1.03	0.06	1.13	0.01	1.25	0.04
Q165H-E170A-P174R	1.18	0.02	1.40	0.09	1.06	0.01	1.14	0.04

Supplementary Table 21: Fluorescence intensity ratios (I_{rel} = I_{mut} · I_{Halo}^{-1}) of all dimmer variants in combination with eight fluorophores. For SiR-CA three biological replicates with each *N* = 4 samples were measured and the mean of the three replicates is given with its sd. For all other measurements the mean of one replicate and its sem (*N* = 4 samples) is given.

Variant	SiR	sd	JF_{646}	sem	JF_{635}	sem	JF_{614}	sem
M175W	0.55	0.03	0.81	0.01	N/D	N/D	N/D	N/D
V167P	0.35	0.02	0.57	0.01	N/D	N/D	N/D	N/D
T148V	1.01	0.04	1.20	0.02	N/D	N/D	N/D	N/D
L161W	0.47	0.03	0.73	0.01	N/D	N/D	N/D	N/D
Q165W	0.47	0.03	0.66	0.01	N/D	N/D	N/D	N/D
T172F	0.26	0.02	0.40	0.00	N/D	N/D	N/D	N/D
T172K	0.33	0.02	0.50	0.01	N/D	N/D	N/D	N/D
T172R	0.16	0.02	0.28	0.00	N/D	N/D	N/D	N/D
G171W	0.23	0.00	0.31	0.00	0.05	0.00	0.03	0.00
P174W	0.27	0.00	0.47	0.00	0.16	0.01	0.18	0.00

Variant	CPY	sem	MaP618	sem	TMR	sem	MaP555	sem
M175W	0.35	0.00	0.40	0.00	0.56	0.02	0.66	0.00
V167P	0.76	0.01	0.03	0.00	0.89	0.02	0.58	0.01
T148V	0.97	0.02	0.35	0.00	0.89	0.02	0.95	0.01
L161W	0.64	0.01	0.68	0.01	0.61	0.01	0.62	0.00
Q165W	0.49	0.01	0.51	0.01	0.23	0.01	0.20	0.00
T172F	0.62	0.01	0.03	0.00	0.76	0.03	0.39	0.00
T172K	0.75	0.03	0.03	0.00	0.68	0.02	0.44	0.00
T172R	0.45	0.01	0.02	0.00	0.60	0.02	0.25	0.01
G171W	0.18	0.00	0.02	0.00	0.07	0.00	0.05	0.00
P174W	0.19	0.00	0.14	0.00	0.28	0.00	0.27	0.00

Supplementary Table 22: Linear fit correlating I_{rel} of different fluorophores with their D_{50} according to Supplementary Equation 9. ***a*** y-offset and its standard error $\mathbf{se_a}$, ***b*** slope and its standard error $\mathbf{se_b}$, and $\boldsymbol{R^2}$ the squared correlation coefficient are given (Figure 35C).

	a	$\mathbf{se}_a$	***b***	$\mathbf{se}_b$	$\boldsymbol{R^2}$
$\boldsymbol{I_{rel}}$	1.027	0.036	0.0050	8.4E−4	0.716

Supplementary Table 23: Mean values and intensity ratios found by live-cell confocal microscopy for SiR-CA in combination with different HaloTag variants. Means and ratios are given with their 90% confidence interval. Three independent biological replicates were performed and *N* = number of cells are directly given in the table.* Dimmer variants (Figure 37A).

Name	***N***	**Mean**	$\boldsymbol{I_{rel\text{-}SiR}}$
M174L	67	0.900±0.024	1.03±0.04
E170K	63	0.899±0.023	1.03±0.04
Q165H	54	0.87±0.03	1.00±0.04
Q165W*	55	0.427±0.018	0.49±0.03
G161W*	58	0.142±0.007	0.162±.009
P175H	55	1.01±0.04	1.16±0.06
P175L	55	1.03±0.03	1.18 ±0.05
P175W*	60	0.221±0.006	0.25±0.01
Q165H-P175R	61	1.02±0.03	1.17±0.05
Q165H-P175L	57	0.98±0.03	1.12±0.05
HaloTag	49	0.87±0.03	1.00±0.04

6.3 Supplementary equations

Mathematical description of the PA-SiR equilibrium system and the associated assumptions

Starting with equilibrium system (1) different assumptions were made depending on the conditions used resulting in four equilibrium systems (2) – (5).

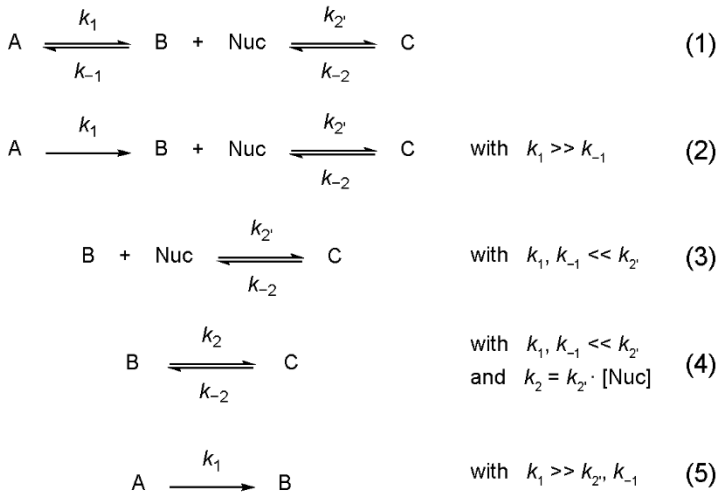

Derivation of the parameters used to treat equilibrium system (4)

$$\frac{-d[B]}{dt} = k_2[B] - k_{-2}[C]$$

Supplementary Equation 1: Differential rate equation for compound B.

$$[B_{tot}] = [B] + [C]$$

Supplementary Equation 2: Boundary conditions for the equilibrium system (4).

$$\frac{-d[B]}{dt} = k_2[B] - k_{-2}([B_{tot}] - [B])$$

$$\frac{-d[B]}{dt} = k_2[B] - k_{-2}[B_{tot}] + k_{-2}[B]$$

$$\frac{-d[B]}{dt} = (k_2 + k_{-2})[B] - k_{-2}[B_{tot}]$$

$$\frac{-d[B]}{dt} = k_{app}[B] - d$$

Supplementary Equation 3: Step-by-step simplification of the differential rate equation for B (Supplementary Equation 1) using the boundary conditions from Supplementary Equation 2. $k_{app} = k_2 + k_{-2}$ and $d = k_{-2} \cdot [B_{tot}]$.

$$[B](t) = c_1 e^{-k_{app}t} + \frac{d}{k_{app}} = c_1 e^{-(k_2 + k_{-2})t} + \frac{k_{-2}[B_{tot}]}{k_2 + k_{-2}}$$

Supplementary Equation 4: Solution of the differential equation.

Further equations used

$$y(x) = y_0 + A \cdot e^{\frac{-(x-x_0)}{\tau}}$$

Supplementary Equation 5: Mono-exponential curve.

$$y(x) = y_0 + \frac{A}{w \cdot \sqrt{\frac{\pi}{2}}} \cdot e^{\frac{-2(x-x_c)^2}{w^2}}$$

Supplementary Equation 6: Gaussian function.

$$y(x) = \frac{a}{1 + e^{-k(x-x_c)}}$$

Supplementary Equation 7: Sigmoidal logistic function.

$$y(x) = A1 + \frac{A2 - A1}{1 + 10^{(LOGx0-x)\cdot p}}$$

Supplementary Equation 8: Sigmoidal dose response curve with variable hill slope given by parameter p.

$$y(x) = a + bx$$

Supplementary Equation 9: Linear function.

$$X^2 = \sum_{i=1}^{n} (y_i - \hat{y}_i)^2$$

Supplementary Equation 10: Definition of X^2.

$$R^2 = 1 - \frac{\sum_{i=1}^{n}(y_i - \hat{y}_i)^2}{\sum_{i=1}^{n}(y_i - \overline{y}_i)^2}$$

Supplementary Equation 11:Definition of R^2.

6.4 Supplementary NMR spectra

57

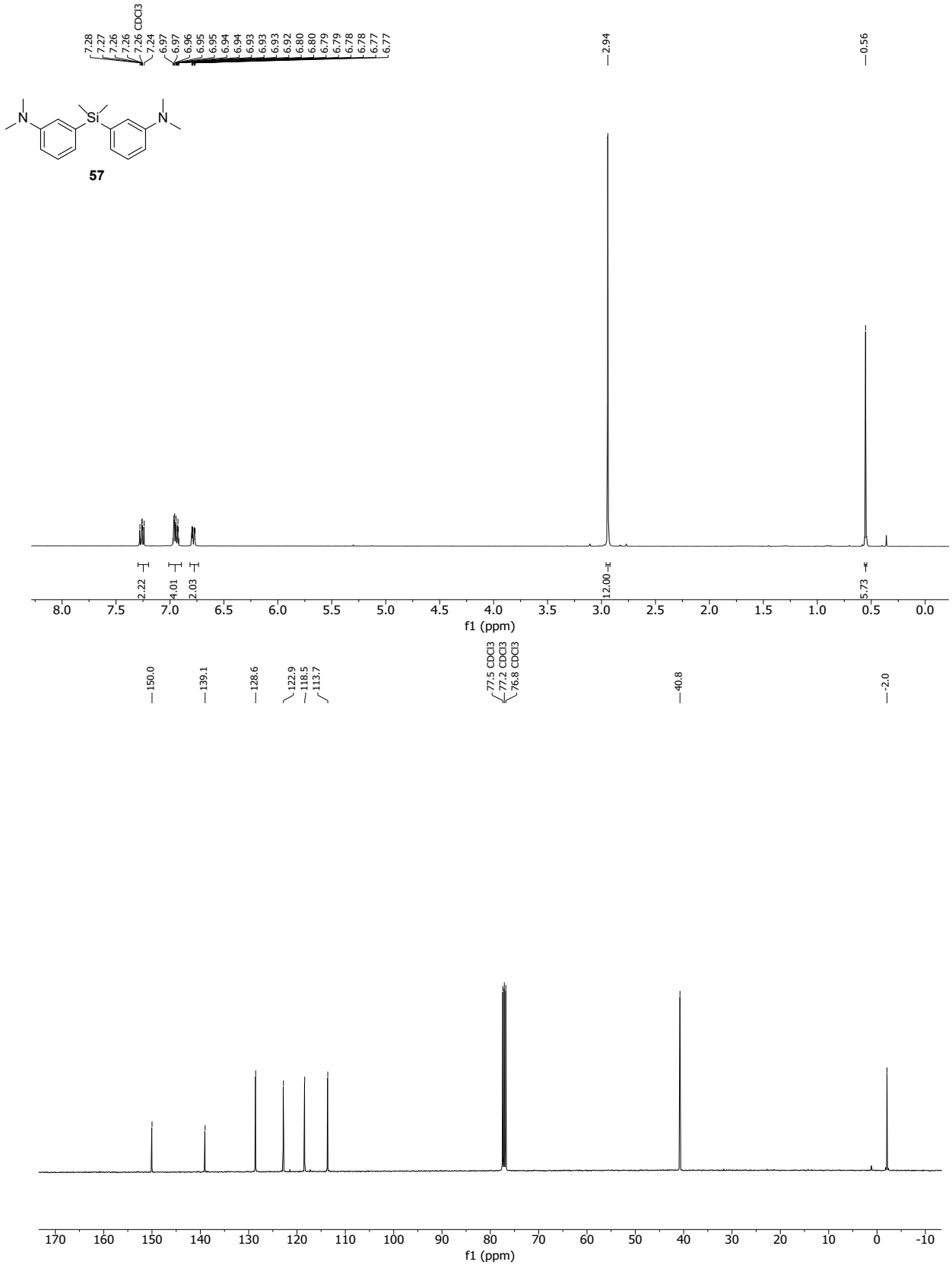
7.28
7.27
7.26
7.26
7.26 CDCl3
7.24
6.97
6.97
6.96
6.95
6.95
6.94
6.94
6.93
6.93
6.92
6.80
6.80
6.79
6.79
6.78
6.78
6.77
6.77
2.94
0.56
Si
N
N
57
2.22
4.01
2.03
12.00
5.73
f1 (ppm)
150.0
139.1
128.6
122.9
118.5
113.7
77.5 CDCl3
77.2 CDCl3
76.8 CDCl3
40.8
-2.0
f1 (ppm)

58

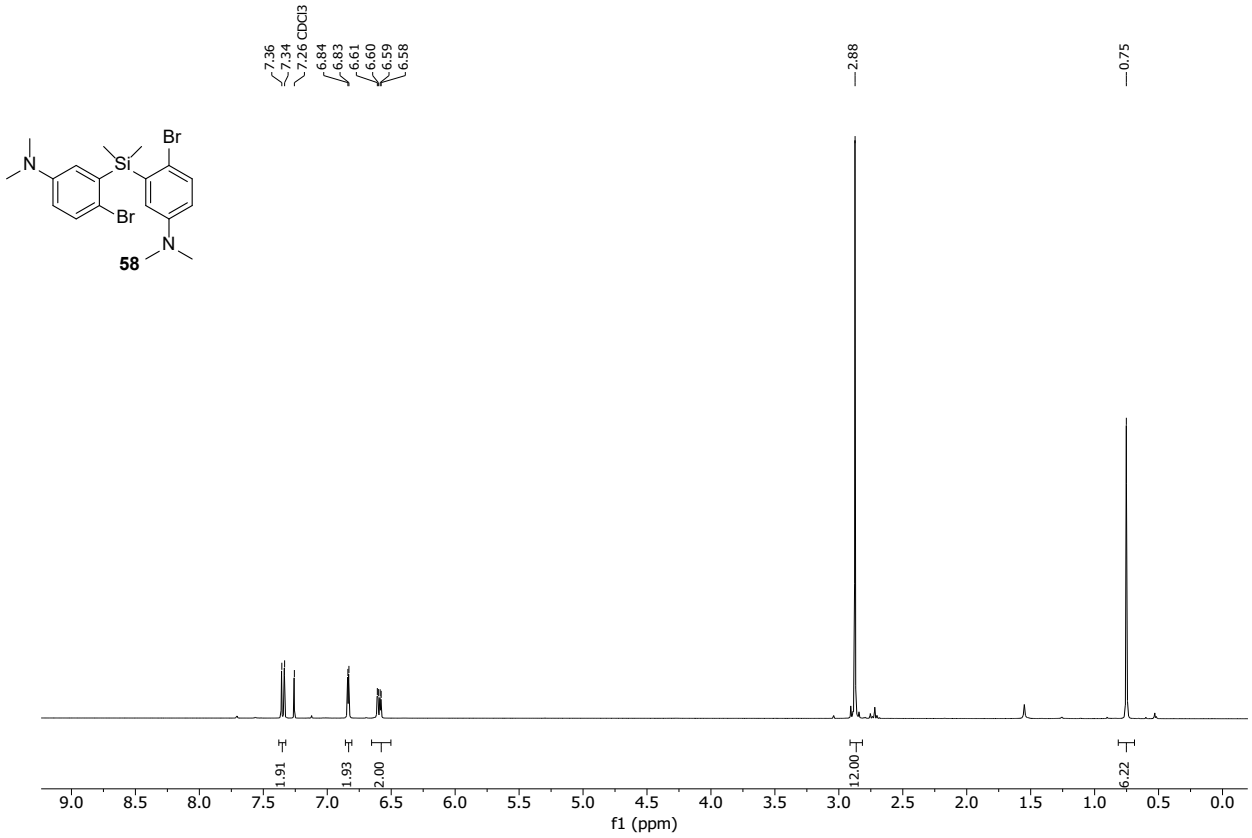
7.36
7.34
7.26 CDCl3
6.84
6.83
6.61
6.60
6.59
6.58
2.88
0.75
Br
Si
N
Br
N
58
1.91
1.93
2.00
12.00
6.22
f1 (ppm)

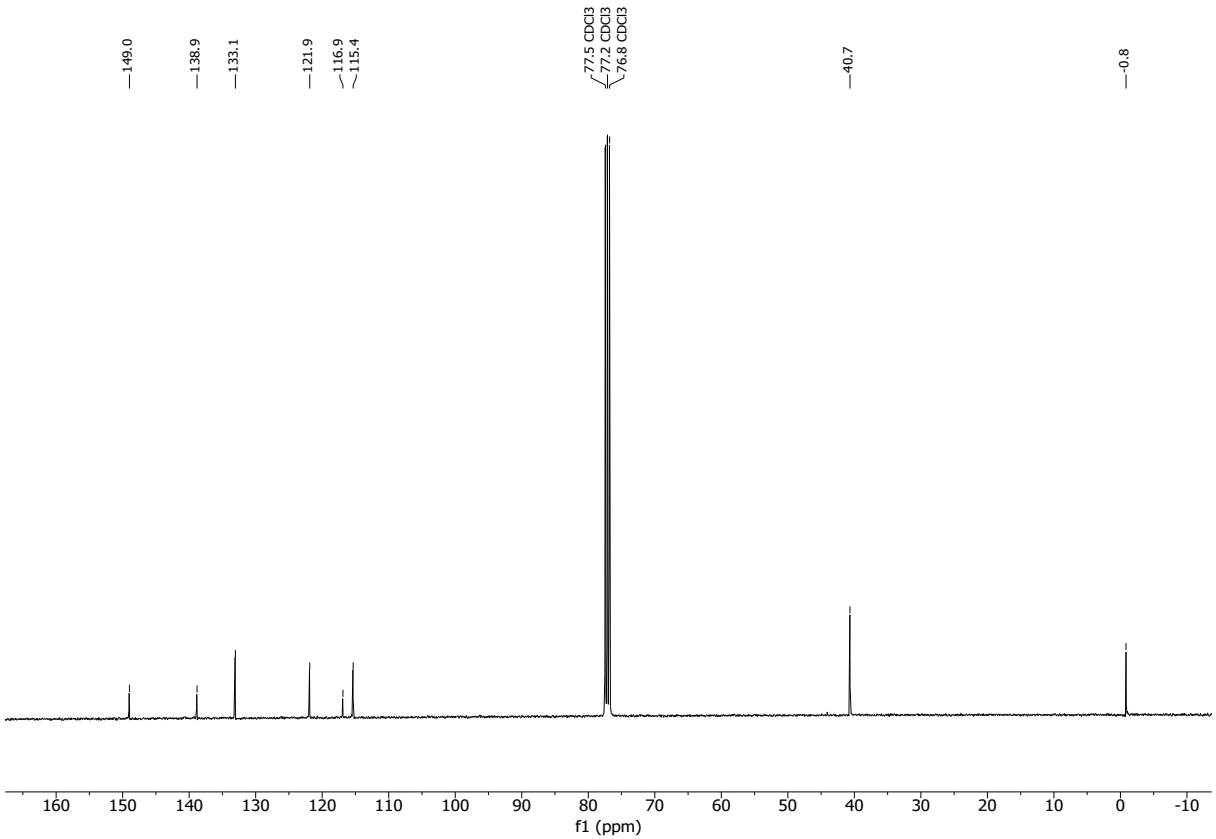
149.0
138.9
133.1
121.9
116.9
115.4
77.5 CDCl3
77.2 CDCl3
76.8 CDCl3
40.7
-0.8
f1 (ppm)

PA-SiR 41

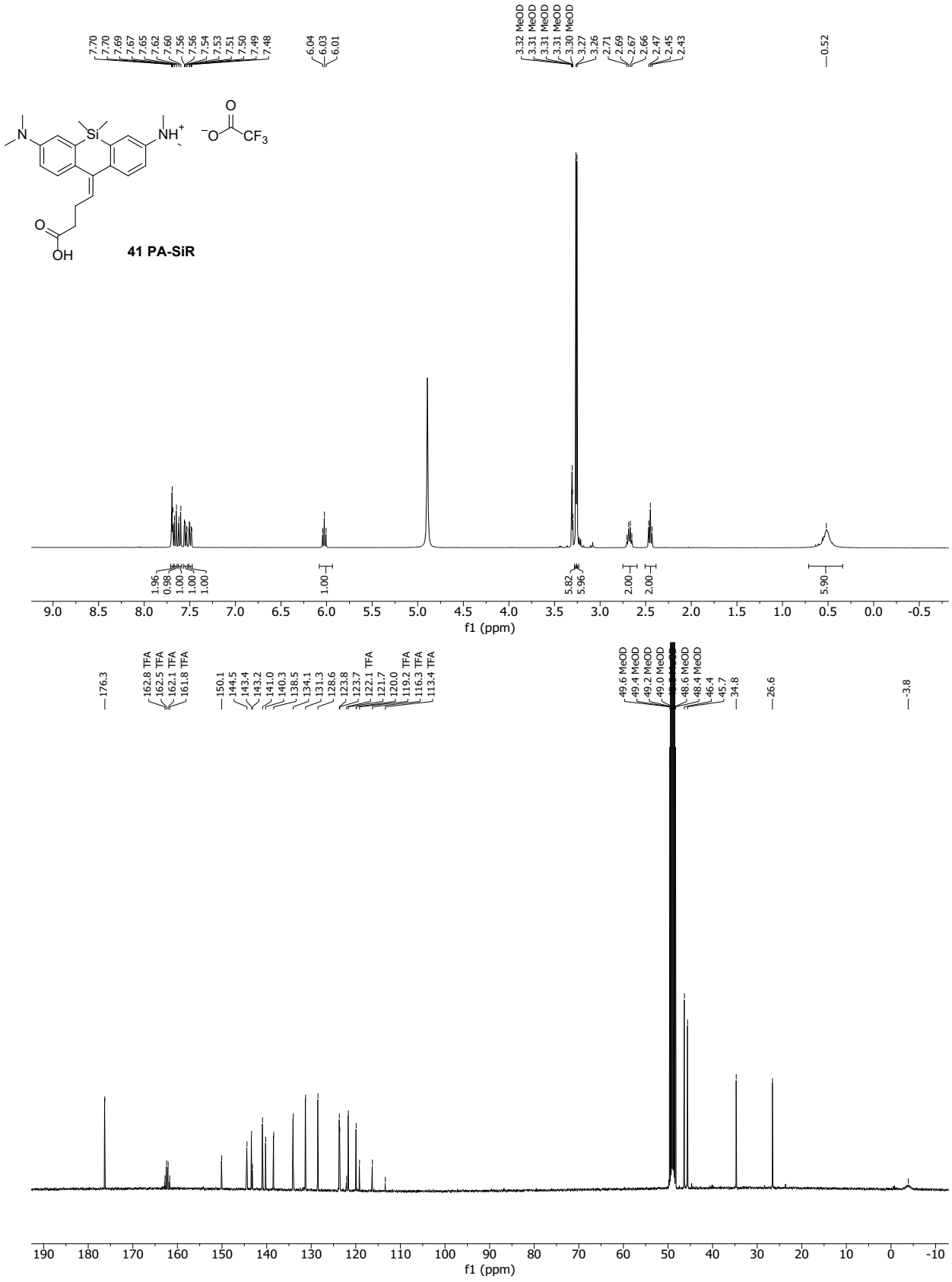
7.70
7.70
7.69
7.67
7.65
7.62
7.60
7.56
7.56
7.54
7.53
7.51
7.50
7.49
7.48
6.04
6.03
6.01
3.32 MeOD
3.31 MeOD
3.31 MeOD
3.31 MeOD
3.30 MeOD
3.27
3.26
2.71
2.69
2.67
2.66
2.47
2.45
2.43
0.52
O
N
Si
NH+
O
CF3
O
OH
41 PA-SiR
1.96
0.98
1.00
1.00
1.00
1.00
5.82
5.96
2.00
2.00
5.90
f1 (ppm)
176.3
162.8 TFA
162.5 TFA
162.1 TFA
161.8 TFA
150.1
144.5
143.4
143.2
141.0
140.3
138.5
134.1
131.3
128.6
123.8
123.7
122.1 TFA
121.7
120.0
119.2 TFA
116.3 TFA
113.4 TFA
49.6 MeOD
49.4 MeOD
49.2 MeOD
49.0 MeOD
48.6 MeOD
48.4 MeOD
46.4
45.7
34.8
26.6
-3.8
f1 (ppm)

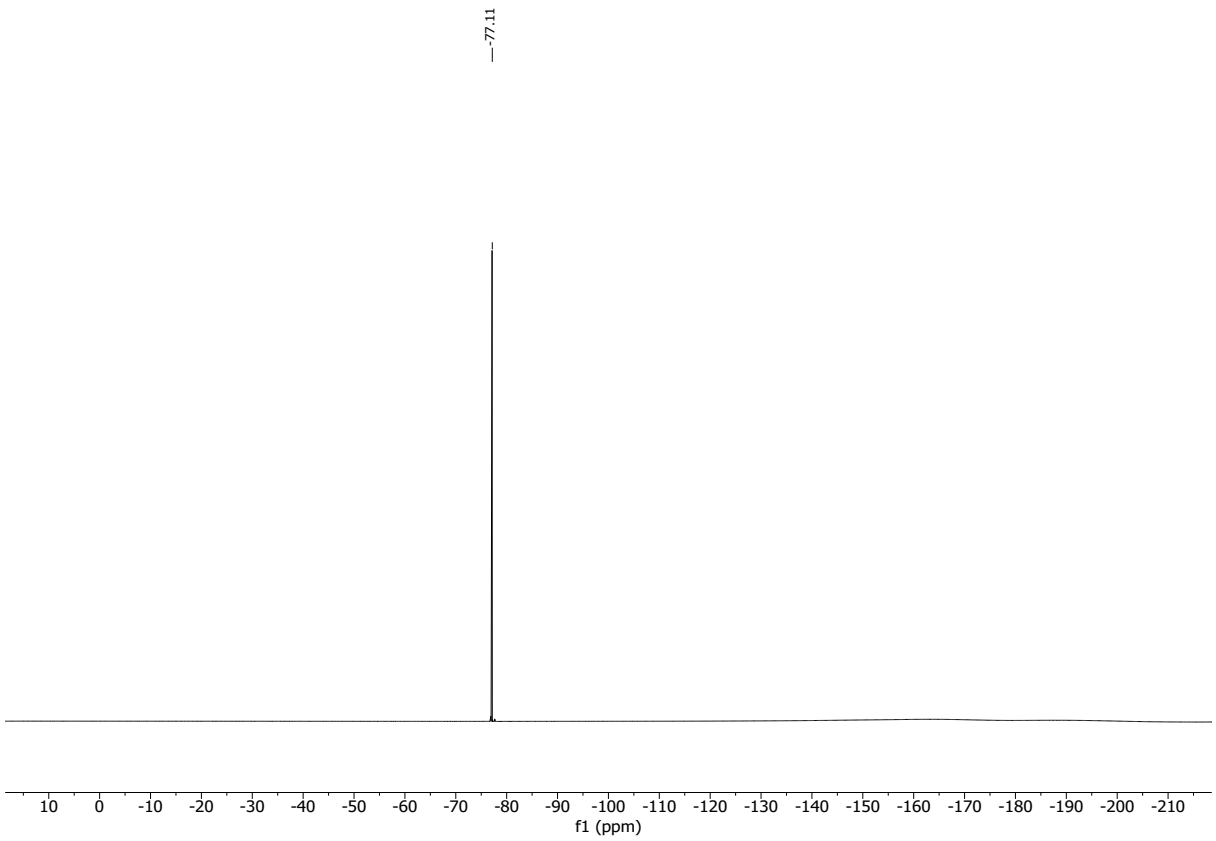
-77.11
10 0 -10 -20 -30 -40 -50 -60 -70 -80 -90 -100 -110 -120 -130 -140 -150 -160 -170 -180 -190 -200 -210
f1 (ppm)

43

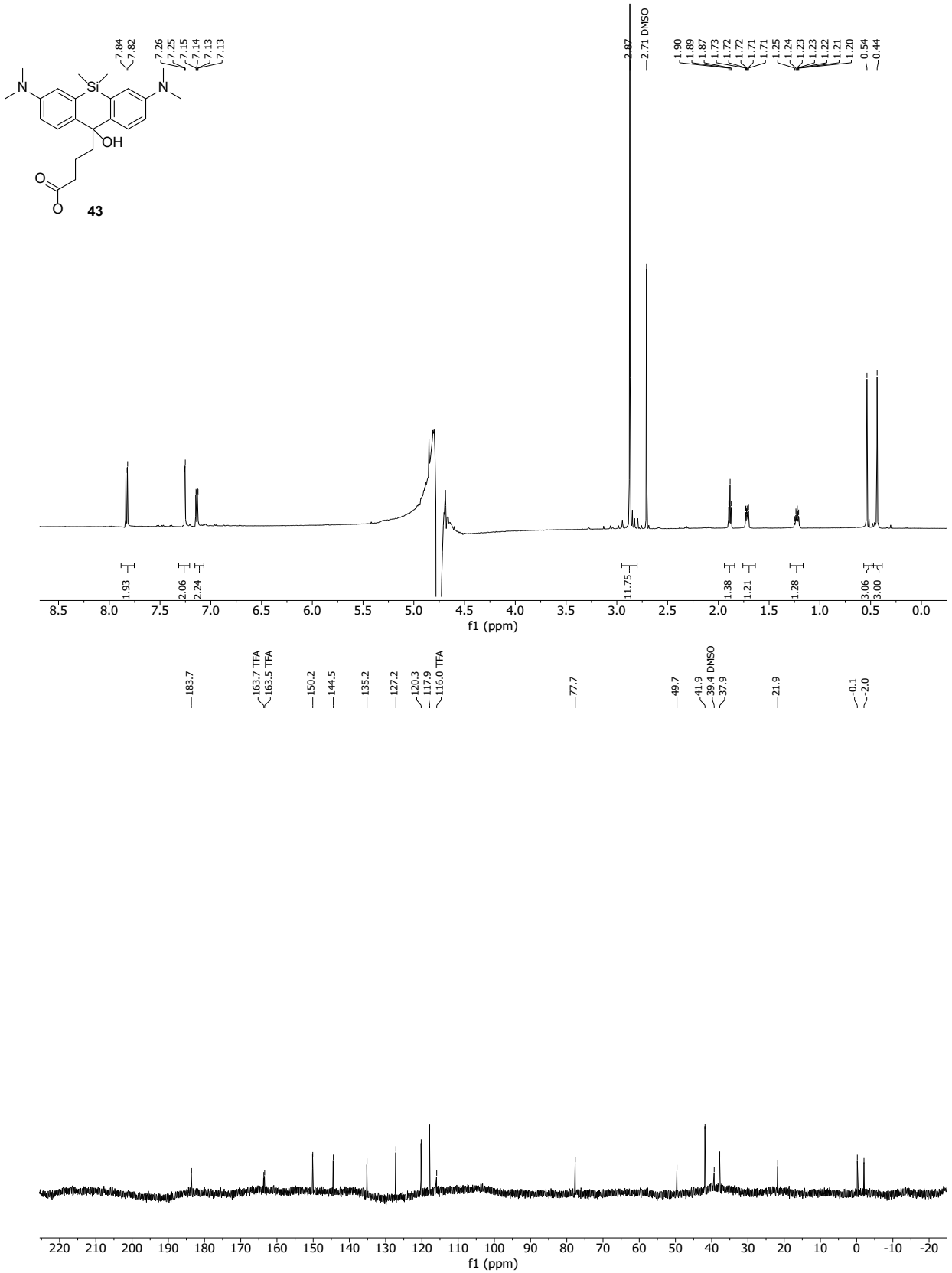
7.84
7.82
7.26
7.25
7.15
7.14
7.13
7.13
2.87
2.71 DMSO
1.90
1.89
1.87
1.73
1.72
1.72
1.71
1.71
1.25
1.24
1.23
1.23
1.22
1.21
1.20
0.54
0.44
1.93
2.06
2.24
11.75
1.38
1.21
1.28
3.06
3.00
f1 (ppm)
183.7
163.7 TFA
163.5 TFA
150.2
144.5
135.2
127.2
120.3
117.9
116.0 TFA
77.7
49.7
41.9
39.4 DMSO
37.9
21.9
-0.1
-2.0
f1 (ppm)

60

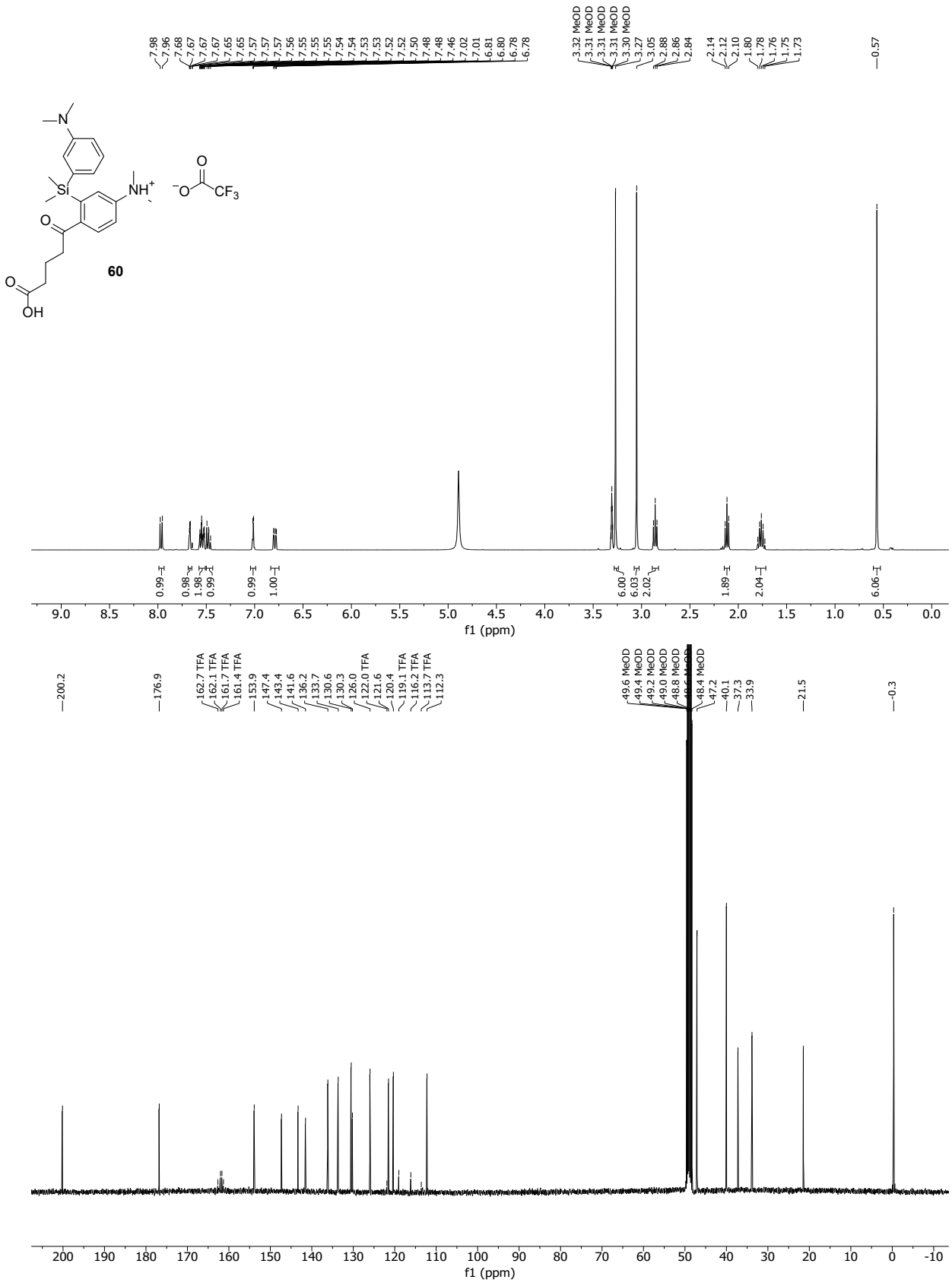
7.98
7.96
7.68
7.67
7.67
7.67
7.65
7.65
7.57
7.57
7.57
7.56
7.55
7.55
7.55
7.54
7.54
7.53
7.53
7.52
7.52
7.50
7.48
7.48
7.46
7.02
7.01
6.81
6.80
6.78
6.78
3.32 MeOD
3.31 MeOD
3.31 MeOD
3.31 MeOD
3.30 MeOD
3.27
3.05
2.88
2.86
2.84
2.14
2.12
2.10
1.80
1.78
1.76
1.75
1.73
0.57
N
Si
NH+
O
O
O
O
CF3
OH
60
0.99
0.98
1.98
0.99
0.99
1.00
6.00
6.03
2.02
1.89
2.04
6.06
f1 (ppm)
200.2
176.9
162.7 TFA
162.1 TFA
161.7 TFA
161.4 TFA
153.9
147.4
143.4
141.6
136.2
133.7
130.6
130.3
126.0
122.0 TFA
121.6
120.4
119.1 TFA
116.2 TFA
113.7 TFA
112.3
49.6 MeOD
49.4 MeOD
49.2 MeOD
49.0 MeOD
48.8 MeOD
48.4 MeOD
47.2
40.1
37.3
33.9
21.5
-0.3
f1 (ppm)

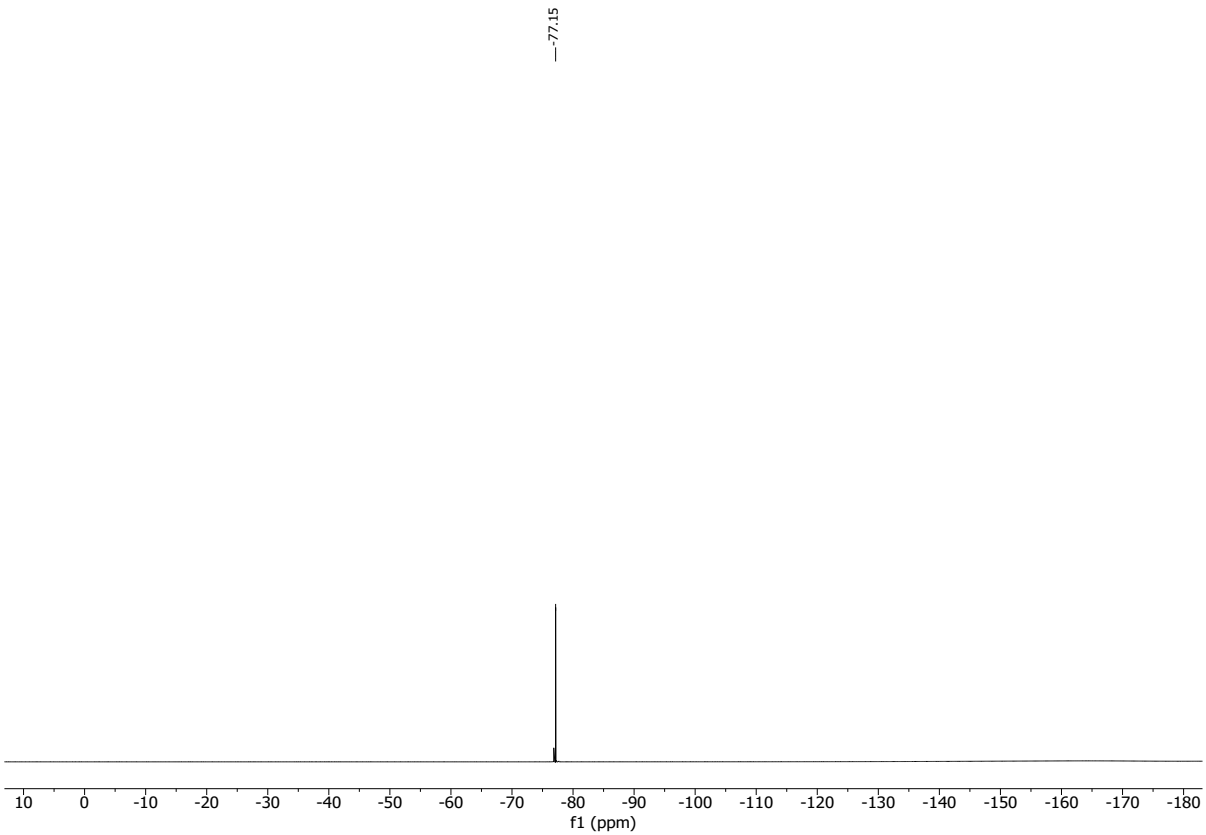
—77.15
10
0
-10
-20
-30
-40
-50
-60
-70
-80
-90
-100
-110
-120
-130
-140
-150
-160
-170
-180
f1 (ppm)

62

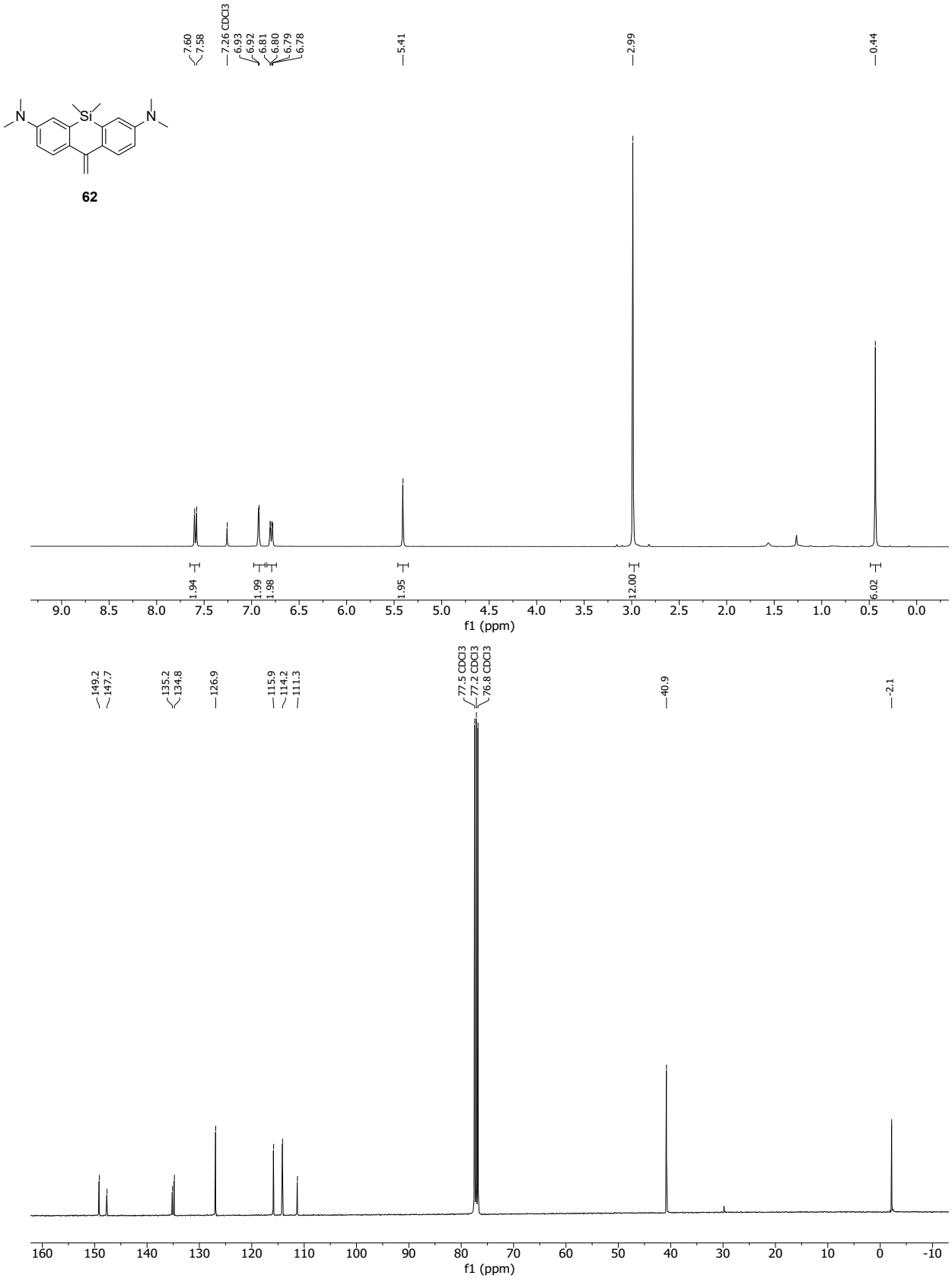
7.60
7.58
7.26 CDCl3
6.93
6.92
6.81
6.80
6.79
6.78
5.41
2.99
0.44
1.94
1.99
1.98
1.95
12.00
6.02
f1 (ppm)
149.2
147.7
135.2
134.8
126.9
115.9
114.2
111.3
77.5 CDCl3
77.2 CDCl3
76.8 CDCl3
40.9
-2.1
f1 (ppm)

65

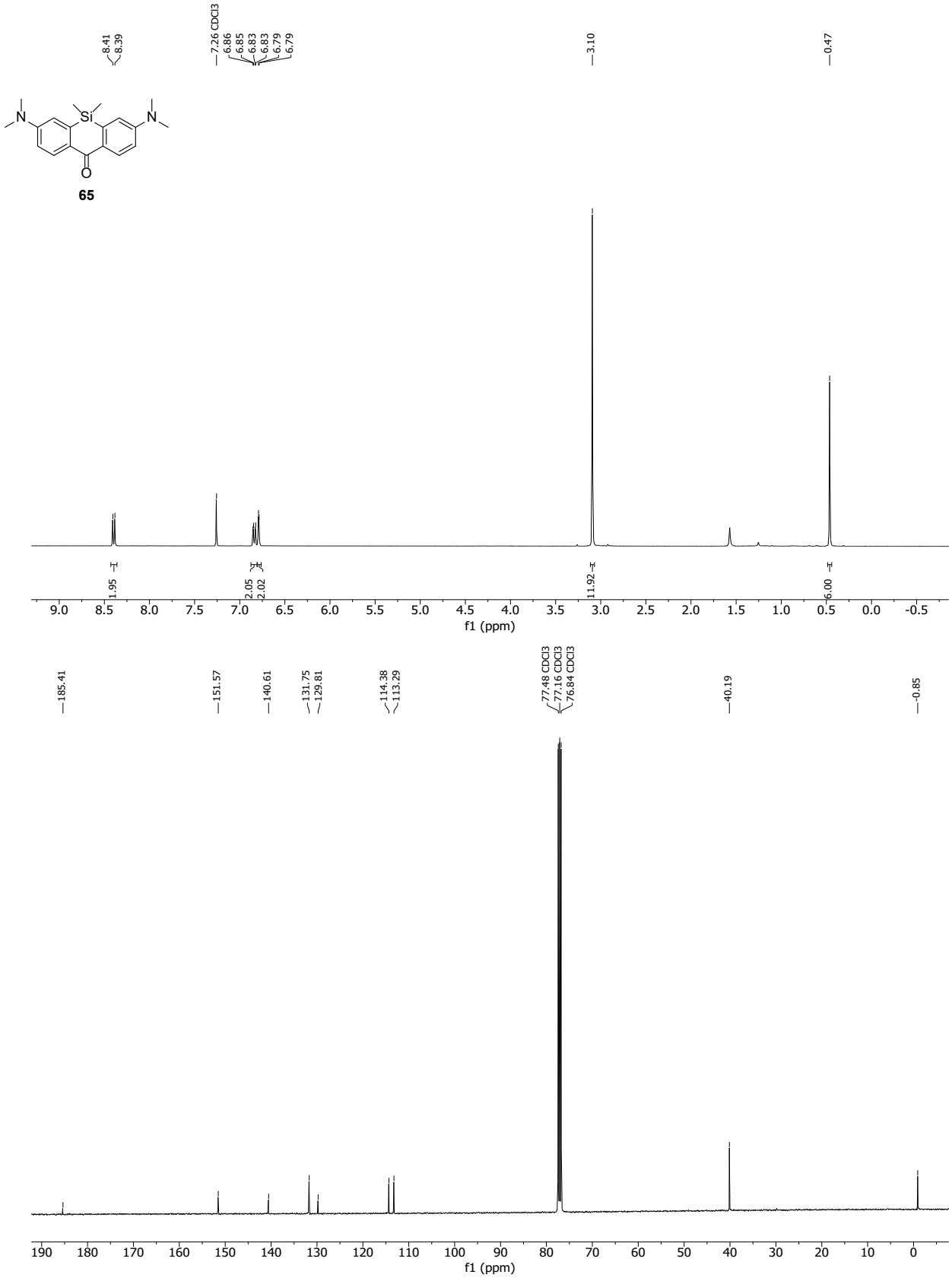
8.41
8.39
7.26 CDCl3
6.86
6.85
6.83
6.83
6.79
6.79
3.10
0.47
65
1.95
2.05
2.02
11.92
6.00
f1 (ppm)
185.41
151.57
140.61
131.75
129.81
114.38
113.29
77.48 CDCl3
77.16 CDCl3
76.84 CDCl3
40.19
-0.85
f1 (ppm)

69

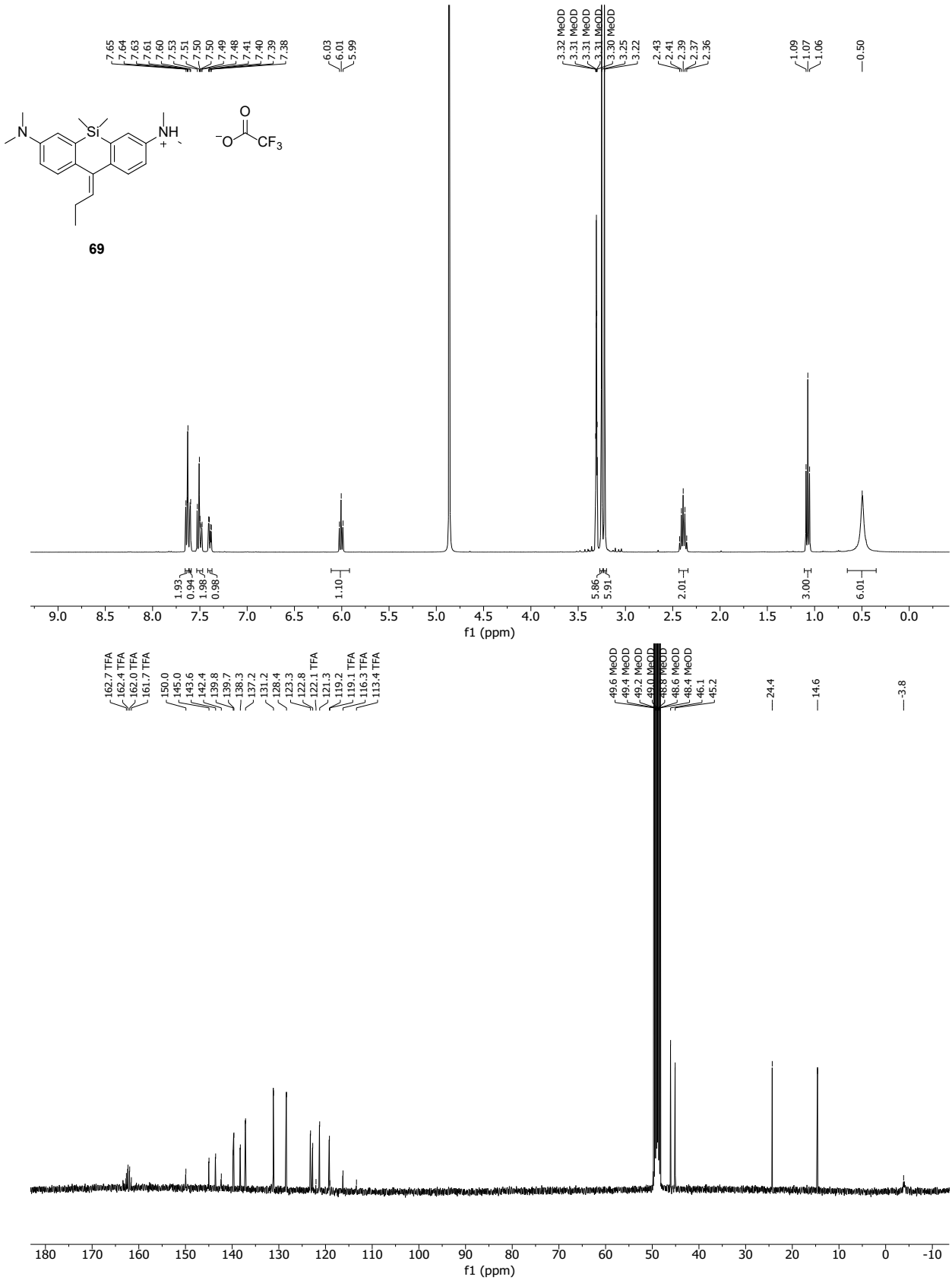
7.65
7.64
7.63
7.61
7.60
7.53
7.51
7.50
7.50
7.49
7.48
7.41
7.40
7.39
7.38
6.03
6.01
5.99
3.32 MeOD
3.31 MeOD
3.31 MeOD
3.31 MeOD
3.30 MeOD
3.25
3.22
2.43
2.41
2.39
2.37
2.36
1.09
1.07
1.06
0.50
N
Si
NH
O
O
CF3
69
1.93
0.94
1.98
0.98
1.10
5.86
5.91
2.01
3.00
6.01
f1 (ppm)
162.7 TFA
162.4 TFA
162.0 TFA
161.7 TFA
150.0
145.0
143.6
142.4
139.8
139.7
138.3
137.2
131.2
128.4
123.3
122.8
122.1 TFA
121.3
119.2
119.1 TFA
116.3 TFA
113.4 TFA
49.6 MeOD
49.4 MeOD
49.2 MeOD
49.0 MeOD
48.8 MeOD
48.6 MeOD
48.4 MeOD
46.1
45.2
24.4
14.6
3.8
f1 (ppm)

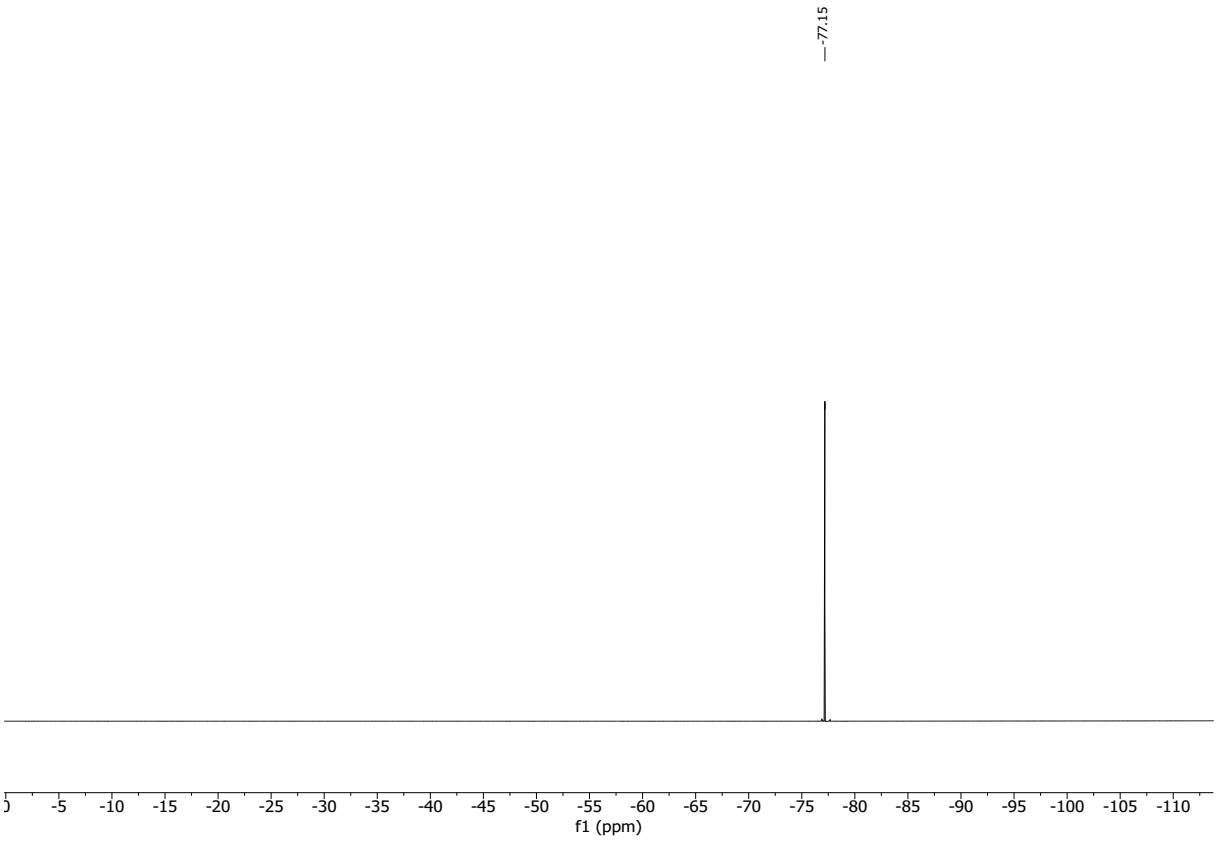
-77.15
0
-5
-10
-15
-20
-25
-30
-35
-40
-45
-50
-55
-60
-65
-70
-75
-80
-85
-90
-95
-100
-105
-110
f1 (ppm)

133

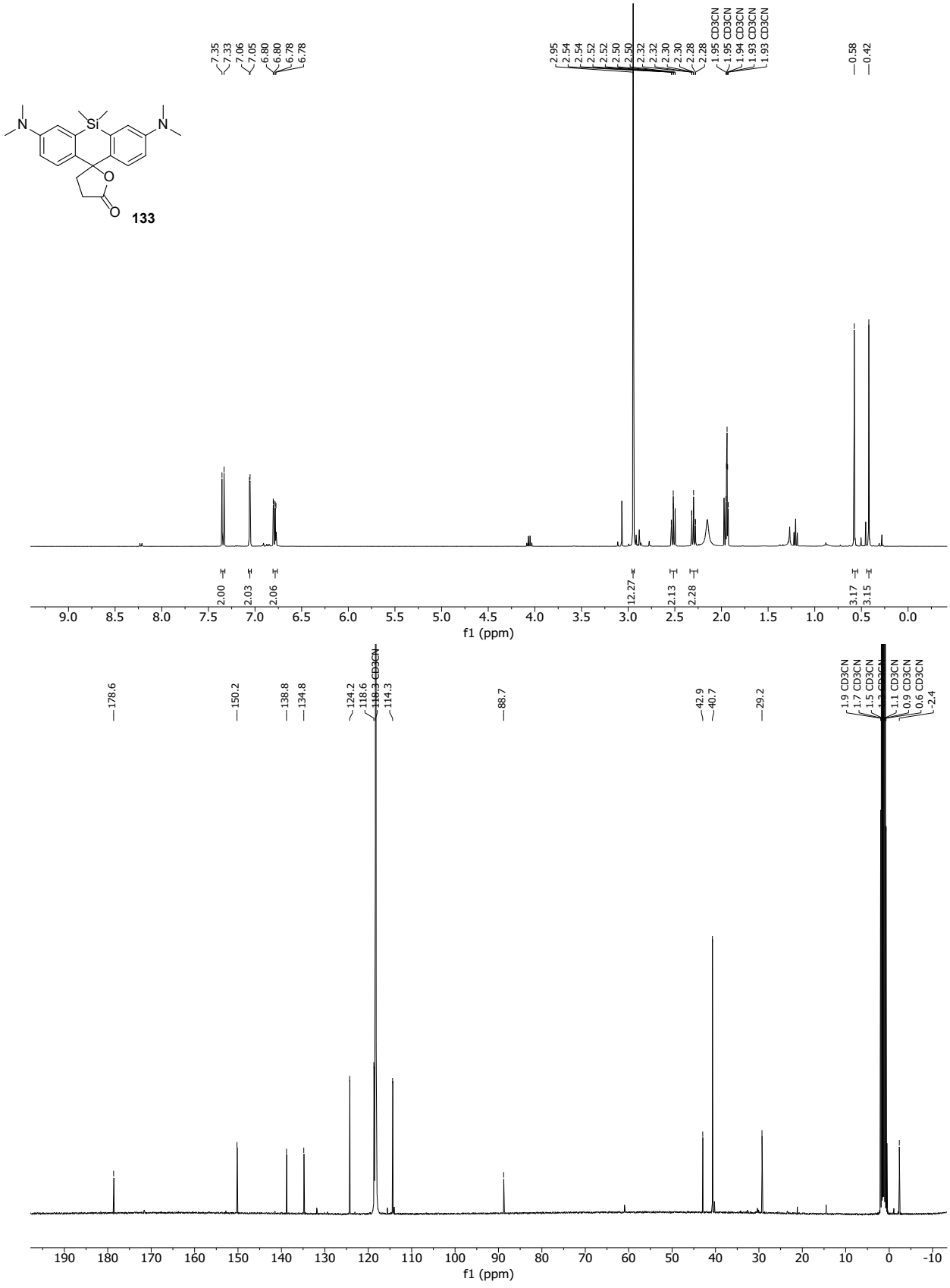
7.35
7.33
7.06
7.05
6.80
6.80
6.78
6.78
2.95
2.54
2.54
2.52
2.52
2.50
2.50
2.32
2.32
2.30
2.30
2.28
2.28
1.95 CD3CN
1.95 CD3CN
1.94 CD3CN
1.93 CD3CN
1.93 CD3CN
0.58
0.42
N
Si
N
O
O
133
2.00
2.03
2.06
12.27
2.13
2.28
3.17
3.15
9.0 8.5 8.0 7.5 7.0 6.5 6.0 5.5 5.0 4.5 4.0 3.5 3.0 2.5 2.0 1.5 1.0 0.5 0.0
f1 (ppm)
178.6
150.2
138.8
134.8
124.2
118.6
118.3 CD3CN
114.3
88.7
42.9
40.7
29.2
1.9 CD3CN
1.7 CD3CN
1.5 CD3CN
1.1 CD3CN
0.9 CD3CN
0.6 CD3CN
-2.4
190 180 170 160 150 140 130 120 110 100 90 80 70 60 50 40 30 20 10 0 -10
f1 (ppm)

PA-SiR-C3

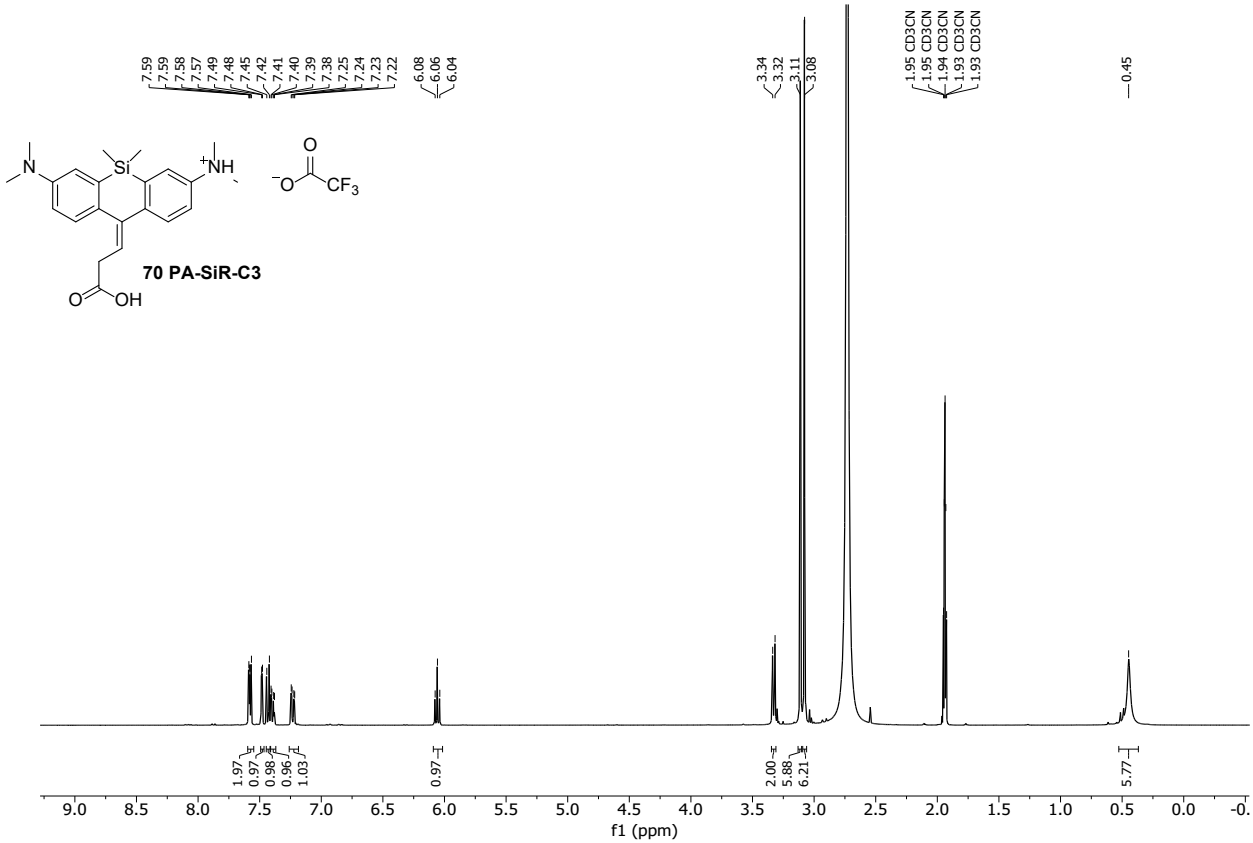

70 PA-SiR-C3

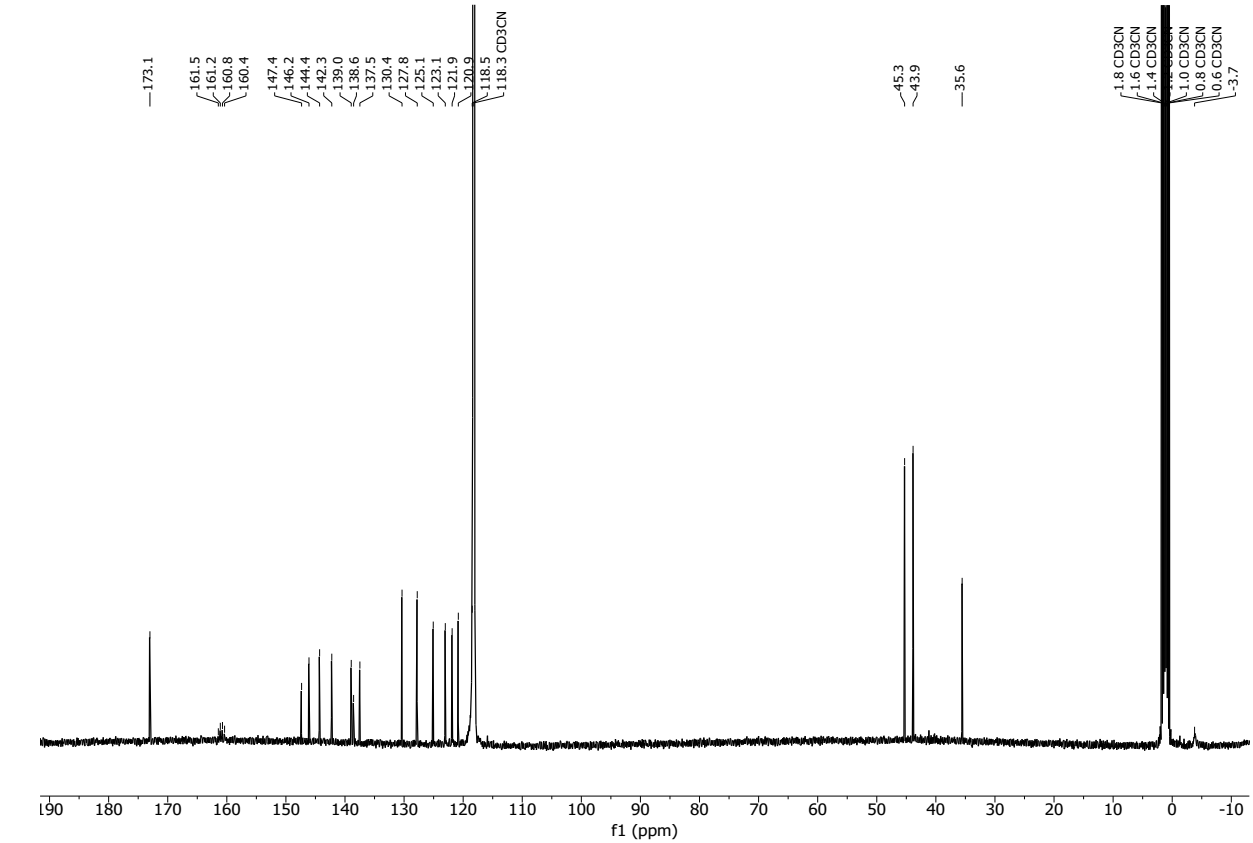

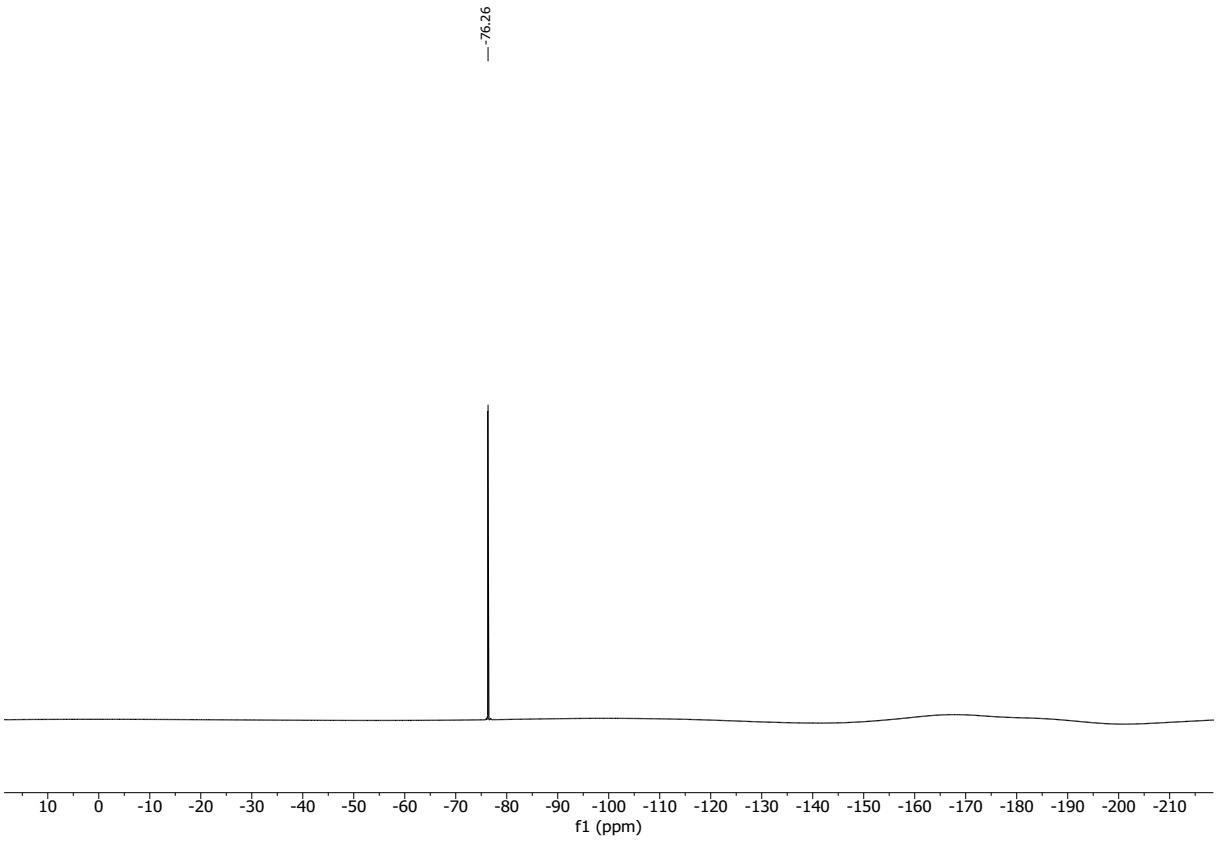
-76.26
10
0
-10
-20
-30
-40
-50
-60
-70
-80
-90
-100
-110
-120
-130
-140
-150
-160
-170
-180
-190
-200
-210
f1 (ppm)

71

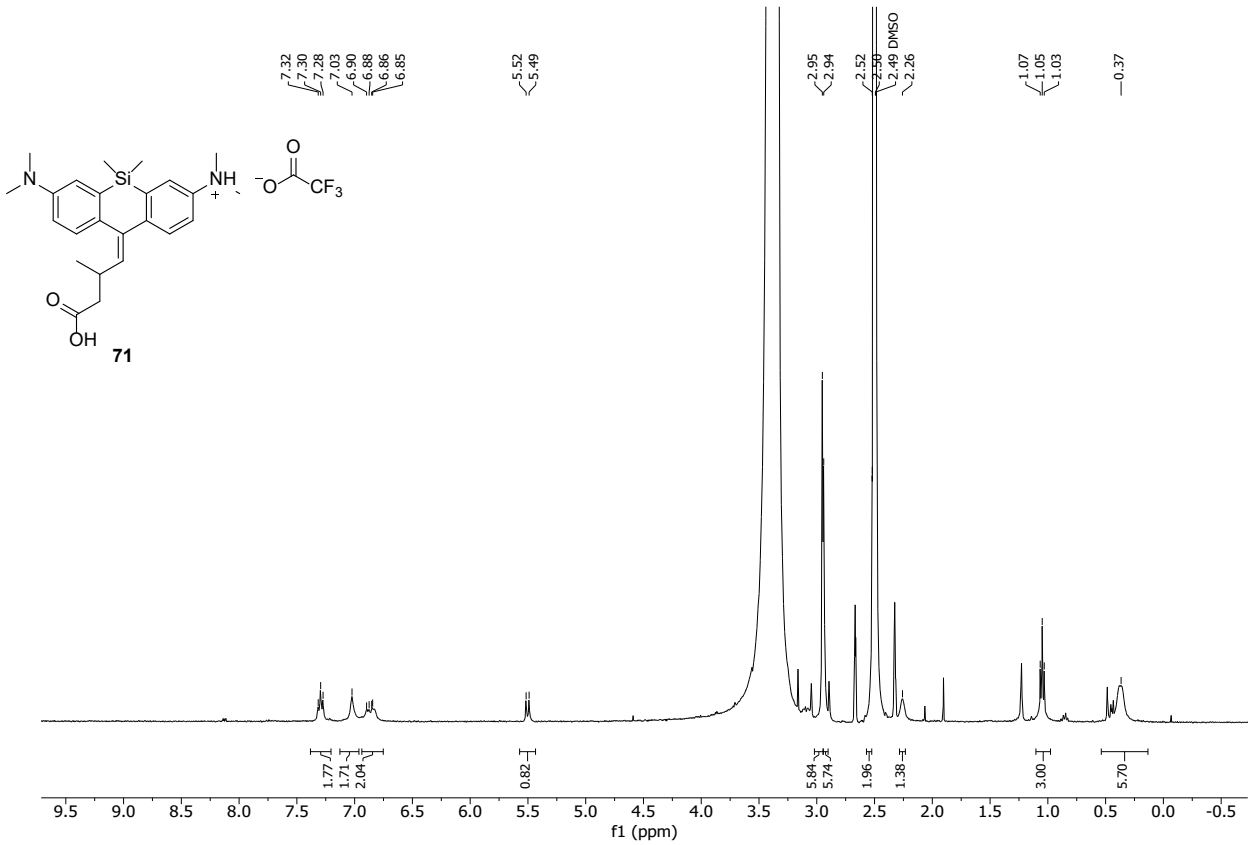
7.32
7.30
7.28
7.03
6.90
6.88
6.86
6.85
5.52
5.49
2.95
2.94
2.52
2.50
2.49 DMSO
2.26
1.07
1.05
1.03
0.37
1.77
1.71
2.04
0.82
5.84
5.74
1.96
1.38
3.00
5.70
f1 (ppm)

100

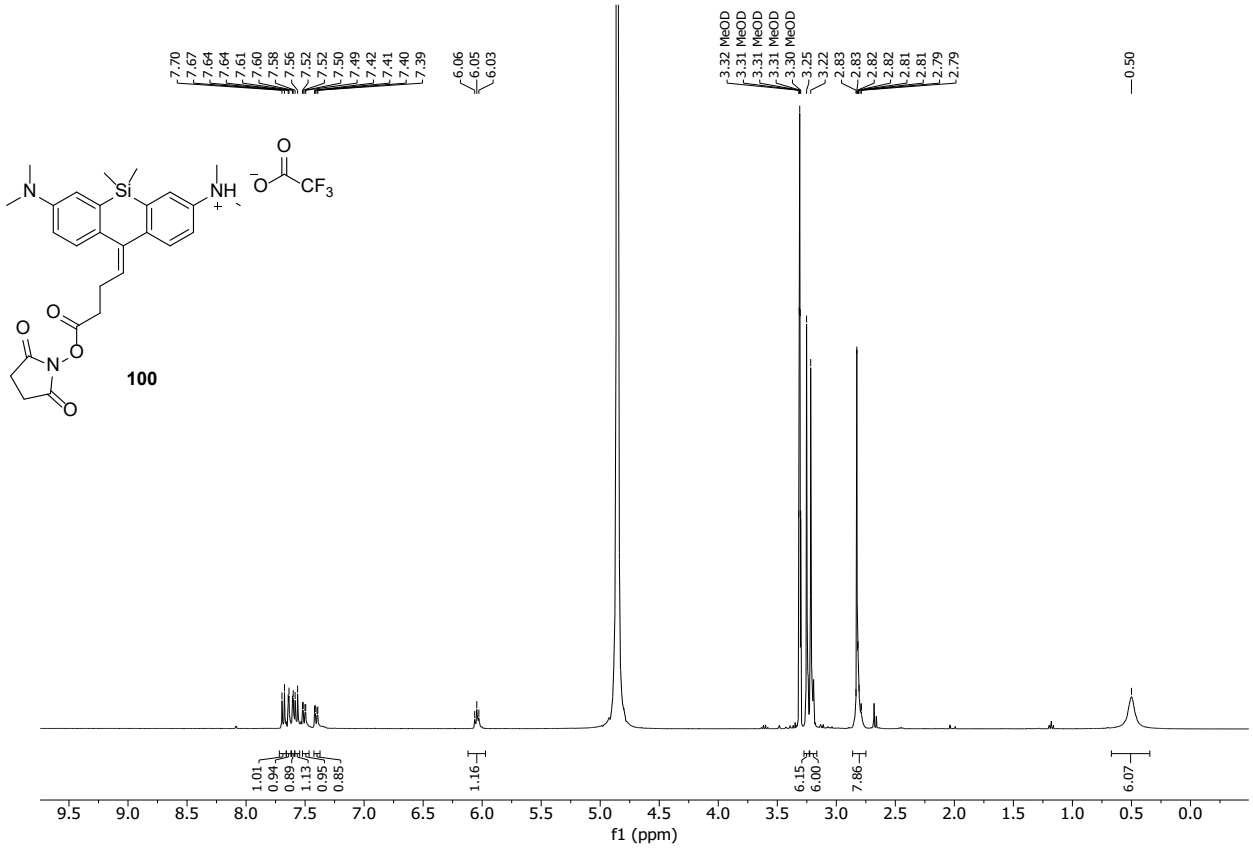
7.70
7.67
7.64
7.64
7.61
7.60
7.58
7.56
7.52
7.52
7.50
7.49
7.42
7.41
7.40
7.39
6.06
6.05
6.03
3.32 MeOD
3.31 MeOD
3.31 MeOD
3.31 MeOD
3.30 MeOD
3.25
3.22
2.83
2.83
2.82
2.82
2.81
2.81
2.79
2.79
0.50
1.01
0.94
0.89
1.13
0.95
0.85
1.16
6.15
6.00
7.86
6.07
f1 (ppm)

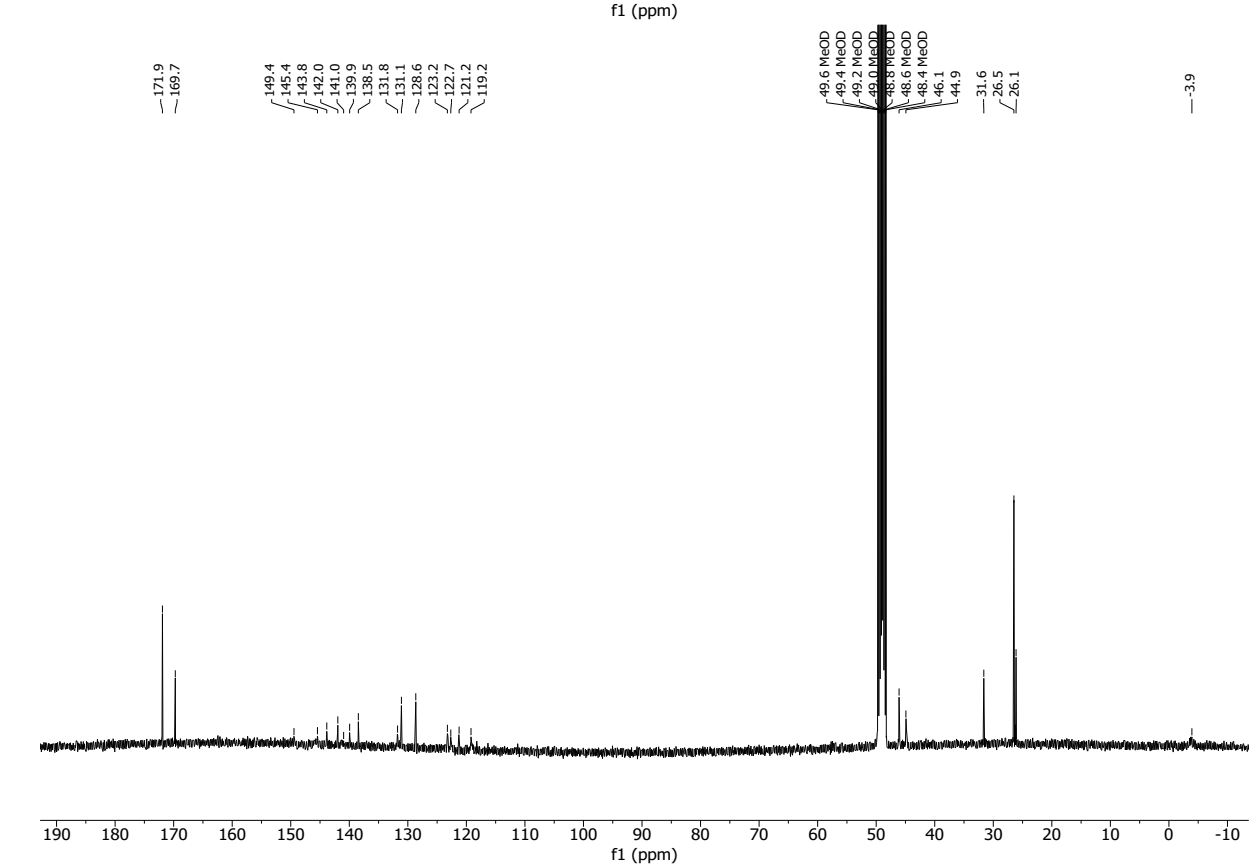
171.9
169.7
149.4
145.4
143.8
142.0
141.0
139.9
138.5
131.8
131.1
128.6
123.2
122.7
121.2
119.2
49.6 MeOD
49.4 MeOD
49.2 MeOD
49.0 MeOD
48.8 MeOD
48.6 MeOD
48.4 MeOD
46.1
44.9
31.6
26.5
26.1
-3.9
f1 (ppm)

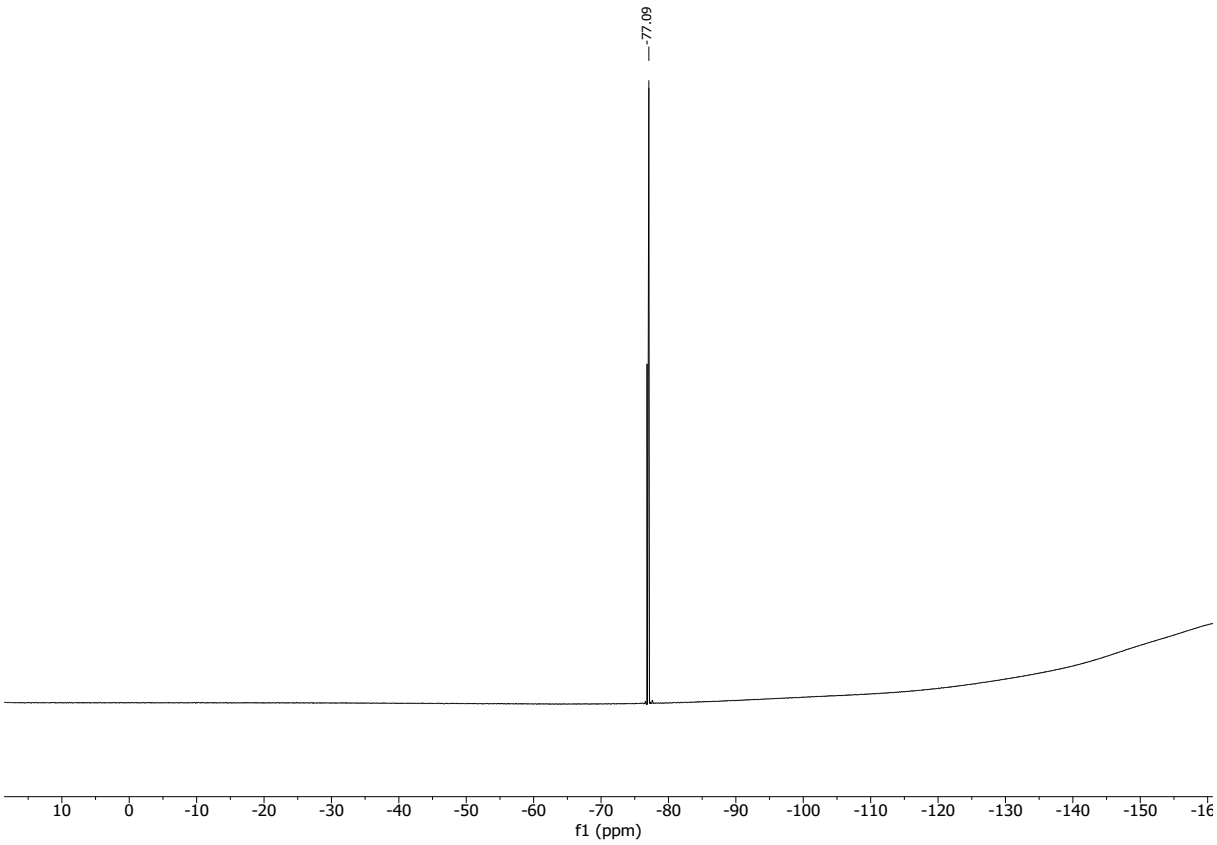
-77.09
10
0
-10
-20
-30
-40
-50
-60
-70
-80
-90
-100
-110
-120
-130
-140
-150
f1 (ppm)

PA-SiR-BG

103 PA-SiR-BG

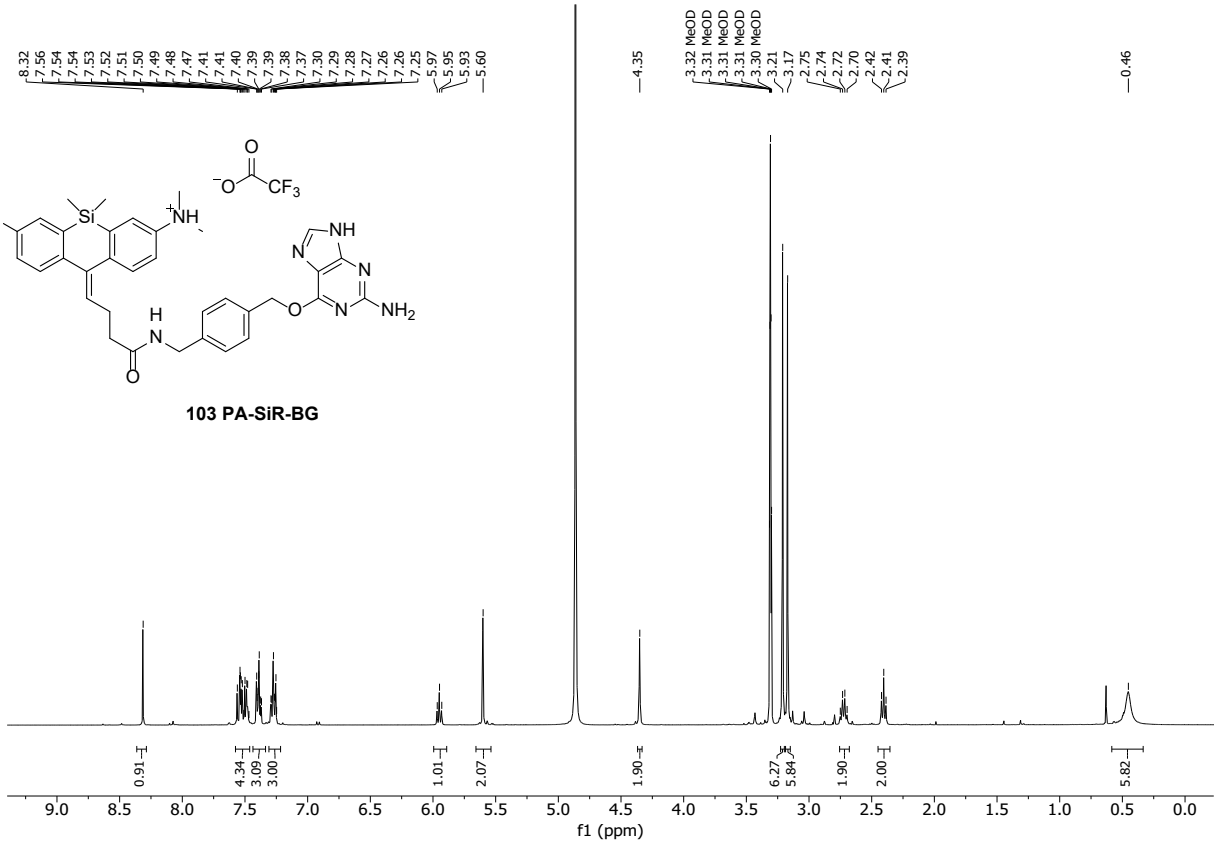

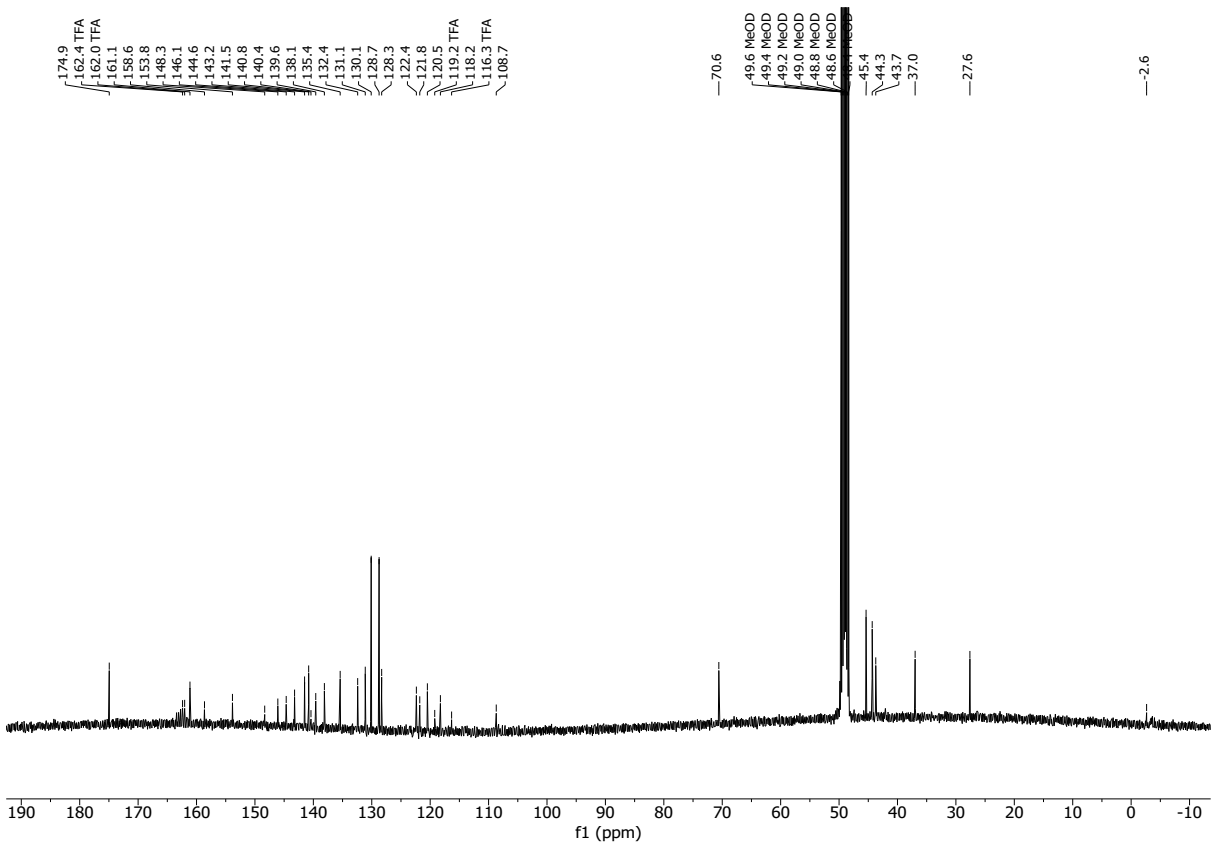

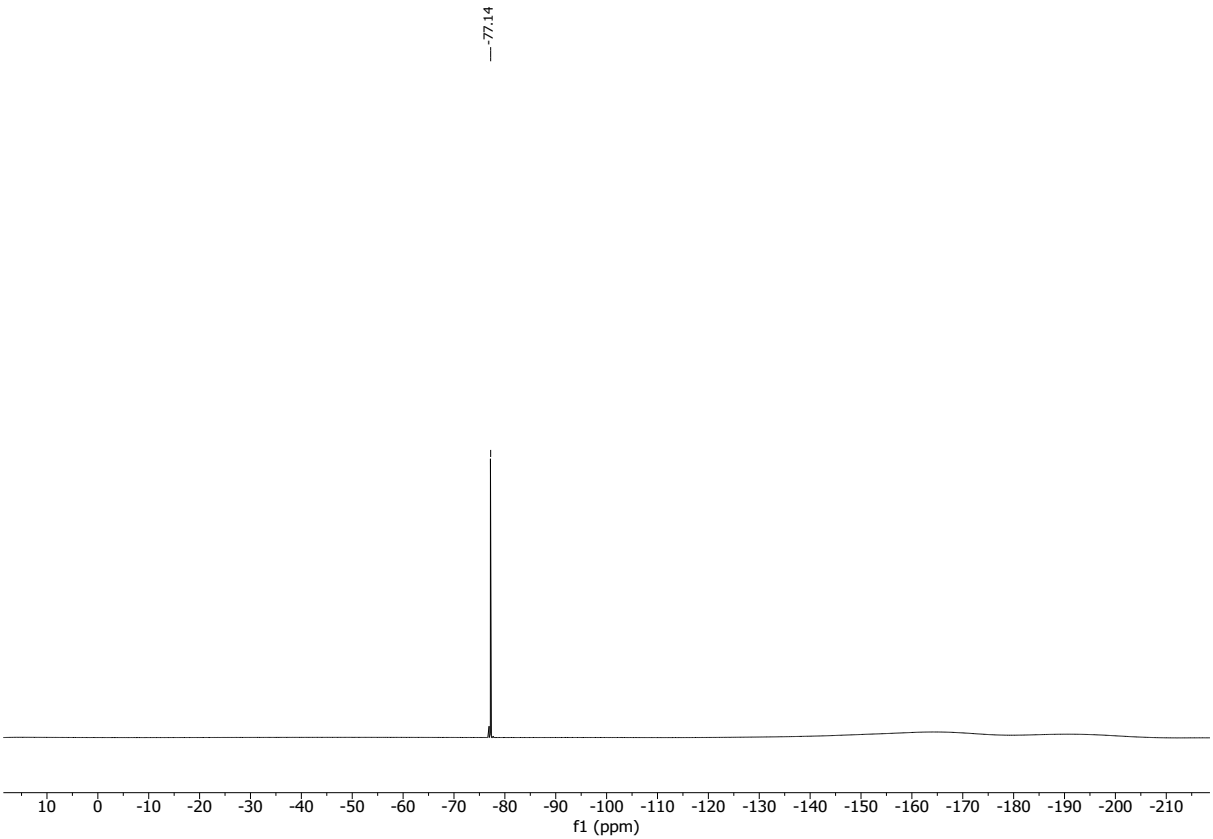
-77.14
10
0
-10
-20
-30
-40
-50
-60
-70
-80
-90
-100
-110
-120
-130
-140
-150
-160
-170
-180
-190
-200
-210
f1 (ppm)

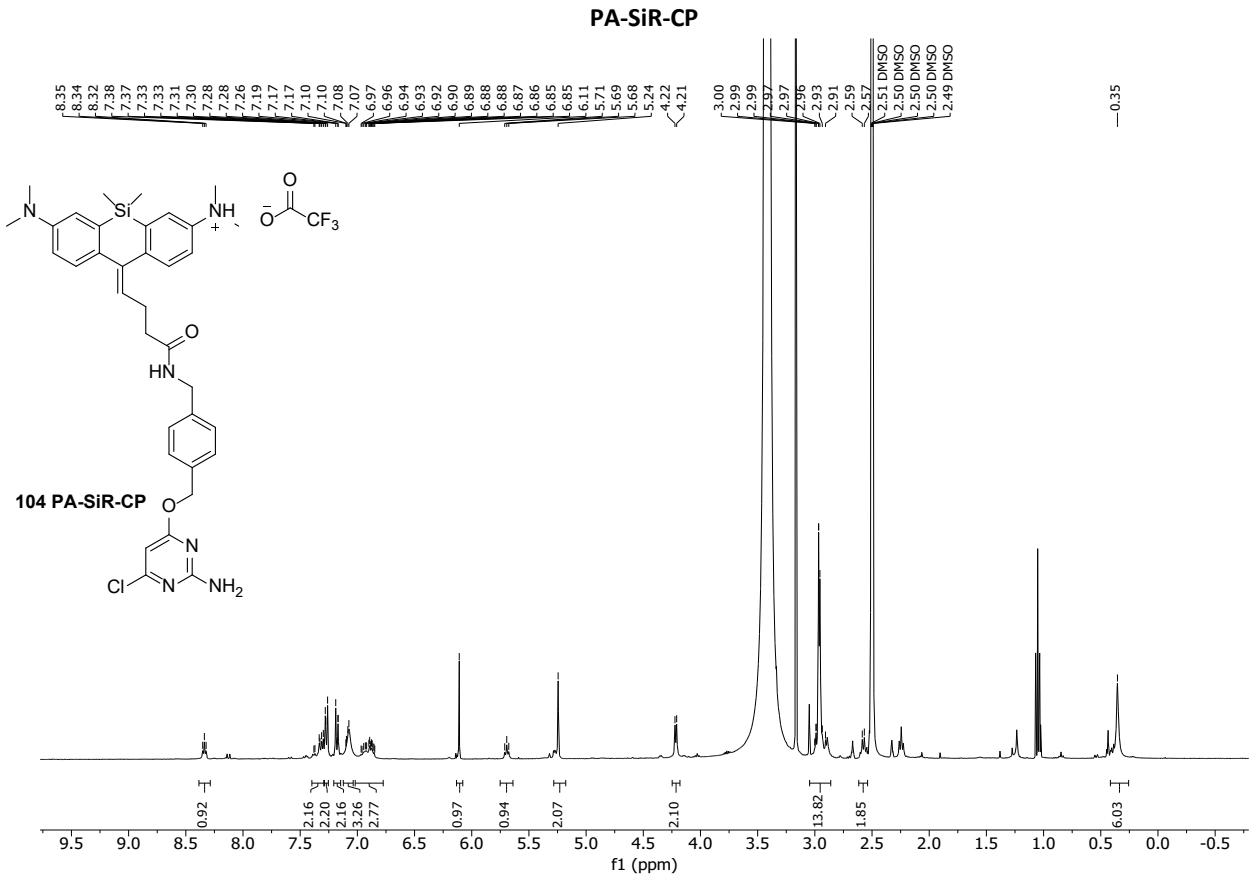
PA-SiR-CP
104 PA-SiR-CP
f1 (ppm)

PA-SiR-CA

105 PA-SiR-CA

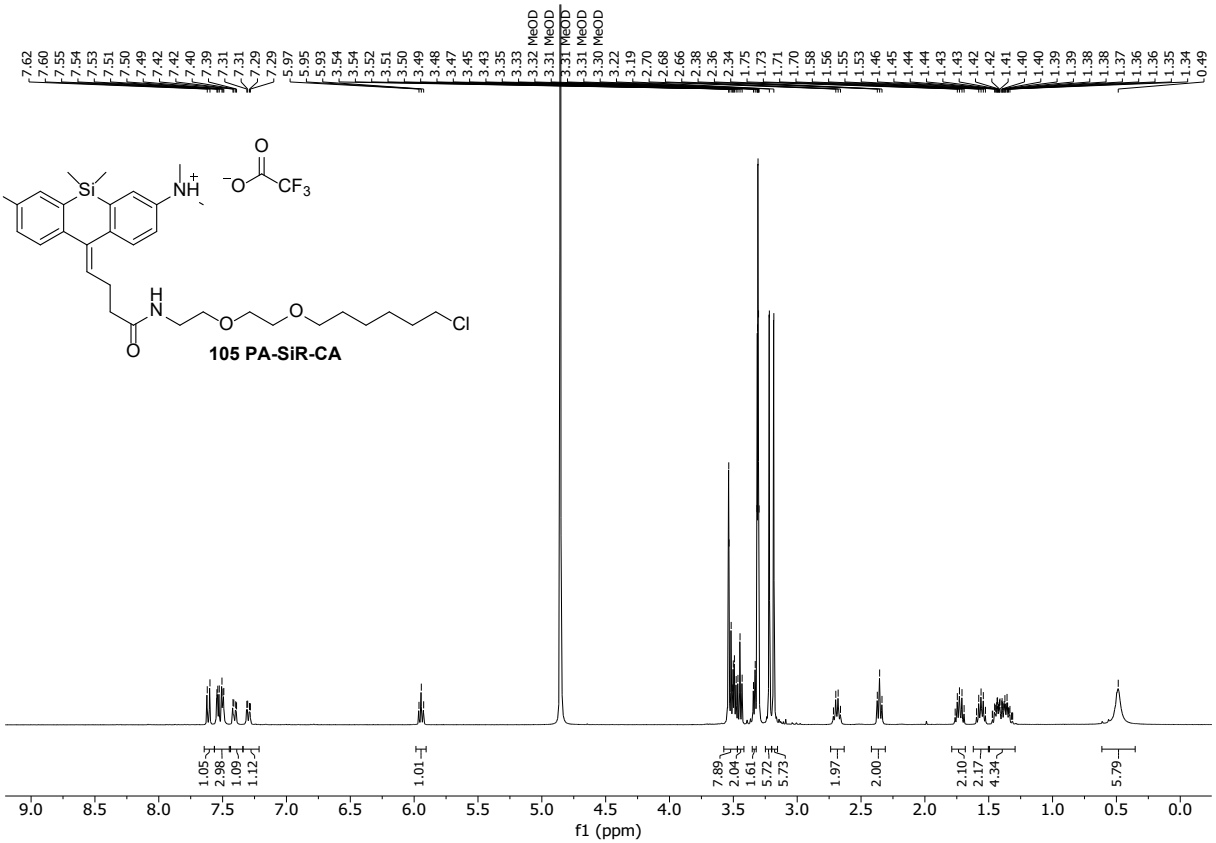

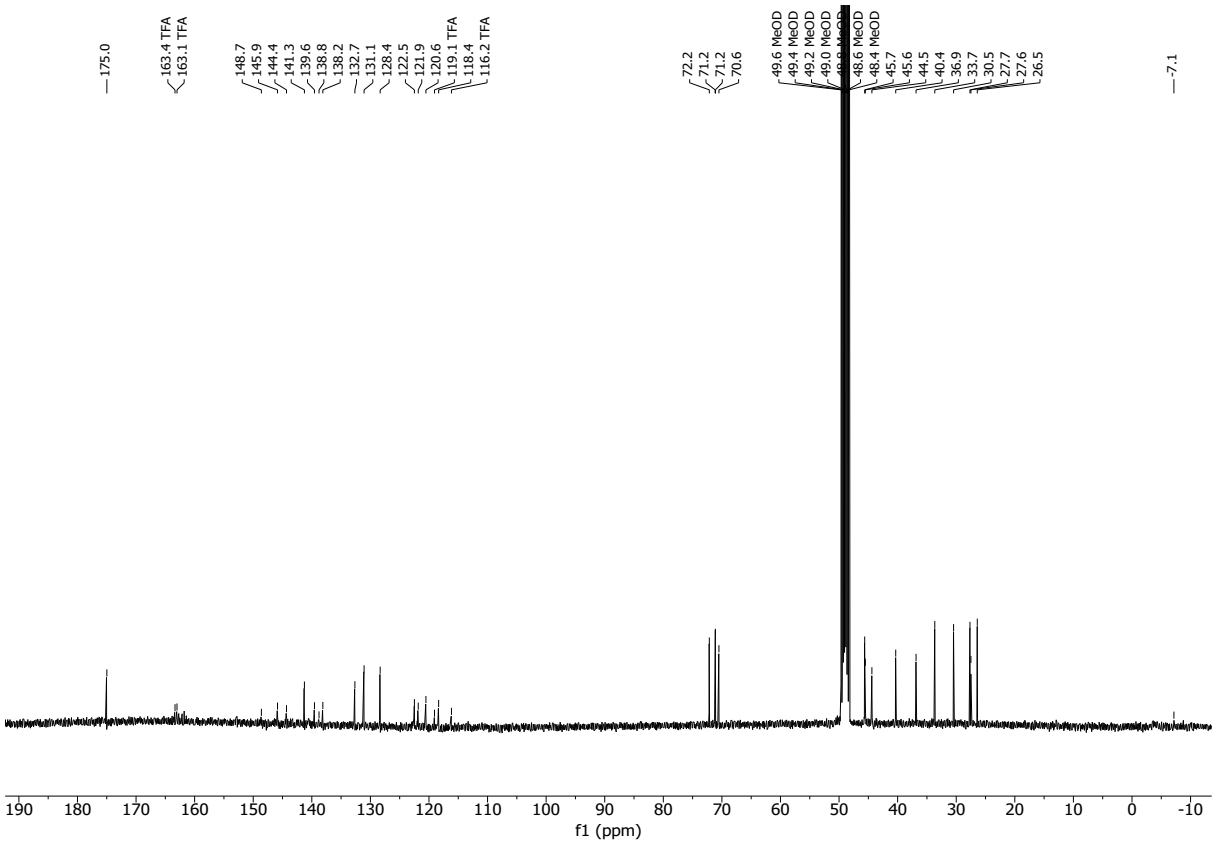

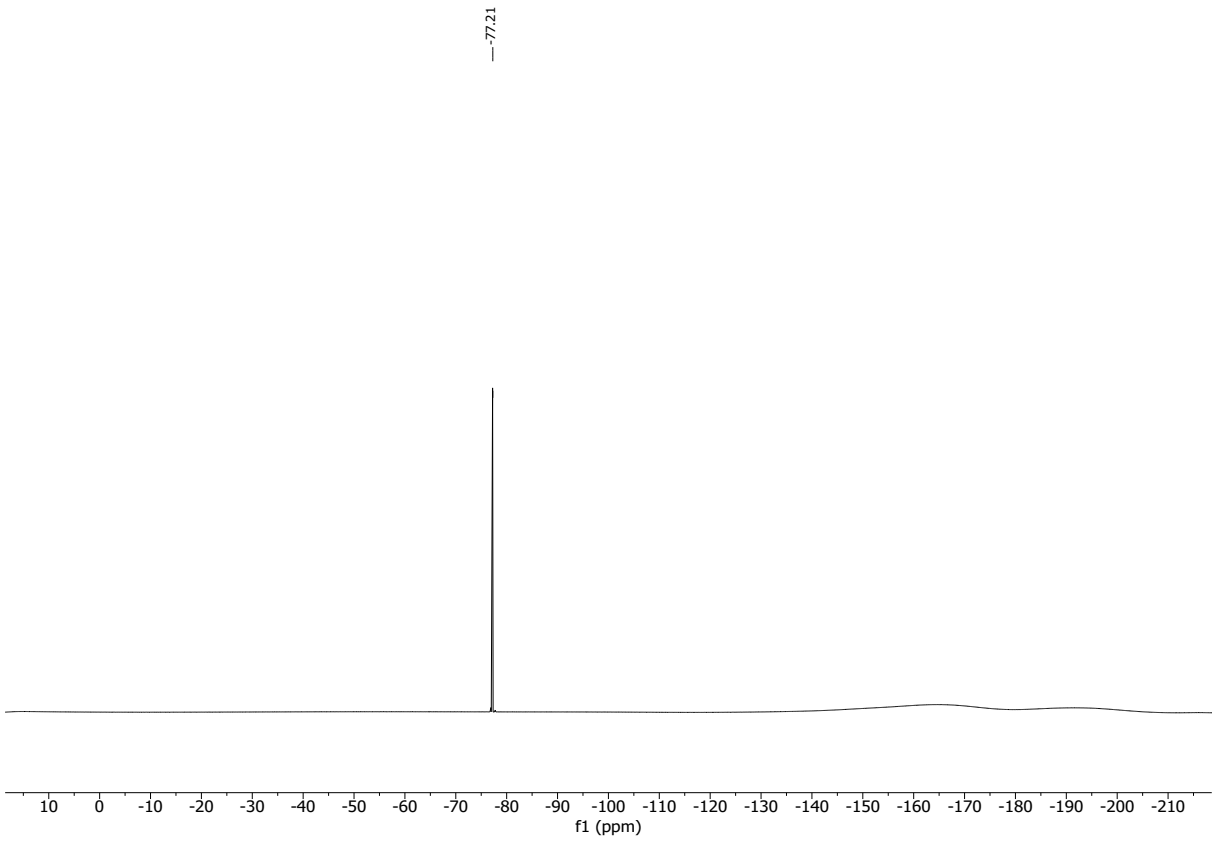
-77.21
10
0
-10
-20
-30
-40
-50
-60
-70
-80
-90
-100
-110
-120
-130
-140
-150
-160
-170
-180
-190
-200
-210
f1 (ppm)

139

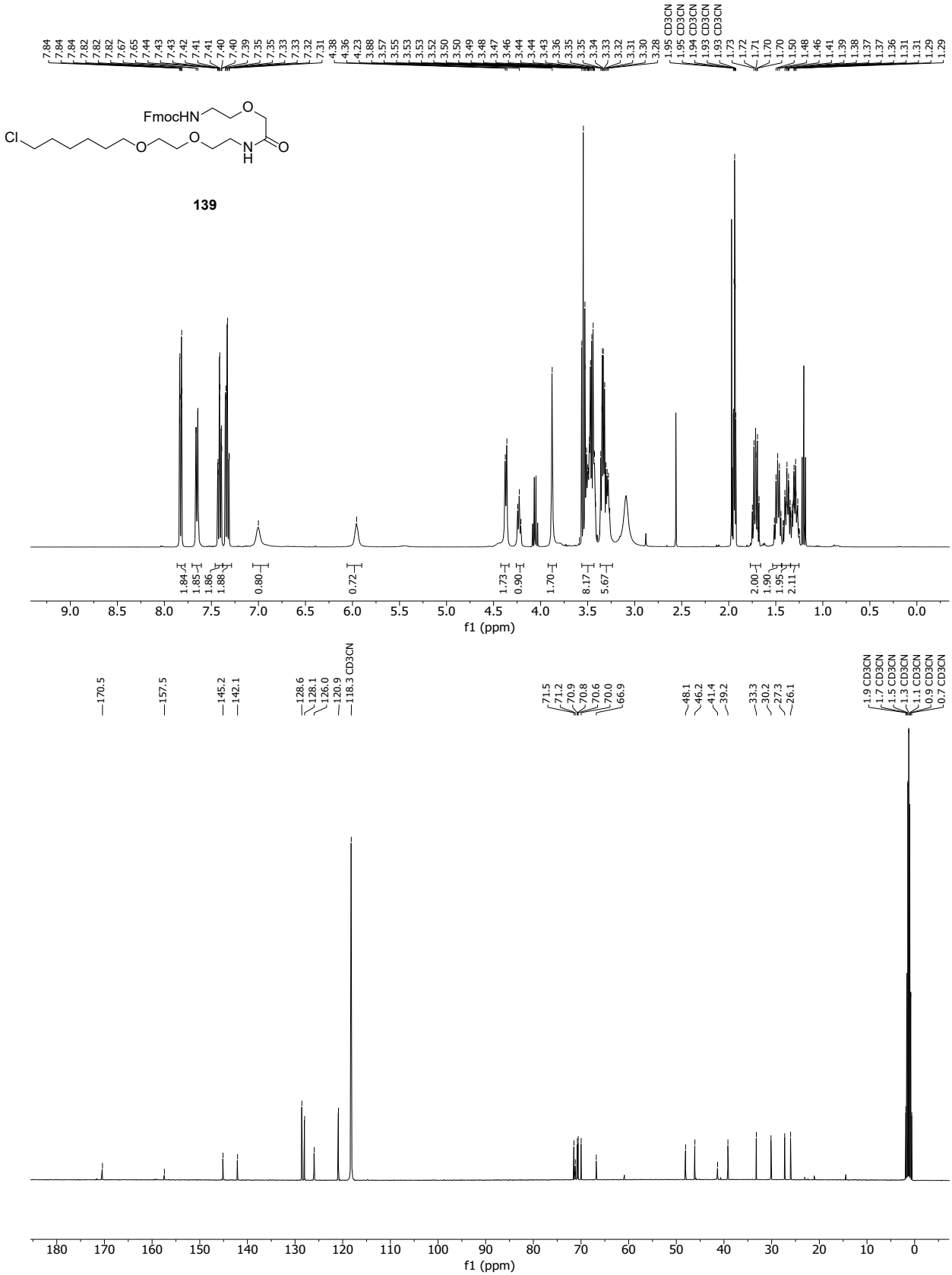

106

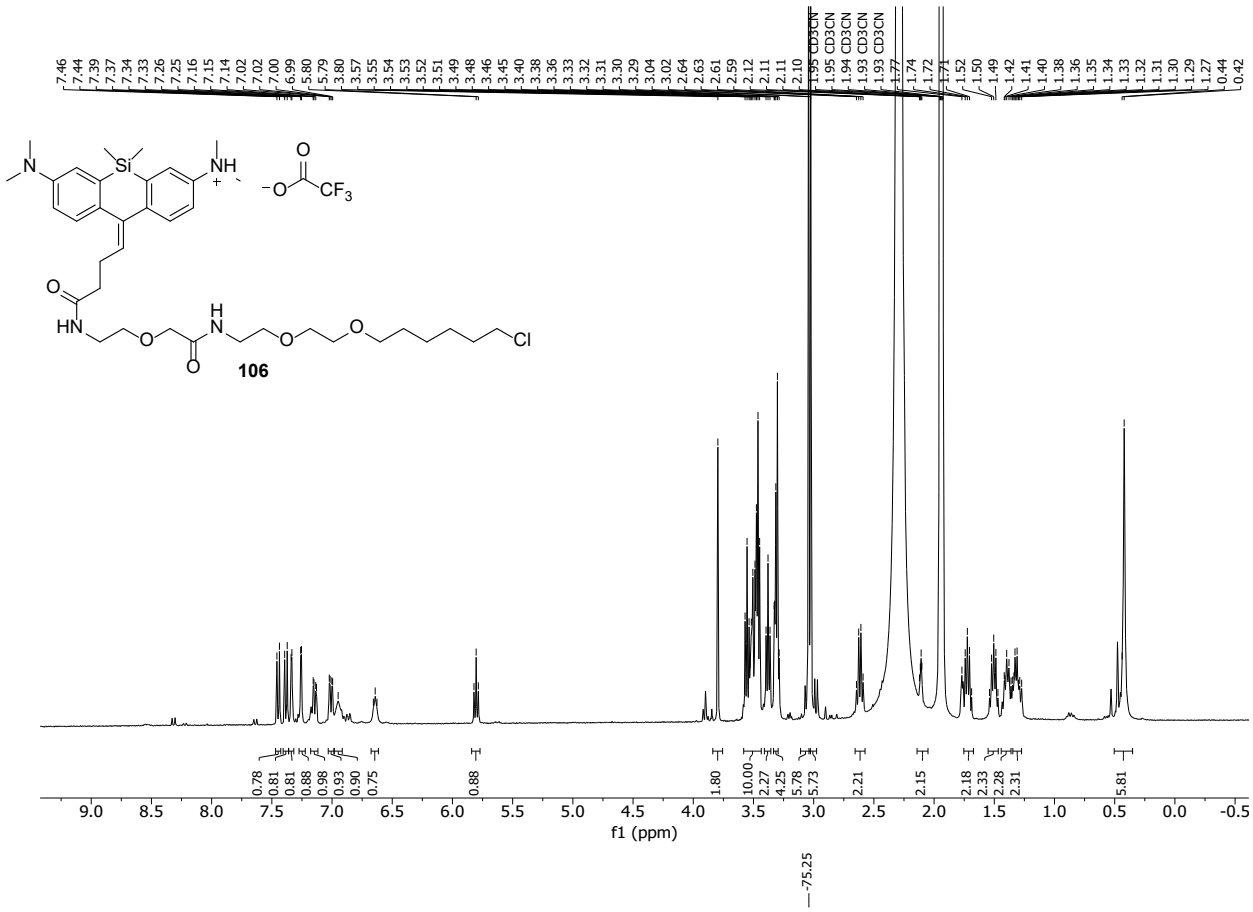

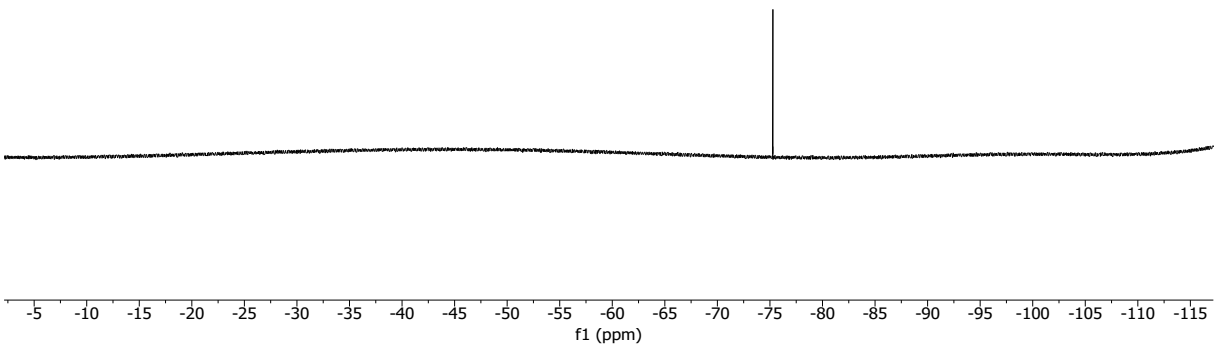

141

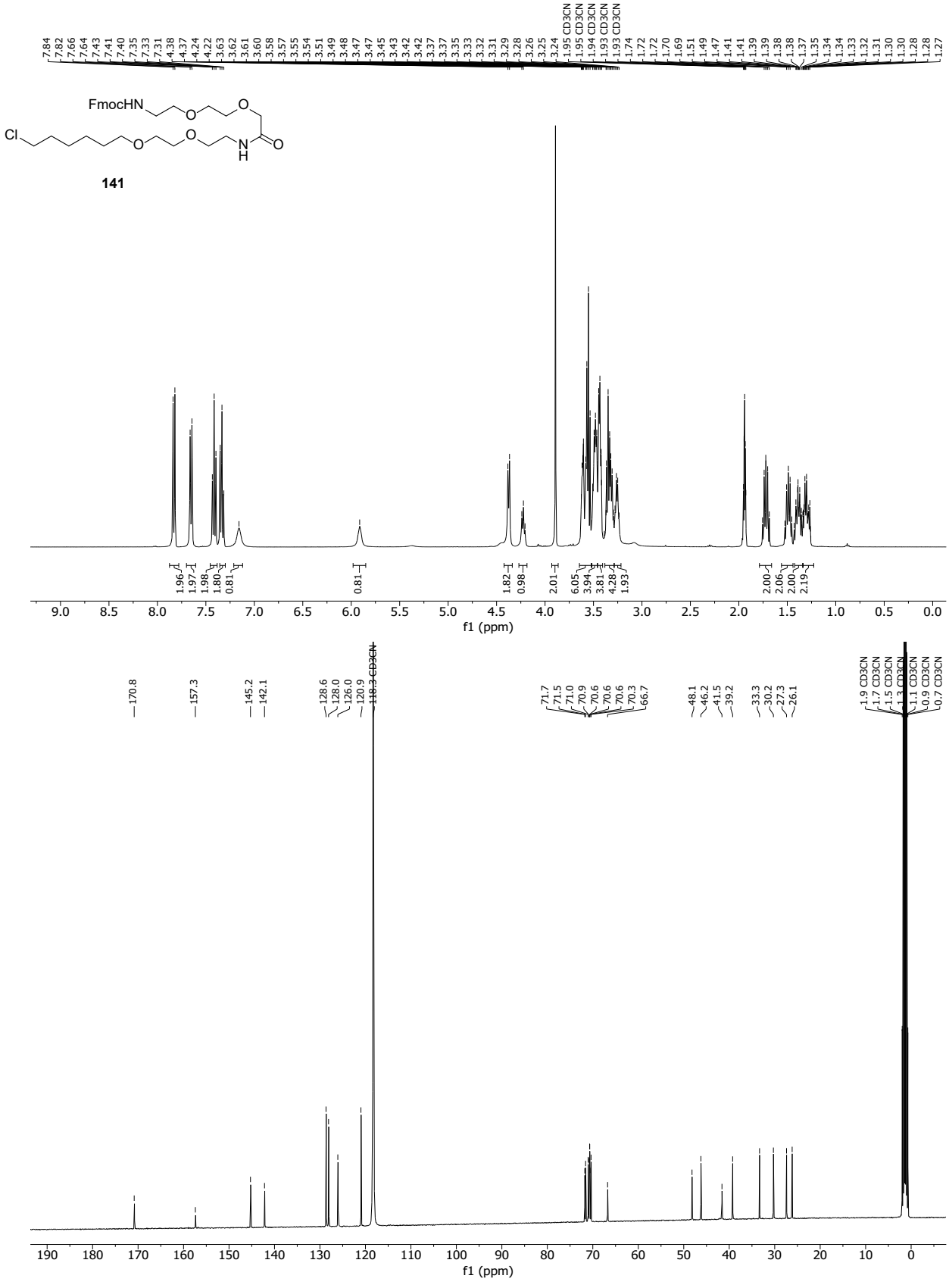

107

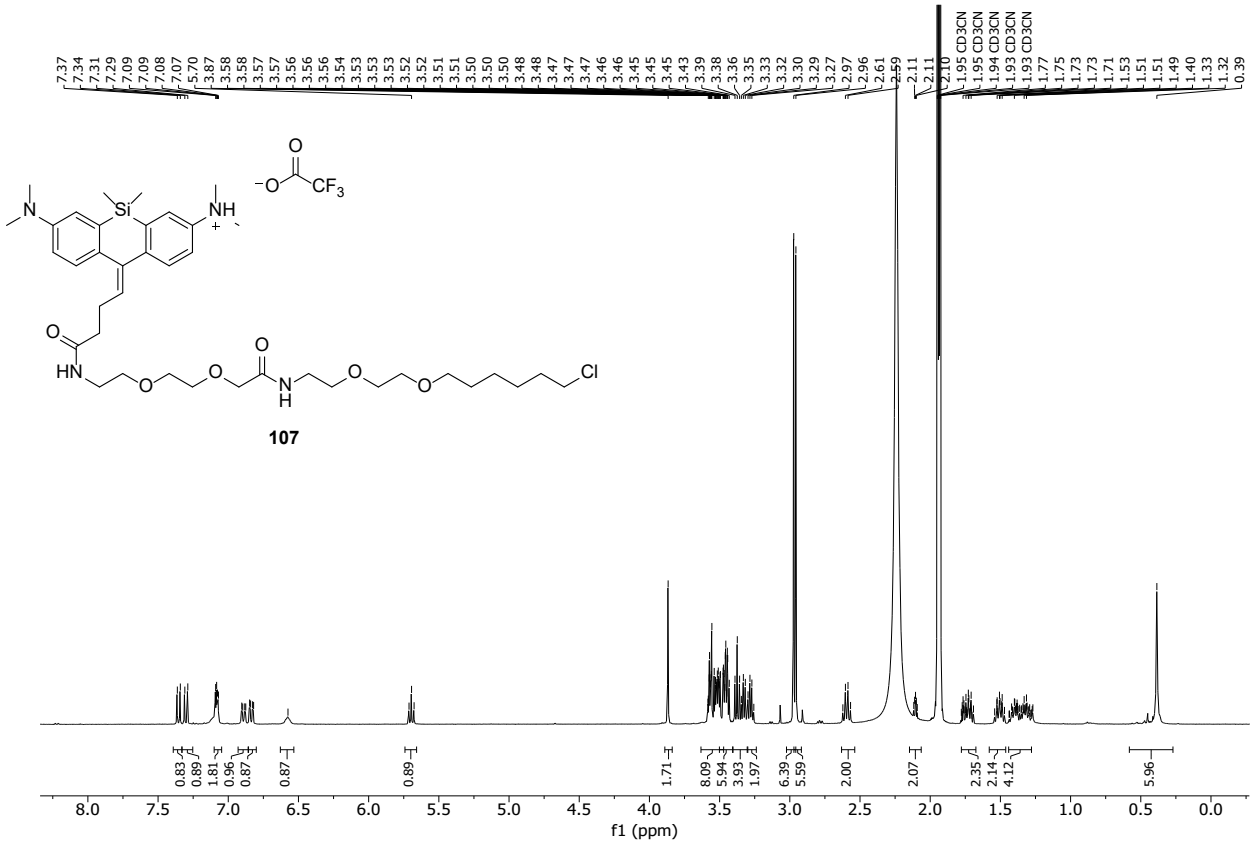
7.37 7.34 7.31 7.29 7.09 7.09 7.08 7.07 5.70 3.87 3.58 3.58 3.57 3.57 3.56 3.56 3.56 3.54 3.53 3.53 3.53 3.52 3.52 3.51 3.51 3.50 3.50 3.50 3.48 3.48 3.47 3.47 3.47 3.46 3.46 3.45 3.45 3.45 3.43 3.39 3.38 3.36 3.35 3.33 3.32 3.30 3.29 3.27 2.97 2.96 2.61 2.59 2.11 2.11 2.10 1.95 CD3CN 1.95 CD3CN 1.94 CD3CN 1.93 CD3CN 1.93 CD3CN 1.77 1.75 1.73 1.73 1.71 1.53 1.51 1.51 1.49 1.40 1.33 1.32 0.39
O
−O
CF3
N
Si
NH
+
O
HN
O
O
O
N
H
O
O
Cl
107
0.83 0.89 1.81 0.96 0.87 0.87 0.89 1.71 8.09 5.94 3.93 1.97 6.39 5.59 2.00 2.07 2.35 2.14 4.12 5.96
8.0 7.5 7.0 6.5 6.0 5.5 5.0 4.5 4.0 3.5 3.0 2.5 2.0 1.5 1.0 0.5 0.0
f1 (ppm)
-75.29
-5 -10 -15 -20 -25 -30 -35 -40 -45 -50 -55 -60 -65 -70 -75 -80 -85 -90 -95 -100 -105 -110 -115
f1 (ppm)

143

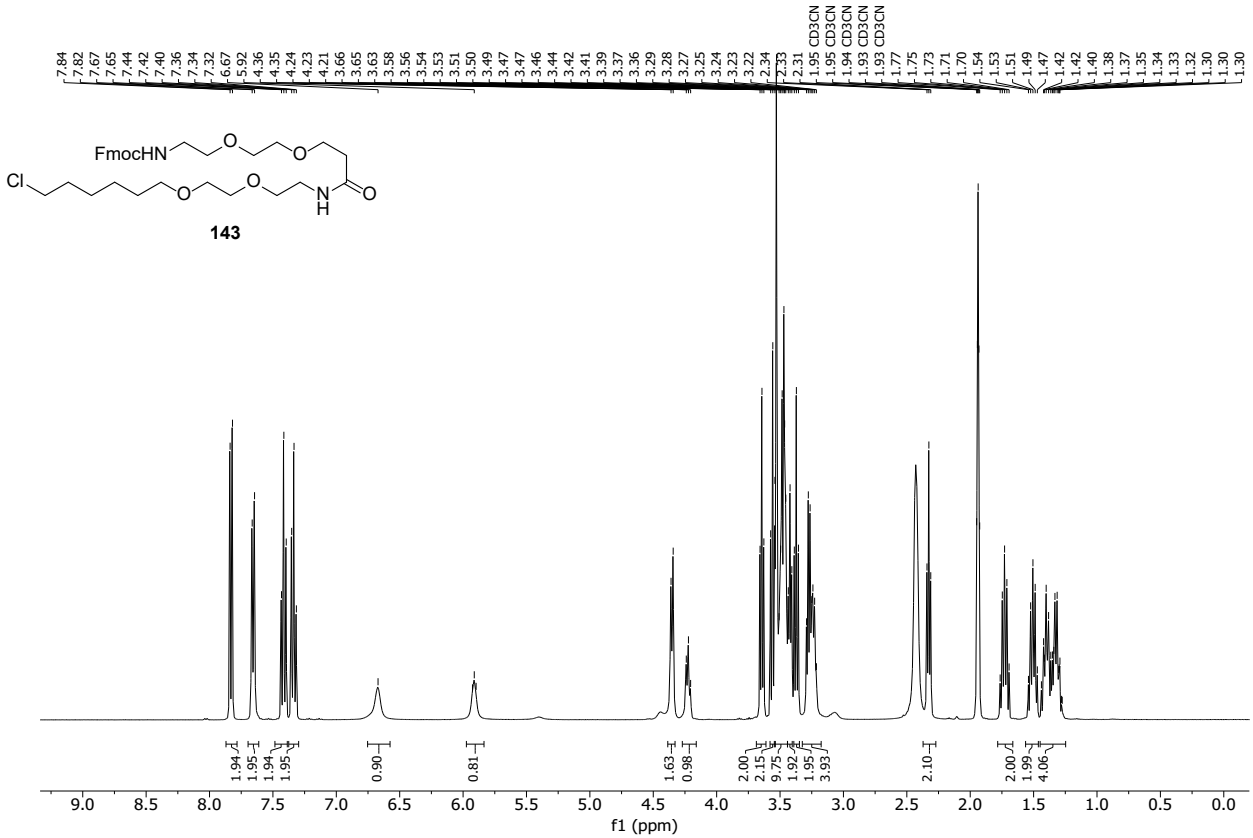

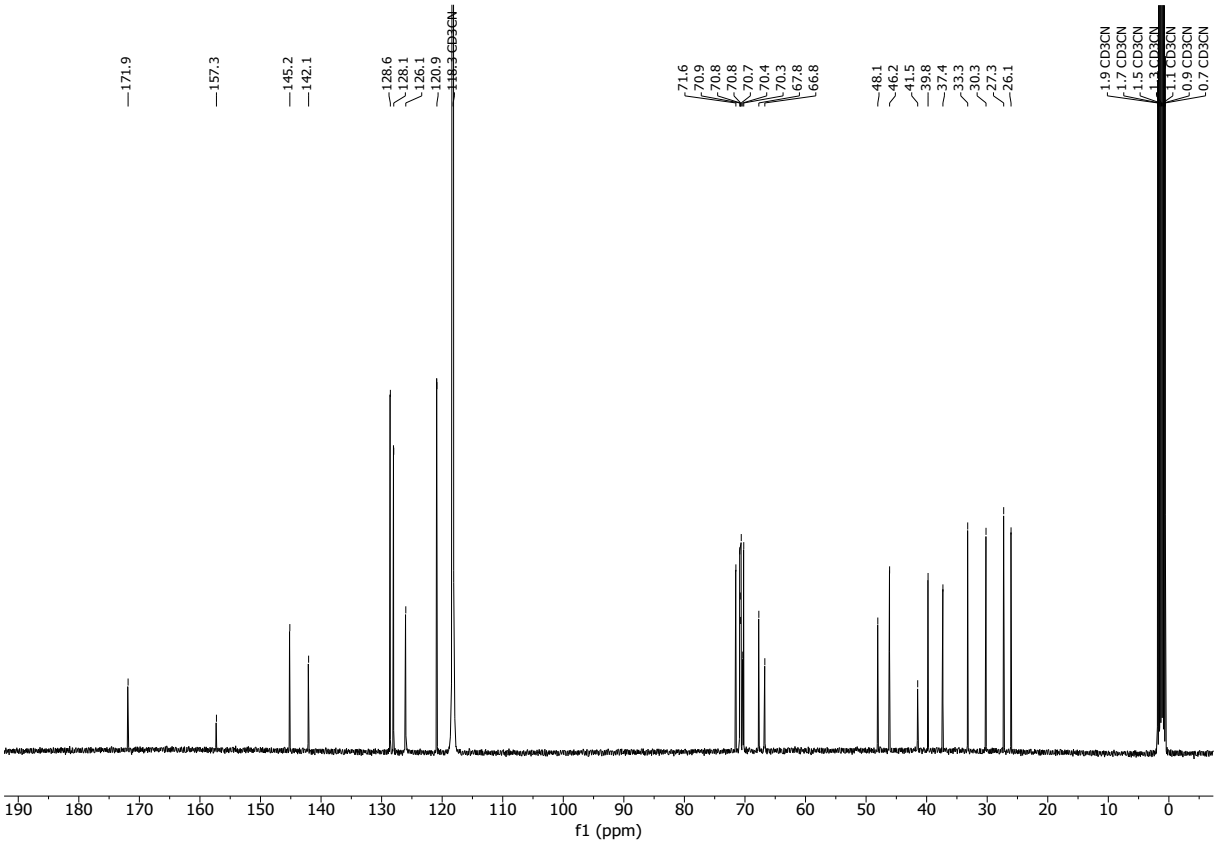

108

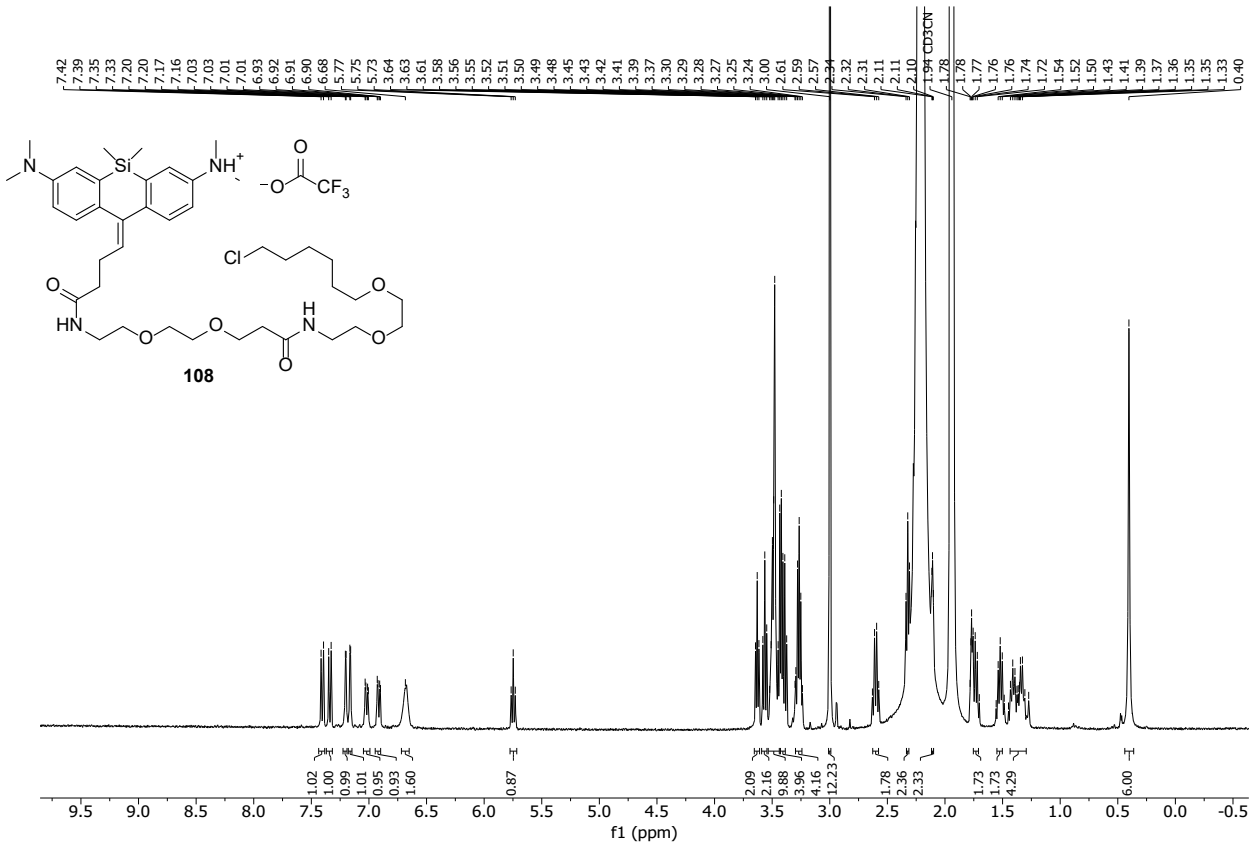

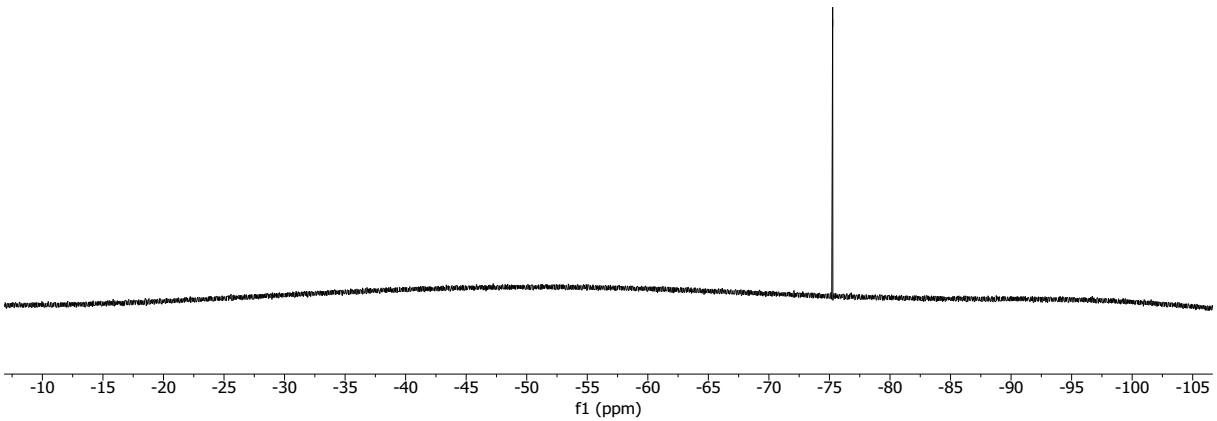

PA-SiR-jasplakinolide

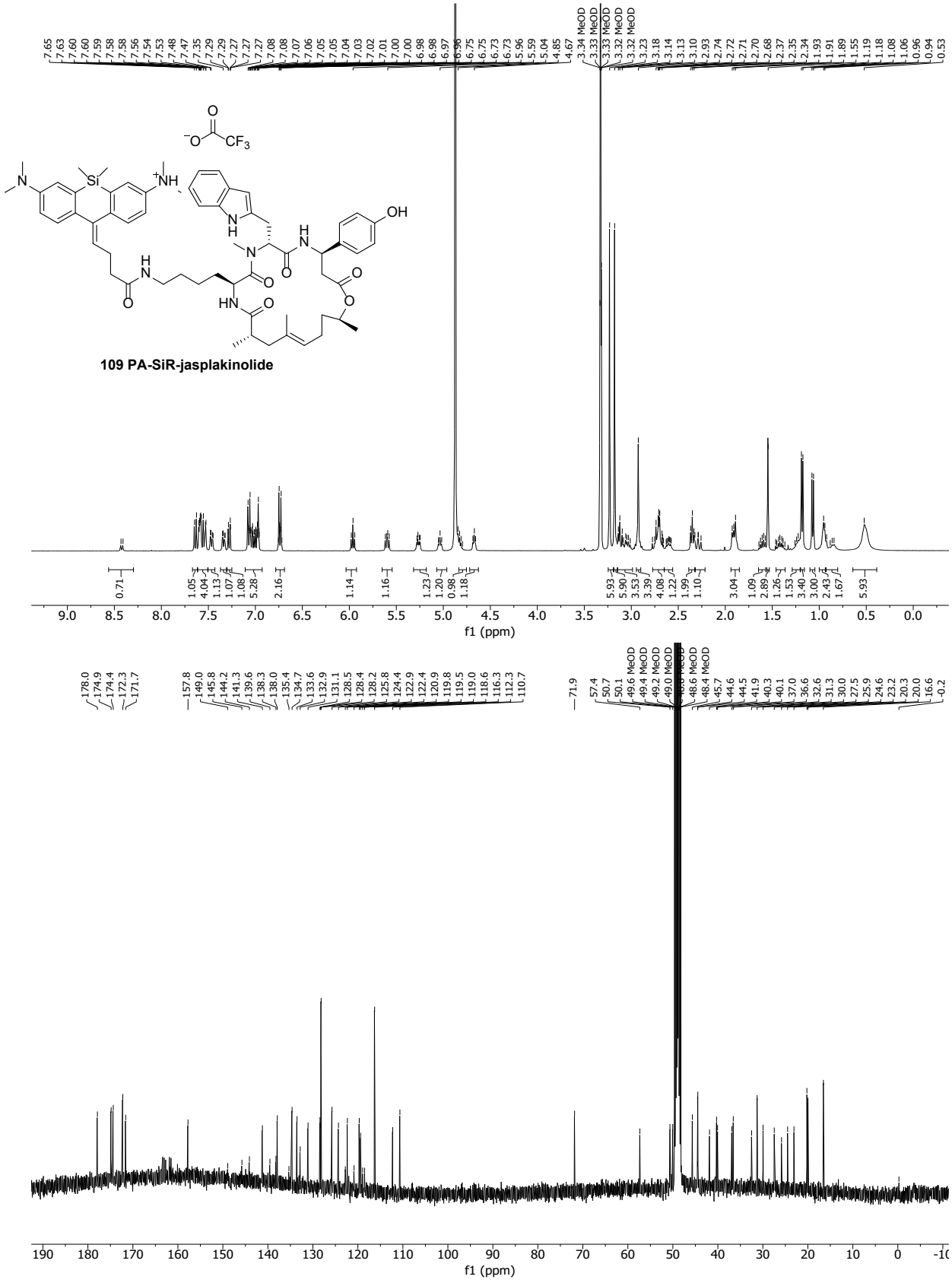

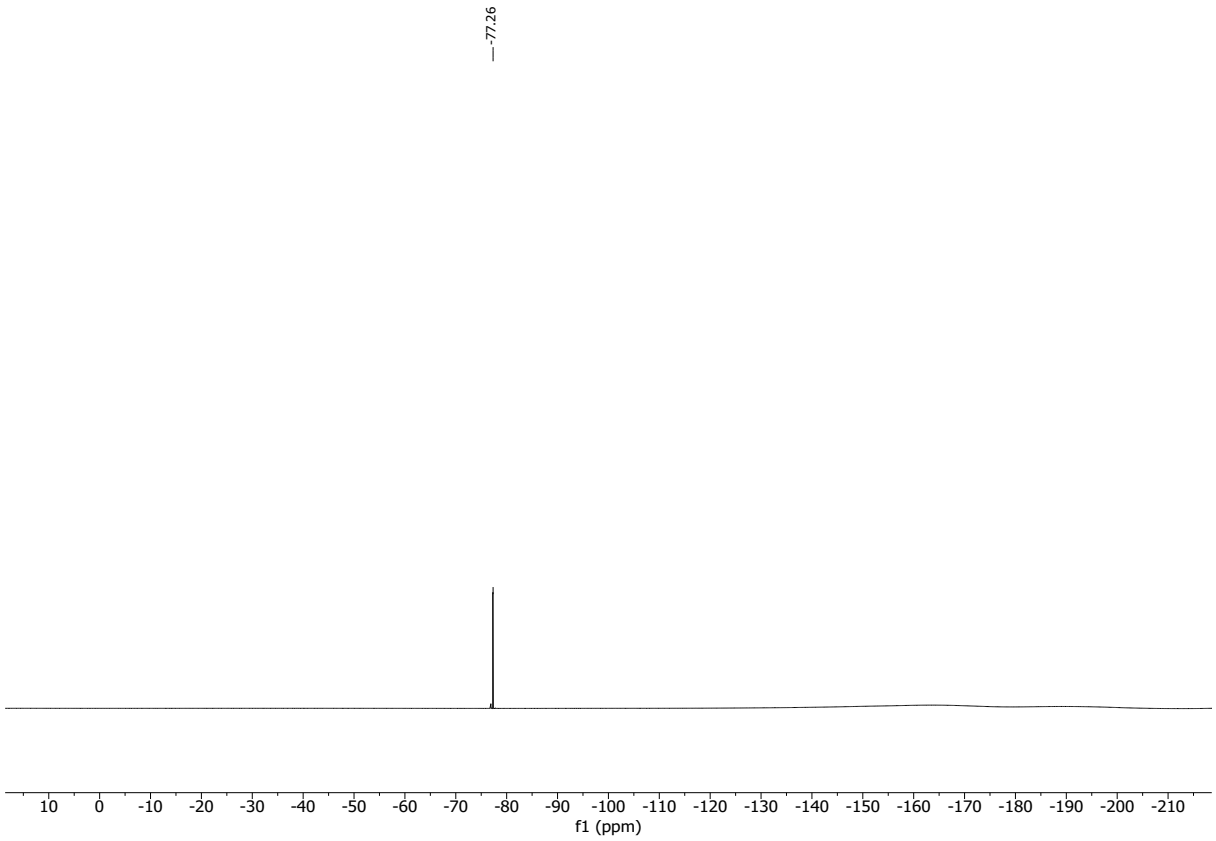
-77.26
10 0 -10 -20 -30 -40 -50 -60 -70 -80 -90 -100 -110 -120 -130 -140 -150 -160 -170 -180 -190 -200 -210
f1 (ppm)

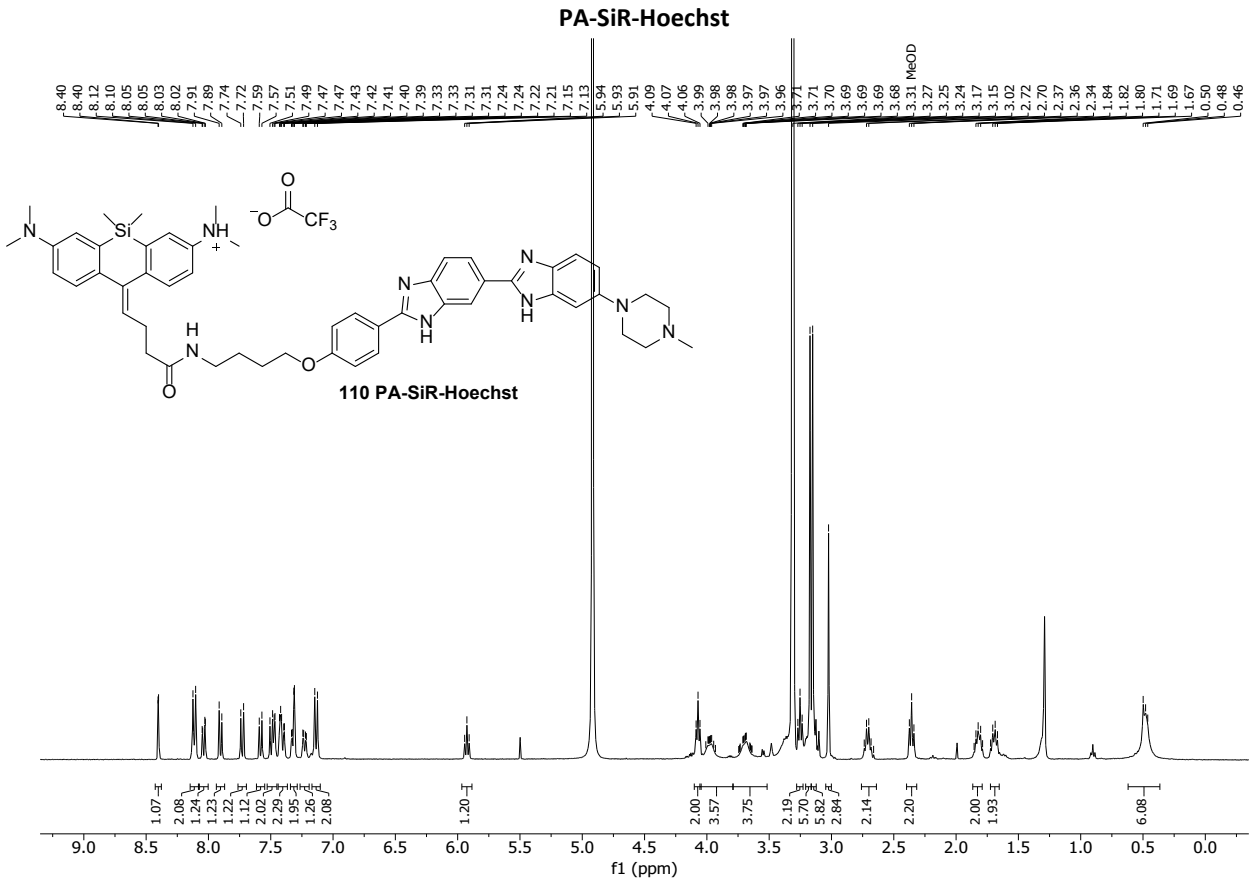
PA-SiR-Hoechst
110 PA-SiR-Hoechst
f1 (ppm)

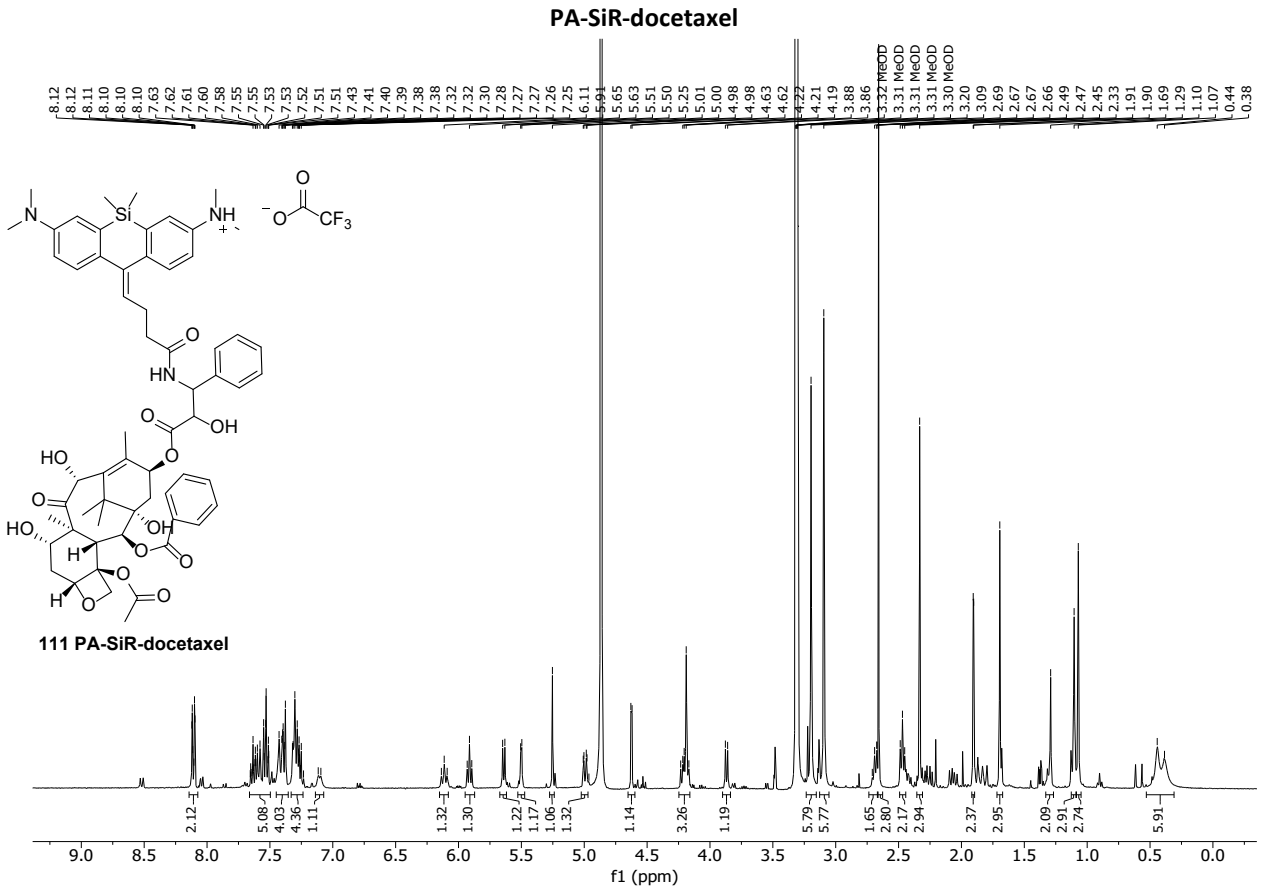
PA-SiR-docetaxel
111 PA-SiR-docetaxel
f1 (ppm)

PA-SiR-cabazitaxel

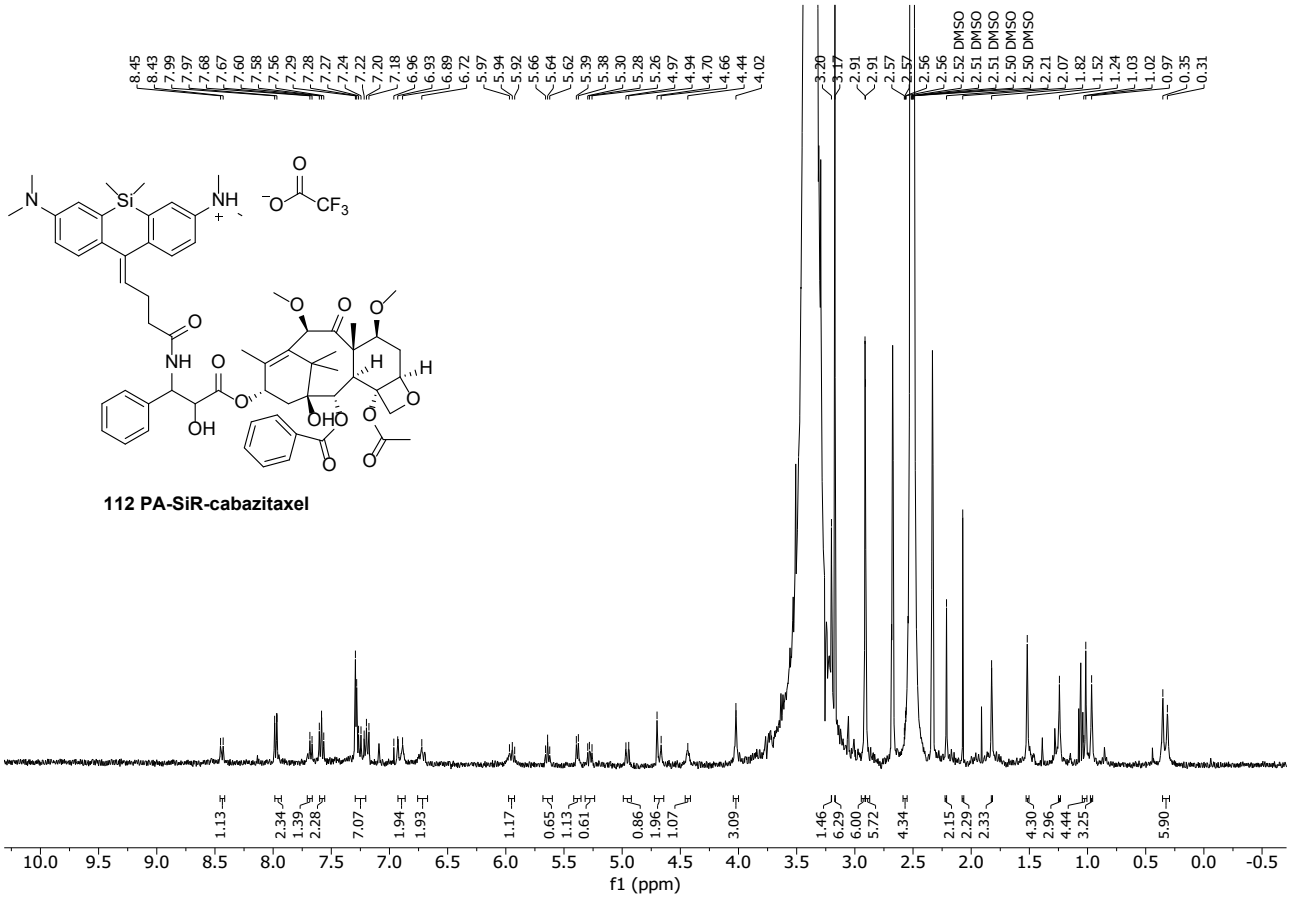

112 PA-SiR-cabazitaxel

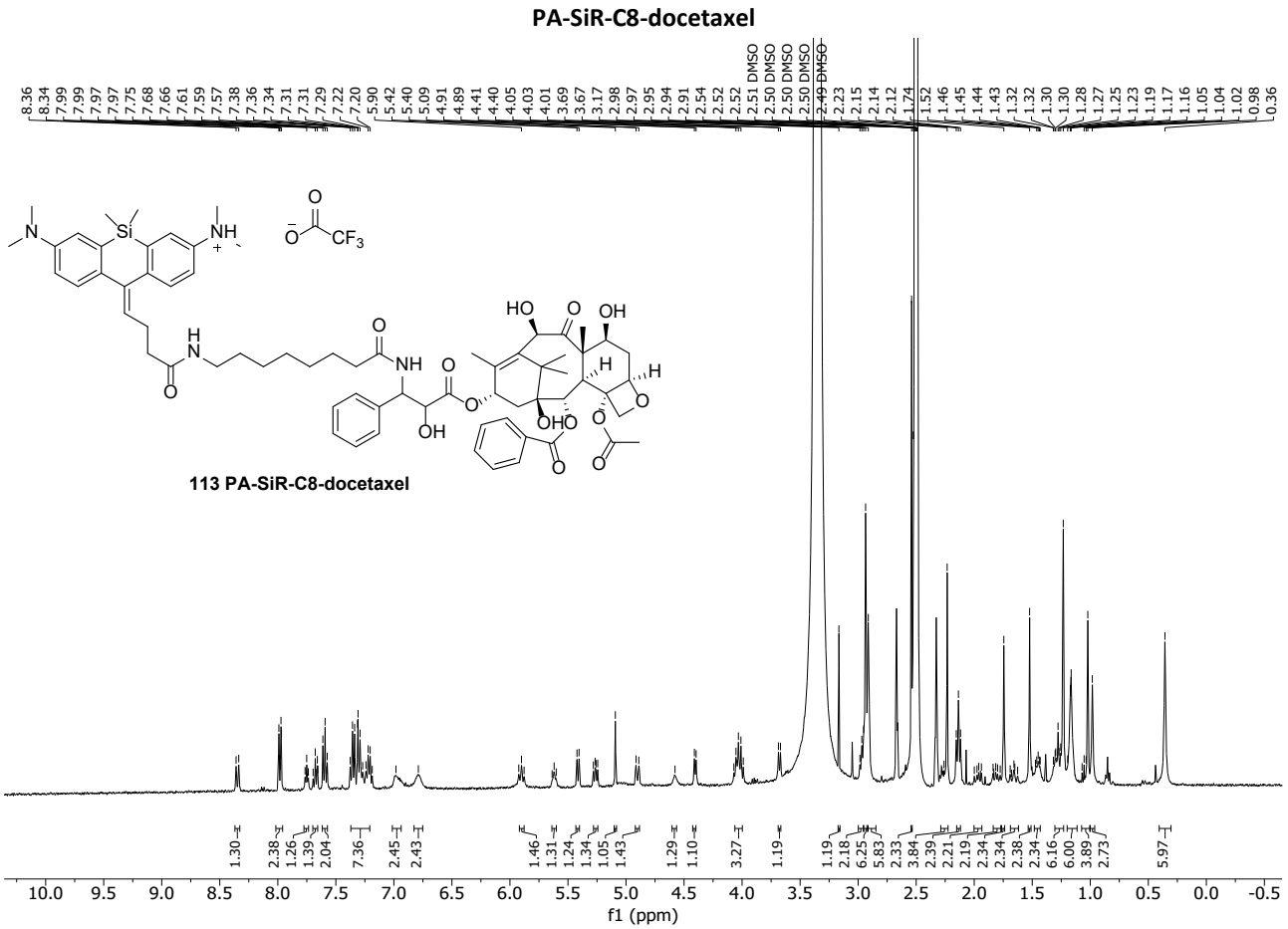
PA-SiR-C8-docetaxel
113 PA-SiR-C8-docetaxel
f1 (ppm)

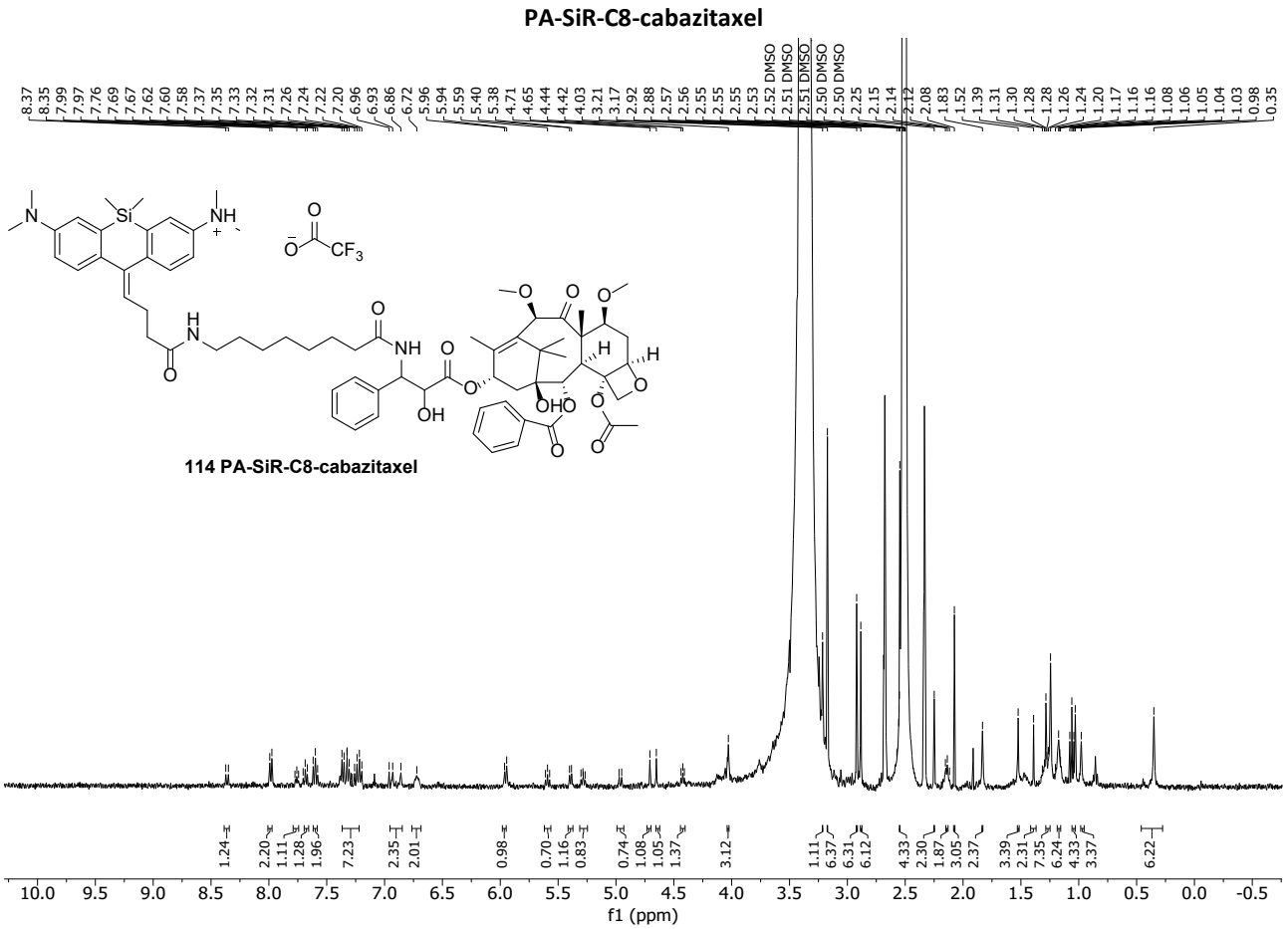
PA-SiR-C8-cabazitaxel
114 PA-SiR-C8-cabazitaxel
f1 (ppm)

PA-SiR-C3-CA

116 PA-SiR-C3-CA

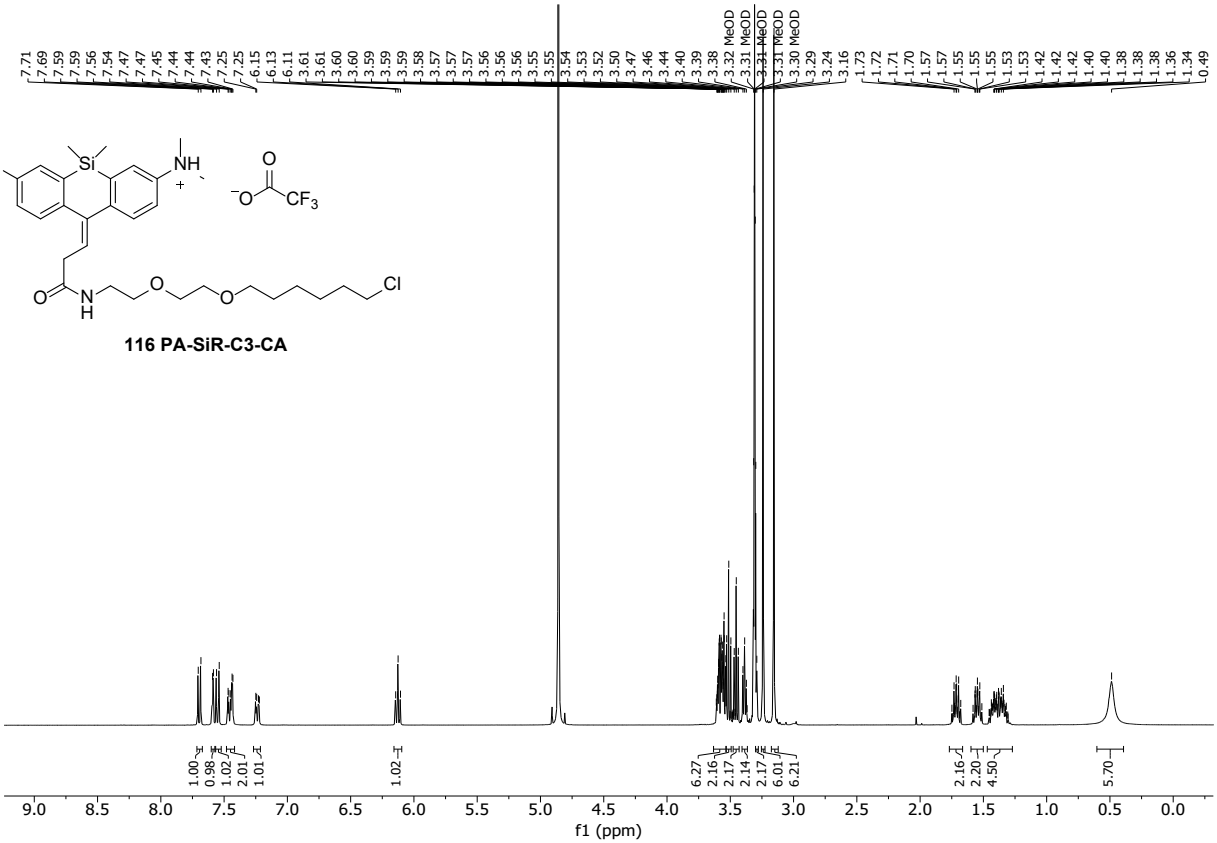

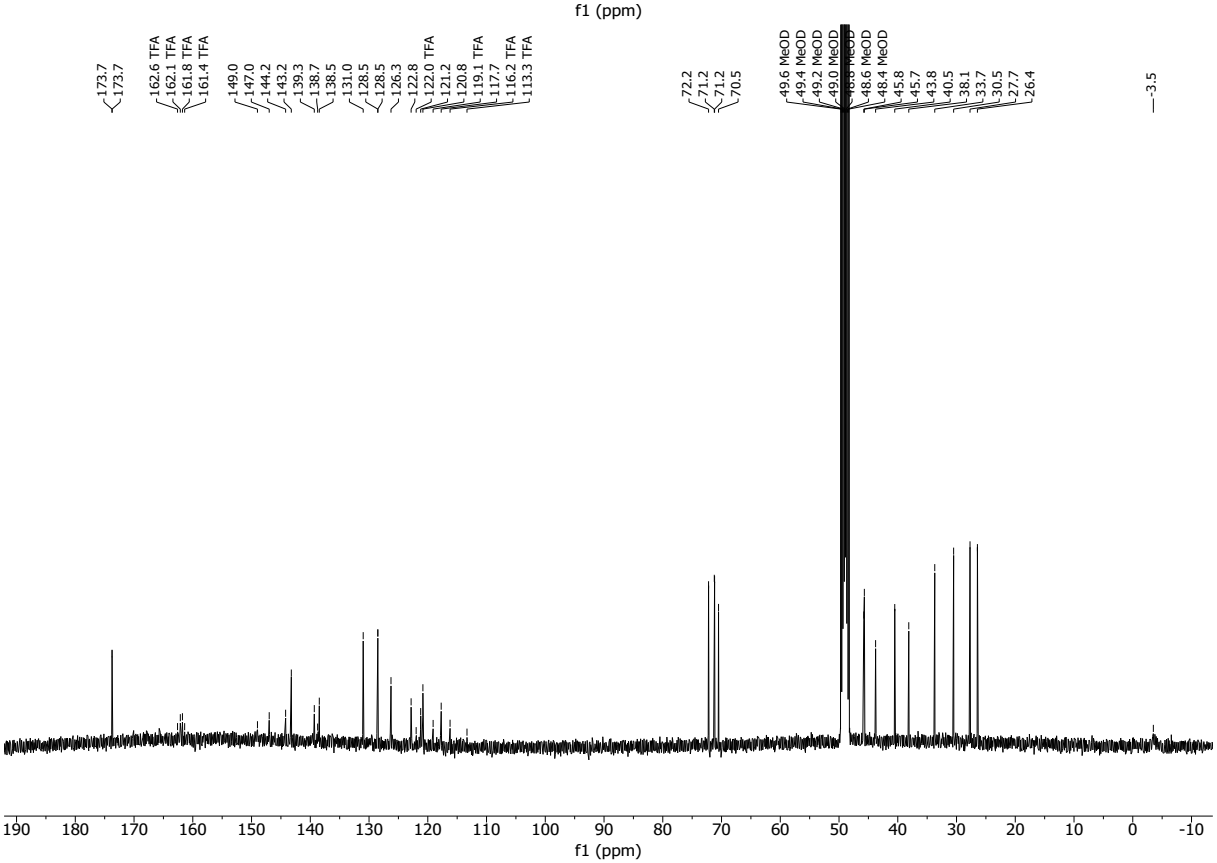

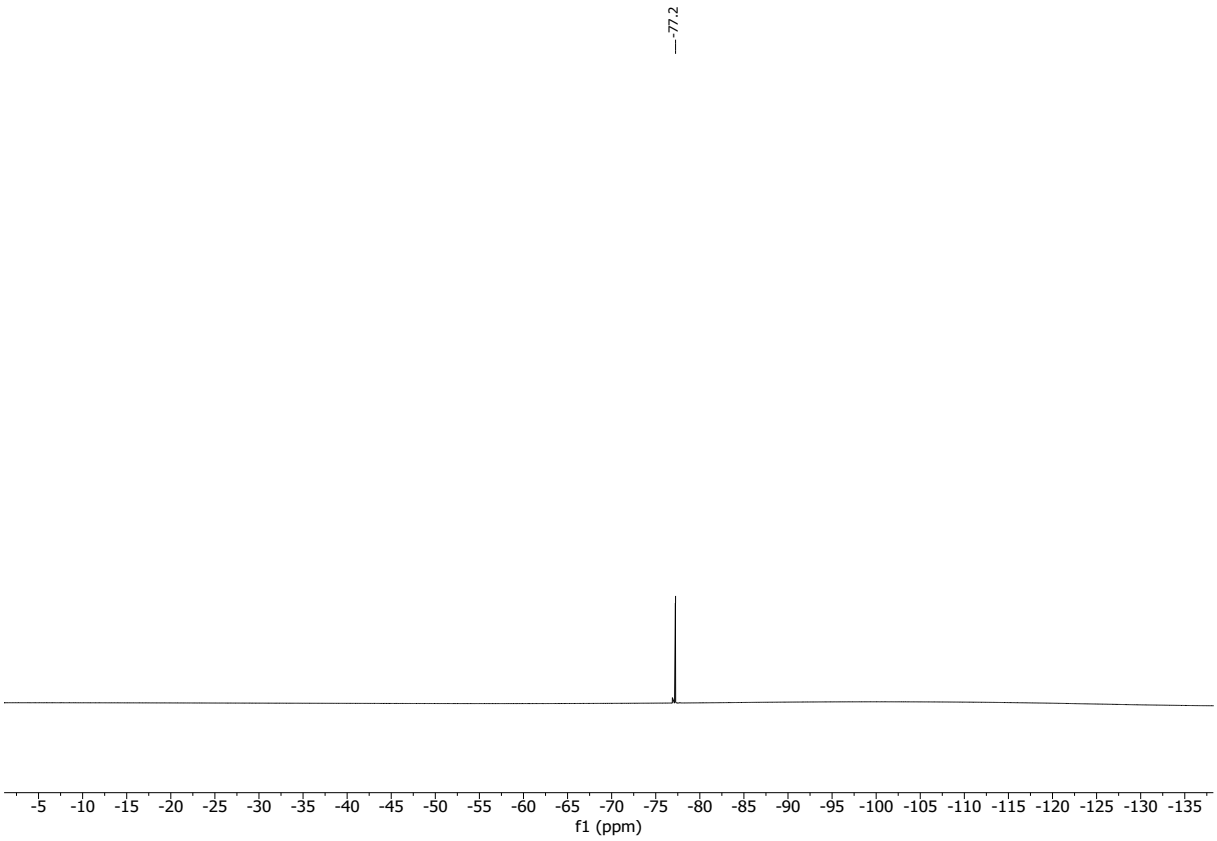
-77.2
-5 -10 -15 -20 -25 -30 -35 -40 -45 -50 -55 -60 -65 -70 -75 -80 -85 -90 -95 -100 -105 -110 -115 -120 -125 -130 -135
f1 (ppm)

153

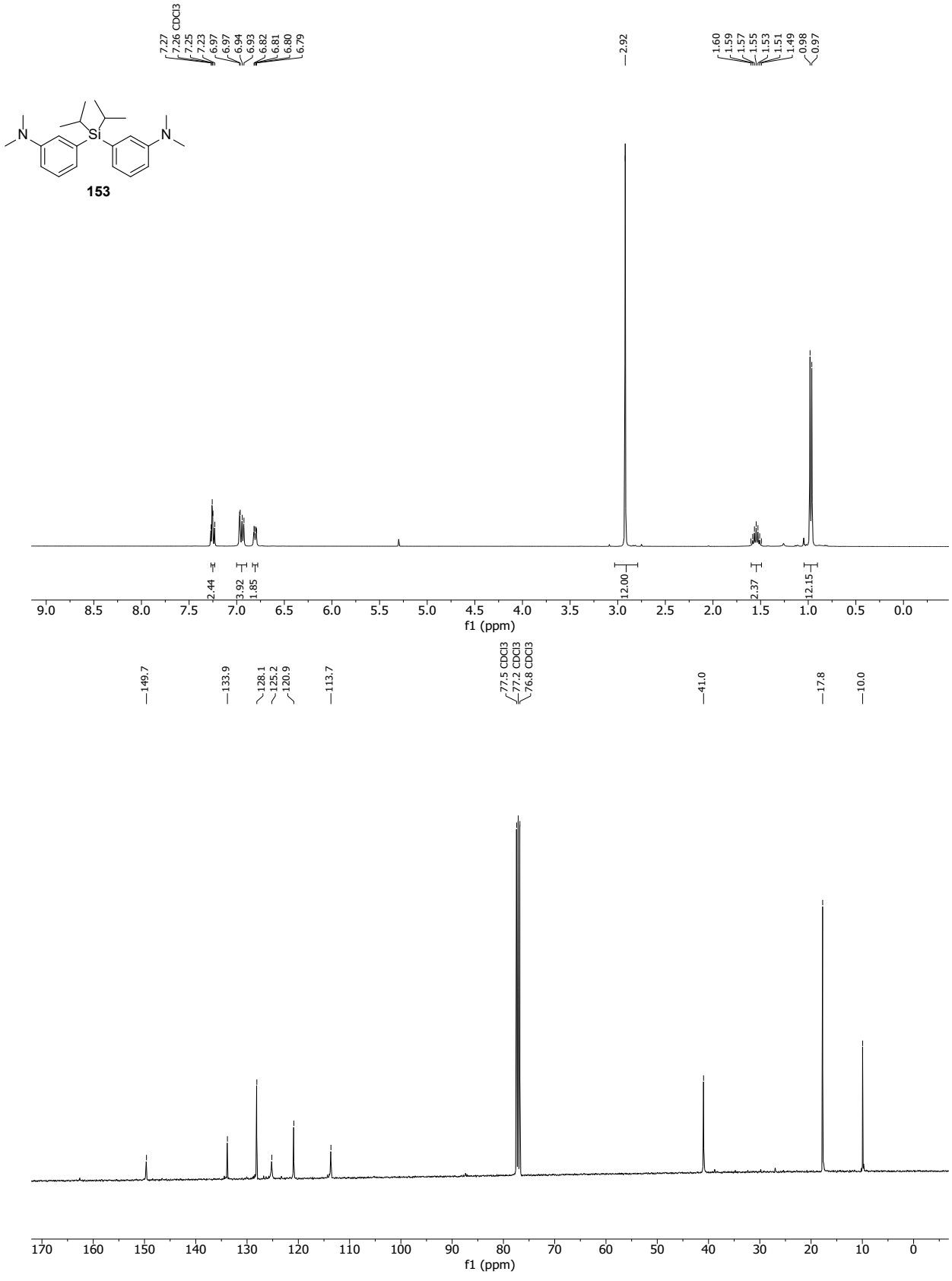
7.27
7.26 CDCl3
7.25
7.23
6.97
6.97
6.94
6.93
6.82
6.81
6.80
6.79
2.92
1.60
1.59
1.57
1.55
1.53
1.51
1.49
0.98
0.97
153
2.44
3.92
1.85
12.00
2.37
12.15
f1 (ppm)
149.7
133.9
128.1
125.2
120.9
113.7
77.5 CDCl3
77.2 CDCl3
76.8 CDCl3
41.0
17.8
10.0
f1 (ppm)

154

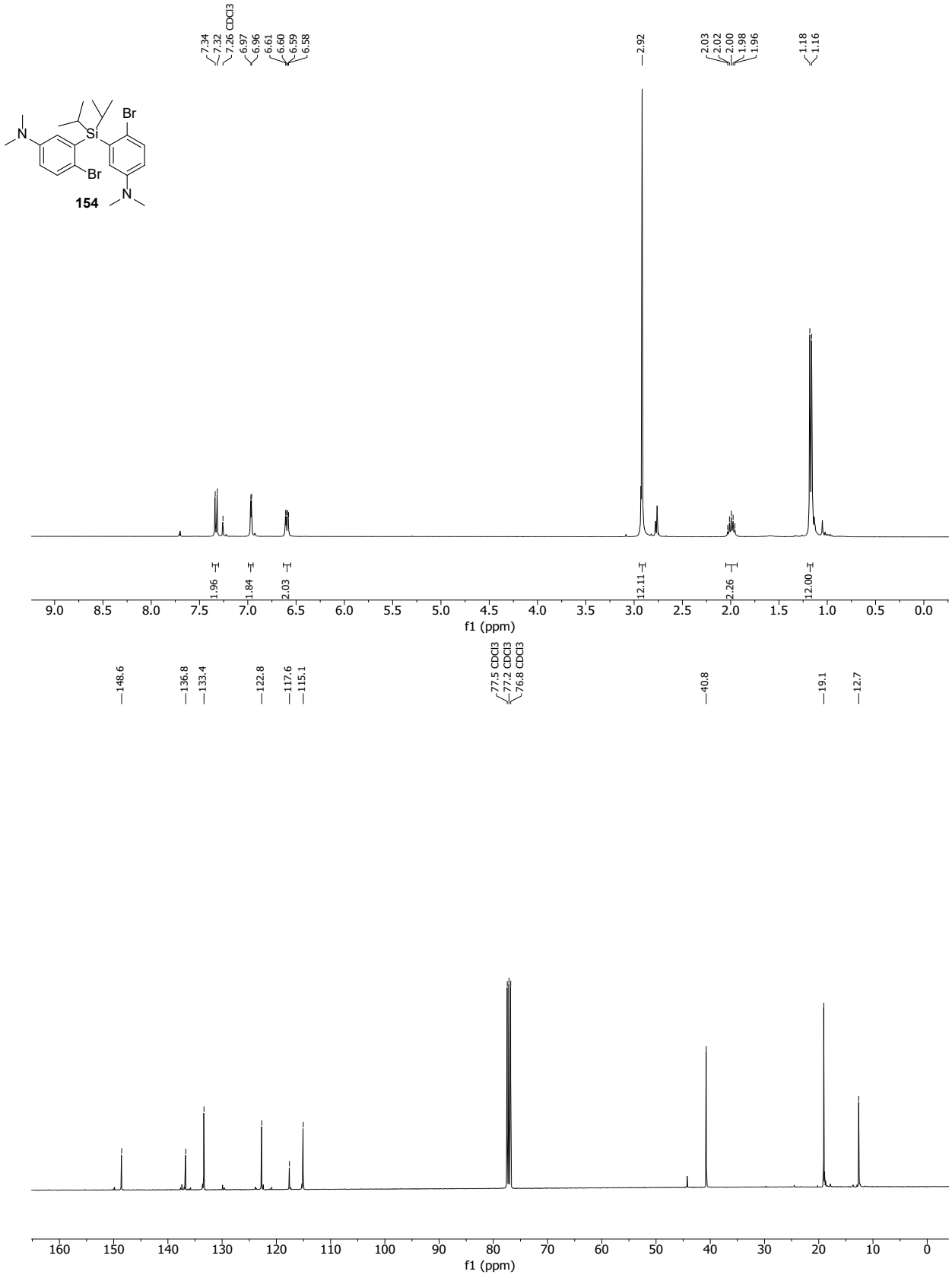
7.34
7.32
7.26 CDCl3
6.97
6.96
6.61
6.60
6.59
6.58
2.92
2.03
2.02
2.00
1.98
1.96
1.18
1.16
Br
Si
N
Br
N
154
1.96
1.84
2.03
12.11
2.26
12.00
f1 (ppm)
148.6
136.8
133.4
122.8
117.6
115.1
77.5 CDCl3
77.2 CDCl3
76.8 CDCl3
40.8
19.1
12.7
f1 (ppm)

72

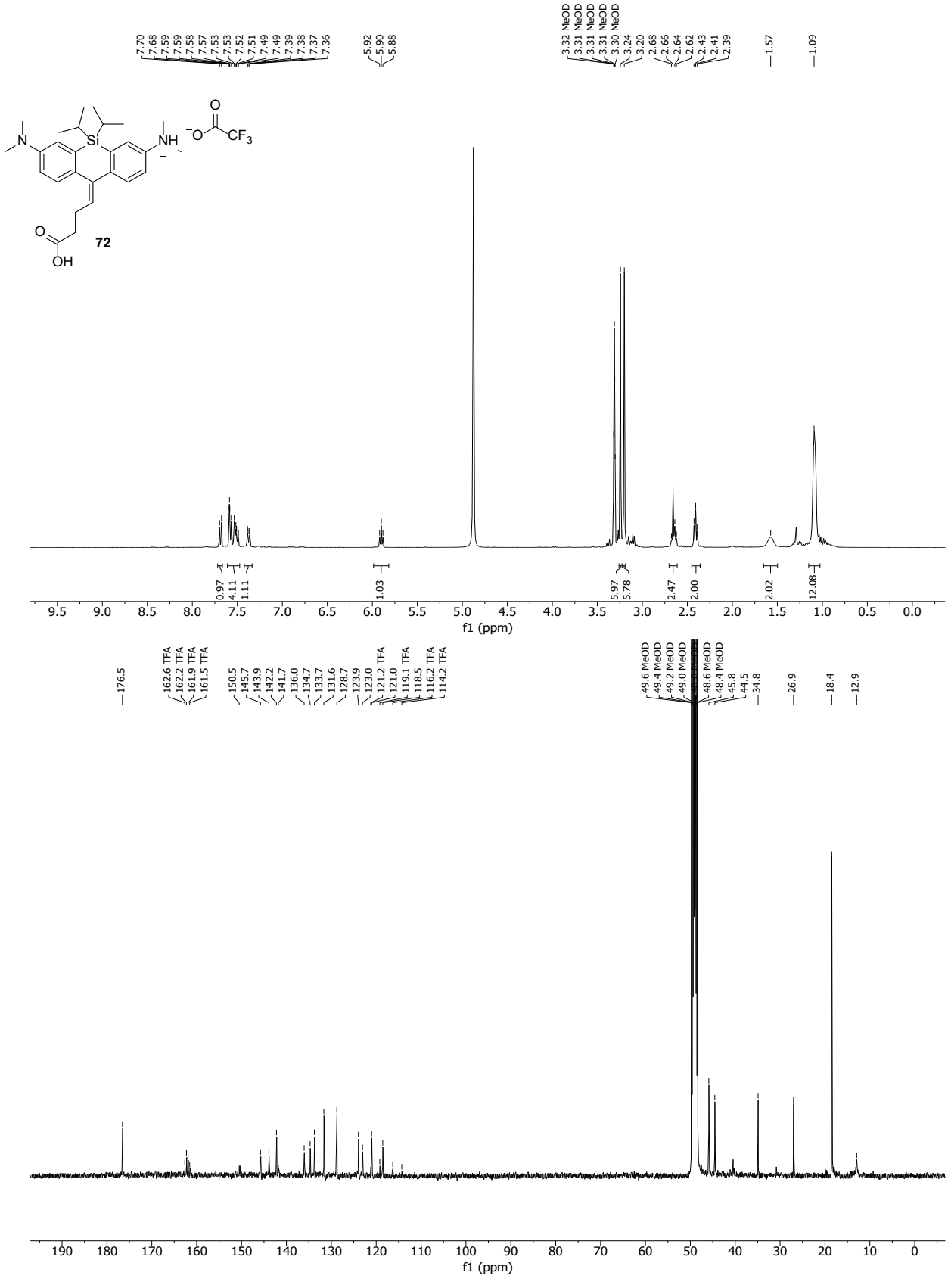
7.70
7.68
7.59
7.59
7.59
7.58
7.57
7.53
7.53
7.52
7.51
7.49
7.49
7.39
7.38
7.37
7.36
5.92
5.90
5.88
3.32 MeOD
3.31 MeOD
3.31 MeOD
3.31 MeOD
3.30 MeOD
3.24
3.20
2.68
2.66
2.64
2.62
2.43
2.41
2.39
1.57
1.09
O
O
CF3
N
Si
NH
+
O
OH
72
0.97
4.11
1.11
1.03
5.97
5.78
2.47
2.00
2.02
12.08
f1 (ppm)
176.5
162.6 TFA
162.2 TFA
161.9 TFA
161.5 TFA
150.5
145.7
143.9
142.2
141.7
136.0
134.7
133.7
131.6
128.7
123.9
123.0
121.2 TFA
121.0
119.1 TFA
118.5
116.2 TFA
114.2 TFA
49.6 MeOD
49.4 MeOD
49.2 MeOD
49.0 MeOD
48.6 MeOD
48.4 MeOD
45.8
44.5
34.8
26.9
18.4
12.9
f1 (ppm)

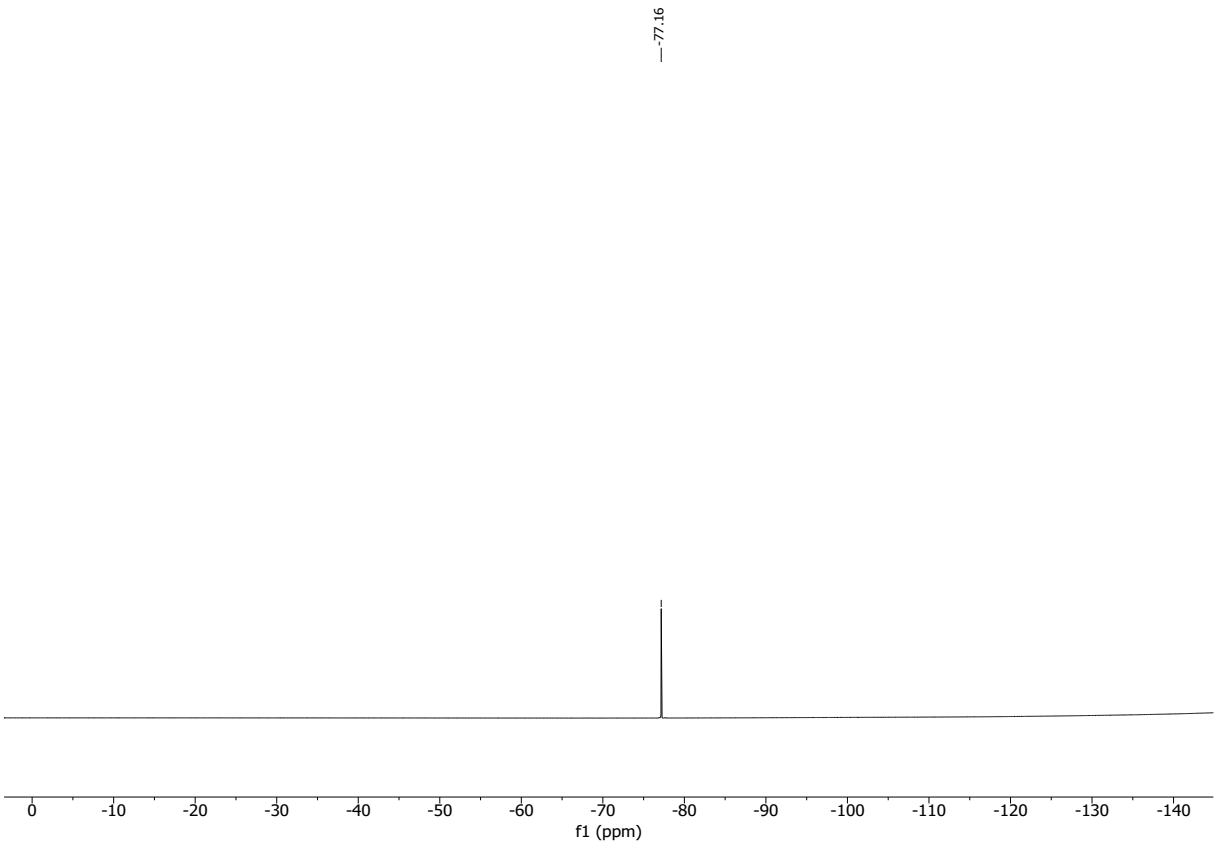
-77.16
0
-10
-20
-30
-40
-50
-60
-70
-80
-90
-100
-110
-120
-130
-140
f1 (ppm)

117

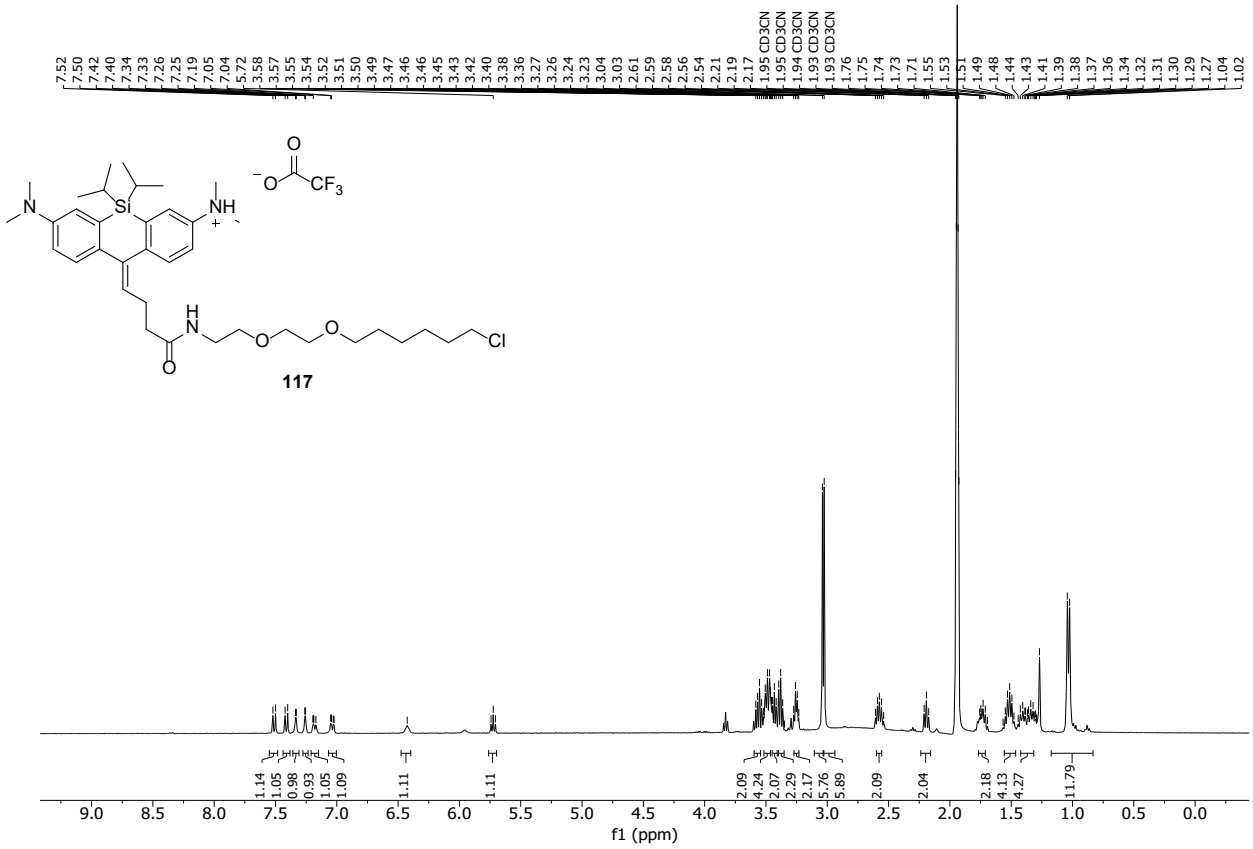
7.52 7.50 7.42 7.40 7.34 7.33 7.26 7.25 7.19 7.05 7.04 5.72 3.58 3.57 3.55 3.54 3.52 3.51 3.50 3.49 3.47 3.46 3.46 3.45 3.43 3.42 3.40 3.38 3.36 3.27 3.26 3.24 3.23 3.04 3.03 2.61 2.59 2.58 2.56 2.54 2.21 2.19 2.17 1.95 CD3CN 1.95 CD3CN 1.94 CD3CN 1.93 CD3CN 1.93 CD3CN 1.76 1.75 1.74 1.73 1.71 1.55 1.53 1.51 1.49 1.48 1.44 1.43 1.41 1.39 1.38 1.37 1.36 1.34 1.32 1.31 1.30 1.29 1.27 1.04 1.02
O
O
CF3
N
Si
NH
H
N
O
O
O
Cl
O
117
1.14 1.05 0.98 0.93 1.05 1.09 1.11 1.11 2.09 4.24 2.07 2.29 2.17 5.76 5.89 2.09 2.04 2.18 4.13 4.27 11.79
9.0 8.5 8.0 7.5 7.0 6.5 6.0 5.5 5.0 4.5 4.0 3.5 3.0 2.5 2.0 1.5 1.0 0.5 0.0
f1 (ppm)

156

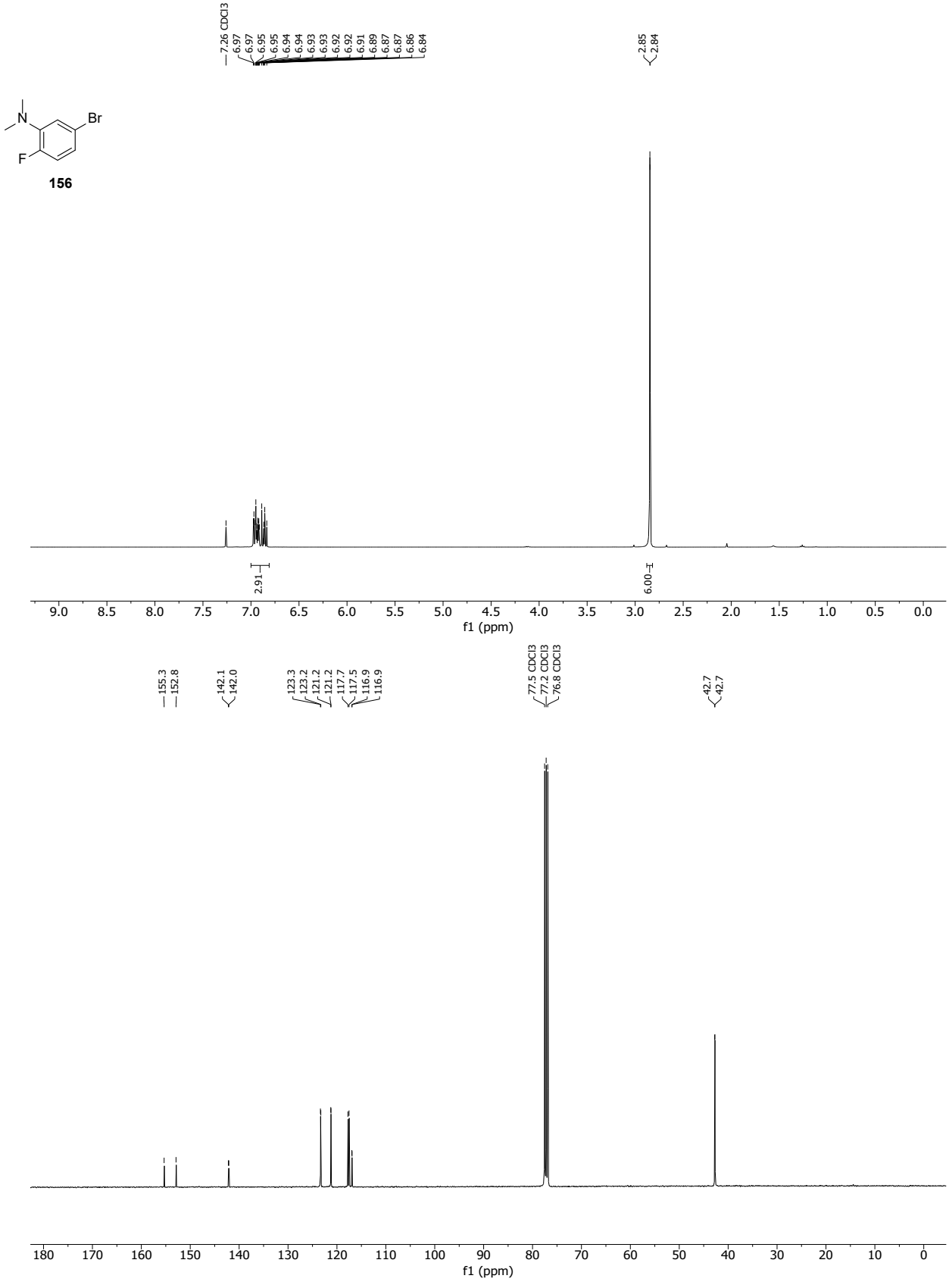
7.26 CDCl3
6.97
6.97
6.95
6.95
6.94
6.94
6.93
6.93
6.92
6.92
6.91
6.89
6.87
6.87
6.86
6.84
2.85
2.84
N
Br
F
156
2.91
6.00
f1 (ppm)
155.3
152.8
142.1
142.0
123.3
123.2
121.2
121.2
117.7
117.5
116.9
116.9
77.5 CDCl3
77.2 CDCl3
76.8 CDCl3
42.7
42.7
f1 (ppm)

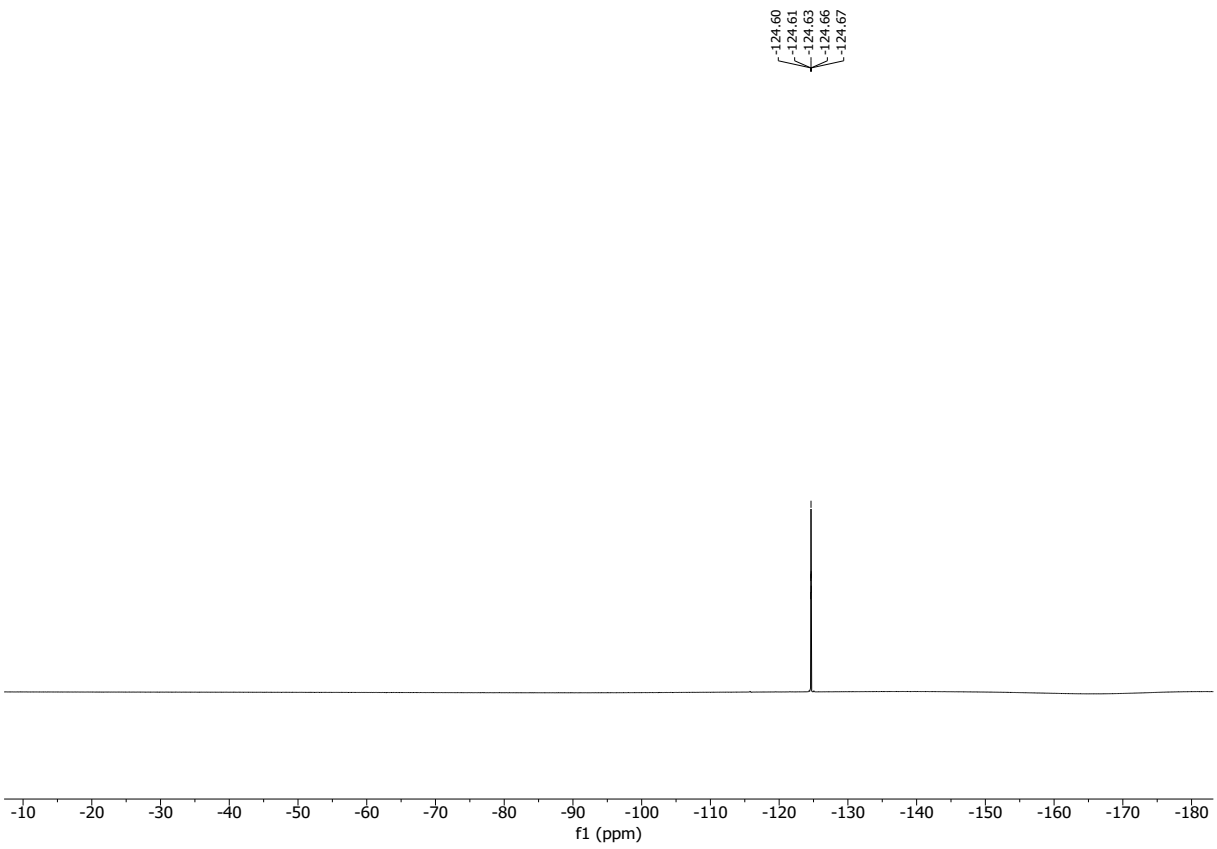
-124.60
-124.61
-124.63
-124.66
-124.67
-10
-20
-30
-40
-50
-60
-70
-80
-90
-100
-110
-120
-130
-140
-150
-160
-170
-180
f1 (ppm)

157

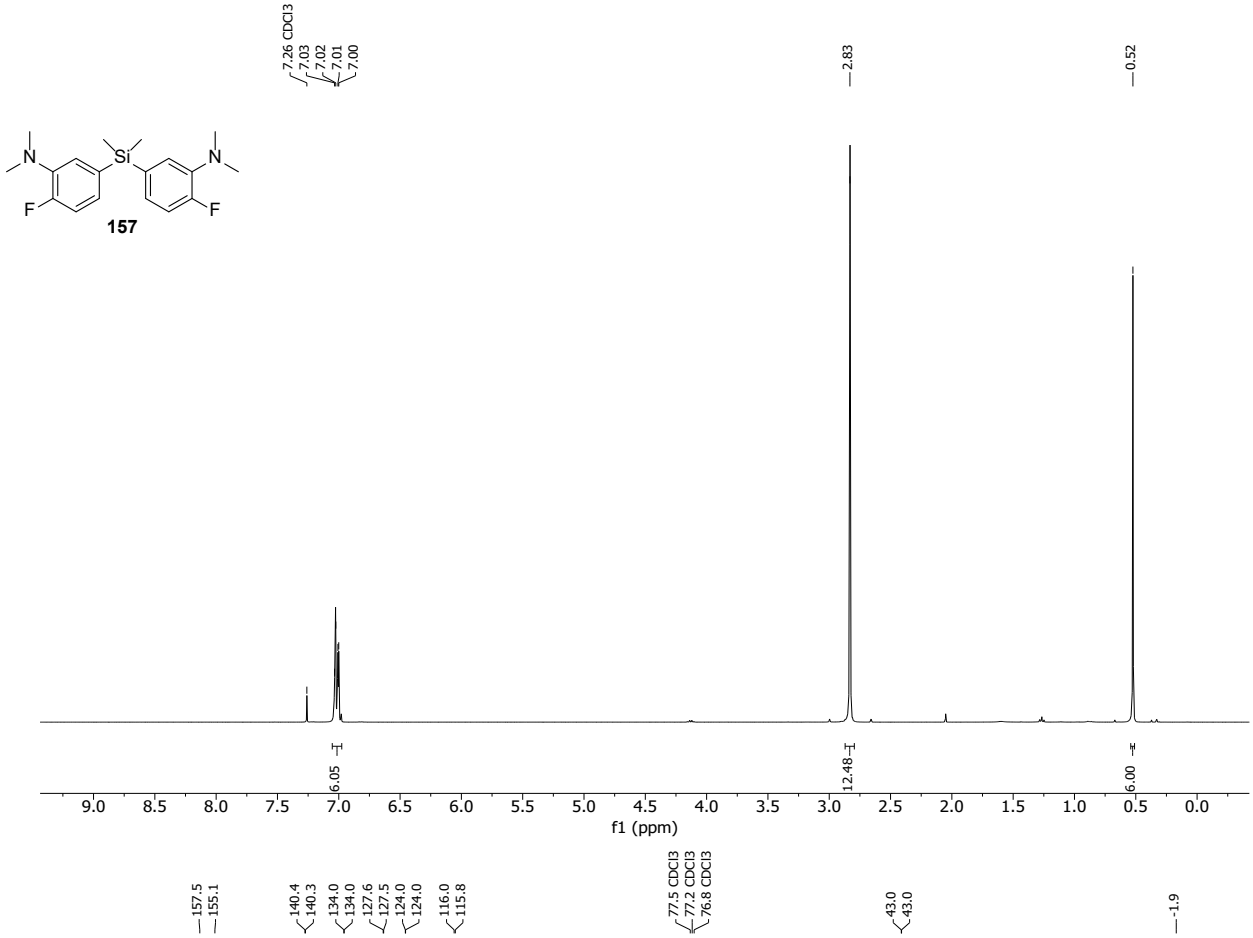
7.26 CDCl3
7.03
7.02
7.01
7.00
2.83
0.52
N
Si
N
F
F
157
6.05
12.48
6.00
f1 (ppm)

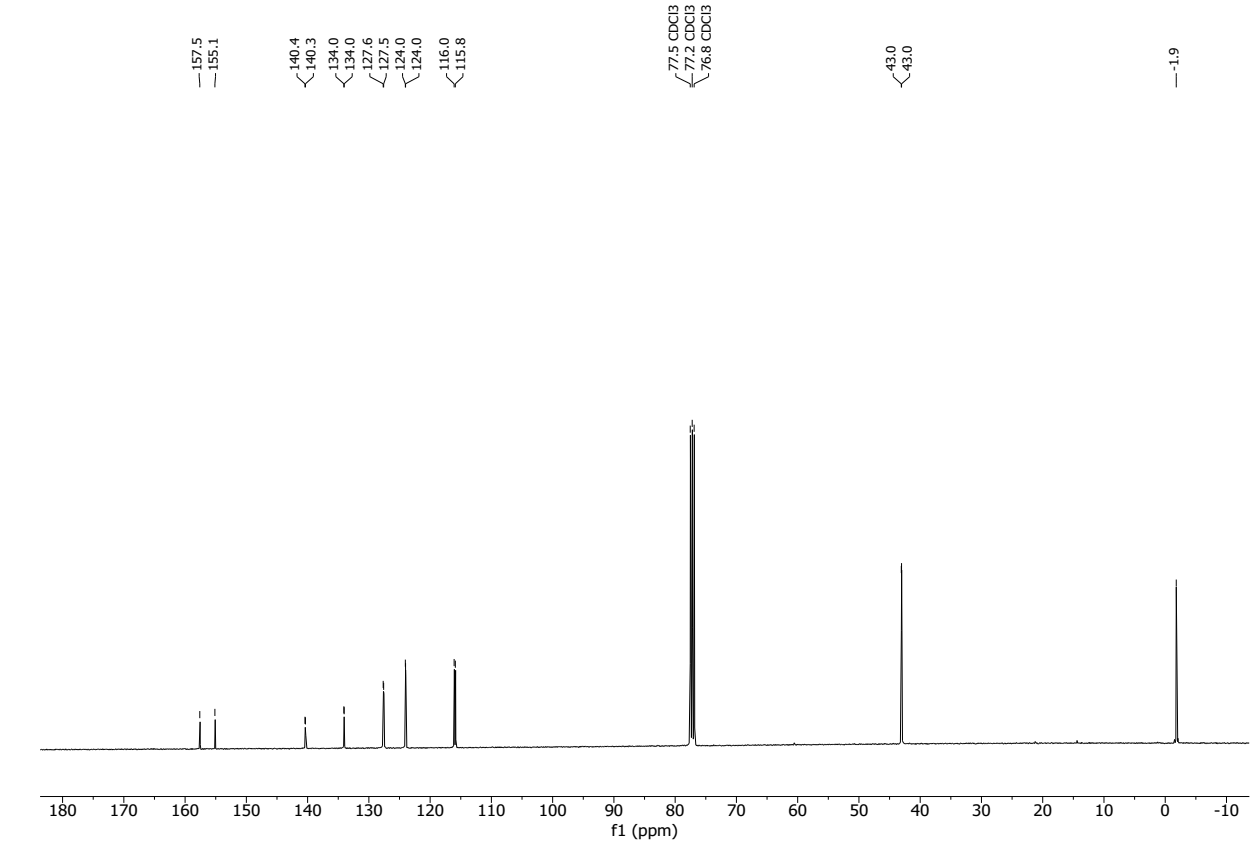
157.5
155.1
140.4
140.3
134.0
134.0
127.6
127.5
124.0
124.0
116.0
115.8
77.5 CDCl3
77.2 CDCl3
76.8 CDCl3
43.0
43.0
-1.9
f1 (ppm)

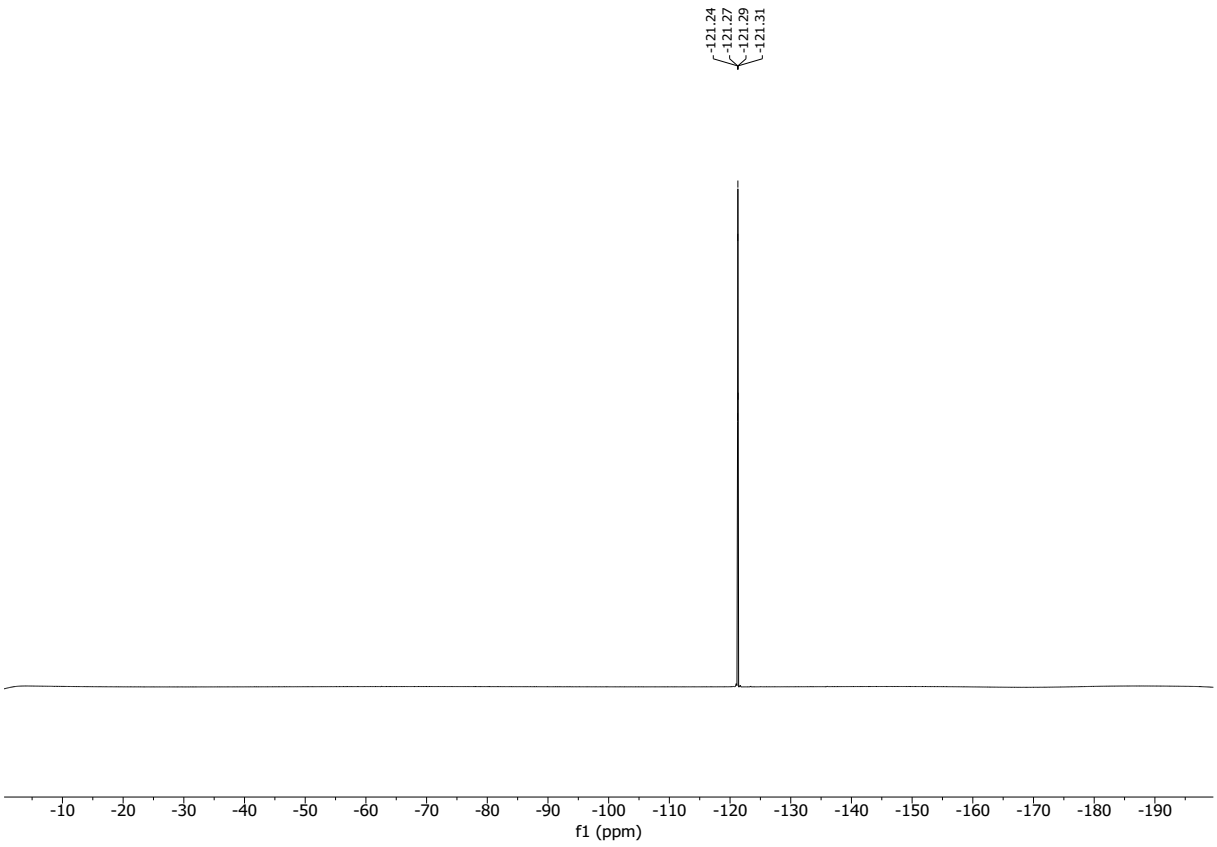
-121.24
-121.27
-121.29
-121.31
-10
-20
-30
-40
-50
-60
-70
-80
-90
-100
-110
-120
-130
-140
-150
-160
-170
-180
-190
f1 (ppm)

158

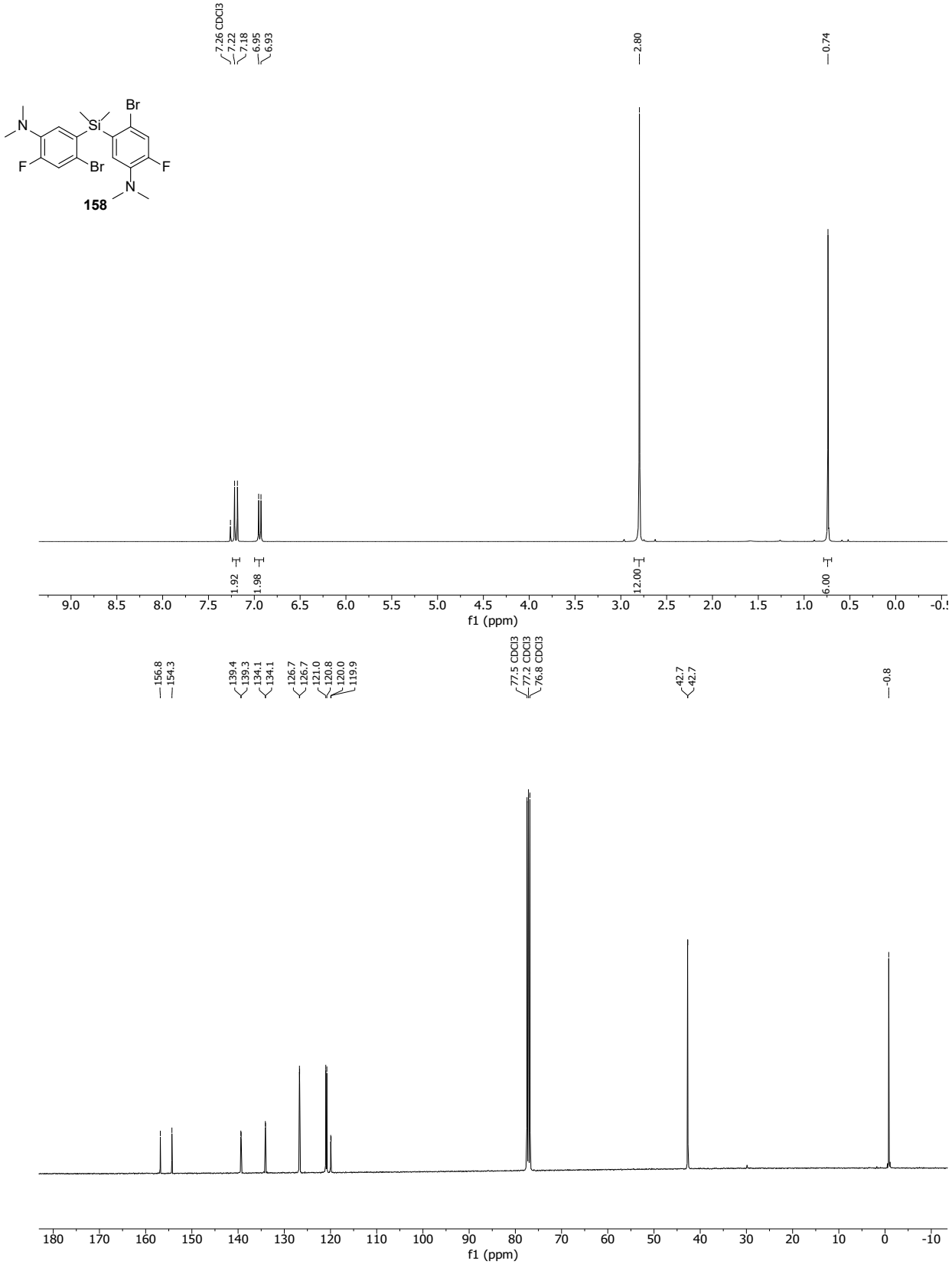
7.26 CDCl3
7.22
7.18
6.95
6.93
2.80
0.74
Br
Si
N
F
Br
F
N
158
1.92
1.98
12.00
6.00
f1 (ppm)
156.8
154.3
139.4
139.3
134.1
134.1
126.7
126.7
121.0
120.8
120.0
119.9
77.5 CDCl3
77.2 CDCl3
76.8 CDCl3
42.7
42.7
-0.8
f1 (ppm)

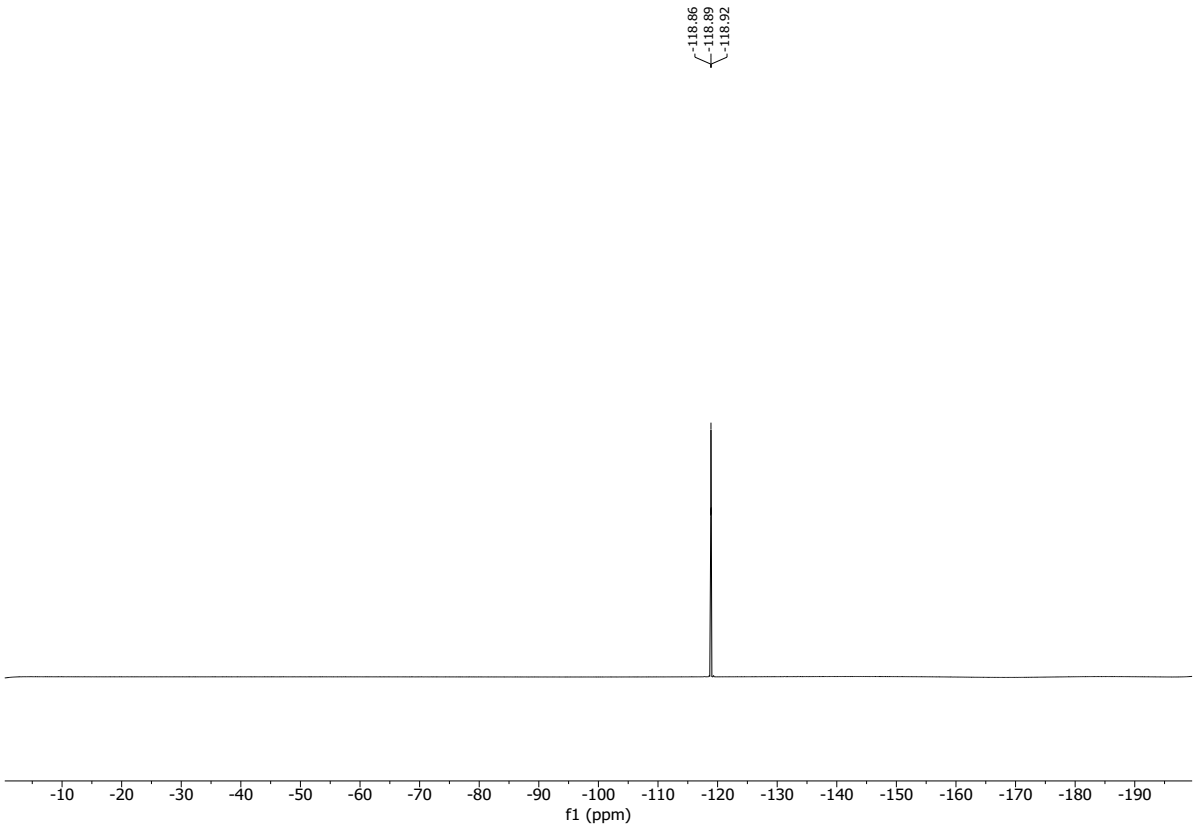
-118.86
-118.89
-118.92
-10
-20
-30
-40
-50
-60
-70
-80
-90
-100
-110
-120
-130
-140
-150
-160
-170
-180
-190
f1 (ppm)

73

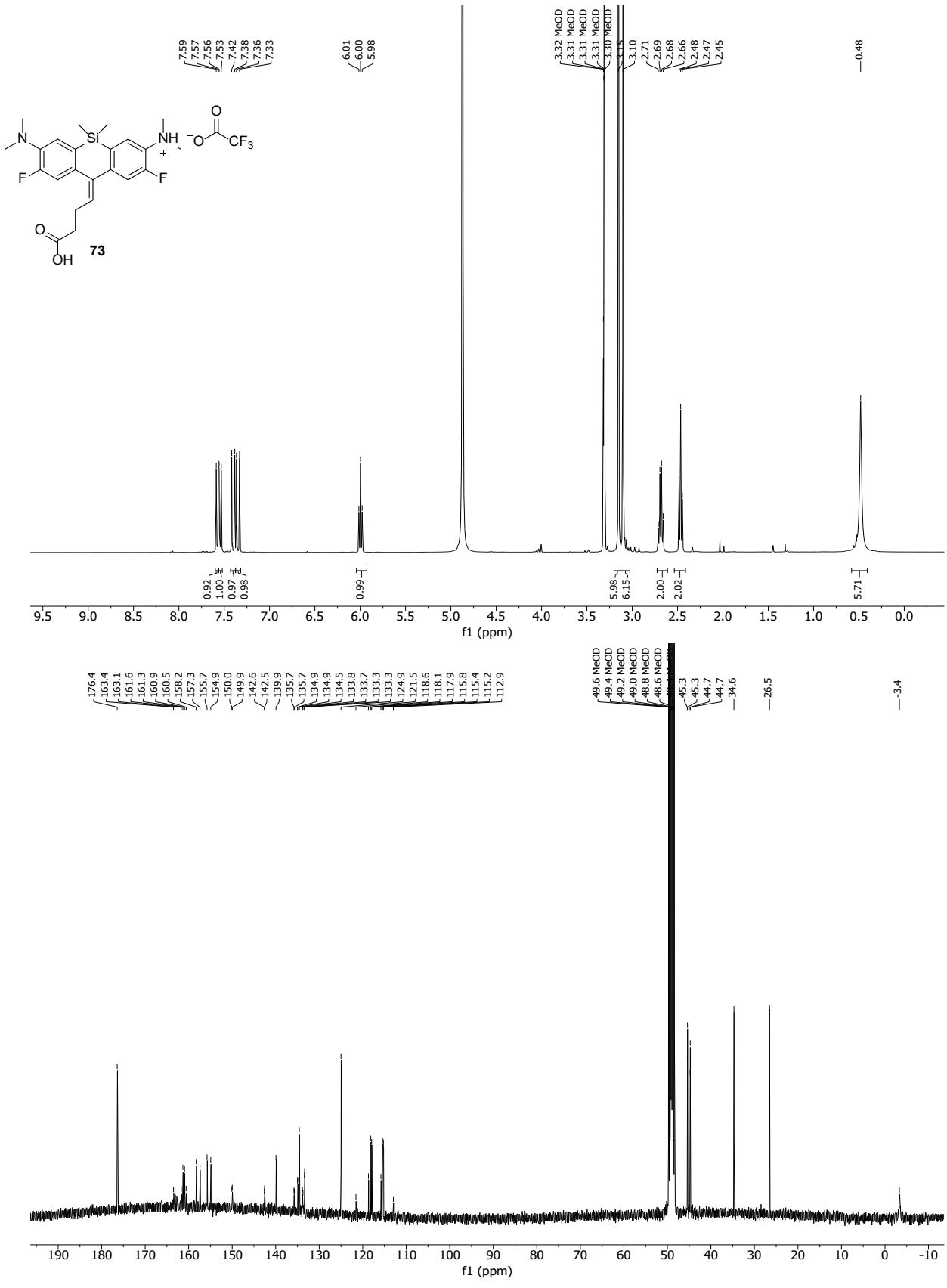
7.59
7.57
7.56
7.53
7.42
7.38
7.36
7.33
6.01
6.00
5.98
3.32 MeOD
3.31 MeOD
3.31 MeOD
3.31 MeOD
3.30 MeOD
3.15
3.10
2.71
2.69
2.68
2.66
2.48
2.47
2.45
0.48
0.92
1.00
0.97
0.98
0.99
5.98
6.15
2.00
2.02
5.71
f1 (ppm)
176.4
163.4
163.1
161.6
161.3
160.9
160.5
158.2
157.3
155.7
154.9
150.0
149.9
142.6
142.5
139.9
135.7
135.7
134.9
134.9
134.5
133.8
133.7
133.3
133.3
124.9
121.5
118.6
118.1
117.9
115.8
115.4
115.2
112.9
49.6 MeOD
49.4 MeOD
49.2 MeOD
49.0 MeOD
48.8 MeOD
48.6 MeOD
45.3
45.3
44.7
44.7
34.6
26.5
-3.4
f1 (ppm)

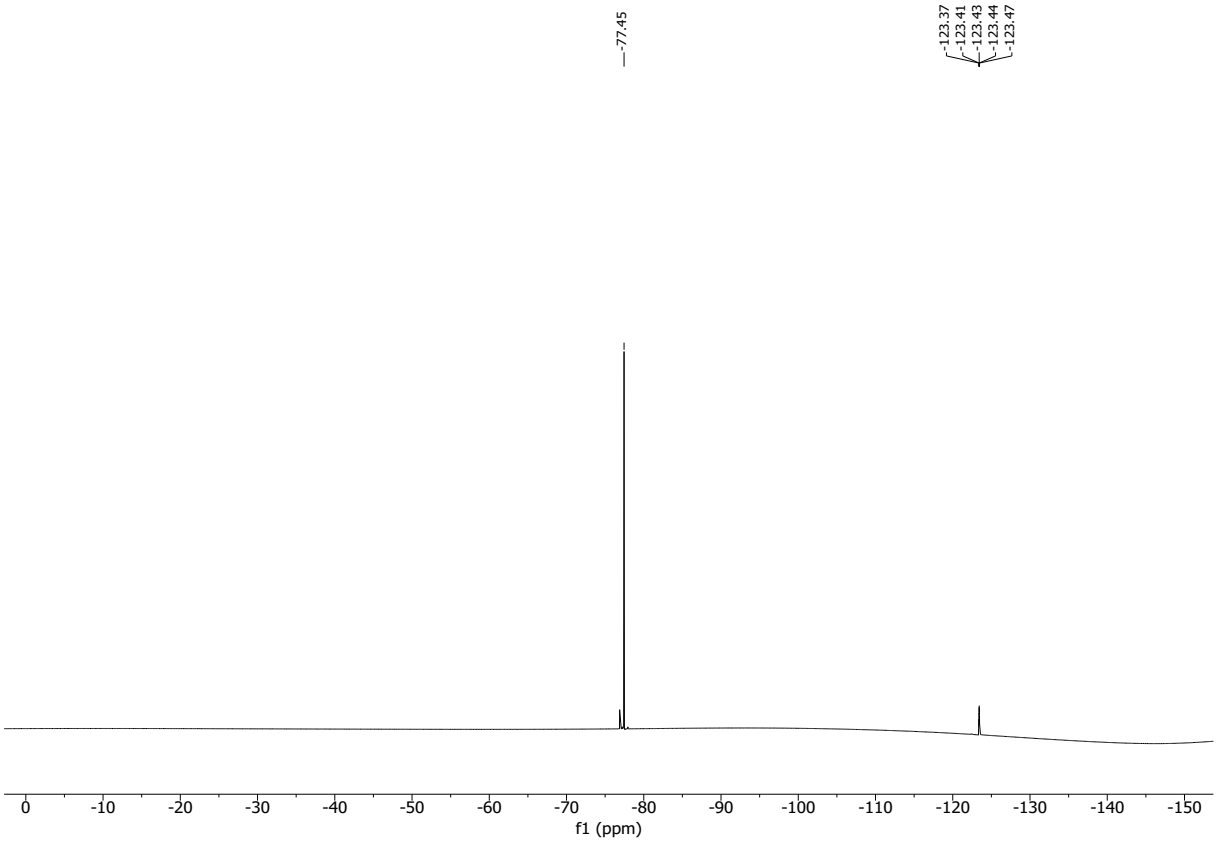
-77.45
-123.37
-123.41
-123.43
-123.44
-123.47
0
-10
-20
-30
-40
-50
-60
-70
-80
-90
-100
-110
-120
-130
-140
-150
f1 (ppm)

118

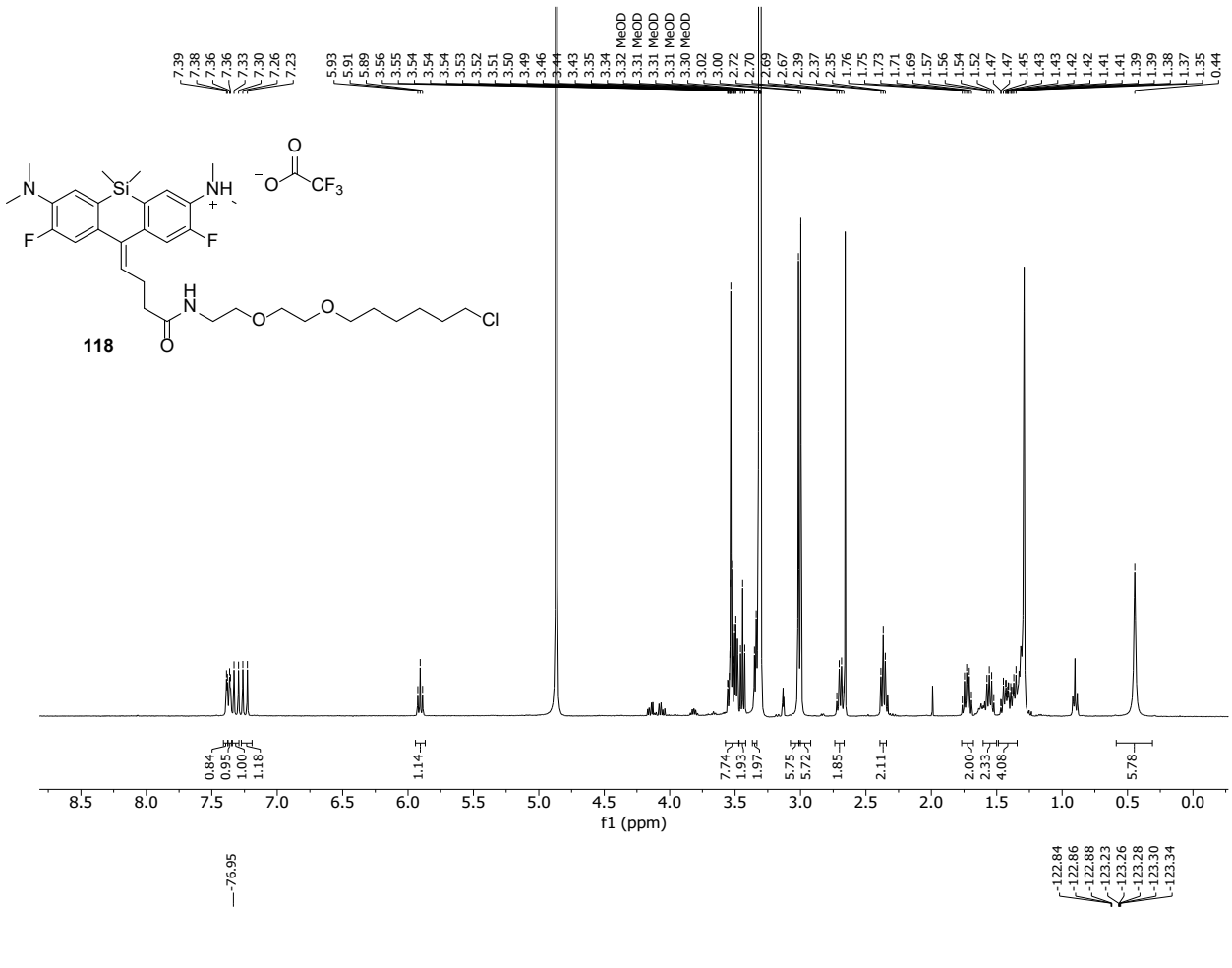
7.39
7.38
7.36
7.36
7.33
7.30
7.26
7.23
5.93
5.91
5.89
3.56
3.55
3.54
3.54
3.54
3.53
3.52
3.51
3.50
3.49
3.46
3.44
3.43
3.35
3.34
3.32 MeOD
3.31 MeOD
3.31 MeOD
3.31 MeOD
3.30 MeOD
3.02
3.00
2.72
2.70
2.69
2.67
2.39
2.37
2.35
1.76
1.75
1.73
1.71
1.69
1.57
1.56
1.54
1.52
1.47
1.47
1.45
1.43
1.43
1.42
1.42
1.41
1.41
1.39
1.39
1.38
1.37
1.35
0.44
118
0.84
0.95
1.00
1.18
1.14
7.74
1.93
1.97
5.75
5.72
1.85
2.11
2.00
2.33
4.08
5.78
f1 (ppm)

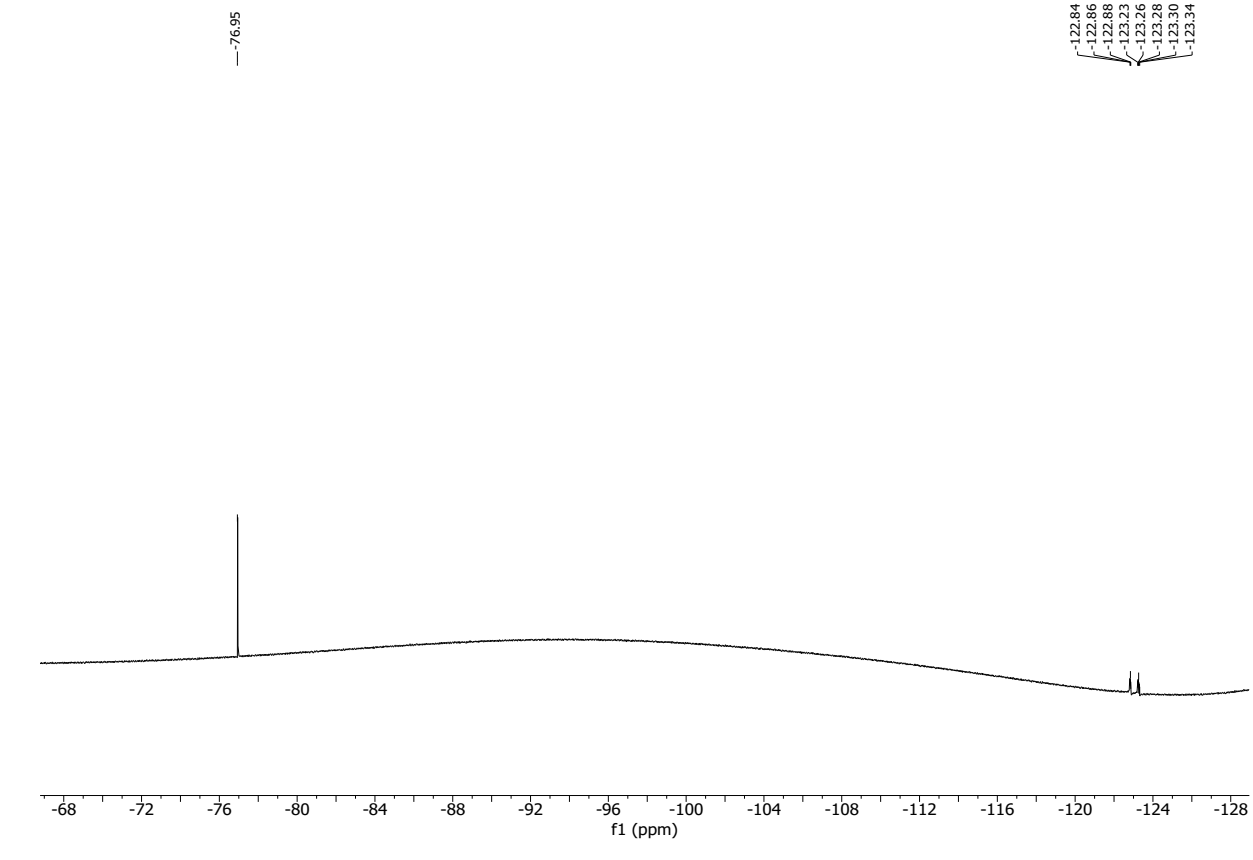
-76.95
-122.84
-122.86
-122.88
-123.23
-123.26
-123.28
-123.30
-123.34
f1 (ppm)

161

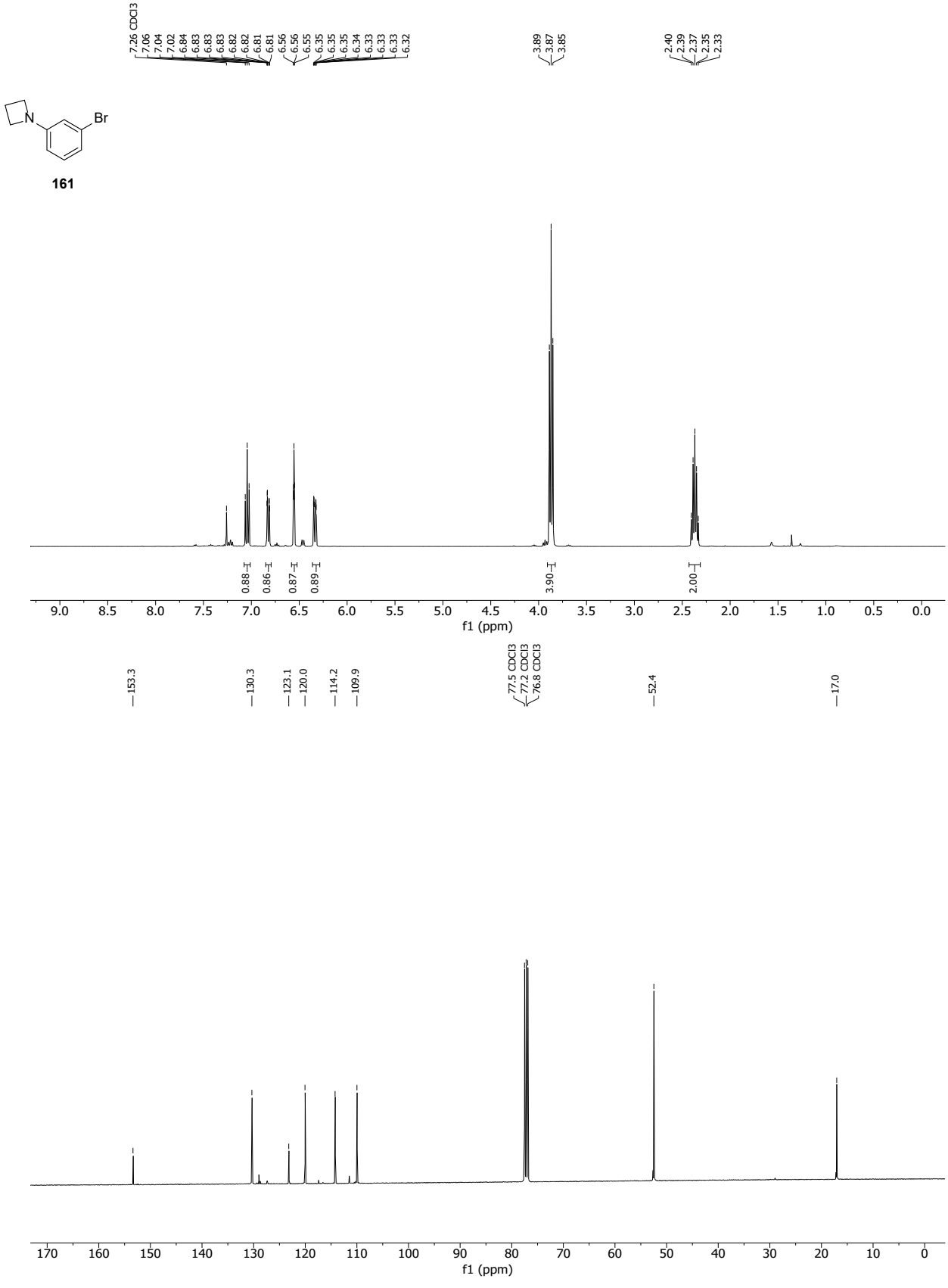
7.26 CDCl3
7.06
7.04
7.02
6.84
6.83
6.83
6.83
6.82
6.82
6.81
6.81
6.56
6.56
6.55
6.35
6.35
6.35
6.34
6.33
6.33
6.33
6.32
3.89
3.87
3.85
2.40
2.39
2.37
2.35
2.33
N
Br
161
0.88
0.86
0.87
0.89
3.90
2.00
f1 (ppm)
153.3
130.3
123.1
120.0
114.2
109.9
77.5 CDCl3
77.2 CDCl3
76.8 CDCl3
52.4
17.0
f1 (ppm)

162

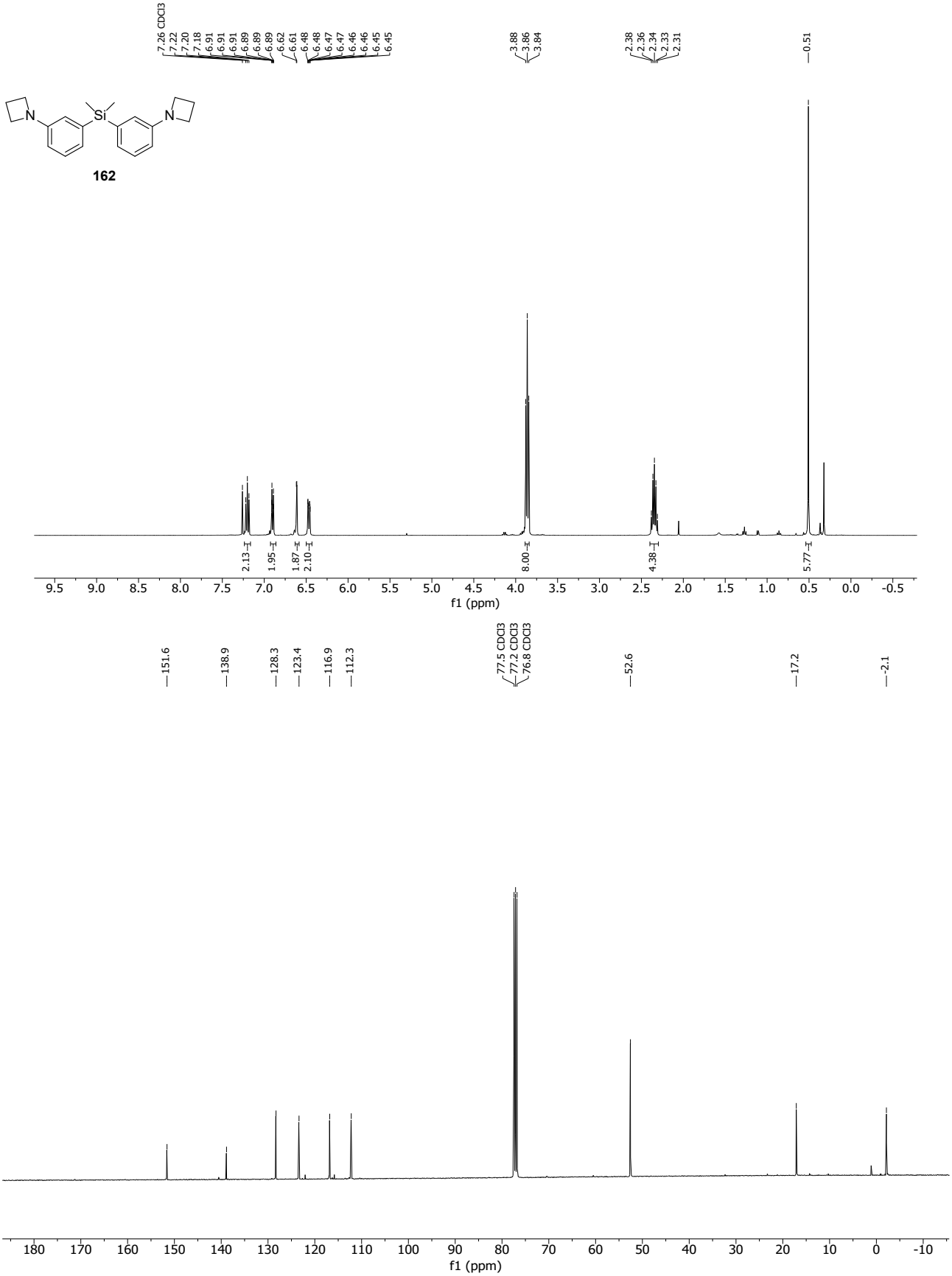
7.26 CDCl3
7.22
7.20
7.18
6.91
6.91
6.91
6.89
6.89
6.89
6.62
6.61
6.48
6.48
6.47
6.47
6.46
6.46
6.45
6.45
3.88
3.86
3.84
2.38
2.36
2.34
2.33
2.31
0.51
N
Si
N
162
2.13
1.95
1.87
2.10
8.00
4.38
5.77
9.5 9.0 8.5 8.0 7.5 7.0 6.5 6.0 5.5 5.0 4.5 4.0 3.5 3.0 2.5 2.0 1.5 1.0 0.5 0.0 -0.5
f1 (ppm)
151.6
138.9
128.3
123.4
116.9
112.3
77.5 CDCl3
77.2 CDCl3
76.8 CDCl3
52.6
17.2
-2.1
180 170 160 150 140 130 120 110 100 90 80 70 60 50 40 30 20 10 0 -10
f1 (ppm)

163

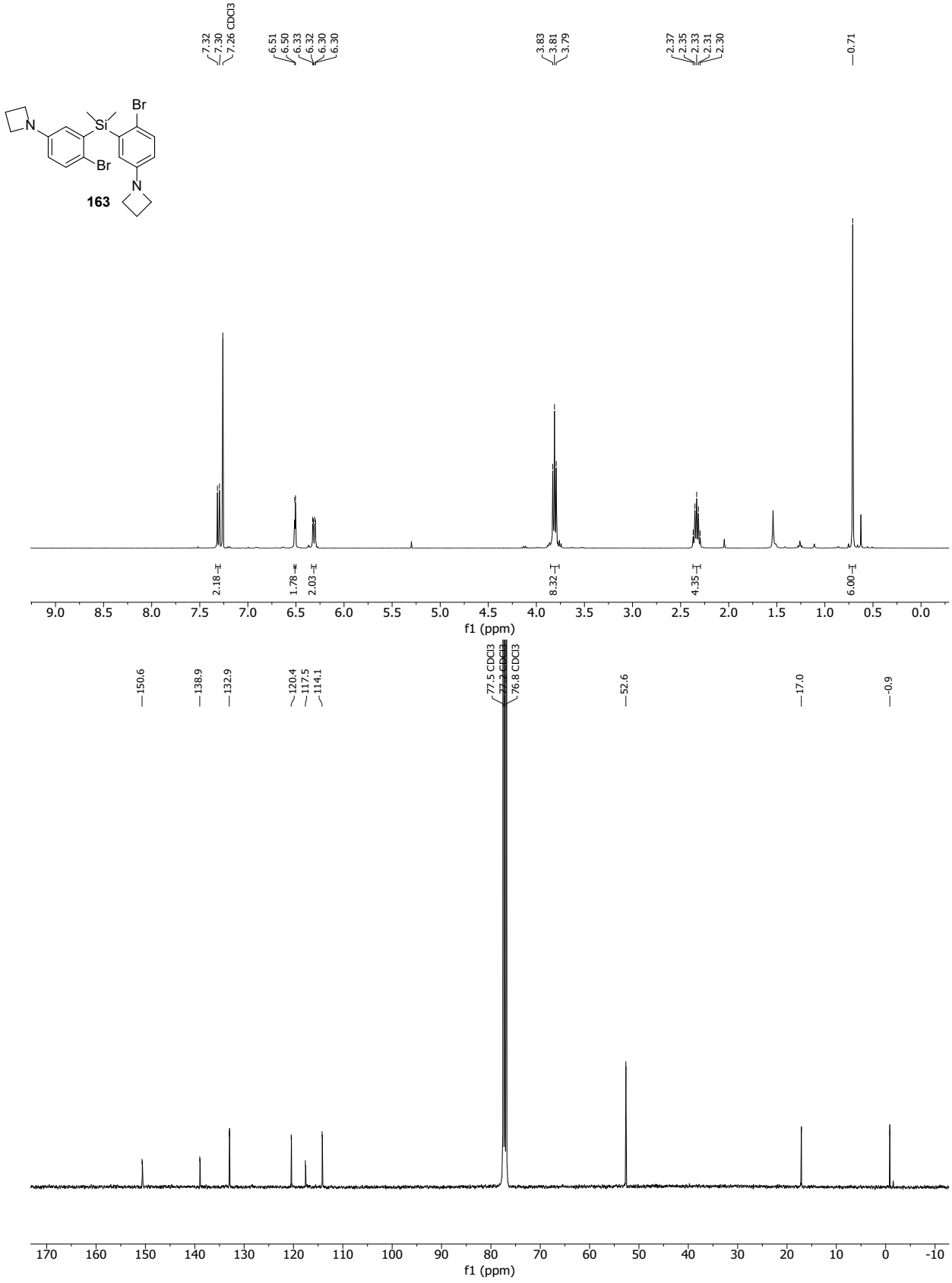
7.32
7.30
7.26 CDCl3
6.51
6.50
6.33
6.32
6.30
6.30
3.83
3.81
3.79
2.37
2.35
2.33
2.31
2.30
0.71
Br
Si
Br
N
N
163
2.18
1.78
2.03
8.32
4.35
6.00
f1 (ppm)
150.6
138.9
132.9
120.4
117.5
114.1
77.5 CDCl3
77.3 CDCl3
76.8 CDCl3
52.6
17.0
-0.9
f1 (ppm)

164

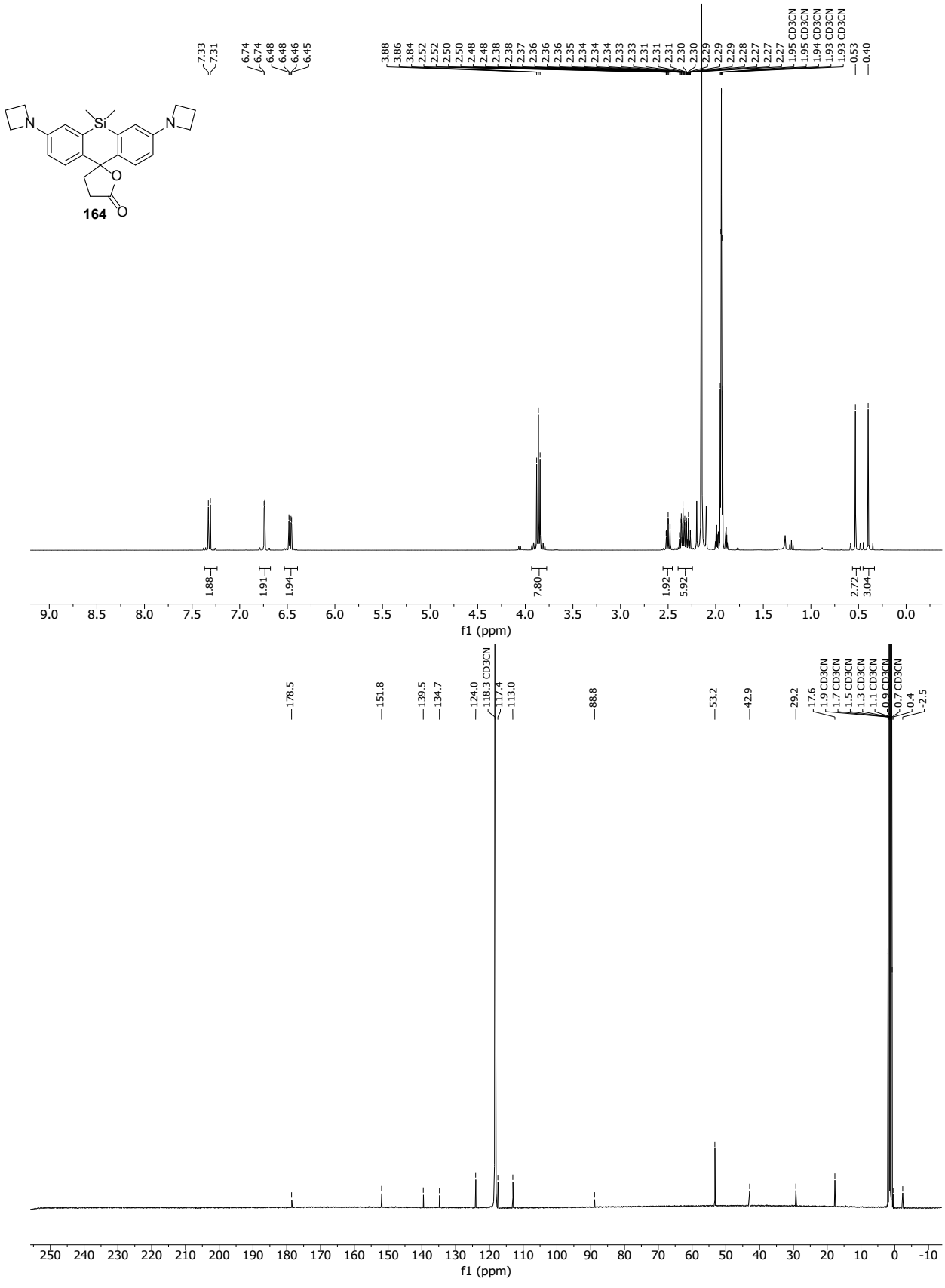
7.33
7.31
6.74
6.74
6.48
6.48
6.46
6.45
3.88
3.86
3.84
2.52
2.52
2.50
2.50
2.48
2.48
2.38
2.38
2.37
2.36
2.36
2.36
2.35
2.34
2.34
2.34
2.33
2.33
2.31
2.31
2.31
2.30
2.30
2.29
2.29
2.29
2.28
2.27
2.27
2.27
1.95 CD3CN
1.95 CD3CN
1.94 CD3CN
1.93 CD3CN
1.93 CD3CN
0.53
0.40
Si
N
N
O
O
164
1.88
1.91
1.94
7.80
1.92
5.92
2.72
3.04
f1 (ppm)
178.5
151.8
139.5
134.7
124.0
118.3 CD3CN
117.4
113.0
88.8
53.2
42.9
29.2
17.6
1.9 CD3CN
1.7 CD3CN
1.5 CD3CN
1.3 CD3CN
1.1 CD3CN
0.9 CD3CN
0.7 CD3CN
0.4
-2.5
f1 (ppm)

74

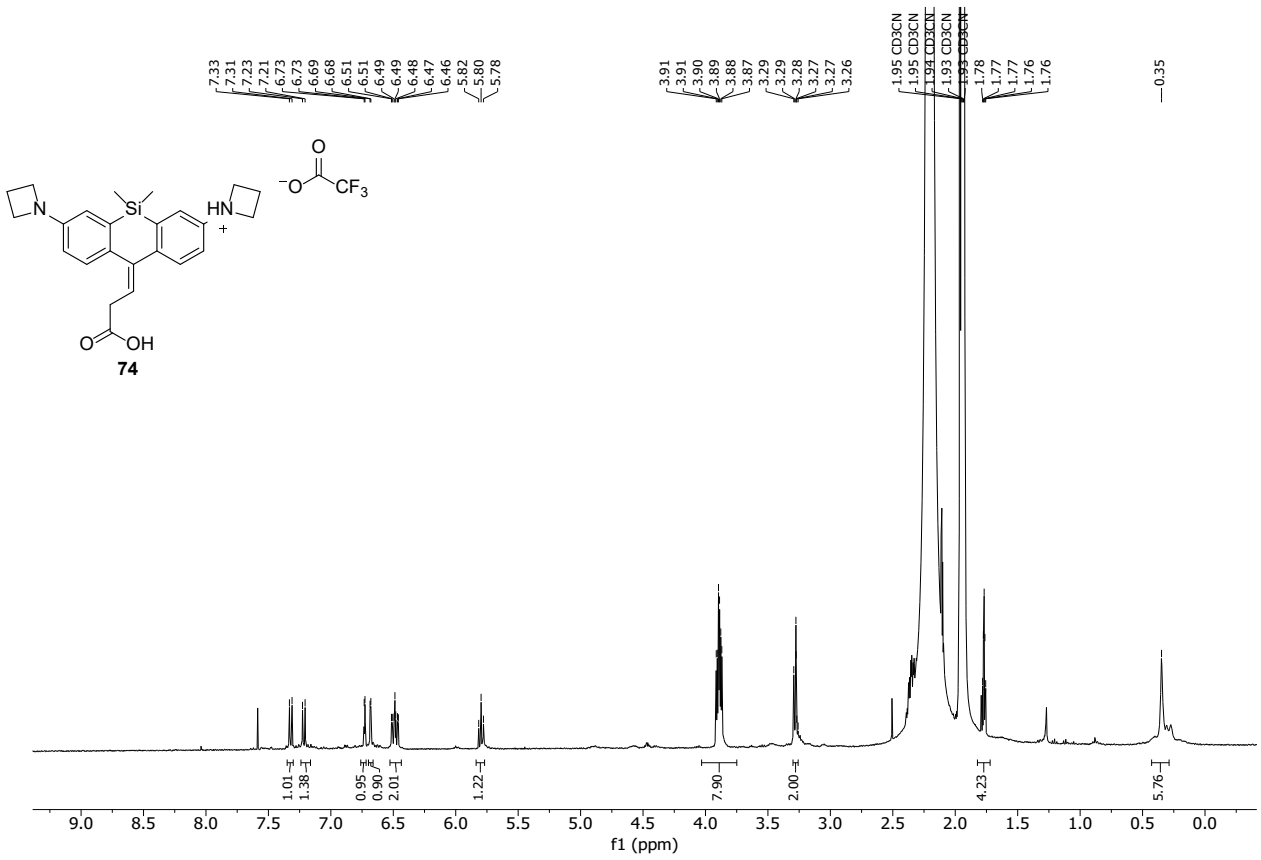
7.33
7.31
7.23
7.21
6.73
6.73
6.69
6.68
6.51
6.51
6.49
6.49
6.48
6.47
6.46
5.82
5.80
5.78
3.91
3.91
3.90
3.89
3.88
3.87
3.29
3.29
3.28
3.27
3.27
3.26
1.95 CD3CN
1.95 CD3CN
1.94 CD3CN
1.93 CD3CN
1.93 CD3CN
1.78
1.77
1.77
1.76
1.76
0.35
O
⁻O
CF3
N
Si
HN
+
O
OH
74
1.01
1.38
0.95
0.90
2.01
1.22
7.90
2.00
4.23
5.76
9.0
8.5
8.0
7.5
7.0
6.5
6.0
5.5
5.0
4.5
4.0
3.5
3.0
2.5
2.0
1.5
1.0
0.5
0.0
f1 (ppm)

166

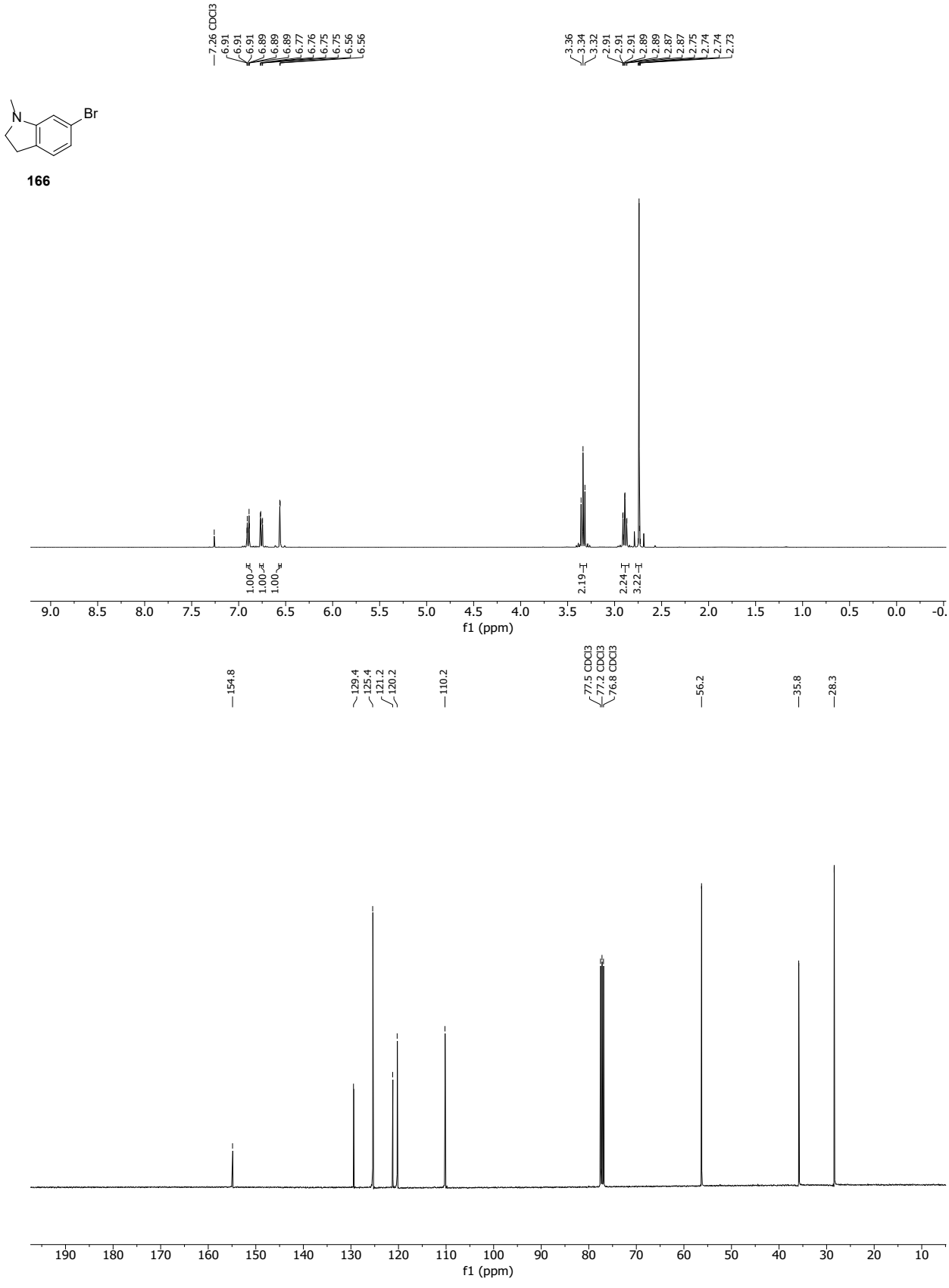
7.26 CDCl3
6.91
6.91
6.89
6.89
6.89
6.77
6.76
6.75
6.75
6.56
6.56
3.36
3.34
3.32
2.91
2.91
2.91
2.89
2.89
2.87
2.87
2.75
2.74
2.74
2.73
N
Br
166
1.00
1.00
1.00
2.19
2.24
3.22
f1 (ppm)
154.8
129.4
125.4
121.2
120.2
110.2
77.5 CDCl3
77.2 CDCl3
76.8 CDCl3
56.2
35.8
28.3
f1 (ppm)

167

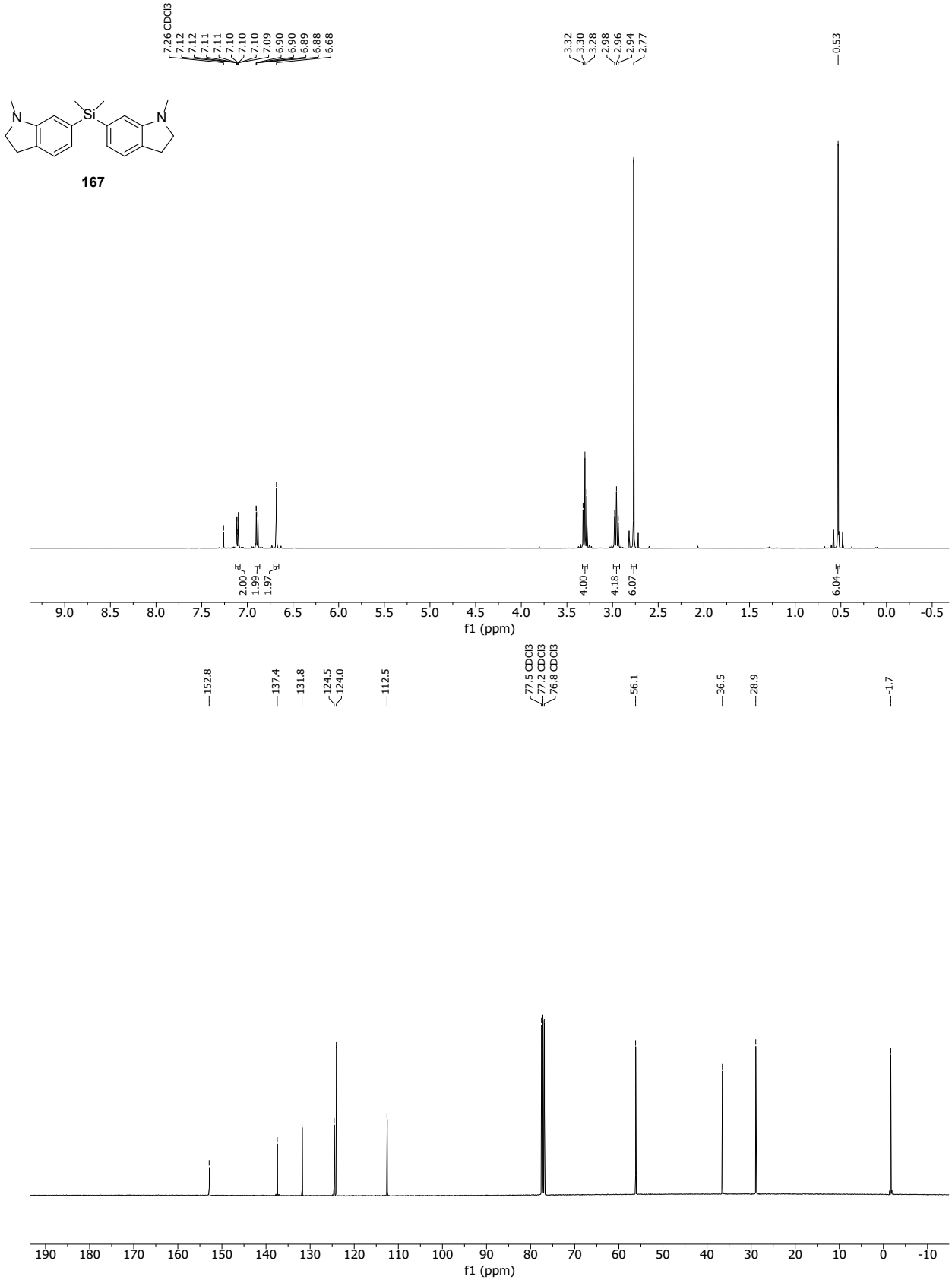
7.26 CDCl3
7.12
7.12
7.11
7.11
7.10
7.10
7.10
7.09
6.90
6.90
6.89
6.88
6.68
3.32
3.30
3.28
2.98
2.96
2.94
2.77
0.53
2.00
1.99
1.97
4.00
4.18
6.07
6.04
f1 (ppm)
152.8
137.4
131.8
124.5
124.0
112.5
77.5 CDCl3
77.2 CDCl3
76.8 CDCl3
56.1
36.5
28.9
-1.7
f1 (ppm)

76

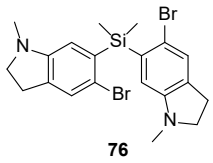
Br
N
Si
Br
N

76

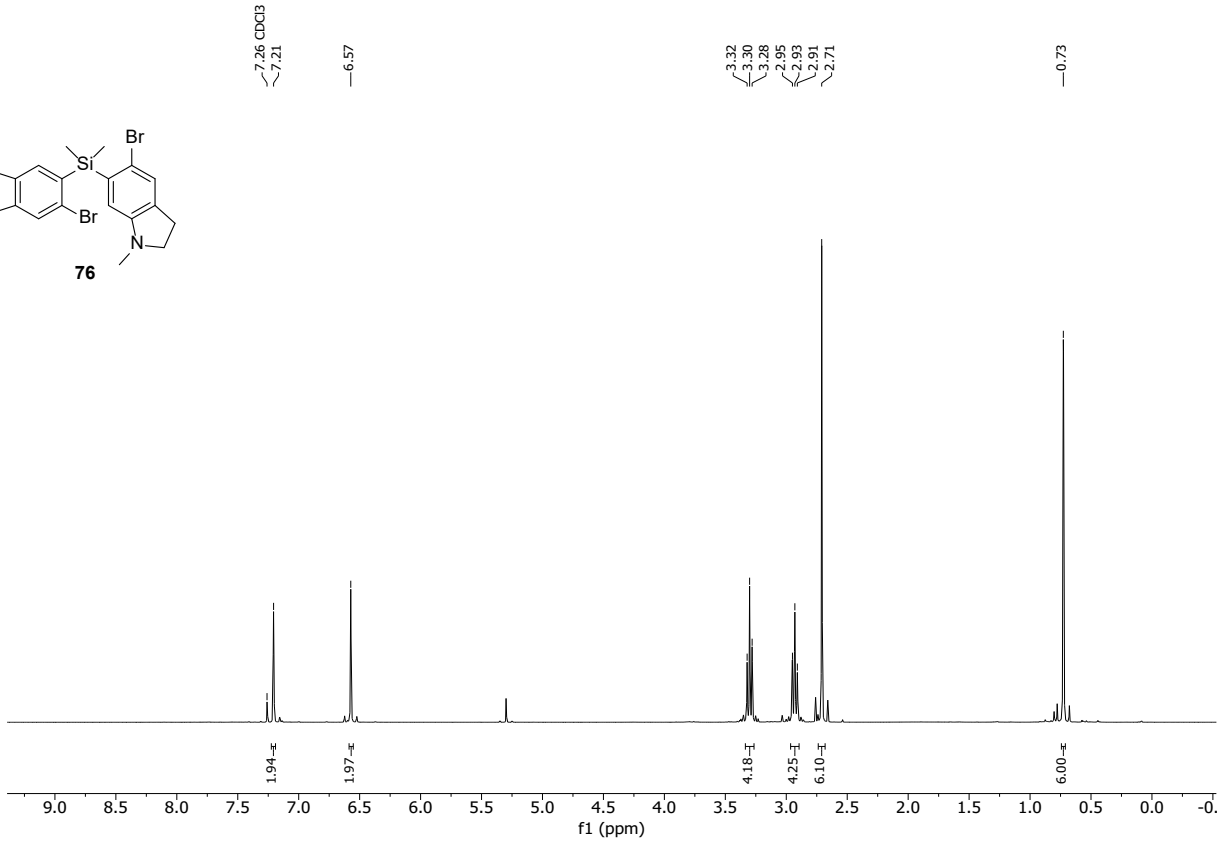
7.26 CDCl3
7.21
6.57
3.32
3.30
3.28
2.95
2.93
2.91
2.71
0.73
1.94
1.97
4.18
4.25
6.10
6.00
f1 (ppm)

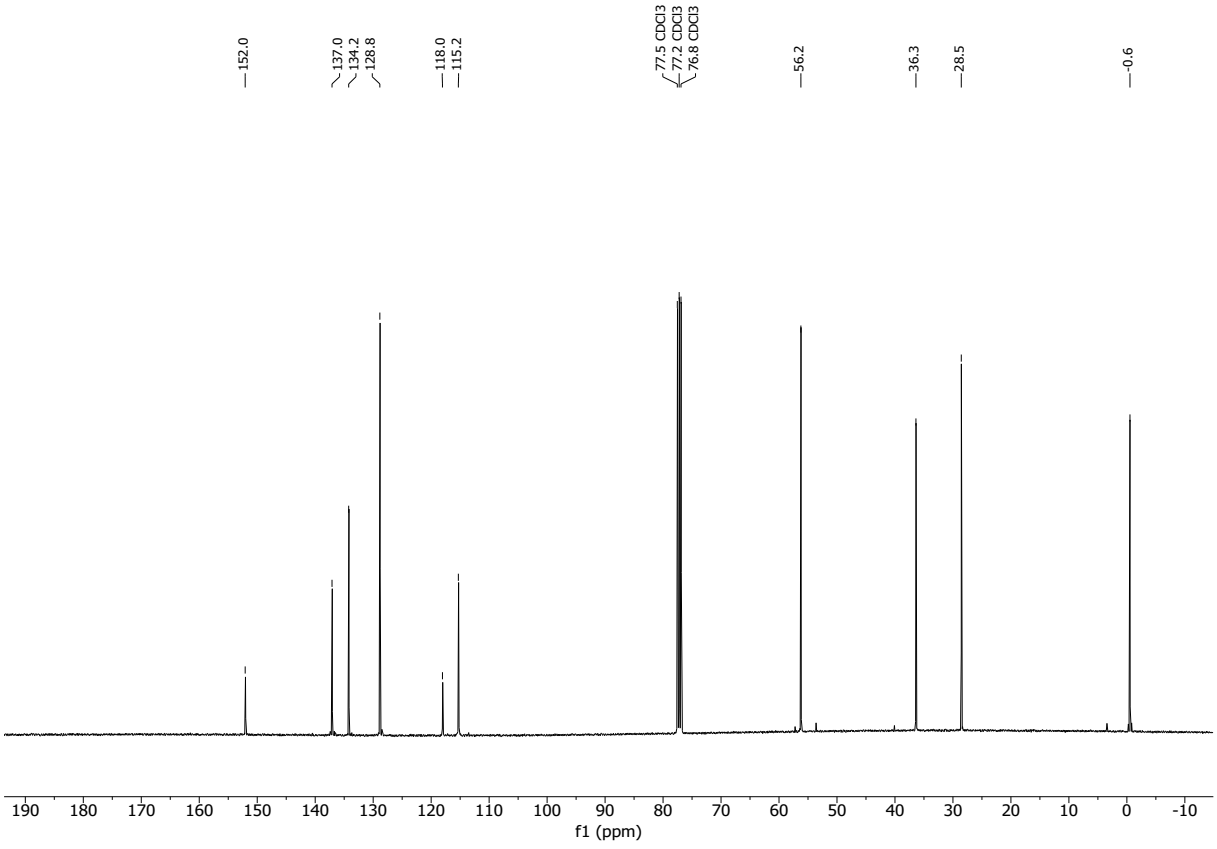
152.0
137.0
134.2
128.8
118.0
115.2
77.5 CDCl3
77.2 CDCl3
76.8 CDCl3
56.2
36.3
28.5
-0.6
f1 (ppm)

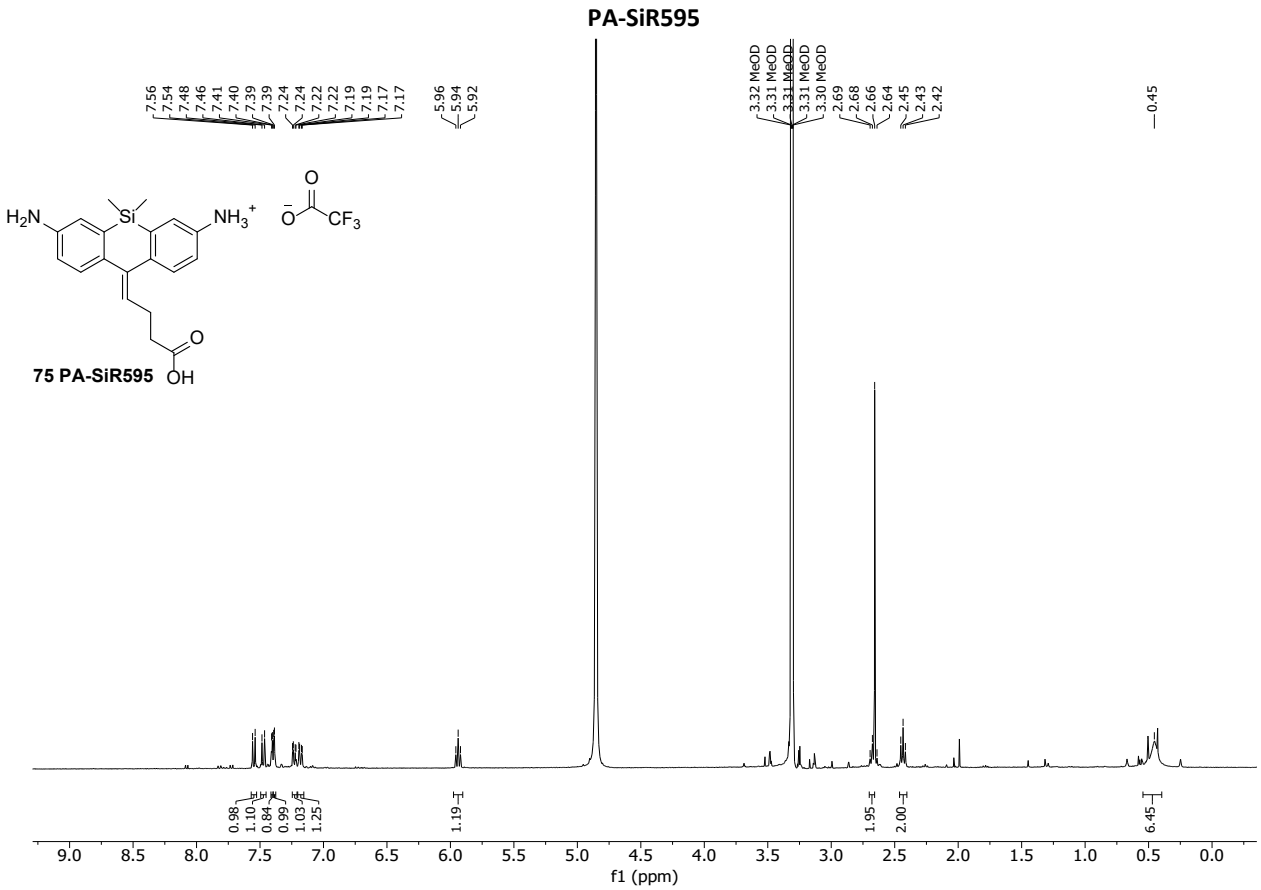
PA-SiR595
7.56
7.54
7.48
7.46
7.41
7.40
7.39
7.39
7.24
7.24
7.22
7.22
7.19
7.19
7.17
7.17
7.17
5.96
5.94
5.92
3.32 MeOD
3.31 MeOD
3.31 MeOD
3.31 MeOD
3.30 MeOD
2.69
2.68
2.66
2.64
2.45
2.43
2.42
0.45
H2N
Si
NH3+
O
O
CF3
O
OH
75 PA-SiR595
0.98
1.10
0.84
0.99
1.03
1.25
1.19
1.95
2.00
6.45
9.0
8.5
8.0
7.5
7.0
6.5
6.0
5.5
5.0
4.5
4.0
3.5
3.0
2.5
2.0
1.5
1.0
0.5
0.0
f1 (ppm)

82

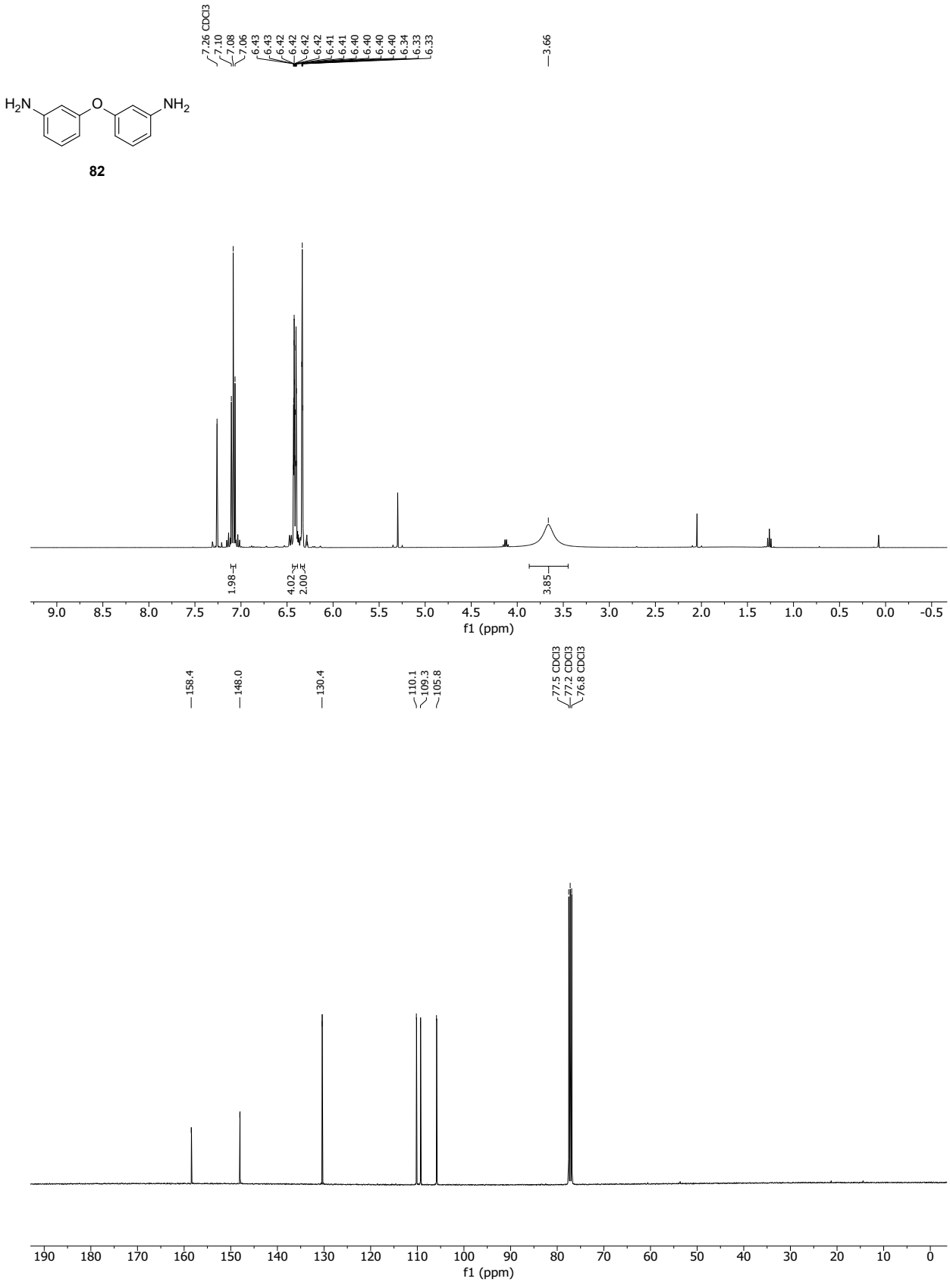
7.26 CDCl3
7.10
7.08
7.06
6.43
6.43
6.42
6.42
6.42
6.42
6.41
6.41
6.40
6.40
6.40
6.40
6.34
6.33
6.33
3.66
H2N
O
NH2
82
1.98
4.02
2.00
3.85
f1 (ppm)
158.4
148.0
130.4
110.1
109.3
105.8
77.5 CDCl3
77.2 CDCl3
76.8 CDCl3
f1 (ppm)

84

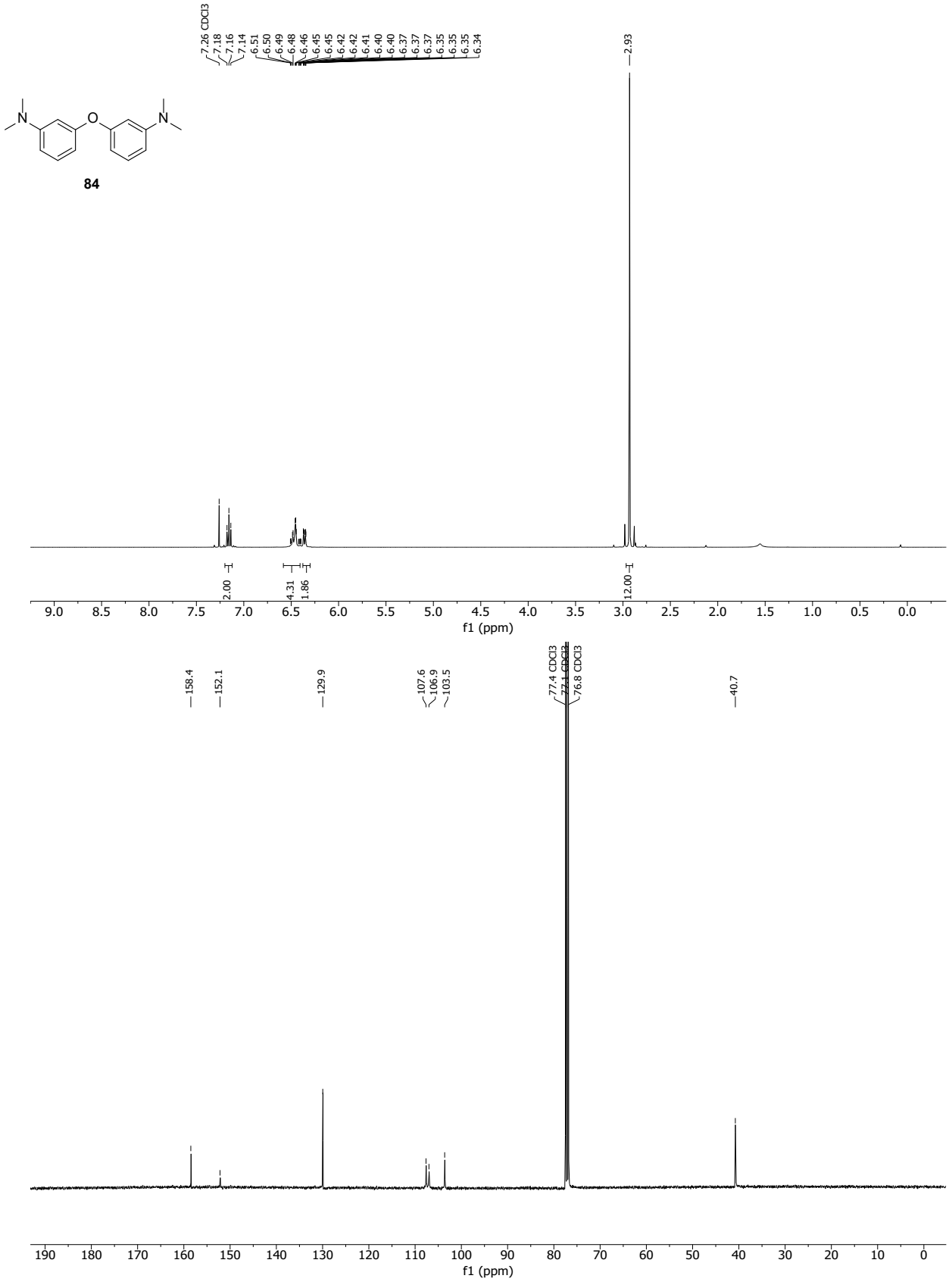
7.26 CDCl3
7.18
7.16
7.14
6.51
6.50
6.49
6.48
6.46
6.45
6.45
6.42
6.42
6.41
6.40
6.40
6.37
6.37
6.35
6.35
6.34
2.93
2.00
4.31
1.86
12.00
f1 (ppm)
158.4
152.1
129.9
107.6
106.9
103.5
77.4 CDCl3
77.1 CDCl3
76.8 CDCl3
40.7
f1 (ppm)

84

86

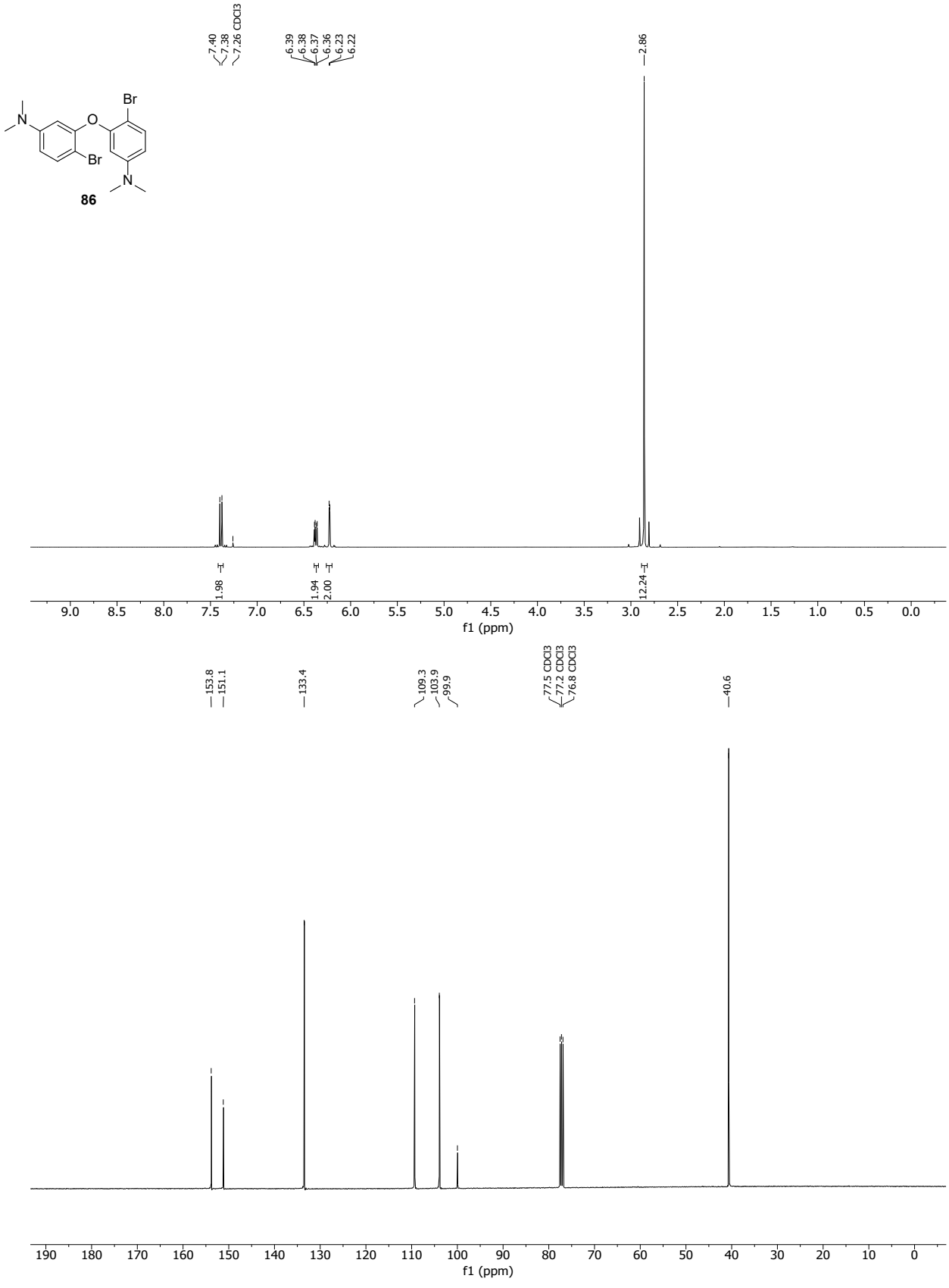
7.40
7.38
7.26 CDCl3
6.39
6.38
6.37
6.36
6.23
6.22
2.86
Br
N
O
Br
N
86
1.98
1.94
2.00
12.24
f1 (ppm)
153.8
151.1
133.4
109.3
103.9
99.9
77.5 CDCl3
77.2 CDCl3
76.8 CDCl3
40.6
f1 (ppm)

83

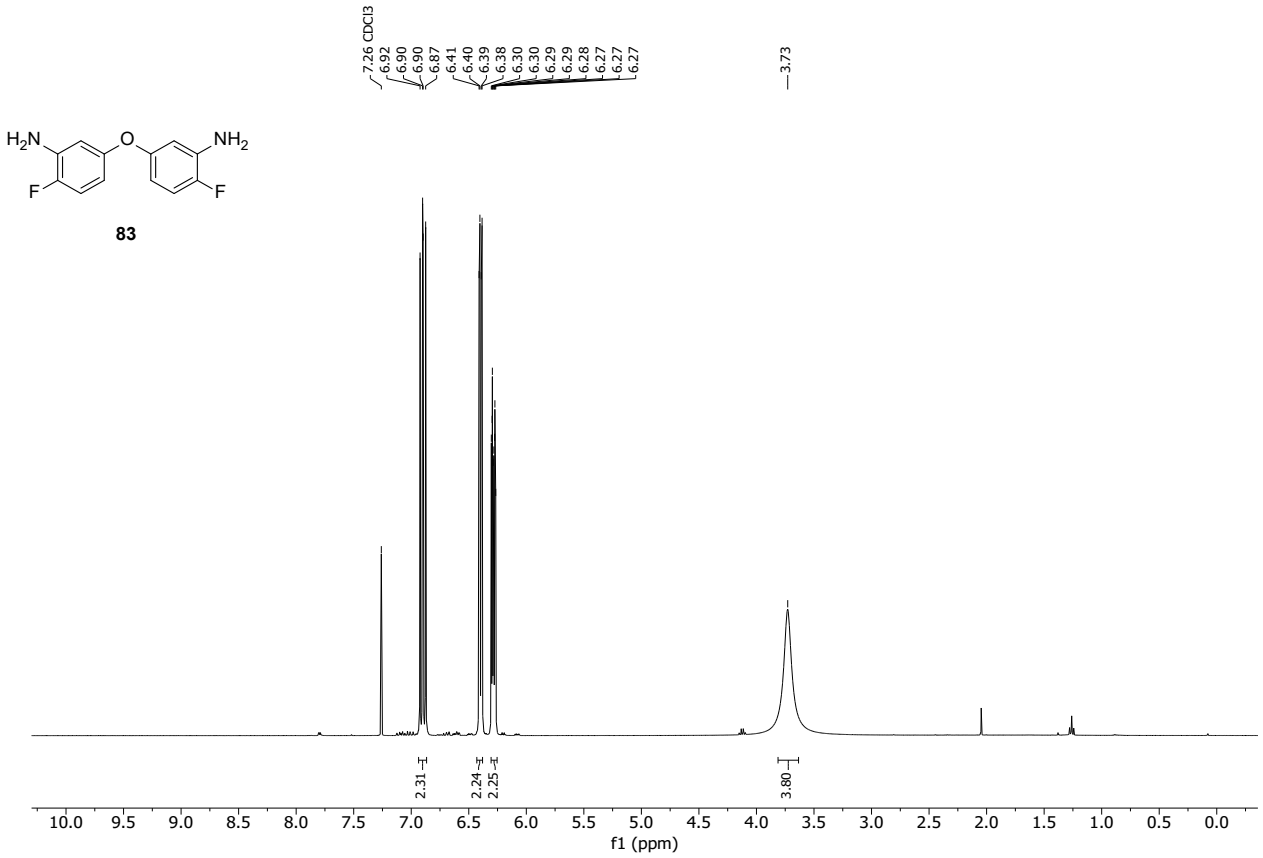
7.26 CDCl3
6.92
6.90
6.90
6.87
6.41
6.40
6.39
6.38
6.30
6.30
6.29
6.29
6.28
6.27
6.27
6.27
3.73
H2N
O
NH2
F
F
83
2.31
2.24
2.25
3.80
f1 (ppm)

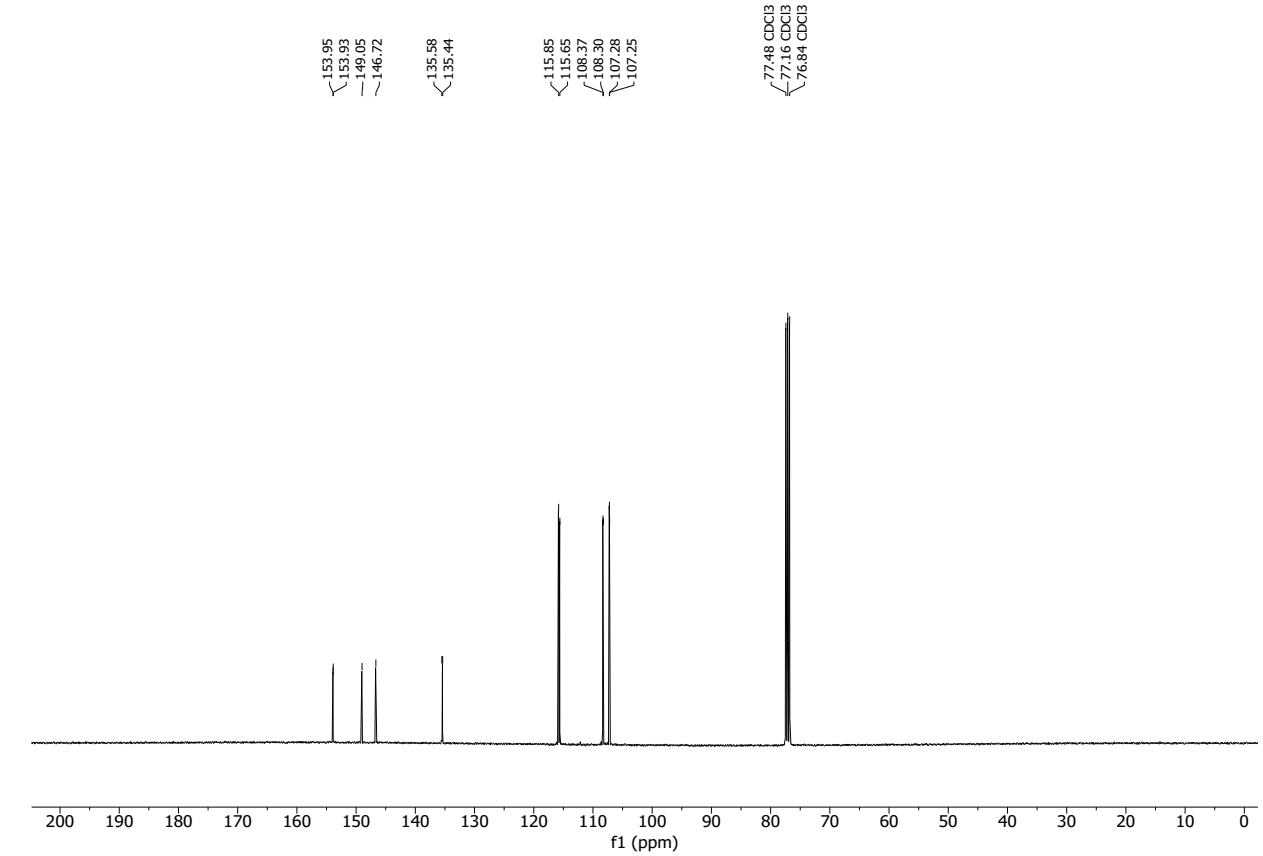
153.95
153.93
149.05
146.72
135.58
135.44
115.85
115.65
108.37
108.30
107.28
107.25
77.48 CDCl3
77.16 CDCl3
76.84 CDCl3
f1 (ppm)

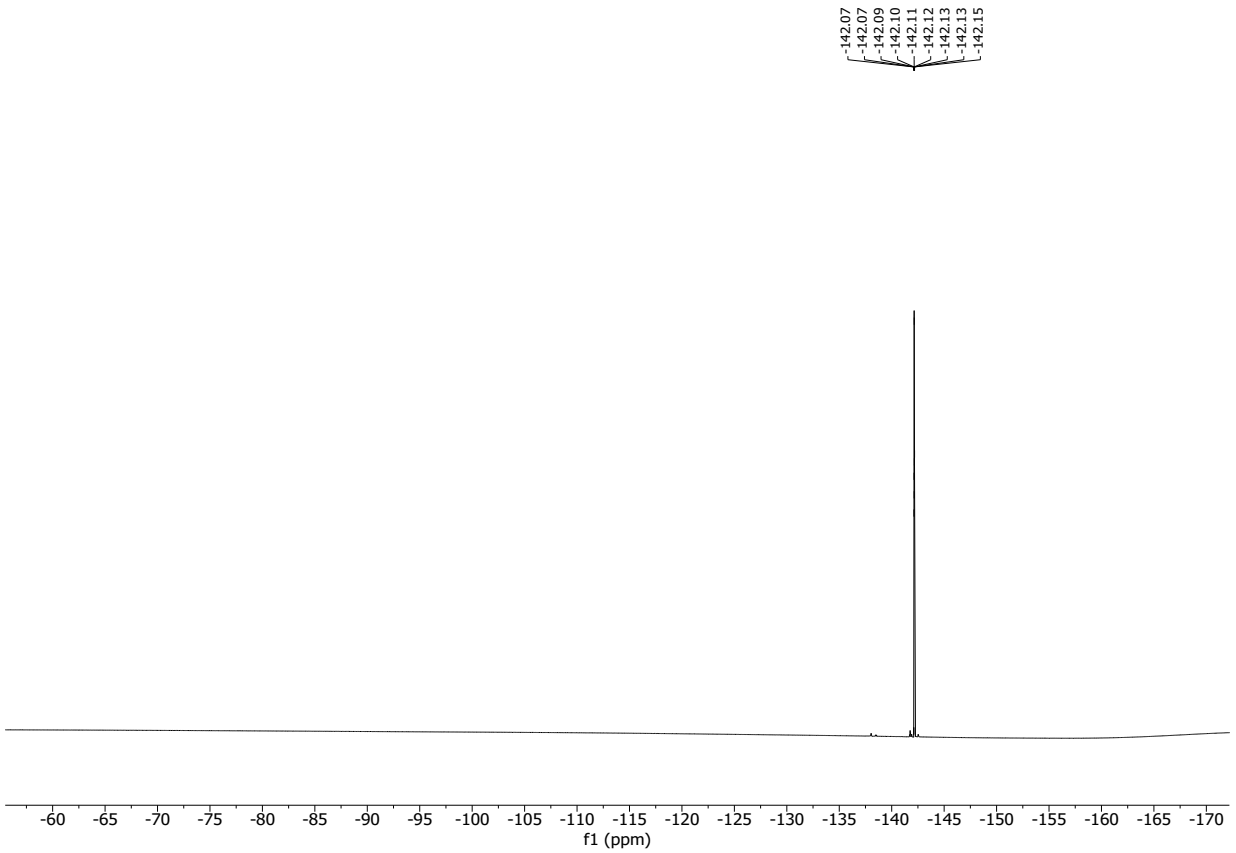
-142.07
-142.07
-142.09
-142.10
-142.11
-142.12
-142.13
-142.13
-142.15
-60 -65 -70 -75 -80 -85 -90 -95 -100 -105 -110 -115 -120 -125 -130 -135 -140 -145 -150 -155 -160 -165 -170
f1 (ppm)

85

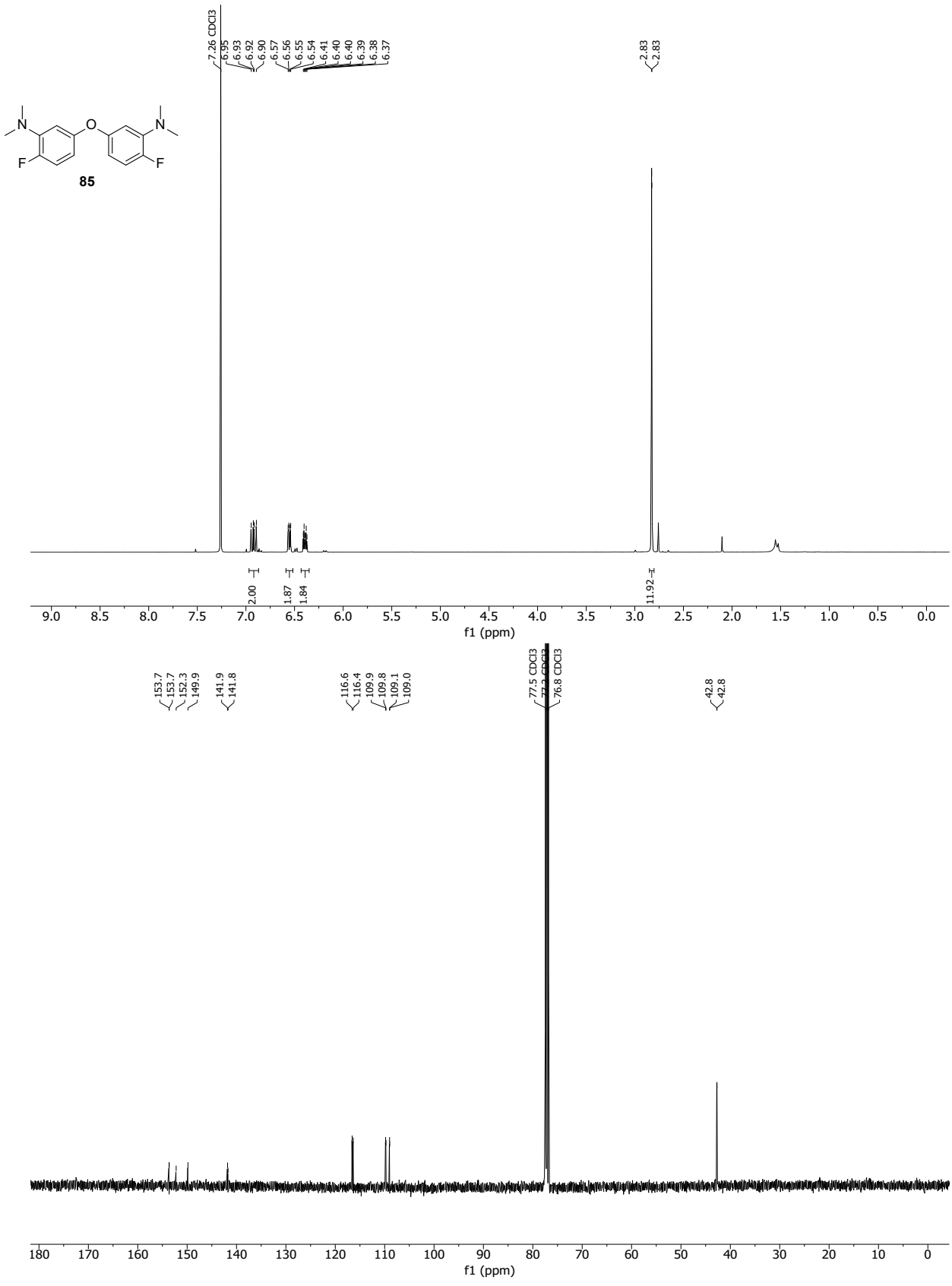
7.26 CDCl3
6.95
6.93
6.92
6.90
6.57
6.56
6.55
6.54
6.41
6.40
6.40
6.39
6.38
6.37
2.83
2.83
2.00
1.87
1.84
11.92
f1 (ppm)
153.7
153.7
152.3
149.9
141.9
141.8
116.6
116.4
109.9
109.8
109.1
109.0
77.5 CDCl3
76.8 CDCl3
42.8
42.8
f1 (ppm)

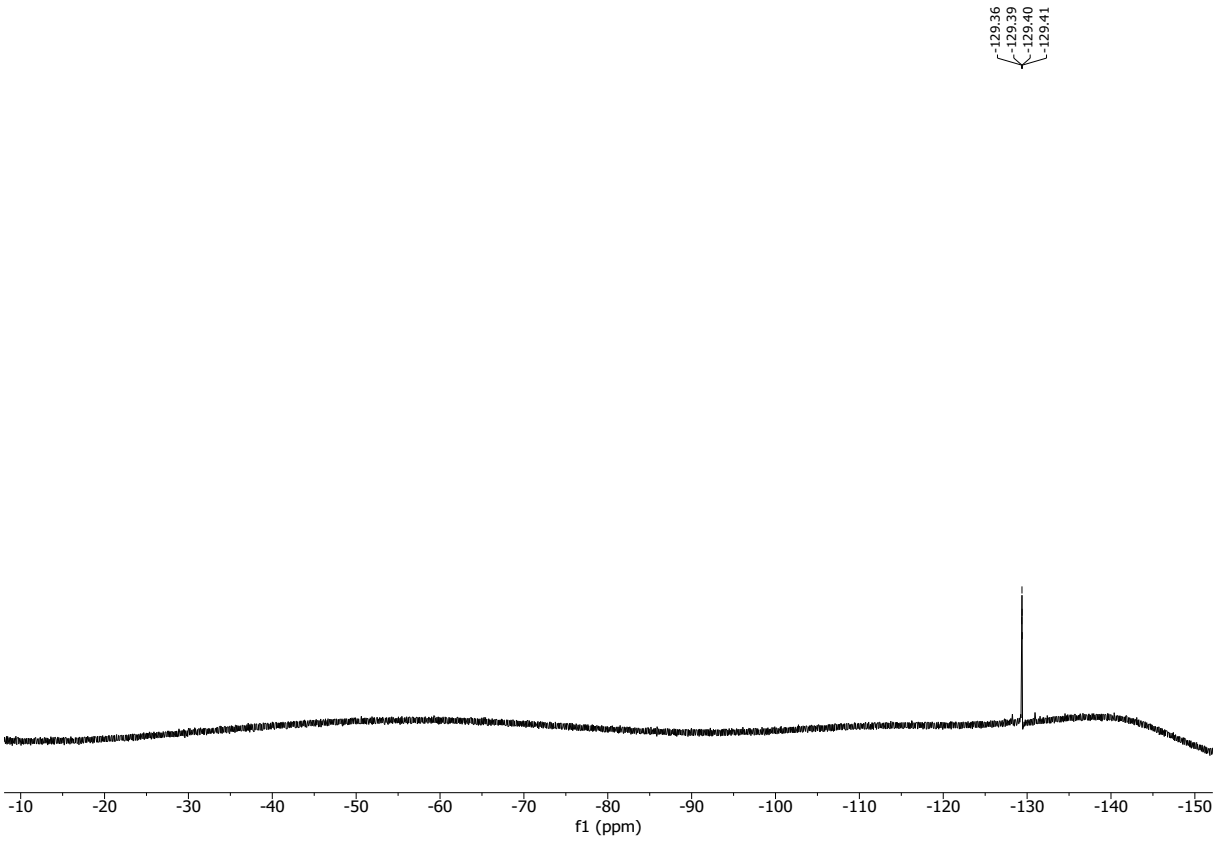
-129.36
-129.39
-129.40
-129.41
-10
-20
-30
-40
-50
-60
-70
-80
-90
-100
-110
-120
-130
-140
-150
f1 (ppm)

87

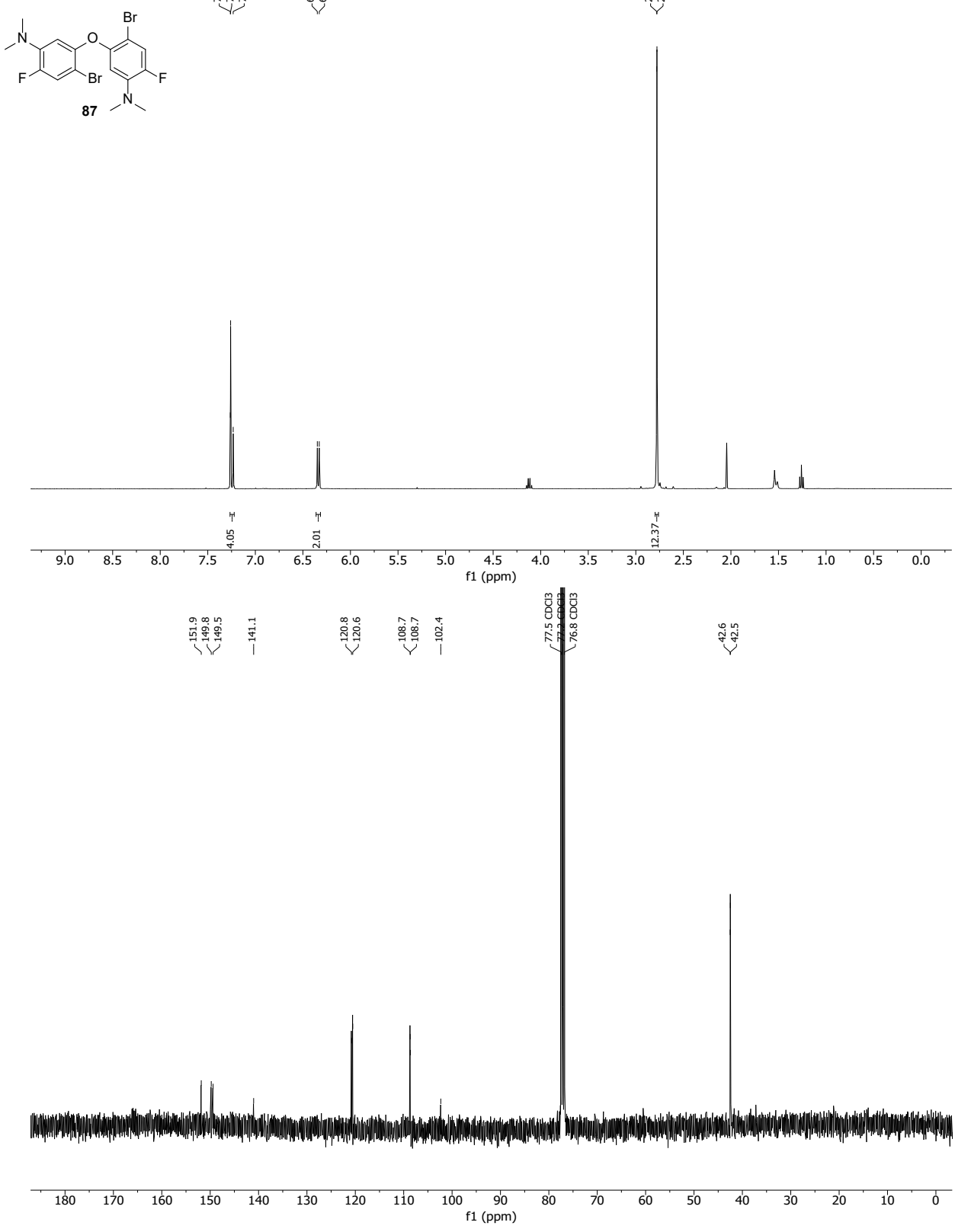
7.26
7.26 CDCl3
7.23
6.35
6.33
2.78
2.78
Br
N
O
F
Br
F
N
87
4.05
2.01
12.37
f1 (ppm)
151.9
149.8
149.5
141.1
120.8
120.6
108.7
108.7
102.4
77.5 CDCl3
77.3 CDCl3
76.8 CDCl3
42.6
42.5
f1 (ppm)

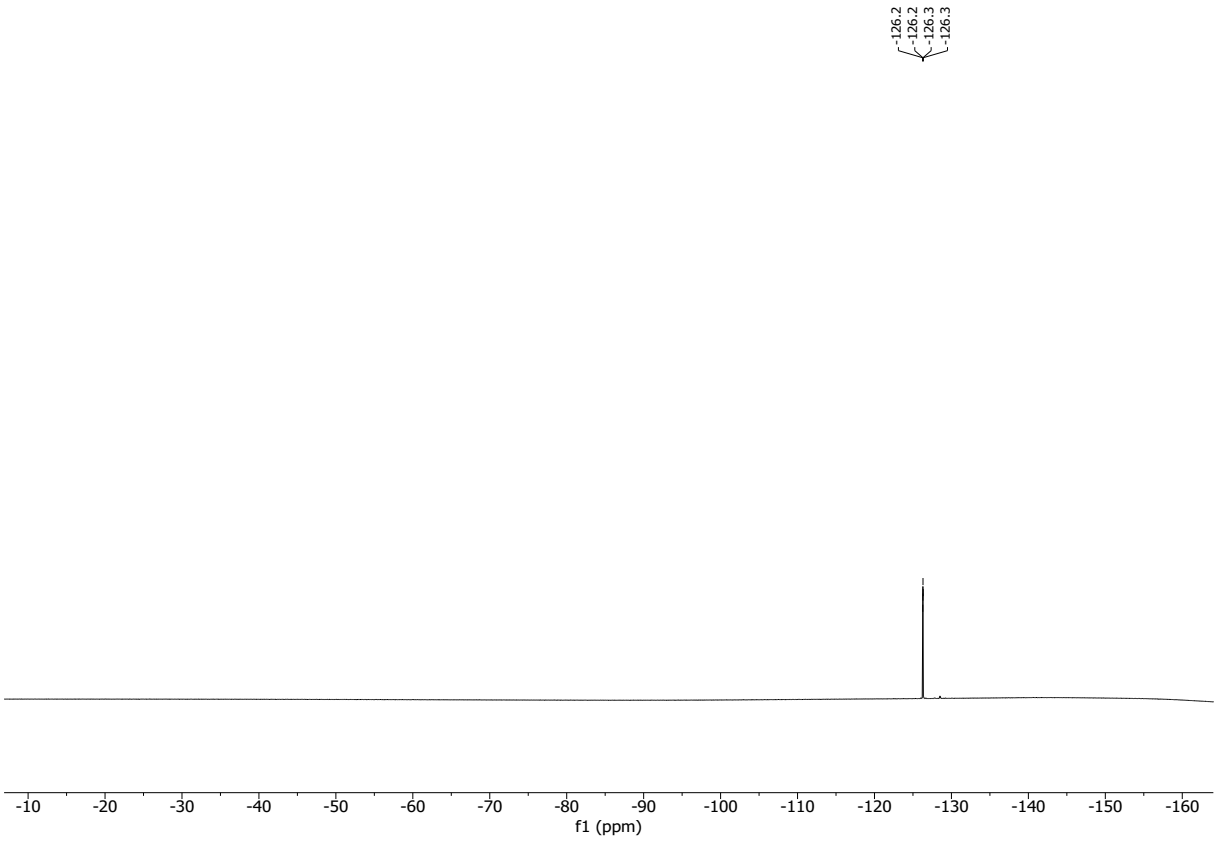
-126.2
-126.2
-126.3
-126.3
-10
-20
-30
-40
-50
-60
-70
-80
-90
-100
-110
-120
-130
-140
-150
-160
f1 (ppm)

90 DMSO-d_6 and CD_3CN

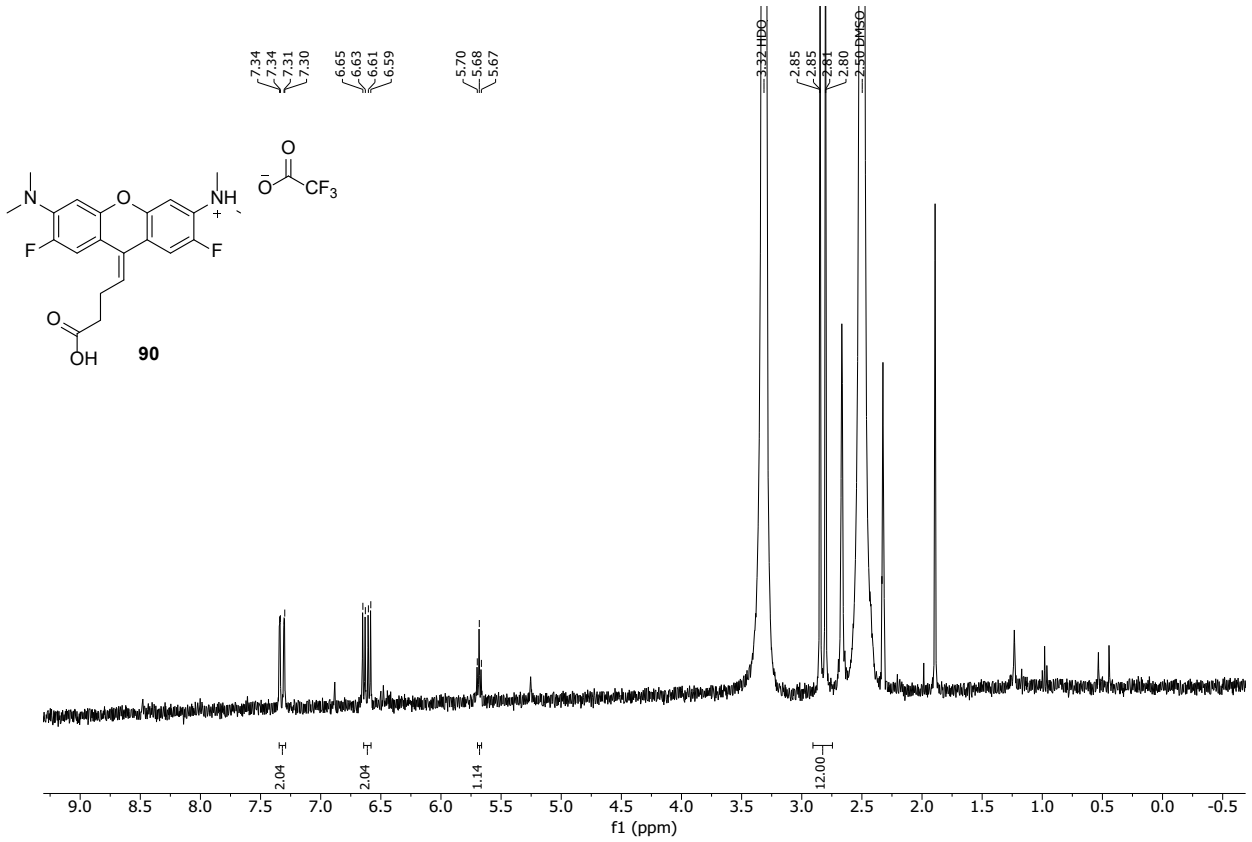

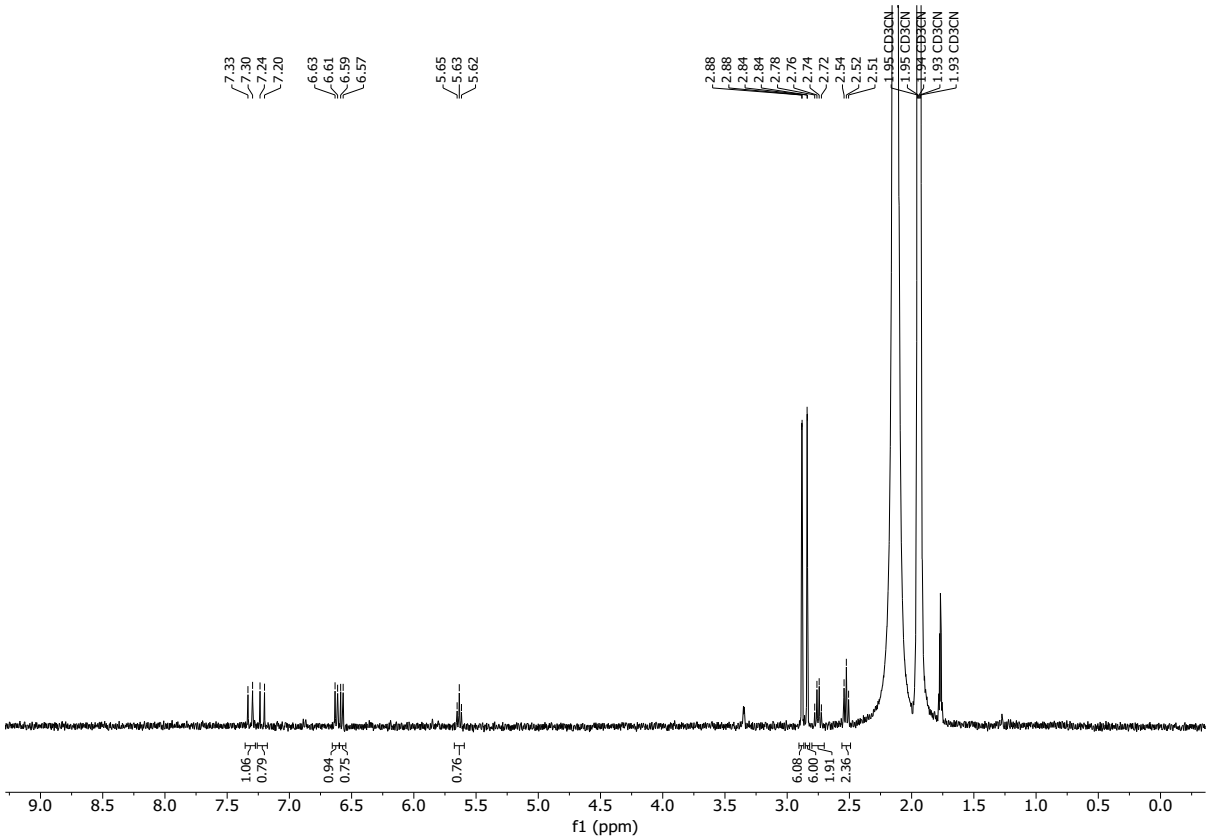

93

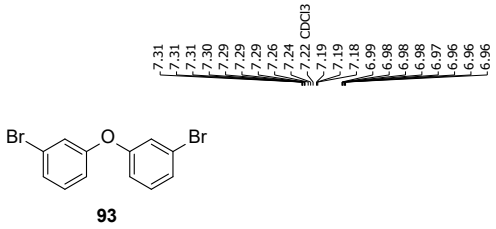
7.31
7.31
7.31
7.30
7.29
7.29
7.29
7.26
7.24
7.22 CDCl3
7.19
7.19
7.18
6.99
6.98
6.98
6.98
6.97
6.96
6.96
6.96
Br
O
Br

93

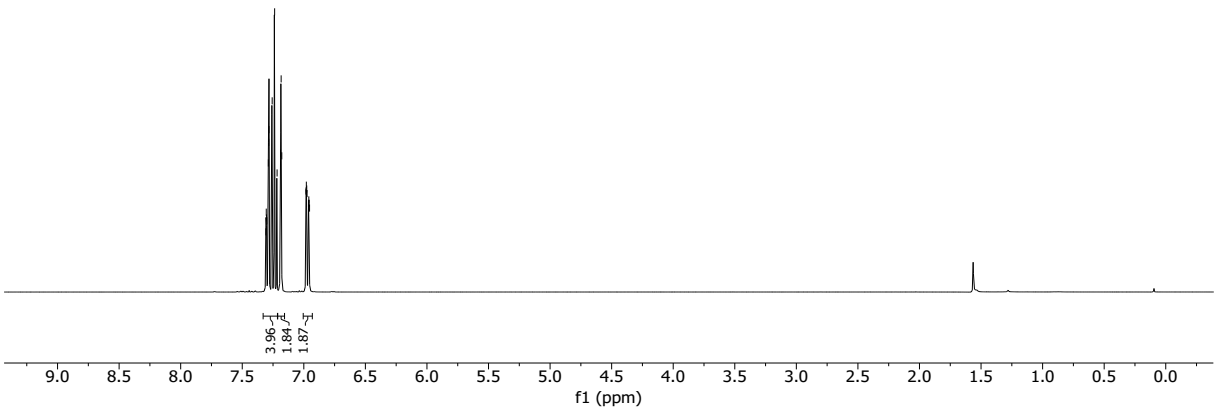
3.96
1.84
1.87
9.0
8.5
8.0
7.5
7.0
6.5
6.0
5.5
5.0
4.5
4.0
3.5
3.0
2.5
2.0
1.5
1.0
0.5
0.0
f1 (ppm)

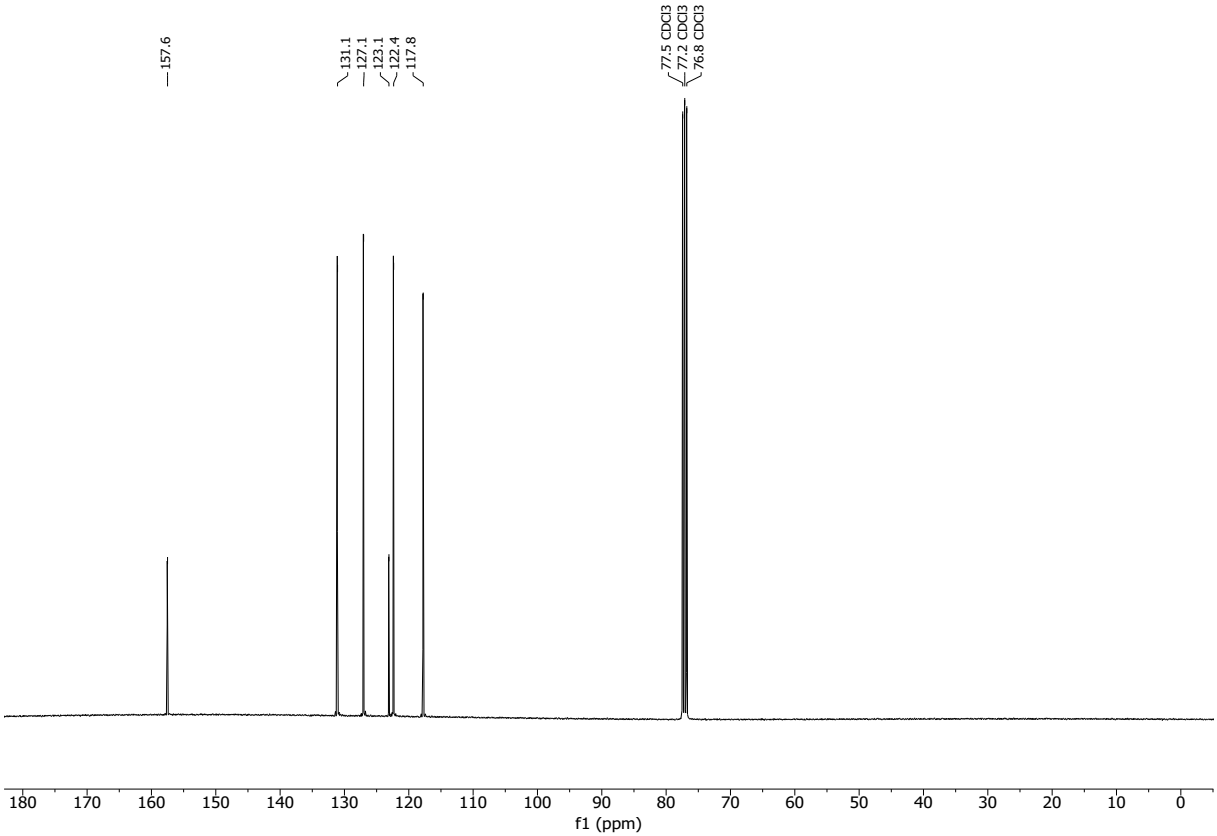
157.6
131.1
127.1
123.1
122.4
117.8
77.5 CDCl3
77.2 CDCl3
76.8 CDCl3
180
170
160
150
140
130
120
110
100
90
80
70
60
50
40
30
20
10
0
f1 (ppm)

95

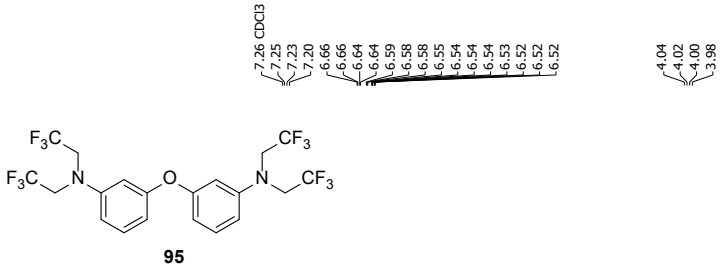
7.26 CDCl3
7.25
7.23
7.20
6.66
6.64
6.64
6.59
6.58
6.58
6.55
6.54
6.54
6.54
6.53
6.52
6.52
6.52
4.04
4.02
4.00
3.98
F3C
CF3
F3C
N
O
N
CF3
95

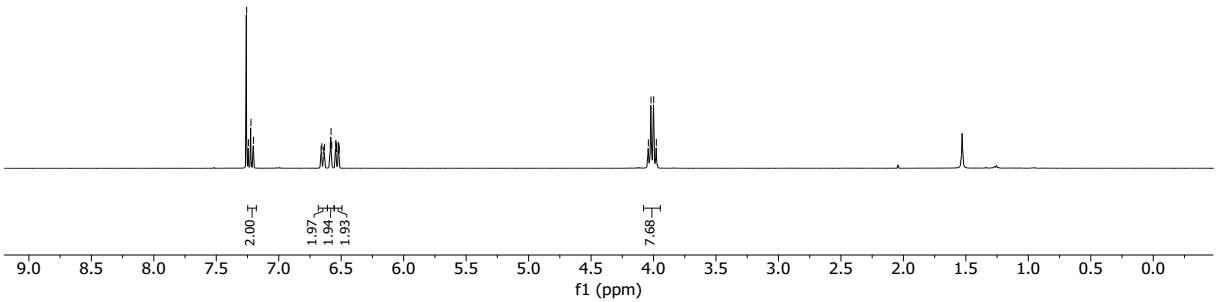
2.00
1.97
1.94
1.93
7.68
9.0
8.5
8.0
7.5
7.0
6.5
6.0
5.5
5.0
4.5
4.0
3.5
3.0
2.5
2.0
1.5
1.0
0.5
0.0
f1 (ppm)

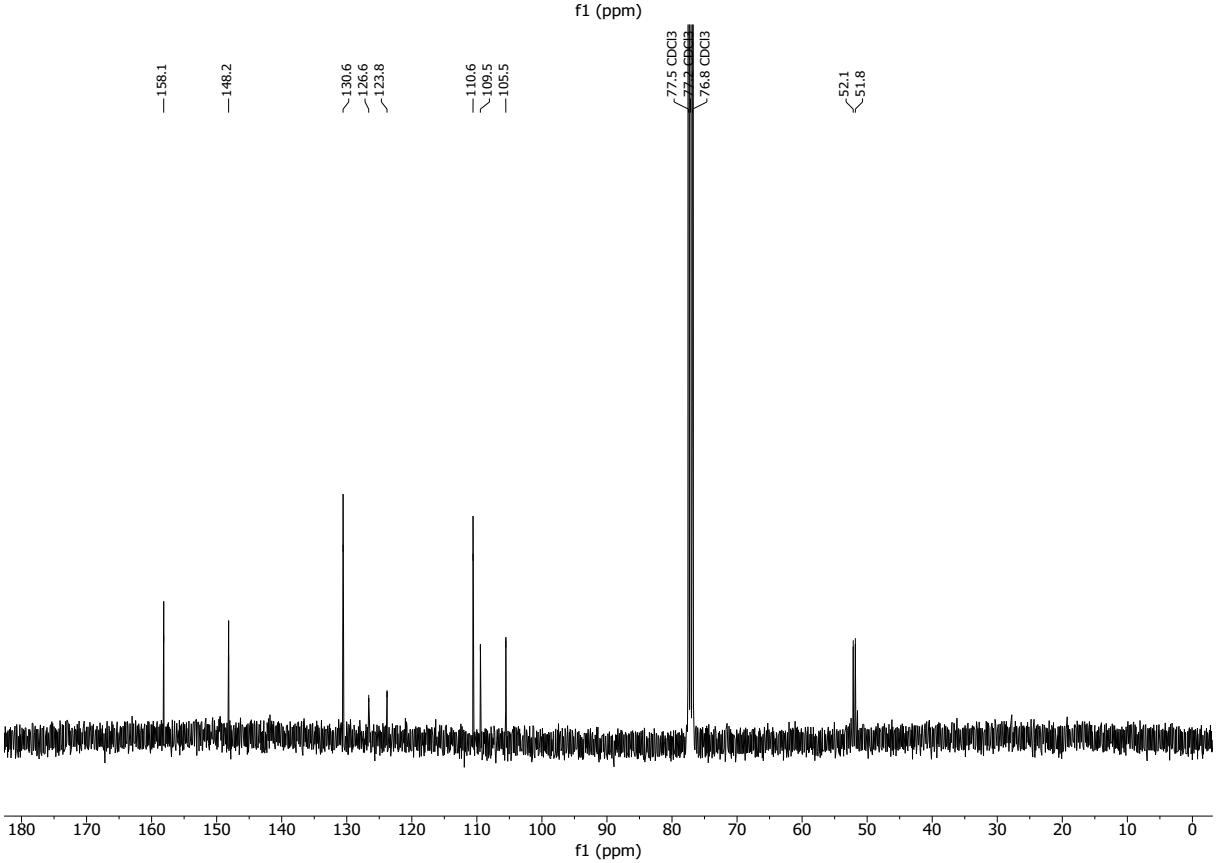
158.1
148.2
130.6
126.6
123.8
110.6
109.5
105.5
77.5 CDCl3
77.2 CDCl3
76.8 CDCl3
52.1
51.8
180
170
160
150
140
130
120
110
100
90
80
70
60
50
40
30
20
10
0
f1 (ppm)

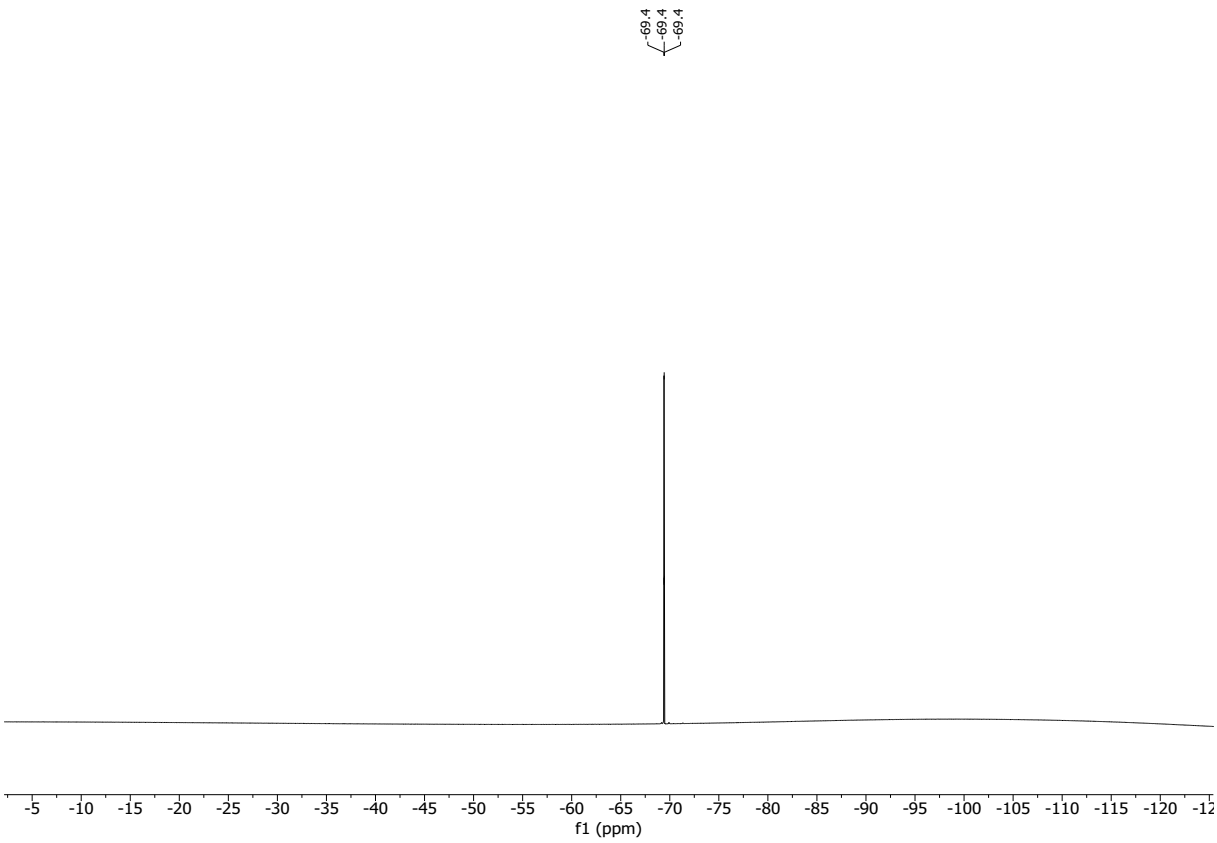
-69.4
-69.4
-69.4
-5 -10 -15 -20 -25 -30 -35 -40 -45 -50 -55 -60 -65 -70 -75 -80 -85 -90 -95 -100 -105 -110 -115 -120 -12
f1 (ppm)

96

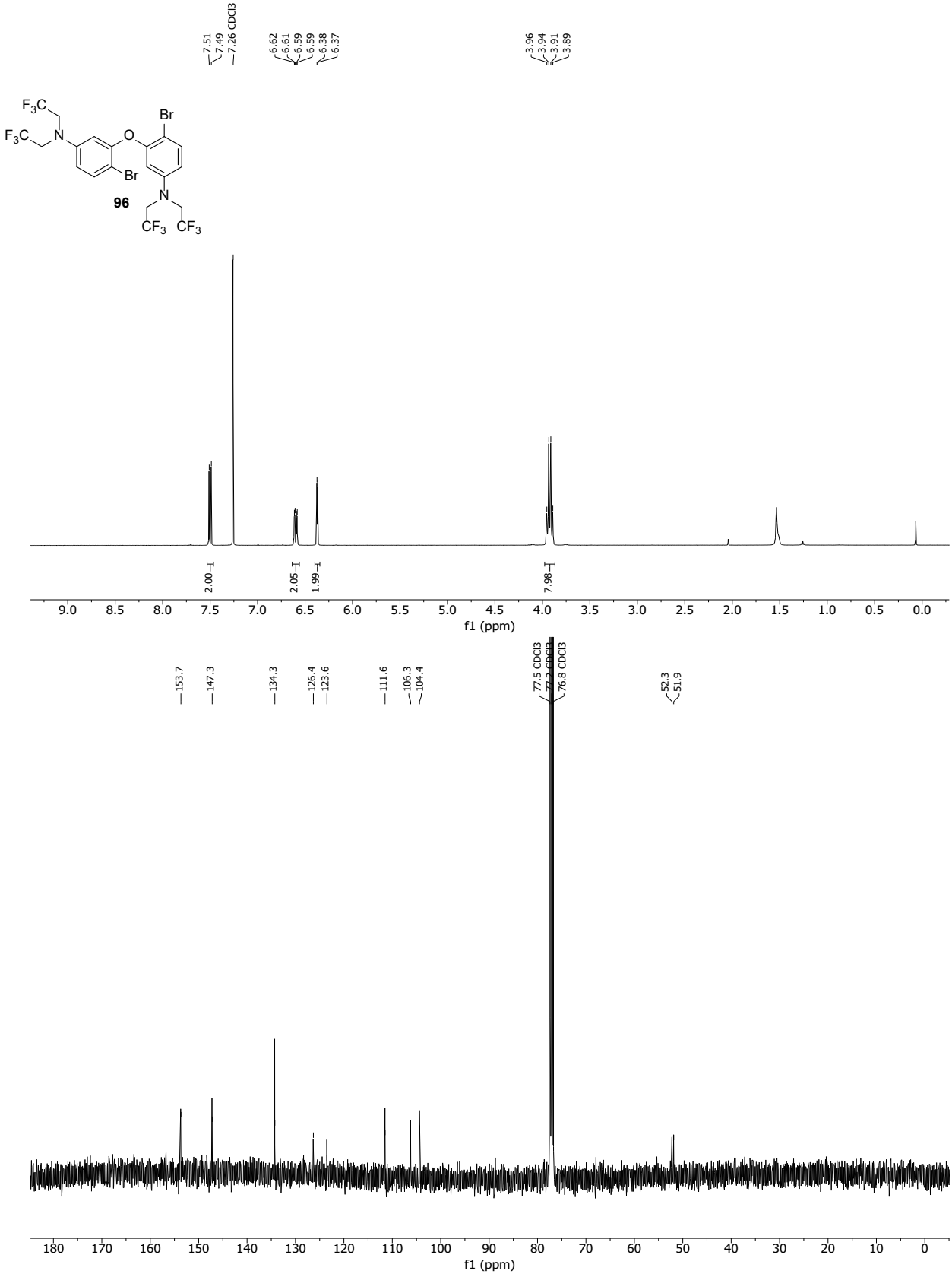
7.51
7.49
7.26 CDCl3
6.62
6.61
6.59
6.59
6.38
6.37
3.96
3.94
3.91
3.89
F3C
F3C
N
O
Br
Br
96
N
CF3
CF3
2.00
2.05
1.99
7.98
f1 (ppm)
153.7
147.3
134.3
126.4
123.6
111.6
106.3
104.4
77.5 CDCl3
77.3 CDCl3
76.8 CDCl3
52.3
51.9
f1 (ppm)

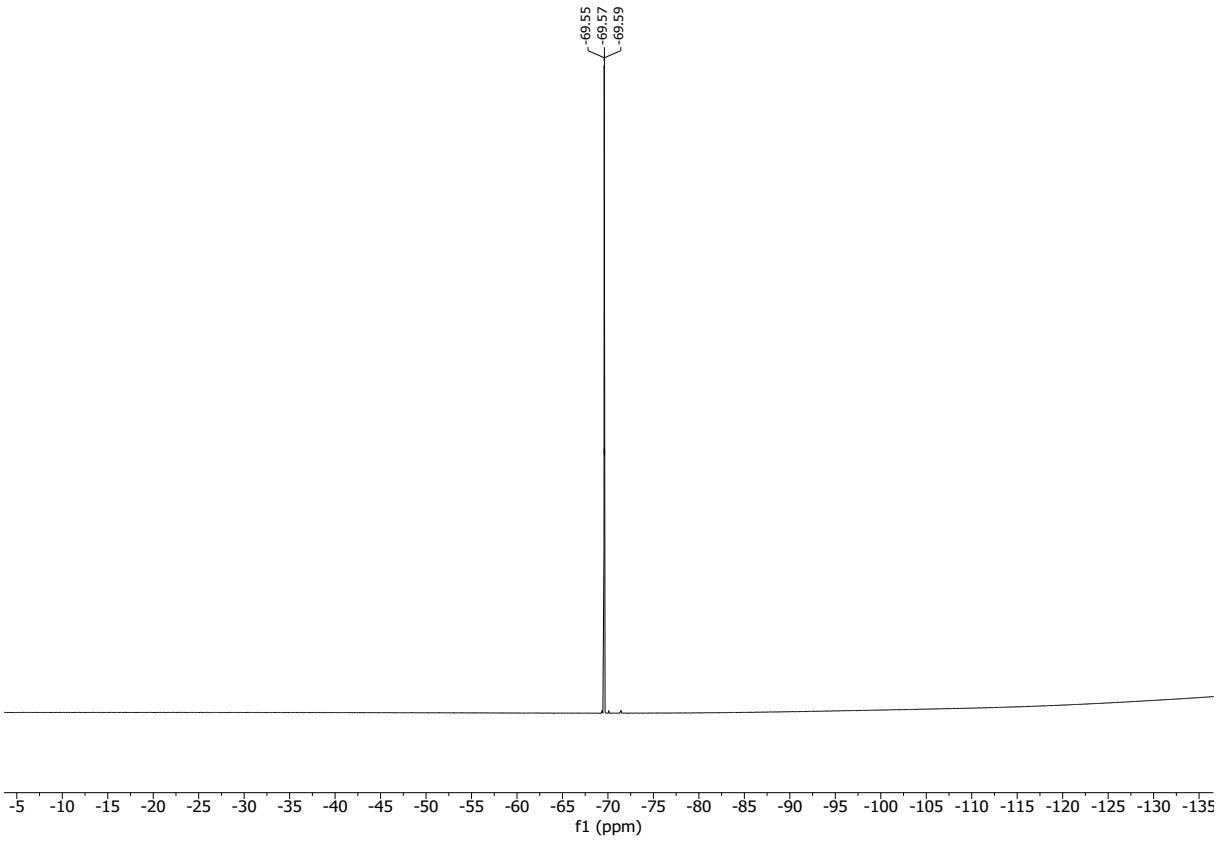
-69.55
-69.57
-69.59
-5 -10 -15 -20 -25 -30 -35 -40 -45 -50 -55 -60 -65 -70 -75 -80 -85 -90 -95 -100 -105 -110 -115 -120 -125 -130 -135
f1 (ppm)

97 and **98**


8.47
8.44
7.57
7.56
7.55
7.54
7.49
7.46
7.37
7.36
6.85
6.84
6.83
6.82
6.80
6.80
6.78
6.76
6.75
6.71
6.70
5.72
5.71
5.69
4.59
4.57
4.55
4.53
4.26
4.24
4.22
4.21
4.19
4.16
3.62
3.61
3.60
3.59
3.58
2.78
2.76
2.74
2.72
2.61
2.59
2.58
2.54
2.52 HDO
2.50
2.02
2.00
1.98
1.98
1.97
1.95 CD3CN
1.95 CD3CN
1.94 CD3CN
1.93 CD3CN
1.93 CD3CN
97
98
2.01
2.20
0.31
2.00
1.18
0.33
0.33
8.09
2.48
2.36
0.68
2.16
0.64
1.96
f1 (ppm)
-69.8
-69.9
-69.9
-76.6
f1 (ppm)

173

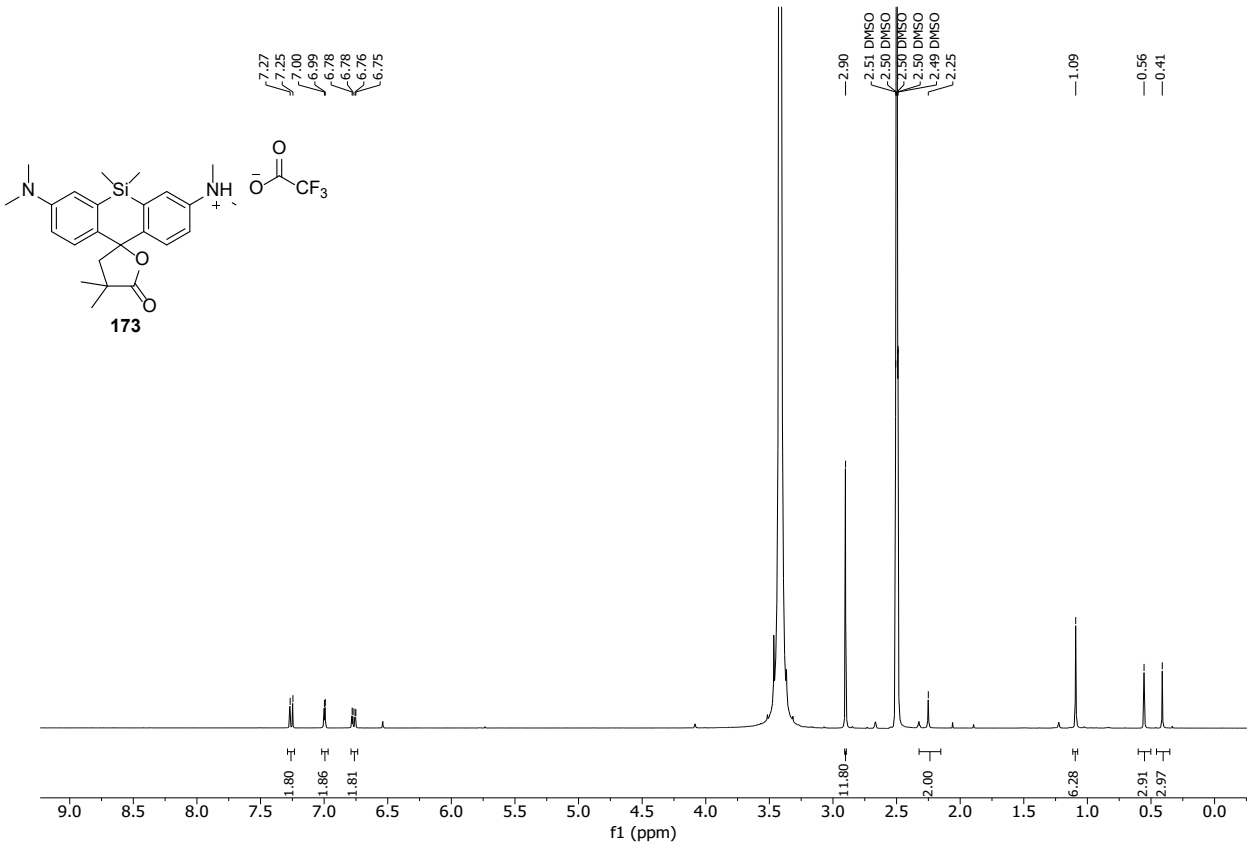
7.27
7.25
7.00
6.99
6.78
6.78
6.76
6.75
2.90
2.51 DMSO
2.50 DMSO
2.50 DMSO
2.50 DMSO
2.49 DMSO
2.25
1.09
0.56
0.41
1.80
1.86
1.81
11.80
2.00
6.28
2.91
2.97
f1 (ppm)
182.3
158.4 TFA
158.0 TFA
147.7
141.7
133.6
122.4
117.0
114.1
83.8
56.3
40.9
40.4
40.1 DMSO
39.9 DMSO
39.7 DMSO
39.5 DMSO
39.3 DMSO
39.1 DMSO
38.9 DMSO
26.9
0.4
-2.8
f1 (ppm)

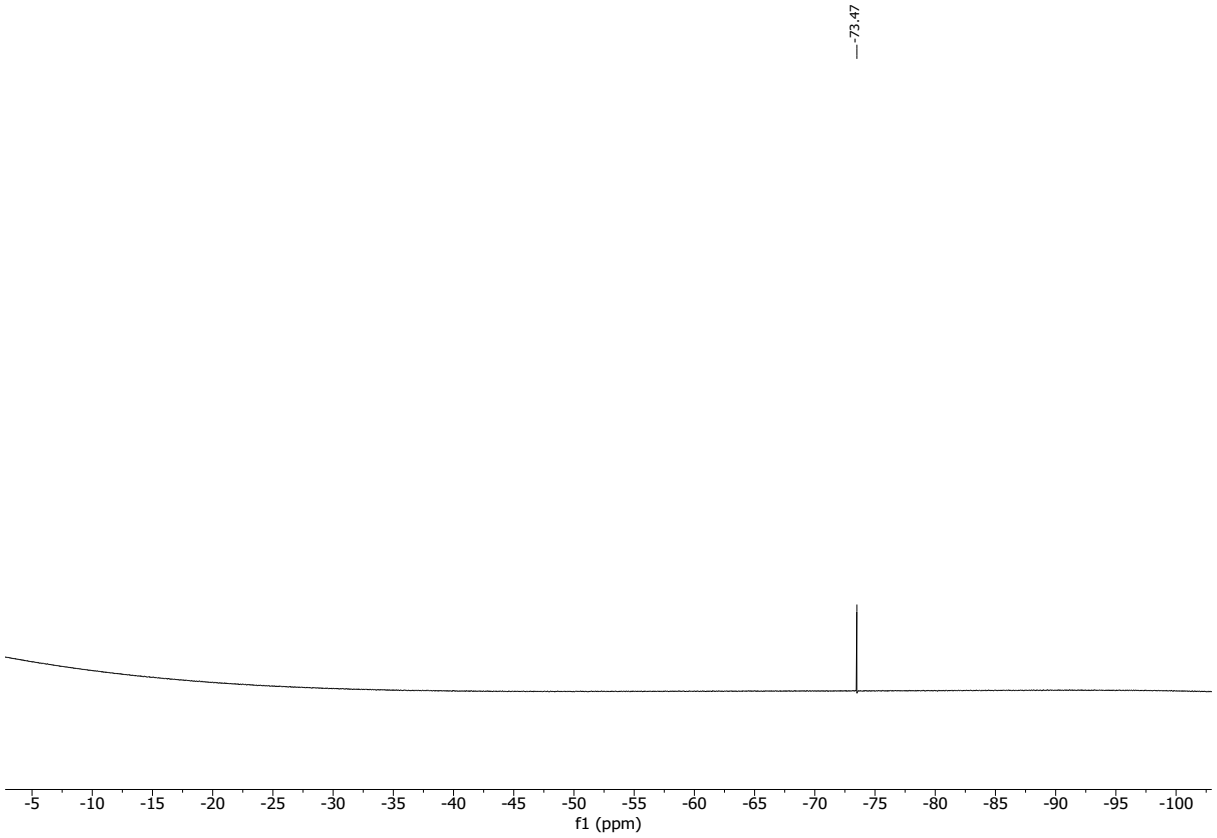
-73.47
-5
-10
-15
-20
-25
-30
-35
-40
-45
-50
-55
-60
-65
-70
-75
-80
-85
-90
-95
-100
f1 (ppm)

175

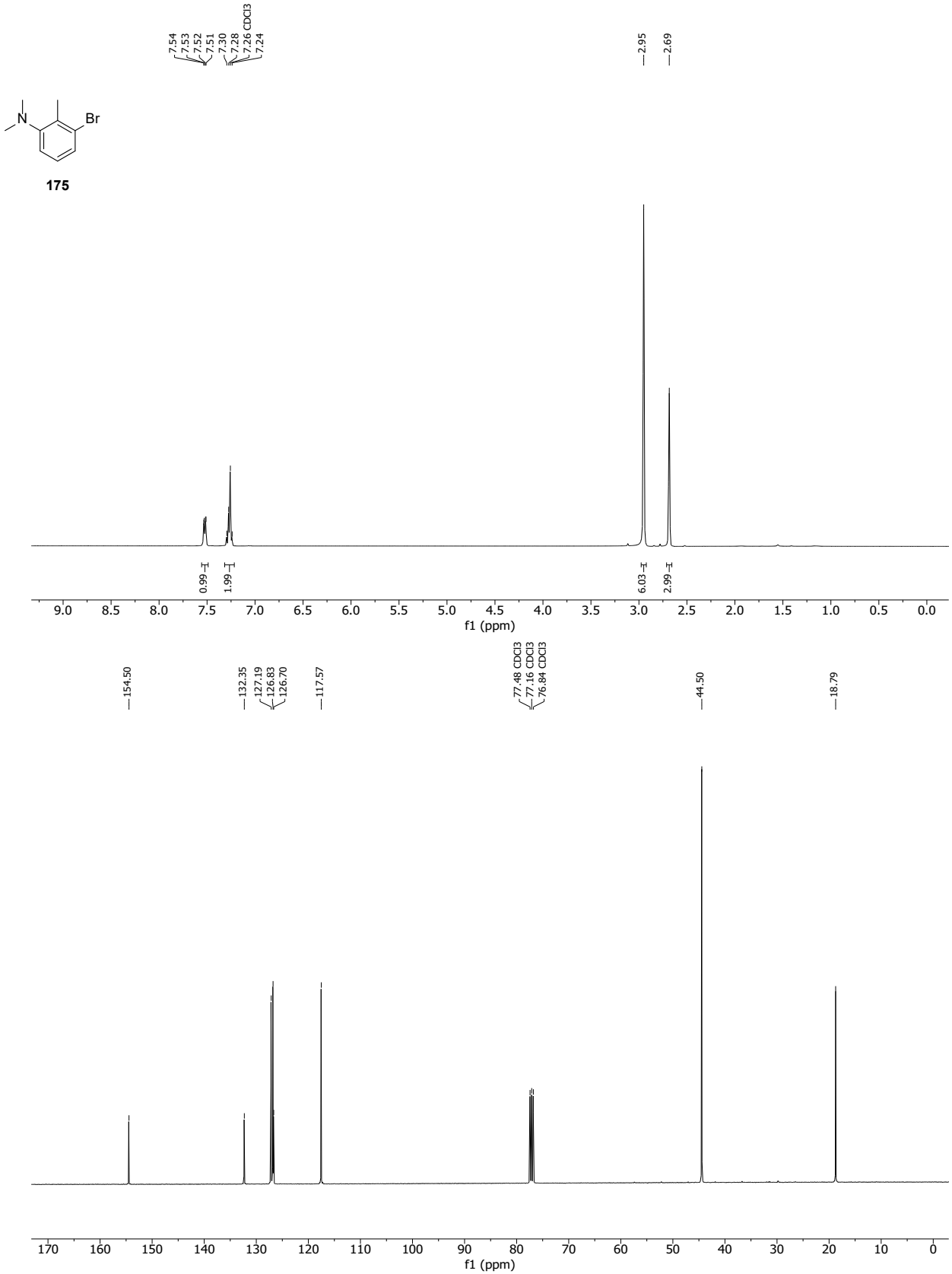
7.54
7.53
7.52
7.51
7.30
7.28
7.26 CDCl3
7.24
2.95
2.69
N
Br
175
0.99
1.99
6.03
2.99
f1 (ppm)
154.50
132.35
127.19
126.83
126.70
117.57
77.48 CDCl3
77.16 CDCl3
76.84 CDCl3
44.50
18.79
f1 (ppm)

176

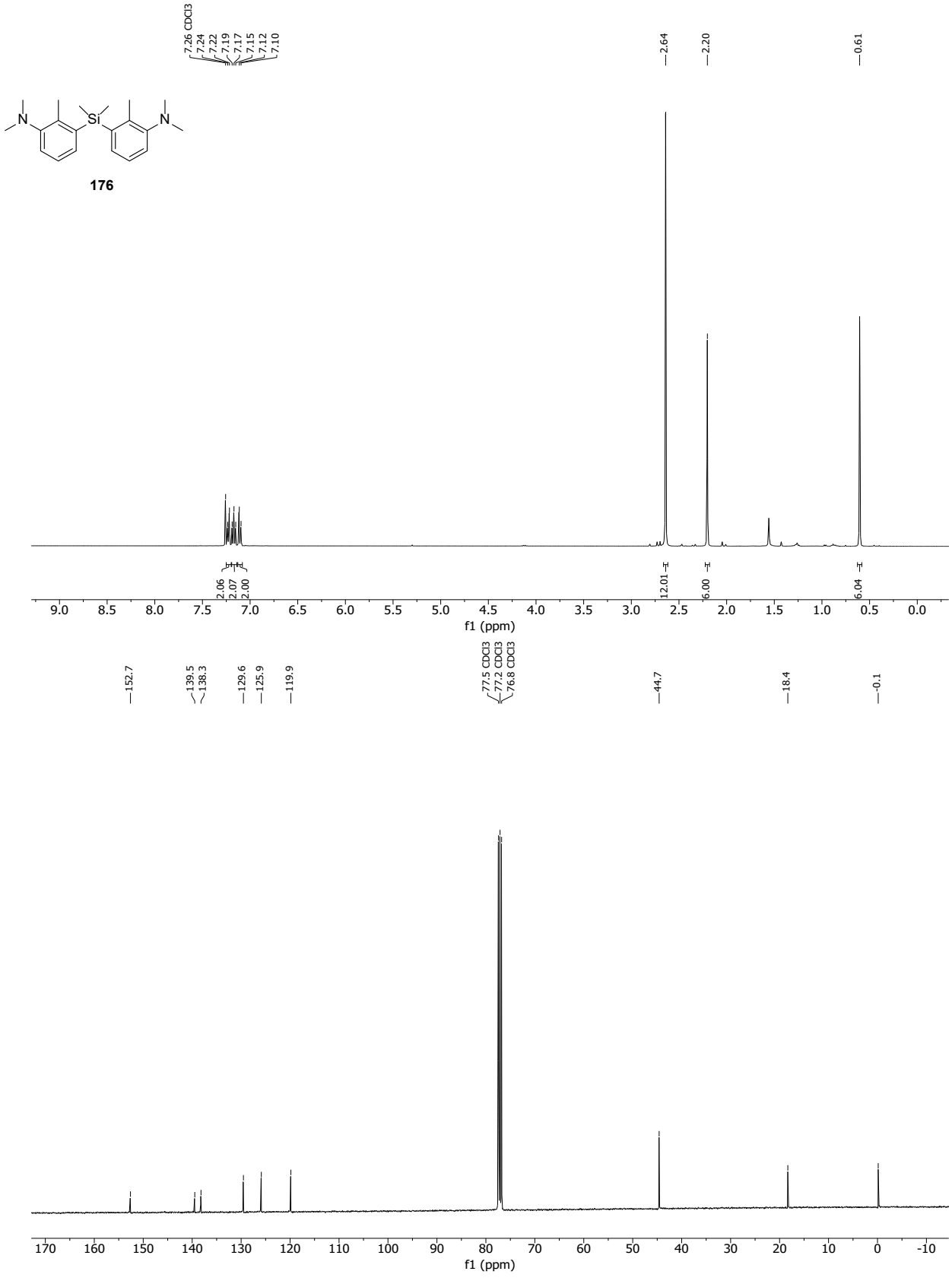
7.26 CDCl3
7.24
7.22
7.19
7.17
7.15
7.12
7.10
2.64
2.20
0.61
N
Si
N
176
2.06
2.07
2.00
12.01
6.00
6.04
f1 (ppm)
152.7
139.5
138.3
129.6
125.9
119.9
77.5 CDCl3
77.2 CDCl3
76.8 CDCl3
44.7
18.4
-0.1
f1 (ppm)

177

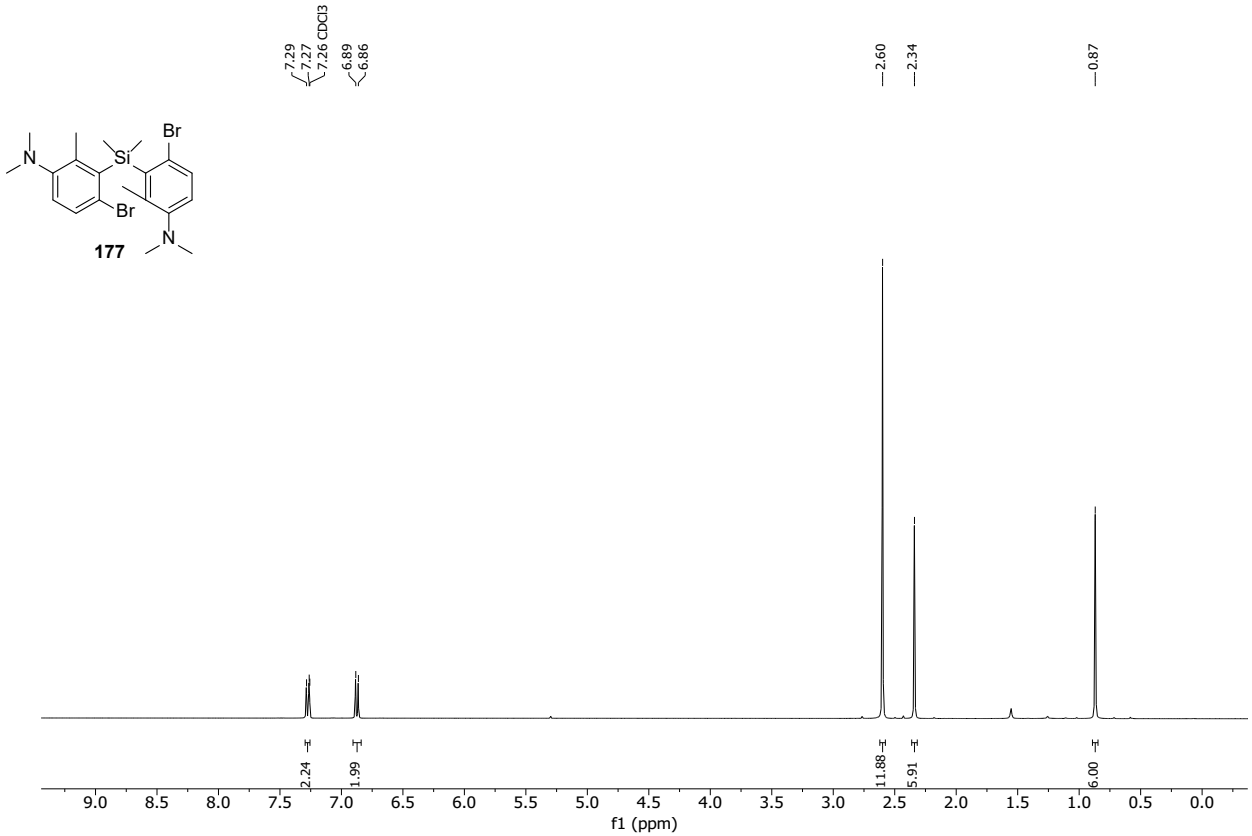
7.29
7.27
7.26 CDCl3
6.89
6.86
2.60
2.34
0.87
Br
N
Si
Br
N
177
2.24
1.99
11.88
5.91
6.00
f1 (ppm)

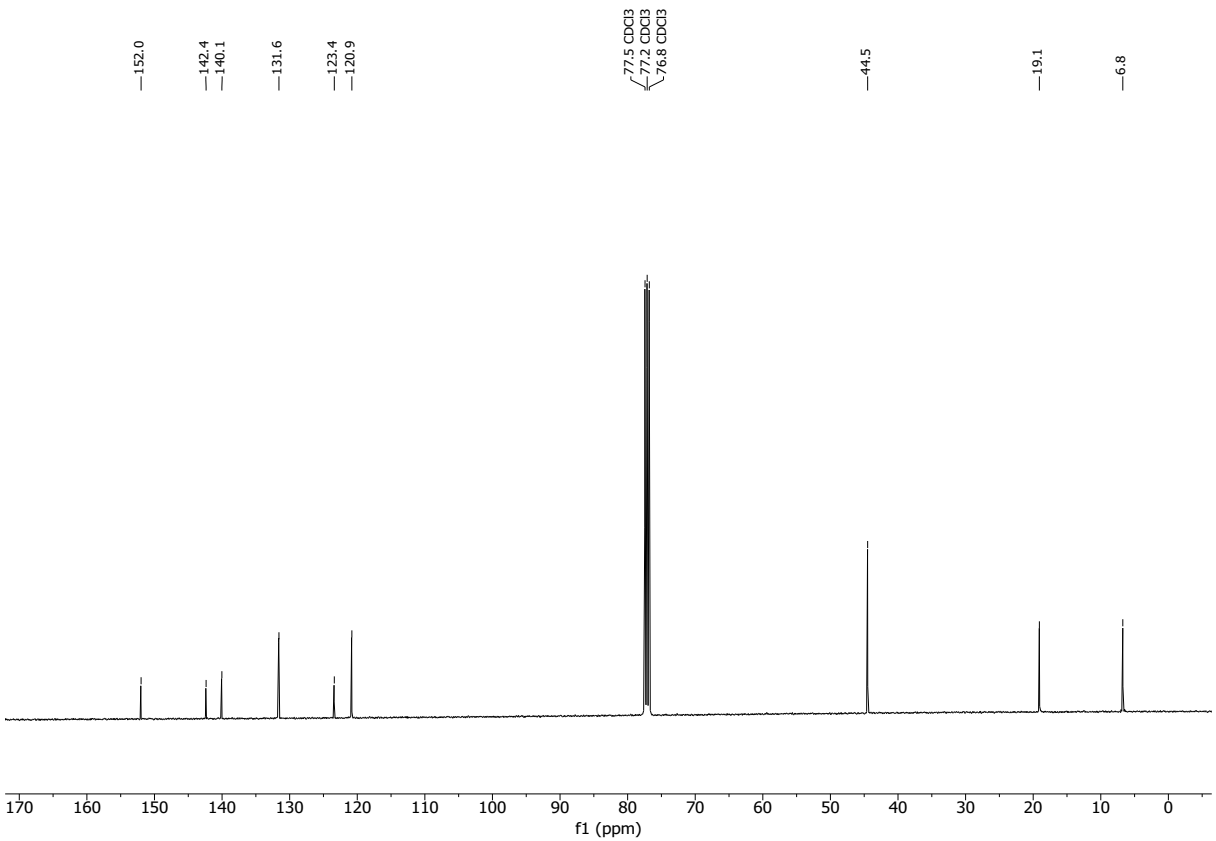
152.0
142.4
140.1
131.6
123.4
120.9
77.5 CDCl3
77.2 CDCl3
76.8 CDCl3
44.5
19.1
6.8
f1 (ppm)

179

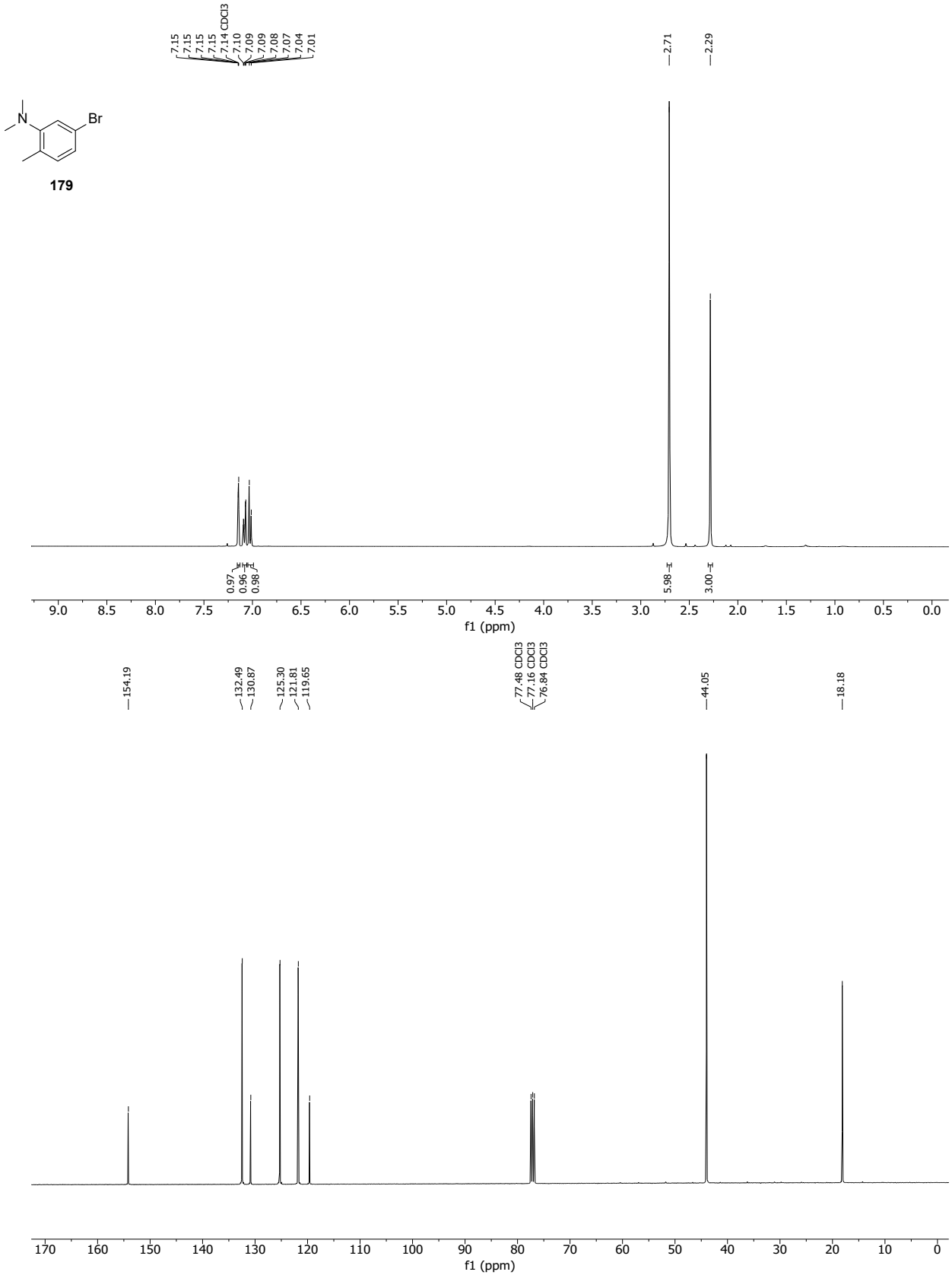
7.15
7.15
7.15
7.15
7.14 CDCl3
7.10
7.09
7.09
7.08
7.07
7.04
7.01
2.71
2.29
N
Br
179
0.97
0.96
0.98
5.98
3.00
f1 (ppm)
154.19
132.49
130.87
125.30
121.81
119.65
77.48 CDCl3
77.16 CDCl3
76.84 CDCl3
44.05
18.18
f1 (ppm)

180

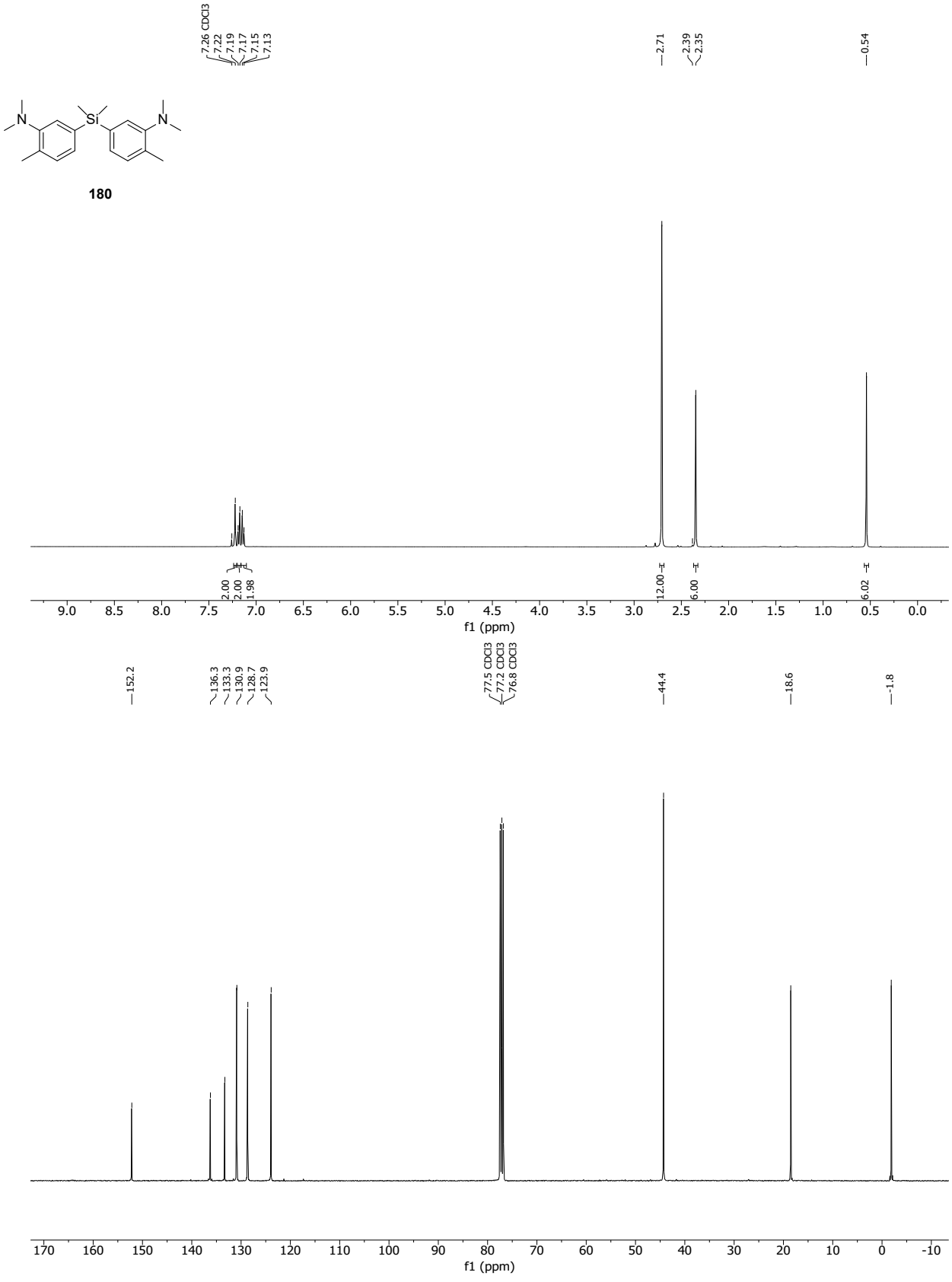
7.26 CDCl3
7.22
7.19
7.17
7.15
7.13
2.71
2.39
2.35
0.54
N
Si
N
180
2.00
2.00
1.98
12.00
6.00
6.02
9.0 8.5 8.0 7.5 7.0 6.5 6.0 5.5 5.0 4.5 4.0 3.5 3.0 2.5 2.0 1.5 1.0 0.5 0.0
f1 (ppm)
152.2
136.3
133.3
130.9
128.7
123.9
77.5 CDCl3
77.2 CDCl3
76.8 CDCl3
44.4
18.6
-1.8
170 160 150 140 130 120 110 100 90 80 70 60 50 40 30 20 10 0 -10
f1 (ppm)

181

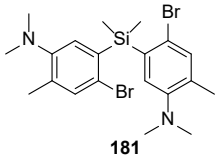
Br
N
Si
Br
N

181

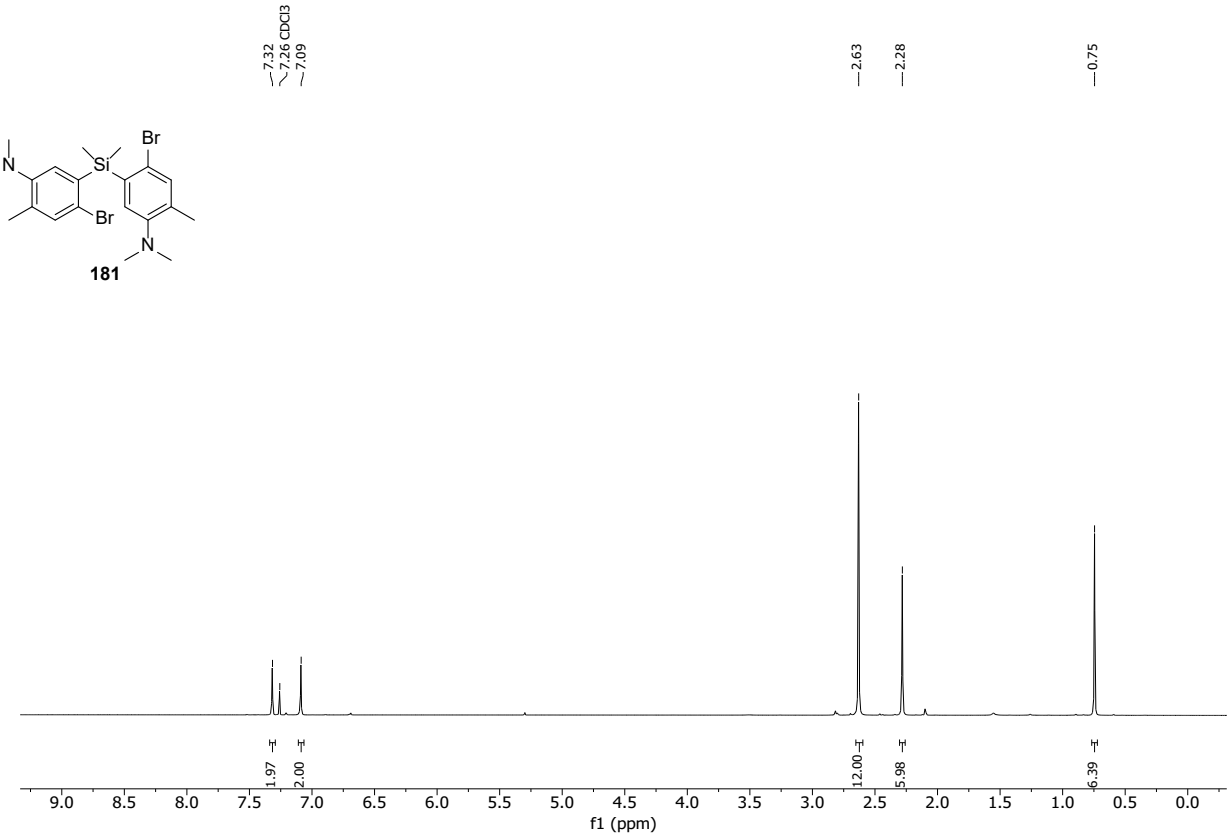
7.32
7.26 CDCl3
7.09
2.63
2.28
0.75
1.97
2.00
12.00
5.98
6.39
f1 (ppm)

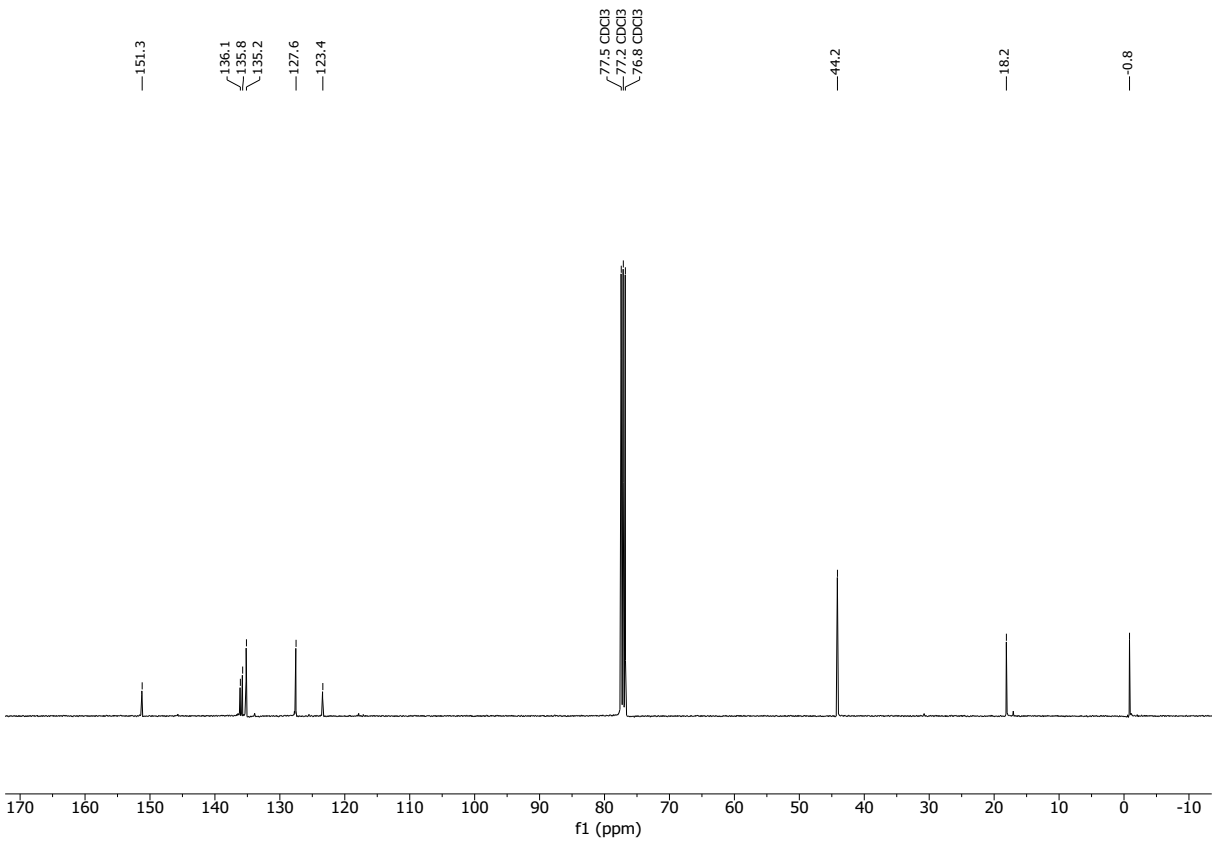
151.3
136.1
135.8
135.2
127.6
123.4
77.5 CDCl3
77.2 CDCl3
76.8 CDCl3
44.2
18.2
-0.8
f1 (ppm)